FACULTY
OF MATHEMATICS
AND PHYSICS
Charles University

DOCTORAL THESIS

Filip Šebesta

Computational Study of Organometallic Interactions with Models of DNA/RNA and Proteins Using Tools of Quantum Chemistry and Molecular Mechanics

Department of Chemical Physics and Optics

Supervisor of the doctoral thesis:
Prof. RNDr. Ing. Jaroslav Burda, DrSc.

Study programme: Physics
Specialization: Biophysics, chemical and macromolecular physics

Prague 2017

I declare that I carried out this doctoral thesis independently, and only with the cited sources, literature and other professional sources.

I understand that my work relates to the rights and obligations under the Act No. 121/2000 Coll., the Copyright Act, as amended, in particular the fact that the Charles University has the right to conclude a license agreement on the use of this work as a school work pursuant to Section 60 paragraph 1 of the Copyright Act.

In…..... date.....

First of all, I would like to thank my family for support during my whole studies. I would like to express my sincere gratitude to my supervisor Prof. Jaroslav Burda for his advices, motivation and patience during my research. My thanks also go to all co-workers on articles.

Title: Computational Study of Organometallic Interactions with Models of DNA/RNA and Proteins Using Tools of Quantum Chemistry and Molecular Mechanics.

Author: Filip Šebesta

Department: Department of Chemical Physics and Optics

Supervisor of the doctoral thesis: Prof. RNDr. Ing. Jaroslav Burda, DrSc., Department of Chemical Physics and Optics

Abstract:

Methods of computational chemistry represent an important tool in development of novel materials or drugs. In this thesis, they are used for investigation of Pt anticancer drugs. Interaction of five hydrated Pt(II) complexes with guanine as a small model of DNA is studied at the DFT level. Several Pt(IV) complexes exhibit less side effects and overcome some resistances of cisplatin, nevertheless they must be reduced to their Pt(II) analogues to obtain anticancer activity due to their high kinetic inertness. Therefore, reduction potentials for eleven Pt(IV) complexes are determined using DFT and post-Hartree-Fock methods. The kinetics of reduction play more important role. Thus, we study reaction mechanisms for reduction of tetraplatin by deoxyguanosine monophosphate and satraplatin by ascorbic acid. In both mechanisms the kinetic model for side reactions is employed since reducing agents occur in different protonation states.

From the perspective of interaction of metals with thymine, proton transfer is of great importance. It is shown that the presence of hydrated metal cations - Mg^{2+}, Zn^{2+}, Hg^{2+} leads to a significant decrease of activation barriers for the N3↔O3 proton transfer. The QM/MM umbrella sampling MD method is employed in a study of binding of the hydrated mercury cation to the N3 position in order to see dynamic effects. The obtained results are compared with DFT calculations. The bonding and Lennard-Jones parameters consistent with General Amber Force Field for all the first row transition metal, Ru, Rh, Pt, and Hg cations are also estimated.

Keywords: DFT, QM/MM MD, platinum, mercury, cancer

Contents

List of Abbreviations

AA	Ascorbic Acid
BCP	Bond Critical Point
CC	Coupled Clusters
CCSD	Coupled Clusters included single and double excitations
CCSD(T)	CCSD with perturbation estimation of triple excitation contribution
CDDP	cisplatin (cis- $Pt(NH_3)_2Cl_2$)
CI	Configuration Interaction
C-PCM	Conductor-like Polarizable Continuum Model
DFT	Density Functional Theory
dGMP	deoxyguanosine monophosphate
DPCM	Dielectric Polarizable Continuum Model
EA	Electron Affinity
EDA	Energy Decomposition Analysis
ETS	Extended Transition State theory
FEP	Free Energy Perturbation
FTIR	Fourier-Transformed Infrared Spectroscopy
GAFF	General Amber Force Field
GD3BJ	D3 version of Grimme's dispersion with Becke-Johnson damping
GGA	General Gradient Approximation
GPK potential	Generalized Phillips-Kleinmann potential
GSH	Glutathione
HEG	Homogeneous Electron Gas
HF	Hartree-Fock
HOMO	Highest Occupied Molecular Orbital
HPLC	High-Performance Liquid Chromatography
IEF-PCM	Integral Equation Formalism variant of PCM
IP	Ionization Potential
JM118	cis,cis-$Pt^{II}(NH_3)(cha)Cl_2$, cha=cyclohexaneamine
JM216	satraplatin, trans,cis,cis-$Pt^{IV}(CH_3COO)_2(NH_3)(cha)Cl_2$
LCAO	Linear Combination of Atomic Orbitals
LDA	Local Density Approximation
LJ	Lennard-Jones
LSDA	Local Spin-Density Approximation

LUMO	Lowest Unoccupied Molecular Orbital
LYP	Lee, Yang, Parr correlation functional
M06-L, M11-L, MN12-L	Local Minnesota MGGA functionals
MD	Molecular Dynamics
MGGA	Meta-GGA
MM	Molecular Mechanics
MP2	second order of MPPT
MPPT	Møller-Plesset Perturbation Theory
NBO	Natural Bonding Orbital
NHO	Natural Hybrid Orbital
NMR	Nuclear Magnetic Resonance
NOCV	Natural Orbitals for Chemical Valence
OP	One-Parameter Progressive Functional
OSET	Outer Sphere Electron Transfer
PAET	Proton-Assisted Electron Transfer
PBE	GGA functional of Perdrew, Burke, Ernzerhof
PCM	Polarizable Continuum Model
PT	Proton Transfer
PW91	Perdew−Wang correlation functional
QTAIM	Quantum Theory of Atoms in Molecules
RC	Reaction Coordinate
REF	Reaction Electronic Flux
RI	Resolution of Identity
SAPT	Symmetry Adapted Perturbation Theory
SCRF	Self Consistent Reaction Field
TPSS	MGGA functional of Tao, Perdrew, Staroverov, and Scuseria
UAHF	United Atom for Hartree-Fock model for cavity construction
UAKS	United Atom for Kohn-Sham model for cavity construction
UI	Umbrella Integration
WHAM	Weighted Histogram Analysis Method
XC	Exchange-Correlation
ZORA	Zero-Order Relativistic Approximation

1 Introduction

Chemistry of transition metal complexes is currently of great importance, as these compounds represent significant artificial catalysts. Transition metals are also present in active centers of enzymes, used as drugs and have many other applications. Their advantage dwells in a possibility to create a lot of spatial arrangements of ligands in well-defined positions and to occur in different spin states as it follows from the ligand field theory. All these properties can be used during synthesis of successful active compounds. Since the related chemical experiments are often quite expensive owing to need of highly purified compounds, many of these experiments are initially carried out *in silico*, which has been enabled by development of computational chemistry. Its real boom is connected with an increase of the computational power of computers in the last thirty years. Today we are able to address systems of millions of atoms using molecular mechanical (MM) simulations based on the classical mechanics obtaining basic information about its structure. Nevertheless, if we want to deal with a study of chemical reactions or we are interested in electronic properties, this approach is not sufficient and quantum chemistry methods must be considered. Even for small systems this problem is too difficult to be solved exactly so that several approximations have been developed in the past. For example, density functional theory (DFT), which scales as $O(N^3)$ with a number of electrons, enables study of thousands of atoms in its roughest form. On the other hand, if one needs to reach chemical accuracy of 1 kcal·mol^{-1}, a more accurate method with higher scaling must be chosen. The golden standard in quantum chemistry is represented by the CCSD(T) method. Nonetheless, it scales as $O(N^7)$. Hence, it is obvious that with increasing accuracy of the quantum mechanical (QM) calculations the size of a system, which can be solved in reasonable time, decreases rapidly. Moreover, an impact of surroundings on the course of a reaction or electronical properties is often non-negligible and must be taken into account as in the case of active centers of enzymes. Fortunately, a whole system has not to be described at the same level of theory and for peripheral regions, a method with lower computational demands can be used. Frequently the molecular mechanical description is sufficient. Such an approach is called hybrid QM/MM technique.

1.1 Pt(II) and Pt(IV) complexes as anticancer drugs

Calculations presented in this thesis are especially focused on interaction of transition metal complexes with small biomolecules, particularly DNA bases, nucleotides or ascorbic acid. A prevailing part is devoted to reduction of Pt(IV) complexes, which represent prospective anticancer ‘pro-drugs’. In fact, several Pt(II)

complexes are currently the only approved drugs among transition metal complexes. For the first time, anticancer activity was observed for cisplatin (CDDP, cis-$Pt(NH_3)_2Cl_2$) when in 1965 prof. Barnett Rosenberg[1] ascertained that this compound prevents cell division of bacteria Escherichia Coli. It lasted next thirteen years until CDDP was approved for medical use.[2] These days, it is used for treatment of a wide spectrum of tumors including bladder, advanced cervical, ovarian, non-small cell lung, testicular cancer and squamous cell carcinoma of head and neck.[3] Success of its activity dwells in appropriate reaction kinetics in living organisms. In fact, it must initially be activated in a two-step hydration process, a substitution of the chloro ligands by water, in order to enable sufficiently rapid course of subsequent reactions. Nevertheless, the rate constant for the reverse process is by approximately one order of magnitude higher[4-6] so the reaction is possible solely in environment with a low concentration of chloride anions. Since their concentration is roughly five times higher in the bloodstream (100 mM) than in the cytoplasm (20 mM), occurrence of the hydrated CDDP in the blood is very low and thus also its reactivity.[7] After its active transfer into a cell via copper transporter CTR1 or pure diffusion through a membrane,[7-9] it becomes less intact and can interact with proteins or other biomolecules. However, the lowest concentration of chlorides is in cellular nuclei (4mM), which favors interaction of CDDP with DNA.

A supposed mechanism of its action represents binding to two adjacent guanine bases forming Pt cross-link. This causes bending of DNA double helix of 20-40 degrees towards the major groove. Precisely, CDDP binds to the nitrogens N7 of guanine bases which are accessible from the major groove.[2] The preference to binding to the guanine bases is given by an appropriate orientation of the dipole moment of this base.[2] Such a bend of double helix prevents transcription and/or replication. As a consequence, formation of the Pt cross-links can lead to apoptosis of the cell. A structural arrangement of the Pt cross-link in the helix was addressed using different computation tools. Investigating cisplatin adducts with DNA oligomers, from dimers to dodecamers, Platts et al.[10,11] concluded that QM/MM calculations are able to provide geometries comparable with structures obtained from NMR experiments. Baik et al.[12] and Eriksson et al.[13] dealt with kinetics of formation of monofunctional and bifunctional adducts with purine bases showing that lower barriers are connected with binding to guanine in both steps – forming Pt-N7 bonds. It is emphasized that an initial stabilization of CDDP plays a crucial role for the reaction rate.[13] The thermodynamic and geometry parameters for CDDP adducts with isolated DNA bases or dinucleotides (d(GpG), d(GpA), d(ApG), d(ApA)) were also studied in our group.[14-16]

Nevertheless, lack of selectivity and many side effects as nephrotoxicity, ototoxicity, neurotoxicity and nausea/vomiting represent serious limitations.[2] In addition, intrinsic or acquired resistance against several tumors was observed.[17] As a

consequence, novel anticancer drugs have been developed. These days, other Pt(II) drugs of the second and third generation, e.g. carboplatin[18,19] and oxaliplatin,[20-22] are clinically approved for treatment of ovarian cancer and adjuvant and metastatic colorectal cancer.[3] A set of currently investigated compounds further involves Au(I) complexes, which are associated with inhibition of the thioredoxin reductase, Ir(III), Ga(III), and As(III) compounds, which increase levels of reactive oxygen species, or multi-targeted Ru(II) complexes.[23] Another group represents octahedral Pt(IV) complexes. Their mechanism of action is more complex in comparison with Pt(II) complexes due to their high kinetic inertness. This means that a substitution of ligands occurs very slowly. On the other hand, this property can be used for fine-tuning of these prospective anticancer drugs.

The study of Raynaud et al.[24] showed that square planar Pt(II) complex JM118 (cis,cis-$Pt^{II}(NH_3)(cha)Cl_2$, cha=cyclohexaneamine) represents the most abundant Pt compound after incubation of satraplatin (JM216, trans,cis,cis-$Pt^{IV}(CH_3COO)_2(NH_3)(cha)Cl_2$) in patients' plasma filtrates. In fact, based on the DFT calculations the hydration of JM216 passes via a direct S_N2 mechanism with a very low probability since the corresponding barriers are more than 32 $kcal \cdot mol^{-1}$ high.[25] Hence, it is generally assumed that Pt(IV) 'pro-drugs' must initially be reduced to their Pt(II) analogues and subsequently the mechanism of action of Pt(II) complexes can proceed. Reduction of Pt(IV) complexes is accompanied by a release of two (axial) ligands.[23,26,27] Therefore, the fine-tuning of Pt(IV) 'pro-drugs' particularly occurs via their axial ligands.[28-30]

Reduction potentials have experimentally been determined for miscellaneous prospective Pt(IV) pro-drugs using cyclic voltammetry.[31-34] For cisplatin derivatives the redox potentials were also determined by Baik et al.[35] using combined experimental and computational approach when the two-electron uptake was considered to be a two-step process. It was concluded that a decisive factor for the value of the reduction potential represents acceptance of the first electron. Simultaneously, an increasing magnitude of redox potentials of Pt(IV) compounds in order complexes possessed hydroxo, acetato, and chloro axial ligands follows from experimental measurements.[33] As to reduction mechanisms of Pt(IV) complexes, a situation is more complicated since it is not known which reducing agents are responsible for this process in living organisms. There are only several indications coming from experiments. A higher reduction rate is associated with higher concentrations of glutathione (GSH, γ-L-glutamyl-L-cysteinylglycine) in cancer cell lines.[23] Lemma et al.[36] showed in another study that JM216 can be reduced by ascorbic acid (AA). However, the pertinent pseudo-first-order rate constant is relatively strongly dependent on its concentration. Thus, there is a question whether its common concentration in cells is sufficient to ensure a satisfactory reaction rate.

Based on *in vitro* experimental measurements (NMR, HPCL, FTIR), a reduction mechanism for tetraplatin ($PtCl_4$(dach), dach = diaminocyclohexane) in the presence of deoxyguanosine monophosphate (dGMP) was proposed by Choi et al.[37-39] The reaction starts with a substitution of one of chloro ligands by dGMP. The corresponding decrease in concentration of tetraplatin is described by a sigmoidal curve in experiments,[40] which indicates that the substitution is autocatalyzed. Therefore, a so-called Basolo-Pearson[41] mechanism is assumed. In the next step, a nucleophilic attack of the 5'-hydroxo (3'-dGMP) or 5'-phosphate (5'-dGMP) group to the C8 position occurs. Subsequently, the axial ligands are released simultaneously with reduction of the platinum complex. The reaction is completed by a hydrolysis of the chelate structure of oxidized dGMP leading to the final 8-oxo-dGMP product. It should be remembered that Basolo-Pearson mechanism the is only applicable for complexes with Cl or similarly small axial ligands.[38]

Despite relatively fast reduction, tetraplatin has not recently been considered as prospective anticancer drug since it exhibits ten times higher neurotoxicity than cisplatin.[42] On the other hand, for satraplatin no neurotoxicity, nephrotoxicity, and ototoxicity have been observed.[43] Nevertheless, its effectivity was not confirmed in Phase II and Phase III clinical trials where its activity against small-cell lung, castrate resistant prostate and ovarian cancer, and squamous cancer of the cervix and was investigated. Due to its mild side effects, it has recently been involved in Phase I clinical trials on children with refractory solid tumors.[44]

1.2 Interaction of the hydrated Hg^{2+} cation with thymine

Within this thesis, the interaction of the hydrated Hg^{2+} cation with thymine is also explored. At first, an impact of the presence of the Hg^{2+} cation on the rate of the N3↔O2 proton transfer is discussed and compared with an influence of the hydrated Mg^{2+} and Zn^{2+} cations. In fact, spontaneous mutations associated with proton transfers in DNA structure can lead to important health disorders as cancer. Therefore, such protons transfers and rare forms of DNA bases have been investigated since Löwdin's study in 1963.[45] Although experimental examination of the rare forms of bases in DNA double helix is difficult, there is also a structural evidence for their occurrence.[46] On the other hand, proton transfers in Watson-Crick base pairs have been broadly investigated using computation tools,[47-50] when also changes of the electronic chemical potential along the reaction coordinate have been analysed.[51] Stability of binding sites of almost all keto/enol forms of adenosine (A), guanine (G), cytosine (C), and thymine (T) for biologically relevant Na^+, Mg^{2+}, and Zn^{2+} cations were scrutinized by Kabeláč[52] at the RI-MP2/TZVPP level showing that a rare enol form of thymine provides better stabilization than the canonical form.

Thus, proton transfers play a crucial role in binding of metals to DNA bases, particularly during formation of metal bridged mismatches.[53] The occurence of such strusctures has been confirmed experimentally.[54,55] In 2007, an evidence of formation of T(N3)-Hg(II)-T(N3) linkages was provided based on ^{15}N NMR chemical shifts and ^{15}N-^{15}N J couplings.[55] The first crystal structure of such consecutive mercury linkages was published for the DNA dodecamer d(CGCGATTTCGCG) with T:T mismatches seven years later.[56] Using the isothermal titration calorimetry, the reaction Gibbs free energy of -8 kcal·mol^{-1} associated with formation of the T(N3)-Hg(II)-T(N3) linkage was obtained.[57] This result is in accord with the calculated value by Yamaguchi et al.[58] at the ONIOM QM/QM level for a DNA trimer model. A detailed reaction mechanism was proposed by Šebera et al.[53] where the corresponding energy profile was determined at the ONIOM B3LYP/BP86 level for the same models with the $[Hg(H_2O)_4OH]^+$ cluster. In the beginning of the reaction, the $[Hg(H_2O)_4OH]^+$ cluster is located in the major groove in the proximity of the T:T mismatch.

Since DNA with T:T mismatches is an efficient target for Hg(II) cations, it could be used for detection of mercury pollution in environment. In addition, several metal cations can be kept between consecutive pyrimidine:pyrimidine mismatches,[56,59] which leads to an idea that such a material can be considered for construction of electric nano-devices.

Here, we only concentrate on binding of the hydrated Hg^{2+} cation to the isolated thymine from a dynamical perspective as the N3↔OH proton transfer plays an important role within this reaction. For this purpose, the QM/MM MD technique is employed.

Necessity of the QM/MM approach for metal complexes simulations motivated us to estimate molecular mechanical (MM) parameters for transition metal cations. We determined bonding parameters as well as Lennard-Jones parameters, which are of the main interest from the viewpoint of the QM/MM method. The parameters are obtained on the basis of QM potential energy surface scans for small model complexes and are estimated for all first row transition metals and ruthenium, rhodium, platinum and mercury.

2 Theory

The description of used methods for determination of atomic structures and molecular mechanisms is presented for deeper understanding of obtained results. They are arranged from the simplest methods to more advanced ones, i.e. from molecular mechanics passing the quantum chemistry methods to the hybrid QM/MM technique. In the frame of QM methods also basics of different analyses of the electron density distribution are presented and a special subchapter is devoted to calculations of free energies. Since studied reactions occur in water solutions, an implicit solvation model is included into QM calculations therefore its basics are briefly discussed, too.

2.1 Molecular mechanics

In this approach, atoms are treated as charged spheres further characterized by their mass and polarizability. The total potential energy E is described by empirical potentials. In our case, the expression for the bonding energy consists of harmonic terms for bond lengths and bond angles and a periodic potential for description of torsion angles

$$E_{bonding} = \sum_{i}^{N_{bonds}} \frac{k_i^b}{2}(r_i - r_i^0)^2 + \sum_{i}^{N_{angles}} \frac{k_i^a}{2}(\phi_i - \phi_i^0)^2 + \sum_{i}^{N_{torsions}} k_i^t \left(1 + \cos\left(n_i\omega_i - \omega_i^0\right)\right). \quad (1)$$

The summations are taken over all bonds, bond angles, and dihedral angles present in a system. The k_i^b, k_i^a, and k_i^t denote pertinent force constants which are part of empirical force fields together with the equilibrium distances r_i^0 and angles φ_i^0 and ω_i^0.

The second part of total potential energy, non-bonding contribution, concerns atoms which are separated by more than three bonds or are not part of the same molecule. It consists of the classical Coulomb electrostatic term and van der Waals interaction represented by Lennard-Jones potential[60]

$$E_{non-bonding} = \frac{1}{2}\sum_{i,j}^{N} \frac{1}{4\pi\varepsilon_0}\frac{q_i q_j}{r_{ij}} + \frac{1}{2}\sum_{i,j}^{N} \varepsilon_{ij}\left[\left(\frac{r_{ij}^0}{r_{ij}}\right)^{12} - 2\left(\frac{r_{ij}^0}{r_{ij}}\right)^{6}\right], \quad (2)$$

where q_i stands for atomic charges and r_{ij} denotes the distance between atoms.

2.2 Molecular dynamics

Within MM framework, time development of a molecular system is described using Hamilton canonical equations of classical mechanics, which leads to the well-known equations of motion

$$\dot{\boldsymbol{r}} = \frac{\boldsymbol{p}}{m}, \qquad \dot{\boldsymbol{p}} = \boldsymbol{F}, \qquad \boldsymbol{F} = -\nabla E \tag{3}$$

Integrating them and discretizing the time, the propagators for development of a system can be obtained. A broadly used propagator with relatively high numerical stability is represented by Velocity Verlet algorithm[61,62] according which positions of atoms in the next step are determined as

$$\begin{aligned} \boldsymbol{r}(t+\Delta t) &= \boldsymbol{r}(t) + \boldsymbol{v}(t)\Delta t + \frac{1}{2}\boldsymbol{a}(t)(\Delta t)^2, \\ \boldsymbol{v}(t) &= \boldsymbol{v}(t-\Delta t) + \frac{1}{2}\big(\boldsymbol{a}(t-\Delta t) + \boldsymbol{a}(t)\big)\Delta t, \\ m\boldsymbol{a}(t) &= -\nabla\big(E(t)\big). \end{aligned} \tag{4}$$

The global error for this propagator is $O(\Delta t^3)$ in the positions and $O(\Delta t^2)$ in the velocities.

When only such propagators are used, the total energy is conserved and the system represents a microcanonical ensemble. Nevertheless, simulations of real systems must frequently be performed at given temperature T and pressure p to obtain physically plausible data. The temperature of a considered system in molecular dynamics (MD) is determined on the basis of the equipartition theorem

$$\frac{N_f}{2} k_b T = \langle \sum_i \frac{1}{2} m_i {v_i}^2 \rangle \tag{5}$$

where N_f stands for a number of degrees of freedom and k_b is Boltzmann constant. To keep temperature at a given average value, velocities of atoms must be scaled in the course of simulations or extra terms must be added to a considered Hamiltonian. Within Berendsen thermostat[63] the change in temperature is proportional to the difference between the current and final temperature. The scaling factor λ for velocities follows from this approximation:

$$\lambda = \left[1 + \frac{\Delta t}{\tau}\left(\frac{T_0}{T} - 1\right)\right]^{1/2}. \tag{6}$$

Nevertheless, this scaling perturbs the canonical distribution and hence it is especially used for equilibration of systems.

2.3 QM methods

In quantum chemistry, molecules are considered as a system of electrons and nuclei, which is most often described using the non-relativistic time-independent Schrödinger equation with Hamiltonian

$$\hat{H} = -\sum_{A}^{N}\frac{\Delta_A}{2M_A} - \sum_{i}^{n}\frac{\Delta_i}{2} - \sum_{A}^{N}\sum_{i}^{n}\frac{Z_A}{r_{iA}} + \frac{1}{2}\sum_{i}^{n}\sum_{j}^{n}\frac{1}{r_{ij}} + \frac{1}{2}\sum_{A}^{N}\sum_{B}^{N}\frac{Z_A Z_B}{R_{AB}} \qquad (7)$$

The nuclei are denoted using large letters A, B and electrons using small letters i, j. The equation (7) is presented in the atomic units, where reduced Planck constant $\hbar$, mass of electron m_e, elementary charge e and Coulomb constant $1/(4\pi\varepsilon_0)$ are equal to unit by definition. These units will be used in a majority of following equations. To facilitate solution of the considered Schrödinger equation with Hamiltonian (7), Born-Oppenheimer approximation is adopted.[64]

When stationary points on the potential energy surface (PES) are searched in QM calculations, only the electronical problem given by Hamiltonian

$$\hat{H}_e = -\sum_{i}^{n}\frac{\Delta_i}{2} - \sum_{A}^{N}\sum_{i}^{n}\frac{Z_A}{r_{iA}} + \frac{1}{2}\sum_{i}^{n}\sum_{j\neq i}^{n}\frac{1}{r_{ij}} + \frac{1}{2}\sum_{A}^{N}\sum_{B\neq A}^{N}\frac{Z_A Z_B}{R_{AB}} \qquad (8)$$

is solved and subsequently positions of nuclei are shifted based on the calculated energy gradient. Corresponding molecular forces $\boldsymbol{F_A}$ are determined according to expression

$$\begin{aligned}\boldsymbol{F_A} = -\frac{\partial E_e}{\partial \boldsymbol{R_A}} = &-\left\langle \varphi \middle| Z_A\left(\sum_{i}^{n}\frac{\boldsymbol{r}_i - \boldsymbol{R}_A}{|\boldsymbol{r}_i - \boldsymbol{R}_A|^3} - Z_B\sum_{B\neq A}^{N}\frac{\boldsymbol{R}_B - \boldsymbol{R}_A}{|\boldsymbol{R}_B - \boldsymbol{R}_A|^3}\right)\middle|\varphi\right\rangle \\ &- 2\left\langle \frac{\partial\varphi}{\partial \boldsymbol{R}_A}\middle|\hat{H}_e\middle|\varphi\right\rangle .\end{aligned} \qquad (9)$$

The first term represents Hellmann-Feynman force[65] and the second term is so-called Pulay's correction,[66] which is connected with incompleteness of the basis set. If the accurate wave function was known this term would disappear. Then positions of the nuclei are developed using one of optimization algorithms as steepest descent,[67] conjugate gradients[68,69] or quasi Newton methods.[67]

2.4 Electronic wave function

The system with more electrons must be described by many body wave function which can be considered as a product of one-electron wave functions. Nevertheless, it is neccessary to require antisymmetry of the total electronic wave function. This can be satisfied in the easiest way by Slater determinant

$$\Theta(x_1, x_2, \dots, x_N) = \frac{1}{\sqrt{N!}} \sum_{\pi \in P} sgn(\pi) \pi \left\{ \psi_1(\boldsymbol{x_1}) \chi_1(\sigma_{z_1}) \dots \psi_N(\boldsymbol{x_N}) \chi_N(\sigma_{z_N}) \right\}. \quad (10)$$

The summation is taken over all permutations π of electrons and $\psi_i(\boldsymbol{x})$ denotes the spatial part and $\chi_i(\sigma_z)$ the spin part of the one-electron spin-orbitals $\varphi_i(\boldsymbol{x})$. It is also appropriate to require orthonormality of one-electron molecular orbitals i.e. their overlap matrix *S* is the identity matrix

$$S_{ij} = \int \psi_i^*(\boldsymbol{x}) \psi_j(\boldsymbol{x}) d\boldsymbol{x} = \delta_{ij} \quad (11)$$

Commonly, the molecular orbitals are considered as linear combination of atomic orbitals Φ_μ (LCAO approach) located on individual atoms i.e.

$$\psi_i = \sum_{\mu}^{N_B} c_{\mu i} \Phi_\mu \,, \quad (12)$$

where $c_{\mu i}$ represent expansion coefficients.

The atomic orbital Φ_μ can be described by Slater-type orbitals (generalized hydrogen functions). Their radial part is defined as

$$R(r) = N r^{n-1} e^{-\zeta r} \,, \quad (13)$$

where *n* represents the principal quantum number and *N* normalization constant. Factor ζ is related to an extent of shielding of the nuclear charge by other electrons. The angular part is given by spherical harmonics. The second choice represents Gaussian-type orbitals. However, these orbitals exhibit incorrect behavior since their decrease towards infinity is too rapid and they do not have a cusp at the position of nucleus. From this reason, the atomic orbitals are not described by one gaussian function, but rather by a contracted Gaussian basis function i.e. linear combination of Gaussian functions with constant coefficients c_i

$$R^{GTO}(r) = \sum_{i=1}^{N} c_i e^{-\alpha_i r^2} \,, \quad (14)$$

where *N* typically ranges between three and six. The angular part, in this case, is considered as a product of cartesian functions, for example *yz* for d_{yz} orbital. Except atomic orbitals which are occupied in isolated atoms (concept of the minimal basis set), other basis functions are added to increase flexibility of a given basis set. It can be difusse or polarization[70] functions. The former are basis functions whose angular moment is not greater than the highest angular moment in the minimal basis set; however, the exponential factor is small which ensures a more diffuse character of the basis set. These functions are particularly important in description of anionic and excited states. In the case of polarization functions, basis functions with higher angular moment than in the minimal basis set are added, which enables better adaptation of molecular orbitals along chemical bonds.

2.5 Electronic problem

When the Slater determinant is substituted into the expression for the electronic energy $E_e = \langle \Theta | H_e | \Theta \rangle$ with electronic Hamiltonian H_e from equation (8), only several terms survive due to considered orthonormality of the molecular spin-orbitals φ$_i$ ($\varphi_i = \psi_i \chi_i$)

$$\begin{aligned} E_e = \sum_i^n \int \varphi_i^*(\tau) \hat{H}^{core} \varphi_i(\tau) d\tau \\ + \frac{1}{2} \sum_{j \neq i}^n \left(\int \varphi_i^*(\tau_1) \varphi_j^*(\tau_2) \frac{1}{r_{ij}} \varphi_i(\tau_1) \varphi_j(\tau_2) d\tau_1 d\tau_2 \right. \\ \left. - \int \varphi_i^*(\tau_1) \varphi_j^*(\tau_2) \frac{1}{r_{ij}} \varphi_j(\tau_1) \varphi_i(\tau_2) d\tau_1 d\tau_2 \right) \\ \hat{H}^{core} = -\frac{\Delta_i}{2} - \sum_A^N \frac{Z_A}{r_{iA}} . \end{aligned} \tag{15}$$

Spin-orbitals corresponding to the ground state of a molecule can subsequently be obtained using Ritz-Rayleigh variational principle along with a condition on preservation of orthonormality of spin-orbitals, which is applied using the Lagrange multipliers ε_{ij}. This approach leads to the well-known Hartree-Fock (HF) equations[71]

$$\left(\hat{H}_i^{core} + \sum_{j \neq i}^n \hat{J}_{ij} - \hat{K}_{ij} \right) \varphi_i(\tau_1) = \hat{f}_i \varphi_i(\tau_1) = \varepsilon_i \varphi_i(\tau_1) , \tag{16}$$

where the coulombic and exchange terms are given by

$$\begin{aligned} \hat{J}_{ij} \varphi_i(\tau_1) = \int \varphi_j^*(\tau_2) \frac{1}{r_{ij}} \varphi_j(\tau_2) d\tau_2 \varphi_i(\tau_1) , \\ \hat{K}_{ij} \varphi_i(\tau_1) = \int \varphi_j^*(\tau_2) \frac{1}{r_{ij}} \varphi_i(\tau_2) d\tau_2 \varphi_j(\tau_1) . \end{aligned} \tag{17}$$

The left side of equation (16) is called Fock operator f_i.

Let‘s initially consider a closed-shell system with an even number of electrons. Then, if the LCAO expansion of molecular orbitals (12) is substituted into the relation (16) for the electronic energy, we obtained

$$\sum_\nu \left[\langle \mu | \hat{H}^{core} | \nu \rangle + \sum_{\lambda,\sigma} P_{\lambda\sigma} \left(\langle \mu\lambda | \nu\sigma \rangle - \frac{1}{2} \langle \mu\lambda | \sigma\nu \rangle \right) \right] c_{\nu i} = \varepsilon_i \sum_\nu S_{\mu\nu} c_{\nu i} . \tag{18}$$

This relation is reffered to as Roothaan-Hall equations,[72] where $S_{\mu\nu}$ is the overlap matrix between atomic orbitals. Density matrix $P_{\lambda\sigma}$ is defined as

$$P_{\lambda\sigma} = 2\sum_{j}^{N/2} c_{\lambda j} c_{\sigma j}^{*} \tag{19}$$

and two-electron integrals are given by the relation

$$\langle \mu\lambda|\nu\sigma\rangle = \int \Phi_{\mu}^{*}(\boldsymbol{x}_1)\Phi_{\lambda}^{*}(\boldsymbol{x}_2)\frac{1}{r_{ij}}\Phi_{\nu}(\boldsymbol{x}_1)\Phi_{\sigma}(\boldsymbol{x}_2)d\boldsymbol{x}_1 d\boldsymbol{x}_2 \tag{20}$$

Equation (18) can also be rewritten in the matrix form $\boldsymbol{FC} = \boldsymbol{ESC}$, which represents a generalized eigenvalue problem with Fock matrix **F.** It can be transformed to a standard eigenvalue problem by the symmetrical or canonical transformation. Pertinent transformation matrices are $\mathbf{X}=\mathbf{S}^{-1/2}$ and $\mathbf{X}=\mathbf{U}\mathbf{s}^{-1/2}$,[71] respectively, where **U** is a unitary matrix that makes the overlap matrix diagonal and **s** represents the vector of eigenvalues of the overlap matrix. This integro-differential equations are solved in a self-consistent manner since Fock matrix depends on the expansion coefficients $c_{\mu i}$.

If the differences of the density matrix elements $P_{\mu\nu}$ and the change in the total energy

$$E = \frac{1}{2}\left(\sum_{i}^{occ}\varepsilon_i + \sum_{\mu\nu} P_{\mu\nu}H_{\mu\nu}\right) \tag{21}$$

$\left(\text{where } H_{\mu\nu} = \langle\mu|H^{core}|\nu\rangle\right)$ between the previous and current step are sufficiently small, the last expansion coefficients and electronic energy is considered as the result. If not, new Fock matrix is built and equations (18) are solved again. The procedure is repeated unless converegence criteria are fulfilled.

In the case of open shell systems, the equations (18) are split into two sets of Pople-Nesbet equations[73]

$$\sum_{\nu}\left[H_{\mu\nu} + \sum_{\lambda,\sigma} P_{\lambda\sigma}\langle\mu\lambda|\nu\sigma\rangle - P_{\lambda\sigma}^{\tau}\langle\mu\lambda|\sigma\nu\rangle\right]c_{\nu i}^{\tau} = \varepsilon_i^{\tau}\sum_{\nu} S_{\mu\nu}c_{\nu i}^{\tau}\ , \qquad \tau \in \alpha,\beta \tag{22}$$

for electrons with α and β spins which are coupled together via the density matrix $P_{\lambda\sigma}$. The density matrices for electrons with α and β spins are defined as

$$P_{\lambda\sigma}^{\alpha} = \sum_{j}^{N_\alpha} c_{\lambda j}^{\alpha}\left(c_{\sigma j}^{\alpha}\right)^{*}\ , \qquad P_{\lambda\sigma}^{\beta} = \sum_{j}^{N_\beta} c_{\lambda j}^{\beta}\left(c_{\sigma j}^{\beta}\right)^{*}\ , \qquad P_{\lambda\sigma} = P_{\lambda\sigma}^{\alpha} + P_{\lambda\sigma}^{\beta}\,. \tag{23}$$

2.6 Post-Hartree-Fock methods

In the above mentioned equations, correlation between electrons with (predominantly) opposite spin is not included. The pertinent correlation energy E_{corr} for post-Hartree-Fock (post-HF)[71] methods is defined as

$$E_{corr} = E_{exact} - E_{HF}\,. \tag{24}$$

Here, only two of these methods will be mentioned: Møller-Plesset perturbation theory (MPPT)[74] and the coupled cluster (CC) method.[75] In MPPT the energy up to the first order correction is equal to the total energy obtained at the HF level. Therefore, the first contribution to the total energy beyond the HF method represents the second order term

$$E_0^{(2)} = \sum_{n\neq 0} \frac{\left|\left\langle \psi_0^{(0)} \middle| \hat{V} \middle| \psi_n^{(0)} \right\rangle\right|^2}{E_0^{(0)} - E_n^{(0)}} = \frac{1}{4} \sum_{a,b,r,s} \frac{|\langle ab \| rs \rangle|^2}{\varepsilon_a + \varepsilon_b - \varepsilon_r - \varepsilon_s}, \tag{25}$$

$$\langle ij \| kl \rangle = \langle ij | kl \rangle - \langle ij | lk \rangle.$$

In this equation, indices *a* and *b* label occupied molecular spin-orbitals and *r* and *s* virtual molecular spin-orbitals determined at the HF level. It can also be stated that from higher states $\psi_n^{(0)}$, only double excitations contribute to the second order correction, since a contribution from single excitations is zero on the basis of Brillouin's theorem and from the Slater-Condon rules it follows that expressions including triple and higher excitations are also equal to zero. Since MPPT is not variational and the second order correction is always negative for the ground state, the total energy at the MP2 level can be lower than the exact energy. Nevertheless, in comparison with the truncated CI (configuration interaction) methods, MPPT is size consistent in each order.

The CC method[75,76] is also not variational, but it is size consistent and provides a large portion of the correlation energy in relatively low computational time. The wave funcion is given by the exponential ansatz

$$|\Phi_{CC}\rangle = e^{\hat{T}} |\Phi_{HF}\rangle\,, \tag{26}$$

where Φ_{HF} represents HF wave function in the form of Slater determinant. $\hat{T}$ is a cluster operator, which is defined as a sum of single $\hat{\tau}_1$, double $\hat{\tau}_2$ and higher-excitation operators i.e. $\hat{T} = \sum_\mu \hat{T}_\mu = \sum_\mu t_\mu \hat{\tau}_\mu$ with amplitudes t_μ. If the cluster operator includes all possible excitations operators then the CC wave function corresponds to the full CI wave function, since the full CI wave function can be written in the product form

$$|\Phi_{CC}\rangle = \prod_\mu \left(1 + t_\mu \hat{\tau}_\mu\right) |\Phi_{HF}\rangle\,, \tag{27}$$

where μ denotes all possible excitations in the system. Nevertheless, the lower excitations contribute more to the total correlation energy, so the complete cluster operator can be truncated in the way that contains only single and double excitation operators (CCSD method).

A variational solution of the CC method is ineffective and a projective method is rather used

$$\langle \Phi_{HF}|\bar{H}|\Phi_{HF}\rangle = E\,, \\ \langle \mu|\bar{H}|\Phi_{HF}\rangle = 0 \tag{28}$$

Introducing the similarity-transformed Hamiltonian $\bar{H}$

$$e^{-\hat{T}}\hat{H}e^{\hat{T}}|\Phi_{HF}\rangle = \bar{H}|\Phi_{HF}\rangle = E|\Phi_{HF}\rangle\,. \tag{29}$$

Here μ denotes the excitation (single, double, etc.). An advantage of this approach dwells in the fact that the expansion can be truncated easily for example

$$\hat{T} = \hat{T}_1 + \hat{T}_2\ . \tag{30}$$

Further, it is appropriate to make use of the Baker-Campbell-Hausdorff expansion of the similarity-transformed Hamiltonian $\bar{H}$

$$e^{-\hat{T}}\hat{H}e^{\hat{T}} = \hat{H} + \left[\hat{H},\hat{T}\right] + \frac{1}{2!}\left[\left[\hat{H},\hat{T}\right],\hat{T}\right] + \frac{1}{3!}\left[\left[\left[\hat{H},\hat{T}\right],\hat{T}\right],\hat{T}\right] + \cdots. \tag{31}$$

Since Hamiltonian includes just one- and two-electron operators, only several terms from the expansion survives. Since the resulting equations are non-linear in amplitudes t_μ, they are frequently solved using quasi-Newton methods.[76]

2.7 Density functional theory

Since the inclusion of the correlation energy at the post-HF level is relatively time demanding for larger systems, the density functional theory (DFT) represents a more effective method. Within this method the correlation energy is approximated using a correlation functional of the electron density. This approach is based on the two Hohenberg-Kohn (H-K) theorems[77]when the first one states that the external potential v_{ext} is uniquely determined by the electron density ρ and vice versa. The second H-K theorem says that a universal energy functional of the electronic density F[ρ] exists so that the total energy is just minimized for the ground state electron density ρ_0 in the space of v-representable densities

$$E_{v_{ext}}[\rho_0] = F[\rho_0] + \int v_{ext}(\boldsymbol{x})\rho_0(\boldsymbol{x})d\boldsymbol{x}\ \leq F[\rho] + \int v_{ext}(\boldsymbol{x})\rho(\boldsymbol{x})d\boldsymbol{x}\,. \tag{32}$$

The electronic energy can also be written in the form

$$E = \langle\varphi_\rho|\hat{T} + \hat{V}_{ee}|\varphi_\rho\rangle + \int v_{ext}(\boldsymbol{x})\rho(\boldsymbol{x})d\boldsymbol{x}\,, \tag{33}$$

where $\hat{T}$ denotes the kinetic operator and $\hat{V}_{ee}$ is an operator of mutual interactions between electrons. Such a definition represents a starting point for a variational principle known as Levy-Lieb constrained search.[78,79] It consists of two step minimization

$$E_0 = \min_{\rho}\left[\min_{\varphi\to\rho}\langle\varphi|\hat{T}+\hat{V}_{ee}|\varphi\rangle + \int v_{ext}(\boldsymbol{x})\rho(\boldsymbol{x})d\boldsymbol{x}\right], \tag{34}$$

where the minimization is taken over all N-representable electron densities. For Coulomb potential, the electron density should also comply with Kato's cusp condition[80] at a nucleus position $\mathbf{x_0}$

$$\left.\frac{\partial\rho(\boldsymbol{x})}{\partial\boldsymbol{x}}\right|_{x=x_0} = -2Z\rho(\boldsymbol{x_0}). \tag{35}$$

Nevertheless, an explicit form of the universal functional is not known and moreover suggested functionals for kinetic energy do not provide sufficiently accurate results. Therefore, Kohn-Sham approach[81,82] proves successful in the current quantum chemistry, where the 3N-dimensional wave function ψ_S in the form of Slater determinant is used for determination of the three dimensional electron density

$$\rho(\boldsymbol{x}) = \sum_{i=1}^{occ}|\varphi_i(\boldsymbol{x})|^2. \tag{36}$$

Within this method, the energy is split into several terms

$$E - \int v_{ext}(\boldsymbol{x})\rho(\boldsymbol{x})d\boldsymbol{x} = T_S + J + (T - T_S) + (V_{ee} - J), \tag{37}$$

where T_S is kinetic energy for the non-interacting system of electrons

$$T_S = -\frac{1}{2}\sum_{i=1}^{occ}\int \varphi_i(\boldsymbol{x})\nabla^2\varphi_i(\boldsymbol{x})d\boldsymbol{x}\ . \tag{38}$$

J corresponds to the Coulomb term from HF method and can easily be expressed in terms of the electron density. The remaining two contributions on the right side of the equation (37) are not known explicitly and they are included into a so-called exchange-correlation functional $E_{xc}[\rho]$, so the energy is expressed as

$$E[\rho] = T_S + J[\rho] + E_{xc}[\rho] + \int v_{ext}(\boldsymbol{x})\rho(\boldsymbol{x})d\boldsymbol{x}\ . \tag{39}$$

When the above expression for the electronic energy is varied with respect to spin-orbitals along with a requirement of spin-orbital orthonormality, Kohn-Sham equations are obtained

$$\left(-\frac{\Delta}{2} + v_{eff}(\boldsymbol{x})\right)\varphi_i(\boldsymbol{x}) = \epsilon_i\varphi_i(\boldsymbol{x}),$$
$$v_{eff}(\boldsymbol{x}) = \int\frac{\rho(\boldsymbol{x}')}{|\boldsymbol{x}-\boldsymbol{x}'|}d\boldsymbol{x}' + v_{ext}(\boldsymbol{x}) + v_{xc}(\boldsymbol{x}), \qquad v_{xc} = \frac{\partial E_{XC}}{\partial\rho}. \tag{40}$$

These equations are non-linear integro-differential and must be solved using the iterative procedure. The term v_{xc} is the exchange-correlation potential whose exact form is not known. Nevertheless, a large number of approximations have been developed up to these days. The first of them was established based on the calculations with the homogeneous electron gas (HEG) leading to the relation

$$v_x^{HEG}(\boldsymbol{x}) = -\left(\frac{3}{\pi}\right)^{\frac{1}{3}} \rho^{\frac{1}{3}}(\boldsymbol{x}) \tag{41}$$

for the exchange part of the v_{xc} potential.

Since this functionals depends solely on the electron density locally, this approach is called local density approximation (LDA). In order to enable calculation of spin polarized systems, also local spin-density approximation (LSDA) was formulated, where the exchange-correlation potential depends on densities ρ^{α} and ρ^{β} of alpha and beta electrons. For this purpose, spin polarization parameter ζ [83] is introduced by the relation

$$\zeta = \frac{\rho^{\alpha} - \rho^{\beta}}{\rho^{\alpha} + \rho^{\beta}}. \tag{42}$$

Then within the discussed method, the exchange potential v_x^{LSDA} can be written in the form

$$v_x(\rho, \zeta) = v_x^P(\rho) + \left(v_x^F(\rho) - v_x^P(\rho)\right) f(\zeta), \tag{43}$$

where v_x^P and v_x^F are exchange potential for spin-compensated HEG and spin–completely-polarized HEG, respectively.[84] A form of function $f(\zeta)$ can be found in ref. 85. The pertinent correlation functional $v_C(\rho, \zeta)$ was parametrized by Vosko, Wilk and Nusair[85] on the basis of Monte Carlo simulations.

However, LDA (LSDA) approach possesses several shortcomings e.g. provides too short bonds, small gaps in the solid state physics or unreliable activation barriers. In other words, it is not appropriate for description of molecules where the electron density changes rapidly. From this point, behavior of the exchange-correlation functionals can be improved by making them dependent also on the gradients of the electron density $\nabla\rho$ and kinetic energy density τ, which leads to general gradient approximation (GGA) and meta-GGA (MGGA), respectively. Hence, a general form of the exchange-correlation potentials is

$$\begin{aligned} E_{xc}^{GGA} &= \int \rho(\boldsymbol{x}) v_{xc}\left(\rho^{\alpha}(\boldsymbol{x}), \rho^{\beta}(\boldsymbol{x}), \nabla\rho^{\alpha}(\boldsymbol{x}), \nabla\rho^{\beta}(\boldsymbol{x})\right) d\boldsymbol{x}, \\ E_{xc}^{MGGA} &= \int \rho(\boldsymbol{x}) v_{xc}\left(\rho^{\alpha}(\boldsymbol{x}), \rho^{\beta}(\boldsymbol{x}), \nabla\rho^{\alpha}(\boldsymbol{x}), \nabla\rho^{\beta}(\boldsymbol{x}), \tau^{\alpha}, \tau^{\beta}\right) d\boldsymbol{x}. \end{aligned} \tag{44}$$

Within GGA approach, Becke[86] proposed his form for the exchange functional

$$E_X^{B88} = E_X^{LDA} - \beta \sum_\sigma \int \rho_\sigma^{\frac{4}{3}}(\boldsymbol{x}) \frac{s_\sigma^2}{1 + 6\beta s_\sigma \, argsinh \, s_\sigma} d\boldsymbol{x}, \qquad s_\sigma(\boldsymbol{x}) = \frac{|\nabla \rho_\sigma|}{\rho_\sigma^{4/3}} \quad (45)$$

based on the requirement of its correct asymptotic behavior $\lim_{r\to\infty} v_x(r) \approx -1/2r$ and satisfaction of other fundamental physical conditions. The parameter β (= 0.0042 a.u.) was determined by fitting ab-initio results for noble gases.

The correlation functionals can be divided into two classes:[87] a) Colle-Salvetti-type functionals and b) density gradient approximation-type functionals. The Colle-Salvetti-type functionals are derived from uncorrelated HF wave function multiplied by a correlation function[88] of explicit interelectron distances

$$\psi(\boldsymbol{x_1}, .., \boldsymbol{x_n}) = \psi_{HF}(\boldsymbol{x_1}, .., \boldsymbol{x_n}) \prod_{i<j} \left(1 - e^{-\beta^2 r_{ij}^2}\right) \left(1 - \Phi(\boldsymbol{R}) \left(1 + \frac{r_{ij}}{2}\right)\right). \quad (46)$$

Representatives of this class are Lee-Yang-Parr (LYP) functional[89] and one-parameter progressive (OP) functional.[90] In the case of density gradient approximation-type functionals, their form follows from requirements of behavior of the electron density in limit cases and for example, PW91 and PBE functionals[91] belong to this class.[91] The correlation and exchange PBE functionals do not furthermore included any fitted parameter. Similarly, MGGA functional of Tao, Perdew, Staroverov, and Scuseria (TPSS)[92] is non-empirical. On the contrary, Truhlar's set of Minnesota MGGA functionals (M06-L,[93] M11-L,[94] MN12-L,[95] etc.) are highly parametrized e.g. 58 parameters for the MN12-L functional.

An important concept is represented by inclusion of the exact HF exchange into the exchange functionals because of wrong description of electron density in molecular bonds by functionals derived from the HEG model. This is done based on the adiabatic connection concept when the exchange-correlation potential v_{XC}^{λ} is considered to be dependent on a parameter λ

$$E_{XC} = \int_0^1 d\lambda \, v_{XC}^{\lambda} \, . \quad (47)$$

Here, zero value of the parameter λ corresponds to the non-interacting Kohn-Sham reference system and λ=1 to inclusion of the entire interaction. Within such an approach, Becke[96] suggested his three-parameter functional

$$E_{XC} = E_{XC}^{LSDA} + a_0(E_X^{HF} - E_X^{LSDA}) + a_X E_X^{B88} + a_C E_C^{PW91} \, . \quad (48)$$

Fitting energies to the G1 molecule set, parameter values a_0 = 0.20, a_X = 0.72, and a_C = 0.81 were obtained. Functionals that contain exact the HF exchange are called hybrid and for majority of pure functionals, also their hybrid modifications have been developed.

2.8 Grimme's empirical dispersion corrections

Despite the inclusion of correlation energy in the DFT approach, lack of dispersion interaction in the case of standard XC functionals represents a serious shortcoming. This problem has been addressed by Grimme et al. who simply added an empirical term into the Kohn-Sham equations. One of its most recent form[97] is

$$E_{disp}^{D3(BJ)} = -\frac{1}{2}\sum_{A\neq B} s_6 \frac{C_6^{AB}}{R_{AB}^6 + [f(R_{AB}^0)]^6} + s_8 \frac{C_8^{AB}}{R_{AB}^8 + [f(R_{AB}^0)]^8}$$
$$f(R_{AB}^0) = a_1 R_{AB}^0 + a_2\,, \qquad R_{AB}^0 = \sqrt{\frac{C_8^{AB}}{C_6^{AB}}}\,, \tag{49}$$

where s_8, a_1, and a_2 are parameters which are fitted to 130 references from non-covalent interaction energy benchmark sets for overall considered density functionals. The s_6 parameter is set to 1 in accord with gas of weakly interacting atoms. The atom-pair wise specific dispersion coefficients C_6^{AB} are determined via Casimir-Polder formula from calculated polarizabilities at the time-dependent DFT level. The cut-off radii R_{AB} are identified with the distance between atoms where the interaction energy (determined without dispersion corrections) reaches a chosen value (between 2 and 10 kcal·mol^{-1}).

2.9 Relativistic calculations

Use of the non-relativistic Schrödinger equation is justifiable for light atoms; nevertheless, in the case of heavy atoms, relativistic effects play a non-negligible role. A famous example of their importance represents different colors of silver and gold when the relativistic effects are responsible for the yellowish color of gold. Since inner electrons close to heavy nuclei move with a velocity approaching to the speed of light, a contraction of inner s orbitals occurs. Also outer orbitals are influenced directly or indirectly via interaction with electrons in the contracted inner orbitals. Relativistic calculations can be performed by solving Dirac equation

$$\hat{H}^D \begin{pmatrix}\phi\\ \chi\end{pmatrix} = \begin{pmatrix}V + c^2 & c\boldsymbol{\sigma}\cdot\boldsymbol{\pi}\\ c\boldsymbol{\sigma}\cdot\boldsymbol{\pi} & V - c^2\end{pmatrix}\cdot\begin{pmatrix}\phi\\ \chi\end{pmatrix} = \varepsilon\begin{pmatrix}\phi\\ \chi\end{pmatrix}, \tag{50}$$

or one of its approximations. In Dirac Hamiltonian H_D, c represents the speed of light and momentum $\boldsymbol{\pi}$ is equal to $\boldsymbol{p}$ *-qA(r,t)/c.* Matrices σ_i are Pauli spin matrices and V represents a sum of an external potential $v_{ext}(\boldsymbol{x_i}, t)$ and interaction between electrons. Spinors Φ and χ are called large and small components.

Four-component Dirac Hamiltonian is usually transformed into a two-component Hamiltonian. For example, after some manipulations Hamiltonian in so-called zeroth order regular approximation (ZORA)[98,99] can be obtained:

$$\hat{H}^{ZORA} = V + \boldsymbol{\pi}\frac{c^2}{2c^2 - V}\boldsymbol{\pi} + \frac{c^2}{(2c^2 - V)^2}\boldsymbol{\sigma}\cdot(\boldsymbol{\nabla}V \times \boldsymbol{\pi}). \tag{51}$$

2.10 Pseudopotentials

Another elegant way how to include at least some relativistic effects for heavy atoms into non-relativistic calculations represents employment of pseudopotentials.[100] Within this method, an influence of inner electrons of heavy atoms is replaced by a potential which is determined on the basis of accurate relativistic calculations. Another advantage dwells in reduction of a number of electrons in regarded systems since the core electrons do not participate in chemical bonds and can be energetically well-separated from valence electrons. Let's consider a system described by Schrödinger equation with an effective Hamiltonian for one-electron orbitals

$$\hat{H}_{eff}|\psi_a\rangle = \varepsilon_a|\psi_a\rangle\,, \quad a \in \{v, c\}, \tag{52}$$

where indices *v* and *c* denotes orbitals occupied by valence and core electrons and pertinent energies. In such a case, a pseudovalence wave function ψ_p for each valence electron can be defined as a sum of this valence wave function and a linear combination of the orbitals for core electrons

$$|\psi_p\rangle = |\psi_v\rangle + \sum_c k_c|\psi_c\rangle\,. \tag{53}$$

After introduction of the generalized Phillips-Kleinmann (GPK) potential[101]

$$\hat{V}^{GPK} = -\hat{H}_{eff}\hat{P}^c - \hat{P}^c\hat{H}_{eff} + \hat{P}^c\hat{H}_{eff}\hat{P}^c + \varepsilon_v\hat{P}^c \tag{54}$$

the above equation (52) can be rewritten as $\left(\hat{H}_{eff} + \hat{V}^{GPK}\right)|\psi_p\rangle = \varepsilon_v|\psi_p\rangle$. $\hat{P}^c = \sum_c|\psi_c\rangle\langle\psi_c|$ is a projector on the space of core orbitals. As a result, non-local formalism is obtained, which is not appropriate from the perspective of computational demands. Therefore, a semi-local approximation is introduced[102]

$$\hat{V} = U^{local} + \sum_l^{L_{highest}} [U_l - U^{local}] \sum_m |lm\rangle\langle lm|\,. \tag{55}$$

For the sake of simplicity, the potentials U_l are fitted in the form of gaussian functions[102]

$$U_l(r) = \sum_k A_{kl} r^{n_{kl}} e^{-a_{kl}r^2}\,. \tag{56}$$

2.11 Hybrid QM/MM method

Dealing with large systems, employment of QM methods is demanding from the viewpoint of computational resources and time. Nevertheless, when we are

interested in a course of a chemical reaction, we cannot avoid using of a QM description. Fortunately, a region where the QM description must be employed can be restricted to a relatively small area and rest of the system can be considered at the MM level without a significant loss of accuracy. However, a choice of the core is crucial in calculations. In fact, when the inner (QM) part is selected too small so that a MM approximation is not sufficient beyond the border of the QM region, reliable results cannot be obtained. On the other hand, too large inner region leads to high computational time as speed of QM calculations represent a deciding factor for the whole hybrid QM/MM technique.[103-107] A typical problem addressed by this method is study of interactions of miscellaneous substrates with an enzyme active center, where just the active center (a few amino acid side chains) together with the substrate should represent the QM region.

The total QM/MM energy can be determined within two computational schemes[107] – additive and subtractive. In the former the total energy is defined as a sum of the QM energy of the isolated inner part, the MM energy of the outer region, and an interaction energy between them

$$E = E_{MM}(O) + E_{QM}(I + L) + E_{MM-QM}(O, I)\,. \tag{57}$$

Nevertheless, this formulation is not easy to implement. Therefore, the subtractive scheme is more often used. The total energy is calculated as a sum of MM energy of the whole system plus the difference between QM and MM energies of the inner region

$$E = E_{MM}(O + I) + E_{QM}(I + L) - E_{MM}(I + L)\,. \tag{58}$$

Within both approaches, the interaction energy can be split into three terms

$$E_{MM-QM} = E_{bond} + E_{elst} + E_{vdW} \tag{59}$$

in accord with the molecular mechanics. The first term, the bonding interaction energy, is only taken into account if the border between the regions intersects a chemical bond. In order to keep the correct valence of the QM frontier atoms in QM calculations, a) the molecular orbitals pointed in direction of the interupted bonds can be frozen[108] or b) an additional so-called link atom L[105,106] can be bound to the QM frontier atoms. Ordinarily, the link atom is represented by the hydrogen atom.

Inclusion of the electrostatic interaction E_{elst} between the QM(I) and MM(O) parts can be carried out at several levels. The simpliest method represents a mechanical embedding where the interaction is treated as Coulomb interaction between atomic charges in the inner and outer region. However, the wave function of the QM part remains unpolarized by the MM surroundings. This is corrected in the second approach called electronic embedding where terms corresponding to interaction of the electron density and nuclei in the QM region with atomic charges q from the outer sphere are included in the QM Hamiltonian

$$\hat{H}_{int} = -\sum_{i\in I}\sum_{J\in O}\frac{q_J}{|\boldsymbol{x}_i - \boldsymbol{X}_J|} + \sum_{A\in I+L}\sum_{J\in O}\frac{q_J Z_a}{|\boldsymbol{X}_j - \boldsymbol{X}_A|}. \quad (60)$$

Frequently, the summation are not taken over the whole outer region but only over a layer which surrounds the QM part. When the polarizable force fields are employed in the calculations, then the electric field generated by the charge density of the QM part can further influence the charge distribution of the MM(O) region via polarizability of atoms. The remaining van der Waals energy is almost always included via Lennard-Jones or Buckingham potentials at the MM level.

2.12 Implicit solvation models

Inclusion of explicit surroundings into QM calculations is a difficult task. Nevertheless, it can be involved at the QM/MM level, when the solvent molecules form the outer region. Then, in order to obtain free energy at the given non-zero temperature, we need to perform averaging over a set of states. From this perspective, implicit solvation models[109] represent much cheaper possibility how to include interaction with environment at least to some extent. Within this method the studied system is situated into a cavity inside dielectric continuum whose properties are described by its relative permittivity ε_r and a size of the cavity.

In accord with the additive scheme for QM/MM energy calculation (equation (57)), Hamiltonian, which includes surroundings, can be written in the form

$$\hat{H}^{tot} = \hat{H}^{solute} + \hat{H}^{int} + \hat{H}^{solvent}. \quad (61)$$

Within implicit solvation models, the last term is omitted. We are only interested in the interaction energy. In so-called polarizable continuum models (PCM),[110,111] a molecular system located in a cavity polarizes dielectric continuum, which leads to generation of the charge on the surface Γ of the cavity. Then the surface charge σ influences the charge density of solute. Hence, the interaction term H^{int} is given by

$$H^{int}(\boldsymbol{x}) = \int_{\Gamma}\frac{\sigma(\boldsymbol{s})}{|\boldsymbol{x} - \boldsymbol{s}|}d\boldsymbol{s} \approx \sum_{k}\frac{q_k}{|\boldsymbol{x} - \boldsymbol{s_k}|}. \quad (62)$$

In the calculations, the surface Γ of the cavity is divided into small triangular areas (called tesserae) whose charge is q_k. The surface charge is determined based on the Poisson-Boltzmann equation

$$-\nabla[\varepsilon(\boldsymbol{x})\nabla\varphi(\boldsymbol{x})] = \rho_M(\boldsymbol{x}), \quad (63)$$

where $\rho_M(\boldsymbol{x})$ is the solute charge density, $\varphi(\boldsymbol{x})$ is total potential generated by this density $\rho_M(\boldsymbol{x})$, and the surface charge $\sigma(\boldsymbol{s})$. The Poisson-Boltzmann equation is solved with requirements of a) continuity of the potential $\varphi(\boldsymbol{x})$ on the border

between regions and b) the jump discontinuity of electric intensity in the direction of the normal vector $\boldsymbol{n}$ to the cavity surface

$$\left(\frac{\partial\varphi}{\partial\boldsymbol{n}}\right)_{in} - \varepsilon_r \left(\frac{\partial\varphi}{\partial\boldsymbol{n}}\right)_{out} = 0 \ , \tag{64}$$

as follows from Maxwell's equations. Indices *in* and *out* denote the derivatives inside and outside the cavity, respectively. A solution of the Poisson-Boltzmann equation with these boundary conditions leads to the relation for the surface charge

$$\sigma(\boldsymbol{x}) = \frac{\varepsilon_r - 1}{\varepsilon_0 \varepsilon_r} \left(\frac{\partial\varphi(\boldsymbol{x})}{\partial\boldsymbol{n}}\right)_{in} . \tag{65}$$

Since the magnitude of the surface charges is influenced by the charged density of the solute and vice versa, the problem of interaction with polarized dielectric continuum is solved in an iterative way and the method is called self-consistent reaction field (SCRF).[112,113]

Not only the permittivity of surrounding environment, but also the size of the cavity is of great importance for accuracy of calculations. The cavity is ordinarily constructed as a union of spheres around the atoms. Radii of the spheres are commonly scaled van der Waals radii[114] or they are further modified according to neighboring atoms, hybridization and formal charges (UAHF and UAKS models) as was suggested by Barone et al.[115] This parametrization works fine for organic molecules; nevertheless, it has to be improved for description of transition metal complexes. Therefore, the scaling according to the actual charge Q_{act} instead of the formal charge (as introduced by Orozco and Luque[116]) is necessary. Zimmermann[117] suggested a linear scaling of the size of radii *R(X)* between values corresponding to formal charges in the way

$$R(X) = R_0(X) - \gamma \cdot \left| \frac{Q_{act}(X) - Q_{dep}(X)}{Q_{prot}(X) - Q_{dep}(X)} + Q_{dep}(X) \right| , \tag{66}$$

where R_0 and γ are the radius (without scaling according to the formal charge) and the scaling factor from the original UAKS method. Q_{prot} and Q_{dep} are charges of group *X* in the reference molecules (in both protonated and deprotonated forms cf. ref [115]) determined at the same computational level as the actual charge Q_{act}. This model is referred to as scaled-UAKS.

2.13 Contributions to Gibbs free energy from degrees of freedom

To obtain the total free energy at a given temperature we have to include contributions from kinetic energy of nuclei. From the equipartition theorem (5) it follows that average kinetic energy depends on a number of degrees freedom and thermodynamic temperature. Their contributions to the total energy can be evaluated

within the statistical mechanics. Since a majority of the studied reactions occurs at a constant temperature and pressure, Gibbs free energy $G=U-TS+pV$ represents an appropriate thermodynamic potential. Nevertheless, if an implicit solvation model is used, the entropic contributions to Gibbs free energy are exaggerated. In fact, such determination of thermodynamic quantities corresponds to the model of the ideal gas. This problem was addressed by Wertz[118] in 1980 and recently reformulated by Goddard,[119] when the total entropy calculated in solvent is estimated as

$$S = S_{gas}^{vib} + 0.54 \cdot \left(S_{gas}^{trans} + S_{gas}^{rot} - 14.3\right) + 8.0\,. \tag{67}$$

The contributions from translational and rotational degrees of freedom are scaled by factor of 0.54, which was suggested by Wertz who made an assumption that all molecules loose as much entropy as water during transfer from the gas phase to liquid. This loss represents 46% according to experimental data. The factors of -14.3 and 8.0 cal·mol^{-1}·K^{-1} correspond to the change of entropy caused by an intial compression of ideal gas from 1 atm to concentration of 55 mol·dm^{-3} and a final dilution to concentration of 1 mol·dm^{-3}.

2.14 Free energy calculations and umbrella sampling method

Appropriately performed MD simulations provide a probability distribution of states P in a desired part of the configuration space of a studied system. We are usually interested in its change along a path on a potential energy surface linked with the reaction coordinate (RC) ξ. In such a case, the probability distribution can be expressed as

$$P(\xi) = \frac{\int \delta[\xi'(\boldsymbol{x}) - \xi] e^{-\beta\varepsilon(x)}\, d^N\boldsymbol{x}}{\int e^{-\beta\varepsilon(x)}\, d^N\boldsymbol{x}}, \tag{68}$$

where averaging is taken over all coordinates except the coordinate ξ. From this one-dimensional probability distribution $P(\xi)$, we can obtain free energy profile $F(\xi)$ along RC as

$$F(\xi) = -k_b T ln P(\xi). \tag{69}$$

In order to obtain an accurate free energy profile we need to ensure sufficient sampling of the configuration space, which can be reached by use of, for example, replica exchange molecular dynamics,[120] metadynamics[121] or umbrella sampling technique[122,123] since occurrence of a system in transition regions in classical MD simulations has a low probability. The last two mentioned methods, metadynamics and umbrella sampling, represent bias potential methods. Within the umbrella sampling method, potentials $V_i(\xi)$, usually in the harmonic form, are added along the

RC in order to keep a system in a required region. Then, biased probability distributions $P_i^b(\xi)$ are give as a modification of equation (68)

$$P_i^b(\xi) = \frac{\int \delta[\xi'(\boldsymbol{x}) - \xi] e^{-\beta[\varepsilon(\boldsymbol{x}) + V_i(\xi'(\boldsymbol{x}))]}\, d^N\boldsymbol{x}}{\int e^{-\beta[\varepsilon(\boldsymbol{x}) + V_i\xi'(\boldsymbol{x})]}\, d^N\boldsymbol{x}} = P_i^u(\xi) e^{-\beta V_i(\xi)} \langle e^{-\beta V_i(\xi)} \rangle^{-1}. \tag{70}$$

Within the weighted histogram analysis method (WHAM),[124,125] the total unbiased probability distribution $P^u(\xi)$ is calculated from a weighted average of unbiased probability distributions $P_i^u(\xi)$ over all windows

$$P^u(\xi) = \sum_{i=1}^{n} p_i(\xi)\, P_i^u(\xi)\ , \qquad \sum_{i=1}^{n} p_i(\xi) = 1\ . \tag{71}$$

The weights p_i are determined based on the requirement of minimization of a statistical error made on the unbiased distribution. This leads to the relation

$$p_i(\xi) = \frac{N_i e^{-\beta(V_i(\xi) - A_i)}}{\sum_{j=1}^{n} N_i e^{-\beta(V_j(\xi) - A_j)}}, \tag{72}$$

where quantity A_i complies with the relations

$$e^{-\beta A_i} = \int P^u(\xi) e^{-\beta V_i(\xi)}\, d\xi \ \ resp.\ A_i = -\beta^{-1} \ln\langle e^{-\beta V_i(\xi)} \rangle \tag{73}$$

and corresponds to an additional free energy coming from the bias potential $V_i(\xi)$. Its value is unknown and the equations (71) - (73) must be solved in the interative way. Condition on an overlap between the neighboring biased probability distributions is required for the determination of these weights. An alternative approach to the WHAM method represents Umbrella Integration (UI).[126,127]

In the case of QM/MM MD simulations, a system is developed using a cheap i.e. lower-level QM method for description of the inner part of a system. To increase accuracy, an energy of the system can be recalculated at a higher QM computational level every n-th step. Using the free energy perturbation (FEP) method

$$\Delta F = -\beta\ ln\langle e^{-\beta \Delta H} \rangle_0\ , \qquad \Delta H = H_1 - H_0\ \ , \tag{74}$$

the difference in free energy between these two computational levels can be obtained from the corresponding energy differences $H_1 - H_0$.

2.15 Chemical kinetics

For a general chemical reaction $aA + bB \rightarrow cC + dD$ the reaction rate v is defined as a decrease of concentration of reactants or an increase of concentration of products divided by the corresponding stechiometric coefficient

$$v = -\frac{1}{a}\frac{d[A]}{dt} = -\frac{1}{b}\frac{d[B]}{dt} = \frac{1}{c}\frac{d[C]}{dt} = \frac{1}{d}\frac{d[D]}{dt}\,. \tag{75}$$

Rate constant k is introduced as a ratio of the reaction rate in dependence on instantaneous concentrations of reactants

$$v = k(T)[A]^x[B]^y\,, \tag{76}$$

where exponents x and y are related to the reaction mechanism. Considering a simple reaction profile with one energy barrier, which separates reactant and product regions, the rate constant can be determined according to Eyring's transition state theory[128] as

$$k(T) = \frac{k_b T}{h} e^{-\frac{\Delta G^{\ddagger}}{RT}}\,, \tag{77}$$

where $\Delta G^{\ddagger}$ represents the height of the activation barrier. An activation complex is a structure related to the top of the barrier and is characterized by a vibrational mode corresponding to transfer between the reactant and the product.

Let's look at side reactions when compound A simultaneously reacts with molecules B and C i.e. A+B→D and A+C→E with the rate constants k_1 and k_2, respectively. Then the total change of concentration of compound A is

$$\frac{d[A]}{dt} = -k_1[A][B] - k_2[A][C]. \tag{78}$$

When concentrations of the substances B and C are not independent, for example, they are two different protonation states B^- and BH ($[B^-]+[BH]=[B]_{tot}$) of the same compound coupled by a fast acid-base equilibrium condition, we can write

$$\begin{aligned}\frac{d[A]}{dt} &= -k_1[A][B^-] - k_2[A][BH] = (-k_1x_1 - k_2x_2)[A][B]_{tot} \\ &= -k_{eff}[A][B]_{tot}\,.\end{aligned} \tag{79}$$

x_1 and x_2 represents molar fractions corresponding to abundance of substances B^- and BH, which can be determined using Henderson-Hasselbalch equation. Thus, the effective rate constant k_{eff}, which is observed in experiments, is given as the weighted average of the rate constants in the individual branches. This formalism of side reactions is important when one of the forms B, C is connected with low concentration and simultaneously with a low activation barrier (leading to sufficiently high k).

2.16 Energy decomposition and analyses of the electron density distribution

In order to enable comparison of the strength of chemical bonds or non-covalent interactions between molecules, different computational schemes have been developed. The first class is focused on changes in the electron density distribution as Bader's Quantum Theory of Atom in Molecules (QTAIM) analysis,[129] Natural

Bond Orbitals,[130-132] a concept of the deformation density,[133] and others. The second group contains methods whose substance dwells in decomposition of the interaction energy into physically meaningful contributions. Such methods are represented by Kitaura-Morokuma Energy Decomposition Analyses (EDA),[134] Symmetry Adapted Perturbation Theory (SAPT),[135] Extended Transition State (ETS) scheme,[136] etc.

Here we use the combined ETS-NOCV analysis (ETS in combination with Natural Orbitals for Chemical Valence)[137] which provides both the quantitative and qualitative perspective. Within the ETS approach, the total interaction energy between fragments A and B is decomposed as

$$\Delta E_{int} = E^{AB} - E^{A} - E^{B} = \Delta E_{def} + \Delta E_{elst} + \Delta E_{Pauli} + \Delta E_{orb}\,, \qquad (80)$$

which corresponds to the train of thought when restrictions on the geometry of fragments and the space where the wave function can be optimized are gradually loosened. The first term on the right side represents deformation energy which states the change of the energy accompanied the distortion of the optimal geometries of the monomers into their geometries in the dimer (the total structure). The second expression ΔE_{elst} gives the electrostatic work that is necessary to move the fragments from the infinity to the mutual position in the dimer without any change of the electron density distributions $\rho_0^A(\mathbf{x})$ and $\rho_0^B(\mathbf{x})$ of the isolated monomers. The total Pauli interaction ΔE_{Pauli} can be split into exchange-correlation part ΔE_{XC} and Pauli repulsion $\Delta\tilde{E}_{Pauli}$. The former contribution expresses the difference in the exchange-correlation energy calculated with the total wave function in the form of Hartree product of monomer's wave functions and wave functions of the isolated monomers. The Pauli repulsion $\Delta\tilde{E}_{Pauli}$ gives the energy change when we enable anti-symmetrization of the mentioned Hartree product i.e we consider the wave function in the form of Slater determinant ψ^0.

The last expression ΔE_{orb} is the orbital interaction term which corresponds to transfer of electrons from occupied orbitals on one fragment to virtual orbitals on another fragment. Within the ETS-NOCV analysis the deformation density $\Delta\rho^{orb}$ is introduced for its description by the relation

$$\Delta\rho^{orb} = \rho - \rho^0 = \sum_{\mu}\sum_{\nu} \Delta P_{\mu\nu}^{orb}\lambda_\mu\,\lambda_\nu\,, \qquad (81)$$

where ρ is the ground-state electron density of the dimer and ρ^0 is the electron density corresponding to Slater determinant ψ^0. Then the deformation density is expanded into a set of the orthonormal fragment spin-orbitals λ_i and the deformation density matrix $\Delta P_{\mu\nu}^{orb}$ is defined. By diagonalization of the matrix $\Delta P_{\mu\nu}^{orb}$, NOCV orbitals[138] are obtained as its eigenvectors

$$\Delta P^{orb}\psi_i^{NOCV} = v_i\psi_i^{NOCV}\,. \qquad (82)$$

Owing to the fact that the trace of the deformation density matrix is zero and spin-orbitals λ_i are orthonormal, the opposite eigenvalue to the arbitrary selected eigenvalue v_i can always be found in its spectrum. This property enables to expand the deformation density into pairwise contributions

$$\Delta\rho^{orb}(\boldsymbol{x}) = \sum_{k=1}^{N/2} v_k[-\psi_{-k}^2(\boldsymbol{x}) + \psi_k^2(\boldsymbol{x})]\,, \tag{83}$$

so that individual channels for transfer of electron density can be seen during formation of the dimer from the fragments, for example, formation of sigma bonds, hydrogen bonds, π-donation and π-backdonation. The energy contributions of each channel can be evaluated quantitatively within the ETS approach.

Another approach which provides localized orbitals is Weinhold's Natural Bonding Orbitals (NBO) analysis.[130,131,139] Within this method it is appropriate to describe an electron system using one-electron reduced density

$$\Gamma(1|1') = N\int \psi(1,2,..,N)\psi^*(1',2,..,N)\,d2..dN \tag{84}$$

When it is expanded into the basis of atomic orbitals, its diagonal terms Γ_{ii} represent occupation numbers of these orbitals. A goal of the NBO approach dwells in maximalization of occupation numbers in blocks of Γ matrix. If the basis functions are ordered in the way that basis functions Φ_A localized on center A are together, we obtain blocks Γ_{AA} along diagonal that correspond to projection of the total reduced density into the space spanned by functions Φ_A centered on one nuclei. When the Löwdin orthogonalization within these blocks is performed

$$\Gamma_{AA}h_i^A = p_i^A S_{AA} h_i^A \tag{85}$$

the natural atomic orbitals are obtained as orbitals h_i^A which are doubly occupied. In the following step, larger blocks Γ_{AB} of the reduced density matrix are taken into consideration. They analogously correspond to projection of the total reduced density on subspaces generated by basis functions Φ_A and Φ_B centered on pairs of atoms A and B. The block diagonal reduced density matrix generated by previously obtained atomic orbitals h_i^A and h_i^B is subtracted from this matrix Γ_{AB} i.e.

$$\Gamma'_{AB} = \Gamma_{AB} - \sum_{A,B} p_i^A h_i^A h_i^A\,. \tag{86}$$

As a result of maximalization of occupation number within these matrices Γ'_{AB}, new sets of orbitals are obtained. Each orbital is futher decomposed into two parts localized on atoms A and B, which are called natural hybrid orbitals (NHO). Performing the Löwdin orthogonalization of Γ_{AB}^{NHO} in the space of the pertinent NHOs, resulting 2-center NBOs are given as their linear combination

$$\Omega_{AB} = ah^A + bh^B \tag{87}$$

where coefficients a and b satisfy $a^2 + b^2 = 1$. The partial charge on atom A with proton number Z_A is determined within this method as

$$Q_A = Z_A - Tr\, \Gamma_{AA} \ . \tag{88}$$

Another viewpoint is such that we want to orthogonalize a set of atomic orbitals Φ_i^{AT} with requirement of minimization of the squared deviation of occupied orbitals from these atomic orbitals i.e. to minimize the expression

$$\sum_i w_i \left|\Phi_i^{AT} - \Phi_i\right|^2 , \tag{89}$$

where w_i are occupation numbers.

Within the QTAIM (Quantum Theory of Atoms in Molecules)[129] analysis, the charge density and its gradient vector field play a main role. Extreme points of the gradient vector field represent the basics of the whole theory and are called critical point. Thus, in these points the gradient of the charge density is zero and they can be characterized according to eigenvalues of the pertinent Hessian matrix. Its eigenvalues correspond with curvature of the course of the charge density and its eigenvectors with principle axes. Decisive values are rank i.e. a number of non-zero eigenvalues and signature i.e. a sum of signs of the eigenvalues. A majority of the critical points has rank = 3 and such points are of main interest. There are four kinds of them relative to their signature. Positions of nuclei are associated with maxima of the charge density, where the first derivative is zero in practical calculations, and correspond to the critical points (3,-3) (the labelling is (rank, signature)). The critical points (3,-1), i.e. saddle points, where the charge density has a minimum only in one direction, are always present between the atoms which are connected with a chemical bond. Therefore, they are referred to as bond critical points (BCPs). Their exact position can also be obtained as intersection of boundary between atoms and a so-called atomic interaction line which represents a connecting line between atoms along which the charge density is maximal in comparison with any neighboring line. Within the QTAIM approach, the boundary of atoms are associated with a surface of the zero charge density flux i.e a set of points where

$$\nabla\rho(\boldsymbol{r}) \cdot \boldsymbol{n}(\boldsymbol{r}) = 0 \tag{90}$$

is fulfilled. The vector **n**(**r**) is the normal vector to the surface. The magnitude of the charge density in the critical points (3,-1) can indicate bond strengths.

To appraise spontaneity of an electron density rearrangement, the electronic chemical potential μ can be calculated from the known ionization potential IP and electron affinity EA and/or approximated based on HOMO, LUMO eigenvalues

$$\mu = -\frac{1}{2}(IP + EA) \approx \frac{1}{2}\big(E(HOMO) + E(LUMO)\big) . \tag{91}$$

A rearrangement of the electron density is spontaneous when the magnitude of the electronic chemical potential decreases along the IRC and vice versa. For this purpose, a quantity called reaction electronic flux J (REF)[140] was introduced according to the formula:

$$J(\xi) = -\frac{\partial \mu}{\partial \xi}, \tag{92}$$

where $\partial\xi$ denotes a change along the reaction coordinate. When the calculated REF is positive, the changes in the electron density distribution are spontaneous.

3 Results

3.1 Study on Electronic Properties, Thermodynamic and Kinetic Parameters of the Selected Platinum(II) Derivatives Interacting With Guanine[141]

Recently, miscellaneous prospective Pt(II) anticancer drugs can be found in the literature. Their different large, mostly hydrophobic, ligands should leads to overcoming of cisplatin resistance for some tumors or a decrease of a number of side effects. Nevertheless, a systematic study on an influence of such modifications on the rate of formation of monofunctional adducts with DNA and the corresponding bond strengths has not been published yet. Therefore, we focused on five Pt(II) complexes with observed in vitro anticancer activity - hydrated CDDP, oxaliplatin (DACH), Pt(II) analogue of satraplatin (JM118), cis-Pt(NH_3)Cl_2(piperidine) (Pip), and trans-Pt(NH_3)Cl_2(thiazole) (Tz) complexes. A considered model reaction represents a substitution of an aqua ligand in the hydrated Pt(II) complexes by guanine. Its course is schematically shown in **Fig. 1**. Both semi-hydrated and fully-hydrated complexes are take into consideration, which is indicated by ligand R_3 =

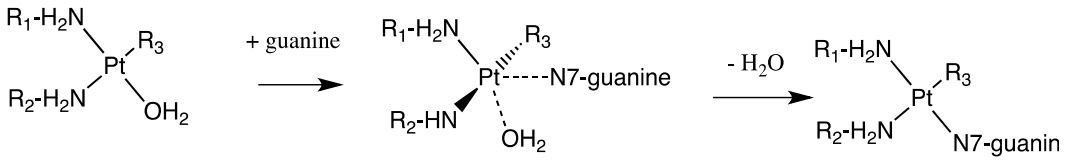

Figure 1: Formation of a monofunctional adduct of the Pt(II) complexes and guanine. R3=Cl^-, OH^- and R1 and R2 ligands are given by regarded complexes.

Cl^-, OH^- in **Fig. 1**. Structures in stationary points on the reaction coordinate are optimized at the B3LYP/6-31+G(d)/IEF-PCM/UFF level. For description of inner electrons of S, Cl, and Pt atoms, Stuttgart energy averaged pseudopotentials are employed. Single-point (SP) calculations for the optimized structures are performed at the B3LYP/6-311++G(2df,2pd)/D-PCM/scaled-UAKS level. Entropic contributions to Gibbs free energy are corrected according to Wertz suggestion (equation (67)). Furthermore, several analyses of the electron density distribution are carried out and binding energies of ligands are corrected to the gas phase Basis Set Superposition Error (BSSE).[142]

All the regarded reactions are exothermic and also exergonic. The corresponding reaction Gibbs free energy is in the range between -16 and -19 kcal·mol^{-1} when the lowest energy decrease is observed for CDDP. On the other hand, the highest one is connected with JM118. The reaction rate increases in the order: DDP-Cl < Pip-Cl < JM118-Cl < DACH-Cl < Tz-Cl for the semi-hydrated Pt(II) complexes and in the order: DACH-OH < DDP-OH < Tz-OH < Pip-OH ≈

JM118-OH for the fully hydrated complexes. In the case of the thiazole complex, the difference in the reaction rate is given by higher trans-effect of Cl^- ligand compared to OH^- ligand. The determined values for CDDP are close to experimental values of Brabec and others [143-147] and also to calculated values by Eriksson et al.[13]

3.2 Redox Potentials for Tetraplatin, Satraplatin, Its Derivatives and Ascorbic Acid; Computational Study[148]

Although the reaction rate represents a decisive factor for majority of reduction reactions of Pt(IV) complexes, their reduction potentials are also of great importance since they enable to estimate possible reducing agents from the thermodynamic perspective. As the experiments indicate, two ligands, mostly the axial ones (L_{AX}), are released along with an uptake of two electrons i.e.

$$Pt(IV) + 2\,e^- \rightarrow Pt(II) + 2\,L_{AX}\,. \tag{93}$$

If the reaction Gibbs free energy ΔG_r^0 is determined for this process, the standard reduction potential E^0 can be calculated according to the relation

$$E^0 = -\frac{\Delta G_r^0}{2F} + E_{SHE}\ , \tag{94}$$

where F is Faraday constant and E_{SHE} absolute potential of standard hydrogen electrode of -4.281 V.[149] In addition, the binding energies (BE) for axial ligands are calculated, since we are interested in the fact if their magnitudes correlate with the calculated redox potentials. They are also corrected to Boys-Bernardi counterpoise error.[142]

In this way, the reduction potentials for eleven Pt(IV) complexes, which are depicted in **Fig. 2** (structures 1-11), are determined. Geometries of these Pt(IV) complexes, their Pt(II) analogues, and axial ligands are optimized at the ω-B97XD/6-31+G(d)/IEF-PCM/UFF level. SP calculations are carried out at the DFT/6-311++G(2df,2pd)/IEF-PCM/scaled-UAKS level with nine functionals - B3LYP,[150] ω-B97XD,[151] PBE1PBE,[152] PBEh1PBE,[153] TPSSTPSS,[92] TPSSh,[92,154] M06-L,[93] M11-L[94] and MN12-L[95]. Grimme's dispersion corrections[97,155] are also employed. For comparison, post-HF methods are additionally considered, namely, MP2 in combination with larger triple-ζ basis set and CCSD(T) together with the 6-31+G(d) basis set.

From the perspective of accuracy of the calculated redox potentials, use of Wertz's correction is necessary, since it leads to a significant decrease of RMSD (root mean square deviation) from experimental values.[31-34] In fact, in comparison with many similar calculations of redox potentials for transition metal complexes, Pt(IV) complexes not only accept two electrons but also a number of particles changes during the reduction and thus also a total number of considered translational and rotational degrees of freedom. Within the DFT calculations, Grimme's

dispersion corrections play a similarly important role since their involvement causes an additional decrease of the RMSD by 100-300 mV. Moreover, inclusion of non-electrostatics solvation contributions to Gibbs free energy leads to a better correlation between the calculated and experimental data. Overall, the lowest RMSDs are determined for Truhlar's MN12-L functional (154 mV), followed by the MP2 method in combination with double-ζ basis set (179 mV) and the CCSD(T) method (234 mV). The higher RMSD at the CCSD(T) can be caused by use of the smaller double-ζ basis.

Besides chloro-forms, we are also interested in the fact how hydration of these complexes influences the magnitude of the reduction potentials. It follows from calculated data that each such substitution is associated with the increase of the

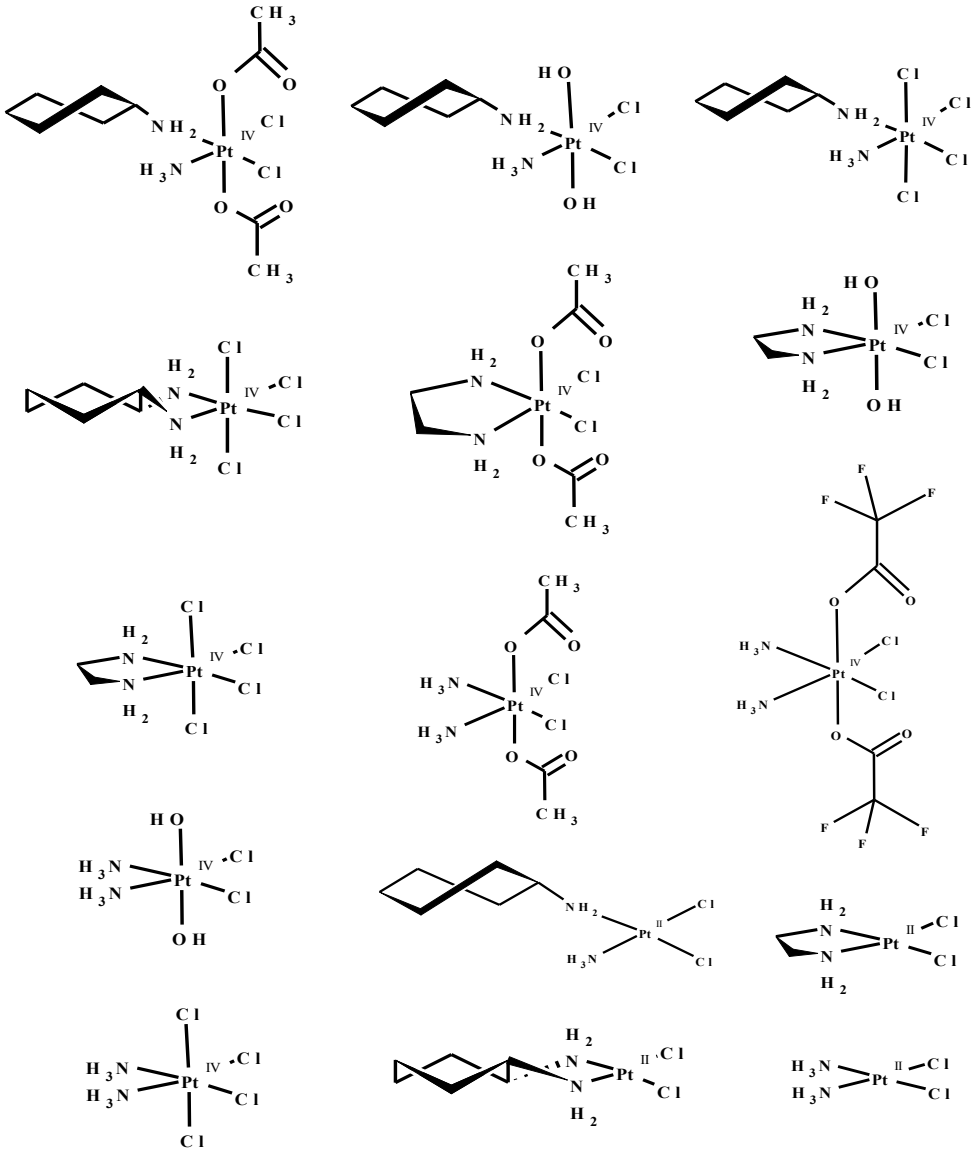

Figure 2: Pt(IV) complexes for which the reduction potential is calculated and their Pt(II) analogues.

reduction potential by approximately 100 mV. Nevertheless, these aqua-forms are not stable at neutral pH and they are converted to the hydroxo form. In this case, the magnitude of the reduction potentials contrarily decreases by roughly 100 mV. Further, we focus on a possible reducing agent – ascorbic acid whose reduction potential strongly depends on solution pH. Despite this fact, the considered post-HF methods in combination with the smaller double-ζ basis set provide very accurate results.

3.3 Reduction of Tetraplatin in the Presence of Deoxyguanosine Monophosphate (dGMP)[156,157]

Although tetaplatin exhibits severe neurotoxicity, it can serve as a convenient model complex. The reaction mechanism of its reduction in the presence of dGMP was suggested by Choi et al.[37] and was described in Introduction. The pertinent scheme is depicted in **Fig. 3**. The whole reaction consists of three parts – a substitution reaction, a reduction step and a final hydrolysis.

All stationary points along the reaction coordinate are optimized at the

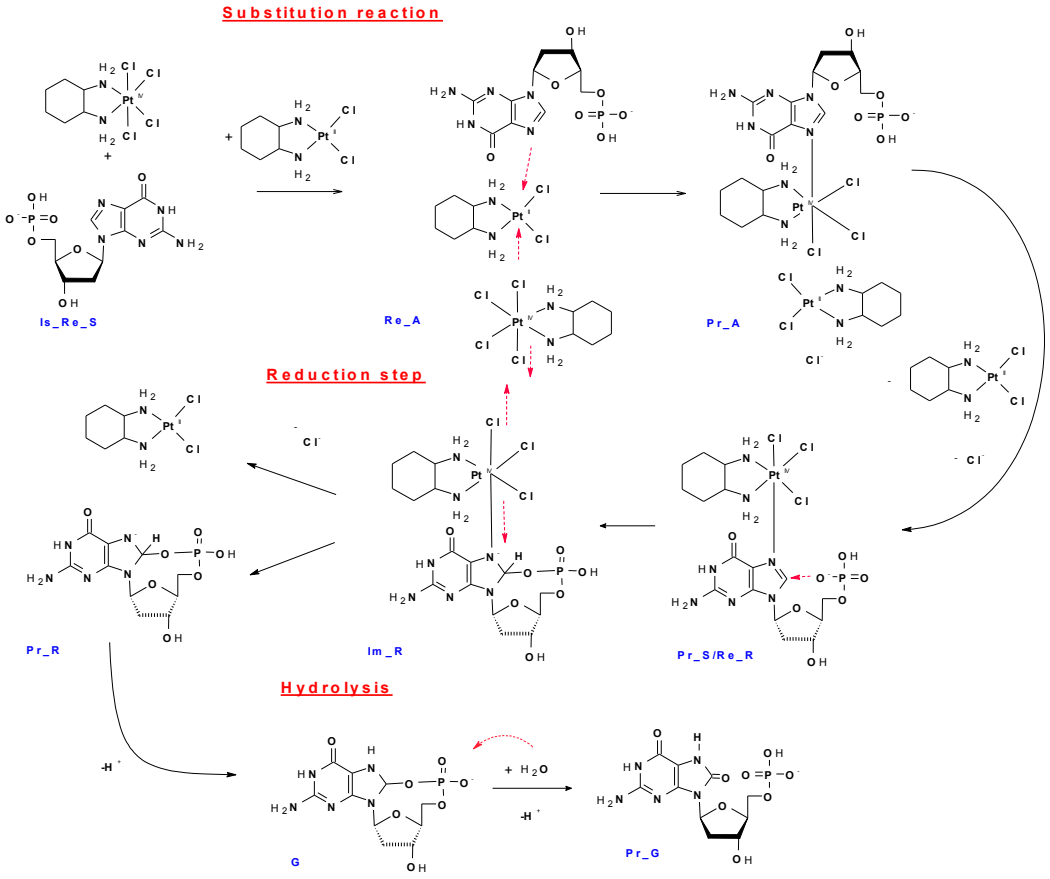

Figure 3: Reaction mechanism for the reduction of tetraplatin in the presence of 5'-dGMP. The reaction is divided into three steps – the substitution, the reduction step and the hydrolysis.

B3LYP-GD3BJ/6-31G(d)/C-PCM/Klamt level and SP calculations are performed at the B3LYP-GD3BJ/6-311++G(2df,2pd) in combination with DPCM/scaled-UAKS and IEF-PCM/scaled-UAKS solvation models in paper III and IV, respectively. Another difference in the used solvation models dwells in cavity scaling around oxygen atoms belonging to the phosphate group. The radii of the corresponding spheres are modified solely for the reduction step and the hydrolysis (within paper III) where phosphate group participates in bond formation or bond breaking. Consideration of Wertz's corrections in paper IV leads to physically more plausible association Gibbs free energies and also reaction Gibbs free energies for the reduction part and the hydrolysis where a number of molecules changes.

All three forms of dGMP - 5'-dGMP, 3'-dGMP, and c-dGMP - are considered. In the first reaction step, the substitution of a chloro ligand by dGMP occurs. The autocatalytic Basolo-Pearson mechanism[41] is employed for this initial part as it was suggested on the basis of experimental measurements.[38] Within this mechanism, the reaction is catalyzed by $PtCl_2$(dach) complex, the product of the reaction. In the reactant structure, the Pt(II) complex is located between dGMP and tetraplatin. Subsequently in the TS (cf. **Fig. 4**), one of axial chloro ligands of Pt(IV) complex is transferred between Pt atoms and simultaneously, the nitrogen N7 approaches to the originally Pt(II) atom whilst the second axial chloro ligand is being released.

The substitution reaction is strongly exergonic for 5'-dGMP and slightly exergonic for 3'-dGMP and c-dGMP. The association energies range from -12 to -9 kcal·mol^{-1} (with inclusion of Wertz's correction). If we focus on the kinetics, activation barriers are relatively low for this pathway, between 14 and 19 kcal·mol^{-1} (cf. **Table 1**). Nevertheless, a situation is not simple since the second pK_a value of the phosphate group is 6.29[158] and 6.14[159] for 5'-dGMP and 3'-dGMP, respectively. Hence, 5'-dGMP and 3'-dGMP occurs in two forms at neutral pH – with the singly

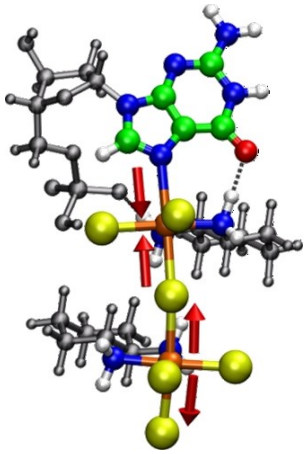

Figure 4: Optimized transition state within the autocatalytic Basolo-Pearson mechanism for the substitution reaction.

protonated and fully deprotonated phosphate group. Exactly, 16% (5'-dGMP) or 12% (3'-dGMP) of molecules possesses the singly protonated phosphate group on the basis of Henderson-Hasselbalch equation. In this case, use of the kinetic model for side reactions is necessary. On the other hand, at pH=8.3 corresponding to the experimental conditions[37,38] more than 99% of the dGMP molecules has fully deprotonated phosphate. When the effective rate constants are determined, fairly good agreement with experimental data is obtained (cf. **Table 1** for pH=8.3). Moreover, analogous energy profiles are constructed for $PtCl_4$(en) and $Pt(NH_3)_2Cl_4$ complexes.

In the following step, the reduction reaction, a nucleophilic attack of group on 5'-end of sugarphosphate to the position of carbon C8 occurs. This group represents the phosphate and hydroxyl in the 5'-dGMP and 3'-dGMP branches, respectively. In the case of the c-dGMP branch, no appropriate group for the nucleophilic attack is available and thus the reaction cannot proceed. Subsequently, the axial ligands are released along with reduction of the Pt complex (cf. **Fig. 3**). The step is completed by a proton transfer in the formed chelate structure of dGMP, namely, the transfer of H8 proton to the N7 position. In the 3'-dGMP branch, a situation is more complicated since the proton from the hydroxyl group must be transferred to an acceptor simultaneously with initial formation of the O-C8 bond. In this study, the phosphate group is chosen as that acceptor.

From the reaction profile depicted in **Fig. 5**, it follows that the initial nucleophilic attack (first activation barrier) represents the rate-determining step for the reduction part and simultaneously it is the highest barrier within the whole mechanism. A formed intermediate (Im_R in **Fig. 3**) has a very low stability since the subsequent activation barriers associated with the release of the axial ligands are less than 4 kcal·mol^{-1} high. In addition, the total decrease of reaction Gibbs free energy is exaggerated in paper III since Wertz's corrections are not employed. If the computational model from paper IV is used and singly protonated phosphate is

		$\Delta G^{\neq}$	**pH=7.0** k^{eff}	**pH=8.3** k^{eff}	$k_{Exp.}$	ΔG_{AS}	ΔG_r
	sp	14.7				-10.8	-13.0
5'-dGMP	fd	17.4	1.8E+01	2.1E+00	4.47	-11.7	-9.2
	sp	18.6				-9.8	-3.4
3'-dGMP	fd	16.4	5.1E+00	5.7E+00	7.25	-9.9	-3.7

Table 1: Thermodynamic and kinetic parameters for the substitution reaction. Effective rate constants k^{eff} (in $M^{-1}\cdot s^{-1}$) are evaluated at neutral pH and pH=8.3 corresponding to experimental conditions. Activation barriers $\Delta G^{\neq}$, association Gibbs free energies ΔG_{AS}, and reaction Gibbs free energies ΔG_r are in kcal·mol^{-1}. The abbreviations sp and fd denote the reaction of dGMP with singly protonated and fully deprotonated phosphate, respectively.

considered in the beginning of reduction step, the heights of activation barriers associated with the nucleophilic attack are closer to experimental results. However, the preference between 3'-dGMP (23.8 kcal·mol^{-1}) and 5'-dGMP branch (21.7 kcal·mol^{-1}) is reverse (cf. **Fig. 5**). The second activation barriers remain without changes. Inclusion of Wertz's correction leads to the fact that the reduction is endergonic (ΔG_r = 9.2 kcal·mol^{-1}) in the 5'-dGMP branch and slightly exergonic (ΔG_r = -1.4 kcal·mol^{-1}) in the 3'-dGMP branch.

The last step, the hydrolysis of the formed chelate structure of dGMP, is by six orders of magnitude faster in the 5'-dGMP branch. The reason is that much stronger ether linkage must be broken in the case of 3'dGMP chelate structure. In total, the hydrolysis represents a strongly exothermic process.

Considering Wertz's corrections, the total reaction is exothermic and exergonic, slightly more in 5'-dGMP branch (ΔG_r = -7.8 kcal·mol^{-1}) in comparison with 3'-dGMP branch (ΔG_r = -5.8 kcal·mol^{-1}). Since the substitution reaction occurs via Basolo-Pearson autocatalytic mechanism as was suggested, the studied reaction mechanism can be considered solely for Pt(IV) complexes with Cl^- or similarly small axial ligands.

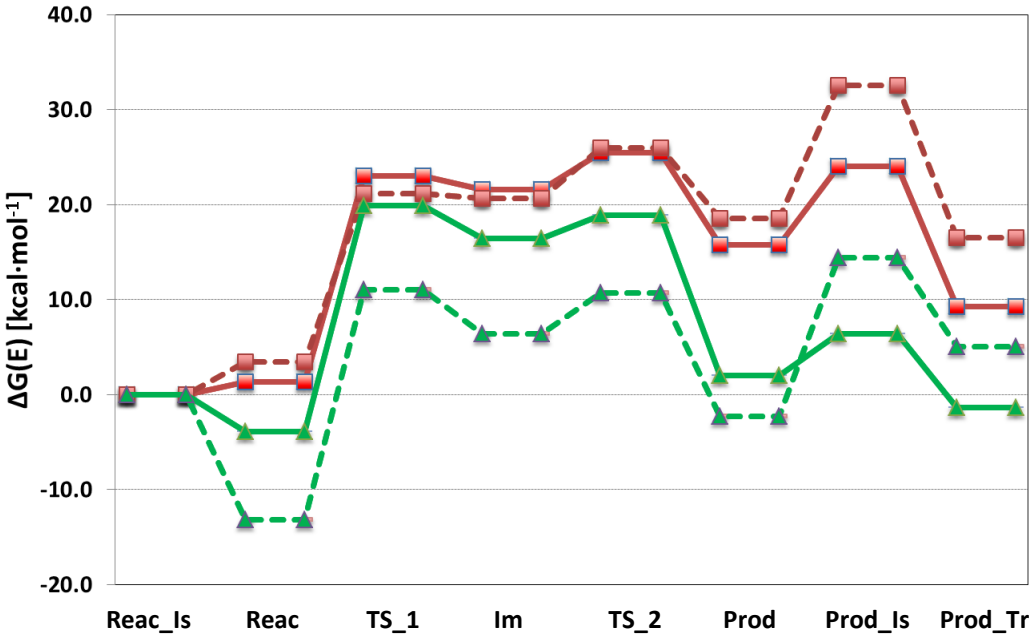

Figure 5: Energy profile of the reduction step. Red lines are associated with the 5'-dGMP branch and green lines with the 3'-dGMP branch. Full lines show the course of Gibbs free energy and dashed lines the course of electronic energy.

3.4 Interactions of Ascorbic Acid with Satraplatin and Its Trans Analogue JM576; DFT Computational Study[160]

Reduction of satraplatin cannot pass via previously described mechanism since its structure does not possess any bridging Cl atom. In fact, the equatorial chloro ligands have in their trans positions ligands (NH_3 or cha) which cannot be released easily. Therefore, another reaction mechanism must be considered in this case. On the basis of the experimental study of Lemma et al,[36] ascorbic acid is chosen as a reducing agent. Previously, this compound has been employed as a reducing agent in reduction of tetra chloro Pt(IV) complexes, both experimentally[161]

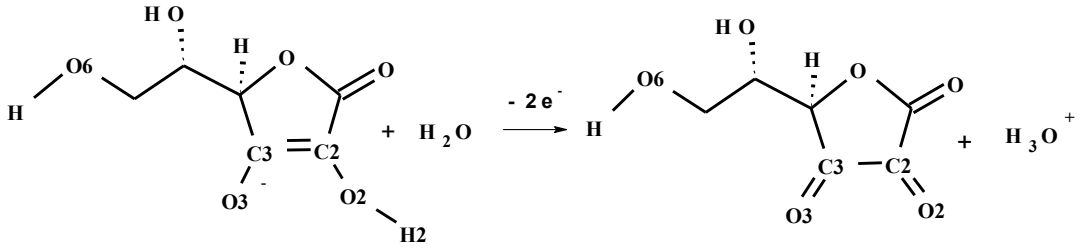

Figure 6: Oxidiation of ascorbic acid at the neutral pH.

and computationally.[162] As mentioned above, its standard reduction potential strongly depends on solution pH since it influences protonation of hydroxyl groups in the C2 and C3 positions where the oxidation of AA occurs. In fact, keto groups are present in the C2 and C3 positions in the oxidized form and protons from these positions must be released during the oxidations, as shown in **Fig. 6**. All three protonation states are taken into account in our calculation. Owing to this fact, two reaction mechanisms are employed – proton-assisted electron transfer (PAET) mechanism for the AAH_2 (fully protonated) and AAH^- (singly deprotonated) forms and outer sphere electron transfer (OSET) for the AA^{2-} (fully deprotonated) form. Within the former mechanism, one proton from the AA moiety is transferred to a aceteto ligand along with the electron transfer (cf. **Fig. 7**).

Geometries of structures involved in the regarded reaction mechanisms are optimized at the B3LYP-GD3BJ/6-31+G(d)/MWB60/C-PCM/Klamt level and SP calculations are carried out at the B3LYP-GD3BJ/6-311++G(2df,2pd)/MWB60/IEF-PCM/scaled-UAKS level.

The reduction for all three branches represents a strongly exergonic reaction when acetates are supposed to be acceptors of the released protons from AA. The reaction Gibbs free energy within the PAET mechanism is approximately -10.0 kcal·mol^{-1}, within OSET its value is much lower, -28.1 kcal·mol^{-1}. A similar picture is also obtained for kinetics. The Gibbs free energy barriers are 28.2 and 28.8 kcal·mol^{-1} in AAH_2 and AAH^- branches whilst the activation barrier for OSET

reaches the height of only 14.7 kcal·mol^{-1}. Since this leads to the difference of ten orders of magnitude between the rate constants in the PAET and OSET mechanisms, the kinetic model for side reactions must be employed to obtain an effective rate constant despite the very low concentration of the AA^{2-} protonation state. In fact, the difference in the rate constants outweighs the difference in the concentrations. The resulting effective rate constant of $2.6 \cdot 10^{-3}$ $M^{-1} \cdot s^{-1}$ is only by one order of magnitude lower than the corresponding experimental value ($5.1 \cdot 10^{-2}$ $M^{-1} \cdot s^{-1}$).

A cysteine molecule with deprotonated thiol group is added into vicinity of ascorbic acid in the AAH^- branch in order to facilitate the proton transfer from AAH^- and to effectively increase an amount of the fully deprotonated form. We denote this mechanism as base-assisted electron transfer and the obtained rate constant of $5.6 \cdot 10^{-3}$ $M^{-1} \cdot s^{-1}$ is twice higher than the previously determined effective rate constant. As a result, presence of an appropriate base in the vicinity of the considered system can make the reduction faster.

Besides satraplatin, we deal with reduction of its trans analogue JM576 (trans,trans,trans-[$PtCl_2(OAc)_2(cha)(NH_3)$]). For this complex, the chloro ligands are released. Similarly to satraplatin, the OSET mechanism is considered in the AAH^- and AA^{2-} branches, which leads to the effective rate constant by one order of magnitude higher in comparison with JM216.

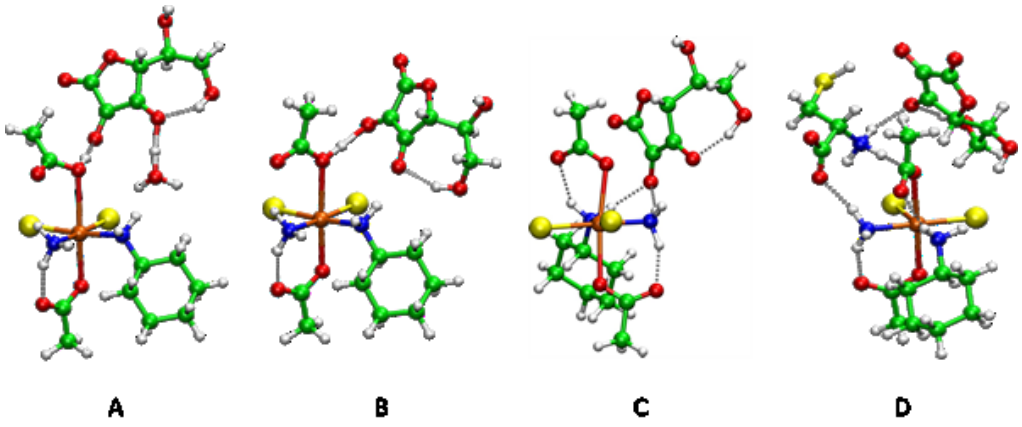

Figure 7: Structures of transition states in proton-assisted (in the AAH_2 (A) and AAH^- (B) branches) and outer sphere electron transfer mechanism (C). The last structure corresponds to TS within base-assisted electron transfer (D) mechanism, where also cysteine is considered.

3.5 Quantum-Mechanical Study of the N3 ↔ O2 Thymine Proton Transfer Including an Influence of Mg^{2+}, Zn^{2+}, and Hg^{2+} Metal Cations[163]

Here, we focus on the proton transfer (PT) from the N3 position to oxygen O2 in thymine. This process is investigated in isolated thymine and also in thymine with a coordinated metal cation to the O4 position. The divalent Mg^{2+}, Zn^{2+}, and Hg^{2+} cations, which are bare or hydrated in this study, are considered. Moreover, the PT assisted by a water molecule or a hexaaqua metal complex of the mentioned cations is taken into account, too. We called the former as a water-assisted PT and the latter as a metal-assisted PT. The course of the metal-assisted PT is depicted in **Fig. 8**.

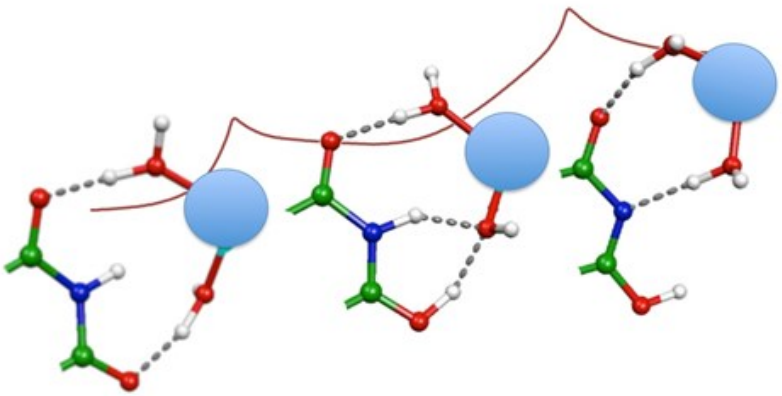

Figure 8: General scheme of the metal assisted N3 ↔ O2 proton transfer in the thymine.

Geometries corresponding to stationary points on the reaction coordinates are optimized at the B3LYP/6-31G(d) in the gas phase. Energy averaged quasirelativistic Stuttgart's pseudopotentials are employed in description of Zn (MWB10) and Hg (MWB60) atoms. For the catalyzed proton transfers, intrinsic reaction coordinates (IRC) are determined and changes of the electron density distribution along IRC are characterized using several analyses.

The N3↔O2 PT leads to the increase of the total Gibbs free energy of 20.9 $kcal \cdot mol^{-1}$ as can be expected. The PT in the isolated base is associated with a very high barrier of 51.1 $kcal \cdot mol^{-1}$ since the transferred proton is not stabilized in the TS structure. If the metal cation is coordinated to the O4 position, the total reaction becomes exergonic because of higher electrostatic stabilization of the enol structure. The bare cations cause the largest energy decrease which diminishes with the presence of aqua ligands thanks to shielding the cation charge. Nevertheless, the activation barriers remain very high in these reaction mechanisms, more than 37 $kcal \cdot mol^{-1}$.

When a water molecule is added in the proximity of nitrogen N3 and oxygen O2, the proton can be transferred via this molecule. In the TS structure, the system can be considered as ion-pair – H_3O^+ and thymine$^-$. Such stabilization of the proton leads to a significant decrease of the activation barrier to 22.4 kcal·mol^{-1}. Even a faster course of the PT can be achieved in the presence of hexaaqua complexes of the regarded divalent cations. In this case, the PT represents a two-step process separated by a metastable intermediate. The first PT occurs from an aqua ligand to oxygen O2 leading to formation of the intermediate: $[M(H_2O)_5OH]^+$ and thymine$^+$. Subsequently, the reaction proceeds with the second PT transfer from the nitrogen N3 to the hydroxo ligand. An ability of Zn^{2+} and Hg^{2+} cations to form dative bonds in contrast to the Mg^{2+} cations leads to the fact that the 'intermediate' is not stable within Mg-assisted proton transfer and only one TS structure is present in its course. The height of the corresponding activation barrier represents 8 kcal·mol^{-1}. In the remaining two cases, both barriers (associated with the first and second PT) are even lower, up to 4.5 kcal·mol^{-1}, when the faster course of the reaction corresponds to the Zn^{2+} cation (cf. **Fig. 9**). It is also shown that an influence of the spin-orbit interaction is negligible in the Hg^{2+} reaction.

Based on the REF analysis, the electronic rearrangement accompanied the first PT is a spontaneous process in all metal-assisted PT cases. On the contrary, the electronic changes associated with the second PT are non-spontaneous (cf. **Fig. 10**).

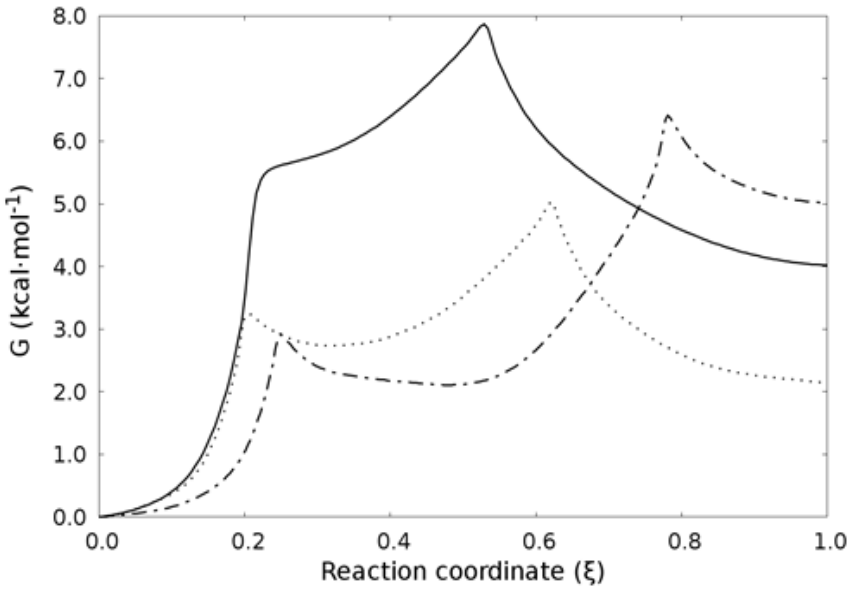

Figure 9: Gibbs free energy profiles for metal-assisted PT in the case of the Mg^{2+} (solid line), Zn^{2+} (dotted line), and Hg^{2+}(dash-dotted line) cations.

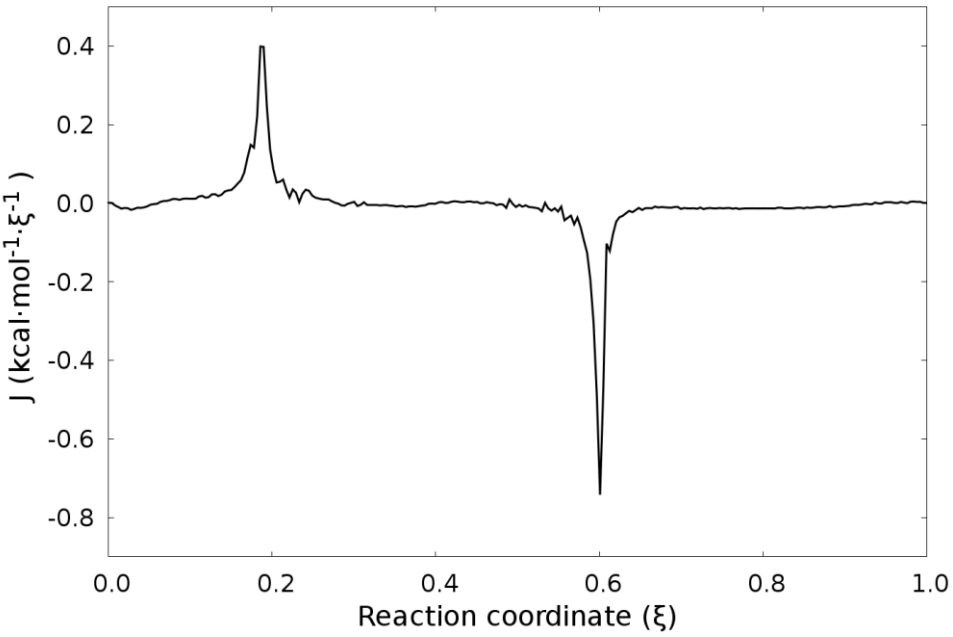

Figure 10: Course of the reaction electronic flux for the Zn-assisted PT mechanism.

3.6 QM/MM Umbrella sampling MD Study of Thymine Interaction with the Mercury Cation in Explicit Water Solution[164]

During formation of mercury linkages between thymine mismatches (T(N3)-Hg(II)-T(N3)), PTs play an important role. Within this study, we only focus on biding of the hydrated Hg^{2+} cation to N1-methylthymine. Since proton transfers can be strongly influenced by dynamic effects, we studied this process using the QM/MM umbrella sampling MD approach. We consider two protonation states of the cation first solvation shell, namely, the clusters $[Hg(H_2O)_5(OH)]^+$ and $Hg(H_2O)_4(OH)_2$ as a part of the inner (QM) region. N1-methylthymine represents the second part (cf. **Fig. 11**). In order to include explicit water solution, the outer (MM) region is formed by a water TIP3P box. The system is developed at the B3LYP-GD3BJ/LANL2DZ/AMBER level and parameters connected with the mercury cation are taken from our previous paper.[165] A final energy profile is constructed using the WHAM method. To increase accuracy, the FEP corrections obtained from energy differences between larger 6-31+G(d)/MWB60 and smaller LANL2DZ basis sets are included. For comparison also DFT calculations are performed with $[Hg(H_2O)_3(OH)]^+$ and $Hg(H_2O)_2(OH)_2$ complexes. Stationary structures along the reaction coordinate are optimized at the ω-B97XD/6-31+G(d)/CPCM/Klamt level

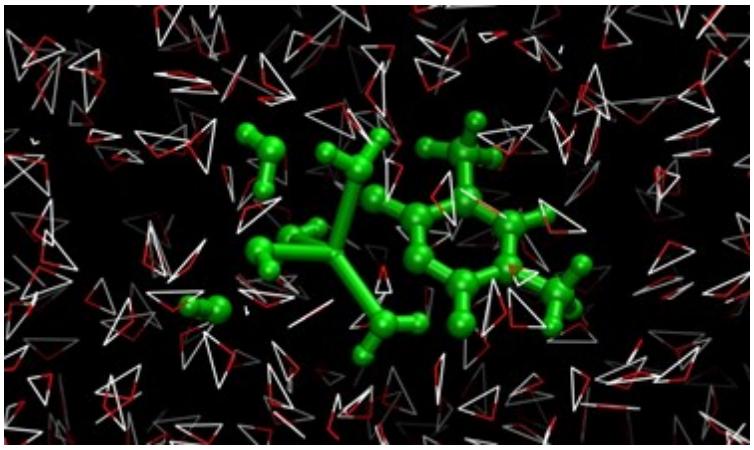

Figure 11: Partitioning of the system in the dihydroxo branch. The green-colored molecules represent the QM part.

and SP calculations are carried out at the B3LYP-GD3BJ/6-311+G(2df,2pd)/DPCM/scaled-UAKS level.

The reaction starts with a PT from the N3 position to a hydroxo ligand and subsequently the mercury cation binds to the free N3 position. When the monohydroxo complex is considered, the DFT calculations at the optimization level provide two activation barriers of 2.8 and 1.5 kcal·mol^{-1}. On the other hand, only one

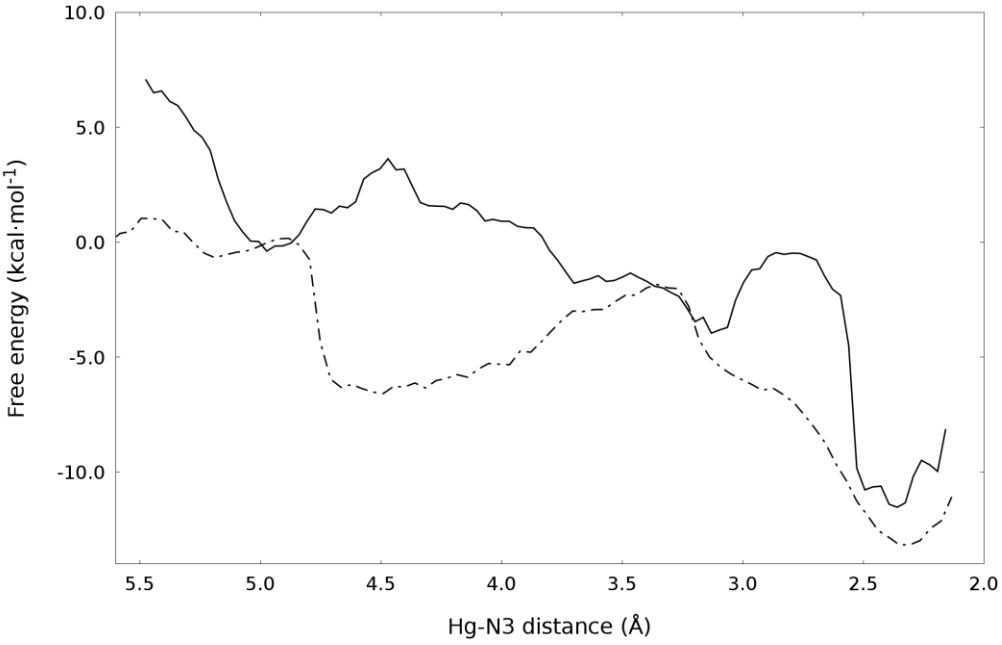

Figure 12: Free energy profiles determined using the QM/MM umbrella sampling MD simulations for the mono- (solid line) and dihydroxo (dash-dotted line) complex. The total profiles are constructed using the WHAM method and corrected by FEP correction determined at the B3LYP-GD3BJ/6-31+G(d)/MWB60 level.

activation barrier of 11.2 kcal·mol^{-1} associated with binding of the Hg^{2+} cation into the N3 position was determined in the dihydroxo branch. In total, the formation of the Hg-N3 bond represents a strongly exergonic process.

The constructed QM/MM free energy profiles (cf. **Fig. 12**) approximately correspond with DFT results when Wertz's corrections are included. The main difference between mono- and dihydroxo branches dwells in the fact that the Hg^{2+} cation is coordinated to the O4 position in the course of the reaction in the monohydroxo branch, while the dihydroxo complex is stabilized only via H-bonds as in the previous study.. Moreover, in the monohydroxo branch two free energy barriers are determined in contrast with one barrier in the dihyhroxo branch. Nevertheless, all activation barriers are lower than 5 kcal·mol^{-1}.

3.7 Estimation of Transition-Metal Empirical Parameters for Molecular Mechanical Force Fields[165]

A set of MM parameters for all the first row transition metals and Ru, Rh, Pt, and Hg metal cations is presented when their common oxidation states are taken into account e.g. II and IV for platinum. Due to large diversity of transition metal complexes where the partial charge of the central atom and binding energies of ligands strongly depend on all presented ligands, determination of MM parameters is not an easy task. In the literature, bonding and non-bonding parameters for individual complexes can be found[166,167] and also Lennard-Jones (LJ) parameters for groups of metal cations have been published.[168-172]

Here, we focus on determination of MM parameters, which are consistent with General Amber Force Field (GAFF). An estimation of bonding parameters, namely, parameters for bonds and bond angles is performed using small homoligated and neutral complexes. These complexes possess a common arrangement associated with the given metal cation, e.g. Pt(II) complexes are square planar, and a multiplicity corresponding to the lowest energy was always searched. Optimizations of the complexes and rigid potential energy surface scans are carried out at the ω-B97XD/6-31+G(d) level with employment of effective core potentials for the metal cations. At the same level, LJ parameters are determined. In this case, fitted potential energy surfaces are obtained by pulling a 'testing' molecule (H_2O, NH_3 and CH_4) around a neutral complex ($M(NH_3)_xCl_y$, $M(H_2O)_x(SH)_y$). All the resulting potential energy curves for the given cation are fitted together in order to obtain one pair of LJ parameters. For the sake of consistence with GAFF, the atomic RESP charges are determined for each complex individually.

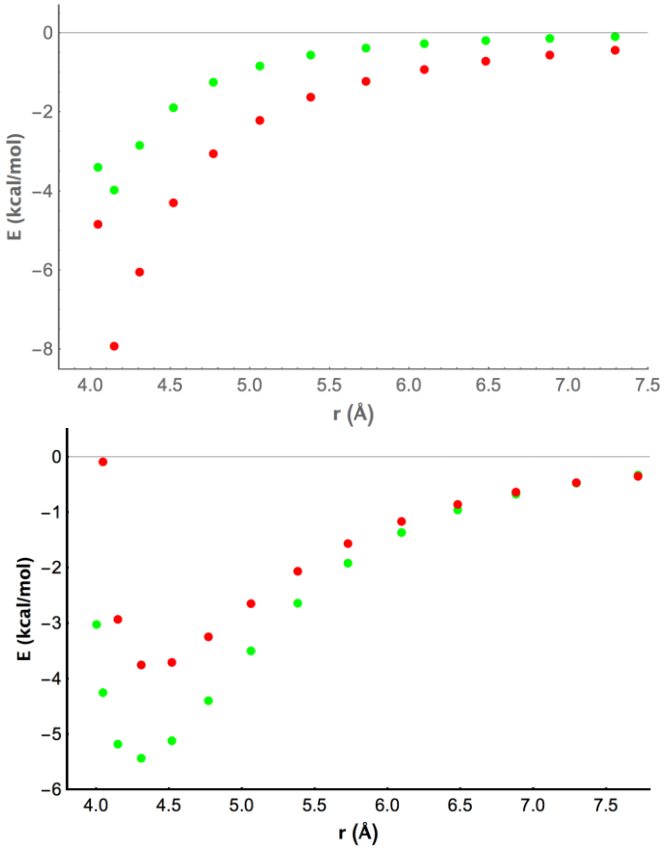

Figure 13: Comparison of QM rigid potential energy surface scans (green dots) with MM non-bonding potentials (red dots) for a) Hg(II), $Hg(CH_3COO)(CH_3CH_2)$/ethanol b) Pt(II), $PtCl(en)OH/(CH_3)_3N$ (en = ethylenediamine)

As verification of the calculated LJ parameters, differences between the QM PES and course of the MM non-bonding energy are analyzed for pulling larger 'testing' molecules as small organic compounds along experimentally studied complexes. In total, nineteen systems are considered, when at least qualitative agreement between the QM and MM profiles is almost achieved as it is depicted in **Fig. 13.**. Further, calculated radial distribution functions Pt-Ow and Pt-Hw for cisplatin (**Fig. 14a**) and its hydrated form $[Pt(NH_3)_2(H_2O)_2]^{2+}$ (**Fig. 14b**) in water solution are compared with clasical MD simulations of Lopes et al. for cisplatin (**Fig. 14c**) and ab-initio Car-Parinello MD results for $[Pt(H_2O)_4]^{2+}$ (**Fig. 14d**).[173-175] Relatively nice agreement in both cases of neutral and charged systems is obtained, since in Car-Parinello MD the first peak of Pt-Ow (oxygen of water) and Pt-Hw (hydrogen of water) radial distribution functions correspond to aqua ligands.

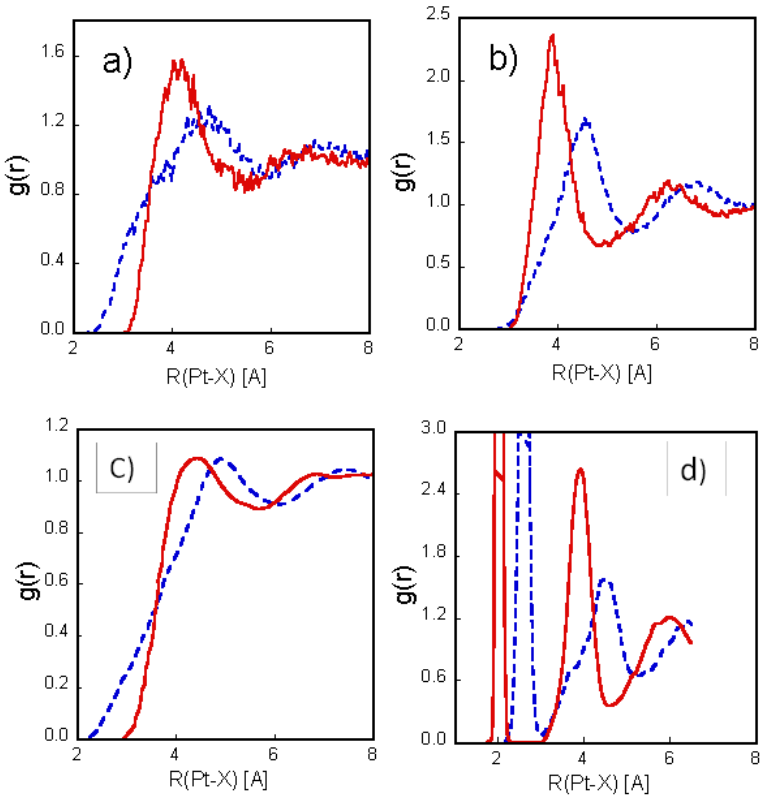

Figure 14: Pt-Ow (red solid lines) and Pt-Hw (blue dashed lines) radial distribution functions for a) $Pt(NH_3)_2Cl_2$ and b) $[Pt(NH_3)_2(H_2O)_2]^{2+}$ complexes obtained with parameters from our study, c) $Pt(NH_3)_2Cl_2$ complex determined by Lopes et al.[173] based on classical MD simulations and d) $[Pt(H_2O)_4]^{2+}$ obtained based on Car-Parinello MD simulations.[175]

4 Conclusions

Interaction of platinum and mercury complexes with small biomolecules as fragments of DNA or ascorbic acid is investigated in this thesis using QM and hybrid QM/MM methods. Within platinum compounds, we focus on prospective anticancer Pt(II) and Pt(IV) drugs. For cisplatin and its derivatives, rate constants for formation of a monoadduct of their semi- and fully-hydrated forms with guanine are determined. Owing to several limitations of approved Pt(II) drugs, new alternatives are searched and Pt(IV) complexes represent a promising possibility. Within proposed mechanism of action, reduction plays a crucial role. Here, reduction potentials for eleven Pt(IV) complexes are calculated and compared with available experimental data. It is shown that inclusion of Wertz's corrections and non-electrostatic solvation contributions is substantial for accuracy of calculated values. Influence of hydration of Pt(IV) complexes on the magnitude of the reduction potentials is also discussed. The detailed reaction mechanisms for reduction of tetraplatin in the presence of dGMP and satraplatin by ascorbic acid are determined at the DFT level. In order to obtain correct effective rate constants, the kinetic model for side reactions is taken into account considering different protonation states of reducing agents. It is shown that in the case of tetraplatin the initial substitution occurs via the autocatalytic Basolo-Pearson mechanism. The rate determining step represents the nucleophilic attack of oxygen on 5'-end of sugarphosphate to the C8 position of guanine in the following step. Although this mechanism is associated with low barriers, its applicability is limited only to complexes with chloro or similarly small axial ligands. As to satraplatin, proton-assisted and outer sphere electron transfer mechanisms are employed according to a protonation state of ascorbic acid. The rate of the reaction strongly depends on amount the fully deprotonated form of ascorbic acid whose relative concentration is very low at neutral pH. It is also ascertained that occurrence of an appropriate base in the proximity of ascorbic acid can make the reaction faster. Obtained kinetic parameters for both studied systems – tetraplatin and satraplatin - are in good agreement with experimental data.

Proton transfers are of great importance in the case of formation of mercury linkages between thymine mismatches. The N3↔O2 proton transfer in thymine is described in the presence of hexaaqua metal complexes. This arrangement significantly facilitates the PT which becomes a two-step process in this case. A PT from the aqua ligand to oxygen O2 initially occurs and subsequently the proton from nitrogen N3 is transferred to the previously formed hydroxo ligand. The first PT is accompanied by a spontaneous rearrangement of the electron density in contrast to the second one. Later, binding of the hydrated Hg^{2+} cation in the form of a mono- or dihydroxo complex to N1-methylthymine is investigated. The QM/MM umbrella

sampling method MD simulations indicate that the monohydroxo complex is stabilized by coordination of the Hg^{2+} cation to oxygen O4 in contrast to the dihydroxo complex. Obtained free energy profiles are compared with static DFT calculations. Necessity of MM parameters for metal cations in QM/MM simulations leads us to their estimation for the all the first row transition metal, Ru, Rh, Pt, and Hg cations based on DFT calculations.

In summary, this thesis provides a comprehensive view on reduction of Pt(IV) complexes and proton transfers in thymine under the influence of hydrated metal cations.

References:

(1) Rosenberg, B.; Van Camp, L.; Krigas, T. *Nature* **1965**, *205*, 698.

(2) *Cisplatin: Chemistry and Biochemistry of a Leading Anticancer Drug*; Lippert, B., Ed.; Wiley-VCH Verlag GmbH: Wienheim, Germany, 1999.

(3) Wheate, N. J.; Walker, S.; Craig, G. E.; Oun, R. *Dalton Transactions* **2010**, *39* 8113.

(4) Burda, J. V.; Zeizinger, M.; Leszczynski, J. *J. Chem. Phys.* **2004**, *120*, 1253.

(5) Berges, J.; Caillet, J.; Langlet, J.; Kozelka, J. *Chem.Phys. Lett.* **2001**, *344*, 573.

(6) Miller, S. E.; Gerard, K. J.; House, D. A. *Inorg. Chim. Acta* **1991**, *190*, 135

(7) Romero-Canelon, I.; Sadler, P. J. *Inorg. Chem.* **2013**, *52*, 12276.

(8) Sinani, D.; Adle, D. J.; Kim, H.; Lee, J. *Journal of Biological Chemistry* **2007**, *282*, 26775.

(9) Safaei, R.; Holzer, A. K.; Katano, K.; Samimi, G.; Howell, S. B. *Journal of Inorganic Biochemistry* **2004**, *98*, 1607.

(10) Gkionis, K.; Mutter, S. T.; Platts, J. A. *RSC Advances* **2013**, *3*, 4066.

(11) Robertazzi, A.; Platts, J. A. *Chem. Eur. J.* **2006**, *12*, 5747.

(12) Baik, M.-H.; Friesner, R. A.; Lippard, S. J. *J. Am. Chem. Soc.* **2003**, *125*, 14082.

(13) Raber, J.; Zhu, C.; Eriksson, L. A. *J. Phys. Chem. B* **2005**, *109*, 11006.

(14) Pavelka, M.; Burda, J. V. *J. Mol. Model.* **2007**, *13*, 367.

(15) Burda, J. V.; Sponer, J.; Leszczynski, J. *Journal of Biological Inorganic Chemistry* **2000**, *5*, 178.

(16) Zeizinger, M.; Burda, J. V.; Leszczynski, J. *Phys. Chem. Chem. Phys.* **2004**, *6*, 3585.

(17) Perez, R. P. *Eur. J. Cancer* **1998**, *34*, 1535.

(18) Canetta, R.; Rozencweig, M.; Carter, S. K. *Cancer Treat Rev.* **1985**, *12*, 125.

(19) Knox, R. J.; Friedlos, F.; Lydall, D. A.; Roberts, J. J. *Cancer Research* **1986**, *46*, 1972.

(20) Spingler, B.; Whittington, D. A.; Lippard, S. J. *Inorg. Chem.* **2001**, *40*, 5596.

(21) Ehrsson, H.; Wallin, I.; Yachnin, J. *Med. Oncol.* **2002**, *19*, 261.

(22) Chval, Z.; Kabelac, M.; Burda, J. V. *Inorganic Chemistry* **2013**, *52*, 5801.

(23) Wexselblatt, E.; Gibson, D. *Journal of Inorganic Biochemistry* **2012**, *117*, 220.

(24) Raynaud, F. I.; Mistry, P.; Donaghue, A.; Poon, G. K.; Kelland, L. R.; Barnard, C. F. J.; Murrer, B. A.; Harrap, K. R. *Cancer Chemotherapy and Pharmacology* **1996**, *38*, 155.

(25) Bradáč, O.; Zimmermann, T.; Burda, J. V. *J. Mol. Model.* **2013**, *19*, 1669.

(26) Nemirovski, A.; Vinograd, I.; Takrouri, K.; Mijovilovich, A.; Rompel, A.; Gibson, D. *Chemical Communications* **2010**, *46*, 1842.

(27) Ravera, M.; Gabano, E.; Zanellato, I.; Bonarrigo, I.; Escribano, E.; Moreno, V.; Font-Bardia, M.; Calvet, T.; Osella, D. *Dalton Transactions* **2012**, *41*, 3313.

(28) Dhar, S.; Lippard, S. J. *Proceedings of the National Academy of Sciences* **2009**, *106*, 22199.

(29) Ang, W. H.; Khalaila, I.; Allardyce, C. S.; Juillerat-Jeanneret, L.; Dyson, P. J. *Journal of the American Chemical Society* **2005**, *127*, 1382.

(30) Barnes, K. R.; Kutikov, A.; Lippard, S. J. *Chemistry & Biology* **2004**, *11*, 557.

(31) Choi, S.; Filotto, C.; Bisanzo, M.; Delaney, S.; Lagasee, D.; Whitworth, J. L.; Jusko, A.; Li, C.; Wood, N. A.; Willingham, J.; Schwenker, A.; Spaulding, K. *Inorg. Chem.* **1998**, *37*, 2500.

(32) Hall, M. D.; Foran, G. J.; Zhang, M.; Beale, P. J.; Hambley, T. W. *Journal of the American Chemical Society* **2003**, *125*, 7524.

(33) Ellis, L.; Er, H.; Hambley, T. *Australian Journal of Chemistry* **1995**, *48*, 793.

(34) Wilson, J. J.; Lippard, S. J. *Inorganic Chemistry* **2011**, *50*, 3103.

(35) McCormick, M. C.; Keijzer, K.; Polavarapu, A.; Schultz, F. A.; Baik, M.-H. *Journal of the American Chemical Society* **2014**, *136*, 8992.

(36) Lemma, K.; Sargeson, A. M.; Elding, L. I. *Journal of the Chemical Society, Dalton Transactions* **2000**, 1167.

(37) Choi, S.; Vastag, L.; Leung, C.-H.; Beard, A. M.; Knowles, D. E.; Larrabee, J. A. *Inorg. Chem.* **2006**, *45*, 10108.

(38) Choi, S.; Vastag, L.; Larrabee, Y. C.; Personick, M. L.; Schaberg, K. B.; Fowler, B. J.; Sandwick, R. K.; Rawji, G. *Inorg. Chem.* **2008**, *47*, 1352.

(39) Choi, S.; Personick, M. L.; Bogart, J. A.; Ryu, D.; Redman, R. M.; Laryea-Walker, E. *Dalton Transactions* **2011**, *40*, 2888.

(40) Choi, S.; Cooley, R. B.; Hakemian, A. S.; Larrabee, Y. C.; Bunt, R. C.; Maupas, S. D.; Muller, J. G.; Burrows, C. J. *J. Am. Chem. Soc.* **2004**, *126*, 591.

(41) Basolo, F.; Pearson, R. G. In *Advances in Inorganic Chemistry and Radiochemistry*; Emeleus, H. J., Sharpe, A. G., Eds.; Academic Press: 1961; Vol. Volume 3, p 1.

(42) O'Rourke, T. J.; Weiss, G. R.; New, P.; Burris, H. A. I.; Rodriguez, G.; Eckhardt, J.; Hardy, J.; Kuhn, J. G.; Fields, S.; Clark, G. M.; Von Hoff, D. D. *Anti-Cancer Drugs* **1994**, *5*, 520.

(43) Bhargava, A.; Vaishampayan, U. N. *Expert Opinion on Investigational Drugs* **2009**, *18*, 1787.

(44) Akshintala, S.; Marcus, L.; Warren, K. E.; Murphy, R. F.; Sissung, T. M.; Srivastava, A.; Goodspeed, W. J.; Goodwin, A.; Brewer, C. C.; Zalewski, C.; King, K. A.; Kim, A.; Figg, W. D.; Widemann, B. C. *Pediatric Blood & Cancer* **2015**, *62*, 603.

(45) Löwdin, P.-O. *Reviews of Modern Physics* **1963**, *35*, 724.

(46) Wang, W.; Hellinga, H. W.; Beese, L. S. *Proceedings of the National Academy of Sciences of the United States of America* **2011**, *108*, 17644.

(47) Florián, J.; Hrouda, V.; Hobza, P. *J. Am. Chem. Soc.* **1994**, *116*, 1457.

(48) Hrouda, V.; Florián, J.; Polášek, M.; Hobza, P. *J. Phys. Chem.* **1994**, *98*, 4742.

(49) Cerón-Carrasco, J. P.; Requena, A.; Michaux, C.; Perpète, E. A.; Jacquemin, D. *The Journal of Physical Chemistry A* **2009**, *113*, 7892.

(50) Jacquemin, D.; Zúñiga, J.; Requena, A.; Céron-Carrasco, J. P. *Accounts of Chemical Research* **2014**, *47*, 2467.

(51) Herrera, B.; Toro-Labbé, A. *J. Phys. Chem. A* **2007**, *111*, 5921.

(52) Kabeláč, M.; Hobza, P. *J. Phys. Chem. B* **2006**, *110*, 14515.

(53) Šebera, J.; Burda, J.; Straka, M.; Ono, A.; Kojima, C.; Tanaka, Y.; Sychrovský, V. *Chem. – Eur. J.* **2013**, *19*, 9884.

(54) Megger, D. A.; Müller, J. *Nucleosides, Nucleotides and Nucleic Acids* **2010**, *29*, 27.

(55) Tanaka, Y.; Oda, S.; Yamaguchi, H.; Kondo, Y.; Kojima, C.; Ono, A. *J. Am. Chem. Soc.* **2007**, *129*, 244.

(56) Kondo, J.; Yamada, T.; Hirose, C.; Okamoto, I.; Tanaka, Y.; Ono, A. *Angewandte Chemie International Edition* **2014**, *53*, 2385.

(57) Torigoe, H.; Ono, A.; Kozasa, T. *Chem. – Eur. J.* **2010**, *16*, 13218.

(58) Yamaguchi, H.; Šebera, J.; Kondo, J.; Oda, S.; Komuro, T.; Kawamura, T.; Daraku, T.; Kondo, Y.; Okamoto, I.; Ono, A.; Burda, J. V.; Kojima, C.; Sychrovský, V.; Tanaka, Y. *Nucleic Acid Res.* **2014**, *42*, 4094.

(59) Benda, L.; Straka, M.; Tanaka, Y.; Sychrovsky, V. *Phys. Chem. Chem. Phys.* **2011**, *13*, 100.

(60) Jones, J. E. *Proceedings of the Royal Society of London. Series A* **1924**, *106*, 463.

(61) Swope, W. C.; Andersen, H. C.; Berens, P. H.; Wilson, K. R. *The Journal of Chemical Physics* **1982**, *76*, 637.
(62) Verlet, L. *Phys. Rev.* **1967**, *159*, 98.
(63) Berendsen, H. J. C.; Postma, J. P. M.; van Gunsteren, W. F.; DiNola, A.; Haak, J. R. *J. Chem. Phys.* **1984**, *81*, 3684.
(64) Born, M.; Oppenheimer, R. *Annalen der Physik* **1927**, *389*, 457.
(65) Piela, L. *Ideas of Quantum Chemistry*; Elsevier Science, 2006.
(66) Pulay, P. *Molecular Physics* **1969**, *17*, 197.
(67) Schlegel, H. B. *Wiley Interdisciplinary Reviews: Computational Molecular Science* **2011**, *1*, 790.
(68) Fletcher, R.; Reeves, C. M. *The Computer Journal* **1964**, *7*, 149.
(69) Polak, B.; Ribiere, G. *Rev. Fr. Inform. Rech. Oper.* **1969**, *16*, 35.
(70) Francl, M. M.; Pietro, W. J.; Hehre, W. J.; Binkley, J. S.; Gordon, M. S.; DeFrees, D. J.; Pople, J. A. *The Journal of Chemical Physics* **1982**, *77*, 3654.
(71) Szabo, A.; Ostlund, N. S. *Modern Quantum Chem.: Introduction to Advanced Electronic Structure Theory*; Dover Publications, Inc.: Mineola, New York, 1996.
(72) Roothaan, C. C. J. *Reviews of Modern Physics* **1951**, *23*, 69.
(73) Pople, J. A.; Nesbet, R. K. *The Journal of Chemical Physics* **1954**, *22*, 571.
(74) Moller, C.; Plesset, M. S. *Physical Review* **1934**, *46*, 618.
(75) Čížek, J. *The Journal of Chemical Physics* **1966**, *45*, 4256.
(76) Helgaker, T.; Jorgensen, P.; Olsen, J. *Molecular Electronic-Structure Theory*; Wiley, 2014.
(77) Hohenberg, P.; Kohn, W. *Physical Review* **1964**, *136*, B864.
(78) Levy, M. *Proceedings of the National Academy of Sciences* **1979**, *76*, 6062.
(79) Lieb, E. H. *International Journal of Quantum Chemistry* **1983**, *24*, 243.
(80) Kato, T. *Communications on Pure and Applied Mathematics* **1957**, *10*, 151.
(81) Parr, R. G.; Yang, W. *Density Functional Theory of Atoms and Molecules*; Oxford University Press: Oxford, 1989.
(82) Kohn, W.; Sham, L. J. *Physical Review* **1965**, *140*, A1133.
(83) Parr, R. G.; Yang, W. *Density-Functional Theory of Atoms and Molecules*; Oxford University Press, 1989.
(84) Barth, U. v.; Hedin, L. *Journal of Physics C: Solid State Physics* **1972**, *5*, 1629.
(85) Vosko, S. H.; Wilk, L.; Nusair, M. *Canadian Journal of Physics* **1980**, *58*, 1200.
(86) Becke, A. D. *Physical Review A* **1988**, *38*, 3098.
(87) Tsuneda, T. *Density Functional Theory in Quantum Chemistry*; Springer Japan, 2014.
(88) Colle, R.; Salvetti, O. *Theoretica chimica acta* **1975**, *37*, 329.
(89) Lee, C.; Yang, W.; Parr, R. G. *Phys. Review B* **1988**, *37*, 785.
(90) Tsuneda, T.; Suzumura, T.; Hirao, K. *The Journal of Chemical Physics* **1999**, *110*, 10664.
(91) Perdew, J. P.; Burke, K.; Ernzerhof, M. *Physical Review Letters* **1997**, *78*, 1396.
(92) Tao, J.; Perdew, J. P.; Staroverov, V. N.; Scuseria, G. E. *Physical Review Letters* **2003**, *91*, 146401.
(93) Zhao, Y.; Truhlar, D. G. *The Journal of Chemical Physics* **2006**, *125*, 194101.
(94) Peverati, R.; Truhlar, D. G. *The Journal of Physical Chemistry Letters* **2012**, *3*, 117.
(95) Peverati, R.; Truhlar, D. G. *Physical Chemistry Chemical Physics* **2012**, *14*, 13171.
(96) Becke, A. D. *The Journal of Chemical Physics* **1993**, *98*, 5648.
(97) Grimme, S.; Ehrlich, S.; Goerigk, L. *J. Comp. Chem.* **2011**, *32*, 1456.

(98) Lenthe, E. v.; Baerends, E. J.; Snijders, J. G. *The Journal of Chemical Physics* **1993**, *99*, 4597.
(99) van Lenthe, E.; Snijders, J. G.; Baerends, E. J. *J. Chem. Phys.* **1996**, *105*, 6505.
(100) Dyall, K. G. *Journal of Chemical Information and Computer Sciences* **2001**, *41*, 30.
(101) Phillips, J. C.; Kleinman, L. *Physical Review* **1959**, *116*, 287.
(102) Andrae, D.; Haussermann, U.; Dolg, M.; Stoll, H.; Preuss, H. *Theor. Chim. Acta* **1990**, *77*, 123.
(103) Bakowies, D.; Thiel, W. *J. Phys. Chem.* **1996**, *100*, 10580.
(104) Warshel, A.; Levitt, M. *Journal of Molecular Biology* **1976**, *103*, 227.
(105) Singh, U. C.; Kollman, P. A. *Journal of Computational Chemistry* **1986**, *7*, 718.
(106) Field, M. J.; Bash, P. A.; Karplus, M. *Journal of Computational Chemistry* **1990**, *11*, 700.
(107) Senn, H. M.; Thiel, W. In *Atomistic Approaches in Modern Biology: From Quantum Chemistry to Molecular Simulations*; Reiher, M., Ed.; Springer Berlin Heidelberg: Berlin, Heidelberg, 2007, p 173.
(108) Théry, V.; Rinaldi, D.; Rivail, J.-L.; Maigret, B.; Ferenczy, G. G. *Journal of Computational Chemistry* **1994**, *15*, 269.
(109) Tomasi, J.; Mennucci, B.; Cammi, R. *Chemical Reviews* **2005**, *105*, 2999.
(110) Miertus, S.; Scrocco, E.; Tomasi, J. *Chem. Phys.* **1981**, *55*, 117.
(111) Cossi, M.; Barone, V. *The Journal of Chemical Physics* **1998**, *109*, 6246.
(112) Cancès, E.; Mennucci, B.; Tomasi, J. *The Journal of Chemical Physics* **1997**, *107*, 3032.
(113) Klamt, A.; Schuurmann, G. *J Chem. Soc.-Perkin Transactions 2* **1993**, 799.
(114) Rappé, A. K.; Casewit, C. J.; Colwell, K. S.; Goddard III, W. A.; Skiff, W. M. *J. Am. Chem. Soc.* **1992**, *114*, 10024.
(115) Barone, V.; Cossi, M.; Tomasi, J. *J. Chem. Phys.* **1997**, *107*, 3210.
(116) Orozco, M.; Luque, F. J. *Chem. Phys.* **1994**, *182*, 237.
(117) Zimmermann, T.; Burda, J. V. *J. Chem. Phys.* **2009**, *131*, 135101.
(118) Wertz, D. H. *J. Am.chem. Soc.* **1980**, *102*, 5316.
(119) Cheng, M.-J.; Nielsen, R. J.; Goddard Iii, W. A. *Chemical Communications* **2014**, *50*, 10994.
(120) Swendsen, R. H.; Wang, J.-S. *Physical Review Letters* **1986**, *57*, 2607.
(121) Laio, A.; Parrinello, M. *Proceedings of the National Academy of Sciences* **2002**, *99*, 12562.
(122) Torrie, G. M.; Valleau, J. P. *Journal of Computational Physics* **1977**, *23*, 187.
(123) Bartels, C.; Karplus, M. *The Journal of Physical Chemistry B* **1998**, *102*, 865.
(124) Souaille, M.; Roux, B. *Comput. Phys. Commun.* **2001**, *135*, 40.
(125) Kumar, S.; Rosenberg, J. M.; Bouzida, D.; Swendsen, R. H.; Kollman, P. A. *J. Comput. Chem.* **1992**, *13*, 1011.
(126) Kästner, J.; Thiel, W. *The Journal of Chemical Physics* **2005**, *123*, 144104.
(127) Kästner, J.; Thiel, W. *The Journal of Chemical Physics* **2006**, *124*, 234106.
(128) Eyring, H. *J. Chem. Phys.* **1935**, *3*, 107.
(129) Bader, R. F. W. *Atoms in Molecules: A Quantum Theory*; Oxford Univ. Press: Oxford, 1990.
(130) Foster, J. P.; Weinhold, F. *J. Am. Chem. Soc.* **1980**, *102*, 7211.
(131) Reed, A. E.; Weinhold, F. *J. Chem. Phys.* **1983**, *78*, 4066.
(132) Reed, A. E.; Weinstock, R. B.; Weinhold, F. *J. Chem. Phys.* **1985**, *83*, 735.

(133) Coppens, P.; Hall, M. B.; Society, A. C. *Electron distributions and the chemical bond*; Plenum Press, 1982.
(134) Kitaura, K.; Morokuma, K. *Int. J. Quantum Chem.* **1976**, *10*, 325.
(135) Jeziorski, B.; Moszynski, R.; Szalewicz, K. *Chemical Reviews* **1994**, *94*, 1887.
(136) Ziegler, T.; Rauk, A. *Theor. Chim. Acta* **1977**, *46*, 1.
(137) Mitoraj, M.; Michalak, A.; Ziegler, T. *J. Chem. Theor. Comput.* **2009**, *5*, 962.
(138) Michalak, A.; Mitoraj, M.; Ziegler, T. *J. Phys. Chem. A* **2008**, *112*, 1933.
(139) Reed, A. E.; Weinstock, R. B.; Weinhold, F. *J. Chem. Phys.* **1985**, *83*, 735.
(140) Flores-Morales, P.; Gutiérrez-Oliva, S.; Silva, E.; Toro-Labbé, A. *Journal of Molecular Structure: THEOCHEM* **2010**, *943*, 121.
(141) Šebesta, F.; Burda, J. V. *Journal of Inorganic Biochemistry* **2017**, *172*, 100.
(142) Boys, S. F.; Bernardi, F. *Mol. Phys.* **1970**, *19*, 553.
(143) Johnson, N. P.; Hoeschele, J. D.; Rahn, R. O. *Chemico-Biological Interactions* **1980**, *30*, 151.
(144) Bernges, F.; Doerner, G.; Holler, E. *Eur. J. Biochem.* **1990**, *191*, 743.
(145) Legendre, F.; Chottard, J.-C. In *Cisplatin*; Lippert, B., Ed.; Wiley-VCH: Weinheim, 1999.
(146) Brabec, V.; Kasparkova, J. *Drug Resistance Updates* **2005**, *8*, 131.
(147) Najajreh, Y.; Kasparkova, J.; Marini, V.; Gibson, D.; Brabec, V. *J Biological Inorg. Chem.* **2005**, *10*, 722.
(148) Šebesta, F.; Baxová, K.; Burda, J. V. *Inorganic Chemistry*, submitted.
(149) Isse, A. A.; Gennaro, A. *The Journal of Physical Chemistry B* **2010**, *114*, 7894.
(150) Becke, A. D. *J. Phys. Chem.* **1993**, *98*, 5648.
(151) Chai, J.-D.; Head-Gordon, M. *Phys. Chem. Chem. Phys.* **2008**, *10*, 6615.
(152) Adamo, C.; Barone, V. *The Journal of Chemical Physics* **1999**, *110*, 6158.
(153) Ernzerhof, M.; Perdew, J. P. *The Journal of Chemical Physics* **1998**, *109*, 3313.
(154) Staroverov, V. N.; Scuseria, G. E.; Tao, J.; Perdew, J. P. *The Journal of Chemical Physics* **2004**, *121*, 11507.
(155) Grimme, S.; Antony, J.; Ehrlich, S.; Krieg, H. *The Journal of Chemical Physics* **2010**, *132*, 154104.
(156) Šebesta, F.; Burda, J. V. *The Journal of Physical Chemistry B* **2017**, *121*, 4400.
(157) Šebesta, F.; Burda, J. V. *Chem. Eur. J.* **2016**, *22*, 1037.
(158) Song, B.; Sigel, H. *Inorg. Chem.* **1998**, *37*, 2066.
(159) Knobloch, B.; Sigel, H.; Okruszek, A.; Sigel, R. K. O. *Organic Biomol. Chem.* **2006**, *4*, 1085.
(160) Šebesta, F.; Burda, J. V. *Inorganic Chemistry* **2017**, submitted.
(161) Dong, J.; Ren, Y.; Huo, S.; Shen, S.; Xu, J.; Tian, H.; Shi, T. *Dalton Transactions* **2016**, *45*, 11326.
(162) Ejehi, Z.; Ariafard, A. *Chemical Communications* **2017**, *53*, 1413.
(163) Šebesta, F.; Brela, M. Z.; Diaz, S.; Miranda, S.; Murray, J. S.; Gutiérrez-Oliva, S.; Toro-Labbé, A.; Michalak, A.; Burda, J. V. *Journal of Computational Chemistry* **2017**, in print.
(164) Šebesta, F.; Burda, J. V. *J. Phys. Chem.* **2017**, submitted.
(165) Šebesta, F.; Sláma, V.; Melcr, J.; Futera, Z.; Burda, J. V. *J. Chem. Theor. Comput.* **2016**, *12*, 3681.
(166) Yao, S.; Plastaras, J. P.; Marzilli, L. G. *Inorg. Chem.* **1994**, *33*, 6061.
(167) Lienke, A.; Klatt, G.; Robinson, D. J.; Koch, K. R.; K.J., N. *Inorg. Chem.* **2001**, *40*, 2352.
(168) Li, X.; Tu, Y.; Tian, H.; Ågren, H. *J. Chem. Phys.* **2010**, *132*, 104505.
(169) Zhao, L.; Liu, L.; Sun, H. *J. Phys. Chem. C* **2007**, *111*, 10610.

(170) Torras, J.; Alemán, C. *J. Phys. Chem. B* **2013**, *117*, 10513.

(171) Bernardes, C. E. S.; Canongia Lopes, J. N.; Minas da Piedade, M. E. *J. Phys. Chem. A* **2013**, *117*, 11107.

(172) Heinz, H.; Vaia, R. A.; Farmer, B. L.; Naik, R. R. *J. Phys. Chem. C* **2008**, *112*, 17281.

(173) Lopes, J. F.; Menezes, V. S. D.; Duarte, H. A.; Rocha, W. R.; De Almeida, W. B.; Dos Santos, H. F. *J Physical Chem. B* **2006**, *110*, 12047.

(174) Melchior, A.; Martínez, J. M.; Pappalardo, R. R.; Marcos, E. S. *J. Chem. Theory Comput.* **2013**, *9*, 4562−4573.

(175) Beret, E. C.; Martinez, J. M.; Pappalardo, R. R.; Marcos, E. S.; Doltsinis, N. L.; Marx, D. *J. Chem. Theory Comput.* **2008**, *4*, 2108.

List of Tables

List of Figures

5 List of publications

I. Šebesta, F.; Burda, J.V.: Study on electronic properties, thermodynamic and kinetic parameters of the selected platinum(II) derivatives interacting with guanine. *J. Inorg. Biochem.*, **2017,** 172, 100.

II. Šebesta, F.; Baxová K.; Burda, J.V.: Redox Potentials for Tetraplatin, Satraplatin, Its Derivatives and Ascorbic Acid; Computational Study. (submitted to Inorganic Chemistry)

III. Šebesta, F. and Burda, J. V.: Reduction process of Tetraplatin in presence of dGMP; Computational DFT Study. *Chemistry – A European Journal* **2016**, *22*, 1037.

IV. Šebesta, F.; Burda, J.V.: Side Reactions with an Equilibrium Constraint: Detailed Mechanism of the Substitution Reaction of Tetraplatin with dGMP as a Starting Step of the Platinum(IV) Reduction Process. J. Phys. Chem. B **2017**, *121*, 4400.

V. Šebesta, F. and Burda, J. V.: Interactions of Ascorbic Acid with Satraplatin and Its Trans Analog JM576; *DFT Computational Study.* (submitted to Inorg. Chem.)

VI. Šebesta, F.; Brela, M.; Diaz, S.; Miranda, S.; Murray, J.; Gutiérrez-Oliva, S.; Toro-Labbé, A.; Michalak, A.; Burda, J.V.: The Influence of the Metal Cations and Microhydration on the Reaction Trajectory of the N3↔O2 Thymine Proton Transfer. Quantum Mechanical Study (in print in J. Comput. Chem.)

VII. Šebesta, F.; Futera, Z; Šebera, J.; Tanaka, Y.; Sychrovský; V.; Burda, J.V.: QM/MM Umbrella sampling MD Study of Thymine Interaction with Mercury Cation in Explicit Water Solution. (submitted to J. Phys. Chem.)

VIII. Šebesta, F.; Sláma, V.; Melcr, J.; Futera, Z.; Burda, J.V.: Estimation of Transition-Metal Parameters for Molecular Mechanical Force Field. *J. Chem. Theory Comput.* **2016***, 12*, 3681

IX. Burda, J. V.; Šebesta F.: Metal Interactions With Nucleobases, Base Pairs, and Oligomer Sequences; Computational Approach. Handbook of Computational Chemistry (review), Springer Science+Business Media Dordrecht **2016**, J. Leszczynski et al. (eds.), Chapter 42, 1827, DOI 10.1007/978-94-007-6169-8_36-2.

6 Attachments

This attachment contains articles stated in List of Publications.

Journal of Inorganic Biochemistry 172 (2017) 100–109

Contents lists available at ScienceDirect

Journal of Inorganic Biochemistry

journal homepage: www.elsevier.com/locate/jinorgbio

Study on electronic properties, thermodynamic and kinetic parameters of the selected platinum(II) derivatives interacting with guanine

Filip Šebesta, Jaroslav V. Burda*

Department of Chemical Physics and Optics, Faculty of Mathematics and Physics, Charles University, Ke Karlovu 3, 121 16 Prague 2, Czech Republic

A B S T R A C T

Interaction of hydrated forms of several potential anticancer agents ($PtCl_2$(diaminocyclohexane), *trans*-[$PtCl_2(NH_3)$(thiazole)], *cis*-[$PtCl_2(NH_3)$(piperidine)], and *cis*-$PtCl_2(NH_3)$(cyclohexylamine) complexes) with guanine are explored and compared with an analogous interaction of cisplatin. Basic electronic properties, binding and stabilization energies are determined and energy profiles for the aquation reaction are estimated at the B3LYP/6-311 + + G(2df,2pd) level of theory. It is found that the substitution reaction is an exothermic and exergonic process with ΔG slightly less negative than − 20 kcal/mol. The largest energy release occurs for PtCl(H_2O)(diaminocyclohexane) complex. The rate constants for the Pt(II) complexes in the chloro- and hydroxo-form are compared and an impact of the ligand in the trans position to water is discussed.

1. Introduction

Platinum(II) complexes represent one of the most important group of anticancer metallodrugs since the Rosenberg's discovery of cisplatin anticancer activities [1]. Many platinum compounds (both Pt(II) and Pt (IV)) were investigated in order to find new and more efficient drugs with smaller side-effects or toxicity. Medical explorations are supported by many in vivo and in vitro experiments, a few representative studies [2–14] can be mentioned from the vast pool of these works. Another reason to find more suitable derivatives of platinum complexes (as well as complexes of some other transition metals) is the resistance of the tumor cells to cisplatin either acquired (when administered repeatedly) or intrinsic. In this way, second- and third-generations of the drugs (like carboplatin [15–16], oxaliplatin [17–20], Pt(IV) complex JM216 (satraplatin) [13,21–24], *cis*-$PtCl_2(NH_3)$(2-methylpyridine) - ADM473 [25,26] or triplatin tetranitrate - BBR3464 [27]) were discovered. Up till now, cisplatin and carboplatin belong to the most often administrated drugs [28]. They have the same final DNA adduct (common also to some other platinum drugs): *cis*-$[Pt(NH_3)_2$-1,2-d(GpG)$]^{2+}$ fragment. These adducts are responsible for a roll of 20–40° between guanine bases [29–30] forming the cross-link and a total bend of the helix to the major groove of ca 20–40° [31–33]. Dickerson et al. [34] examined and solved the structure of these bridges. An similar structural pattern with a cisplatin G-Pt-G bridge [31] was solved later. The cisplatin distortion of the helix was observed by Lilley [35]. *cis*-Pt(II) complexes are able to form also stable interstrand bridges [36]. Spinger et al. [17] explored such an adduct of analogous complex - oxaliplatin with 1,2-d(GpG) intrastrand guanines in an DNA oligomer. Later, other structures of Pt (II) complexes with DNA [37–38] or in a ternary complex of the platinated DNA oligomer with High-Mobility Group (HMG) proteins [39–40] were crystallized and characterized. Sigel and Lippert explored ternary platinum complexes in solution [41]. Various conformers of the cisplatin adduct with d(GpG) were examined by Marzilli et al. [42] where conformation of the sugar-phosphate backbone was also discussed. Recently Reedijk et al. [43] studied on azole *cis/trans*-Pt(II) derivatives showing that trans structures are more active than the cisplatin analogues.

A important insight to the molecular description can be achieved by computational simulations, which reveal the bonding and structural relations in formation of the Pt(II) complexes with nucleobases, amino acid side chains or other systems. Many computational works exploring interactions of Pt(II) complexes with DNA bases were published, too. A possibility of employing Car-Parrinello Molecular Dynamics (CPMD) and combined Molecular mechanics (MM) with CPMD techniques (MM/CPMD) in calculations of the spectroscopic and structural information on novel platinum-based anticancer drugs were discussed by Dal Peraro [44]. An effect of Pt(II) coordination to N7 site of guanine on the strength of the N9-C1′ glycosidic bond was explored by Baik [45]. A reaction mechanism of formation of the $Pt(NH_3)_2$diguanine complexes was also investigated by the same authors [46]. A similar study was published by Eriksson [47] where both reaction steps creating i) a mononucleobase adduct and ii) a Pt(II) cross-link with two guanosines were examined. The first interaction step, formation of a Pt(II) adduct with single nucleobase, was explored also by Chval [48]. The structure

* Corresponding author.
E-mail address: burda@karlov.mff.cuni.cz (J.V. Burda).

http://dx.doi.org/10.1016/j.jinorgbio.2017.04.006
Received 13 December 2016; Received in revised form 6 April 2017; Accepted 8 April 2017
Available online 12 April 2017
0162-0134/

and properties of anhydrotetracycline-Pt(II) complex together with the hydration reaction were studied by Dos Santos et al. [49] A similar rate constant was found as for the cisplatin complex. Other two contributions from the same laboratory consider interaction of cisplatin with guanine [50] and description of cisplatin in explicit water environment using Monte Carlo simulations [51]. Chang [52] performed calculation of the Pt-thiazole complex. Some novel trans-platinum(II) anticancer drugs (with aliphatic amines) were studied at the Density Functional Theory (DFT) level with Becke hybrid functional B3LYP [53] where also the hydration process was examined. Deubel [54] performed DFT calculations with the valence triple-zeta basis set (VTZP) and compared the affinities of cisplatin to N-sites and S-sites of the nucleobases and amino acids side-chains. His conclusions are in very good agreement with our previous calculations of the thermodynamics of aquation of the platinum complexes [55–59] and the interactions with sulphur-containing amino acids [60–61]. Robertazzi and Platts carried out the Quantum Mechanics/Molecular Mechanics (QM/MM) calculations of a cisplatin adduct with octamer of double-stranded DNA sequence [62]. Recently, a work exploring an influence of GC base pairing on the Pt complexes was published [63] where the interbase proton transfer from G to C was analyzed. Wysokinski examined the structural relations with vibrational spectra of (orotato)platinum(II) complex [64]. He compared the experimental data with calculated vibration transitions using DFT method employing Perdew-Wang functional (mPW1PW91 [65]). A lot of studies on properties and chemical behavior of the platinum complexes was published by Ziegler and co-workers [66]. One of their studies deals with the reactivity of methane by $[PtCl_4]^{2-}$ in the acidic aqueous solution. The authors showed that the Pt(II) complex after replacement of two chloro ligands by water becomes active in the H/D exchange reaction [67]. Also dinuclear [68] and trinuclear platinum(II) (BBR3464) complexes [69] were studied using a computational approach. Hofmann et al. [70] studied relations between thermodynamic and kinetic parameters with theoretical predictions for the Pt(II) complexes. Pavelka et al. [71] performed a hydration study of carboplatin. Using the B3LYP/6-311 + +G(2df,2pd) computational level, they found relatively high activation barrier of 30 kcal/mol. Tsipis [72] discussed various aspects of the cisplatin hydrolysis. Some other papers on hydration of the Pt(II) complexes should be mentioned [73–79]. Also, our group has considered the thermodynamics of Pt-bridges formation, an influence of the sugar-phosphate backbone, and analyses of binding energies [80–82].

In this study, a reaction mechanism of five different platinum derivatives (cisplatin, $PtCl_2$(diaminocyclohexane), *cis*-[$PtCl_2(NH_3)$(piperidine)], $PtCl_2(NH_3)$(cyclohexylamine) (JM118) (a metabolite of satraplatin [21]), and *trans*-[$PtCl_2(NH_3)$(thiazole)]) interacting with guanine is studied using quantum mechanical tools. This set of complexes needs to be activated by the hydration reaction first as explored in our previous paper [83]. Therefore, the complexes are considered in both semi-hydrated and fully-hydrated forms. The semi-hydrated complexes mean structures, where one of the Cl^- ligands is substituted by water. In the fully-hydrated complexes one of the Cl^- ligands is substituted by water and the other one by OH^- group. In this way, both types of complexes have the same total charge for the sake of comparison. Also, this form represents one of the most abundant structures in solution [84]. Hereafter, the semi-hydrated Pt(II) complexes are labeled in the text as: DDP-Cl - for monochloro-cisplatin, DACH-Cl for PtCl(H_2O)(diaminocyclohexane), JM118-Cl for PtCl(H_2O)(NH_3)(cyclohexylamine), Pip-Cl for *cis*-[PtCl(H_2O)(NH_3)(piperidine)], and Tz-Cl for *trans*-[PtCl(H_2O)(NH_3)(thiazole)]; their structural formulas are displayed in Scheme 1. The corresponding fully-hydrated complexes are labeled with extension −OH instead of −Cl.

2. Computational details

A geometry of all stationary points on the considered reaction coordinates: isolated reactants, supermolecules of reactant associates (containing both interacting molecules: Pt(II) complex and guanine, as an H-bonded system), transition states, product associates and isolated products were optimized using hybrid density functional B3LYP and 6-31 + G(d) basis set. The Stuttgart energy averaged relativistic (MWB) pseudopotentials were used for the description of the inner electrons of the Pt (MWB-60), S and Cl (MWB-10) atoms. The original pseudoorbitals were extended by the set of 1f(Pt) (α_f(Pt) = 0.980), 1d(S) (α_d(S) = 0.498), and 1d(Cl) (α_d(Cl) = 0.618) polarization functions. Supermolecular approach directly allows for an energy comparison of individual structures within the given reaction coordinate. The optimizations were performed in implicit water solution simulated by the Integral Equation Formalism of the Polarizable Continuum Model (IEF-PCM) method with Universal Force-Field (UFF) model for cavity construction. Various arrangements of guanine and Pt(II) complexes in the reactant associates were considered and the structure with the lowest energy was chosen for further single point energy calculations. The same procedure was employed for determination of 'optimal' water orientation in product associates and also for the frequency analyses. The character of the transition states was confirmed by existence of a single negative eigenvalue of the hessian matrix corresponding to the appropriate antisymmetric stretching mode. Single point (SP) calculations were performed on optimized structures using the B3LYP functional and 6-311 + +G(2df,2pd) basis set. The original base of pseudoorbitals on Pt, Cl, and S was augmented by an appropriate set of diffuse functions (Pt: α_s = 0.0075, α_p = 0.013, and α_d = 0.025, exponents for α_s(S), α_p(S), α_s(Cl), and α_p(Cl) were taken from the 6-311 + G set [85]). Similarly polarization functions were added for the sake of basis set consistency with exponents: α_{f1}(Pt) = 1.419, α_{f2}(Pt) = 0.466, α_g(Pt) = 1.208; α_{d1}(Cl) = 1.500, α_{d2}(Cl) = 0.375, α_f(Cl) = 0.700; α_{d1}(S) = 0.918, α_{d2}(S) = 0.289, α_f(S) = 0.568 [55,86]. The Natural Bonding Orbital (NBO) partial charges were used for rescaling of the atomic radii of Cl, O, and S atoms within cavity construction for the Dielectric-PCM with scaled-United-Atom Kohn-Sham radii (D-PCM/scaled-UAKS model) as recommended by Zimmermann [87]. Evaluation of the Basis Set Superposition Error (BSSE) corrections determined within the PCM model suffers with serious drawback as described in our previous studies [61,88–90]. Within the PCM scheme there are two possibilities how to evaluate BSSE corrections. a) Using for fragments the cavity of the whole supermolecule and then electronic density can be also localized on ghost Atomic Orbital (AO) functions correctly but with wrong (unphysical) induced charges on some parts of a cavity surface. b) Using a physically correct small cavity of the given fragment with ghost AO outside. Then various corrections on escaped charge density spoil the BSSE treatment. Therefore, all the SP calculations were performed in implicit solvent while the counterpoise corrections were determined at the same level in vacuum for solvent geometries. The Gibbs free energy was also evaluated with Wertz's correction [91–92] G(W) = H-TS(W) where the entropy contributions from translational and rotational degrees of freedom are scaled in solvent according to the equation: $TS(W) = TS_{vib} + T[0.54\cdot(S_{gas}^{trans} + S_{gas}^{rot} - 14.3) + 8.0]$.

Association energies of the reactants and products in supermolecular model and binding energies (*BE*) of the Pt coordinated ligands in the stationary points of the reaction coordinate were determined according to the equation: $BE = E_{complex} - E_L - E_{CL}$ where E_L is the BSSE corrected energy of the given ligand calculated with the ghost atomic orbitals on the complementary part of the whole structure and E_{CL} is energy of that complementary part calculated in analogous way. Also, the binding energies were determined for all the Pt ligands in isolated complexes.

The NBO analysis was performed in order to get a deeper insight into the electron distribution within the systems. It also clarifies the geometrical changes along the reaction pathway. Bader's Quantum Theory of Atoms-In-Molecules (QTAIM) analysis was employed for the evaluation of electron densities in bond critical points (BCPs). These densities complement information on binding interactions between Pt atom and individual ligands.

Gibbs free energies of activation barriers $\Delta G^{\#}$ correspond to the rate

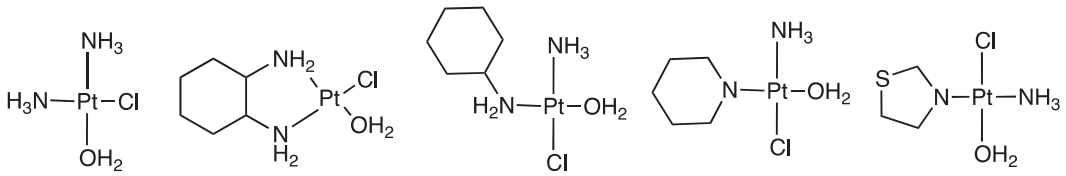

DDP-Cl DACH-Cl JM118-Cl Pip-Cl Tz-Cl

Scheme 1. Structural formulas of chosen semi-hydrated Pt(II) complexes.

constants $k^{TST}(T = 298\ \mathrm{K})$ of the substitution reaction based on the Eyring's Transition State Theory according to the formula: $k^{TST}(T) = \frac{kT}{h}\cdot\exp(-\Delta G^{\neq}/kT)$. The $k^{TST}(298)$ constants were evaluated using the single point energies considering corrections on the nuclear degrees of freedom from the optimization level. All the electronic structure calculations were carried out with the Gaussian 09 program packages. NBO analysis [93–95] were performed using genNBO v.5.9 program [95] and QTAIM analysis [96] as coded in Keith's program AIMAll v.14 [97]. The Extended Transition State (ETS) method for energy decomposition analysis combined with the Natural Orbitals for Chemical Valence (NOCV) theory [98–99] as implemented in Amsterdam Density Functional (ADF-2014) program was employed for deeper insight to the character of the Pt(II) coordinate bonds. Visualizations of results were enabled by Molden v 5.1 [100], VMD v1.92 [101], and GaussView v. 5 programs.

3. Results and discussion

The interaction of the set of Pt(II) complexes with guanine is explored according to the general picture depicted in Scheme 2. Such an interaction can occur after the activation process of these complexes, which is represented by the hydration reaction as described in our previous study [83]. Here, we focus on the fact to which extent individual ligands of the Pt(II) complexes can influence interaction of these complexes with DNA nucleobases.

3.1. Geometry parameters

First the optimization of all the stationary points from the reaction coordinate (the isolated reactants, reactant associates, TS structures, and product complexes both associated and isolated) was performed for semi-hydrated (monochloro-monoaqua) and fully-hydrated (monohydroxo-monoaqua) forms of the chosen platinum(II) complexes. The obtained Pt—X coordination bond lengths are compiled for the isolated complexes in Table 1 and for the reactant supermolecules, transition states, and product supermolecules in Supplementary Information Table S1. In these tables, as well as in the text hereafter, label G stands for guanine and N(trans) signs Pt—N coordination of the Y-ligand in trans position to aqua ligand or guanine (Y = diaminocyclohexane, cyclohexylamine, piperidine or thiazole). Pt—N(cis) labels coordination of ammonia ligand. Global minima of the supermolecular reactant complexes in their semi-hydrated form are displayed in Fig. 1.

Discussing the length of Pt—N(cis) and Pt—N(trans) bonds, the dative strength of the ligand in the trans-position to the corresponding amino group in the given complex plays an important role. In the case of the reactants complexes, a relatively weak trans-influence of aqua-ligand allows shorter Pt—N(trans) distances. Replacing aqua ligand by guanine in the product state, these Pt—N(trans) bonds become substantially longer (about ca 0.03 Å) since guanine exhibits a higher donation strength than other Y-ligands. The only exception is Tz-complex, which is transplatin derivative. One of the shortest Pt—N bonds occurs in the case of DACH complex (2.027 Å). In the case of Tz structures shorter Pt—N(trans) bond speaks out about a stronger trans-influence of thiazole ligand in comparison with ammonia, which is caused by the back-donation from the Pt occupied orbital to the virtual

Table 1
Optimized Pt—X bond lengths (in Å) for the isolated structures of reactants and products; N(cis) means amino-group with Pt—N in cis-position to aqua/guanine ligands, N(trans) in trans-position.

Complex	O(H_2O)	Cl/O(OH)	N(cis)	N(trans)
Reactants				
DDP-Cl	2.112	2.355	2.075	2.028
DDP-OH	2.107	2.004	2.093	2.031
DACH-Cl	2.116	2.355	2.072	2.027
DACH-OH	2.113	2.015	2.088	2.033
JM118-Cl	2.12	2.350	2.076	2.033
JM118-OH	2.124	2.003	2.098	2.030
Pip-Cl	2.128	2.352	2.078	2.037
Pip-OH	2.124	2.004	2.099	2.033
Tz-Cl	2.134	2.316	2.063[b]	2.031[a]
Tz-OH	2.148	1.976	2.061[b]	2.031[a]

Complex	N7(G)	Cl/O(OH)	N(cis)	N(trans)
Products				
DDP-Cl	2.040	2.363	2.070	2.066
DDP-OH	2.039	2.014	2.085	2.057
DACH-Cl	2.048	2.372	2.063	2.057
DACH-OH	2.04	2.021	2.08	2.056
JM118-Cl	2.044	2.364	2.072	2.068
JM118-OH	2.046	2.015	2.087	2.061
Pip-Cl	2.049	2.370	2.071	2.079
Pip-OH	2.046	2.015	2.087	2.066
Tz-Cl	2.042	2.353	2.059[b]	2.037[a]
Tz-OH	2.056	2.007	2.055[b]	2.037[a]

[a] Thiazole ligand.
[b] Ammonia ligand.

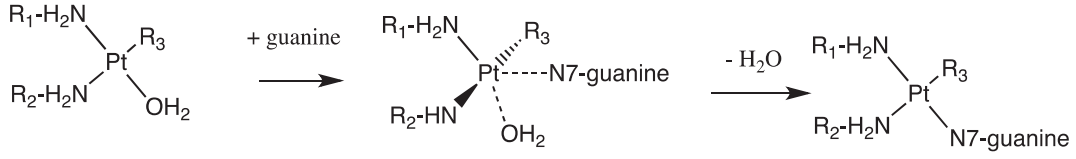

Reactant **TS** **Product**

Scheme 2. Substitution of aqua-ligand by guanine. $R_3 = Cl^-$ or OH^-.

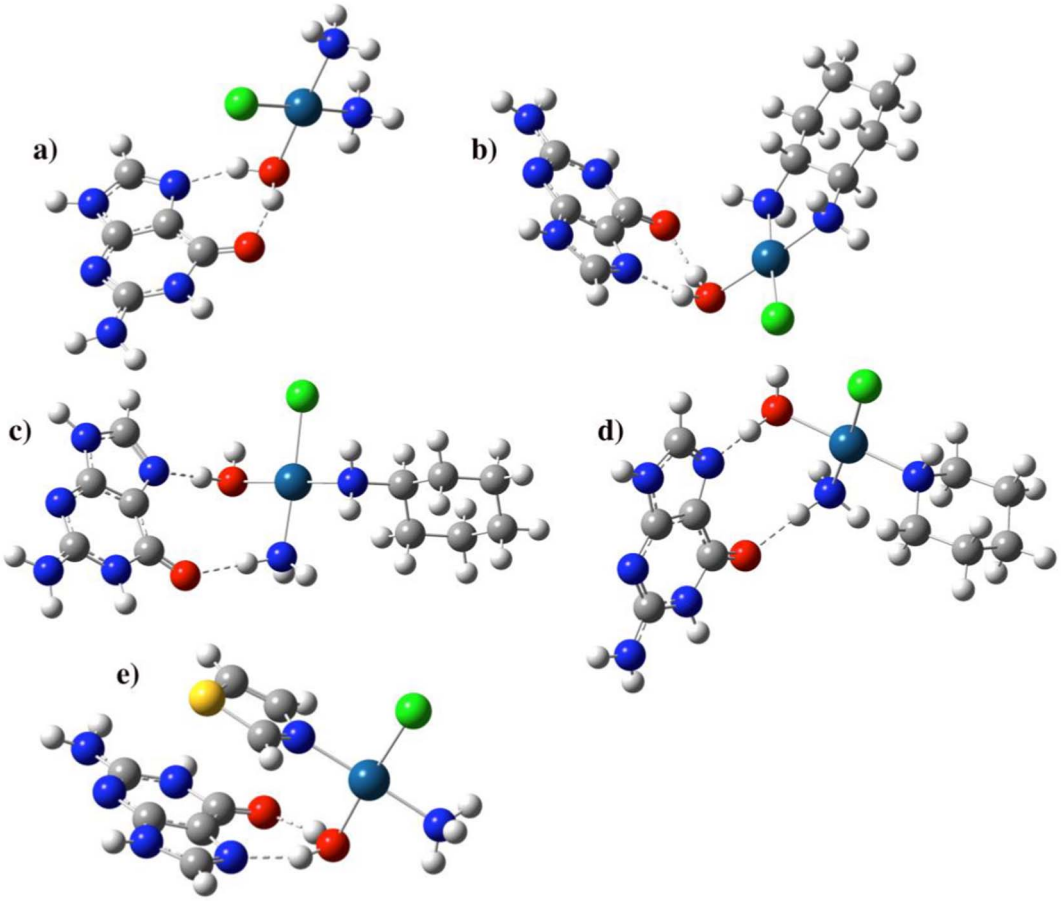

Fig. 1. Global minima of the chloro-forms of the associated reactant complexes: a) DDP-Cl…guanine, b) DACH-Cl…guanine, c) JM118-Cl…guanine, d) Pip-Cl…guanine, e) Tz-Cl…guanine.

antibonding π orbital of thiazole. This situation is discussed in the part devoted to electronic properties. Comparing the trans-influence of Cl^- and OH^- ligands, markedly longer Pt—N(cis) bonds occur in hydroxo-complexes than in chloro-ones demonstrating higher trans-influence of OH-group. The same conclusion follows also from BE in Table 4 and QTAIM analyses presented in Table 7. Comparing these Pt-X distances from Table 1 with corresponding ones from the supermolecular model in Table S1 the effect of H-bonded guanine (in the reactants) or water (in the products) is distinctly visible. H-bonds in the reactant associates occur between O6 and N7 guanine sites and polarized H atoms of the aqua and/or the ammonia ligands, which usually cause small shortening of the corresponding Pt—O/N bonds. In the product associates, the released water molecule predominately interacts with N1 and N2 sites of guanine or with hydroxo-ligand.

As to the Pt—Cl/OH distances, the shortest bond occurs in the Tz complexes, ca 2.316 and 1.976 Å due to weak dative ability of the aqua ligand in the trans position since Tz belongs to transplatin analogues. In the remaining Pt(II) complexes, the Cl/OH ligands are located opposite to N(cis) amino position. The reason why NH_3 ligand is in trans position to Cl/OH is a consequence of the stronger trans-influence of the Y-ligands in comparison with the ammonia. In the aquation process, the first chloro-ligand is released and replaced by water in the original (dichloro) complexes just in trans position to Y-ligand, for further details see study [83].

In the transition states, the Pt—O bond length of exchanging water is always a little bit shorter than the corresponding Pt—N7 bond of guanine, which is in agreement with the Hammond's postulate since the substitution reactions are exergonic and therefore a closer similarity of the TS state to the reactant can be expected.

3.2. Energy profile

Energy characteristics of the substitution reactions of the Pt-aqua complexes with guanine in water solution (DPCM) are presented in Table 2 and the corresponding energy reaction profile is plotted in Fig. 2. The assumption on activation of (generally all) chloro-containing metallodrugs is based on the fact that the aqua-forms are less stable i.e., more reactive than the original chloro-complexes. Therefore starting from the aqua-platinum(II) complexes, most of the substitution reactions are exothermic and exergonic. According to Martin [84], such a species (monoaqua-monohydroxo-complex) is more probable in water solution of cisplatin than 2+ charged diaqua-form. Moreover in our models, both of the semi-hydrated and fully-hydrated forms have the same total charge, which also allows an easier comparison of the interaction with guanine for the both Pt—Cl and Pt—OH complexes. Usually, when the total Gibbs free energies of the isolated reactant and products are not corrected according to Wertz's suggestion, a visibly lower value is obtained relative to energy of the corresponding supermolecules. This fact is connected with the higher entropy contribution of translation and rotation degree of freedom in comparison with vibrational degrees, to which they transform in supermolecular picture of reactant and/or product associates. There is already several discussions on the effect of entropy contributions when number of particles is changed within the association process, cf. e.g. ref. [91, 102]. From the first part of Table 2 it can be noticed that including Wertz's correction leads to an improvement in the description of association energies in water solution giving reasonably small negative values of ca −4 to −5 kcal/mol. Without these corrections the association energies become even positive so that a) the reaction would scarcely occur and b) the examined supermolecular structures would not be stable. In all the

Table 2
Energy characteristics from the reaction profile (in kcal/mol) for the substitution of aqua ligand by guanine in chosen Pt(II) complexes - without (ΔG(W)) and with inclusion of non-electrostatic contributions of cavitation energies ($\Delta G(W)^{NE}$).

	ΔE(B1)	ΔG(W)	ΔE(B2)	ΔG(W)	$\Delta G(W)^{NE}$
Association energy					
DDP-Cl	− 20.3	− 15.1	− 12.0	− 6.8	− 4.0
DDP-OH	− 18.3	− 13.8	− 12.2	− 7.8	− 4.8
DACH-Cl	− 20.7	− 15.9	− 12.1	− 7.3	− 3.6
DACH-OH	− 19.0	− 16.3	− 11.9	− 9.2	− 5.4
JM118-Cl	− 20.1	− 16.2	− 11.8	− 7.9	− 5.0
JM118-OH	− 22.1	− 17.6	− 14.8	− 10.4	− 4.1
Pip-Cl	− 20.1	− 15.0	− 12.5	− 7.4	− 4.0
Pip-OH	− 17.4	− 13.3	− 11.1	− 7.0	− 3.6
Tz-Cl	− 20.8	− 16.3	− 12.1	− 7.6	− 5.4
Tz-OH	− 19.8	− 15.8	− 11.6	− 7.6	− 4.0
Reaction energy					
DDP-Cl	− 23.7	− 23.3	− 18.1	− 17.7	− 16.0
DDP-OH	− 22.2	− 22.4	− 18.0	− 18.2	− 16.7
DACH-Cl	− 24.0	− 24.9	− 18.1	− 19.1	− 16.8
DACH-OH	− 21.6	− 23.4	− 17.0	− 18.8	− 16.8
JM118-Cl	− 23.3	− 25.7	− 18.0	− 20.4	− 18.0
JM118-OH	− 24.4	− 26.0	− 19.0	− 20.6	− 18.7
Pip-Cl	− 21.6	− 22.6	− 18.4	− 19.4	− 17.5
Pip-OH	− 21.9	− 23.2	− 17.6	− 18.9	− 17.0
Tz-Cl	− 25.7	− 25.6	− 20.2	− 20.1	− 18.2
Tz-OH	− 23.3	− 24.3	− 18.7	− 19.6	− 17.5
Activation barrier					
DDP-Cl	17.5	17.5	17.6	17.6	18.9
DDP-OH	17.0	17.4	17.6	18.0	19.0
DACH-Cl	18.6	16.8	17.4	15.7	16.5
DACH-OH	18.3	19.3	18.4	19.5	20.0
JM118-Cl	18.7	17.5	16.7	15.5	16.8
JM118-OH	19.2	17.6	19.7	18.1	16.9
Pip-Cl	18.7	17.2	17.8	16.2	16.9
Pip-OH	18.6	17.7	17.2	16.2	17.0
Tz-Cl	13.3	14.0	12.9	13.6	15.0
Tz-OH	16.1	16.9	16.2	17.0	17.5

cases two H-bonds are formed, usually N7…H(aq) and O6…H(amino). Association energies are slightly stronger than H-bonds within water molecules themselves. Therefore, also Gibbs free energy for formation of such structures is always negative. Although the electronic energies ΔE(B2) for both Cl- and OH-forms are very similar electron densities in BCPs of these H-bonds are visibly larger for Cl-complexes than for OH-ones. Also, comparing BCP electronic densities, practically twice higher value can be systematically found in the case of N7…H(aqua) than O6…H(amino), which gives an estimation of the proportionality of these two H-bonds, cf. Table 7.

Considering the Gibbs free reaction energies, all the explored processes are quite exothermic and exoergic, which is not surprising due to the fact that relatively weaker Pt-O(aqua) bond is replaced by much stronger Pt-N7 coordination, cf. Table 4 for binding energies. The highest release of Gibbs free reaction energy is obtained for the JM118-OH complex, ΔG = − 18.7 and the lowest for cisplatin-Cl: − 16.0 kcal/mol. From this, it follows (cf. also the middle part of Table 2) that the energy variation is very small. A similar conclusion was made for the aquation process of the same series of Pt(II) complexes considered in our previous paper [83].

The activation energies of the substitution reaction for all the explored Pt(II) complexes are collected in the last section of Table 2. The reaction barriers for the Cl-forms are connected with generally slightly lower energies than OH-forms. Comparing with cisplatin, all the other chloro-complexes have reaction barriers lower at least by 2 kcal/mol. It means that these complexes interact with guanine a little bit faster than cisplatin itself. The lowest activation barrier occurs in the Tz-Cl complex due to stronger trans-effect of chloro-ligand in comparison with all the considered amino-ligands. As to the complexes in OH-form, in Tz-OH structure the Oh ligand has lower trans-effect than Cl-form (comparable with trans-effect of amino-ligands), which is connected with the visibly higher barrier, fairly similar to the other *cis*-Pt(II) complexes. Among the OH-complexes, the piperidine and cyclohexylamine structures exhibit the lowest height of activation barriers: − 17.0 kcal/mol. In this case heterocyclic nitrogen of piperidine, similarly to pyridine, has higher trans-effect than aliphatic amines but still lower than trans-effect of chloro-ligands as also follows from the reaction rates for complexes in the Cl-form. Reaction profiles of the Gibbs free energy are drawn in Fig. 2a for the chloro-complexes and in Fig. 2b for the complexes with hydroxo-group.

Based on the Eyring's TST, the rate constants k (T = 298 K) are determined and collected in Table 3. The rate constants for the Pt(II) complexes with monochloro ligand can be ordered: DDP-Cl < Pip-Cl < JM118-Cl < DACH-Cl < Tz-Cl and the rate constants for the complexes containing OH^- ligand increases in row: DACH-OH < DDP-OH < Tz-OH < Pip-OH ≈ JM118-OH. It can be concluded that the kinetic preference differs quite substantially from the similar order

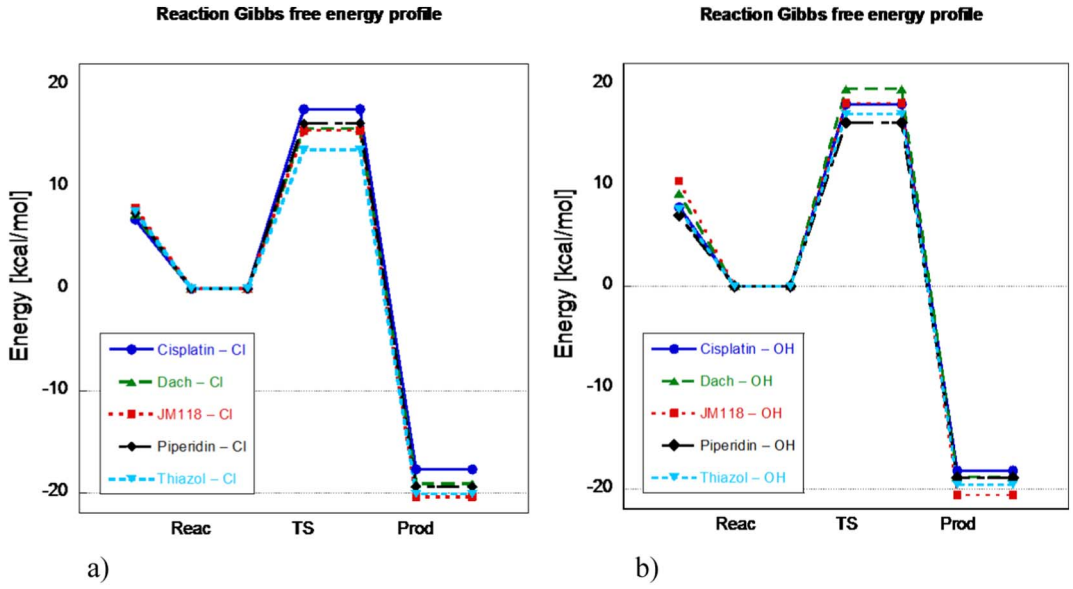

Fig. 2. Gibbs free energy profiles of the reactions of a) semi-hydrated and b) fully-hydrated Pt(II) complexes with guanine at the B3LYP/6-311 + + G(2df,2pd)/DPCM/sUAKS computational model starting from isolated reactants.

Table 3
Rate constants at $T = 298$ K (in $M^{-1} s^{-1}$) for the reactions of Pt(II) complexes with guanine - without (k_a) and with inclusion of non-electrostatic contributions of cavitation energies (k_a^{NE}).

	k_a	k_a^{NE}
DDP-Cl	7.80E − 01[a]	7.59E − 02
DDP-OH	3.94E − 01[a]	7.28E − 02
DACH-Cl	2.09E + 01	5.06E + 00
DACH-OH	3.01E − 02	1.25E − 02
JM118-Cl	2.71E + 01	3.12E + 00
JM118-OH	3.19E − 01	2.67E + 00
Pip-Cl	7.71E + 00	2.49E + 00
Pip-OH	7.89E + 00	2.19E + 00
Tz-Cl	6.64E + 02	6.58E + 01
Tz-OH	2.16E + 00	8.84E − 01

[a] Experimental values for substitution reaction including DDP is k(DDP-Cl) = 0.3 and k(DDP-H_2O) = 140 according to ref. [104] k(DDP-Cl) = 0.34 or 0.20 ref. [105] and k (DDP-Cl) = 2.5 and k(DDP-H_2O) = 42 ref. [106–107], and ref. [108].

of the rate constants for the activation process by aquation reaction of the same series of dichloro-Pt(II) complexes where they were ordered as: Tz < JM 118 < DDP < Pip [83].

3.3. Binding, and stabilization energies

Energy decomposition into stabilization and binding energies (*BE*) gives an insight to the energetics inside the (super)molecules, which can be also directly comparable with electron densities of BCP of the individual bonds. BEs of all the platinum coordinate bonds and complex stabilization energies of the isolated reactant and product complexes are collected in Table 4. Here it can be noticed that BEs of aqua and amino-ligands in the reactant are higher in semi-hydrated complexes than in fully-hydrated ones, which is a consequence of the lower trans-influence of the Cl ligand in comparison with the OH ligand (as already discussed in part Geometry parameters). From the differences between BEs of aqua-ligand and guanine it is also clear that an extent of the reaction energies represents ca 20 kcal/mol as it should generally follow from enthalpy estimation based on energies of constituted bonds.

Table 4
Bonding energies BE (in kcal/mol) for isolated reactants and products of reactions of Pt (II) complexes and stability of the complexes; N(cis) means amino-group with Pt—N in cis-position to aqua/guanine ligands, N(trans) in trans-position.

Complex	H_2O/G	Cl/OH	N(cis)	N(trans)	Stab
Reactants					
DDP-Cl	− 30.9	− 30.6	− 47.9	− 58.0	− 219.8
DDP-OH	− 26.6	− 38.1	− 45.6	− 54.7	− 225.4
DACH-Cl	− 28.2	− 37.4	− 120.9		− 237.0
DACH-OH	− 25.1	− 44.2	− 114.0		− 226.4
JM118-Cl	− 29.4	− 39.3	− 47.4	− 64.4	− 229.8
JM118-OH	− 27.0	− 43.0	− 44.3	− 60.0	− 231.3
Pip-Cl	− 28.7	− 36.8	− 47.2	− 64.4	− 217.8
Pip-OH	− 25.4	− 44.2	− 45.0	− 60.7	− 224.2
Tz-Cl	− 27.7	− 47.4	− 47.4[b]	− 50.3[a]	− 219.8
Tz-OH	− 26.8	− 53.8	− 45.1[b]	− 47.2[a]	− 225.4
Products					
DDP-Cl	− 50.9	− 36.8	− 48.9	− 49.2	− 238.5
DDP-OH	− 47.0	− 42.0	− 46.5	− 46.1	− 243.6
DACH-Cl	− 48.0	− 35.1	− 112.6		− 254.5
DACH-OH	− 44.5	− 39.0	− 104.5		− 244.8
JM118-Cl	− 48.9	− 37.4	− 48.6	− 55.4	− 248.3
JM118-OH	− 45.6	− 41.6	− 46.6	− 51.2	− 249.5
Pip-Cl	− 48.3	− 38.3	− 47.4	− 56.3	− 238.7
Pip-OH	− 45.4	− 40.4	− 46.8	− 51.8	− 243.2
Tz-Cl	− 49.6	− 39.0	− 47.2[b]	− 51.8[a]	− 238.5
Tz-OH	− 47.3	− 44.0	− 42.9[b]	− 48.2[a]	− 243.6

[a] Thiazole ligand.
[b] Ammonia ligand.

Table 5
Association/bonding energies (in kcal/mol) of water and guanine ligands in the super-molecular structures of reactants transition states and products.

Complex	Reactants		TS		Products	
	G	H_2O	G	H_2O	G	H_2O
DDP-Cl	− 12.6	− 41.2	− 12.2	− 6.9	− 49.7	− 6.2
DDP-OH	− 11.4	− 36.7	− 10.3	− 6.7	− 47.6	− 8.1
DACH-Cl	− 12.1	− 39.2	− 10.8	− 3.2	− 48.2	− 2.7
DACH-OH	− 10.8	− 35.4	− 8.4	− 4.0	− 47.8	− 7.3
JM118-Cl	− 12.3	− 39.5	− 12.4	− 4.5	− 47.7	− 5.1
JM118-OH	− 14.6	− 35.8	− 11.1	− 4.0	− 45.4	− 7.6
Pip-Cl	− 13.1	− 39.1	− 13.6	− 5.2	− 47.2	− 4.6
Pip-OH	− 12.0	− 35.5	− 11.3	− 4.4	− 47.5	− 1.4
Tz-Cl	− 12.5	− 40.3	− 12.4	− 9.6	− 49.7	− 4.4
Tz-OH	− 11.9	− 36.9	− 12.0	− 6.7	− 49.0	− 7.1

Table 4 shows that the structures with the DACH ligand have visibly larger BEs – more than twice as BEs of other amino-ligands, showing a synergy effect of the bidentate character of this ligand. Nevertheless, BEs of the remaining two dative bonds (Pt—O(aq) and Pt—Cl/Pt—OH) are not substantially influenced by these larger values, being still comparable with analogous energies of e.g., JM118 of Pt-Pip complex. Also, it is worth to notice that visibly reduced BEs (ca by 10 kcal/mol) occur in Y-ligand when more weakly bonded aqua ligand is replaced by N7 site of guanine with a higher trans influence. When stabilization energies are compared it follows from the last column of Table 4 that all these structures have quite comparable stabilization energy with very few exceptions like DACH-Cl complex, which is slightly more stabilized mainly due to the already mentioned stronger Pt—N(amino) coordination covalent bonds. Slightly higher stabilization is also noticeable in the OH-forms than in Cl-forms due to stronger BE of Pt—OH bond.

In Table 5 BEs of exchanging ligands (water and guanine) are collected. From this table it can be noticed that some of BEs for water in TS are even lower than BEs of H-bonded molecule in products. In the remaining cases are both BEs very similar - within a few kcal/mol. The same is true also for H-bonded guanine in the reactant supermolecule in comparison with 'partially bonded' guanine in TS. An analogous picture was also noticeable in our previous studies [59,103], too. Despite the very weak 'coordination', the TS structures exhibit an vibrational antisymmetric stretching mode confirming the associative mechanism of the substitution reaction.

3.4. NBO, MO, and QTAIM analyses

NBO partial charges of the isolated reactants and products are collected in Table 6 and of the supermolecular reactants, transition states, and products in SI Table S2.

These tables show that the Pt atom has always a relatively large positive value indicating the extent of electron donation from its ligands. The NBO partial charge δ(Pt) is larger for the OH-forms of the Pt complexes than for the Cl-forms. This demonstrates that the donation from the chloro-ligand is larger, which also partially corresponds with a more diffuse character of the Cl atom. The aqua-ligand in the reactants has small positive charge (since oxygen partially donates its electron pair to platinum cation) while the water molecule in the product supermolecules is practically electroneutral (cf. Table S2). In the transition states, the charge of water is only slightly more positive than in the product states confirming the very weakly bonding character, see also the discussion to Table 5 above. Inversely, guanine is electroneutral in the reactant state since the association means only a weak perturbation from the isolated molecule. Nevertheless, fairly large positive charge transfer occurs in the products complexes. In several TS structures, a positive partial charge of guanine is quite tiny sometimes even lower than in the reactant state. As to a comparison of individual Y-ligands, it can be noticed that the weakest donation occurs in Tz-

Table 6
NBO partial charges (in e) for whole ligand units (guanine, aqua, DACH, etc.) in the isolated Pt(II) complexes of reactants and products.

Complex	Pt	Cl/OH	H_2O/G	Y (trans)	NH_3(cis)
Reactants					
DDP-Cl	0.730	− 0.604	0.204	0.306[a]	0.364
DDP-OH	0.806	− 0.601	0.187	0.269[a]	0.339
DACH-Cl	0.731	− 0.626	0.191	0.704	
DACH-OH	0.804	− 0.617	0.170	0.643	
JM118-Cl	0.714	− 0.600	0.199	0.301	0.386
JM118-OH	0.795	− 0.606	0.182	0.260	0.369
Pip-Cl	0.720	− 0.601	0.198	0.295	0.388
Pip-OH	0.794	− 0.602	0.183	0.259	0.367
Tz-Cl	0.748	− 0.531	0.189	0.325	0.269
Tz-OH	0.835	− 0.544	0.171	0.307	0.232
Products					
DDP-Cl	0.692	− 0.606	0.297	0.299[a]	0.317
DDP-OH	0.776	− 0.610	0.270	0.261[a]	0.303
DACH-Cl	0.710	− 0.632	0.277	0.645	
DACH-OH	0.789	− 0.627	0.254	0.585	
JM118-Cl	0.672	− 0.600	0.289	0.302	0.337
JM118-OH	0.762	− 0.607	0.265	0.261	0.319
Pip-Cl	0.662	− 0.598	0.299	0.302	0.335
Pip-OH	0.759	− 0.606	0.270	0.258	0.319
Tz-Cl	0.714	− 0.587	0.292	0.322	0.259
Tz-OH	0.805	− 0.593	0.249	0.307	0.231

[a] NH_3 ligand of Pt.

Table 7
QTAIM analysis of the isolated structures of reactant and products: BCPs electron density (in 10^{-2} e/Å^3) for Pt—X coordination bonds.

X	Cl/O(OH)	O(H_2O)/N7(G)	N(cis)	N(trans)
Reactants				
DDP-Cl	8.74	8.53	11.37	12.73
DDP-OH	12.42	8.79	10.62	12.54
DACH-Cl	8.67	8.43	11.70	13.01
DACH-OH	12.04	8.68	11.07	12.76
JM118-Cl	8.85	8.38	11.33	12.88
JM118-OH	12.46	8.15	10.47	12.90
Pip-Cl	8.83	8.20	11.30	12.87
Pip-OH	12.44	8.37	10.47	12.89
Tz-Cl	9.72	8.24	11.66	12.28
Tz-OH	13.44	7.66	11.67	12.23
Products				
DDP-Cl	8.58	11.98	11.57	11.55
DDP-OH	12.09	11.94	10.93	11.72
DACH-Cl	8.32	11.68	12.02	12.06
DACH-OH	11.81	11.83	11.35	11.97
JM118-Cl	8.58	11.86	11.56	11.78
JM118-OH	12.10	11.72	10.90	11.89
Pip-Cl	8.49	11.78	11.60	11.63
Pip-OH	12.10	11.72	10.88	11.88
Tz-Cl	8.83	12.06	11.91	12.12
Tz-OH	12.40	11.39	11.94	12.06

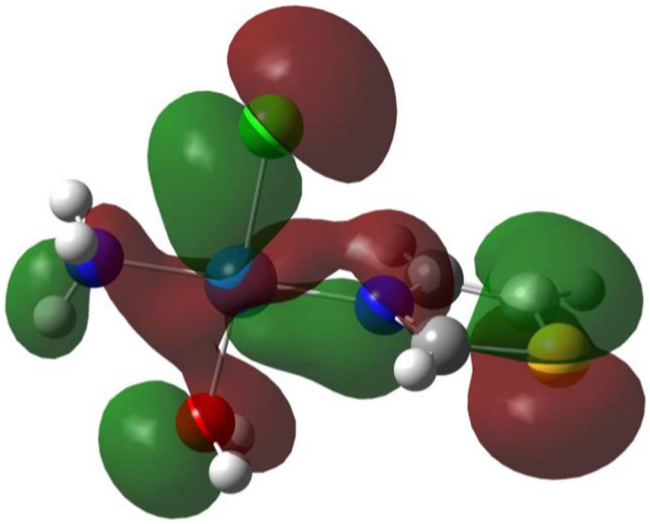

Fig. 3. 32nd MO of Tz-Cl complex with back-donation character: Pt → N.

complexes. On the contrary, the highest donation can be seen in the JM118 and Pt-Pip complexes (as also follows from the smallest δ(Pt) values in Table 6).

Thiazole-ligand poses a π-conjugated system and, in this way, it can allow for the π back-donation from the occupied Pt lone pair of appropriate d_π AO character to the π^* unoccupied MO of thiazole. Therefore a possibility of strengthening by a π back-donation effect was search and indeed the 32nd MO has an appropriate character with π-back-donation as it is depicted in Fig. 3. Also, from the ETS-NOCV analysis performed for this complex using ADF program it was found based on diagonalization of deformation density matrix that the second pair of eigenvalues has the corresponding π-character with energy of − 8.6 kcal/mol while the first pair has σ-character with energy of − 48.0 kcal/mol. Both these deformation densities are drawn in Fig. 4.

The QTAIM analysis of electron density in BCPs of the Pt-X coordinated bonds of the isolated reactant and product complexes are displayed in Table 7 and the corresponding values for the super-molecular structures of reactants, transition states, and products are shown in SI Table S3. In Table 7 it is possible to distinguish coordinate covalent bonds between Pt and its ligands confirming that the Pt-N (trans) bonds in the reactants are visibly stronger than Pt—O(aqua) bonds. The electron densities in Pt—Cl BCPs are about 0.03 e/Å^3 smaller

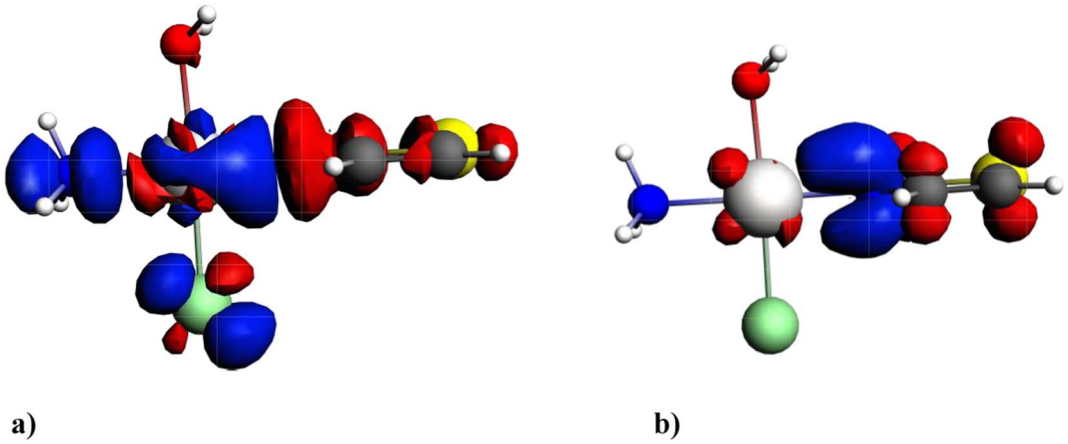

Fig. 4. First two diagonal deformation densities with a) σ- and b) π-character; blue areas of increased and red areas with decreased electron densities.

than corresponding values of Pt-OH, which again demonstrates higher dative strength of the OH–ligands. Also, we can compare the BCPs densities of individual ligands, which can be sorted in the row: DACH ≈ JM118 ≈ Pip > DDP > Tz for both OH- and Cl-forms of the complexes. For the completeness it should be mentioned that guanine has comparable dative ability as DACH ligand. Table S3 shows that quite low BCPs electron densities were found for exchanging ligands in the TS states (comparable with H-bond values as mentioned above and as also follows from the Table 5 for BEs). Interestingly, in these structures which has a well-known trigonal-bipyramidal character, the BCP densities of ligand in equatorial position Pt—N(trans) achieve in TS state its maxima due to weak competition from H_2O/G exchanging ligands.

4. Conclusions

In this study the series of Pt(II) complexes with promising anticancer properties is explored. The activated (monoaqua-monochloro- and monoaqua-monohydroxo-) forms of these compounds are assumed for substitution reaction where the aqua-ligand is replaced by guanine. All required structures for determining thermodynamic and kinetic characteristics were optimized at the B3LYP/6-31 + G(d)/IEF-PCM/UFF computational level. The Stuttgart energy averaged relativistic pseudopotentials were used for the outer electrons of the S, Cl, and Pt atoms. Energy and electronic properties were evaluated for the optimized structures using the B3LYP/6-311 + + G(2df,2pd)/DPCM/scaled-UAKS model. For scaling of UAKS cavities the procedure recommended by Zimmermann [87] was applied. The substitution reaction is exothermic and exergonic with ΔG slightly less negative values than − 20 kcal/mol and the largest energy release occurs for complex JM118. The rate constants for the Pt(II) complexes with chloro ligand can be ordered: DDP-Cl < Pip-Cl < JM118-Cl < DACH-Cl < Tz-Cl and for the OH-complexes: DACH-OH < DDP-OH < Tz-OH < Pip-OH ≈ JM118-OH. As to kinetics, practically all derivatives replace aqua-ligand by guanine faster than cisplatin in both semi- and fully-activated forms. The only exception is DACH-OH form, which interacts slightly slower.

Acknowledgement

Authors are grateful to project No 16-06240S from Grant Agency of the Czech Republic for financial support of this study. Also the Charles University Grant Agency No. 1145016 has to be acknowledged for additional support (FŠ). Authors also appreciated an access to computing and storage facilities of the National Grid Infrastructure MetaCentrum, provided under the program 'Projects of Large Infrastructure for Research, Development, and Innovations' (LM2010005).

Appendix A. Supplementary data

For further details on coordinate-covalent bond lengths, NBO charges, and QTAIM densities in BCPs of stationary points from reaction coordinate see Supplementary information. Supplementary data associated with this article can be found in the online version, at doi:http://dx.doi.org/10.1016/j.jinorgbio.2017.04.006.

References

[1] B. Rosenberg, L. Van Camp, J.L. Trosko, V.H. Mansour, Platinum drugs; a new class of potent antitumor agents, Nature 222 (1969) 385–391.
[2] N. Farrell, L.F. Povirk, Y. Dange, G. DeMasters, M.S. Gupta, G. Kohlhagen, Q.A. Khan, Y. Pommier, D.A. Gewirtz, Cytotoxicity, DNA strand breakage and DNA–protein crosslinking by a novel transplatinum compound in human A2780 ovarian and MCF-7 breast carcinoma cells, Biochem. Pharmacol. 68 (2004) 857–866.
[3] E.Y. Bivian-Castro, M. Roitzsch, D. Gupta, B. Lippert, Synthesis and X-ray crystal structure analysis of 1:1 and 1:2 complexes of cisplatin with the model nucleobase 9-methyladenine in its protonated form and a unique HNO_3 adduct of cis-[(NH_3)(2)Pt(9-MeAH-N7)(2)](4 +), Inorg. Chim. Acta 358 (7) (2005) 2395–2402.
[4] V. Beljanski, J.M. Villanueva, P.W. Doetsch, G. Natile, L.G. Marzilli, Marked dependence on carrier-ligand bulk but not on carrier-ligand chirality of the duplex versus single-strand forms of a DNA oligonucleotide with a series of G-Pt(II)-G intrastrand cross-links modeling cisplatin-DNA adducts, J. Am. Chem. Soc. 127 (45) (2005) 15833–15842.
[5] V. Marini, P. Christofis, O. Novakova, J. Kasparkova, N. Farrell, V. Brabec, Conformation, protein recognition and repair of DNA interstrand and intrastrand cross-links of antitumor trans-[PtCl2(NH_3)(thiazole)], Nucleic Acids Res. 33 (18) (2005) 5819–5828.
[6] Y. Najajreh, J. Kasparkova, V. Marini, D. Gibson, V. Brabec, Structural characterization and DNA interactions of new cytotoxic transplatin analogues containing one planar and one nonplanar heterocyclic amine ligand, J. Biological Inorg. Chem. 10 (7) (2005) 722–731.
[7] G. Giannikopoulos, C.-L. Teo, M.D. Hall, R.R. Fenton, T.W. Hambley, The synthesis and in vitro Cytotoxicity of two trans-platinum complexes of heterocyclic amines, Aust. J. Chem. 56 (2003) 685–689.
[8] K.R. Barnes, S.J. Lippard, Cisplatin and related anticancer drugs: recent advances and insights, Metal Ions in Biolgical Systems, Vol 42: Metal Complexes in Tumor Diagnosis and as Anticancer Agents, Vol. 42 2004, pp. 143–177.
[9] J. Malina, M. Voitiskova, V. Brabec, C.I. Diakos, T.W. Hambley, DNA adducts of the enantiomers of the Pt(II) complexes of the ahaz ligand (ahaz = 3-aminohexahydroazepine) and recognition of these adducts by HMG domain proteins, Biochem. Biophys. Res. Commun. 332 (4) (2005) 1034–1041.
[10] V. Brabec, J. Kasparkova, Modifications of DNA by platinum complexes — relation to resistance of tumors to platinum antitumor drugs, Drug Resist. Updat. 8 (3) (2005) 131–146.
[11] M. Carlone, L.G. Marzilli, G. Natile, Platinum complexes with only one purine ligand (guanine, deoxyguanine, or adenine) flanked by two cis-NH(CH3) groups — informative models for assessing the interaction of purine C6 substituents with cis-amines, Eur. J. Inorg. Chem. 7 (2005) 1264–1273.
[12] D. Bhattacharyya, P.A. Marzilli, L.G. Marzilli, Exploring the universality of unusual conformations of the 17-membered Pt(d(G*pG*)) macrochelate ring. Dependence of conformer formation on a change in bidentate carrier ligand from an sp(3) to an sp(2) nitrogen donor, Inorg. Chem. 44 (21) (2005) 7644–7651.
[13] K. Wosikowski, L. Lamphere, G. Unteregger, V. Jung, F. Kaplan, J.P. Xu, B. Rattel, M. Caligiuri, Preclinical antitumor activity of the oral platinum analog satraplatin, Cancer Chemother. Pharmacol. 60 (2007) 589–600.
[14] F. Huq, J.Q. Yu, H. Daghriri, P. Beale, Studies on activities, cell uptake and DNA binding of four trans-planaramineplatinum(II) complexes of the form: trans-PtL(NH_3)Cl2, where L¼2-hydroxypyridine, imidazole, 3-hydroxypyridine and imidazo(1,2-a)pyridine, J. Inorg. Biochem. 98 (2004) 1261–1270.
[15] R. Canetta, M. Rozencweig, S.K. Carter, Carboplatin: the clinical spectrum to date, Cancer Treat. Rev. 12 (1985) 125–136.
[16] R.J. Knox, F. Friedlos, D.A. Lydall, J.J. Roberts, Mechanism of cytotoxicity of anticancer platinum drugs: evidence that cis-diamminedichloroplatinum(II) and cis-diammine-(1,1-cyclobutanedicarboxylato)platinum(II) differ only in the kinetics of their interaction with DNA, Cancer Res. 46 (4_Part_2) (1986) 1972–1979.
[17] B. Spingler, D.A. Whittington, S.J. Lippard, 2.4 A crystal structure of an oxaliplatin 1,2-d(GpG) intrastand cross-link in a DNA dodecamer duplex, Inorg. Chem. 40 (2001) 5596–5602.
[18] H. Ehrsson, I. Wallin, J. Yachnin, Pharmacokinetics of oxaliplatin in humans, Med. Oncol. 19 (4) (2002) 261–265.
[19] Z. Chval, M. Kabelac, J.V. Burda, Mechanism of the cis-Pt(1R,2R-DACH)(H2O)(2)(2 +) intrastrand binding to the double-stranded (pGpG)center dot(CpC) dinucleotide in aqueous solution: a computational DFT study, Inorg. Chem. 52 (10) (2013) 5801–5813.
[20] M.G. Apps, E.H.Y. Choi, N.J. Wheate, The state-of-play and future of platinum drugs, Endocrine-related Cancer 22 (4) (2015) 219–233.
[21] O. Bradáč, T. Zimmermann, J.V. Burda, Can satraplatin be hydrated before the reduction process occurs? The DFT computational study, J. Mol. Model. 19 (2013) 1669–1678.
[22] S. Akshintala, L. Marcus, K. Warren, R. Murphy, T. Sissung, A. Srivastava, W. Goodspeed, A. Goodwin, C. Brewer, C. Zalewski, K. King, A. Kim, W. Figg, B. Widemann, Phase 1 trial and pharmacokinetic study of the oral platinum analog satraplatin in children and young adults with refractory solid tumors including brain tumors, Pediatr. Blood Cancer 62 (2015) 603–610.
[23] F. Šebesta, J.V. Burda, Reduction mechanism of satraplatin in water solution; thermodynamic, kinetic computational study, J. Phys. Chem. A (2016) (submitted).
[24] L.R. Kelland, G. Abel, M.J. McKeage, M. Jones, P.M. Goddard, M. Valenti, B.A. Murrer, K.R. Harrap, Preclinical antitumor evaluation of bis-acetato-ammine-dichloro-cyclohexylamine platinum(IV): an orally active platinum drug, Cancer Res. 53 (1993) 2581–2586.
[25] J. Holford, F. Raynaud, B.A. Murrer, K. Grimaldi, J.A. Hartley, M. Abrams, L.R. Kelland, ADM 473, Anticancer Drug Des. 13 (1998) 1–8.
[26] F.I. Raynaud, F.E. Boxall, P.M. Goddard, M. Valenti, M. Jones, B.A. Murrer, M. Abrams, L.R. Kelland, cis-Amminedichloro(2-methylpyridine) platinum(II) (AMD473), a novel sterically hindered platinum complex: in vivo activity, toxicology, and pharmacokinetics in mice, Clin. Cancer Res. 3 (1997) 2063–2074.
[27] N.J. Wheate, S. Walker, G.E. Craig, R. Oun, The status of platinum anticancer drugs in the clinic and in clinical trials, Dalton Trans. 39 (2010) 8113–8127.
[28] W. Kaim, B. Schwederski, Bioinorganic Chem.: Inorganic Elements in the Chem. of Life, John Wiley & Sons Ltd, Chichester, England, 1994.

[29] D. Yang, S.S.G.E. van Boom, J. Reedijk, J.H. van Boom, A.H.-J. Wang, Structure and isomerization of an intrastrand cisplatin-cross-linked octamer DNA duplex by NMR analysis, Biochemist 34 (1995) 12912–12921.
[30] A. Gelasco, S.J. Lippard, NMR solution structure of a DNA dodecamer duplex containing a cis-diammineplatinum(II) d(GpG) intrastrand cross-link, the major adduct of the anticancer drug cisplatin, Biochemist 37 (1998) 9230–9238.
[31] P.M. Takahara, A.C. Rosenzweig, C.A. Frederick, S.J. Lippard, Crystal structure of a double-stranded DNA containing the major adduct of the anticancer drug cisplatin, Nature 377 (1995) 649–655.
[32] P.M. Takahara, C.A. Frederick, S.J. Lippard, Crystal structure of the anticancer drug cisplatin bound to duplex DNA, J. Am. Chem. Soc. 118 (1996) 12309–12321.
[33] S.U. Dunham, S.U. Dunham, C.J. Turner, S.J. Lippard, Solution structure of a DNA duplex containing a nitroxide spin-labeled platinum d(GpG) intrastrand cross-link refined with NMR-derived long-range electron-proton distance restraints, J. Am. Chem. Soc. 120 (1998) 5395–5403.
[34] R.M. Wing, P. Pjura, H.R. Drew, R.E. Dickerson, The primary mode of binding of cisplatin to a B-DNA dodecamer: C-G-C-G-A-A-T-T-C-G-C-G, EMBO J. 3 (1984) 1201–1212.
[35] D.M.J. Lilley, Cisplatin adducts in DNA: Distortion and recognition, J. Biol. Inorg. Chem. 1 (1996) 189–191.
[36] F. Coste, J.M. Malinge, L. Serre, W. Shepard, M. Roth, M. Leng, C. Zelwer, Crystal structure of a double-stranded DNA containing a cisplatin interstrand cross-link at 1.63 Angstrom resolution: hydration at the platinated site, Nucleic Acids Res. 27 (1999) 1837–1845.
[37] A.P. Silverman, W. Bu, S.M. Cohen, S.J. Lippard, 2.4-A crystal structure of the asymmetric platinum complex {Pt(ammine)(cyclohexylamine)}2 + bound to a dodecamer DNA duplex, J. Biol. Chem. 277 (2002) 49743–49754.
[38] G.N. Parkinson, G.M. Arvanitis, L. Lessinger, S.L. Ginell, R. Jones, B. Gaffney, H.M. Berman, Crystal and molecular structure of a new Z-DNA crystal form: d [CGT(2-NH2-A)CG] and its platinated derivative, Biochemist 34 (1995) 15487–15495.
[39] U.-M. Ohndorf, M.A. Rould, Q. He, C.O. Pabo, S.J. Lippard, Molecular basis for recognition of cisplatin-modified DNA by high-mobility-group proteins, Nature 399 (1999) 708–712.
[40] E.R. Jamieson, S.J. Lippard, Structure, recognition, and processing of cisplatin-DNA adducts, Chem. Rev. 99 (1999) 2467–2498.
[41] H. Sigel, B. Song, G. Oswald, B. Lippert, Acid-base and metal-ion-binding properties of the quaternary [cis-(NH_3)2Pt(dGuo)(dGMP)] complex formed between cis-diammineplatinum(II), 2′-deoxyguanosine (dGuo), and 2′-deoxyguanosine 5′-monophosphate (dGMP2-) in aqueous solution, Chem. Eur. J. 4 (6) (1998) 1053–1060.
[42] K.M. Williams, T. Scarcia, G. Natile, L.G. Marzilli, Imprinting structural information from a GpG ligand into the configuration of a chiral diamine ligand through second-sphere communication in platinum(II) complexes, Inorg. Chem. 40 (2001) 445–454.
[43] E. Pantojaa, A. Gallipolia, S. van Zutphena, D.M. Tookeb, A.L. Spekb, C. Navarro-Ranningerc, J. Reedijk, In vitro antitumor activity and interaction with DNA model bases of cis-[PtCl2(iPram)(azole)] complexes and comparison with their trans analogues, Inorg. Chim. Acta 359 (13) (2006) 4335–4342.
[44] M. Dal Peraro, P. Ruggerone, S. Raugei, F.L. Gervasi, P. Carloni, Investigating biological systems using first principles Car–Parrinello molecular dynamics simulations, Curr. Opin. Struct. Biol. 17 (2) (2007) 149–156.
[45] M.-H. Baik, R.A. Friesner, S.J. Lippard, Theoretical study on the stability of N-glycosyl bonds: why does N7-platination not promote depurination? J. Am. Chem. Soc. 124 (2002) 4495–4503.
[46] M.H. Baik, R.A. Friesner, S.J. Lippard, Theoretical study of cisplatin binding to purine bases: why does cisplatin prefer guanine over adenine? J. Am. Chem. Soc. 125 (46) (2003) 14082–14092.
[47] J. Raber, C. Zhu, L.A. Eriksson, Theoretical study of cisplatin binding to DNA: the importance of initial complex stabilisation, J. Phys. Chem. 109 (2005) 11006–11015.
[48] Z. Chval, M. Šíp, Transition states of cisplatin binding to guanine and adenine: ab initio reactivity study, Collect. Czechoslov. Chem. Commun. 68 (6) (2003) 1105–1118.
[49] H.F. Dos Santos, B.L. Marcial, C.F. De Miranda, L.A.S. Costa, W.B. De Almeida, Structure and properties of the 5a,6-anhydrotetracycline-platinum(II) dichloride complex: a theoretical ab initio study, J. Inorg. Biochem. 100 (10) (2006) 1594–1605.
[50] L.A. Costa, T.W. Hambley, W.R. Rocha, W.B. Almeida, H.F. Dos Santos, Kinetics and structural aspects of the cisplatin interactions with guanine: a quantum mechanical description, Int. J. Quant. Chem. 106 (2006) 2129–2144.
[51] J.F. Lopes, V.S.D. Menezes, H.A. Duarte, W.R. Rocha, W.B. De Almeida, H.F. Dos Santos, Monte Carlo simulation of cisplatin molecule in aqueous solution, J. Physical Chem. B 110 (24) (2006) 12047–12054.
[52] G.R. Chang, L.X. Zhou, D. Chen, Theoretical investigation of detailed thermodynamic character of possible difunctional adducts model, Chin. J. Struct. Chem. 25 (5) (2006) 533–542.
[53] Q.H. Yuan, L.X. Zhou, Hydrolysis process of the anticancer agents novel non-classical trans-platinum(II) with aliphatic amines, Chin. J. Struct. Chem. 26 (8) (2007) 962–972.
[54] D.V. Deubel, On the competition of the purine bases, functionalities of peptide side chains, and protecting agents for the coordination sites of dicationic cisplatin derivatives, J. Am. Chem. Soc. 124 (2002) 5834–5842.
[55] J.V. Burda, M. Zeizinger, J. Sponer, J. Leszczynski, Hydration of cis- and trans-platin: a pseudopotential treatment in the frame of a G3-type theory for platinum complexes, J. Chem. Phys. 113 (6) (2000) 2224–2232.
[56] M. Zeizinger, J.V. Burda, J. Šponer, V. Kapsa, J. Leszczynski, A systematic ab initio study of the hydration of selected palladium square-planar complexes. A comparison with platinum analogues, J. Phys. Chem. A 105 (34) (2001) 8086–8092.
[57] J.V. Burda, M. Zeizinger, J. Leszczynski, Activation barriers and rate constants for hydration of platinum and palladium square-planar complexes: an ab initio study, J. Chem. Phys. 120 (3) (2004) 1253–1262.
[58] J.V. Burda, M. Zeizinger, J. Leszczynski, Hydration process of an activation of trans- and cisplatin complexes in anticancer treatment. DFT and ab initio computational study of thermodynamic and kinetic parameters, J. Comput. Chem. 26 (2005) 907–914.
[59] T. Zimmermann, J. Leszczynski, J.V. Burda, Activation of the cisplatin and transplatin complexes in solution with constant pH and concentration of chloride anions; quantum chemical study, J. Mol. Model. 17 (2011) 2385–2393.
[60] T. Zimmermann, M. Zeizinger, J.V. Burda, Cisplatin interaction with cysteine and methionine; theoretical DFT study, J. Inorg. Biochem. 99 (2005) 2184–2196.
[61] T. Zimmermann, Z. Chval, J.V. Burda, Cisplatin interaction with cysteine and methionine in aqueous solution: computational DFT/PCM study, J. Phys. Chem. B 113 (10) (2009) 3139–3150.
[62] A. Robertazzi, J.A. Platts, A QM/MM study of cisplatin-DNA oligonucleotides: from simple models to realistic systems, Chem. Eur. J. 12 (22) (2006) 5747–5756.
[63] T. Matsui, Y. Shigeta, K. Hirao, Influence of Pt complex binding on the guanine-cytosine pair: a theoretical study, Chem. Phys. Lett. 423 (4–6) (2006) 331–334.
[64] R. Wysokinski, K. Hernik, R. Szostak, D. Michalska, Electronic structure and vibrational spectra of cis-diammine-(orotato)platinum(II), a potential cisplatin analogue: DFT and experimental study, Chem. Phys. 333 (1) (2007) 37–48.
[65] C. Adamo, V. Barone, Exchange functionals with improved long-range behavior and adiabatic connection methods without adjustable parameters: The mPW and mPW1PW models, J. Chem. Phys. 108 (1998) 664–675.
[66] J. Cooper, T. Ziegler, A density functional study of S(N)2 substitution at square-planar platinum(II) complexes, Inorg. Chem. 41 (25) (2002) 6614–6622.
[67] H.J. Zhu, T. Ziegler, A theoretical study of the original Shilov reaction involving methane activation by platinum tetrachloride (PtCl42-) in an acidic aqueous solution, J. Organomet. Chem. 691 (21) (2006) 4486–4497.
[68] H. Erturk, A. Hofmann, R. Puchta, R. van Eldik, Influence of the bridging ligand on the substitution behaviour of dinuclear Pt(II) complexes. An experimental and theoretical approach, Dalton Trans. 22 (2007) 2295–2301.
[69] L. Hao, Y. Zhang, H.W. Tan, G.J. Chen, Theoretical investigation of interaction between unclassical trinuclear antitumor platinum complex and DNA duplex, Chem. J. Chin. Univ.-Chin. 28 (6) (2007) 1160–1164.
[70] A. Hofmann, D. Jaganyi, O.Q. Munro, G. Liehr, R. van Eldik, Electronic tuning of the lability of Pt(II) complexes through - acceptor effects. Correlations between thermodynamic, kinetic, and theoretical parameters, Inorg. Chem. 42 (2003) 1688–1700.
[71] M. Pavelka, M.F.A. Lucas, N. Russo, On the hydrolysis mechanism of the second-generation anticancer drug carboplatin, Chem. Eur. J. 13 (36) (2007) 10108–10116.
[72] A.C. Tsipis, M.P. Sigalas, Mechanistic aspects of the complete set of hydrolysis and anation reactions of cis- and trans-DDP related to their antitumor activity modeled by an improved ASED-MO approach, J. Mol. Struct. (Theochem.) 584 (2002) 235–248.
[73] C. Zhu, J. Raber, L.A. Eriksson, Hydrolysis process of the second generation platinum-based anticancer drug cis-amminedichlorocyclohexylamineplatinum(II), J. Phys. Chem. B 109 (2005) 12195–12205.
[74] T. Song, P. Hu, Insight into the solvent effect: a density functional theory study of cisplatin hydrolysis, J. Chem. Phys. 125 (2006) 091101.
[75] M. Jia, W. Qu, Z. Yang, G. Chen, Theoretical study on the factors that affect the structure and stability of the adduct of a new platinum anticancer drug with a duplex DNA, Int. J. Modern Phys. B 19 (2005) 2939–2949.
[76] A. Robertazzi, J.A. Platts, Hydrogen bonding, solvation, and hydrolysis of cisplatin: a theoretical study, J. Comput. Chem. 25 (8) (2004) 1060–1067.
[77] A. Robertazzi, J.A. Platts, Hydrogen bonding and covalent effects in binding of cisplatin to purine bases: ab initio and atoms in molecules studies, Inorg. Chem. 44 (2) (2005) 267–274.
[78] Y. Zhang, Z. Guo, X.-Z. You, Hydrolysis theory for cisplatin and its analogues based on density functional studies, J. Am. Chem. Soc. 123 (2001) 9378–9387.
[79] J.K.C. Lau, D.V. Deubel, Hydrolysis of the anticancer drug cisplatin: pitfalls in the interpretation of quantum chemical calculations, J. Chem. Theory Comput. 2 (1) (2006) 103–106.
[80] J.V. Burda, J. Leszczynski, How strong can the bend be on a DNA helix from cisplatin? DFT and MP2 quantum chemical calculations of cisplatin-bridged DNA purine bases, Inorg. Chem. 42 (22) (2003) 7162–7172.
[81] M. Zeizinger, J.V. Burda, J. Leszczynski, The influence of a sugar-phosphate backbone on the cisplatin-bridged BpB models of DNA purine bases. Quantum chemical calculations of Pt(II) bonding characteristics, Chem. Phys. 6 (10) (2004) 3585–3590.
[82] M. Pavelka, J. Burda, V., Pt-bridges in various single-strand and double-helix DNA sequences. DFT and MP2 study of the cisplatin coordination with guanine, adenine, and cytosine, J. Mol. Model. 13 (2007) 367–379.
[83] O. Bradáč, T. Zimmermann, J.V. Burda, Comparison of the electronic properties, and thermodynamic and kinetic parameters of the aquation of selected platinum (II) derivatives with their anticancer IC50 indexes, J. Mol. Model. 14 (8) (2008) 705–716.
[84] R.B. Martin, Platinum complexes and binding to N(7) and N(1) of purines, in: B. Lippert (Ed.), Cisplatin, Wiley-VCH, Weinheim, 1999, pp. 183–206.
[85] T. Clark, J. Chandrasekhar, P.V.R. Schleyer, J. Comput. Chem. 4 (1983) 294.
[86] J.V. Burda, N. Runeberg, P. Pyykko, Chemical bonds between noble metals and

noble gases. Ab initio study of the neutral diatomics NiXe, PdXe and PtXe, Chem. Phys. Lett. 288 (5–6) (1998) 635–641.
[87] T. Zimmermann, J.V. Burda, Charge-scaled cavities in polarizable continuum model: determination of acid dissociation constants for platinum-amino acid complexes, J. Chem. Phys. 131 (2009) 135101.
[88] M. Pavelka, M. Šimánek, J. Šponer, J.V. Burda, Copper cation interactions with biologically essential types of ligands: a computational DFT study, J. Phys. Chem. A 110 (2006) 4795–4809.
[89] M. Pavelka, J.V. Burda, Computational study of redox active centres of blue copper proteins: a computational DFT study, Mol. Phys. 106 (24) (2008) 2733–2748.
[90] J.V. Burda, A. Toro-Labbe, S. Gutierrez-Oliva, J.S. Murray, P.A. Politzer, Reaction force decomposition of activation barriers to elucidate solvent effects, J. Phys. Chem. A 111 (13) (2007) 2455–2457.
[91] D.H. Wertz, J. Am. Chem. Soc. 102 (1980) 5316.
[92] M.-J. Cheng, R.J. Nielsen, W.A. Goddard III, Chem. Commun. 50 (2014) 10994.
[93] J.P. Foster, F. Weinhold, Natural hybrid orbitals, J. Am. Chem. Soc. 102 (1980) 7211–7218.
[94] A.E. Reed, F. Weinhold, Natural bond orbital analysis of near-Hartree-Fock water dimer, J. Chem. Phys. 78 (6) (1983) 4066–4073.
[95] F. Weinhold, NBO 5.0 Program 5.0, University of Wisconsin, Madison, Wisconsin 53706: Wisconsin, 2001.
[96] R.W.F. Bader, Atoms in Molecules: A Quantum Theory, Clarendon Press, Oxford, U.K., 1990.
[97] T.A. Keith, A.I.M. All, http://aim.tkgristmill.com, (2009).
[98] M. Mitoraj, A. Michalak, T. Ziegler, A combined charge and energy decomposition scheme for bond analysis, J. Chem. Theor. Comput. 5 (2009) 962.
[99] M. Mitoraj, A. Michalak, T. Ziegler, On the nature of the agostic bond between metal centers and beta-hydrogen atoms in alkyl complexes. An analysis based on the extended transition state method and the natural orbitals for chemical valence scheme (ETS-NOCV), Organometallics 28 (2009) 3727–3741.
[100] G. Schaftenaar, J.H. Noordik, Molden: a pre- and post-processing program for molecular and electronic structures, J. Comput.-Aided Mol. Des. 14 (2000) 123–134, http://www.cmbi.ru.nl/molden/.
[101] W. Humphrey, A. Dalke, K. Schulten, VMD — visual molecular dynamics, J. Molec. Graphics 14 (1996) 33–38.
[102] J.K.C. Lau, D.V. Deubel, Loss of ammine from platinum(II) complexes: implications for cisplatin inactivation, storage, and resistance, Chem.-a Eur. J. 11 (9) (2005) 2849–2855.
[103] Z. Chval, Z. Futera, J.V. Burda, Comparison of hydration reactions for “piano-stool” RAPTA-B and [Ru(η6 − arene)(en)Cl] + complexes: density functional theory computational study, J. Chem. Phys. 134 (2011) 024520.
[104] N.P. Johnson, J.D. Hoeschele, R.O. Rahn, Kinetic-analysis of the in vitro binding of radioactive cis-dichlorodiammineplatinum(II) and trans-dichlorodiammineplatinum(II) to DNA, Chem. Biol. Interact. 30 (2) (1980) 151–169.
[105] N.P. Johnson, J.L. Butour, J. Am. Chem. Soc. 103 (1981) 7351–7354.
[106] W. Schaller, H. Reisner, E. Holler, Biochemistry 26 (1987) 943–951.
[107] F. Bernges, G. Doerner, E. Holler, Eur. J. Biochem. 191 (1990) 743.
[108] F. Legendre, J.-C. Chottard, Kinetics and selectivity of DNA-platination, in: B. Lippert (Ed.), Cisplatin, Wiley-VCH, Weinheim, 1999.

Redox Potentials for Tetraplatin, Satraplatin, Its Derivatives and Ascorbic Acid; *Computational Study.*

Filip Šebesta, Katarína Baxová, Jaroslav V. Burda*

Department of Chemical Physics and Optics, Faculty of Mathematics and Physics, Charles University, Ke Karlovu 3, 121 16 Prague 2, Czech Republic

*corresponding author: burda@karlov.mff.cuni.cz

Abstract

Redox potentials of the Pt(IV) complexes like satraplatin, tetraplatin and several others are determined at the DFT level (with B3LYP, ω-B97XD, PBE1PBE, TPSSTPSS, M06-L, M11-L and MN12-L functionals) and compared with post-Hartree-Fock methods MP2 and CCSD(T). Calculations are performed in water solution employing an implicit solvation model. An impact of replacement of a chloro ligand by water - hydration in the equatorial plane of the complexes is also explored. Further, an influence of solvent pH on the magnitude of the redox potentials is discussed for such hydrated complexes. The obtained results are compared with available experimental data, which leads to RMSD of ca 0.23 V using the CCSD(T)/6-31+G(d)/IEF-PCM/scaled-UAKS level. The distribution of electron density is analyzed at the B3LYP/6-311++G(2df,2pd) level. Also, binding energies of (axial) ligands are compared with the redox potential. Since the Pt(IV) complexes are considered in framework of anticancer treatment, possible reducing agents in bio-environment is searched. Therefore the reduction potential of different protonation states of ascorbic acid is also presented.

Introduction

Cisplatin (cis-diammine-dichloro-platinum(II)) and other Pt(II) complexes like oxaliplatin, carboplatin, nedaplatin, etc. are well known for their anticancer activity. It is generally accepted that a nature of their activity dwells in formation of cross-links in the DNA double helix where the Pt(II) complexes preferably bind to N7 nitrogen atoms of two adjacent guanine nucleobases. Nevertheless, in order to enable the cross-link formation, the complexes must be activated by the hydration reaction, which means a replacement of chloro-ligand(s) by water. In the case of cisplatin, this

reaction is characterized by activation barriers of ca 23 - 25 kcal·mol^{-1} according to experimental data.[1] The theoretical calculations in the implicit solvent give only slightly higher barriers of 24.7 and 26.7 kcal·mol^{-1} for the replacement of the first and second chloro-ligand, respectively.[2] The reaction Gibbs free energies for these two steps are 6.5 and 10.5 kcal·mol^{-1}, respectively. It means that the activation reaction is an endoergic process, which is actually enabled or driven due to L'Chaterier - van Hoff - Brown thermodynamic principle as a consequence of a very low concentration of chloride anions in cytosol and especially in environment of a cellular nucleus. An analogous energy profile was also obtained for JM118 (*cis*-ammine- (cyclohexylamine)-dichloro-platinum (II)) complex (cf. structure **12** in **Scheme 1**).

Potential anticancer Pt(IV) drugs are characterized by their quite high kinetical inertness. This fact is also supported by theoretically determined reaction barriers, e.g. more than 32 kcal·mol^{-1} for the hydration process of satraplatin (JM216, bis-acetato-ammine-(cyclohexylamine)-dichloro-platinum (IV)) and JM149 (the analogous structure like satraplatin where bis-acetato ligands are replaced by bis-hydroxo ligands), cf. **1** and **2** in **Scheme 1**.[2] Hence, it can be assumed that Pt(IV) complexes must be initially reduced and subsequently their reduced forms activated via the described hydration reaction. This also corresponds to the experimental data, which show that the major metabolite of JM216 in patient's plasma (ca 6 hours after administration) is JM118 complex.[3] However, the second most abundant structure is quite surprisingly hydrated JM216. This indicates that hydration can also pass via another reaction mechanism than the 'direct hydration' as considered in ref. 2.

Nevertheless, it still remains a question, which biomolecules can be considered as reductants and which reaction mechanism is responsible for reduction of Pt(IV) complexes. In general, glutathione (GSH) or ascorbic acid (AA) can be assumed as common molecules present in cells. However, in vitro experiments showed that GSH is probably not employed in the reduction process of Pt(IV) derivatives of picoplatin (cis-amminedichloro(2-methylpyridine)platinum(II))[4] and in the case of AA the available experimental studies[5-7] diverge in its impact on the reduction of satraplatin. Simultaneously, it was found that reduction of Pt(IV) complexes can rapidly occur in the presence of metalloproteins (cytochrome c and hemoglobin) together with NADH dehydrogenase.[5] For Pt(IV) drugs with chloro or hydroxo ligands in the axial positions, there exists a pathway via Basolo-Pearson

autocatalytic reaction[8-9] where the axial ligand can be substituted by a reducing agent (dGMP) and the subsequent reduction leads to formation of the corresponding square planar Pt(II) complexes.[10-11] Moreover, several other Pt(II) complexes were detected in assays after reduction, nevertheless they cannot be expected as products formed by releasing of axial ligands.[3-4, 12] Another special case represents photoactivated Pt(IV) diazide complexes, which can be easily reduced under irradiation at the appropriate wavelength.[13]

Satraplatin represents one of the best-known complex of this class. Its activity against small-cell lung cancer, ovarian cancer and squamous cancer of the cervix was investigated in Phase II clinical trials and against castrate resistant prostate cancer in Phase III study.[14] Nevertheless, only limited activity is noticed, but the toxicity profile was satisfactory. No neurotoxicity, ototoxicity and nephrotoxicity were observed in comparison with side effects of cisplatin. Recently its impact on children with refractory solid tumors was studied in Phase I trials.[15] In experimental studies, another representative of Pt(IV) complexes - tetraplatin (tetrachloro-(D,L-trans)l,2-diaminocyclohexaneplatinum(IV)) is frequently used. However, it is no longer considered as potential drug due to its high neurotoxicity, which is ten times higher than in the case of cisplatin.[16-17]

Redox potentials of miscellaneous metallo-complexes were examined in many theoretical studies using different computational techniques. Small octahedral complexes of iron, ruthenium and osmium were investigated by Rulisek.[18] He recommended to use the DFT(PBE)/def2-TZVP/COSMO-RS model for determination of redox potentials providing results with the maximal deviation of 0.1 V from experimental values for $[M(H_2O)_6]^{+2/+3}$ and $[M(NH_3)_6]^{+2/+3}$ redox pairs. However, for highly charged -4/-3 redox pairs the calculated values did not reach desired accuracy. The situation was partially overcome by employing the variable-temperature H-atom abstraction/addition methodology[19] into the calculation scheme. In this approach the redox potential for a highly charged redox pair is calculated based on the redox potential for the -1/0 redox pair formed from the initial complexes by protonation of ligands. It further requires determination of the temperature dependence of Gibbs free energy difference between complex pairs, which have the same charge, and differs by one hydrogen atom. This leads to the fact that the redox potential are computed from supposedly more accurately determined energy differences: between structures with a lower charge (in absolute value) than

the charge of reduced complex and between structures with the same charge. This approach leads to the mean unsigned error of approximately 0.15 V for complexes of seven different transition metals, which already represents an acceptable deviation. Kvapilova et al.[20] investigated an influence of explicit counterions (PF_6^-,$N(CH_3)_4^+$) in the calculations on values of redox potentials of chromium aminocarbene complexes. Simultaneously, surrounding acetonitrile environment was considered at the level of the implicit solvent in these DFT calculations. Inclusion of the explicit counterions itself into the model leads to a decrease of mean average error by 23 mV to 88 mV. Demissie et al.[21] determined redox potentials for iridium and ruthenium complexes as photocatalysts. Besides ground-state redox potentials also the excited state redox potentials, which are important for these compounds, were obtained based on the time-dependent DFT approach. The calculations were performed in acetonitrile employing Born-Haber thermodynamic cycle.

Focusing on reducing agents, the reduction potentials of AA and NADH (exactly methyl-nicotineamide) were investigated using the DFT and very accurate calculations (G3B3, G3MP2) by Matsui et al.[22-23] Solvent was simulated using the C-PCM/UFF model and solvation energy of the proton was established from a linear fit of the dependence of experimental values of pK_a for small alcohols on corresponding computed reaction Gibbs free energies. The calculated redox potential of fully protonated AA (cf. **Fig. 3**) is in the range 0.40 - 0.50 V, while in the literature the experimental value of 0.06 V [24] can usually be found for pH=7. In fact, the redox potential is strongly dependent on pH. In 1933, the relation $E_0(AA) = 375 - 60 . pH$ (mV) was published by Green,[25] however this dependence was found problematic for solutions with pH greater than ca 5.75 due to deprotonation of alcohol groups. Later, Ball[26] determined the redox potential of 326 mV at pH=1.05, 136 mV at pH=4.58 and 51 mV at pH=7.24. For methyl-nicotineamide (as a model structure for NADH) the reduction potential of -0.29 V was calculated (G3MP2) by Matsui in comparison with experimental value of -0.32 V for NADH.[27] Recently, the redox potentials and pK_a values of DNA bases and their derivatives were investigated by Schlegel.[28] The SMD implicit solvent model was employed and pH dependent redox potentials were determined based on the calculated pK_a values.

In this study, we focus on determination of the redox potential of four Pt(IV) complexes - $Pt(NH_3)(cha)Cl_2X_2$ and $Pt(dach)Cl_4$ (where X = CH_3COO, OH, Cl; cha = cyclohexylamine, and dach = diaminocyclohexane), where the reduced complex is

formed by cleaving off the axial ligands X. The redox potential is also calculated for the hydrated complexes where one or both equatorial chloro ligands are substituted by aqua ligands. The calculated binding energies of all ligands in complexes and some electronic structure analyses are presented, too.

Computational details

All calculations were carried out in Gaussian 09. The structures were optimized at the DFT level with the hybrid ω-B97XD functional and 6-31+G(d) basis set in gas phase and subsequently were re-optimized in solvent simulated using the IEF-PCM implicit solvation model with UFF radii for cavity construction. For platinum and chlorine atoms, the Stuttgart-Dresden effective core potentials (MWB-60 and MWB-10, respectively) were used, while the corresponding basis set of pseudoorbitals were appropriately extended by diffuse and polarization functions in order to keep balanced basis set. This basis set is labeled as B1 level hereafter. Frequency analyses were performed at the same level. To find the lowest-lying structure, several conformations were considered for each studied complexes.

Final energies were determined from single-point (SP) calculations at the DFT and MP2 levels using 6-311++G(2df,2pd) basis set in combination with original pseudoorbitals extended with diffuse and 2fg polarization functions[29-31] (this basis set is labeled as B2 in further text) and at the CCSD(T) level with smaller 6-31+G(d) basis set. The single-point DFT calculations were performed with B3LYP,[32] ω-B97XD,[33] PBE1PBE,[34] PBEh1PBE,[35] TPSSTPSS,[36] TPSSh,[36-37] M06-L,[38] M11-L[39] and MN12-L[40] functionals. In the case of B3LYP, PBE1PBE, TPSSTPSS and M06-L functionals, Grimme's empirical dispersion contributions[41-42] were added. In all SP calculations, the IEF-PCM implicit solvation model is combined with UAKS (United Atom Kohn-Sham cavities[43]) radii scaled according to actual NBO charges: scaled-UAKS.[44] It means that in the case of CCSD(T) SP calculations the model was CCSD(T)/B1/IEF-PCM/scaled-UAKS while for the remaining DFT functionals and MP2 method the model was Method/B2/IEF-PCM/scaled-UAKS.

Within the scaled-UAKS model the radius of sphere around group X is scaled linearly with the actual charge Q_{act} between values, which corresponds to formal charges in UAKS model i.e. according to the formula:

$$R(X) = R_0(X) - \gamma \cdot \left| \frac{Q_{act}(X) - Q_{deprot}(X)}{Q_{prot}(X) - Q_{deprot(X)}} + Q_{deprot}(X) \right|, \qquad (1)$$

where R_0 and γ denotes the initial radius and the scaling factor from the standard UAKS model. The radius R_0 is taken according to the original study. Q_{deprot} is NPA charge of individual (negatively charged) group X and Q_{prot} stands for NPA charge of group X in a (neutral) reference molecule (usually CH_3-X). The NPA charges used for scaling are determined by SP calculation at the B3LYP/6-31++G(d,p)/IEF-PCM/UAKS level of theory.

Since the calculated entropic contributions to Gibbs free energies are based on partition sums for ideal gas, it is needed to reduce them when we considered a reaction in solvent. Using free volume theory, Okuno[45] proposed the formula for entropy in solution as:

$$\Delta S_{liq} = \Delta S_{gas} + R \ ln \ (10^{2m-2} \ m) \qquad (2)$$

where *m* is the overall order of the reaction. As a result the free energy is corrected by 6.1 kcal·mol^{-1} in the case of a trimolecular reaction at 298.15 K. Another approach was suggested by Wertz[46] and reformulated by Cheng et al.[47] Its substance dwells in rescaling of the translational and rotational contributions to the total entropy and inclusion of volume changes leading to the expression for calculation of Gibbs free energy:

$$G = H + G_{solv} - TS_{vib} - T[0.54 \cdot \left(S_{gas}^{trans} + S_{gas}^{rot} - 14.3\right) + 8.0] \qquad (3).$$

Reduction of Pt(IV) complexes is considered in the way that after receiving of two electrons from a reducing agent, Pt(II) analogue is formed and axial ligands L_{AX} are simultaneously released. The described process is summarized by equation

$$Pt(IV) + 2\, e^- \rightarrow Pt(II) + 2\, L_{AX}. \qquad (5)$$

Standard redox potential E^0 is associated with standard Gibbs free energy ΔG_r^0 of the above reaction by relation

$$E^0 = -\frac{\Delta G_r^0}{2F} + E_{SHE}\,, \qquad (6)$$

where F is Faraday constant and E_{SHE} represents standard hydrogen electrode potential of -4.281 V.[48]

Except redox potentials, binding energies (BE) for all ligands in the studied complexes are determined including the counterpoise correction[49] according to:

$$BE(L_{AX}) = -(E^C(Pt\_L_{EQ}\_L_{AX\,2}) - E^C(Pt\_L_{EQ}\_L_{AX}) - E^C(L_{AX}) + \Delta BSSE)\,. \quad (7)$$

where ΔBSSE is Boys-Bernardi[49] counterpoise error determined in gas phase:

$$\Delta BSSE = -E(Pt\_L_{EQ}\_L_{AX}\_Bq[L_{AX}]) + E(Pt\_L_{EQ}\_L_{AX}) - E(Bq[Pt\_L_{EQ}\_L_{AX}]\_L_{AX}) + E(L_{AX})\,.$$

Here, Bq[X] signs the ghost part X where only basis set functions are located. The energies E^C are determined in SP calculations at the B3LYP-GD3BJ/B2/IEF-PCM/scaled-UAKS level for optimized geometries. At the same computational level, electronic properties are determined, i.e. atomic partial charges using natural population analysis (NPA) by the NBO v 5.9 program[50] and Bader's AIM analysis of electron density by the AIMAll v 14 program.[51]

Results and Discussion

Binding energies

First, a set of eleven Pt(IV) compounds were optimized at B1 level. It contains $Pt(NH_3)(cha)Cl_2X_2$ structures with axial ligands: X = CH_3COO – satraplatin JM216 (**1**), OH – JM149 (**2**), Cl (**3**), tetraplatin - $Pt(dach)Cl_4$ (**4**), $Pt(en)Cl_2X_2$ structures, where $(NH_3)(cha)$ ligands are replaced by bidentate (en) ligand, with the same set of X-ligands (**5**), (**6**), and (**7**), and analogously $Pt(NH_3)Cl_2X_2$ group: (**8**), (**10**), and (**11**). Since reduction potential of trifluoroacetic acid derivative of the complex (**8**) is experimentally known we added this form to the considered species. All the examined molecules are depicted in **Scheme 1** together with their reduced forms: $Pt(NH_3)(cha)Cl_2$ (JM118 - **12**), $Pt(dach)Cl_2$ (**13**), $Pt(en)_2Cl_2$ (**14**), and $Pt(NH_3)_2Cl_2$ (cisplatin - **15**). In the case of $Pt(NH_3)(cha)Cl_2X_2$ and tetraplatin, monoaqua and diaqua complexes are also considered. Here, the replacement of the chloro ligand in the trans position to cyclohexylamine ligand by a water molecule is expected as monoaqua form since **cha** ligand is characterized by greater trans-influence in comparison with ammine ligand making its trans ligand predisposed to water exchange. This follows also from **Table 1** where BE of chloro ligand in the trans position to **cha** ligand is about 2 kcal·mol^{-1} smaller than BE of the adjacent chloro ligand in the trans position to NH_3 in the case of complexes **2** and **3**. In JM216 (**1**), the determined BEs indicate the opposite trend, which is a consequence of a

hydrogen bonding between ammine ligand and acetate. This H-bond causes strengthening of Pt-NH_3 coordination and consequently weakening of the Pt-Cl bond in the trans-position to this NH_3 ligand (trans influence). The interaction of dach ligand with platinum is stronger than sum of both interactions of cha and NH_3 ligands in complex **3**, which is also confirmed by higher electron density in BCP on Pt-N bonds for tetraplatin by about 0.005 $e \cdot a_b^{-3}$.

BEs of the axial ligands in the studied complexes should have close connection to the redox potential due to the fact that actually these ligands are split off the during reduction process when square-planar Pt(II) complexes are formed. From **Table 2** it follows that in solution the strongest BEs of axial ligands to platinum atom are determined for acetato ligands in satraplatin **1** and JM149 **2**. In satraplatin, hydrogen bonds between acetates and amino groups represent an additional contribution compared to other considered complexes. The electron densities in BCPs of these hydrogen bonds are 0.037 $e \cdot a_b^{-3}$ and 0.027 $e \cdot a_b^{-3}$, which indicate quite strong non-covalent interactions. This fact is also confirmed by the ETS-NOCV analysis carried out for partitioning of the system into one acetate ligand and the remaining part of complex where the third highest contribution to orbital energy corresponds to the hydrogen bond and it represents about 5-6 % of the total orbital interaction (cf. **Fig. 1**). Slightly weaker BE (about 1 $kcal \cdot mol^{-1}$) is observed for the axial hydroxo ligands in **2** (except diaqua-form of the complex). BE of axial chloro ligands in **3** is substantially lower – ca about 8 $kcal \cdot mol^{-1}$ in comparison with structure **1**. Replacement of both ammine and cha ligands by bidentate dach ligand in tetraplatin leads to only marginal changes in BEs of the axial chloro ligands. According to the gas phase calculations, BEs of hydroxo ligands is larger than BEs of the acetato ligands (cf. **Table 3**). This fact is also in accord with shorter bond lengths and larger magnitude of the electron density in the corresponding BCPs (cf. **Table 2**), which indicates that the coordinate-covalent bond between Pt atom and the axial ligands is stronger in the case of JM149. The partial charge of oxygen in the hydroxo ligand is significantly lower compared to the binding atom of the acetato ligands, which points to larger electrostatic enhancement. As to the chloro axial ligands, the lower BE values from **Table 2** are also supported by BCP electron densities, which are approximately about 25% lower in comparison with structures **1** and **2**.

If we compare both the monohydrated and dihydrated complexes, the first substitution of the equatorial chloro ligand leads to an increase of BEs of axial ligand by 9 kcal·mol^{-1} at complexes with **cha** ligand, and about 7 kcal·mol^{-1} at tetraplatin, cf. **Table 2**. The replacement of the second chloro ligand further raises the BEs by 6-9 kcal·mol^{-1}. This is a result of weaker donation of the neutral aqua ligands compared to the charged chloro ligands, which leads to higher donation from the remaining ligands, cf. **Tables 1** and **2**. This is also documented by an increase of electron density in BCPs between these atoms and Pt. However, the monoaqua Pt(IV) complexes are not usually stable at neutral pH and converts to the hydroxo complexes as follows from the calculated pK_as for aqua ligand in the range between 0 and 3 (determined at CCSD(T) level). For these hydroxo complexes different behavior is observed. The equatorial hydroxo ligand is bound more strongly than chloro ligands due to higher electrostatic enhancement. As a consequence the BEs of axial ligands slightly decrease by approximately 1 kcal·mol^{-1} compared to the corresponding chloro forms. Nevertheless, the electron density in BCPs of Pt-L_{AX} bonds does not nearly differ (±0.0002 e·a_b^{-3}) for the both chloro and hydroxo form while after the substitution of the equatorial chloro ligand by neutral water the electron density in the BCPs of corresponding Pt-L_{AX} bonds increases more significantly - by 0.003-0.004 e·a_b^{-3}.

In the reduced Pt(II) complexes, a decrease of the partial charge of Pt atom by ca 0.7 e is observed in comparison with the Pt(IV) complexes containing axial hydroxo and acetato ligands and by 0.4 e in complexes with axial chloro ligands. The decrease of Pt partial charge corresponds also with decrease of BE of equatorial ligands up to 10 kcal·mol^{-1}. Similar changes are visible in the BCPs electron densities of Pt-L_{EQ} ligands, which are diminished by 0.004-0.010 e·a_b^{-3}.

Redox potentials

Redox potentials for the studied Pt(IV) complexes were determined at the 16 levels including two different kinds of the corrections to entropic contributions in solvent. Final values of the redox potentials together with available experimental data[52-55] are presented in **Table 4** for the selected (discussed) methods. Complete data of all the considered methods are collected in **Table S1** in Supplementary Material. From these tables it follows that one of the best agreement with measured data is achieved at the CCSD(T) level employing Wertz's correction. The RMSD from experimental

results (considering complexes **1**, **4**, **5**, **6**, **7**, **8**, **9**, **10** and **11**) represents 234 mV, which is about twice lower than in the case when these corrections are not included. Also the Okuno's corrections provide a visible improvement of calculated redox potentials. This shows that the entropic contributions are really overestimated in standard PCM approach and should be reduced. In comparison with most of previous calculations of redox potentials where only the charge of a considered complex was changed and number of ligands remained conserved, here the complexes loose two axial ligands within the reduction process. This is a result of the fact, that two accepted electrons during the reduction enter the d_{z^2} orbital (LUMO in Pt(IV) complexes, cf. **Fig. 2**), which destabilizes ligands in the axial positions. The described change of number of particles in the reaction course leads to the additional problems with nuclear degrees of freedom within evaluation of reaction Gibbs free energy. These contributions can reach up to 30 kcal·mol^{-1} in the case of our complexes, which represent a significant part of total reaction Gibbs free energy. Application of the Wertz's correction decreases them approximately to one half of the original uncorrected values.

As to accuracy of the considered methods we can compare CCSD(T) and MP2/B2 calculations with Wertz's corrections. Determining RMSD just for complexes with axial chloro ligands, the difference is more than 250 mV. For the other group of complexes (with hydroxo or acetate axial ligands - **1**, **2**, **5**, **6**, **8**, **9** and **10**) the analogous difference is much smaller - up to 60 mV. It should be mentioned that the lowest RMSD (179 mV) from post-HF methods is obtained using the MP2/B1+W computational level. This method systematically provides lower values by 100-200 mV than the CCSD(T) approach. Finally, the redox potentials determined at the regarded DFT levels do not reach accuracy of the post-HF methods except MN12-L and TPSSTPSS-GD3BJ functionals. Results obtained using MN12-L functional (+ Wertz's correction) represents the best agreement with experimental data (RMSD = 154 mV). Applying Grimme's dispersion corrections introduces another important feature how to decrease the RMSD by 100-300mV especially with inclusion of non-electrostatic solvation contributions within the PCM scheme. The RMSDs of other commonly used functionals: ω-B97XD, B3LYP-GD3BJ, and PBE1PBE- GD3BJ are visibly higher: 741, 628, and 482 mV, respectively, cf. **Table 4** and results for complete set of explored methods can be found in **Table S1** in Supplementary Material. The systematically highest deviations from experimental

values come from the calculated redox potentials of bis-acetato complexes **5** and **8,** which are strongly overestimated for all the considered methods. Nevertheless, the reduction potential of the bis-acetato complex **1** is determined relatively correctly (in comparison with the other complexes). In fact, on the contrary to the complexes **5** and **8**, its experimental value is taken from Choi's study[52] whose results are in very good agreement with our CCSD(T) calculations (RMSD of 64 mV). On the other hand, Baik et al.[56] assumed in their study that the reduction of Pt(IV) complexes represents two single electron transfers where acceptance of the first electron leads to formation of the six-coordinate Pt(III) complex while the second electron transfer is accompanied with releasing of the axial ligands. The first step is not as much thermodynamically favorable as the second one which is decisive for the magnitude of the redox potential. Moreover, on the basis of the work of Savéant[57] they claimed that the standard reduction potential does not correspond with peak potential E_{pc} from cyclic voltammetry and its value can be estimated as $(E_{pc}+E_{pc/2})/2$ where $E_{pc/2}$ is potential at the half-height of the peak. In this way, the calculated values of redox potentials are not so positive. The reduction potential of AA is determined with sufficient accuracy only at the post-HF levels with smaller 6-31+G(d) basis set. In this case, all the DFT functionals fail, providing highly overestimated values.

Another comparison is focused on differences between the potentials obtained within the same experimental group. It means that only relative differences of redox potentials (measured by the same technique in each group, e.g. in the case Choi's data just differences between complexes 1-4-7 and in the case of Hambley's results differences between complexes 5-6-8-10-11) were compared with analogous calculated differences in order to minimize error from different experimental conditions. From this viewpoint, the lowest RMSD is connected with CCSD(T) approach (137 mV) followed by CCSD (163 mV) and MP2/B1 (184 mV) methods. The DFT-D methods do not provide much worse deviations: 186 mV for TPSSTPSS-GD3BJ and 184 mV for ω-B97XD are the most successful functionals in this case. We also tried to consider the potential of SHE as a parameter determined by the least-square fitting procedure within each method. The obtained values lie between 4.26 V and 5.12 V. The closest values to the reference SHE potential of 4.28 V are connected with MN12-L/6-311++G(2df,2pd) (E_{SHE} = 4.26 V) and MP2/6-31+G(d) (E_{SHE} = 4.36 V) computational levels. The fitting of the SHE potential in calculations of reduction potentials decreases the RMSDs up to values of 200 mV for

all the methods where the lowest RMSD (128 mV) corresponds to CCSD(T). Also, the correlation coefficients are quite interesting, giving us some information how well trends of the reduction potentials are described. The highest correlation with experimental data is observed at the MN12-L, CCSD(T), and TPSSTPSS-GD3BJ levels (in the descending order). The correlation coefficients for other methods together with values of the fitted SHE potentials can be found in **Table S1** in Supplementary materials. As a result of the performed comparisons, hereafter only the results obtained at the CCSD(T) level with Wertz corrections will be discussed.

From the experimental results it was found that redox potentials are dependent on the axial ligands. It was observed for $PtCl_2(en)X_2$ complexes that the potential increases in order OH < OAc < Cl. These experiments[53] were performed relative to Ag/AgCl electrode obtaining: -884, -505, and -224 mV for X = OH, OAc, and Cl, respectively. The calculated redox potentials for $Pt(NH_3)Cl_2(cha)X_2$ complexes (**1**,**2**,**3**) show not only the same trend as for $PtCl_2(en)X_2$ complexes but also the differences between the individual reduction potentials are quite similar (cf. **Table 4**). This behavior nicely correlates with gas phase BEs of the axial ligands. In the literature,[52] a dependence of the reduction potential on the electron-withdrawing power and the volume (bulkiness) of axial ligands is also discussed – the larger axial ligand, the higher reduction potential. But we rather focus on the volume of the equatorial ligands. Based on experimental data in **Table 4** it can be noticed that in the row of $Pt(NH_3)_2Cl_4$ **(11)**, $Pt(en)Cl_4$ **(7)**, and $Pt(dach)Cl_4$ **(4)** complexes the redox potential increases with the bulkiness of the equatorial ligands. However, the calculated values exhibit an opposite trend (actually quite systematically for all the employed methods), despite the fact that magnitudes of BEs for their axial chloro ligands is in good accord with experimental data: -42.3 (**11**), -40.3 (**7**) and -39.5 (**4**) kcal·mol^{-1}. The same is true for electron densities in BCPs of these Pt-Cl(axial) (0.0945 (**11**), 0.0941 (**7**), 0.0939 e·a_b^{-3} (**4**)).

The hydration of Pt(IV) complexes in the equatorial plane, substituting one of the chloro ligands, leads to an increase of the reduction potentials by roughly 100 mV per each substituted chloro ligand. The largest increase is observed for satraplatin and represents ca 120 mV per one substitution. This change is caused by a lower stability of the hydrated Pt(IV) complexes in comparison with the hydrated Pt(II) complexes, which can be explained by the electrostatic reasons - a negatively charged ligand coordinates more strongly to the central atom with higher partial

charge (oxidation number). However, as already mentioned above, the monoaqua Pt(IV) complexes are not stable at neutral pH and convert to hydroxo-forms according to calculated pK_a values, cf. **Table 3**. The hydroxo complexes exhibit quite different behavior of the reduction potential, which is lower than potential of original Pt(IV) complexes (with equatorial dichloro ligands). The difference is approximately -100 mV (cf. **Table 4**). Hence, it can be concluded that the hydration does not facilitate the reduction process, which is particularly important for reduction of satraplatin (with experimentally estimated reduction potential: -53 ± 60 mV)[52] by AA considering that its reduction potential is ca 60 mV.[24] Nevertheless, as mentioned in Introduction, the reduction potential of AA strongly depends on solvent pH - its reduction potential decreases with increasing pH. In fact, oxidation of AA is described by **Scheme 2** and magnitude of its reduction potential depends on protonation of O2 and O3 sites. Experimentally determined pK_a values[58] represent 4.1 and 11.6 and three corresponding protonation states are depicted in **Fig. 3**. The calculated difference in the reduction potentials of the fully protonated (**I** in **Fig. 3**) and singly-deprotonated (**II** in **Fig.** 3) form of AA is ca 300 mV, where our best estimation give values 346 mV and 41 mV, respectively. This fairly fits to the experimental results obtained by Ball (326 mV (pH=1.05) and 51 mV (pH=7.24))[26] and usually presented experimental value of 60 mV[24] at neutral pH. Furthermore, Matsui et al.[22] determined reduction potential for fully protonated AA in the range 400-500 mV. On the contrary to AA, whose reduction potential is relatively high, reducing agents as GSH (with reduction potential -230 mV) or NADH (-320 mV) can be taken into consideration for reduction of all mentioned Pt(IV) complexes except compounds with axial hydroxo ligands according to our calculations. However, Pt(IV) complexes are known for their kinetic inertness and an important role is played by an individual reduction mechanism. For example, it was experimentally shown that Pt(IV) derivatives of picoplatin are not reduced in the presence of GSH.[4]

Conclusion

Redox potentials for several Pt(IV) complexes are determined using selected QM methods. On the contrary to majority of previous calculations, a number of molecules changes in the course of the reduction process due to the Pt-L_{AX} bond

cleavage. We showed that in this case contributions from translational and rotational degrees of freedom to Gibbs free energy have to be corrected in order to reach sufficient accuracy when the reaction is considered in a water solution. The best results are provided by the MN12-L functional, which gives RMSD of 0.15 V after employing Wertz's correction and the IEF-PCM/scaled-UAKS implicit solvation model. Nevertheless, when a systematic error is removed by least-square fitting the SHE potential for experimentally known reduction potential the CCSD(T) method becomes the best-performing with RMSD of 0.13 V. The post-HF methods in combination with 6-31+G(d) basis set are also suitable for determination of reduction potential of organic molecules as documented in the case of ascorbic acid. The increasing magnitude of the reduction potential in the series of OH^-, Ac, and Cl^- is obtained in accord with experiments. Nevertheless, the dependence on the type of the equatorial ligand (dach, en, $(NH_3)_2$) was not reproduced. Furthermore, an influence of a possible hydration of the Pt(IV) complexes in their equatorial plane was studied. The dependence on pH of solution is observed, since in strongly acid solutions magnitude of the reduction potential is visibly high (in presence of aqua-ligands) and it decreases in less acidic and basic solutions where complexes with hydroxo-ligands occur. For the chosen Pt(IV) complexes, gas phase BEs of the axial ligands correlate well with the reduction potentials. Also the effect of trans-influence is discussed in the case of the equatorial ligands.

Acknowledgement:

Authors are grateful to Grant Agency of Czech Republic project No 16-06240S for supporting this study. Additional support (for FŠ) was obtained from the Grant Agency of Charles University. No.1145016. Access to computing facilities owned by parties and projects contributing to the National Grid Infrastructure MetaCentrum, provided under the program 'Projects of Large Infrastructure for Research, Development, and Innovations' (LM2010005) is highly appreciated.

References:

1. Arpalahti, J.; Mikola, M.; Mauristo, S., cisplatin eq. K. *Inorg. Chem.* **1993,** *32*, 3327.
2. Bradáč, O.; Zimmermann, T.; Burda, J. V., Can Satraplatin be hydrated before the reduction process occurs? The DFT computational study. . *J. Mol. Model.* **2013,** *19*, 1669-168.

3. Raynaud, F. I.; Mistry, P.; Donaghue, A.; Poon, G. K.; Kelland, L. R.; Barnard, C. F. J.; Murrer, B. A.; Harrap, K. R., Biotransformation of the platinum drug JM216 following oral administration to cancer patients. *Cancer Chemotherapy and Pharmacology* **1996,** *38*, 155-162.
4. Ravera, M.; Gabano, E.; Zanellato, I.; Bonarrigo, I.; Escribano, E.; Moreno, V.; Font-Bardia, M.; Calvet, T.; Osella, D., Synthesis, characterization and antiproliferative activity on mesothelioma cell lines of bis(carboxylato)platinum(iv) complexes based on picoplatin. *Dalton Transactions* **2012,** *41* (11), 3313-3320.
5. Carr, J.; Tingle, M.; McKeage, M., Satraplatin activation by haemoglobin, cytochrome C and liver microsomes in vitro. *Cancer Chemotherapy and Pharmacology* **2006,** *57* (4), 483-490.
6. Lemma, K.; Sargeson, A. M.; Elding, L. I., Kinetics and mechanism for reduction of oral anticancer platinum(IV) dicarboxylate compounds by L-ascorbate ions. *Journal of the Chemical Society, Dalton Transactions* **2000,** (7), 1167-1172.
7. Wexselblatt, E.; Gibson, D., What do we know about the reduction of Pt(IV) pro-drugs? *Journal of Inorganic Biochemistry* **2012,** *117*, 220-229.
8. Basolo, F.; Messing, A. F.; Wilks, P. H.; Wilkins, R. G.; Pearson, R. G., Proceedings International Symposium on the Chemistry of the Co-ordination CompoundsMechanisms of exchange and substitution reactions in platinum (IV) complexes. *Journal of Inorganic and Nuclear Chemistry* **1958,** *8*, 203-208.
9. Basolo, F.; Pearson, R. G., Mechanisms of Substitution Reactions of Metal Complexes. In *Advances in Inorganic Chemistry and Radiochemistry*, Emeleus, H. J.; Sharpe, A. G., Eds. Academic Press: 1961; Vol. Volume 3, pp 1-89.
10. Ariafard, A.; Ghohe, N. M.; Abbasi, K. K.; Canty, A. J.; Yates, B. F., Theoretical Investigation into the Mechanism of 3′-dGMP Oxidation by [PtIVCl4(dach)]. *Inorganic Chemistry* **2013,** *52* (2), 707-717.
11. Choi, S.; Vastag, L.; Leung, C.-H.; Beard, A. M.; Knowles, D. E.; Larrabee, J. A., Kinetics and Mechanism of the Oxidation of Guanosine Derivatives by Pt(IV) Complexes. *Inorg. Chem.* **2006,** *45* (25), 10108-10114.
12. Nemirovski, A.; Vinograd, I.; Takrouri, K.; Mijovilovich, A.; Rompel, A.; Gibson, D., New reduction pathways for ctc-[PtCl2(CH3CO2)2(NH3)(Am)] anticancer prodrugs. *Chemical Communications* **2010,** *46* (11), 1842-1844.
13. Mackay, F. S.; Woods, J. A.; Heringová, P.; Kašpárková, J.; Pizarro, A. M.; Moggach, S. A.; Parsons, S.; Brabec, V.; Sadler, P. J., A potent cytotoxic photoactivated platinum complex. *Proceedings of the National Academy of Sciences* **2007,** *104* (52), 20743-20748.
14. Bhargava, A.; Vaishampayan, U. N., Satraplatin: leading the new generation of oral platinum agents. *Expert Opinion on Investigational Drugs* **2009,** *18* (11), 1787-1797.
15. Akshintala, S.; Marcus, L.; Warren, K. E.; Murphy, R. F.; Sissung, T. M.; Srivastava, A.; Goodspeed, W. J.; Goodwin, A.; Brewer, C. C.; Zalewski, C.; King, K. A.; Kim, A.; Figg, W. D.; Widemann, B. C., Phase 1 trial and pharmacokinetic study of the oral platinum analog satraplatin in children and young adults with refractory solid tumors including brain tumors. *Pediatric Blood & Cancer* **2015,** *62* (4), 603-610.
16. O'Rourke, T. J.; Weiss, G. R.; New, P.; Burris, H. A. I.; Rodriguez, G.; Eckhardt, J.; Hardy, J.; Kuhn, J. G.; Fields, S.; Clark, G. M.; Von Hoff, D. D., Phase I clinical trial of ormaplatin (tetraplatin, NSC 363812). *Anti-Cancer Drugs* **1994,** *5* (5), 520-526.

17. Schilder, R. J.; LaCreta, F. P.; Perez, R. P.; Johnson, S. W.; Brennan, J. M.; Rogatko, A.; Nash, S.; McAleer, C.; Hamilton, T. C.; Roby, D.; Young, R. C.; Ozols, R. F.; O'Dwyer, P. J., Phase I and Pharmacokinetic Study of Ormaplatin (Tetraplatin, NSC 363812) Administered on a Day 1 and Day 8 Schedule. *Cancer Research* **1994,** *54* (3), 709-717.
18. Rulíšek, L., On the Accuracy of Calculated Reduction Potentials of Selected Group 8 (Fe, Ru, and Os) Octahedral Complexes. *The Journal of Physical Chemistry C* **2013,** *117* (33), 16871-16877.
19. Bím, D.; Rulíšek, L.; Srnec, M., Accurate Prediction of One-Electron Reduction Potentials in Aqueous Solution by Variable-Temperature H-Atom Addition/Abstraction Methodology. *The Journal of Physical Chemistry Letters* **2016,** *7* (1), 7-13.
20. Kvapilová, H.; Hoskovcová, I.; Ludvík, J.; Záliš, S., Theoretical Predictions of Redox Potentials of Fischer-Type Chromium Aminocarbene Complexes. *Organometallics* **2014,** *33* (18), 4964-4972.
21. Demissie, T. B.; Ruud, K.; Hansen, J. H., DFT as a Powerful Predictive Tool in Photoredox Catalysis: Redox Potentials and Mechanistic Analysis. *Organometallics* **2015,** *34* (17), 4218-4228.
22. Matsui, T.; Kitagawa, Y.; Okumura, M.; Shigeta, Y., Accurate Standard Hydrogen Electrode Potential and Applications to the Redox Potentials of Vitamin C and NAD/NADH. *The Journal of Physical Chemistry A* **2015,** *119* (2), 369-376.
23. Psciuk, B. T.; Schlegel, H. B., Computational Prediction of One-Electron Reduction Potentials and Acid Dissociation Constants for Guanine Oxidation Intermediates and Products. *The Journal of Physical Chemistry B* **2013,** *117* (32), 9518-9531.
24. Loach, P. A.; Fasman, G. D., *Handbook of Biochemistry and Molecular Biology*. 1976; Vol. I.
25. Green, D. E., The potentials of ascorbic acid. *Biochemical Journal* **1933,** *27* (4), 1044-1048.
26. Ball, E. G., STUDIES ON OXIDATION-REDUCTION: XXIII. ASCORBIC ACID. *Journal of Biological Chemistry* **1937,** *118* (1), 219-239.
27. David F. Wilson; Maria Erecińska, a.; Dutton, P. L., Thermodynamic Relationships in Mitochondrial Oxidative Phosphorylation. *Annual Review of Biophysics and Bioengineering* **1974,** *3* (1), 203-230.
28. Thapa, B.; Schlegel, H. B., Calculations of pKa's and Redox Potentials of Nucleobases with Explicit Waters and Polarizable Continuum Solvation. *The Journal of Physical Chemistry A* **2015,** *119* (21), 5134-5144.
29. Burda, J. V.; Zeizinger, M.; Sponer, J.; Leszczynski, J., Hydration of cis- and trans-platin: A pseudopotential treatment in the frame of a G3-type theory for platinum complexes. *Journal of Chemical Physics* **2000,** *113* (6), 2224-2232.
30. Burda, J. V.; Runenberg, N.; Pyykko, P., Chemical bond between noble metals and noble gases. Ab initio study of the neutral diatomics NiXe, PdXe, and PtXe. *Chem. Phys. Letters* **1998,** *288*, 635-641.
31. Zeizinger, M.; Burda, J. V.; Šponer, J.; Kapsa, V.; Leszczynski, J., A Systematic ab Initio Study of the Hydration of Selected Palladium Square-Planar Complexes. A Comparison with Platinum Analogues. *J. Phys. Chem. A,* **2001,** *105* (34), 8086-8092.
32. Becke, A. D., Density Functional thermochemistry. III. The role of exact exchange. *J. Phys. Chem.* **1993,** *98*, 5648-5652.

33. Chai, J.-D.; Head-Gordon, M., Long-range corrected hybrid density functionals with damped atom-atom dispersion corrections,. *Phys. Chem. Chem. Phys.* **2008,** *10*, 6615-20.
34. Adamo, C.; Barone, V., Toward reliable density functional methods without adjustable parameters: The PBE0 model. *The Journal of Chemical Physics* **1999,** *110* (13), 6158-6170.
35. Ernzerhof, M.; Perdew, J. P., Generalized gradient approximation to the angle- and system-averaged exchange hole. *The Journal of Chemical Physics* **1998,** *109* (9), 3313-3320.
36. Tao, J.; Perdew, J. P.; Staroverov, V. N.; Scuseria, G. E., Climbing the Density Functional Ladder: Nonempirical Meta\char21{}Generalized Gradient Approximation Designed for Molecules and Solids. *Physical Review Letters* **2003,** *91* (14), 146401.
37. Staroverov, V. N.; Scuseria, G. E.; Tao, J.; Perdew, J. P., Erratum: "Comparative assessment of a new nonempirical density functional: Molecules and hydrogen-bonded complexes" [J. Chem. Phys. 119, 12129 (2003)]. *The Journal of Chemical Physics* **2004,** *121* (22), 11507-11507.
38. Zhao, Y.; Truhlar, D. G., A new local density functional for main-group thermochemistry, transition metal bonding, thermochemical kinetics, and noncovalent interactions. *The Journal of Chemical Physics* **2006,** *125* (19), 194101.
39. Peverati, R.; Truhlar, D. G., M11-L: A Local Density Functional That Provides Improved Accuracy for Electronic Structure Calculations in Chemistry and Physics. *The Journal of Physical Chemistry Letters* **2012,** *3* (1), 117-124.
40. Peverati, R.; Truhlar, D. G., An improved and broadly accurate local approximation to the exchange-correlation density functional: The MN12-L functional for electronic structure calculations in chemistry and physics. *Physical Chemistry Chemical Physics* **2012,** *14* (38), 13171-13174.
41. Grimme, S.; Ehrlich, S.; Goerigk, L., Effect of the damping function in dispersion corrected density functional theory. . *J. Comp. Chem.* **2011,** *32*, 1456-65.
42. Grimme, S.; Antony, J.; Ehrlich, S.; Krieg, H., A consistent and accurate ab initio parametrization of density functional dispersion correction (DFT-D) for the 94 elements H-Pu. *The Journal of Chemical Physics* **2010,** *132* (15), 154104.
43. Barone, V.; Cossi, M.; Tomasi, J., A new definition of cavities for the computation of solvation free energies by the polarizable continuum model. *J. Chem. Phys.* **1997,** *107* (8), 3210-3221.
44. Zimmermann, T.; Burda, J. V., Charge-scaled cavities in polarizable continuum model: Determination of acid dissociation constants for platinum-amino acid complexes. *J. Chem. Phys.* **2009,** *131*, 135101.
45. Okuno, Y., Theoretical Investigation of the Mechanism of the Baeyer-Villiger Reaction in Nonpolar Solvents. *Chemistry – A European Journal* **1997,** *3* (2), 212-218.
46. Wertz, D. H., Relationship between the Gas-Phase Entropies of Molecules and Their Entropies of Solvation in Water and 1-Octanol. . *J. Am.chem. Soc.* **1980,** *102*, 5316-5322.
47. Cheng, M.-J.; Nielsen, R. J.; Goddard Iii, W. A., A homolytic oxy-functionalization mechanism: intermolecular hydrocarbyl migration from M-R to vanadate oxo. *Chemical Communications* **2014,** *50* (75), 10994-10996.
48. Isse, A. A.; Gennaro, A., Absolute Potential of the Standard Hydrogen Electrode and the Problem of Interconversion of Potentials in Different Solvents. *The Journal of Physical Chemistry B* **2010,** *114* (23), 7894-7899.

49. Boys, S. F.; Bernardi, F., The Calculation of Small Molecular Interactions by the Differences of Separate Total Energies. Some Procedures with Reduced Errors. *Mol. Phys.* **1970,** *19*, 553-566.
50. Glendening, E. D.; Badenhoop, K.; Ree, A. E.; Carpenter, J. E.; Bohmann, J. A.; Morales, M.; Weinhold, F. *NBO v 5.9 Program* 5.0; University of Wisconsin, Madison, Wisconsin 53706: Wisconsin, 2001.
51. Keith, T. A. *AIM All*, http://aim.tkgristmill.com: 2014.
52. Choi, S.; Filotto, C.; Bisanzo, M.; Delaney, S.; Lagasee, D.; Whitworth, J. L.; Jusko, A.; Li, C.; Wood, N. A.; Willingham, J.; Schwenker, A.; Spaulding, K., Reduction and Anticancer Activity of Platinum(IV) Complexes. *Inorg. Chem.* **1998,** *37* (10), 2500-2504.
53. Ellis, L.; Er, H.; Hambley, T., The Influence of the Axial Ligands of a Series of Platinum(IV) Anti-Cancer Complexes on Their Reduction to Platinum(II) and Reaction With DNA. *Australian Journal of Chemistry* **1995,** *48* (4), 793-806.
54. Hall, M. D.; Foran, G. J.; Zhang, M.; Beale, P. J.; Hambley, T. W., XANES Determination of the Platinum Oxidation State Distribution in Cancer Cells Treated with Platinum(IV) Anticancer Agents. *Journal of the American Chemical Society* **2003,** *125* (25), 7524-7525.
55. Wilson, J. J.; Lippard, S. J., Synthesis, Characterization, and Cytotoxicity of Platinum(IV) Carbamate Complexes. *Inorganic Chemistry* **2011,** *50* (7), 3103-3115.
56. McCormick, M. C.; Keijzer, K.; Polavarapu, A.; Schultz, F. A.; Baik, M.-H., Understanding Intrinsically Irreversible, Non-Nernstian, Two-Electron Redox Processes: A Combined Experimental and Computational Study of the Electrochemical Activation of Platinum(IV) Antitumor Prodrugs. *Journal of the American Chemical Society* **2014,** *136* (25), 8992-9000.
57. Costentin, C.; Robert, M.; Savéant, J.-M., Electron transfer and bond breaking: Recent advances. *Chemical Physics* **2006,** *324* (1), 40-56.
58. In *The Merck Index - An Encyclopedia of Chemicals, Drugs, and Biologicals*, O'Neil, M. J., Ed. Merck and Co., Inc.: Whitehouse Station, NJ, 2006; p 136.

Table 1: Binding energies (in kcal·mol^{-1}) of equatorial ligands in considered Pt(IV) complexes (determined at B3LYP/B2/IEFPCM/scaled-UAKS level and corrected to gas phase counterpoise error) and the partial charge on Pt atom (in e).

	Equatorial ligands/Charge	Neutral	Monoaqua	Monohydroxo	Diaqua
1	cha	45	61	39	64
	NH_3	49	48	43	64
	$Cl/H_2O/OH/H_2O$	38	32	54	33
	$Cl/Cl/Cl/H_2O$	37	46	36	31
	δ(Pt)	1.252	1.362	1.365	1.495
2	cha	44	61	39	66
	NH_3	40	46	40	60
	$Cl/H_2O/OH/H_2O$	35	25	48	27
	$Cl/Cl/Cl/H_2O$	37	46	33	28
	δ(Pt)	1.251	1.359	1.357	1.483
3	cha	45	67	42	71
	NH_3	44	47	43	67
	$Cl/H_2O/OH/H_2O$	40	30	56	32
	$Cl/Cl/Cl/H_2O$	43	51	39	34
	δ(Pt)	0.957	1.077	1.092	1.206
4	dach	104	127	96	155
	$Cl/H_2O/OH/H_2O$	40	29	53	33
	$Cl/Cl/Cl/H_2O$	40	47	35	33
	δ(Pt)	0.967	1.083	1.102	1.212
12	cha	42	53	40	37
	NH_3	39	41	39	52
	$Cl/H_2O/OH/H_2O$	31	24	41	26
	$Cl/Cl/Cl/H_2O$	32	37	31	26
	δ(Pt)	0.554	0.668	0.643	0.794
13	dach	94	108	89	86
	$Cl/H_2O/OH/H_2O$	30	23	39	25
	$Cl/Cl/Cl/H_2O$	30	35	30	25
	δ(Pt)	0.557	0.670	0.640	0.795

	5	**6**	**7**	**8**	**9**	**10**	**11**	**14**	**15**
Cl	36	33	40	41	48	39	45	31	34
en/NH_3	106	99	103	48	48	43	45	94	41
δ(Pt)	1.252	1.254	0.968	1.249	1.242	1.234	0.957	0.554	0.552

Table 2: Pt-L_{AX} bond lengths (in Å), electron densities (in $e \cdot a_b^{-3}$) in corresponding BCPs, partial charges (in e) of the binding atoms of the axial ligands and binding energies (in $kcal \cdot mol^{-1}$) of the axial ligands. Column Equat. signs non-amino equatorial ligands

	Equat.	Lengths	BCP(Pt-L_{AX}))	Charge(L_{AX})	BE
1	Cl_2	2.019	0.1187	-0.686	49
	$(H_2O)Cl$	2.011	0.1224	-0.688	58
	$(OH)Cl$	2.016	0.1189	-0.694	48
	$(H_2O)_2$	2.003	0.1260	-0.701	64
2	Cl_2	2.010	0.1267	-1.029	48
	$(H_2O)Cl$	2.000	0.1307	-1.025	58
	$(OH)Cl$	2.008	0.1265	-1.051	47
	$(H_2O)_2$	1.992	0.1338	-1.024	66
3	Cl_2	2.350	0.0941	-0.443	41
	$(H_2O)Cl$	2.342	0.0967	-0.428	49
	$(OH)Cl$	2.348	0.0940	-0.459	40
	$(H_2O)_2$	2.330	0.0997	-0.411	57
4	Cl_2	2.350	0.0939	-0.448	40
	$(H_2O)Cl$	2.339	0.0969	-0.433	47
	$(OH)Cl$	2.347	0.0937	-0.464	38
	$(H_2O)_2$	2.329	0.0996	-0.418	56
5	Cl_2	2.019	0.1184	-0.692	48
6	Cl_2	2.008	0.1269	-1.035	49
7	Cl_2	2.349	0.0941	-0.449	40
8	Cl_2	2.019	0.1187	-0.680	52
9	Cl_2	2.015	0.1177	-0.649	48
10	Cl_2	2.007	0.1274	-1.044	50
11	Cl_2	2.348	0.0945	-0.443	42

Table 3: Gas phase binding energies (in $kcal \cdot mol^{-1}$) of the axial ligands in the considered Pt(IV) complexes which are determined at the B3LYP/B2 level and corrected to the counterpoise error. The pK_a values correspond to equatorial aqua (hydroxo) ligand in the monohydrated complexes.

	Axial ligands	Neutral	Monoaqua	Diaqua	pK_a
1	CH_3COO^-	172	271	368	1.2
2	OH^-	194	295	396	2.6
3	Cl^-	156	252	350	0.4
4	Cl^-	155	252	355	1.8

Table 4: Redox potentials (in mV) determined within the IEF-PCM/scaled-UAKS model. The redox potential for ascorbic acid is presented for the fully protonated (I), singly deprotonated (II) and twice deprotonated (III) form.

Complex	Axial ligand	Equatorial ligand	Form	B3LYP-D3/B2+W	TPSS-D3/B2+W	MN12-L/B2+W	MP2/B1+W	MP2/B2+W	CCSD(T)/B1	CCSD(T)/B1+O	CCSD(T)/B1+W [f]	Experiment
1	AcO	cha	Cl_2	476	81	-159	-78	51	365	232	8	-53 ± 60 [a]
			$(H_2O)Cl$	534	105	-87	47	158	485	353	129	
			$(OH)Cl$	368	-20	-276	-144	-1	260	128	-96	
			$(H_2O)_2$	605	161	-52	187	298	611	479	256	
2	OH		Cl_2	-15	-404	-802	-486	-372	-194	-327	-434	
			$(H_2O)Cl$	56	-357	-761	-377	-283	-89	-222	-329	
			$(OH)Cl$	-87	-473	-884	-506	-405	-249	-381	-488	
			$(H_2O)_2$	133	-300	-728	-273	-170	9	-124	-230	
3	Cl		Cl_2	541	155	-18	26	-86	421	289	211	
			$(H_2O)Cl$	647	246	59	155	39	535	403	326	
			$(OH)Cl$	415	30	-173	-78	-178	278	145	68	
			$(H_2O)_2$	713	296	83	249	132	615	483	406	
4	Cl	dach	Cl_2	466	80	-111	-79	-158	315	182	105	107 ± 19 [a]
			$(H_2O)Cl$	548	150	-55	-2	-94	389	257	180	
			$(OH)Cl$	382	3	-216	-160	-239	205	72	-5	
			$(H_2O)_2$	636	226	0	114	11	495	363	286	
5	AcO	en	Cl_2	426	35	-201	-135	-23	315	183	-38	-326 [b]
6	OH		Cl_2	-69	-457	-870	-560	-465	-259	-391	-497	-664 [b]
7	Cl		Cl_2	476	93	-101	-62	-162	338	206	130	37 ± 53 [a]
8	AcO	$(NH_3)_2$	Cl_2	443	47	-200	-87	37	343	211	-8	-443 [c]
9	fAcO		Cl_2	885	508	231	358	456	797	665	423	207 [d]
10	OH		Cl_2	-23	-415	-813	-485	-381	-198	-330	-436	-683 [c]
11	Cl		Cl_2	523	140	-41	32	-66	412	280	206	-63 [c]
RMSD				628	266	154	179	266	507	384	234	
AA			I	853	683	483	331	674	329	329	346	60 [e]
			II	491	353	201	62	338	33	33	41	
			III	-207	-297	-423	-499	-320	-563	-563	-564	

a) Ref. [52], b) Ref. [53] , c) Ref. [54], d) Ref. [55], e) Ref. 24

f) W means Wertz and O - Okuno entropy corrections evaluated at the optimization level; they represent constant a term for the given complex within all methods.

Schemes:

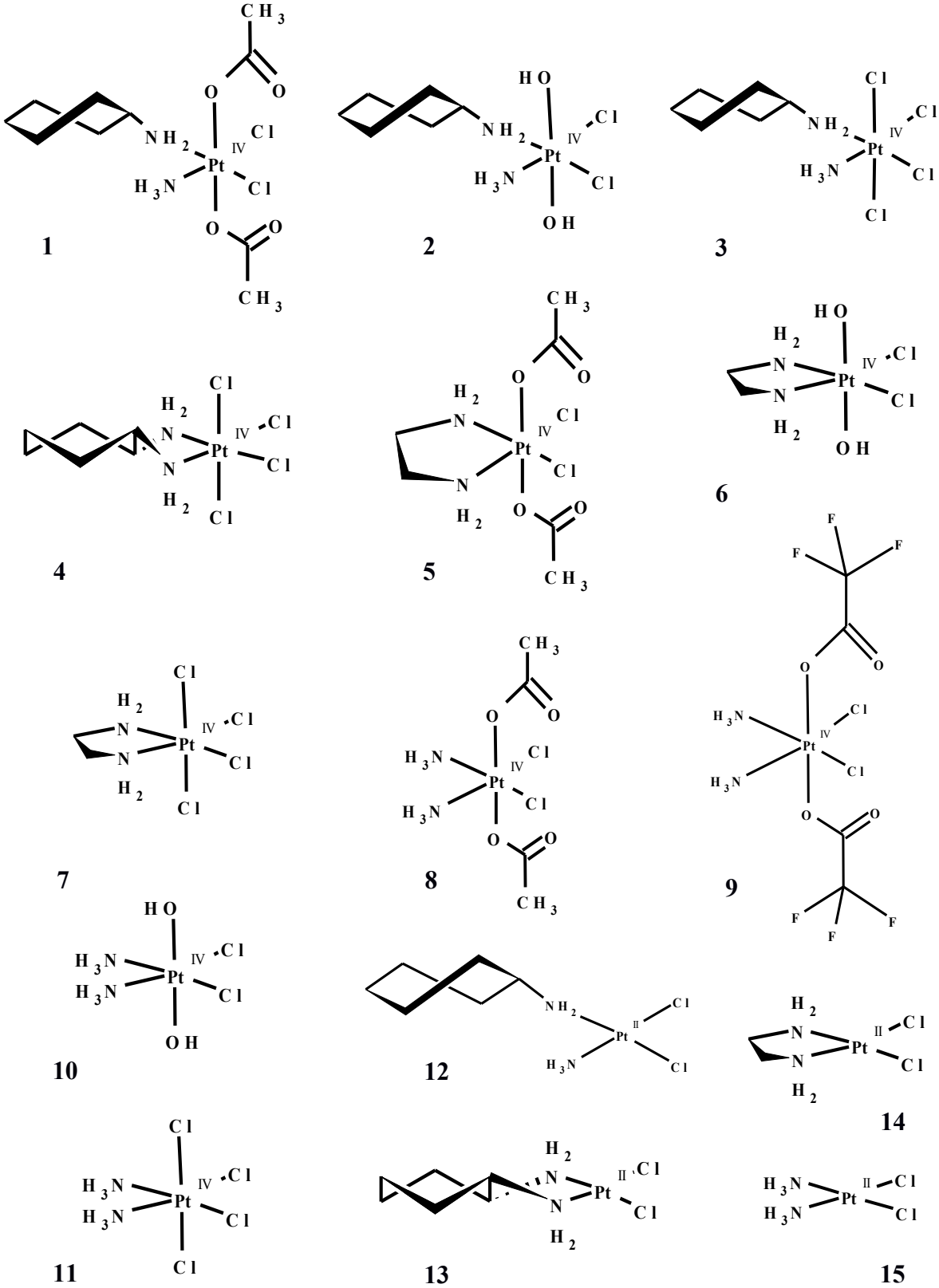

Scheme 1: The considered Pt(IV) complexes and their reduced analogues

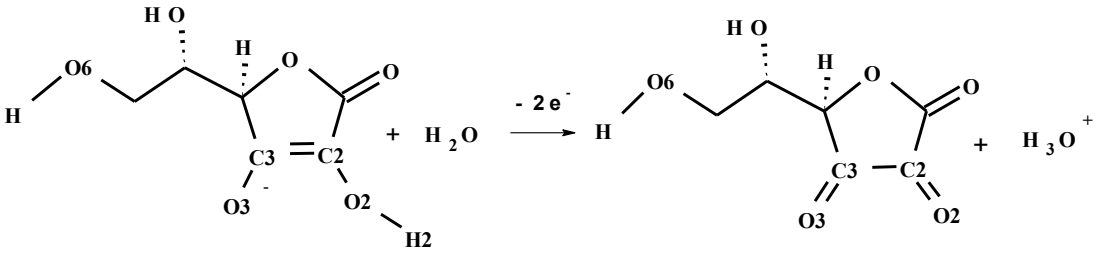

Scheme 2: Considered oxidation of ascorbic acid at neutral pH. Numbering for important oxygen atoms is stated.

Figures:

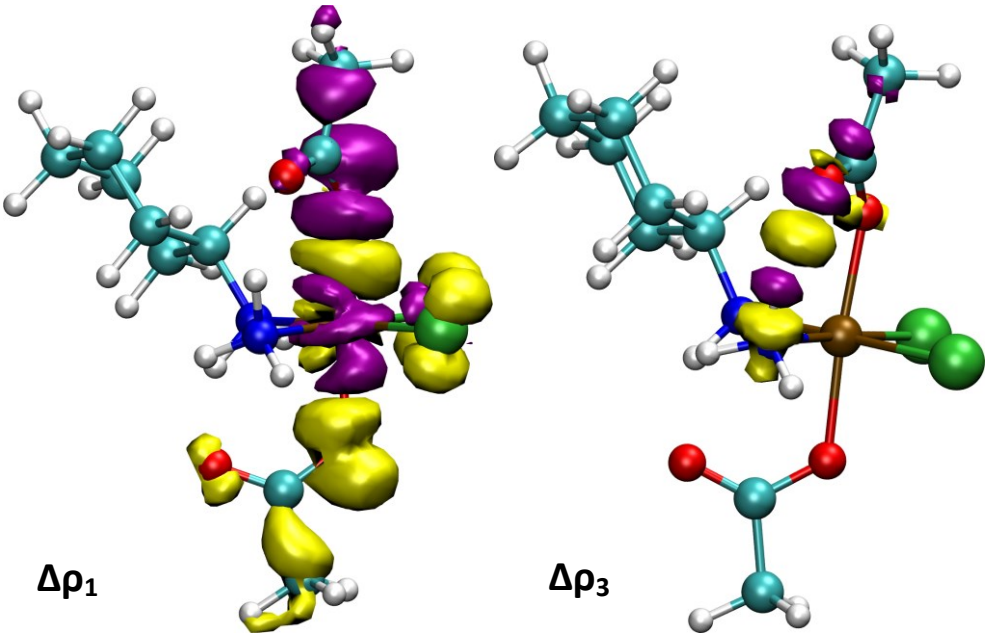

Figure 1: Contours of deformation densities $\Delta\rho_1$ and $\Delta\rho_3$ from ETS-NOCV analysis. Yellow regions correspond to an increase of electron density and purple ones to a decrease. The value of deformation density on contours is ±0.002 a.u.

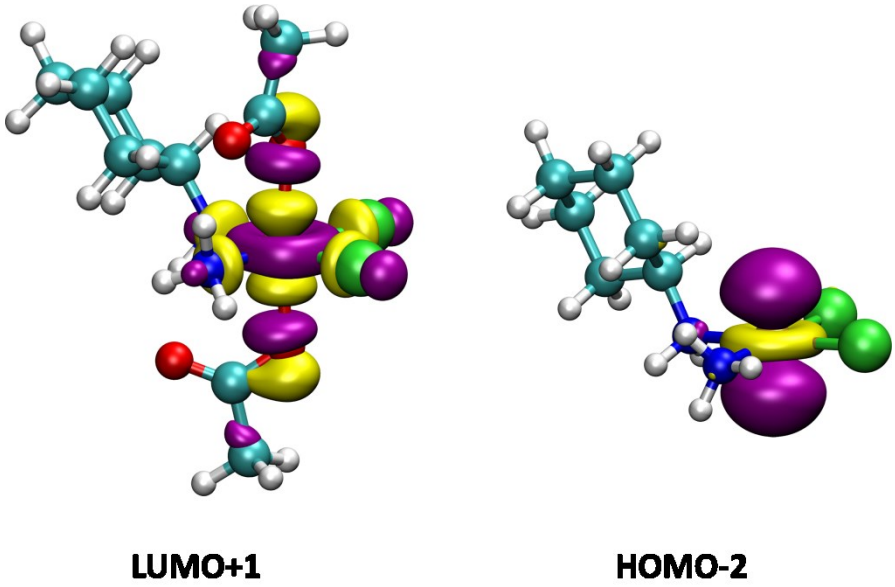

Figure 2: Canonical molecular orbitals – LUMO+1 on satraplatin and HOMO-2 on JM118.

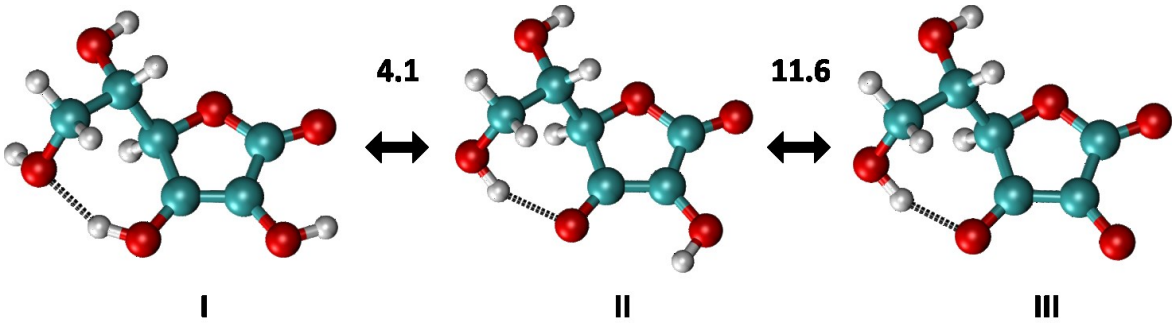

Figure 3: Three protonation states of ascorbic acid and corresponding experimental pK_a values.

ChemPubSoc Europe

DOI: 10.1002/chem.201503555

CHEMISTRY A European Journal Full Paper

Anticancer Drugs |*Hot Paper*|

Reduction Process of Tetraplatin in the Presence of Deoxyguanosine Monophosphate (dGMP): A Computational DFT Study

Filip Šebesta and Jaroslav V. Burda*[a]

Abstract: The reduction mechanism of $[Pt^{IV}(dach)Cl_4]$ (dach = diaminocyclohexyl) in the presence of dGMP was studied. The first step is substitution of a chloro ligand by dGMP, followed by nucleophilic attack of a phosphate or sugar oxygen atom to the C8-position of guanine. Subsequent reduction forms the $[Pt^{II}(dach)Cl_2]$ complex. The whole process is completed by a hydrolysis. Two different pathways for the substitution reaction were examined: a direct associative and a Basolo–Pearson autocatalytic mechanism. All the explored structures were optimized at the B3LYP-D3/6-31G(d) level and by using the COSMO solvation model with Klamt's radii. Single-point energetics was determined at the B3LYP-GD3BJ/6-311++G(2df,2pd)/PCM/scaled-UAKS level. Activation barriers were used for an estimation of the rate constants and these were compared with experimental values. It was found that the rate-determining step is the nucleophilic attack with a slightly faster performance in the 3′-dGMP branch than in the case of 5′-dGMP with activation barriers of 21.1 and 20.4 kcal mol^{-1} (experimental: 23.8 and 23.2 kcal mol^{-1}). The reduction reaction is connected with an electron flow from guanine. The product of the reduction reaction is a chelate structure, which dissociates within the last reaction step, that is, a hydrolysis reaction. The whole redox process (substitution, reduction, and hydrolysis) is exergonic by 34 and 28 kcal mol^{-1} for 5′-dGMP and 3′-dGMP, respectively.

Introduction

Platinum complexes as well as several other transition-metal compounds play an important role in antitumor treatment.[1,2] Especially, square-planar Pt^{II} complexes like cisplatin (*cis*-diamminedichloroplatinum(II), approved as an anticancer drug first in 1978), oxaliplatin ([(1*R*,2*R*)-cyclohexane-1,2-diamine]-(ethanedioato-O,O′)platinum(II)), and carboplatin (*cis*-diammine-(cyclobutane-1,1-dicarboxylate-O,O′)platinum(II)) are currently the most frequently used cytostatic metallodrugs. However, new agents are still being searched for because there are a large number of negative side effects of the contemporary drugs, which are also resistant to some types of tumors. Nowadays, the attention is particularly focused on complexes of Pt^{IV},[3,4] Ru^{II},[5,6] Ir^{III},[7] Au,[8,9] and some others.[10] These compounds are usually prepared in a form of "pro-drugs", which must be first activated in an organism. This fact is believed to lead to a smaller number of side effects (if the activation process can be regulated) and their easier administration. Such classes of compounds are non-specific; however, they can be characterized by higher kinetic inertness. This property enables for example, oral administration of Pt^{IV} complexes like satraplatin (bis(acetate)amminedichloro(cyclohexylamine)platinum(IV)), which is still under clinical testing.[3] The hydration process (which means replacement of some of the chloro ligands by water molecules) is a standard mechanism of activation for generally all chloro-ligand-containing complexes. However, this process occurs with a very low probability in the case of Pt^{IV} complexes.[11] The corresponding energy barriers are estimated up to 40 kcal mol^{-1} in comparison with 23 kcal mol^{-1} of cisplatin. Such a high activation barrier means that the hydration process of Pt^{IV} complexes is kinetically forbidden and therefore their reduction has to occur first followed by hydration of the corresponding Pt^{II} forms.

Tetraplatin (tetrachloro-(D,L-*trans*)-[(1*R*,2*R*)-cyclohexane-1,2-diamine]-platinum(IV)) is one of the more reactive Pt^{IV} complexes.[12–14] Unfortunately, investigation of its anticancer activity was stopped after revealing that this compound has ten times higher neurotoxicity than cisplatin.[15,16] Nevertheless, clarification of its activation mechanism can help to understand the reduction processes of similar Pt^{IV} complexes. The reduction mechanism of tetraplatin in the presence of deoxyguanosine monophosphate (dGMP) was suggested by Choi et al.[17–20] and it is shown in Scheme 1. According to IR and NMR spectroscopy, and liquid chromatography (HPLC)/mass spectrometry measurements, an intermediate, where dGMP is bound to Pt through a Pt–N7(dGMP) interaction, is initially formed in a substitution reaction. A sigmoidal shape of the kinetic curves indicates an autocatalytic course of this first reaction.[19,20] The subsequent reduction reaction occurs only if the

[a] *F. Šebesta, Prof. Dr. J. V. Burda*
Department of Chemical Physics and Optics
Faculty of Mathematics and Physics, Charles University
Ke Karlovu 3, 121 16 Prague 2 (Czech Republic)
E-mail: burda@karlov.mff.cuni.cz

Supporting information for this article is available on the WWW under http://dx.doi.org/10.1002/chem.201503555.

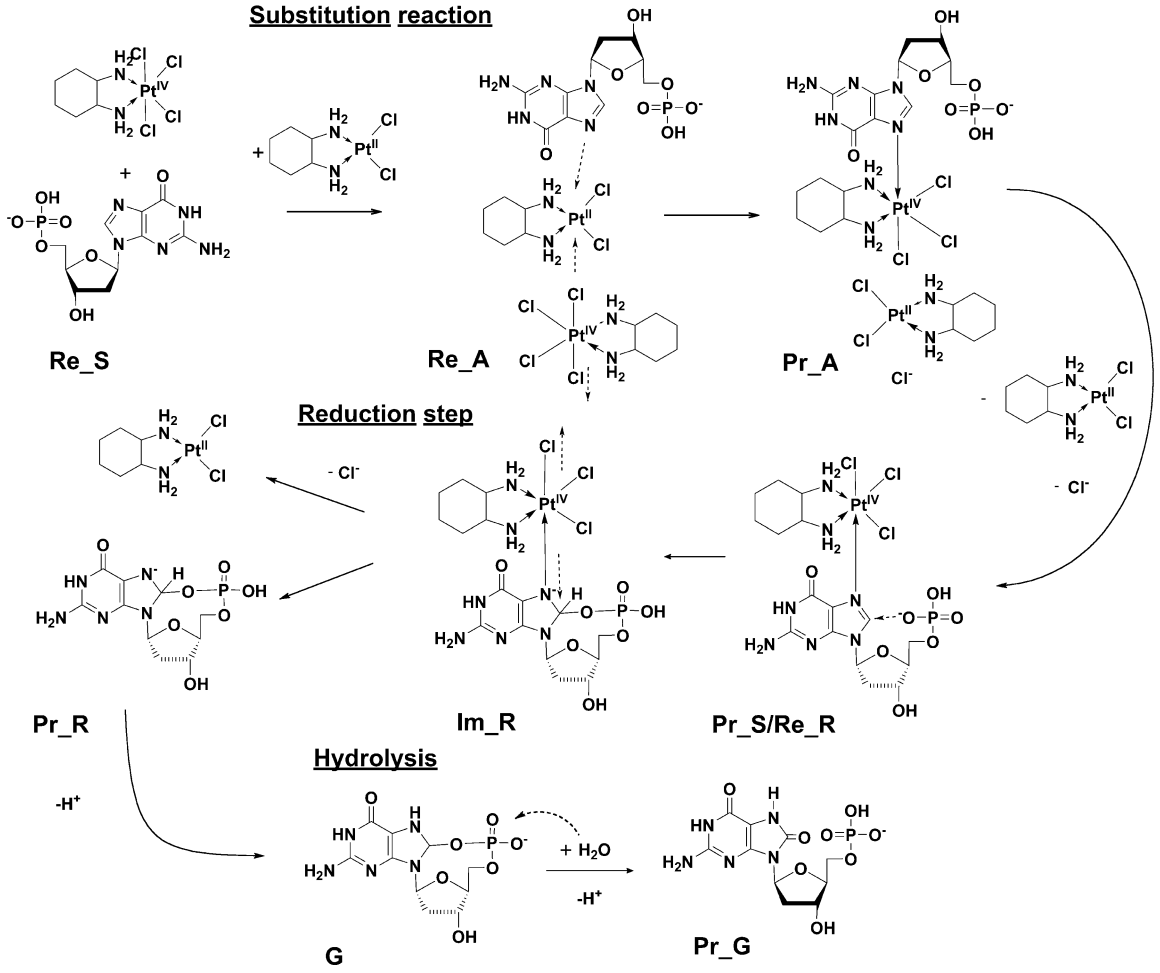

Scheme 1. Representation of the explored mechanism. Labels of the structures are composed from three parts: 1) The abbreviations "Re", "TS", and "Pr" are used for reactants, transition states, and products, respectively. 2) Reaction step: "S" is used for the associative mechanism of the substitution, "A" is used for the autocatalytic mechanism of the substitution, "R" is used for the reduction reaction, and "G" is used for hydrolysis. 3) The basic labels can be extended after underscore with "5", "3", or "c" to determine in which branch, that is, 5′-dGMP, 3′-dGMP, or cGMP, they are involved, or with "E" or "A" in order to emphasize that substitution occurs into the equatorial or axial position, respectively (for example Pr_S_5E).

given form of dGMP has a suitable group for an nucleophilic attack to the C8-position, which can be, for example, 5′-dGMP, 3′-dGMP, or 5′-d[GTTTT]-3′. On the other hand, this reaction cannot proceed in the case of cGMP, 5′-d[TTGTT]-3′, or 5′-d[TTTTG]-3′ structures[20] because oxygen in an appropriate position suitable for nucleophilic attack is missing. The two-electron transfer results in the formation of (reduced) $[Pt^{II}(dach)Cl_2]$ (dach = diaminocyclohexyl) complex and 8-oxo-deoxyguanosine-monophosphate (8-oxo-dGMP).

As to computational activities within the anticancer Pt^{IV} complexes, systematic exploration of ^{195}Pt NMR chemical shifts was performed by Tsipis et al.[21] for a large set of Pt^{II} and Pt^{IV} complexes in implicit water solution. The calculated shifts were compared with experimental values demonstrating fair agreement. A similar topic was also explored by Vicha et al.[22] In contrast to previous authors, they used the relativistic approach, that is, the two-component zeroth-order regular approximation (SO-ZORA) with the PBE0/TZP/COSMO computational level for successful determination of the NMR shielding constants. Another interesting paper was recently published by Wilson et al.[23] where, by combining experimental and computational tools, the oxidation of platinum(II) complexes with iodobenzene dichloride in DMF was studied, yielding the respective platinum(IV) analogues. Time-dependent (TD)-DFT/LANL2DZ/COSMO approach was employed for the determination of the singlet excited states of both sets of Pt^{II} and Pt^{IV} complexes. The calculations confirmed that the quenching of an excitation state (originally based on the LUMO in the Pt^{II} complex) arises from the presence of metal-based d orbitals energetically positioned between the HOMO and the LUMO of the fluorophore ligand. Similar supporting calculations on diazido-platinum(IV) complexes were performed by Zhao et al.[24] where thirty-two singlet and eight triplet excited states with the corresponding oscillator strengths were determined by using a TD-DFT(PBE1PBE/LanL2DZ/CPCM) model. Based on a metal–ligand charge-transfer (LMCT) process of the azido ligand they confirm the dissociative character of the low-lying exited states. Quantum chemistry parameters (for example, dipole moments, solvation energies, electrostatic potential, and partial charges) were used in quantitative structure–activity relationship (QSAR) investigations for novel cytotoxic Pt^{IV} complexes by Varbanov et al.[25a]

In our previous paper, we showed that high activation barriers of the direct hydration of satraplatin (JM216) and its dihydroxo derivative (JM149) can be considered as a reason that hydration is a kinetically forbidden reaction.[11] Herein, we focus on tetraplatin as another representative of Pt^{IV} complexes. A set of all three forms of dGMP, that is, 5′-dGMP, 3′-dGMP, and cGMP, is investigated and compared with experimental results. The detailed energy profile of the whole process is determined by using DFT calculations together with several analyses of the electron density distribution.

Computational details

All geometries of the studied complexes were optimized at the DFT level with the hybrid B3LYP functional using Grimme's empirical dispersion corrections[25b] and the 6-31G(d) basis set.[25c] Stuttgart–Dresden effective core potentials (labeled as MWB-60) were used for the description of platinum atom.[25d] The original pseudoorbitals were extended by polarization and diffuse functions in order to keep a consistent basis set. In the case of the double zeta 6-31++G(d,p) basis set extension for the Pt atom contained diffuse and polarization functions.[26a] A water solution was simulated by the COSMO implicit solvent model with Klamt radii for the cavity construction.[26b] Contributions from nuclear degrees of freedom to the Gibbs free energy were obtained based on the canonical ensemble (with harmonic oscillator and rigid rotor models) at the same level (hereafter labeled as B1 level).

In accord to the previous study of cisplatin reactions,[27–29] the single-point (SP) energy calculations were performed at the B3LYP-GD3BJ/6-311++G(2df,2pd) level and the DPCM/scaled-UAKS (United Atom Kohn–Sham cavities[30]) implicit solvent model. In this case the original pseudoorbitals for the Pt atom were extended by a 2fg basis set[26a] (labeled as B2, all polarization and diffuse functions are also included in the Supporting Information). The radius of the spheres around heavy atoms in the scaled-UAKS cavity model is calculated according to reference [27] by using Equation (1).

$$R(X) = R_0(X) - \gamma\left|\frac{Q_{act}(X) - Q_{deprot}(X)}{Q_{prot}(X) - Q_{deprot}(X)} + Q_{deprot}(X)\right| \quad (1)$$

where R_0 is a radius taken from the standard UAKS model without a correction to the formal charge and γ is a factor in the UAKS model due to the formal charges. The suggested value is 0.3 for all negatively charged groups[30] but it differs for positively charged groups according to its central atom. It is 0.26 for oxygen (the other factors can be found in Ref. [30]). The expressions Q_{deprot} and Q_{prot} represent the partial charges of the reference molecule as described in references [27,30]. The expression Q_{act} corresponds to the actual partial charge of the group in the given structure. The scaling is performed for chlorines and groups containing oxygen atoms with the exception of the phosphate group. The radii of the spheres on nitrogen and carbon atoms are not scaled in our calculations in correspondence with the original UAKS model.[30]

The rate constants k of the explored reactions were determined from the heights of the activation barriers $\Delta G^{\neq}$ at T = 298.15 K according to the transition state theory (TST) of Eyring[31] by using Equation (2).

$$k = \frac{k_B T}{h} e^{\frac{\Delta G^{\neq}}{k_B T}} \quad (2)$$

The natural population analysis (NPA) charges were determined by using the NBO v 5.9 program[32a] for the wave function obtained from the SP calculation at the B2 computational level. All optimization and SP calculations were performed by using the Gaussian 09 software package.[32b] The Bader's AIM analysis[33] was carried out by using the program AIMAll v.14 of Keith[34] for the electron densities determined at the B2 level. In addition for the optimized structures of selected platinum complexes, electrostatic, steric, and orbital contributions to the total binding energy between Pt and the chloro ligands were obtained by ETS-NOCV analysis[35a] (extended transition state for energy decomposition analysis combined with the natural orbitals for chemical valence analysis) as programmed in the ADF 2014 program.[35b] The corresponding electron density was determined by using scalar ZORA Hamiltonian at the B3LYP-GD3BJ/TZ2P level where the 4d frozen-core approximation was used for Pt atom.[35c] At the same level bond orders were also evaluated according to the approach of Nalewajski and Mrozek.[36] The symmetry-adapted intermolecular perturbation theory (DFT-SAPT)[37a] as coded in the MOLPRO 2012 program[37b] was applied for energy decomposition of the Pt^{II}/Pt^{IV} core in the autocatalytic substitution reaction.

The whole reduction process studied in this paper can be divided into three parts: a substitution reaction passing through 1) an associative mechanism (S) or 2) an autocatalytic mechanism (A), a reduction reaction (R), and finally a hydrolysis reaction (G), leading to the formation of the 8-oxo-dGMP. In each reaction, "Re" stands for the reactants, "TS" for the transition states, "Pr" for the products, and "Im" for the intermediates. Therefore, we label structures for easier orientation like Pr_A, which can be further extended by "5", "3", or "c" to specify the considered variant of dGMP and/or by "E" or "A" to emphasize whether the substitution occurs into an equatorial or axial position (for example, Pr_S_5A or Pr_S_5E; see also Scheme 1).

Results and Discussion

Reactants

Tetraplatin is a molecule with C_2 symmetry where effects of *trans* influence and electrostatic interaction with neighboring ligands leads to the fact that bonds between the Pt atom and the axial chloro ligands and between the Pt atom and the equatorial chloro ligands are very similar. It follows from the ETS-NOCV analysis that smaller orbital contribution to the bonding energy together with a larger Pauli repulsion term are compensated in the case of the axial chloro ligands by higher electrostatic interactions and a steric term. The similarity of the both axial and equatorial Pt–Cl bonds is also noticeable from the bond lengths and a Nalewajski and Mrozek bond order analysis[36] evaluated by using the ADF program[35b] and collected in Table 1. Besides tetraplatin, two other platinum derivatives with ethylendiamino (en) and two ammine ligands are employed because these complexes are also explored in the autocatalytic mechanism of the substitution reaction.

Deoxyguanosine monophosphate (dGMP) is the second reactant and it is considered in the variants 5′-dGMP, 3′-dGMP, or cGMP (all structures are depicted in Scheme 2 together with the atom numbering used herein). For the simulation of the whole set of reactions, it is important to know the extent of protonation of the phosphate group in solution at a neutral

Table 1. Parameters for bonds between the platinum atom and the axial or equatorial chloride ligands in $[Pt^{IV}(dach)Cl_4]$.

	Pt–Cl_e	Pt–Cl_a	Pt–Cl_e	Pt–Cl_a	Pt–Cl_e	Pt–Cl_a
	$Pt^{IV}(dach)Cl_4$		$Pt^{IV}(en)Cl_4$		$Pt^{IV}(NH_3)_2Cl_4$	
bond length [Å]	2.367	2.368	2.365	2.367	2.361	2.367
bond index	0.738	0.672	0.737	0.686	0.750	0.691
electron density in the BCP [$e\,a_0^{-3}$]	0.0913	0.0917	0.0918	0.0918	0.0923	0.0920
Contributions to the bonding energy						
electrostatic	−187	−215	−192	−217	−120	−218
Pauli repulsion	120	132	121	131	123	131
steric	−67	−83	−70	−85	−77	−86
orbital	−105	−94	−109	−96	−110	−96
total bonding	−175	−181	−182	−186	−190	−186

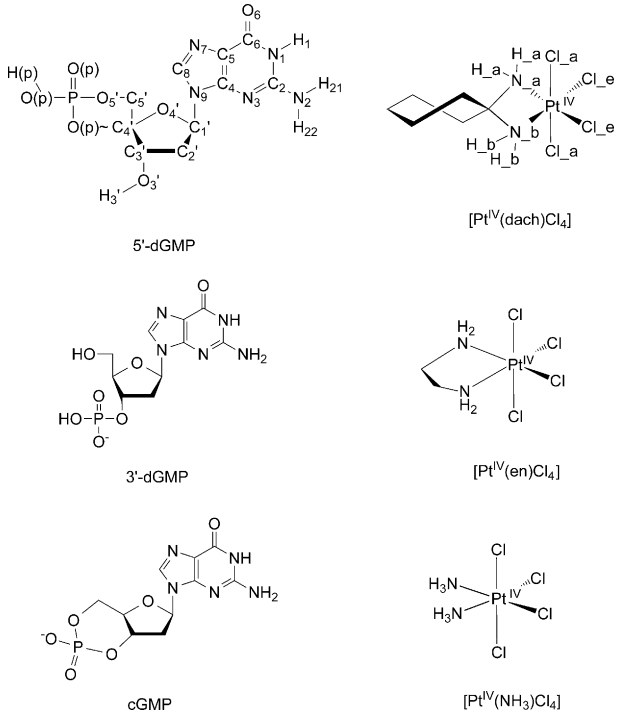

Scheme 2. Numbering of 5′-dGMP and labels of $[Pt^{IV}(dach)Cl_4]$. The atoms in the amino group of the dach ligand, closer to the O6 atom within the reaction course, are labeled with "a" (that is, N_a, H_a) and atoms of the second amino group with "b" (N_b, H_b).

pH value (in cells) and/or pH 8.3, which was used in the experimental assays. As the experimental pK_a values are not available for all of the explored complexes, we tried to estimate these values according to a previously suggested methodology based on the DPCM method with scaled UAKS cavities, which has been successfully applied before.[27–29] Our calculations of pK_a constants suggest that a singly protonated phosphate group will dominate (80%) in the case of 5′-dGMP, whereas there will be only 39% of single-protonated 3′-dGMP molecules at a neutral pH value. The cGMP form should have the phosphate group in the fully deprotonated form (compare Table 2). According to experimentally determined pK_a constants, that is, 0.35 and 6.29 for 5′-dGMP[38] and 6.14 (pK_a of the first deprotonation stage was not reported) for 3′-dGMP[39]

Table 2. Calculated pK_a values of the phosphate group in 5′-dGMP, 3′-dGMP, and cGMP.

pK_a	5′-dGMP		3′-dGMP		cGMP		Phosphoric acid	
	calcd	exp.[a]	calcd	exp.[b]	calcd	exp.	calcd	exp.[c]
1	−0.8	0.35 ± 0.2	−3.2		2.7	–	−1.9	2.1
2	7.6	6.29 ± 0.01	6.8	6.14 ± 0.01	–	–	6.5	7.2
3							10.2	12.3

[a] Reference [38]. [b] Reference [39]. [c] Reference [46]. The negative value of −1.9 for phosphoric acid means that according to our calculations this acid will deprotonate at relatively higher concentration of protons, that is, we overestimates its acidity.

it will be approximately 16% of 5′-dGMP and 12% of 3′-dGMP molecules in the singly protonated state according to the Henderson–Hasselbach equation in solution with a neutral pH value.

We examined several conformations of dGMP (with various mutual orientations of the guanine and the sugar–phosphate moieties). The *syn* conformation has lower energy than the *anti* conformation for all studied geometries of dGMP in the protonated state. Especially, the position of the phosphate group in the 5′-dGMP molecule enables a strong stabilization by hydrogen bonding between the phosphate group and the N3 and H22 atoms from the guanine. The Gibbs free energy differences are within 4.0 kcal mol^{-1} in the PCM solvation model as can be seen in Table 3.

Table 3. Energy differences (in [kcal mol^{-1}]) between the *syn* and *anti* conformers at the B2 level.

	5′-dGMP	3′-dGMP	cGMP
ΔE	5.2	2.8	−0.3
ΔG	3.8	2.9	1.3

Substitution reaction

The whole process starts with the replacement of one of the tetraplatin chloro ligands by dGMP, where coordination occurs through a covalent bond between the Pt atom and the N7

atom of the guanine base. According to the structural features of tetraplatin it is not clear if the substitution preferably occurs to the axial or equatorial position because similar Pt–Cl bond strengths and other physicochemical characteristics (mentioned above in the paragraph devoted to tetraplatin) do not indicate a visible preference. Therefore, both positions are considered possible in the calculations.

The substitution reaction is mostly exergonic and strongly exothermic as follows from the reaction energies collected in Table 4. In the case of 5′-dGMP, the most stable product is

Table 4. Thermodynamic and kinetic parameters of the substitution reaction at 298 K at the B2 level. Energies are given in [kcal mol^{-1}]. The associative mechanisms of [Pt^{IV}(dach)Cl$_4$].

		ΔE_r	ΔG_r	$\Delta E^{\neq}$	$\Delta G^{\neq}$	k [L mol^{-1} s^{-1}]
axial association	5′-dGMP	−13.8	−8.4	42.0	43.4	9.5×10^{-20}
	3′-dGMP	−5.8	1.2	38.9	41.5	2.4×10^{-18}
	cGMP	−10.3	−0.9	41.9	43.6	7.1×10^{-20}
equatorial association	5′-dGMP	−13.0	−5.4	37.6	38.1	7.0×10^{-16}
	3′-dGMP	−12.4	−3.7	38.4	40.2	2.0×10^{-17}
	cGMP	−13.1	−4.5	39.7	41.2	3.9×10^{-18}

Pr_S_5A with the guanine being coordinated to the axial position of tetraplatin. The Pr_S_5E conformer, which is coordinated in the equatorial position, is 3.0 kcal mol^{-1} higher in energy. An opposite situation occurred in the case of 3′-dGMP where the structure with an equatorial coordination of GMP (that is, Pr_S_3E) is about 4.9 kcal mol^{-1} more preferable over the Pr_S_3A conformer. All four geometries are displayed in Figure S1 in the Supporting Information. The explanation of the different stabilities can be partially searched in the additional weak interactions between dGMP and tetraplatin. The reaction Gibbs free energy for the Pr_S_5A product formation is −8.4 kcal mol^{-1}, and −3.7 kcal mol^{-1} for Pr_S_3E.

The substitution reaction can occur through two possible pathways: 1) a non-catalytic pathway by the associative mechanism and 2) an autocatalytic mechanism. The transition state of the associative mechanism has an imaginary mode represented by antisymmetric stretching vibration for the simultaneous leaving of the chloro ligand and approaching of the N7 site of the guanine and reverse. Within this pathway, the chloro ligands in both the equatorial and the axial positions can be substituted. The corresponding transition states TS_S_5A and TS_S_5E are displayed with the imaginary vibration modes shown by arrows in Figure 1a. Despite the fact that the Pt–N7 and Pt–Cl bond lengths in the TS_S structures are relatively longer in comparison with our previous calculations on cisplatin or satraplatin complexes,[11,29] the AIM analysis confirms the bond critical points (BCPs) between the Pt and N7 atoms as well as between Pt and the leaving chloride atom (Cl_l). Nevertheless, the electron density in these BCPs is very low, even lower than the density in the BCP of the O6···H_a hydrogen bond.

The energy profile of the associative mechanism is summarized in Table 4. From this it can be concluded that the

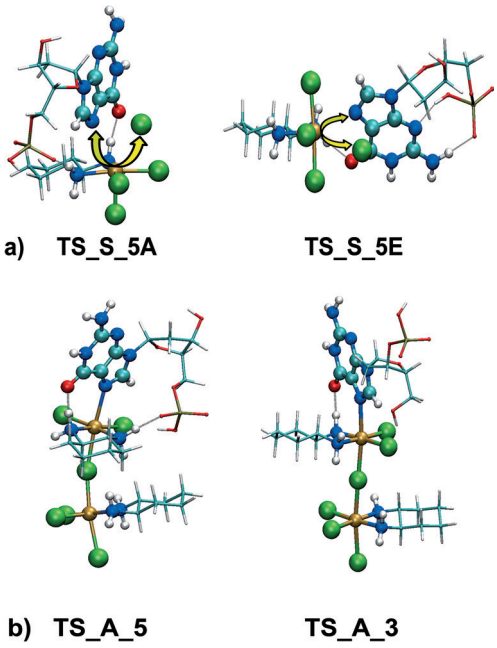

Figure 1. a) Transition states for the substitution of 5′-dGMP in the equatorial and axial position in the associative mechanism. b) Transition-state structures involved in the autocatalytic mechanism for the substitution of 3′-dGMP and 5′-dGMP.

activation barriers are more than 38 kcal mol^{-1} high in both the 3′- and 5′-dGMP branches. Thus, the reaction will occur by the described mechanism with a very low probability. As a consequence, the rate constants predicted according to the transition state theory of Eyring are smaller than 10^{-15} L mol^{-1} s^{-1}.

The second pathway is represented by Basolo–Pearson autocatalytic mechanism.[19,40] It is assumed that the reaction is catalyzed by traces of reduced Pt^{II} complex, which is located between the dGMP and the Pt^{IV} complex. In the reactant (Re_A), mutual positions of dGMP and the Pt^{II} complex are stabilized by O6···H_a hydrogen bonds and, in the case of the 5′-dGMP branch, also by O(p)···H_b hydrogen bonds (for the atomic notation, see Scheme 2). The dispersion interaction is another important stabilizing contribution, which keeps the plane of guanine almost parallel to the plane of the Pt^{II} complex.

The associate of both Pt complexes is a core of the reaction center. To gain a deeper insight into stable minima of this Pt^{II}/Pt^{IV} core structure, a MP2 optimization (MP2/6-31G(d)/CPCM/Klamt) was carried out for a [Pt(en)Cl$_2$]/[Pt(en)Cl$_4$] model. In this way, three lowest minima, A_1, A_2, and A_3, were obtained. They are displayed in Figure 2. The association Gibbs free energies, determined at the MP2/6-311++G(2df,2pd)/PCM/sUAKS computational level, are −2.4, 3.5, and 8.8 kcal mol^{-1} for A_1, A_2, and A_3, respectively. The stabilization of the Pt^{II}/Pt^{IV} structure can be divided into two main contributions: 1) The electrostatic interaction stabilizes mainly an antiparallel arrangement of the complexes (A_1 and A_2), whereas it has a lower effect in a parallel arrangement (A_3) where the dipole–dipole interaction of both Pt complexes is repulsive; and 2) the dispersion interaction, which stabilizes both the par-

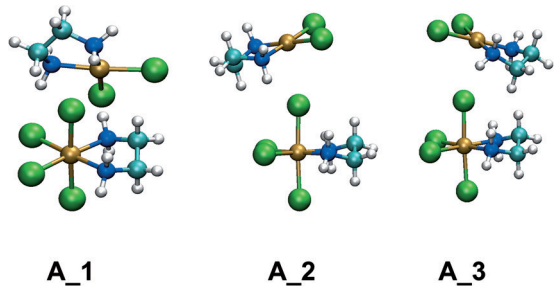

Figure 2. Stable structures of the $[Pt^{IV}(en)Cl_4]/[Pt^{II}(en)Cl_2]$ associate optimized at the MP2/6-31G(d)/CPCM/Klamt level.

allel and antiparallel orientations. However, in the case of the parallel orientation of the Pt^{II}/Pt^{IV} core, the dispersion term dominates in the total stabilization. This picture follows from the energy decomposition performed by the DFT-SAPT:B3LYP/6-31+G(d) method. The individual energy terms are collected in Table 5. The A_1 structure forms the core arrangement of

Table 5. Energy decomposition [kcal mol^{-1}] by using SAPT2 at the B3LYP/6-31+G(d) level in the gas phase.

	Electrostatics	Induction	Exchange	Dispersion	Total ($E(1)+E(2)$)
A_1	−30.2	−9.2	26.8	−10.8	−23.4
A_2	−18.5	−4.6	17.3	−6.4	−12.2
A_3	2.0	−4.6	17.5	−6.9	8.0

the reactant geometries. Its stability is strengthened by two additional weak interactions between the amino groups and the chloro ligands and dispersion interaction between the Pt^{II} ion and the H_a atom. The distance $d[Pt^{II}\cdots H\_a] = 2.33$ Å is close to the value of 2.55 Å for purely dispersion interaction between water and cisplatin as reported by Beret et al.[41] Moreover, in the A_1 structure a fairly high induction contribution is also noticeable (twice as high as in the other two structures) (compare Table 5). The total association energy of A_1 is −2.4 kcal mol^{-1} at the MP2 level. Nevertheless, when this energy was evaluated at the B2 level (with the solvent model), its value increased to 3.2 kcal mol^{-1} (Table 6). The antiparallel arrangement (A_2) is basically present in the TS structures and it is about 5 kcal mol^{-1} less stable at the MP2 level in comparison with the A_1 structure.

Exploring the trimer arrangement, there is the question whether the Pt^{IV}/Pt^{II} complex is more stable and dGMP associates afterwards or whether the Pt^{II} complex links with dGMP first and tetraplatin affiliates subsequently. The pair association energies from the first two columns of Table 6 show that the $[Pt(dach)Cl_2]$/dGMP structures are generally slightly less stable (up to 6 kcal mol^{-1} for 3′-dGMP) than the Pt^{IV}/Pt^{II} core. The total association of Re_A is significantly exothermic (ΔE^{As} is less than −18 kcal mol^{-1}), whereas the final ΔG^{As} value is close to +10 kcal mol^{-1} due to the prevailing entropy term. From Table 7 it follows that the difference between the electronic and the Gibbs free energy is quite large for all of the associates. The entropic contribution $-T\Delta S$ to ΔG^{As} corresponding

Table 6. Pair association energies (in [kcal mol^{-1}]) of the $[Pt^{IV}Cl_4X]/[Pt^{II}Cl_2X]$ complexes (X = dach, en, or $(NH_3)_2$) and $[Pt^{II}Cl_2X]$ with 5′-dGMP, 3′-dGMP, and cGMP at the B2 level.

	$Pt^{II}Cl_2$(dach)		$Pt^{II}Cl_2$(en)		$Pt^{II}(NH_3)_2Cl_2$	
	ΔE^{As}	ΔG^{As}	ΔE^{As}	ΔG^{As}	ΔE^{As}	ΔG^{As}
$Pt^{IV}Cl_4X$	−10.9	2.5	−9.4	3.2	−9.8	3.5
5′-dGMP	−9.4	4.3	−9.8	3.2	−9.1	5.8
3′-dGMP	−4.4	9.4	−4.8	5.7	−6.6	9.2
cGMP	−9.1	7.3	−8.8	6.5	−10.5	6.7

to the formation of Re_A from isolated molecules is in the range 25–30 kcal mol^{-1} due to the fact that a trimolecular aggregation must occur. Then the entropic contribution ΔS_T related to translational degrees of freedom of isolated components is not compensated by the part of entropy coming from vibrational degrees of freedom ΔS_V of the whole aggregate. When the structures are bound weakly, the value for ΔS_V is smaller, which leads to larger differences between the values for ΔE and ΔG, particularly in the case of association of several molecules.

The calculated activation barriers of the autocatalytic mechanism (Figure 3) are close to the experimental values: 14.7 versus 16.6 kcal mol^{-1} for 5′-dGMP and 18.6 versus 16.3 kcal mol^{-1} for 3′-dGMP. Our estimation of the Gibbs activation barrier in the cGMP branch is 16.1 kcal mol^{-1}. The predicted reaction preference is in favor for 5′-dGMP on the contrary to the experimental results. This preference is a consequence of the higher stabilization of the TS structure caused by the stronger hydrogen bonds between the phosphate group and the amino group of the dach ligand. This could be probably improved by using a more realistic solvation model.

It can be stated that the substitution reaction occurs only to the axial position of the Pt^{IV} complex (replacing only the axial chloro ligand) because reasonably low activation barriers were found only in the case of the autocatalytic mechanisms, as can be seen in Tables 4 and 7. The catalytic enhancement of the substitution reaction by the Pt^{II} complex can be understood in analogy to the proton transfer between two water molecules. The electron density of the breaking H–O bond is smoothly decreasing simultaneously as the new O–H bond is formed. This is exactly the case of the Pt^{IV}–Cl_m–Pt^{II} bonding picture (as follows for example from the AIM analysis; also the second-order perturbation theory energies from the NBO analysis indicate that the chloro ligand Cl_m is well stabilized by interaction of lone-pair electrons with vacant orbitals on both Pt atoms; see Table S1 in the Supporting Information).

In the transition state TS_A (see Figure 1 b), the process of synproportionation of both Pt atoms occurs, that is, their partial charges become practically equal as follows from Table S2 in the Supporting Information. The chloride ligand located between both Pt atoms (Cl_m) is moved from the former tetraplatin to the Pt^{II} complex and simultaneously the Pt–N7 bond is formed on the opposite side of the Pt^{II} complex (see Figure 1 b). The equatorial plane of the Pt^{IV} complex becomes nearly parallel to the plane of the Pt^{II} complex. In this structure, both cyclohexane rings are in an antiparallel orientation in the 3′-dGMP and cGMP reaction branches. In the case of 5′-dGMP,

Table 7. Thermodynamic and kinetic parameters of the substitution reaction at 298 K at the B2 level. Energies are given in [kcal mol^{-1}]. The autocatalytic mechanism.

		ΔE^{As}	ΔG^{As}	ΔE_r	ΔG_r	$\Delta E^{\neq}$	$\Delta G^{\neq}$	k [L mol^{-1} s^{-1}]
[Pt^{IV}(dach)Cl_4]								
	5′-dGMP	−18.4	8.7	−13.8	−8.4	13.5	14.7	1.1×10^{2}
	3′-dGMP	−19.9	9.6	−5.8	1.2	18.1	18.6	1.5×10^{-1}
	cGMP	−20.0	10.3	−10.3	−0.9	18.4	16.1	9.3
experiment	5′-dGMP[a]						16.6 ± 1.4	$4\times10^{\pm1}$[c]
	5′-dGMP[b]						16.0	(11.1 ± 2.2)[d]
	3′-dGMP[a]						16.3 ± 0.2	(7.2 ± 3.1)
[Pt^{IV}(en)Cl_4]								
	5′-dGMP	−19.0	7.9	−13.6	−7.2	12.0	12.4	5.0×10^{3}
	3′-dGMP	−18.8	9.3	−5.9	1.1	17.6	20.0	1.5×10^{-2}
	cGMP	−18.3	11.3	−5.6	0.5	16.2	15.7	20
experiment	5′-dGMP[b]						15.5	(25.2 ± 4.1)[b]
[$Pt^{IV}(NH_3)_2Cl_4$]								
	5′-dGMP	−21.1	8.6	−15.3	−8.5	12.6	10.5	1.3×10^{5}
	3′-dGMP	−21.1	8.5	−6.9	−0.9	17.6	18.0	3.8×10^{-1}
	cGMP	−21.6	9.1	−8.5	−0.6	18.2	16.5	4.7
experiment	5′-dGMP[b]						14.8	85.8 ± 6.2[c]

[a] Reference [20]. [b] Reference [19]. [c] According to the accuracy of the activation barrier (16 ± 1.4) rate constant is estimated in the range 0.4–45.1. [d] Rate constants determined at pH 8.3 with initial concentrations of 1:0.2:20 mM of Pt^{IV} complex/Pt^{II} complex/5′-dGMP.

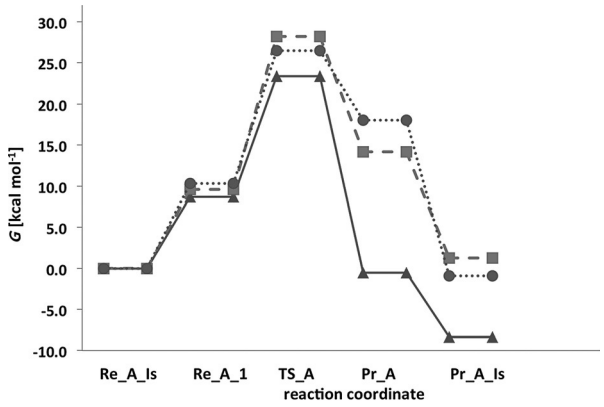

Figure 3. Gibbs free energy profiles for the autocatalytic mechanism of 5′-dGMP (solid line with triangles), 3′-dGMP (dashed line with squares), and cGMP (dotted line with circles) determined at the B2 level. The label "Is" corresponds to the isolated reactants and/or products.

the dach ligands come closer to each other so that their orientation is nearly perpendicular (the C_2 pseudo-axes of the dach ligands are approximately orthogonal), as is shown in Figure 1b for TS_A_5. In the case of 5′-dGMP, the additional interaction between the phosphate group and the amino group is also strengthened (shorter bond length with higher electron density in the BCP). It means that the TS structure of 5′-dGMP is energetically lower than the corresponding 3′-dGMP and cGMP structures. Similar oxidation states of both Pt atoms in TS_A can be also reflected by the fact that the exchanged chloro ligand Cl_m is practically in the center between both Pt atoms and the interaction with them is rather strong and symmetrical; the electron density in the corresponding BCPs is in average 0.07 e a_0^{-3}, whereas its original value in the Pt^{IV}–Cl bond was 0.09 e a_0^{-3}. The electron transfer occurring between the Pt^{II} and Pt^{IV} complexes is also supported by some electron density coming from guanine (as can be noticed in the last line of Table S2 in the Supporting Information). This is also linked with an increase of the charge of the C8 atom, which facilitates a consequent oxygen attack in the reduction reaction.

Influence of various Pt ligands on the autocatalytic course

The effect of various kinds of amino ligands (i.e., X = dach, en, and diammine) is also compared. When the core Pt^{II}/Pt^{IV} structure with dach, en, and diammine ligands is considered, the most stable arrangement of the reactants is similar to the structure A_1 in all three cases. The mutual differences in the association energies vary within 1 kcal mol^{-1} (Table 6, first line). A similar trend was also observed in the stability of various Pt^{II}–X complexes with dGMP (see the pair association energies in the individual lines of Table 6). In analogy, the total association energies $\Delta E^{As}/\Delta G^{As}$ of the whole reactant structures (Re_A) differ only by a few kcal mol^{-1} for the particular type of dGMP (Table 7). They mainly depend on the fact whether the Pt^{II}–X complex is stabilized by interaction with the phosphate (5′-dGMP, cGMP) or hydroxy group (3′-dGMP).

In an experimental study,[19] rate constants were obtained for the reaction of [Pt(dach)Cl_4], [Pt(en)Cl_4], and [Pt$(NH_3)_2Cl_4$] with 5′-dGMP (Table 7). The measured rate constants of the substitution reaction decrease from [Pt$(NH_3)_2Cl_4$] to [Pt(dach)Cl_4]. Despite the fact that the experimental rate constants differ nearly by an order of magnitude (11–86 L mol^{-1} s^{-1}), only quite a small energy difference of 1.4 kcal mol^{-1} is obtained after "transformation" according to the TST of Eyring into activation barriers. In our calculations this energy difference is slightly larger (4.2 kcal mol^{-1}). The monotonous decrease of the activation barrier $\Delta G^{\neq}$ in structures with 5′-dGMP follows from Table 7. The decrease of the activation barriers by passing from the dach to the en ligand can be explained by the different mutual orientation of the dach ligands versus the orientation of the en ligands in TS_A. Although the C_2 axes of the en ligands stay close to the antiparallel arrangement (with higher electrostatic stabilization), the corresponding "axes" are nearly

perpendicular in the case of the dach ligands. This less-stable arrangement of the dach ligands is probably caused by their fairly hydrophobic character. Passing from the Pt–en to the Pt–diammine TS structure, an additional decrease of the Gibbs energy is due to the (overestimated) entropy factor as follows from a comparison of the corresponding $\Delta E^{\neq}$ and $\Delta G^{\neq}$ values in Table 7.

Reduction reaction

This reaction starts with a nucleophilic attack of an oxygen atom of the phosphate group (in the case of 5′-dGMP) or O5′ oxygen of ribose (in the case of 3′-dGMP) to the C8 site of guanine. This attack leads to an increase of the positive charge on the C8 atom. The reaction cannot proceed in the case of cGMP where no appropriate attacking group is available.

As we are exploring derivatives of 8-oxo-dGMP, it is highly important to know in which reaction stage the deprotonation of the H8 atom occurs. Therefore the pK_a(H8) calculation was performed concluding that in neutral solution both reactants, Re_R_5 and Re_R_3 (Figure 4) are H8-deprotonated with very low probability at the beginning of the reduction reaction. This is in accord with experimentally known guanosine monophosphate forms. The activation barriers for nucleophilic attack to deprotonated C8 position are higher than 35 kcal mol^{-1}[11] (cf. also Ariafard et al.[42a,b]). Such a conclusion is easy to understand because after deprotonation the decrease of the positive charge on the C8 atom occurs, making the nucleophilic attack to this site more energy demanding.

In the reaction mechanism, the existence of an intermediate state is assumed where the O–C8 bond is formed in the first reaction step despite the fact that such an intermediate (that is, Im_R, Figure 4) is quite unstable. Coordination of platinum to both the N7 atom of the guanine and the Cl ligands are also still present in the Im_R structure. As to the reaction rate, the energy barrier associated with the formation of the O–C8 bond is the most demanding from the whole set of explored reactions. The calculated activation barrier is 21.1 kcal mol^{-1} in the case of 5′-dGMP, which is about 2.7 kcal mol^{-1} lower in comparison with experimental data. Such a difference is comparable with our previous calculations[42c,43] where it is demonstrated that the B3LYP functional underestimates the activation barriers by a similar amount of energy. In the case of 3′-dGMP, the B3LYP calculation gives a slightly lower energy barrier of 20.4 kcal mol^{-1} compared to the experimental value (23.2 kcal mol^{-1}) (see Table 8 and Figure 5).

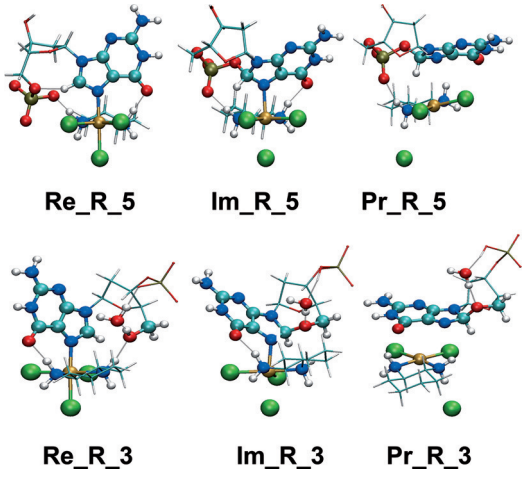

Figure 4. Optimized structures of the stationary points in the reduction mechanism in the 5′-dGMP (top) and 3′-dGMP (bottom) branches.

The difference between the oxygen attacks from a phosphate group (5′-dGMP) or a hydroxy group (3′-dGMP) partially dwell also in the fact that H5′ proton transfer from hydroxy group has to occur simultaneously (or before) the nucleophilic attack itself. According to pK_a calculations, the phosphate group should be fully deprotonated in the reactant Re_R at neutral pH. Therefore, this group can still be considered as an acceptor of the H5′ proton. One explicit water molecule has to be included to the system to enable such an additional proton transfer (PT). This PT from a sugar hydroxy group occurs simultaneously with the O5′ atom binding to the C8 site of guanine so that the H5′ hydrogen is released together with the formation of the O–C8 bond.

During this step an electron transfer occurs from the phosphate group to the guanine moiety and to a region of the axial chloride ligand (Cl_a). This electron transfer can be basically considered as a rotation of the HOMO−1 orbital (electron pair localized at the phosphate group) of the reactant Re_R to unoccupied orbitals (see Figure 6). From the partial charges obtained from the natural population analysis, it follows that the electron density of the phosphate group decreases monotonously from the Re_R to Im_R structure and similarly the charge of the planar [Pt(NH$_2$)$_2$Cl$_2$] structure decreases. Nevertheless, the partial charge of the Pt atom remains practically unchanged in this first step (see Table S3 in the Supporting Information).

The second reaction step, that is Im_R→Pr_R, is connected with a very low energy barrier because the Im_R complex is not too stable. The simultaneous elongation of the Pt–Cl_a and Pt–N7 bonds in TS2_R (symmetrical stretching vibrational mode) corresponds to the imaginary mode of the TS structure. Slightly behind the TS2_R point, the electron transfer is completed and the C8–H8, Pt–N7, and Pt–Cl bonds are broken practically simultaneously. From AIM and NBO analyses

Table 8. Thermodynamic and kinetic parameters for the reduction step calculated at the B2 level. Results are determined at 298 K and energies are given in [kcal mol^{-1}].

	$\Delta G_1^{\neq}$	k_1 [s^{-1}]	$\Delta G_2^{\neq}$	k_2 [s^{-1}]	ΔE_r	ΔG_r	$\Delta G_{exp}^{\neq}$ [a]	k_{exp} [s^{-1}]
5′-dGMP	21.1	2.1×10^{-3}	3.9	8.5×10^{9}	16.1	−14.2	23.8±1.2	$(2\pm1)\times10^{-5}$
3′-dGMP	20.4	7.5×10^{-3}	2.4	1.1×10^{11}	10.6	−18.5	23.2±2.3	$(6\pm4)\times10^{-5}$

[a] Reference [20].

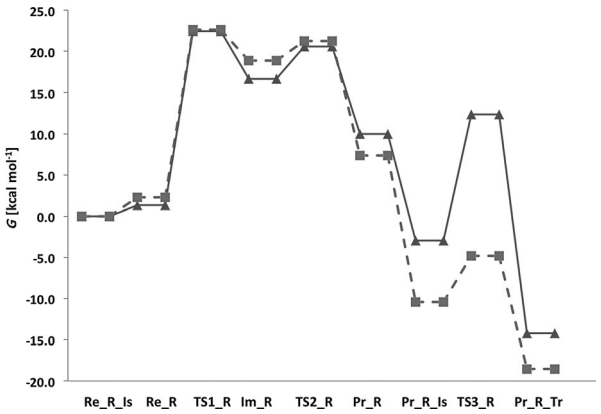

Figure 5. Gibbs free energy profiles of the reduction reaction in the 5′-dGMP branch (solid line with triangles) and in the 3′-dGMP branch (dashed line with squares) at the B2 level. The label "Is" corresponds to the isolated reactants and/or products, "Tr" represents a conformer with a proton transferred from the C8 to the N7 site.

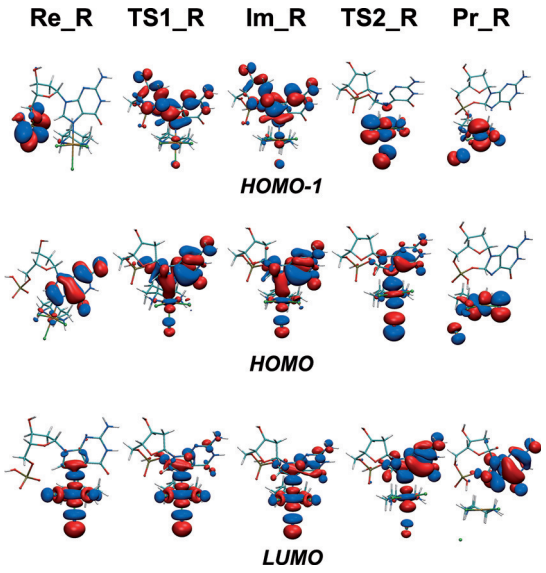

Figure 6. Frontier orbitals of the stationary structures in the reduction reaction with 5′-dGMP.

of the reduction (reaction) coordinate follows that the C8–H8 bond should be present until the axial ligands of the Pt are released completely. In the Pr_R products, the total charge of the guanine uniquely demonstrates its oxidation. Also, the NPA charge of $[Pt(NH_2)_2Cl_2]$ confirms the reduction of the Pt complex (see Table S3 in the Supporting Information). The reduction is also visible from the rotation of the occupied "π orbital of guanine" and the virtual "d_{z^2} atom orbital (AO) of Pt" for the second reaction step from Im_R to Pr_R, displayed in Figure 6.

The activation barrier related to the second step does not substantially influence the reaction rate because its height is lower than 4 kcal mol^{-1} in both dGMP branches. It demonstrates that decomposition of the Im_R complex is a fast and exergonic step.

In the product of the reduction process, negative pK_a(H8) value of approximately −15 and a fairly positive pK_a(N7) value of approximately ten were determined for both the Pr_R_5 and Pr_R_3 structure. Therefore the H8 proton is released and actually transferred to the N7 atom. The calculated energy barrier (TS3_R) is about 15 kcal mol^{-1} in the 5′-dGMP case and 6 kcal mol^{-1} in the 3′-dGMP case. It means that the considered H8→H7 PT is a relatively fast and exergonic process, connected with the release of −11 and −8 kcal mol^{-1} in the case of G_5 and G_3 branch, respectively. The considered PT is the third step and completes the reduction reaction.

We also tried to evaluate the activation barrier related to the deprotonation of the H8 proton in the Im_R structure immediately after the nucleophilic attack. For this process, a quite high barrier can be estimated (more than 30 kcal mol^{-1}). It is known[44] that a contribution from nuclear quantum mechanical (NQM) effects can modify the reaction rate of a proton transfer, nevertheless, such a change introduced by NQM effects will not play such an important role in our case. Liu and Warshel[44] demonstrated on the transfer of hydride in dihydrofolate reductase that this contribution represents approximately 7% of the total reaction rate.

The whole reduction reaction is endothermic. Nevertheless, the entropic term plays a crucial role due to the decomposition of the original associated system into several parts within the reaction course. Therefore the whole reaction is exergonic: the change of the Gibbs energy is approximately −14 kcal mol^{-1} in the 5′-dGMP branch and about −19 kcal mol^{-1} in the 3′-dGMP branch, as can be seen in Figure 5.

Hydrolysis

The G_5 structure, resulting from the reduction reaction, must be finally hydrolyzed to break the chelate structure P–O–C8 forming the 8-oxo-5′-dGMP according to the experimental study.[18,20] Nevertheless, the formation of 8-oxo-3′-dGMP (after breaking of C′–O–C8) was not observed so it is a question whether the reaction is kinetically or thermodynamically forbidden. To calculate the activation barrier, one explicit water molecule has to be taken into account. Proton transfer to the N7 site (from the C8-position as described in a previous section) stabilizes the 8-oxo-dGMP structure (Cysewski[45] calculated pK_a(N7–H) = 9.5) in both G_5 and G_3 reaction branches. Simultaneously with this PT also weakening of the P–O8 or C5′–O8 bonds occurs.

Two different possibilities for approaching of the water molecule to the G_5 chelate were chosen. In the first case, water is located between the H7 atom and the phosphate group (Figure 7, G1_5 structure) whereas it is placed outside the phosphate group in the second pathway (Figure 7, G2_5 structure). In the first pathway, the mechanism is nearly dissociative. In fact, water must initially break a P–O bond because it is located in the vicinity of the P–O8–C8 bonds. In the second pathway, oxygen atoms of the phosphate group together with oxygen of water form an electrostatically more convenient trigonal-bipyramidal arrangement in the TS_G2_5 structure.

The height of the Gibbs free energy barriers in the first (dissociative) mechanism is predicted to be 33 kcal mol^{-1} whereas only 10 kcal mol^{-1} are required in the second pathway. Therefore, only the second mechanism is explored in the case of the

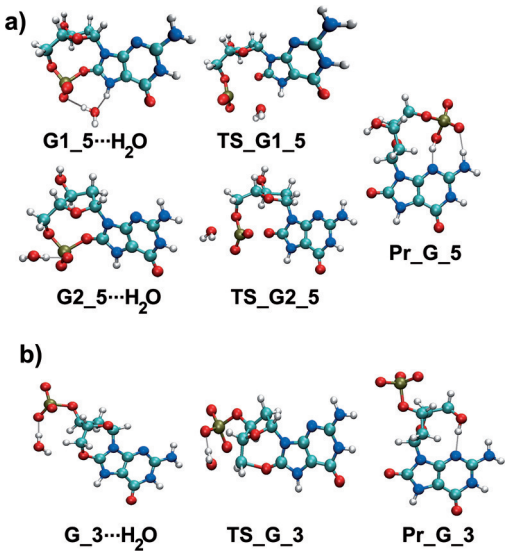

Figure 7. a) Reaction mechanism of the hydrolysis of the P–O8 bond with water localized between a phosphate group and the H7 atom (G1 pathway) and an outside phosphate group (G2 pathway. b) C5′–O8 bond (G2 pathway).

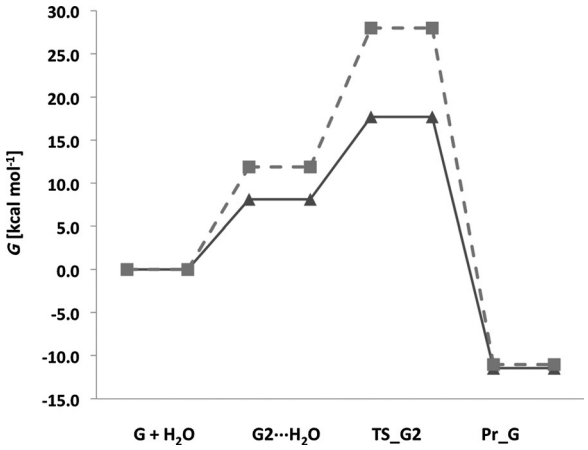

Figure 8. Gibbs free energy profiles of the hydrolysis of the 5′-dGMP branch (solid line with triangles) and the 3′-dGMP branch (dashed line with squares) at the B2 level. The label "G+H_2O" means the isolated reactants and "G2···H_2O" corresponds to supermolecular structures of the second pathway.

3′-dGMP branch. It was found that breaking of the stronger ether C5′–O8 bond is more demanding. The electron density in the BCP of the C5′–O8 bond is nearly twice as large as the corresponding value in the BCP of the P–O8 bond. Consequently, the activation barrier reaches the height of approximately 16 kcal mol^{-1} (Figure 8). The corresponding rate constant in the 5′-dGMP branch determined according to the TST of Eyring is 5.7×10^5 L mol^{-1} s^{-1}. The rate constant in the 3′-dGMP branch is about 10 L mol^{-1} s^{-1}. The hydrolysis is an exergonic reaction releasing about 11 kcal mol^{-1} for both G_5 and G_3 branches, as can be seen in Figure 8.

Conclusion

A detailed mechanism of the reduction process of tetraplatin with dGMP is studied by using the DFT method. The B3LYP-GD3BJ/6-31G(d)/COSMO computational level was chosen for optimization of all studied systems. The reaction energy surface and electronic properties were determined by using the 6-311++G(2df,2pd) basis set with consistent extension of pseudoorbitals[29] and DPCM/scaled-UAKS cavities.[27]

The total reduction mechanism was composed of three consequent reactions, that is, substitution, reduction, and hydration. It was shown that the substitution process occurs by the Basolo–Pearson autocatalytic mechanism. In this pathway only substitution of an axial chloro ligand is possible. Activation barriers were estimated to be 15, 16, and 19 kcal mol^{-1} for the 5′-dGMP, cGMP, and 3′-dGMP forms, respectively. The reaction is exothermic for all three dGMP forms.

The reduction reaction is the rate-determining process. It consists of three steps where first the nucleophilic attack by a phosphate (5′-dGMP) or a hydroxy (3′-dGMP) oxygen atom occurs, forming a relatively unstable chelate structure with the O–C8 bond. The reaction barrier for this step is about 21 and 20 kcal mol^{-1}, respectively, which according to the TST of Eyring can be translated into rate constants of 2.1×10^{-3} and 7.4×10^{-3} s^{-1} for 5′-dGMP and 3′-dGMP, respectively. The faster reaction rate in the case of 3′-dGMP corresponds to the experimental data.[20] In the second step the electron transfer from the guanine base to the platinum complex is carried out. Shortly after TS2, simultaneous breaking of both the Pt–N7 and Pt–Cl_a bonds occurs, releasing a chloride anion and forming a reduced square-planar Pt^{II} complex and 8-oxo-dGMP in the chelate form. The reduction reaction is exergonic also due to the third step; proton transfer from the C8 to the N7 site of guanine.

A hydration reaction finalizes the whole redox process. In this stage the chelate form is broken and regular 8-oxo-dGMP is formed. In both branches, the hydration barriers are relatively low (about 10 and 16 kcal mol^{-1} for 5′- and 3′-dGMP, respectively).

Summarizing, the total redox process is exothermic and exergonic. The corresponding change of the electronic energy is −15 and −17 kcal mol^{-1} for 5′-dGMP and 3′-dGMP, respectively, and the difference of the Gibbs energy is −34 and −28 kcal mol^{-1} in the 5′-dGMP and 3′-dGMP branch, respectively. The rate-determining step is the first activation barrier in the reduction reaction, which amounts 21.1 and 20.4 kcal mol^{-1} for the 5′-dGMP and 3′-dGMP reactions, respectively. Finally, an increase of the reaction rate of the substitution reaction is observed when the dach ligand is replaced by en or NH_3 groups.

Acknowledgements

The authors are grateful to a Grant Agency of Czech Republic project No P208/12/0622 for supporting this study. Additional support (for F.Š.) was obtained from the Grant Agency of Charles University. No. 532212. Access to computing facilities owned by parties and projects contributing to the National Grid Infrastructure MetaCentrum, provided under the program

"Projects of Large Infrastructure for Research, Development, and Innovations" (LM2010005) is highly appreciated.

Keywords: density functional calculations · kinetics · platinum · redox chemistry · thermodynamics

[1] B. Rosenberg in *Cisplatin* (Ed.: B. Lippert), Wiley-VCH, Weinheim, **1999**, p. 3.
[2] B. Rosenberg, L. Van Camp, J. L. Trosko, V. H. Mansour, *Nature* **1969**, *222*, 385.
[3] S. Akshintala, L. Marcus, K. Warren, R. Murphy, T. Sissung, A. Srivastava, W. Goodspeed, A. Goodwin, C. Brewer, C. Zalewski, K. King, A. Kim, W. Figg, B. Widemann, *Pediatr Blood Cancer* **2015**, *62*, 603.
[4] K. Wosikowski, L. Lamphere, G. Unteregger, V. Jung, F. Kaplan, J. P. Xu, B. Rattel, M. Caligiuri, Cancer *Chemother. Pharmacol.* **2007**, *60*, 589.
[5] A. E. Egger, C. G. Hartinger, A. K. Renfrew, P. J. Dyson, *J. Biol. Inorg. Chem.* **2010**, *15*, 919.
[6] R. Pettinari, F. Marchetti, F. Condello, C. Pettinari, G. Lupidi, R. Scopelliti, S. Mukhopadhyay, T. Riedel, P. Dyson, *Organometallics* **2014**, *33*, 3709.
[7] V. Novohradsky, Z. Liu, M. Vojtiskova, P. J. Sadler, V. Brabec, J. Kasparkova, *Metallomics* **2014**, *6*, 682.
[8] M. D. Zivkovic, S. Rajkovic, M. I. Djuran, *Bioorg. Chem.* **2008**, *36*, 161.
[9] L. Maiore, M. A. Cinellu, S. Nobili, I. Landini, E. Mini, C. Gabbiani, L. Messori, *J. Inorg. Biochem.* **2012**, *108*, 123.
[10] I. Romero-Canelón, P. J. Sadler, *Inorg. Chem.* **2013**, *52*, 12276.
[11] O. Bradáč, T. Zimmermann, J. V. Burda, *J. Mol. Model.* **2013**, *19*, 1669.
[12] S. Choi, S. Delaney, L. Orbai, E. J. Padgett, A. S. Hakemian, *Inorg. Chem.* **2001**, *40*, 5481.
[13] S. Choi, C. Filotto, M. Bisanzo, S. Delaney, D. Lagasee, J. L. Whitworth, A. Jusko, C. Li, N. A. Wood, J. Willingham, A. Schwenker, K. Spaulding, *Inorg. Chem.* **1998**, *37*, 2500.
[14] A. Vekris, D. Meynard, M.-C. Haaz, M. Bayssas, J. Bonnet, J. Robert, *Cancer Res.* **2004**, *64*, 356.
[15] T. J. O'Rourke, G. R. Weiss, P. New, H. A. Burris, G. Rodriguez, J. Eckhardt, J. Hardy, J. G. Kuhn, S. Fields, G. M. Clark, D. D. Von Hoff, *Anticancer Drugs* **1994**, *5*, 520.
[16] M. McKeage, F. Boxall, M. Jones, K. Harrap, *Cancer Res.* **1994**, *54*, 629.
[17] S. Choi, R. B. Cooley, A. S. Hakemian, Y. C. Larrabee, R. C. Bunt, S. D. Maupas, J. G. Muller, C. J. Burrows, *J. Am. Chem. Soc.* **2004**, *126*, 591.
[18] S. Choi, R. B. Cooley, A. Voutchkova, C. H. Leung, L. Vastag, D. E. Knowles, *J. Am. Chem. Soc.* **2005**, *127*, 1773.
[19] S. Choi, L. Vastag, Y. C. Larrabee, M. L. Personick, K. B. Schaberg, B. J. Fowler, R. K. Sandwick, G. Rawji, *Inorg. Chem.* **2008**, *47*, 1352.
[20] S. Choi, L. Vastag, C.-H. Leung, A. M. Beard, D. E. Knowles, J. A. Larrabee, *Inorg. Chem.* **2006**, *45*, 10108.
[21] A. C. Tsipis, I. N. Karapetsas, *Dalton Trans.* **2014**, *43*, 5409.
[22] J. Vícha, M. Patzschke, R. Marek, *Phys. Chem. Chem. Phys.* **2013**, *15*, 7740.
[23] J. J. Wilson, S. J. Lippard, *Inorg. Chim. Acta* **2012**, *389*, 77.
[24] Y. Zhao, J. A. Woods, N. J. Farrer, K. S. Robinson, J. Pracharova, J. Kasparkova, O. Novakova, H. Li, L. Salassa, A. M. Pizarro, G. J. Clarkson, L. Song, V. Brabec, P. J. Sadler, *Chem. Eur. J.* **2013**, *19*, 9578.
[25] a) H. P. Varbanov, M. A. Jakupec, A. Roller, F. Jensen, M. Galanski, B. K. Keppler, *J. Med. Chem.* **2013**, *56*, 330; b) S. Grimme, S. Ehrlich, L. Goerigk, *J. Comput. Chem.* **2011**, *32*, 1456; c) W. J. Hehre, R. Ditchfield, J. A. Pople, *J. Chem. Phys.* **1972**, *56*, 2257; d) D. Andrae, U. Häußermann, M. Dolg, H. Stoll, H. Preuß, *Theor. Chim. Acta* **1990**, *77*, 123.
[26] a) J. V. Burda, M. Zeizinger, J. Šponer, J. Leszczynski, *J. Chem. Phys.* **2000**, *113*, 2224; b) A. Klamt in *Encyclopedia of Computational Chemisty* (Ed.: P. v. R. Schleyer), John Wiley & Sons, Ltd., Chichester, UK, **1998**.
[27] T. Zimmermann, J. V. Burda, *J. Chem. Phys.* **2009**, *131*, 135101.
[28] L. Michera, M. Nekardova, J. V. Burda, *Phys. Chem. Chem. Phys.* **2012**, *14*, 12571.
[29] T. Zimmermann, J. Leszczynski, J. V. Burda, *J. Mol. Model.* **2011**, *17*, 2385.
[30] V. Barone, M. Cossi, J. Tomasi, *J. Chem. Phys.* **1997**, *107*, 3210.
[31] H. Eyring, *J. Chem. Phys.* **1935**, *3*, 107.
[32] a) NBO v 5.9, 5.0 ed., E. D. Glendening, K. Badenhoop, A. E. Ree, J. E. Carpenter, J. A. Bohmann, M. Morales, F. Weinhold, University of Wisconsin, Madison, WI (USA), **2001**.. b) M. J. Frisch, G. W. Trucks, H. B. Schlegel, G. E. Scuseria, M. A. Robb, J. R. Cheeseman, G. Scalmani, V. Barone, B. Mennucci, G. A. Petersson, H. Nakatsuji, M. Caricato, X. Li, H. P. Hratchian, A. F. Izmaylov, J. Bloino, G. Zheng, J. L. Sonnenberg, M. Hada, M. Ehara, K. Toyota, R. Fukuda, J. Hasegawa, M. Ishida, T. Nakajima, Y. Honda, O. Kitao, H. Nakai, T. Vreven, J. A. Montgomery, Jr., J. E. Peralta, F. Ogliaro, M. Bearpark, J. J. Heyd, E. Brothers, K. N. Kudin, V. N. Staroverov, R. Kobayashi, J. Normand, K. Raghavachari, A. Rendell, J. C. Burant, S. S. Iyengar, J. Tomasi, M. Cossi, N. Rega, J. M. Millam, M. Klene, J. E. Knox, J. B. Cross, V. Bakken, C. Adamo, J. Jaramillo, R. Gomperts, R. E. Stratmann, O. Yazyev, A. J. Austin, R. Cammi, C. Pomelli, J. W. Ochterski, R. L. Martin, K. Morokuma, V. G. Zakrzewski, G. A. Voth, P. Salvador, J. J. Dannenberg, S. Dapprich, A. D. Daniels, O. Farkas, J. B. Foresman, J. V. Ortiz, J. Cioslowski, D. J. Fox, Gaussian 09, Revision D.01, Gaussian Inc., Wallingford CT, **2009**.
[33] R. F. W. Bader, *Atoms in Molecules: A Quantum Theory*, Oxford University Press, Oxford, **1990**.
[34] T. A. Keith, http://aim.tkgristmill.com, **2014**.
[35] a) M. Mitoraj, A. Michalak, T. Ziegler, *J. Chem. Theor. Comput.* **2009**, *5*, 962; b) E. J. Baerends, T. Ziegler, J. Autschbach, D. Bashford, A. Bérces, F. M. Bickelhaupt, C. Bo, P. M. Boerrigter, L. Cavallo, D. P. Chong, L. Deng, R. M. Dickson, D. E. Ellis, M. van Faassen, L. Fan, T. H. Fischer, C. Fonseca Guerra, M. Franchini, A. Ghysels, A. Giammona, S. J. A. van Gisbergen, A. W. Götz, J. A. Groeneveld, O. V. Gritsenko, M. Grüning, S. Gusarov, F. E. Harris, P. van den Hoek, C. R. Jacob, H. Jacobsen, L. Jensen, J. W. Kaminski, G. van Kessel, F. Kootstra, A. Kovalenko, M. V. Krykunov, E. van Lenthe, D. A. McCormack, A. Michalak, M. Mitoraj, S. M. Morton, J. Neugebauer, V. P. Nicu, L. Noodleman, V. P. Osinga, S. Patchkovskii, M. Pavanello, P. H. T. Philipsen, D. Post, C. C. Pye, W. Ravenek, J. I. Rodríguez, P. Ros, P. R. T. Schipper, H. van Schoot, G. Schreckenbach, J. S. Seldenthuis, M. Seth, J. G. Snijders, M. Solà, M. Swart, D. Swerhone, G. te Velde, P. Vernooijs, L. Versluis, L. Visscher, O. Visser, F. Wang, T. A. Wesolowski, E. M. van Wezenbeek, G. Wiesenekker, S. K. Wolff, T. K. Woo, A. L. Yakovlev, ADF2014, SCM, Amsterdam, NL, **2014**; c) E. van Lenthe, R. van Leeuwen, E. J. Baerends, J. G. Snijders, *Int. J. Quant. Chem.* **1996**, *57*, 281.
[36] R. F. Nalewajski, J. Mrozek, A. Michalak, *Int. J. Quantum Chem.* **1997**, *61*, 589.
[37] a) A. Hesselmann, G. Jansen, J. Schütz, *J. Chem. Phys.* **2005**, *122*, 014103; b) H.-J. Werner, P. J. Knowles, G. Knizia, F. R. Manby, M. Schütz, P. Celani, W. Györffy, D. Kats, T. Korona, R. Lindh, A. Mitrushenkov, G. Rauhut, K. R. Shamasundar, T. B. Adler, R. D. Amos, A. Bernhardsson, A. Berning, D. L. Cooper, M. J. O. Deegan, A. J. Dobbyn, F. Eckert, E. Goll, C. Hampel, A. Hesselmann, G. Hetzer, T. Hrenar, G. Jansen, C. Köppl, Y. Liu, A. W. Lloyd, R. A. Mata, A. J. May, S. J. McNicholas, W. Meyer, M. E. Mura, A. Nicklass, D. P. O'Neill, P. Palmieri, D. Peng, K. Pflüger, R. Pitzer, M. Reiher, T. Shiozaki, H. Stoll, A. J. Stone, R. Tarroni, T. Thorsteinsson, M. Wang, MOLPRO, version 2012.1, **2012**.
[38] B. Song, H. Sigel, *Inorg. Chem.* **1998**, *37*, 2066.
[39] B. Knobloch, H. Sigel, A. Okruszek, R. K. O. Sigel, *Org. Biomol. Chem.* **2006**, *4*, 1085.
[40] F. Basolo, R. G. Pearson in *Advances in Inorganic Chemistry and Radiochemistry, Vol. 3* (Eds.: H. J. Emeleus, A. G. Sharpe), Academic Press, New York, **1961**, p. 1.
[41] E. C. Beret, J. M. Martinez, R. R. Pappalardo, E. S. Marcos, N. L. Doltsinis, D. Marx, *J. Chem. Theory Comput.* **2008**, *4*, 2108.
[42] a) A. Ariafard, N. M. Ghohe, K. K. Abbasi, A. J. Canty, B. F. Yates, *Inorg. Chem.* **2013**, *52*, 707; b) A. Ariafard, E. S. Tabatabaie, S. Aghmasheh, S. Najaflo, B. F. Yates, *Inorg. Chem.* **2012**, *51*, 8002; c) Z. Futera, J. V. Burda, *J. Comput. Chem.* **2014**, *35*, 1446.
[43] Z. Futera, J. Klenko, J. E. Sponer, J. Sponer, J. V. Burda, *J. Comput. Chem.* **2009**, *30*, 1758.
[44] H. Liu, A. Warshel, *J. Phys. Chem. B* **2007**, *111*, 7852.
[45] P. Cysewski, *Comp. Meth. Sci. Technol.* **2010**, *16*, 51.
[46] *CRC Handbook of Chemistry and Physics*, CRC Press, Boca Raton, **2005**.

Received: September 5, 2015
Revised: October 15, 2015
Published online on December 10, 2015

THE JOURNAL OF PHYSICAL CHEMISTRY B

Article

pubs.acs.org/JPCB

Side Reactions with an Equilibrium Constraint: Detailed Mechanism of the Substitution Reaction of Tetraplatin with dGMP as a Starting Step of the Platinum(IV) Reduction Process

Filip Šebesta and Jaroslav V. Burda*

Department of Chemical Physics and Optics, Faculty of Mathematics and Physics, Charles University, Ke Karlovu 3, 121 16 Prague 2, Czech Republic

ABSTRACT: Two possible pathways of the substitution reaction within the reduction process of the $Pt^{IV}(DACH)Cl_4$ by dGMP are compared: associative reaction course and autocatalytic Basolo−Pearson mechanisms. Since two forms: single-protonated and fully deprotonated phosphate group of dGMP are present in equilibrium at neutral and mildly acidic solutions, consideration of a side reactions scheme with acido-basic equilibrium-constraint is a very important model for obtaining reliable results. The examined complexes are optimized at the B3LYP-GD3BJ/6-31G(d) level with the COSMO implicit solvation model and Klamt's radii used for cavity construction. Energy characteristics and thermodynamics for all reaction branches are determined using the B3LYP-GD3BJ/6-311++G(2df,2pd)/IEF-PCM/scaled-UAKS level with Wertz's entropy corrections. Rate constants are estimated for each individual branch according to Eyring's transition state theory (TST), averaged according to equilibrium constraint and compared with available experimental data. The determined reaction barriers of the autocatalytic pathway fairly correspond with experimental values. Furthermore, autocatalytic reaction of tetraplatin and its two analogues complexes $[Pt^{IV}(en)Cl_4$ and $Pt^{IV}(NH_3)_2Cl_4]$ are explored and compared with measured data in order to examined general reaction descriptors.

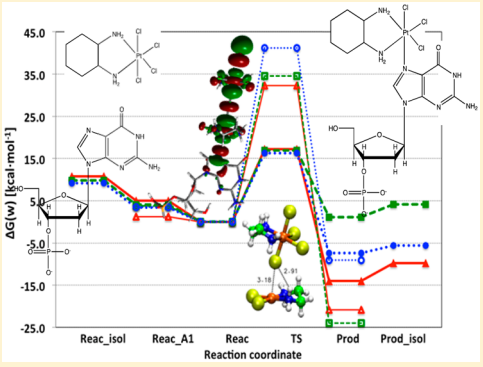

INTRODUCTION

Since Rosenberg's discovery of cisplatin anticancer activity, many platinum complexes together with several other transition metal compounds have been examined as possible metallodrugs.[1] Besides cisplatin (cis-diamminedichloroplatinum(II)), also carboplatin (*cis*-diammine-(cyclobutane-1,1-dicarboxylate-*O*,*O*′)platinum(II)), and oxaliplatin ([(1*R*,2*R*)-cyclohexane-1,2-diamine]-(ethanedioato-*O*,*O*′)platinum(II)) belong among the most frequently used anticancer agents. Nevertheless, since there are a large number of harmful side effects of contemporary drugs new compounds are still examined. Also, many of these drugs are resistant to some types of tumors. Recently, researchers addressed also some other transition metals, e.g., coordination compounds of Ru(II),[2,3] Pt(IV),[4,5] Ir(III),[6−8] and several others.[9−11] These substances can be often administrated in an inactive form being activated in an organism later. Among this family of drugs belongs also Pt(IV) complexes characterized by relatively high kinetic inertness. This feature enables an oral application of compounds like satraplatin (bis(acetate)amminedichloro(cyclohexylamine)-platinum(IV)).[4] For cytostatic metallodrugs containing chloro-ligand(s), the hydration process, i.e., substitution of some of these ligands by water, constitutes an activation step. Nevertheless, the hydration occurs with a very low probability in the case of Pt(IV) complexes[12] due to the relatively high reaction barriers, which are estimated to be more than 30 kcal/mol in comparison with activation barriers of ca. 22−24 kcal/mol in the case of Pt(II) complexes. Therefore, the direct hydration of Pt(IV) complexes can be interpreted as a kinetically forbidden process. It means that the reduction of these Pt(IV) complexes should occur first, followed by the hydration of the corresponding reduced Pt(II) forms, which also confirms the experimental study of Raynaud et al.[13]

The anticancer Pt(IV) complexes were also many times addressed by computational tools. Wilson et al.[14] combined computational and experimental techniques in the study where platinum(IV) complexes were prepared by oxidation of corresponding platinum(II) structures with iodobenzene dichloride in DMF. Singlet excited states of both sets of Pt(II) and Pt(IV) complexes were determined by the TD-DFT/LANL2DZ/COSMO method. The calculations confirmed that the quenching process is enabled by the new character of the excited state, which is based on the presence of one of the metal d-AOs, energetically located between original HOMO and LUMO of the chromophore ligand. Wada et al.[15] explored platinum complexes with 1,4,7-triazacyclononane (tacn) as facial ligands. Octahedral structures were determined via the single-crystal X-ray analysis. In aqueous solutions, a quasi-reversible two-electron redox wave at +0.22 V (vs SCE) was detected. An X-ray analysis of the reduced complex revealed a

Received: February 13, 2017
Revised: April 7, 2017
Published: April 10, 2017

DOI: 10.1021/acs.jpcb.7b01427
J. Phys. Chem. B 2017, 121, 4400−4413

tetra-coordinated square-planar structure, in which both tacn and bpy (bipyridine) were bound to the central Pt as bidentate ligands. The DFT calculations confirmed that structural changes in tacn-ligand facilitate the reversible redox process between octahedral Pt(IV) and square planar Pt(II) complexes. Other calculations performed Zhao et al.[16] for diazido-platinum(IV) complexes where vibrational modes determined by the TD-DFT(PBE1PBE/LanL2DZ/C-PCM) model confirmed the dissociative character of the low-lying excited states connected with metal−ligand charge transfer (LMCT) of azido-ligands. Series of papers was recently published by Tsipis et al.[17,18] where ^{195}Pt NMR chemical shifts were determined for a large set of platinum complexes (both Pt(II) and Pt(IV)) in implicit water solution and compared with measured data. Similar calculations were also performed by Vicha et al.[19] using the PBE0/TZP/COSMO computational level with the two-component zeroth-order regular approximation. Some new Pt(IV) structures were synthesized and characterized among other also by DFT calculations in the Bakalova study.[20] A series of Pt(IV), Pt(II), and Pd(II) complexes have been prepared and examined by IR, H-1, and C-13 NMR spectroscopies.[21] Authors also performed DFT calculations suggesting that in both gas and solution phases the trans isomers are more stable than the cis ones. Both experimental and calculated structural results revealed slightly distorted octahedral (Pt(IV)) and square-planar (Pt(II) and Pd(II)) geometries. Analogous similarities between Pt(II) and Pd(II) were also found in a research paper.[22]

In our study the substitution reaction is explored where one of the Pt−Cl bond is replaced by a Pt−N7 coordination in the system of tetraplatin (tetrachloro-(*d*,*l*-trans)-[(1*R*,2*R*)-cyclohexane-1,2-diamine]platinum(IV)) and dGMP. Tetraplatin itself represents a relatively reactive complex among other Pt(IV) complexes.[23−25] Unfortunately, the clinical tests on its anticancer activity were stopped since very high neurotoxicity[26,27] was found after its administration. Nonetheless, investigation of its reaction mechanism can explain how processes of similar Pt(IV) complexes occur. A series of experimental studies was recently performed by Choi et al.[28−31] who examined interaction of tetraplatin with deoxyguanosine monophosphate (dGMP). Using several measurements: IR, NMR, HPLC, a complex with Pt−N7(dGMP) coordination is formed in the initial substitution step. On the basis of a sigmoidal shape of kinetic curves authors concluded that explored reaction can have an autocatalytic course.[30] In our previous paper, we performed DFT calculations which indicated that activation barriers of the direct hydration of satraplatin (JM216) and its dihydroxo-dichloro derivative (JM149) are very high and lead to a conclusion that the hydration is a kinetically forbidden reaction.[12] Recently the complete reduction process of tetraplatin in the presence of dGMP was studied,[32−34] describing all three steps: substitution, reduction, and hydrolysis. In this contribution, we focus on the substitution reaction connected with formation of the tetraplatin adduct to N7 site of guanine as an important starting point of the reduction process. On the contrary to our previous study,[32] we used different thermodynamic description, including Wertz's entropy corrections and also a kinetic model based on side reactions with an equilibrium constraint, which enables to mix results from competitive reactions in order to obtain reliable data for comparison with experiments.

COMPUTATIONAL DETAILS

Optimization of the studied complexes is performed with the B3LYP functional applying Grimme's empirical dispersion corrections (GD3BJ keyword in Gaussian 09 (g09)). The double-ζ 6-31G(d) basis set is combined with Stuttgart effective energy averaged relativistic core potentials (MWB-60) for the description of the platinum atom. Scalar relativistic effects were shown to be sufficiently treated within these ECPs.[35,36] This approach was found accurate enough as to relativistic effect[36,37] in comparison with other approximations used in our model. The originally suggested set of pseudo-orbitals is augmented by f-polarization functions[38,39] [α_f(Pt) = 0.9593] in order to have a well-balanced basis set. The COSMO implicit solvation model with the cavities constructed based on Klamt's radii is used for simulation of the water environment[40] (hereafter labeled as the B1 level). Entropy and energy contributions from nuclear degrees of freedom, required for evaluation of the Gibbs free energies, are determined at the same B1 level based on canonical partition functions (with harmonic oscillator and rigid rotor models).

The single-point (SP) energy calculations are performed at the B3LYP-GD3BJ/6-311++G(2df,2pd) level with the IEF-PCM/scaled-UAKS (united atom−Kohn−Sham cavities[41]) implicit solvation model. The original pseudoorbitals for Pt atom are extended by a set of 2fg-polarization [α_{f1}(Pt) = 1.4193, α_{f2}(Pt) = 0.4662, α_g(Pt) = 1.2077] and spd-diffuse functions[38,42] [α_s(Pt) = 0.0075, α_p(Pt) = 0.013, α_d(Pt) = 0.025] in accord to the previous studies on cisplatin reactions[42−46] (labeled as the B2 level). In the scaled-UAKS cavity model, radii of the spheres around heavy atoms are modified relative to actual partial charges according to ref:[43,47,48]

$$R(X) = R_0(X) - \gamma \cdot \left| \frac{Q_{act}(X) - Q_{deprot}(X)}{Q_{prot}(X) - Q_{deprot}(X)} + Q_{deprot}(X) \right| \quad (1)$$

where γ is an original scaling factor in the UAKS model suggested according to formal charges by Orozco and Luque[49] and R_0 is a radius from the standard UAKS model without correction to the formal charge. γ was estimated to be 0.3 for all negatively charged groups and 0.26 for positively charged oxygen group. Factors for some other elements can be found in original papers.[41,49] Expressions Q_{deprot} and Q_{prot} are used for partial charges of the scaled group in protonated/deprotonated reference molecules as suggested in refs 41, 43, and 49, and Q_{act} is the partial charge of the given group of the explored structure. In this study, the scaling is applied to chlorines and groups containing oxygen atom with the exception of phosphate group. Radii of cavities around nitrogen and carbon atoms are not scaled in correspondence with the original UAKS model.[41,49] The NBO partial charges are determined using the B3LYP-GD3BJ functional and extended double-ζ 6-31++G-(d,p) basis set augmented consistently by spd-diffuse and f-polarization functions on Pt atom according to ref 38; cf. above. As to the solvation model, the IEF-PCM method with UAKS cavities is applied (together with g09 keyword g03defaults).

The Gibbs free energy was evaluated with Wertz's corrections[50,51] $G(w) = H - TS(w)$ where the entropy contributions from translational and rotational degrees of freedom are scaled in solvent using the following relation:

$$TS(w) = TS_{vib} + T[0.54 \times (S_{gas}^{trans} + S_{gas}^{rot} - 14.3) + 8.0] \quad (2)$$

DOI: 10.1021/acs.jpcb.7b01427
J. Phys. Chem. B 2017, 121, 4400−4413

Table 1. Parameters of the Pt−Cl Bonds for the Axial and Equatorial Ligands in $Pt^{IV}(NN)Cl_4$ Complexes

	$Pt^{IV}(DACH)Cl_4$		$Pt^{IV}(en)Cl_4$		$Pt^{IV}(NH_3)_2Cl_4$	
	Pt−Cl_e	Pt_Cl_a	Pt−Cl_e	Pt_Cl_a	Pt−Cl_e	Pt_Cl_a
bond length [Å]	2.367	2.368	2.365	2.367	2.361	2.367
bond index	0.738	0.672	0.737	0.686	0.750	0.691
electron density in the BCP × 10^2 [$e{\cdot}a_0^{-3}$]	9.13	9.17	9.18	9.18	9.23	9.20
EDA [in kcal/mol]:						
electrostatic	−187	−215	−192	−217	−200	−218
Pauli repulsion	120	131	121	131	123	131
steric	−67	−83	−70	−85	−77	−86
orbital	−105	−94	−109	−96	−110	−96
total	−175	−181	−182	−186	−190	−186

Scheme 1. Labeling and Atom Numbers in 5′-dGMP together with $Pt^{IV}(DACH)Cl_4$[a]

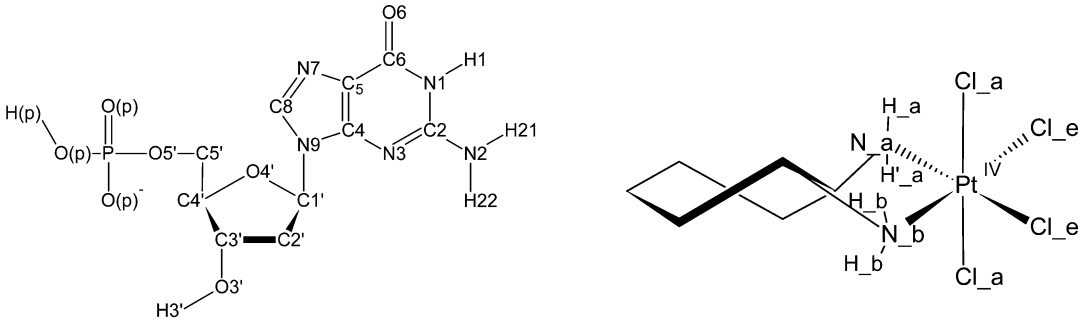

[a]Amino group of DACH ligand, which is closer to O6 of guanine is labeled with "a" (N_a, H_a), the second amino group with "b" (N_b, H_b).

Rate constants k of the explored reactions are estimated based on the heights of activation barriers $\Delta G^{\neq}$ according to Eyring's transition state theory[52] (TST) at T = 298.15 K:

$$k = \frac{k_B T}{h} e^{-\Delta G^{\neq}/k_B T} \quad (3)$$

All calculations of electronic structures are performed using Gaussian 09 software package. The symmetry-adapted intermolecular perturbation theory (DFT-SAPT)[53] from the Molpro 2012 program is applied for decomposition of interaction energy of Pt(II)/Pt(IV) cores in the autocatalytic reaction. In selected structures of platinum complexes, electrostatic, steric and orbital contributions to the total binding energy between Pt and coordinated ligands are obtained by ETS-NOCV analysis[54] (extended transition state for energy decomposition analysis combined with the natural orbitals for chemical valence) using the ADF 2014 program. The electron density is determined using scalar ZORA Hamiltonian at the B3LYP-GD3BJ/TZ2P level with the 4d frozen-core approximation used for Pt atom. At the same level, the bond order analysis is evaluated according to Nalewajski and Mrozek approach.[55] For the analysis of Pt(II)/Pt(IV) cores Averaged Local Ionization Potential (ALIP)[56] is mapped to isodensity surface at 0.001 $e{\cdot}Å^{-3}$. The Bader's QTAIM analysis[57] is performed by AIMAll v.14[58] program for the electron densities determined at the B2 level. At the same computational level also NPA partial charges are determined using the NBO v. 5.9 program[59] and pK_a values are alternatively estimated using CosmoTherm program,[60] too.

As to labeling used in the paper, Re stands for reactants, TS for transition states, Pr for products, and Im for intermediates, which can be further extended by *S* for *associative mechanism* or *A* for *autocatalytic mechanism* eventually followed by *"_5"*, *"_3"* or *"_c"* for more detailed variant of dGMP and by *"E"* or *"A"* in order to emphasize whether the substitution occurs into an equatorial or axial position (e.g., *Pr_S_5A*, *Pr_S_5E*).

RESULTS AND DISCUSSION

Since it is not clear, which chloro-ligand of tetraplatin should be replaced within the associative mechanism, basic electronic characteristics of the complex are evaluated for this molecule with C_2 symmetry. In tetraplatin both axial and equatorial Pt−Cl bonds are relatively similar, cf. Table 1. From the ETS-NOCV energy decomposition analysis (EDA) it follows that the larger orbital contribution for equatorial ligands is compensated by higher term of electrostatic interaction together with the Pauli repulsion in the case of axial chloro-ligands. The analogous conclusion can be drawn from the Nalewajski and Mrozek bond order analysis[55] and also by comparison of the both axial and equatorial Pt−Cl bond lengths and electron densities in bond critical points (BCPs), cf. Table 1. Similar analyses are also performed for two other platinum complexes related to tetraplatin, where DACH ligand is replaced by ethylenediamino ligand (en) and/or by two ammine-ligands, which are considered in the autocatalytic reaction course. Their bonding characteristics are quite close to original tetraplatin complex as follows from corresponding sections of Table 1. As to the dGMP molecule, all three forms are considered: 5′-dGMP, 3′-dGMP, and cGMP in substitution reaction. Atom numbering of both dGMP and Pt(IV) complex used in the paper is presented in Scheme 1. For the determination of an appropriate thermodynamic and kinetic description of the substitution reactions, it is necessary to know a correct protonation state of phosphate groups in solution at

DOI: 10.1021/acs.jpcb.7b01427
J. Phys. Chem. B 2017, 121, 4400−4413

Table 2. pK_a of Phosphoric Acid and the Phosphate Group in 5′-dGMP, 3′-dGMP, and cGMP[a]

	5′-dGMP			3′-dGMP			cGMP			H_3PO_4		
pK_a	calcd	CT	expt[b]	calcd	CT	expt[c]	calcd	CT	expt	calcd	CT	expt[d]
1	−0.8	4.9	0.35	−3.2	3.8		2.7	2.2	–	−1.9	2.5	2.1
2	7.6	6.5	6.29	6.8	5.6	6.14				6.5	4.7	7.2
3										10.2	9.8	12.3

[a]Columns with header CT means values obtained by the CosmoTherm program. [b]Reference 61. [c]Reference 62. [d]Reference 69. RMSD from experimental values is 0.823 for our calculations and 0.968 for CosmoTherm.

Table 3. Association and Reaction Energies and Activation Barriers for the Direct S_N2 Mechanism of Tetraplatin Interaction with dGMP (in kcal/mol) and Rate Constants k (in $M^{-1}\cdot s^{-1}$) at T = 298 K

	B1			B2		
association energies	ΔE	ΔG	ΔG(w)	ΔE	ΔG	ΔG(w)
5′-dGMP, ax,H[a]	−17.3	−6.3	−15.8	−7.4	3.6	−5.9
5′-dGMP, ax	−22.3	−9.3	−18.9	−4.6	8.4	−1.2
5′-dGMP, eq,H	−17.1	−5.7	−15.1	−7.9	3.5	−5.9
5′-dGMP, eq	−18.0	−5.8	−15.3	−7.8	4.4	−5.0
3′-dGMP, ax,H	−18.8	−3.4	−12.9	−7.9	7.5	−2.0
3′-dGMP, ax	−23.3	−7.9	−17.4	−9.6	5.7	−3.8
3′-dGMP, eq,H	−11.2	1.4	−8.0	−4.4	8.2	−1.2
3′-dGMP, eq	−11.8	1.2	−8.2	−5.8	7.2	−2.2
c-dGMP, ax	−16.4	−3.2	−12.6	−4.7	8.5	−0.9
c-dGMP, eq	−16.9	−3.2	−12.6	−7.7	5.9	−3.5
	B1			B2		
reaction energy	ΔE	ΔG	ΔG(w)	ΔE	ΔG	ΔG(w)
5′-dGMP, ax,H	−18.0	−12.6	−17.3	−13.8	−8.4	−13.0
5′-dGMP, ax	−28.5	−22.5	−27.2	−22.2	−16.2	−20.9
5′-dGMP, eq,H	−14.2	−6.6	−11.2	−13.0	−5.4	−10.0
5′-dGMP, eq	−15.6	−9.7	−14.3	−14.6	−8.6	−13.3
3′-dGMP, ax,H	−10.4	−3.3	−7.9	−5.8	1.2	−3.4
3′-dGMP, ax	−11.6	−4.6	−9.2	−9.7	−2.6	−7.2
3′-dGMP, eq,H	−14.2	−5.5	−10.1	−12.4	−3.7	−8.3
3′-dGMP, eq	−14.1	−7.7	−12.3	−12.6	−6.2	−10.8
c-dGMP, ax	−16.4	−7.0	−11.7	−10.3	−0.9	−5.6
c-dGMP, eq	−15.0	−6.4	−11.0	−13.1	−4.5	−9.1
	B1			B2		
TS energies	ΔE	ΔG	ΔG(w)	ΔE	ΔG	ΔG(w)	k
5′-dGMP, ax,H	40.0	41.4	41.4	42.0	43.4	43.4	9.5×10^{-20}
5′-dGMP, ax	34.5	34.8	34.8	33.0	32.2	32.2	1.5×10^{-11}
5′-dGMP, eq,H	38.5	39.0	39.0	37.6	38.1	38.1	7.7×10^{-16}
5′-dGMP, eq	38.6	40.0	40.0	38.1	39.6	39.5	6.8×10^{-17}
3′-dGMP, ax,H	35.3	37.9	37.8	38.9	41.5	41.4	2.7×10^{-18}
3′-dGMP, ax	32.7	33.1	33.0	34.3	34.7	34.6	2.8×10^{-13}
3′-dGMP, eq,H	37.7	39.6	39.5	38.4	40.2	40.2	2.2×10^{-17}
3′-dGMP, eq	37.8	39.6	39.6	39.3	41.1	41.1	5.0×10^{-18}
c-dGMP, ax	42.0	43.7	43.6	41.9	43.6	43.6	7.4×10^{-20}
c-dGMP, eq	38.5	40.0	39.9	39.7	41.2	41.1	4.4×10^{-18}

[a]ax and eq means substitution in axial and equatorial position, respectively; H labels system with singly protonated phosphate group, otherwise fully deprotonated phosphate is considered.

cellular pH (≈7.0) and, for comparison with experimental results,[29] also at pH = 8.3. We evaluated the pK_a of phosphate groups according to the previously suggested scheme using the D-PCM method with the scaled-UAKS cavities as described in ref.[42−44] For a better insight into the accuracy of calculated pK_a values, results of phosphoric acid are also added in Table 2. Moreover, the pK_a values are estimated using electron densities by the CosmoTherm program and for comparison displayed in Table 2. It can be noticed that deprotonation constants are in relatively fair agreement with experiments except of first step where the estimations are quite poor. Nevertheless, even a small deviation from the correct value can cause a relatively large deviation in the solution composition and therefore we decided to work rather with experimental pK_a values in this study. The experimental pK_a constants of 5′-dGMP[61] were determined to 0.35 and 6.29 and to 6.14 for 3′-dGMP[62] (pK_a of the first deprotonation was not present). From the Henderson-Hasselbach equation:

DOI: 10.1021/acs.jpcb.7b01427
J. Phys. Chem. B 2017, 121, 4400−4413

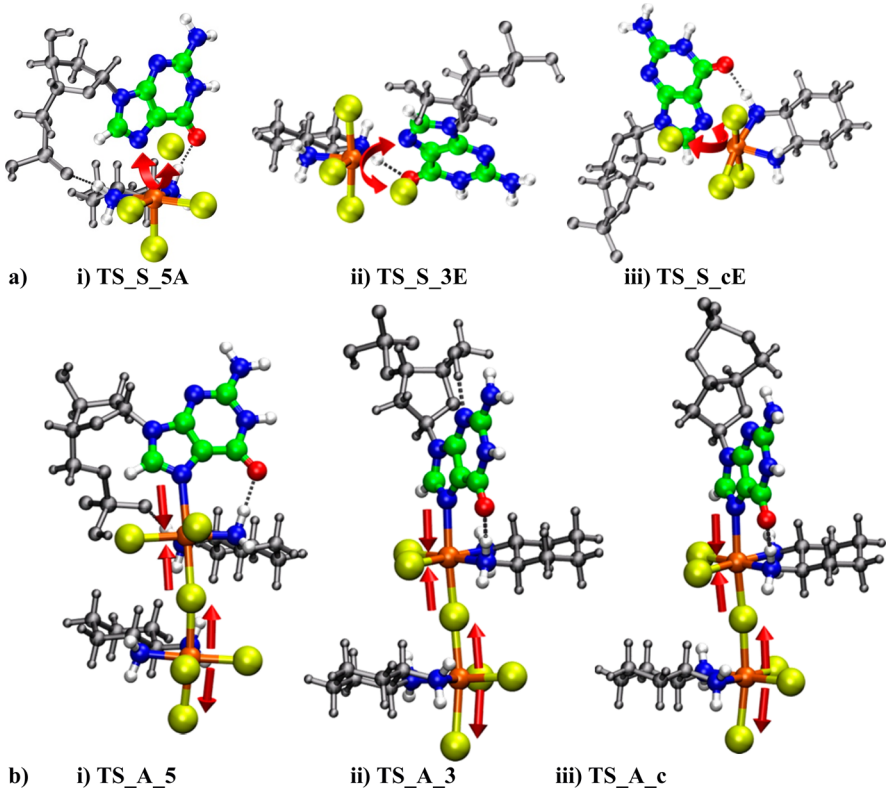

Figure 1. (a) Transition states for substitution of 5′-dGMP in equatorial and axial positions in the associative mechanism. (b) TS structures involved in the autocatalytic mechanism for substitution of 3′-dGMP and 5′-dGMP. Red arrows in the pictures indicate the antisymmetric vibrational mode, which leads to the product formation.

$$pK_a = pH + \log\left(\frac{[HA]}{[A^-]}\right) \quad (4)$$

the composition of solution with neutral pH will consist from ca. 16% of the singly protonated form in the case of 5′-dGMP and about 12% of the singly protonated form in the case of 3′-dGMP molecules.

In the structural search, several conformations of dGMP with various orientations of sugar−phosphate group to nucleobase are considered. The syn-conformations exhibit higher stabilization than anti-conformations for singly protonated states of dGMP. Especially, the position of phosphate group in 5′-dGMP molecule enables a strong stabilization by hydrogen bonding between phosphate group and N3 nitrogen of guanine. On the contrary, the fully deprotonated dGMP structures prefer anti-conformation. The differences of Gibbs free energy of the lowest structures are within 4.0 kcal/mol in the PCM solvation model. Similar conclusions were also published by Shishkin[63] for a pyrimidine nucleobases.

Direct S_N2 Substitution Reaction. Within this mechanism a replacement of one of the tetraplatin chloro-ligands by dGMP is modeled. By the term "direct substitution reaction", we mean a mechanism connected with TS where the imaginary (negative) vibrational mode has character of the antisymmetric stretch: X−Pt−Y (here Cl−Pt−N7). In this way the original Pt−Cl bond is broken simultaneously with Pt−N7 bond formation. Within such a mechanism, energy required for breaking of the bond (Pt−Cl) is (at least) partially compensated by an energy gain of synchronous formation of Pt−N7 bond. The reaction starts by forming an associate supermolecule from both "isolated" (solvated) molecules. While in gas phase the association is always an exothermic reaction in solution usually one kind of H-bonds (with water molecules from solvent) is (partially) replaced by some other weak interactions. Moreover, when Gibbs free energy is considered, two "pairs" of translational and rotational degrees of freedom are reduced to a single set (within the supermolecular model), transforming the other 6 degrees into vibrational contributions. Since the translational and rotational degrees are overestimated in the case of solvent models, the entropy contributions to Gibbs free energy, which generally disfavors formation of arranged systems, are therefore visibly exaggerated. This effect was already realized in 80-ties by Wertz.[50] He performed a deep analysis of these effects suggesting a scaling factor for the entropy contribution. Another interesting approach to reduced entropy was published by Okuno.[64] Recently some more accurate ways for estimation of the Wertz's corrections appeared,[51] which we are using in this paper. Most stable forms of the associate supermolecule correspond to systems with either tetraplatin associates by two H-bonds (Pt−NH···O6 and Pt−NH′...N7) to dGMP resembling a chelate 7-membered ring or by one (stronger) H-bond between Pt−NH···O6 with some additional weaker 'contacts' usually between phosphate group and tetraplatin hydrogens. In Table 3 association energies for the most stable structures in water solution are collected at the both optimization (B1) and SP (B2) levels for both singly protonated (sp) and fully deprotonated (fd) phosphate groups. Clearly, when Wertz's corrections are considered, the association energies (ΔG^{As}) remain negative (attractive interaction) after the supermolecular aggregation and they are up to −6 kcal/mol.

DOI: 10.1021/acs.jpcb.7b01427
J. Phys. Chem. B 2017, 121, 4400−4413

As it was already mentioned, despite the detailed insight into the structural features of tetraplatin, it remains not completely clear if the substitution preferably occurs to the axial or equatorial position. Similar Pt−Cl bond strengths and other bonding characteristics (cf. Table 1) do not indicate a unique preference. Therefore, both positions are considered in this part of calculations. Independently on the type of the ligand, it was found that the substitution reaction is exergonic and strongly exothermic as follows from reaction energies collected in the middle part of Table 3. The most stable product has guanine coordinated to the axial position of tetraplatin (**Pr_S_5A** structure) in the case of 5′-dGMP. The conformer with replaced chloro-ligand in equatorial position (**Pr_S_5E** structure) is by 3 and 8 kcal/mol higher in energy for dGMP with sp- and fd-phosphate group, respectively. In the cases of 3′-dGMP and cGMP, an opposite situation occurs since the structures with equatorial coordination of N7 site of guanine (**Pr_S_3E, Pr_S_cE**) are about 4−5 kcal/mol more stable than the axial conformers. The opposite stability can be partially explained by additional weak interactions between tetraplatin and dGMP (usually by highly polarized hydrogens of Pt−amino groups with oxygens of phosphate, sugar 5′-hydroxyl group or O6 site of guanine). The reaction Gibbs free energies are −20.9, −10.8, and −9.1 kcal/mol for the **Pr_S_5A**, **Pr_S_3E**, and **Pr_S_cE** structures (all in the fd-forms), respectively. The reaction in deprotonated forms occurs more easily mainly due to the electrostatic enhancement. When energy averaging is applied according to eq 5 reaction energies are ΔG_r = −19.6 and −10.4 kcal/mol for **Pr_S_5A** and **Pr_S_3E**; i.e., only minor changes occur in the direct mechanism.

As mentioned at the beginning of this section, transition state of the direct associative mechanism is characterized by the imaginary mode of the antisymmetric stretching vibration with the simultaneously leaving chloro-ligand and the approaching N7 site of guanine and vice versa. Comparing the optimized Pt−N7 and Pt−Cl distances in TS structures with our previous results dealing with cisplatin[65] or satraplatin[12,42] complexes, relatively longer coordinations of Pt cation are obtained in the present study. Despite this fact, the BCPs of Pt−N7 and Pt−Cl of the leaving chloro ligand (**Cl_l**) are detected in the AIM "molecular graph", which confirms the associative mechanism. However, electron densities of the corresponding BCPs are very small, even in comparison with the BCP density of the O6···H_a hydrogen bond. TS structures for all three dGMP conformers are drawn in Figure 1a. When the energy profile of the direct substitution mechanism is constructed, it follows that the activation barrier for each of the examined branches is higher than 32 kcal/mol. Actually the sp-forms of TS structures are connected with markedly higher activation barriers. Visibly lower reaction barriers in fd-3′/5′-dGMP is linked with electrostatic enhancement, which stabilizes the TS structure due to an appropriate orientation of the (charged) phosphate group toward protons of the amino-group of Pt moiety. Using this mechanism, chloro-ligands in the both equatorial and axial positions can be replaced by N7-guanine coordination. From the obtained transition states, it follows that lower activation energies are connected with replacement of chloro ligands in axial position since in this orientation better interaction between Pt complex and phosphate group of dGMP is enabled. Only in the case of cGMP, the TS structure with equatorial coordination represents lower energy pathway due to the low flexibility of the phosphate group. Nevertheless, probability that the reaction occurs via this mechanism is quite low even for the lowest activation barriers and the corresponding rate constants determined according to Eyring's TST are below 10^{-11} $M^{-1}\cdot s^{-1}$ (or below 10^{-10} $M^{-1}\cdot s^{-1}$ for T = 310 K). Clearly, such a reaction mechanism leads to kinetically forbidden reactions. The reaction energy profiles are drawn for both kinds of the associative mechanisms in Figure 2.

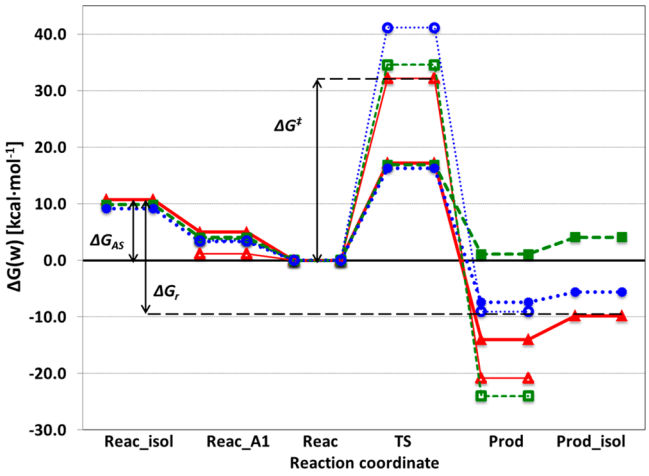

Figure 2. Gibbs free energy profile for the direct S_N2 (thin with empty symbols) and autocatalytic (bold with full symbols) mechanisms of 5′-dGMP (solid red line with triangles), 3′-dGMP (dashed green line with squares) and cGMP (dotted blue and circles) determined at the B2 level. For the energy profile of 5′-dGMP branch meaning of the parameters presented in Tables 3 and 5 is depicted: ΔG_{AS}, association Gibbs energy; ΔG_r, reaction Gibbs energy; and $\Delta G^{\ddagger}$, activation barrier.

Basolo−Pearson Autocatalytic Mechanism.[30,66] This mechanism represents alternative reaction pathway where a reduced Pt(II) complex is expected to catalyze the reaction course. The Pt(II) compound is placed between the dGMP and Pt(IV) molecules.

First, stability of the dinuclear Pt(II)/Pt(IV) core is explored. Since the dispersion interaction represents an important stabilizing contribution, the perturbation theory is used for calculations. The MP2 optimization (MP2/6-31G(d)/C-PCM/Klamt) is carried out for a slightly simpler $Pt(en)Cl_2/Pt(en)Cl_4$ model. The three lowest minima: **A_1**, **A_2**, and **A_3** are displayed in Figure 3. The association Gibbs free energies are evaluated at the MP2/6-311++G(2df,2pd)/IEF-PCM/scaled-UAKS level of theory, and the obtained Gibbs free energies

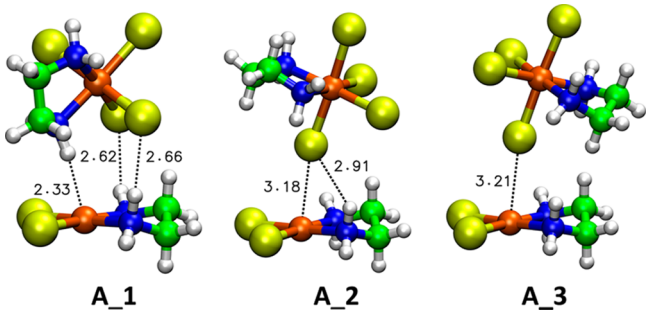

Figure 3. Stable structures of $Pt^{IV}(DACH)Cl_4/Pt^{II}(DACH)Cl_2$ associate optimized at the MP2/6-31G(d)/C-PCM/Klamt level. Distances (in Å) between atoms in important weak interactions are depicted, too.

DOI: 10.1021/acs.jpcb.7b01427
J. Phys. Chem. B 2017, 121, 4400−4413

with Wertz's correction are −11.5, −5.6, and −0.2 kcal/mol for **A_1**, **A_2**, and **A_3**, respectively. An energy decomposition of the interaction energies are calculated using the DFT-SAPT method at the B3LYP/6-31+G(d) level. The obtained energy contributions are summarized in Table 4. There can be seen

Table 4. EDA Obtained by SAPT2 at the B3LYP/6-31+G(d) Level, in kcal/mol

	electrostatics	induction	exchange	dispersion	total
A_1	−30.2	−9.2	26.8	−10.8	−23.4
A_2	−18.5	−4.6	17.3	−6.4	−12.2
A_3	2.0	−4.6	17.5	−6.9	8.0

that the Pt(II)/Pt(IV) core stabilization can be decomposed into two main parts: (a) The electrostatic interaction, which stabilizes an antiparallel amino-ligands arrangement of complexes (**A_1** and **A_2**) and has a negative impact on a parallel arrangement (**A_3**) since the dipole−dipole interaction of both Pt complexes is repulsive in this core structure. Also, a fairly high induction contribution is noticeable in the **A_1** structure (twice as high as in remaining cases). (b) The dispersion contribution stabilizes both the parallel and antiparallel orientations of amino-ligands. Nevertheless, the dispersion represents the most important attractive component in the parallel orientation of the Pt(II)/Pt(IV) core. The **A_1** core (i.e., mildly tilted antiparallel arrangement) was found in the reactant structures of the autocatalytic mechanism.

In the reactant supermolecular structures (**Re_A**), dGMP and Pt(II) complex are associated by O6···H_a H-bond. In the case of 5′-dGMP, the whole system is also linked together via an additional O(p)···H_b H-bond between the phosphate and the amino group of Pt(IV) complex (for atomic notation see Scheme 1). An additional interaction between Pt(II) ion and hydrogen H_a can be noticed, which is common to all the **A_1** core structures. Here a relatively short Pt(II)···H_a distance occurs - usually ca. 2.4 Å (cf. Figure 3), which is similar to the value of 2.55 Å found by Beret et al.[67] for the dispersion interaction between water hydrogen and nucleus of cisplatin. Notice that the recent study of Chval et al.[68] shows that such an interaction is not of a dispersion origin but more or less of a charge transfer character. The total association energy (ΔE^{As}) of **Re_A** complex is quite negative - stabilizing (less than −18 kcal/mol at the B2 computational level). However, the Gibbs free energy ΔG^{As} of the reactant supermolecule without Wertz's correction is up to +10 kcal/mol due to the exaggerated entropy term. Introducing Wertz's correction the ΔG^{As}(w) energy approaches values of −10 kcal/mol. The original (uncorrected) entropic contribution $-T\Delta S$ to ΔG^{As} for the formation of **Re_A** from three isolated parts is in the range 25−30 kcal/mol, cf. part of association energies in Table 5. As stated above, the entropic contribution ΔS_{T+R} corresponding to 12 from 18 translational+rotational degrees of freedom is not properly compensated by the ΔS_V term from vibrational degrees, to which are these above-mentioned degrees transformed in the supermolecular model. Then, the ΔS becomes unrealistic, which causes too large differences between ΔE and ΔG. Applying Wertz's correction, there is still an entropy penalty for formation of a more ordered system but these entropy terms correspond much closer to reality (experiments). In Table 5 it can be seen the differences between electronic and both kinds of Gibbs free energies, which are quite large for the formation of the associates.

It was found that the most stable structures of the reactant supermolecules contain anti-conformation of sugar−phosphate moiety to nucleobase in the singly protonated form of dGMP on the contrary to isolated dGMP and also to the fully deprotonated reactant forms where syn-conformation dominates. The activation barriers calculated from these sp-anti-conformation of dGMP in **Re_A** reactant structures are 14.7 and 18.6, for 5′-dGMP and 3′-dGMP respectively. In the case of fd-syn-form of **Re_A** activation barriers are 17.4, 16.3, and 16.2 kcal/mol, for 5′-dGMP, 3′-dGMP, and cGMP, respectively.

Because of the results from previous paragraph, we have to consider both possible reaction pathways (with two different TS) since one of the reactant (dGMP) occurs in two different forms with comparable concentrations at neutral pH - the single-protonated and fully deprotonated forms (as follows from eq 4). In this case, the total effective reaction rate must be obtained as a weighted average of rates in the sp- and fd-branches unless the rate constants differ substantially (by several order of magnitude). This represents the kinetics of side reactions with constraint of equilibrium condition between concentrations of B and C

$$\mathrm{A} + \mathrm{B} \overset{k_1}{\rightarrow} \mathrm{R} \text{ and } \mathrm{A} + \mathrm{C} \overset{k_2}{\rightarrow} \mathrm{S}$$

where A is dinuclear Pt_2 complex and B and C are sp- and fd-forms of dGMP where B and C concentrations are linked via the fast acido-base equilibrium described by the Henderson−Hasselbach formula eq 4. Then a product ratio [R]/[S] can be determined according to equation:

$$\frac{[\mathrm{R}]}{[\mathrm{S}]} = \frac{k_1[\mathrm{B}]}{k_2[\mathrm{C}]} = \frac{k_1[\mathrm{HB}]}{k_2[\mathrm{B}^-]} = \frac{k_1}{k_2}K_a[\mathrm{H}^+] = \frac{x_1k_1}{x_2k_2} = \frac{k_1^{eff}}{k_2^{eff}}$$

From the activation energies for both sp- and fd- forms of dGMP, the actual k_1 and k_2 rate constants in the individual branches can be determined from eq 3. On the basis of the known pH and pK_a values, concentration respectively molar fractions x_1, x_2 of both acidic and basic form of dGMP can be easily obtained and used for determination of effective rate constants (k_1^{eff}, k_2^{eff}). It is obvious that such a treatment has reason only if both concentrations of the acidic and basic forms are comparable. From Table 5 it follows that for sp-5′-dGMP the distinctly lower activation barrier occurs 14.7 kcal/mol in comparison with fd-form with $\Delta G^{\neq}$ is 17.4 kcal/mol. However, due to low concentration of acidic (sp)- 5′-dGMP vs fd-form (molar ratio x_1:x_2 = 0.163:0.837 at neutral pH) the rate constant k_1 decreases from 105 $M^{-1}\cdot s^{-1}$ to effective value 17.3 $M^{-1}\cdot s^{-1}$ (cf. first line in Table 6b) when it is considered that certain amount of 5′-dGMP is reacting through the fd-form reaction-channel (with rate constant k_2 = 1.12 $M^{-1}\cdot s^{-1}$ and k_2^{eff} = 0.94 $M^{-1}\cdot s^{-1}$).

Then the total effective rate constants k^{eff} and the corresponding effective barrier ΔG^{eff} (for comparison with experimental values) can be obtained as the sum of effective rate constants in both (generally all) reaction channels, since:

$$\begin{aligned}\frac{\mathrm{d}[A]}{\mathrm{d}t} &= -k_1[\mathrm{A}][\mathrm{HB}] - k_2[\mathrm{A}][\mathrm{B}^-] \\ &= -(k_1x_1 + k_2x_2)[\mathrm{A}][\mathrm{B}^{tot}] \\ &= -k^{eff}[\mathrm{A}][\mathrm{B}^{tot}]\end{aligned}$$

Here $[B^{tot}]$ denotes total concentration of the compound B (in our case dGMP) regardless its protonation state. ΔG^{eff} free

DOI: 10.1021/acs.jpcb.7b01427
J. Phys. Chem. B 2017, 121, 4400−4413

Table 5. Energetics and Kinetics of the Individual Reaction Branches in the Basolo−Pearson Autocatalytic Mechanism[a]

		B1			B2			
X		ΔE	ΔG	ΔG(W)	ΔE	ΔG	ΔG(W)	rate constants
				Association Energies				
DACH	5′-dGMP,H	−37.7	−10.6	−30.1	−18.4	8.7	−10.8	
	5′-dGMP	−48.8	−20.9	−40.3	−20.1	7.7	−11.7	
	3′-dGMP,H	−34.4	−3.9	−23.4	−19.9	9.6	−9.8	
	3′-dGMP	−35.1	−6.5	−25.9	−19.1	9.5	−9.9	
	C-dGMP	−33.4	−9.0	−28.5	−20.0	10.3	−9.1	
en	5′-dGMP,H	−36.3	−9.4	−28.5	−19.0	7.9	−11.2	
	5′-dGMP	−47.0	−19.2	−38.3	−22.0	5.8	−13.3	
	3′-dGMP,H	−31.6	−3.5	−22.5	−18.8	9.3	−9.8	
	3′-dGMP	−32.0	−2.7	−21.7	−20.4	9.0	−10.1	
	C-dGMP	−36.9	−7.3	−26.4	−18.3	11.3	−7.8	
$(NH_3)_2$	5′-dGMP,H	−33.7	−3.9	−22.8	−21.1	8.6	−10.2	
	5′-dGMP	−46.3	−15.9	−34.7	−27.2	3.2	−15.6	
	3′-dGMP,H	−30.0	−2.4	−21.2	−21.1	6.5	−12.3	
	3′-dGMP	−30.2	−2.1	−20.9	−21.1	7.0	−11.8	
	C-dGMP	−34.7	−4.0	−22.9	−21.6	9.1	−9.8	
				Reaction Energies				
DACH	5′-dGMP,H	−18.0	−12.6	−17.3	−13.8	−8.4	−13.0	
	5′-dGMP	20.3	−1.5	13.2	−2.0	−23.9	−9.2	
	3′-dGMP,H	−10.4	−3.3	−7.9	−5.8	1.2	−3.4	
	3′-dGMP	25.3	3.0	17.8	13.7	−8.6	6.3	
	C-dGMP	−16.4	−7.0	−11.7	−10.3	−0.9	−5.6	
en	5′-dGMP,H	−17.0	−10.6	−15.2	−13.6	−7.2	−11.8	
	5′-dGMP	21.6	0.3	14.7	−0.1	−21.4	−7.0	
	3′-dGMP,H	−9.8	−2.9	−7.5	−5.9	1.1	−3.5	
	3′-dGMP	19.9	−1.7	12.8	12.4	−9.2	5.2	
	C-dGMP	−12.3	−6.3	−10.9	−5.6	0.5	−4.1	
$(NH_3)_2$	5′-dGMP,H	−14.8	−7.9	−12.5	−15.3	−8.5	−13.1	
	5′-dGMP	19.2	−2.7	11.5	0.9	−21.0	−6.7	
	3′-dGMP,H	−7.5	−1.5	−6.0	−6.9	−0.9	−5.4	
	3′-dGMP	17.4	−2.9	11.4	7.1	−13.2	1.1	
	C-dGMP	−12.0	−4.1	−8.6	−8.5	−0.6	−5.1	
				TS Energies				
DACH	5′-dGMP,H	9.2	10.4	10.4	13.5	14.7	14.7	1.06×10^{2}
	5′-dGMP	13.7	14.6	14.5	16.5	17.4	17.4	1.12×10^{0}
	3′-dGMP,H	14.3	14.8	14.8	18.1	18.6	18.6	1.37×10^{-01}
	3′-dGMP	15.4	15.2	15.2	16.6	16.3	16.3	6.90×10^{0}
	C-dGMP	19.7	17.4	17.5	18.4	16.1	16.2	9.29×10^{0}
en	5′-dGMP,H	13.7	14.1	14.1	12.0	12.4	12.4	4.98×10^{3}
	5′-dGMP	17.5	18.0	18.0	16.3	16.8	16.8	2.95×10^{0}
	5′-dGMP,H	14.3	16.7	16.8	17.6	20.0	20.0	1.45×10^{-02}
	5′-dGMP	14.1	13.6	13.7	17.8	17.3	17.4	1.24×10^{0}
	C-dGMP	18.9	18.3	18.4	16.2	15.7	15.8	1.98×10^{1}
$(NH_3)_2$	5′-dGMP,H	15.9	13.8	13.9	12.6	10.5	10.5	1.27×10^{5}
	5′-dGMP	22.9	19.7	19.7	15.6	12.4	12.5	4.77×10^{3}
	3′-dGMP,H	15.3	15.7	15.8	17.6	18.0	18.1	3.76×10^{-01}
	3′-dGMP	15.1	15.4	15.5	17.2	16.8	16.8	2.95×10^{0}
	C-dGMP	17.3	15.7	15.7	18.2	16.5	16.6	4.74×10^{0}

[a]Energies are in kcal/mol. $Pt(II)Cl_2(X)$/ $Pt(IV)Cl_4(X)$ where X = DACH, en, $(NH_3)_2$ and rate constants (in $M^{-1}\cdot s^{-1}$) at T = 298 K.

energy barrier can subsequently be determined from the known effective rate constant k^{eff} using eq 3. For the total reaction energy ΔG_r^{eff} standard energy averaging can be used:

$$\Delta G_r^{eff} = x_1 \Delta G_{r1} + x_2 \Delta G_{r2} \quad (5)$$

Here ΔG_{ri} are individual reaction Gibbs free energies for sp- and fd-branches. Notice that in this way both rate constants and reaction energies are directly dependent on pH of the solution.

This procedure was applied for both 3′- and 5′-dGMP and all three forms of Pt(IV)/Pt(II) dinuclear cores with DACH, en, and diammine ligands and obtained results are summarized in Table 6 for pH = 7 and 8.3 for a comparison with experimental data.[31] For neutral solutions, the ΔG_r^{eff} energy with Wertz's correction is −9.8 kcal/mol for 5′-dGMP and Pt(IV) complex with DACH ligand while for pH = 8.3 it reduces to −9.2 kcal/mol. All the reaction energies are summarized in Table 6a and the kinetic characteristics in Table 6b. From, e.g., first line of

DOI: 10.1021/acs.jpcb.7b01427
J. Phys. Chem. B 2017, 121, 4400−4413

Table 6. (a) Effective Reaction Gibbs Free Energies ΔG_r^{eff} for solutions with pH = 7 and 8.3 (in kcal/mol) and (b) Activation Barriers and Rate Constants: Effective and Averaged Values of the Basolo−Pearson Autocatalytic Mechanism[a]

(a) Effective Reaction Gibbs Free Energies

		pH = 7	pH = 8.3
DACH	5′-dGMP	−9.8	−9.2
	3′-dGMP	5.1	6.2
	cGMP	−5.6	−5.6
en	5′-dGMP	−7.8	−7.0
	3′-dGMP	4.2	5.2
	cGMP	−4.1	−4.1
$(NH_3)_2$	5′-dGMP	−7.8	−6.8
	3′-dGMP	0.3	1.1
	cGMP	−5.1	−5.1

(b) Activation Barriers and Rate Constants

				pH = 7.0			pH = 8.3		
		$\Delta G^{\ddagger}$(W)	k_1/k_2	k_1^{eff}/k_2^{eff}	k^{eff}	ΔG^{eff}	k_1^{eff}/k_2^{eff}	k^{eff}	ΔG^{eff}
5′-dGMP[d]									
DACH	sp	14.7	1.1×10^{2}	1.7×10^{1}			1.0×10^{0}		
	fd	17.4	1.1×10^{0}	9.4×10^{-01}	1.8×10^{1}	15.7	1.1×10^{0}	2.1×10^{0}	17.0[b,c]
en	sp	12.4	4.8×10^{3}	7.8×10^{2}			4.8×10^{1}		
	fd	16.8	3.0×10^{0}	2.5×10^{0}	7.8×10^{2}	13.5	2.9×10^{0}	5.1×10^{1}	15.1[c]
$(NH_3)_2$	sp	10.5	1.2×10^{5}	1.9×10^{4}			1.1×10^{3}		
	fd	12.5	4.4×10^{3}	3.7×10^{3}	2.3×10^{4}	12.4	4.4×10^{3}	5.5×10^{3}	12.4[c]
3′-dGMP[e]									
DACH	sp	18.6	1.4×10^{-01}	1.7×10^{-02}			9.4×10^{-04}		
	fd	16.4	5.7×10^{0}	5.0×10^{0}	5.1×10^{0}	16.5	5.7×10^{0}	5.7×10^{0}	16.4[b]
en	sp	20.0	1.3×10^{-02}	1.6×10^{-03}			9.1×10^{-05}		
	fd	17.4	1.1×10^{0}	1.0×10^{0}	1.0×10^{-01}	17.5	1.1×10^{0}	1.1×10^{0}	17.3
$(NH_3)_2$	sp	18.1	3.4×10^{-01}	4.1×10^{-02}			2.3×10^{-03}		
	fd	17.5	8.6×10^{-01}	7.5×10^{-01}	8.0×10^{-01}	17.6	8.5×10^{-01}	8.6×10^{-01}	17.6

[a]Energies are in kcal/mol. Pt(II)Cl_2(X)/ Pt(IV)Cl_4(X) where X= DACH, en, $(NH_3)_2$ and rate constants (in $M^{-1}\cdot s^{-1}$) at T = 298 K. [b]Compare with experimental values of 16.6 ± 1.4 and 16.3 ± 0.2 for 5′ and 3′-dGMP respectively, in ref 31. [c]Measured rate constant of 11.1 ± 2.2 for DACH ligand, 25.2 ± 4.1 for (en) ligand and 85.8 ± 6.2 at pH = 8.3 with initial concentrations 1/0.2/20 mM of Pt(IV) complex/Pt(II) complex/5′-dGMP, respectively; in ref 30. [d]5′-dGMP: pK_a = 6.29, pH = 7, [HA] = 0.163, [A] = 0.837; pH = 8.3, [HA] = 0.010, [A] = 0.990. [e]3′-dGMP: pK_a = 6.14, pH = 7, [HA] = 0.121, [A] = 0.879 pH = 8.3, [HA] = 0.007, [A] = 0.993.

Table 6b, it follows that despite visibly lower activation energy of sp-5′-dGMP (14.7 kcal/mol), fd-5′dGMP has dominant concentration and therefore effective activation barrier (ΔG^{eff}) of 5′-dGMP is noticeably higher. When we compare rate constants of the interaction of 3′- and 5′-dGMP with Pt(DACH)Cl_4 in solution with pH = 8.3, we obtain, using the above-mentioned procedure, values of 16.42 and 17.00 kcal/mol, and the experimental values are 16.3 ± 0.2 and 16.6 ± 1.4 for 3′ and 5′-dGMP respectively. So that it can be seen more than fair accord considering the used computational level. Actually, Tables 3 and 5 contain similar energy averaging as to the syn and anti-conformation equilibrium of the 3′- and 5′-dGMP nucleotides in a few cases, too.

In transition state **TS_A**, the synproportionation of Pt atoms from both Pt(IV) and Pt(II) complexes occurs. These structures contain the antiparallel arrangement of the Pt(II)/Pt(IV) core (**A_2**) as can be noticed in Figure 1b. Simultaneously, on the opposite side of the square-planar Pt(II) complex, the Pt−N7 coordination is established. The equatorial plane of Pt(IV) complex becomes practically parallel to the plane of Pt(II). In these TS_A structures, the dipole moments of both bulky cyclohexane rings are in antiparallel orientation in the cases of 3′-dGMP and cGMP forms (**TS_A_3** and **TS_A_c**). However, the C_2 pseudoaxes of both DACH ligands are nearly perpendicular in TS structure with 5′-dGMP as can be seen in Figure 1b: **TS_A_5**. The explanation can be seen in distinctly hydrophobic character of cyclohexane rings, which tend to get to mutual proximity. The unification of oxidation states of both Pt atoms in the transition state correlates with the fact that the exchanged chloro-ligand **Cl_m** is practically in the middle between both metal atoms. Also the electron densities in corresponding BCPs are practically the same—ca. 0.07 $e\cdot a_0^{-3}$. On the contrary, in the reactant and product structures, the corresponding BCPs densities of Pt(II)-Cl_m are less than 0.006 $e\cdot a_0^{-3}$ (if exist) and Pt(IV)-Cl_m is about 0.09 $e\cdot a_0^{-3}$. The analogous conclusion can be also drawn from the frontier MOs picture (cf. Figure 4) where occupation of "d_{z^2}" AO on platinum clearly indicates, which cation is in reduced Pt(II) or in oxidized Pt(IV) state in the reactants and products. On the contrary in TS structure, an equal mixture of AOs belonging to the both Pt atoms is visible in both HOMO and LUMO orbitals. This fact is supported by very similar NBO partial charges on Pt atoms, cf. Table 7. Notice also that the electron transfer from Pt(II) to Pt(IV) complex is partially enhanced by decrease of electron density on the guanine moiety (as can be seen in the last line of Table 7). Since the direct associative mechanism for the substitution reaction has to overcome quite high-energy barriers only the autocatalytic pathway, with activation barriers lower than 20 kcal/mol, represents realistic possibility. Within this mechanism releasing of chloro-ligand in the equatorial position of the Pt-complex can be excluded.

DOI: 10.1021/acs.jpcb.7b01427
J. Phys. Chem. B 2017, 121, 4400−4413

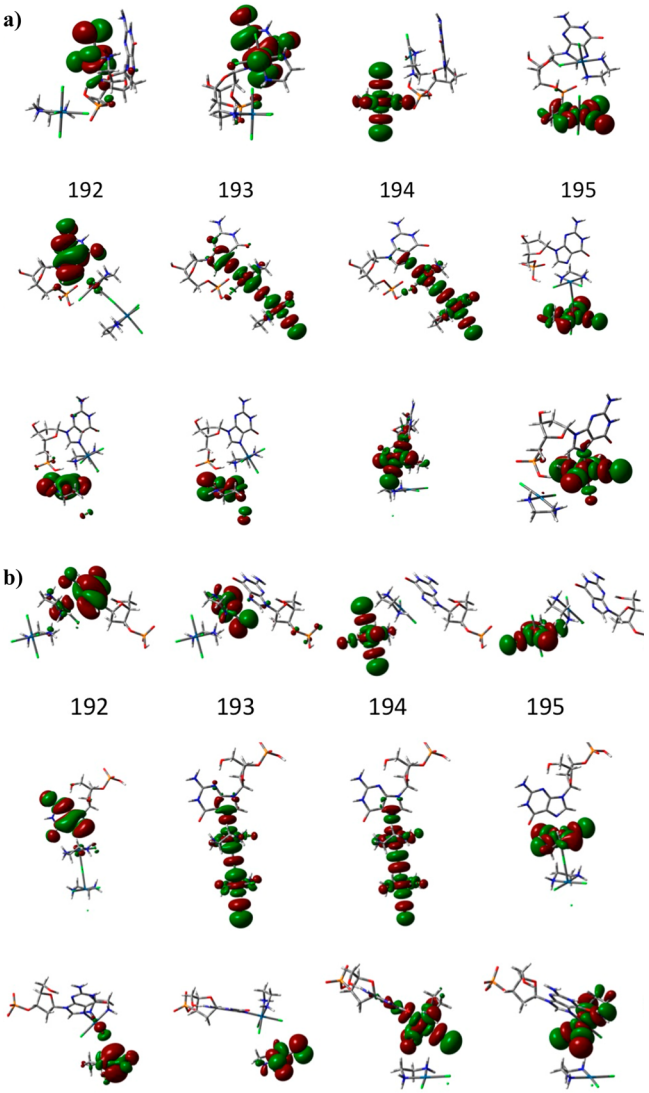

Figure 4. Frontier orbitals of the stationary structures (first line, reactant; second, TS; and third, product) in the synproportionation process within the autocatalytic mechanism with (a) 5′-dGMP and (b) 3′-dGMP. The 192th MO is HOMO−1, 193th is HOMO, etc.

In the case of the autocatalytic mechanism, Pt complexes with the other amino-ligands were explored, too. First, the stability of dinuclear core Pt(II)/Pt(IV) structures with DACH, en, and diammine ligands are compared. It was found that the most stable arrangement is practically the same in all three cases and corresponds to the **A_1** structure. The mutual differences in association energies vary within a few kcal/mol at the B2 level; cf. the same lines in the each ligand section of Association energies in Table 5. The main difference in the Pt(II)···dGMP association energy among various dGMP conformers is connected with the different interacting site of dGMP: phosphate group (in the 5′-dGMP) and hydroxyl group (in the 3′-dGMP). The cGMP conformer is usually too rigid so that its phosphate group cannot effectively interact with the metal core.

Rate constants of the reaction between $Pt(DACH)Cl_4$, $Pt(en)Cl_4$, or $Pt(NH_3)_2Cl_4$ with 5′-dGMP were measured in the laboratory of Choi,[30] cf. footnote of Table 6b. The experimentally determined rate of the substitution reaction increases from $Pt(DACH)Cl_4$ (rate constant of 11 $M^{-1}\cdot s^{-1}$) to $Pt(NH_3)_2Cl_4$ (86 $M^{-1}\cdot s^{-1}$). The relatively large variation of the rate constants results in only quite a small energy difference of 1.4 kcal/mol when it is translated into the language of the heights of activation barriers. This difference can be compared with the calculated value, which is a little bit larger, ca. 4.8 kcal/mol. The decrease of activation barriers has basically two origins. At first, when DACH is replaced by en-ligand, the decrease is connected with the different mutual orientation of both DACH ligands in comparison with the orientation of en ligands. The TS structure with the en-ligand has the mutual orientation of their C2 axes nearly colinear (maximizing electrostatic contribution of the stabilization energy) in analogy with 3′-dGMP and cGMP structures while the corresponding axes are nearly perpendicular in the case of the DACH ligands. This (electrostatically) less stable arrangement of the DACH ligands is probably enforced by fairly hydrophobic character of DACH ligands (cf. discussion above). An additional stabilization of en-containing TS structure occurs due to stronger interaction (with shorter distance) between the negatively charged phosphate group and hydrogen H_b of en-ligand of the originally Pt(II) complex (for the atom numbering see Scheme 1). The second decrease, when en-ligand containing complexes are compared with the systems with two ammine groups, is due to the entropy factor as follows from an additional decrease of Gibbs free energy ($\Delta\Delta G^{\ddagger} = \Delta G^{\ddagger}(\text{en}) - \Delta G^{\ddagger}(\text{diammine})$) in comparison with corresponding electronic energies ($\Delta\Delta E^{\ddagger}$) in Table 5. If we compare the predicted $\Delta G^{\ddagger}$ decrease with the measured data, it can be seen that the trend is reproduced fairly well, despite an underestimation of activation energy of the complex with diammine ligands.

Electronic Density Analyses. NBO, QTAIM, and MO analyses together with construction of maps of molecular electrostatic potentials and ALIP on the 0.001 e·Å^{-3} electron density surface have been performed for a deeper insight into the reaction profile.

MO analysis is used mainly for demonstration of the synproportionation process of both Pt cations within the autocatalytic mechanism displayed for both 5′- and 3′-dGMP branches in Figure 4. Here, occupied MOs of AO-d_{z^2} character (corresponding to Pt(II) complex) give the evidence of reduced Pt(II) moiety and inversely analogous unoccupied MOs of oxidized Pt(IV) moiety within the supermolecular model. From this point, an interesting situation occurs in TS state where d-AOs from both Pt atoms are "symmetrically" combined in both HOMO and LUMO orbitals forming Pt(III)−Pt(III) TS structure.

A similar picture is visible from Table 7 where NBO partial charges are collected. Clear charge unification of both Pt cations occurs in the TS structures. Also, the exchange of charge differences between the reactant and the product can be noticed confirming flipping of the Pt(II) and Pt(IV) oxidation states. As already mentioned, a mild charge transfer (of ca. 0.35e) from guanine to Pt(IV) complex is distinctly seen. Analogous characteristics are obtained for all three kind of the explored platinum complexes containing DACH, en, and $(NH_3)_2$ ligands with very marginal variation.

Within the QTAIM analysis we concentrate on the electron densities of Pt−L BCPs for all ligands and on detection of weak interactions. Comparing three different Pt complexes with DACH, en, and $(NH_3)_2$ ligands, electron densities in corresponding BCPs for Pt−N7 coordination can be approximately ordered DACH ≈ en > ammonia. However, no simple correlation between the activation barriers and the

DOI: 10.1021/acs.jpcb.7b01427
J. Phys. Chem. B 2017, 121, 4400−4413

Table 7. Partial Charges (in e) in the Stationary Points along the Autocatalytic Reaction Course in 3′-GMP and 5′-dGMP Branches

	5′-dGMP			3′-dGMP		
	singly protonated			singly protonated		
	reacn	TS	prod.	reacn	TS	prod.
Pt(IV)	1.007	0.924	0.558	1.005	0.876	0.579
Pt(II)	0.563	0.891	1.086	0.559	0.951	1.078
Cl_m[a]	−0.461	−0.396	−0.422	−0.455	−0.375	−0.414
$Pt^{II}(NH_2)_2Cl_2$	−0.472	−0.071	0.426	−0.454	0.096	0.502
$Pt^{IV}(NH_2)_2Cl_2$	0.379	0.086	−0.649	0.367	−0.031	−0.518
guanine	0.049	0.125	0.386	0.082	0.233	0.434
	5′-dGMP			3′-dGMP		
	fully deprotonated			fully deprotonated		
	reacn	TS	prod.	reacn	TS	prod.
Pt(IV)	1.015	0.913	0.564	1.005	0.887	0.568
Pt(II)	0.561	0.898	1.090	0.566	0.940	1.065
Cl_m[a]	−0.453	−0.394	−0.438	−0.458	−0.378	−0.415
$Pt^{II}(NH_2)_2Cl_2$	−0.521	−0.068	0.409	−0.493	0.068	0.498
$Pt^{IV}(NH_2)_2Cl_2$	0.338	0.053	−0.541	0.359	−0.006	−0.517
guanine	0.037	0.121	0.380	0.051	0.218	0.428

[a]Cl_m = chloro-ligand lying between both Pt atoms.

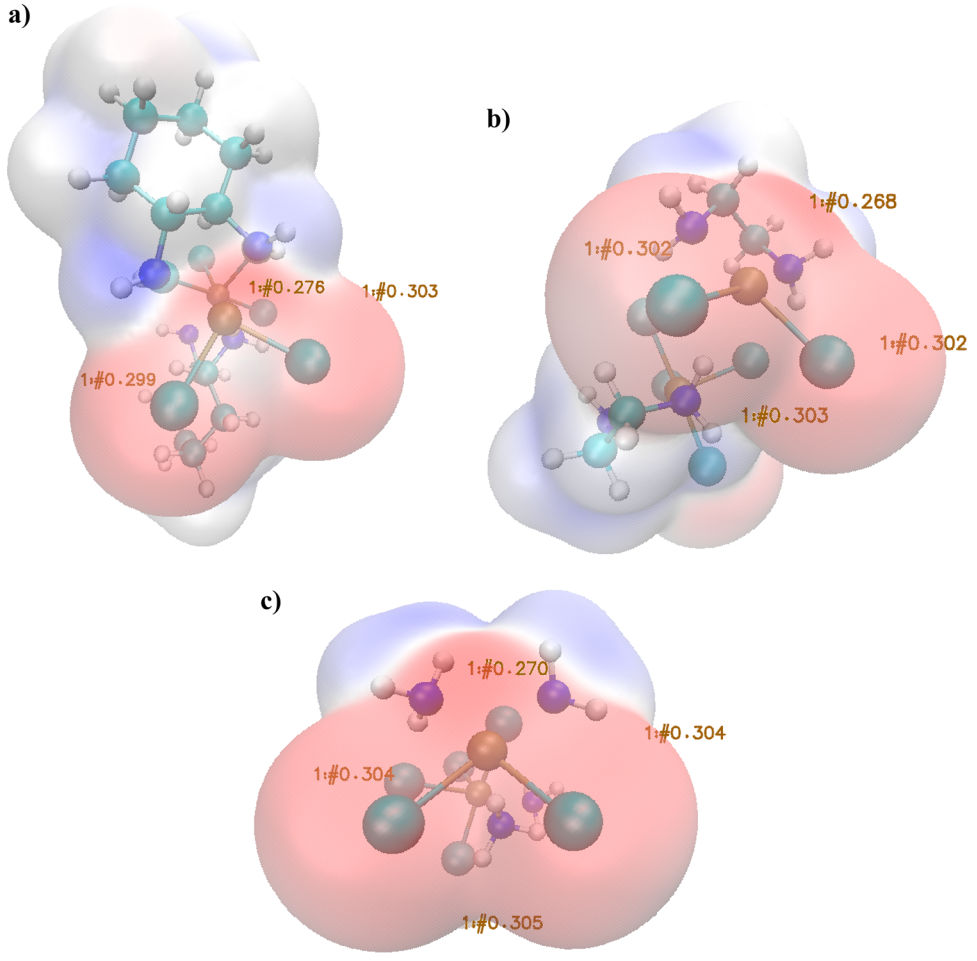

Figure 5. Maps of averaged local ionization potentials and positions of the lowest minima for three Pt(II)/Pt(IV) cores: (a) Pt−DACH with minimum of 0.276; (b) Pt−en, min: 0.268; and (c) Pt−$(NH_3)_2$, min: 0.270 au.

electron densities in the BCPs of Pt−Cl with the shared chloro-ligand or forming Pt−N7 bond in TS structures was found. In the case of Pt(II)/Pt(IV) dinuclear cores, the ALIP analysis as suggested by Politzer is performed. When maps of ALIP projected on the 0.001 e·Å^{-3} electron isodensity surface are analyzed it appears that the lowest minimum (place with most

DOI: 10.1021/acs.jpcb.7b01427
J. Phys. Chem. B 2017, 121, 4400−4413

readily electron detachment) is located just above the Pt atom of the Pt(II) complex. This corresponds to the place where N7 site starts to form Pt−N7 covalent bond after withdrawing two electrons from the Pt(II) complex, cf. Figure 5. This ALIP-value can be compared for all three Pt(II)/Pt(IV) cores estimating the strength of Pt−N7 bond under the influence of various Pt-ligands. Such a trend is in good agreement with electronic activation energies $\Delta E^{\ddagger}$(B2) averaged over all five GMP conformers in Table 5.

CONCLUSIONS

A detailed mechanism of the substitution process of tetraplatin with dGMP is studied using the B3LYP-GD3BJ/6-31G(d)/C-PCM/Klamt model for optimization. Single-point energies and electronic properties are determined using the 6-311++G-(2df,2pd) basis set with consistent extension of pseudoorbitals and IEF-PCM/scaled-UAKS cavities.

The substitution process occurs via the Basolo−Pearson autocatalytic mechanism, since the direct S_N2 mechanism is connected with too high reaction barriers (over 32 kcal/mol). In the autocatalytic pathway, a replacement of the equatorial chloro-ligand is excluded due to geometry reasons. In this study we applied improved Wertz's correction for determination Gibbs free energies with explicit dependence on pH of solution in thermodynamic description of substitution reaction. This improved model is in reasonable agreement with our previous "standard" calculations performed on this reaction.[32] Activation barriers are estimated to be 15.7 (17.0), 16.5 (16.4), and 16.2 kcal/mol for 5′-dGMP, 3′-dGMP, and cGMP conformers, respectively for pH = 7 (and pH = 8.3), which is also in fair agreement with either our previous results or experimental data. The reaction is exothermic for all three dGMP forms. Nevertheless, the improved model leads to the same reaction preference between both dGMP as the experimental observations: slightly more active 3′-dGMP over 5′-dGMP on the contrary to our previous conclusions[32].

Within the autocatalytic mechanism, additional two tetraplatin derivatives are examined. In accord with experimental measurements for 5′-dGMP reductans, an increase of the reaction rate in order: DACH < en < $(NH_3)_2$ is confirmed using both "standard" and "improved" models.

AUTHOR INFORMATION

Corresponding Author

*(J.V.B.) E-mail: burda@karlov.mff.cuni.cz.

ORCID

Jaroslav V. Burda: 0000-0001-9909-8797

Notes

The authors declare no competing financial interest.

ACKNOWLEDGMENTS

This study was supported by the Grant Agency of the Czech Republic, Project No. 16-06240S. F.Š. is thankful for additional support from the Grant Agency of Charles University. No. 1145016. The authors are grateful for generous access to computing facilities of the National Grid Infrastructure MetaCentrum, under the program "Projects of Large Infrastructure for Research, Development, and Innovations" (LM2010005).

REFERENCES

(1) Rosenberg, B.; Van Camp, L.; Trosko, J. L.; Mansour, V. H. Platinum drugs; a new class of potent antitumor agents. *Nature* **1969**, *222*, 385−391.

(2) Egger, A. E.; Hartinger, C. G.; Renfrew, A. K.; Dyson, P. J. Metabolization of [Ru(η6-C6H5CF3) (pta)Cl2]: a cytotoxic RAPTA-type complex with a strongly electron withdrawing arene ligand. *JBIC, J. Biol. Inorg. Chem.* **2010**, *15*, 919−927.

(3) Pettinari, R.; Marchetti, F.; Condello, F.; Pettinari, C.; Lupidi, G.; Scopelliti, R.; Mukhopadhyay, S.; Riedel, T.; Dyson, P. Ruthenium(II)-Arene RAPTA Type Complexes Containing Curcunnin and Bisdemethoxycurcumin Display Potent and Selective Anticancer Activity. *Organometallics* **2014**, *33* (14), 3709−3715.

(4) Akshintala, S.; Marcus, L.; Warren, K.; Murphy, R.; Sissung, T.; Srivastava, A.; Goodspeed, W.; Goodwin, A.; Brewer, C.; Zalewski, C.; King, K.; Kim, A.; Figg, W.; Widemann, B. Phase 1 trial and pharmacokinetic study of the oral platinum analog satraplatin in children and young adults with refractory solid tumors including brain tumors. *Pediatr Blood Cancer* **2015**, *62*, 603−610.

(5) Wosikowski, K.; Lamphere, L.; Unteregger, G.; Jung, V.; Kaplan, F.; Xu, J. P.; Rattel, B.; Caligiuri, M. Preclinical antitumor activity of the oral platinum analog satraplatin. *Cancer Chemother. Pharmacol.* **2007**, *60*, 589−600.

(6) Liu, Z.; Sadler, P. J. Organoiridium Complexes: Anticancer Agents and Catalysts. *Acc. Chem. Res.* **2014**, *47* (4), 1174−1185.

(7) Liu, Z.; Romero-Canelón, I.; Habtemariam, A.; Clarkson, G. J.; Sadler, P. J. Potent Half-Sandwich Iridium(III) Anticancer Complexes Containing C∧N-Chelated and Pyridine Ligands. *Organometallics* **2014**, *33* (19), 5324−5333.

(8) Novohradsky, V.; Liu, Z.; Vojtiskova, M.; Sadler, P. J.; Brabec, V.; Kasparkova, J. Mechanism of cellular accumulation of an iridium(III) pentamethylcyclopentadienyl anticancer complex containing a C,N-chelating ligand. *Metallomics* **2014**, *6* (3), 682−690.

(9) Romero-Canelon, I.; Sadler, P. J. Next-Generation Metal Anticancer Complexes: Multitargeting via Redox Modulation. *Inorg. Chem.* **2013**, *52*, 12276−12291.

(10) Zivkovic, M. D.; Rajkovic, S.; Djuran, M. I. Reaction of [Pt(Gly-Gly-N,N0,O)I] with the N-acetylated dipeptide L-methionyl-L-histidine: Selective platination of the histidine side chain by intramolecular migration of the platinum(II) complex. *Bioorg. Chem.* **2008**, *36*, 161−164.

(11) Maiore, L.; Cinellu, M. A.; Nobili, S.; Landini, I.; Mini, E.; Gabbiani, C.; Messori, L. Gold(III) complexes with 2-substituted pyridines as experimental anticancer agents: Solution behavior, reactions with model proteins, antiproliferative properties. *J. Inorg. Biochem.* **2012**, *108*, 123−127.

(12) Bradáč, O.; Zimmermann, T.; Burda, J. V. Can Satraplatin be hydrated before the reduction process occurs? The DFT computational study. *J. Mol. Model.* **2013**, *19*, 4669−4680.

(13) Raynaud, F. I.; Mistry, P.; Donaghue, A.; Poon, G. K.; Kelland, L. R.; Barnard, C. F. J.; Murrer, B. A.; Harrap, K. R. *Cancer Chemother. Pharmacol.* **1996**, *38*, 155.

(14) Wilson, J. J.; Lippard, S. J. Modulation of ligand fluorescence by the Pt(II)/Pt(IV) redox couple. *Inorg. Chim. Acta* **2012**, *389*, 77−84.

(15) Wada, T.; Enami, K.; Kojima, R.; Okada, T.; Ishikawa, Y.; Miyazato, Y.; Horn, E.; Mochizuki, Y. Reversible Structural Changes Accompanying the Two-Electron Redox Reaction of Pt(tacn) (tacn: 1,4,7-triazacyclononane) Complexes. *Bull. Chem. Soc. Jpn.* **2015**, *88* (9), 1230−1237.

(16) Zhao, Y.; Woods, J. A.; Farrer, N. J.; Robinson, K. S.; Pracharova, J.; Kasparkova, J.; Novakova, O.; Li, H.; Salassa, L.; Pizarro, A. M.; Clarkson, G. J.; Song, L.; Brabec, V.; Sadler, P. J. Diazido Mixed-Amine Platinum(IV) Anticancer Complexes Activatable by Visible-Light Form Novel DNA Adducts. *Chem. - Eur. J.* **2013**, *19* (29), 9578−9591.

(17) Tsipis, A. C.; Karapetsas, I. N. Accurate prediction of Pt-195 NMR chemical shifts for a series of Pt(II) and Pt(IV) antitumor agents by a non-relativistic DFT computational protocol. *Dalton Trans.* **2014**, *43* (14), 5409−5426.

DOI: 10.1021/acs.jpcb.7b01427
J. Phys. Chem. B 2017, 121, 4400−4413

(18) Tsipis, A. C.; Karapetsas, I. N. Prediction of Pt-195 NMR chemical shifts of dissolution products of H-2 Pt(OH)(6) in nitric acid solutions by DFT methods: how important are the counter-ion effects? *Magn. Reson. Chem.* **2016**, *54* (8), 656−664.
(19) Vicha, J.; Patzschke, M.; Marek, R. A relativistic DFT methodology for calculating the structures and NMR chemical shifts of octahedral platinum and iridium complexes. *Phys. Chem. Chem. Phys.* **2013**, *15* (20), 7740−7754.
(20) Bakalova, A.; Buyukliev, R.; Momekov, G. Synthesis, DFT calculations and cytotoxic investigation of platinum complexes with 3-thiolanespiro-5 ′-hydantoin and 4-thio-1H-tetrahydropyranespiro-5 ′-hydantoin. *J. Mol. Struct.* **2015**, *1091*, 118−124.
(21) Sabounchei, S. J.; Shahriary, P.; Salehzadeh, S.; Gholiee, Y.; Chehregani, A. Spectroscopic, theoretical, and antibacterial approach in the characterization of 5-methyl-5-(3-pyridyl)-2, 4-imidazolidene-dione ligand and of its platinum and palladium complexes. *C. R. Chim.* **2015**, *18* (5), 564−572.
(22) Zeizinger, N.; Burda, J. V.; Sponer, J.; Kapsa, V.; Leszczynski, J. A systematic ab initio study of the hydration of selected palladium square-planar complexes. A comparison with platinum analogues. *J. Phys. Chem. A* **2001**, *105* (34), 8086−8092.
(23) Choi, S.; Delaney, S.; Orbai, L.; Padgett, E. J.; Hakemian, A. S. A Platinum(IV) Complex Oxidizes Guanine to 8-Oxo-Guanine in DNA and RNA. *Inorg. Chem.* **2001**, *40*, 5481−5482.
(24) Choi, S.; Filotto, C.; Bisanzo, M.; Delaney, S.; Lagasee, D.; Whitworth, J. L.; Jusko, A.; Li, C.; Wood, N. A.; Willingham, J.; Schwenker, A.; Spaulding, K. Reduction and Anticancer Activity of Platinum(IV) Complexes. *Inorg. Chem.* **1998**, *37* (10), 2500−2504.
(25) Vekris, A.; Meynard, D.; Haaz, M.-C.; Bayssas, M.; Bonnet, J.; Robert, J. Molecular Determinants of the Cytotoxicity of Platinum Compounds: The Contribution of in Silico Research. *Cancer Res.* **2004**, *64* (1), 356−362.
(26) O'Rourke, T. J.; Weiss, G. R.; New, P.; Burris, H. A.; Rodriguez, G.; Eckhardt, J.; Hardy, J.; Kuhn, J. G.; Fields, S.; Clark, G. M.; Von Hoff, D. D. Phase I clinical trial of ormaplatin (tetraplatin, NSC 363812). *Anti-Cancer Drugs* **1994**, *5*, 520−526.
(27) McKeage, M.; Boxall, F.; Jones, M.; Harrap, K. Lack of neurotoxicity of oral bisacetatoamminedichlorocyclohexylamine-platinum(IV) in comparison to cisplatin and tetraplatin in the rat. *Cancer Res.* **1994**, *54*, 629−631.
(28) Choi, S.; Cooley, R. B.; Hakemian, A. S.; Larrabee, Y. C.; Bunt, R. C.; Maupas, S. D.; Muller, J. G.; Burrows, C. J. Mechanism of Two-Electron Oxidation of Deoxyguanosine 5′-Monophosphate by a Platinum(IV) Complex. *J. Am. Chem. Soc.* **2004**, *126* (2), 591−598.
(29) Choi, S.; Cooley, R. B.; Voutchkova, A.; Leung, C. H.; Vastag, L.; Knowles, D. E. Oxidation of Guanosine Derivatives by a Platinum(IV) Complex: Internal Electron Transfer through Cyclization. *J. Am. Chem. Soc.* **2005**, *127*, 1773−1781.
(30) Choi, S.; Vastag, L.; Larrabee, Y. C.; Personick, M. L.; Schaberg, K. B.; Fowler, B. J.; Sandwick, R. K.; Rawji, G. Importance of Platinum(II)-Assisted Platinum(IV) Substitution for the Oxidation of Guanosine Derivatives by Platinum(IV) Complexes. *Inorg. Chem.* **2008**, *47* (4), 1352−1360.
(31) Choi, S.; Vastag, L.; Leung, C.-H.; Beard, A. M.; Knowles, D. E.; Larrabee, J. A. Kinetics and Mechanism of the Oxidation of Guanosine Derivatives by Pt(IV) Complexes. *Inorg. Chem.* **2006**, *45* (25), 10108−10114.
(32) Šebesta, F.; Burda, J. V. Reduction Process of Tetraplatin in the Presence of Deoxyguanosine Monophosphate (dGMP): A Computational DFT Study. *Chem. - Eur. J.* **2016**, *22*, 1037−1047.
(33) Ariafard, A.; Ghohe, N. M.; Abbasi, K. K.; Canty, A. J.; Yates, B. F. Theoretical Investigation into the Mechanism of 3′-dGMP Oxidation by [PtIVCl4(dach)]. *Inorg. Chem.* **2013**, *52* (2), 707−717.
(34) Ariafard, A.; Tabatabaie, E. S.; Aghmasheh, S.; Najaflo, S.; Yates, B. F. Density Functional Theory Studies on the Oxidation of 5′-dGMP and 5′-dAMP by a Platinum(IV) Complex. *Inorg. Chem.* **2012**, *51* (15), 8002−8013.
(35) Burda, J. V.; Runeberg, N.; Pyykko, P. Chemical bonds between noble metals and noble gases. Ab initio study of the neutral diatomics NiXe, PdXe and PtXe. *Chem. Phys. Lett.* **1998**, *288* (5−6), 635−641.
(36) Dyall, K. G. Relativistic effects on the bonding and properties of the hydrides of platinum. *J. Chem. Phys.* **1993**, *98* (12), 9678−9686.
(37) Burda, J. V.; Runeberg, N.; Pyykko, P. Chemical bond between noble metals and noble gases. Ab initio study of the neutral diatomics NiXe, PdXe, and PtXe. *Chem. Phys. Lett.* **1998**, *288*, 635−641.
(38) Burda, J. V.; Zeizinger, M.; Šponer, J.; Leszczynski, J. Hydration of cis- and trans-platin: A pseudopotential treatment in the frame of a G3-type theory for platinum complexes. *J. Chem. Phys.* **2000**, *113* (6), 2224−2232.
(39) Zeizinger, M.; Burda, J. V.; Šponer, J.; Kapsa, V.; Leszczynski, J. A Systematic ab Initio Study of the Hydration of Selected Palladium Square-Planar Complexes. A Comparison with Platinum Analogues. *J. Phys. Chem. A* **2001**, *105* (34), 8086−8092.
(40) Klamt, A.; Schuurmann, G. Cosmo - a New Approach to Dielectric Screening in Solvents with Explicit Expressions for the Screening Energy and Its Gradient. *J. Chem. Soc., Perkin Trans. 2* **1993**, No. 5, 799−805.
(41) Barone, V.; Cossi, M.; Tomasi, J. A new definition of cavities for the computation of solvation free energies by the polarizable continuum model. *J. Chem. Phys.* **1997**, *107* (8), 3210−3221.
(42) Zimmermann, T.; Leszczynski, J.; Burda, J. V. Activation of the cisplatin and transplatin complexes in solution with constant pH and concentration of chloride anions; quantum chemical study. *J. Mol. Model.* **2011**, *17*, 2385−2393.
(43) Zimmermann, T.; Burda, J. V. Charge-scaled cavities in polarizable continuum model: Determination of acid dissociation constants for platinum-amino acid complexes. *J. Chem. Phys.* **2009**, *131*, 135101.
(44) Michera, L.; Nekadova, M.; Burda, J. V. Reactions of cisplatin and glycine in solution with constant pH: a computational study. *Phys. Chem. Chem. Phys.* **2012**, *14*, 12571−12579.
(45) Pavelka, M.; Burda, J. V. Theoretical model of copper Cu(I)/Cu(II) mixed aqua-amine complexes. DFT and ab initio quantum chemical study. *Chem. Phys.* **2005**, *312*, 193−204.
(46) Pavelka, M.; Šimánek, M.; Šponer, J.; Burda, J. V. Copper Cation Interactions with Biologically Essential Types of Ligands: A Computational DFT Study. *J. Phys. Chem. A* **2006**, *110*, 4795−4809.
(47) Zimmermann, T.; Burda, J. V. Reaction of cisplatin with cysteine and methionine at constant pH. *Dalton Trans.* **2010**, *39*, 1295−1301.
(48) Zimmermann, T.; Chval, Z.; Burda, J. V. Cisplatin Interaction with Cysteine and Methionine in Aqueous Solution: Computational DFT/PCM Study. *J. Phys. Chem. B* **2009**, *113* (10), 3139−3150.
(49) Orozco, M.; Luque, F. J. Optimization of the cavity size for ab initio MST-SCRF calculations of monovalent ions. *Chem. Phys.* **1994**, *182*, 237−248.
(50) Wertz, D. H. Relationship between the Gas-Phase Entropies of Molecules and Their Entropies of Solvation in Water and 1-Octanol. *J. Am. Chem. Soc.* **1980**, *102*, 5316−5322.
(51) Cheng, M.-J.; Nielsen, R. J.; Goddard, W. A., III *Chem. Commun.* **2014**, *50*, 10994.
(52) Eyring, H. The Activated Complex in Chemical Reactions. *J. Chem. Phys.* **1935**, *3* (2), 107−115.
(53) Hesselmann, A.; Jansen, G.; Schütz, J. *J. Chem. Phys.* **2005**, *122*, 014103.
(54) Mitoraj, M.; Michalak, A.; Ziegler, T. A Combined Charge and Energy Decomposition Scheme for Bond Analysis. *J. Chem. Theory Comput.* **2009**, *5*, 962.
(55) Nalewajski, R. F.; Mrozek, J.; Michalak, A. Two-electron valence indices from the Kohn-Sham orbitals. *Int. J. Quantum Chem.* **1997**, *61* (3), 589−601.
(56) Sjoberg, P.; Murray, J. S.; Brinck, T.; Politzer, P. Average Local Ionization Energies on the Molecular Surfaces of Aromatic Systems as Guides to Chemical Reactivity. *Can. J. Chem.* **1990**, *68*, 1440.
(57) Bader, R. F. W. *Atoms in Molecules: A Quantum Theory*. Oxford Univ. Press: Oxford, U.K., 1990.
(58) Keith, T. A. *AIM All*, http://aim.tkgristmill.com: 2014.

DOI: 10.1021/acs.jpcb.7b01427
J. Phys. Chem. B 2017, 121, 4400−4413

(59) Glendening, E. D.; Badenhoop, K.; Ree, A. E.; Carpenter, J. E.; Bohmann, J. A.; Morales, M.; Weinhold, F. *NBO v 5.9 Program 5.0*; University of Wisconsin: Madison, WI, 2001.
(60) Eckert, F.; Klamt, A. *COSMOtherm, Version C3.0, Release 16.01*,, COSMOlogic GmbH & Co. KG: Leverkusen, Germany, 2015.: 2015.
(61) Song, B.; Sigel, H. Metal Ion-Coordinating Properties of 2′-Deoxyguanosine 5′-Monophosphate (dGMP2-)1 in Aqueous Solution. Quantification of Macrochelate Formation. *Inorg. Chem.* **1998**, *37* (8), 2066−2069.
(62) Knobloch, B.; Sigel, H.; Okruszek, A.; Sigel, R. K. O. Acid-base properties of the nucleic-acid model 2[prime or minute]-deoxyguanylyl(5[prime or minute][rightward arrow]3[prime or minute])-2[prime or minute]-deoxy-5[prime or minute]-guanylate, d(pGpG)3-, and of related guanine derivatives. *Org. Biomol. Chem.* **2006**, *4* (6), 1085−1090.
(63) Shishkin, O. V.; Gorb, L.; Leszczynski, J.; et al. Conformational Flexibility of Pyrimidine Ring in Nucleic Acid Bases. *J. Biomol. Struct. Dyn.* **2004**, *22*, 227−243.
(64) Okuno, Y. *Chem. - Eur. J.* **1997**, *3*, 212−218.
(65) Šebesta, F.; Burda, J. V. Study on Electronic Properties, Thermodynamic and Kinetic Parameters of the Selected Platinum(II) Derivatives Interacting With Guanine. *J. Inorg. Biochem.* **2016**, DOI: 10.1016/j.jinorgbio.2017.04.006.
(66) Basolo, F.; Pearson, R. G.; Emeleus, H. J.; Sharpe, A. G. Mechanisms of Substitution Reactions of Metal Complexes. *Adv. Inorg. Chem. Radiochem.* **1961**, *3*, 1−89.
(67) Beret, E. C.; Martinez, J. M.; Pappalardo, R. R.; Marcos, E. S.; Doltsinis, N. L.; Marx, D. Explaining Asymmetric Solvation of Pt(II) versus Pd(II) in Aqueous Solution Revealed by Ab Initio Molecular Dynamics Simulations. *J. Chem. Theory Comput.* **2008**, *4* (12), 2108−2121.
(68) Kroutil, O.; Predota, M.; Chval, Z. Pt···H Nonclassical Interaction in Water-Dissolved Pt(II) Complexes: Coaction of Electronic Effects with Solvent-Assisted Stabilization. *Inorg. Chem.* **2016**, *55*, 3252−3264.
(69) *Metallotherapeutic Drugs and Metal-Based Diagnostic Agents: The Use of Metals in Medicine* John Wiley & Sons, Ltd.: 2005.

DOI: 10.1021/acs.jpcb.7b01427
J. Phys. Chem. B 2017, 121, 4400−4413

Interactions of Ascorbic Acid with Satraplatin and Its Trans Analog JM576; *DFT Computational Study.*

Filip Šebesta, Jaroslav V. Burda*

Department of Chemical Physics and Optics, Faculty of Mathematics and Physics, Charles University, Ke Karlovu 3, 121 16 Prague 2, Czech Republic

*corresponding author: burda@karlov.mff.cuni.cz

Keywords: satraplatin, ascorbic acid, reduction, DFT

Abstract

Knowledge of mechanisms for reduction of Pt(IV) anticancer 'pro-drugs' is of great importance since the reduction process can be considered as a necessary step for their activation. Simultaneously, it can be used for 'tuning' of appropriate physico-chemical behavior, especially by a modification of axial ligands. Recently, the reduction of tetraplatin ($Pt(dach)Cl_4$) in the presence of deoxyguanosine monophosphate was broadly addressed by both experimental and computational tools.[1-5] Nevertheless, the assumed mechanism is not generally applicable, e.g. it cannot be used in the case of satraplatin (cis,trans,cis-$[PtCl_2(OAc)_2(cha)(NH_3)]$) and similar complexes with more bulky axial ligands. Therefore in this study we investigate the reduction of satraplatin by ascorbic acid where proton assisted electron transfer and outer sphere electron transfer mechanisms are employed. Also a presence of an additional base is discussed. All three protonation states of ascorbic acid are taken into consideration. An effective rate constant of $2.6 \cdot 10^{-3}$ $M^{-1} \cdot s^{-1}$ is obtained via the kinetic model for side reactions as described recently.[3] For the reduction of satraplatin by fully deprotonated ascorbic acid, changes of the electron density distribution are further analyses using NPA, QTAIM, and reaction electronic flux analysis. Both the electron transfer mechanisms are also explored for the satraplatin trans analog JM576 (trans,trans,trans-$[PtCl_2(OAc)_2(cha)(NH_3)]$). A resulting effective rate constant of $5.1 \cdot 10^{-2}$ $M^{-1} \cdot s^{-1}$ is compared with available experimental data.

Introduction

Satraplatin (JM216, cis,trans,cis-$[PtCl_2(OAc)_2(cha)(NH_3)]$, cha=cyclohexylamine) represents one of the best-known Pt(IV) complexes with promising anticancer activity. Recently, it has been employed in clinical trials, which

focused on its activity with refractory solid tumors.[6] In the past, its activity against small-cell lung cancer, ovarian cancer, squamous cancer of the cervix and castrate resistant prostate cancer was studied. However, the clinical tests were stopped within phase II and/or III of clinical tests,[7] due to an insignificant increase of survivors. Its advantage dwells in a small number of side effects; especially no neurotoxicity, nephrotoxicity and ototoxicity were observed after administration.

In common with other Pt(IV) complexes, satraplatin can be characterized by high kinetical inertness, i.e. it has a low ability to exchange its ligands.[8] Due to this property, the activation mechanism of Pt(IV) complexes has not still been elucidated completely. Nevertheless, early experiments with satraplatin showed[9] that this compound more probably primarily undergoes a reduction process. During this reaction, the axial ligands are released and Pt(II) analog is formed. Interestingly, another Pt(IV) complex was formed in the reaction course with an aqua ligand instead of a chloro ligand.[9] Nevertheless, even in this case it can be expected that the hydration reaction does not pass through the 'direct' reaction mechanism[8] but via another pathway, where an additional molecule probably serves as an interactive medium facilitating the replacement of the chloro ligand by water.

In the Pt(IV) complexes with a chloro or hydroxo ligands in axial positions one can consider a mechanism where the axial ligand is initially replaced by a reducing agent (for example by deoxyguanosine monophosphate (dGMP)) and subsequently both the axial ligands (the reducing agent and the chloro/hydroxo ligand) are released with the simultaneous reduction of the Pt(IV) complex.[1,2,4] However, the 'direct' substitution via S_{N2} mechanism is characterized by too high activation barriers. They are more than 32 kcal·mol^{-1} high in the case of tetraplatin (tetrachloro(D,L-trans)l,2-diaminocyclohexane-platinum(IV)) and dGMP as a reducing agent.[2,3,5] In fact, a preferred pathway for the initial substitution of one of the axial ligand is represented by the autocatalytic mechanism proposed by Basolo and Pearson.[10,11] In this case the substitution is catalyzed by the product state - Pt(II) complex, which is sandwitched by Pt(IV) complex from one side and by dGMP from the other. In the transition state the chloro/hydroxo ligand is transferred from Pt(IV) complex towards Pt(II) complex, so that the ligand has practically same distance to both Pt atoms. Simultaneously dGMP starts to coordinate to Pt(II) complex by N7 site of guanine. Passing the TS structure the other axial Cl/OH ligand is spontaneously released and Pt-N7 coordination completes. In this way synproportionation of the two Pt complexes occurs forming Pt(IV) complex with Pt-N7(dGMP) axial ligand. Nevertheless, for the exchange of larger ligands, like acetyl group, this mechanism is more or less improbable and some other mechanism must be search for.

Reducing agents, which are responsible for reduction of satraplatin, are still uncertain. The performed experiments provide only an indication in this question. It

was found by Ravera[12] that glutathione (GSH) does not reduced bis(carboxylato) Pt(IV) derivatives of picoplatin ($[PtCl_2(mpy)(NH_3)]$) in *in vitro* experiments. On the other hand, the fast reduction of Pt(IV) complexes was observed in the presence of metalloproteins – cytochrome c and hemoglobin – together with NADH.[13] This finding was also confirmed by work of Gibson and Wexselblatt[14] where reduction rates of bis(acetato) Pt(IV) complexes were measured in aqueous extracts of different cells. In the experiment, these extracts were separated into a low molar weight (LMW) and high molar weight (HMW) fractions. The HMW part contains metalloproteins while in the LMW fraction GSH and ascorbic acid (AA) were present. The reduction process was substantially slower for the LMW fraction. However, the reduction rates in unseparated extract correlated with concentration of GSH. Another study of Pichler[15] supports the fact that GSH has nearly no impact on the reduction of different bis(acetato) Pt(IV) complexes.

It was shown that AA is able to reduced JM216 *in vitro* experiments and the process is characterized by relatively high rate constants of 6.8 ± 0.8 (40°C, pH=7.1, 7.5 mM AA, and 0.75 mM platinum)[16] and 0.100 ± 0.003 (35°C, pH=7.1, and 5 mM AA).[17] Moreover, the reaction rate strongly depends on solvent pH. In ref. 17 authors even suppose that the form of AA, which is mainly responsible for the reduction, represents fully deprotonated conformer (AA^{2-})[18] despite the pK_a of AA are 4.1 and 11.6. MacKeage et al.[13] object that the used concentrations of AA are too high in comparison with cellular concentration (usually 50-150 μM), which causes a significant decrease of the reduction rate. The deprotonation of hydroxyl groups in the C2 and C3 positions also influence the magnitude of its reduction potential. This dependence was studied by Ball[19] already in 1937 when a change of the redox potential from 326 mV (at pH=1.05), via 136 mV (at pH=4.58) to 51 mV (at pH=7.24) was determined. These data nicely correlate with our previous CCSD(T) calculations[20] where we obtained the reduction potential of 346mV for fully protonated form (AAH_2) (pH<4.1), 41 mV for singly deprotonated (AAH^-), and -564 mV for fully deprotonated form (AA^{2-}) (pH>11.6). The reduction potential of (-53 ± 60) mV for satraplatin was determined experimentally.[16] Our estimated value is ca 8 mV at the CCSD(T)/6-31+G(d) level, which is within the error bars of the experimental value. According to this result, the reduction of JM216 by AAH^- should be a slightly endergonic process when a water molecule is considered as an acceptor of proton from AAH^-.

AA was also considered as a possible reducing agent for tetrachloro Pt(IV) complexes[21] ($Pt(dach)Cl_4$, $Pt(NH_3)_2Cl_4$) and trans derivatives of satraplatin[17] where the electron transfer is assumed to occur via a chloride bridge. The rate constants for the trans-derivatives of satraplatin (JM394 and JM576) are by ca three orders of magnitude higher[17] than for satraplatin, i.e. 20 and 50 $M^{-1}\cdot s^{-1}$ (at pH=7.12, 5mM AA, and 25°C), respectively. For tetrachloro Pt(IV) complexes the reaction rate is similar

at pH=7.4 and 5mM AA. The reduction of tetraplatin by AAH^- was *in silico* investigated by Ariafard[22] et al. They concluded that the reduction occurs via the 'base-assisted outer sphere' electron transfer characterized by the activation barrier of at most 12.4 kcal·mol^{-1}. In this mechanism a base (fully deprotonated AA) accepts proton from AAH^- during its oxidation and in this way facilitates the reduction process.

In this study, we focus on the reduction of satraplatin by AA considering all three protonation states (AAH_2, AAH^-, AA^{2-}). It means that both proton-assisted and outer sphere electron transfer mechanisms are explored. Further, the reduction of another derivative of satraplatin - JM576 (trans,trans,trans-[$PtCl_2(OAc)_2(cha)(NH_3)$]) is also investigated. In the last section changes in the electron density distribution during the reduction process are discussed in detail.

Computational details

Optimizations and single-point (SP) energy calculations were performed using Gaussian 09 program. The considered structures were optimized at the DFT level with hybrid B3LYP functional[23] and double-zeta 6-31+G(d) basis set. Core electrons of Pt atom were described using Stuttgart-Dresden pseudopotentials (MWB60) and the basis set of pseudoorbitals was extended by diffuse (α_s(Pt)=0.0075, α_p(Pt)=0.013, α_d(Pt)=0.025) and polarization functions (α_f(Pt)=0.9593) in order to keep the whole basis set balanced. Hereinafter, this basis set is denoted as B1. Grimme's dispersion corrections GD3BJ[24,25] were considered in the calculations and for simulation of water solution the C-PCM/Klamt solvation model[26] was used. Frequency analyses were carried out at the same level.

Electronic energies, wave functions, and electron densities for further analyses were obtained at the B3LYP-GD3BJ/6-311++G(2df,2pd)/MWB60 level. In this case, the original pseudo-orbitals of the Pt atom were extended by spd-diffuse functions and by a set of three polarization functions - α_{f1}(Pt)=1.4193, α_{f2}(Pt)=0.4662, α_g(Pt)=1.2077. This basis is labelled as B2 in the text. In accord with our previous calculations the IEFPCM/scaled-UAKS solvation model is employed at the SP level. The scaled-UAKS approach[27] for cavity construction differs from the standard UAKS model[28] by the fact that the radii of spheres around atoms (resp. groups) are reduced according to their actual (NPA) partial charges instead of their formal charges. The scaling of sphere radii is in our study applied only for Cl and O atoms (groups) in consistency with the original UAKS model and the actual partial charges were determined at the B3LYP-GD3BJ/6-31++G(d,p)/MWB60/IEF-PCM/UAKS level using Natural Population Analysis (NPA). All the details can be found in ref. 27.

Since we considered the reaction in solvent environment, entropic contributions to Gibbs energy, which were determined on the basis of partition

functions for ideal gas, needed to be reduced unless exaggerated (de)association energies are obtained. According to studies of Wertz[29] and Goddard[30] the loss of entropy corresponding to translational and rotational degrees of freedom passing from gas phase to liquid represents 46%. The resulting entropy *S* is given by relation:

$$S = S_{gas}^{vib} + 0.54 \cdot \left(S_{gas}^{trans} + S_{gas}^{rot} - 14.3\right) + 8.0\,,$$

where S_{gas}^{trans}, S_{gas}^{rot}, and S_{gas}^{vib} are contributions from translational, rotational, and vibrational degrees of freedom and factors of -14.3 and 8.0 cal·mol^{-1}·K^{-1} correspond to the change of entropy caused by the initial compression of ideal gas from 1 atm to concentration of 55 mol·dm^{-3} and the final dilution to concentration of 1 mol·dm^{-3}. In the text, G(w) stands for Gibbs energy corrected according to Wertz's suggestions.

Changes in the electron density distribution during the examined reactions were studied using NPA and Bader's Atom in Molecules (QTAIM) approach using electron densities obtained at the SP level. The ETS-NOCV (Extended Transition State combined with Natural Orbitals for Chemical Valence) method as coded in ADF2014.04 program was employed for analyses of the deformation densities and interaction energy decompositions using scalar ZORA (zeroth order relativistic approximation) hamiltonian and the B3LYP-GD3/TZ2P level (with 4d frozen core for Pt) .

Results and discussion

Important characteristics for compounds involved in redox reactions represent the reduction potentials as a measure of thermodynamic difficulty to reduce or oxidize these molecules. The more positive the potential is, the greater the species' affinity for electrons and tendency to be reduced is. The determination of this quantity was addressed in our recent paper[20] where also other approaches are mentioned. In **Table 1**, a comparison of the current model values from ref. 20 of reduction potentials is provided for satraplatin and ascorbic acid. Moreover, the reduction potential for JM576 is included, which is by 330 mV higher than potential of satraplatin. This difference is in fairly good accord with experimental results for reduction potentials of Pt(IV) complexes since a release of acetato ligands is more demanding than a release of chloride anions within the reduction process. As it was also shown previously,[20] the B3LYP functional overestimates absolute values of the redox potential by several hundreds mV. Nevertheless, relative differences among various Pt(IV) complexes are quite reliable. For the currently used method the shift represents approximately 600 mV. Also, the difference of 115 mV between the estimated reduction potential of JM216 and AA very well corresponds to the experimentally obtained results. Since the magnitude of the reduction potential of AA strongly depends on solvent pH, analyses of the results must be done with care. Fortunately, it follows from our results that comparing to experimental data we

managed to describe this pH dependency fairly well, too. Such behavior is tightly connected with occurrence of individual protonation states of AA in solution. Since the concentrations of [AAH_2] and [AAH^-] are linked via acid dissociation constant K_{a1} and concentrations [AAH^-] and [AA^{2-}] via acid dissociation constant K_{a2}, then the molar fractions of the protonated forms can be calculated as:

$$[AAH_2] = \frac{[H^+]^2}{X}\,, \qquad [AAH^-] = \frac{K_{a1}[H^+]}{X}\,, \qquad [AA^{2-}] = \frac{K_{a1}K_{a2}}{X}\,,$$

$$X = [H^+]^2 + K_{a1}[H^+] + K_{a1}K_{a2}\,.$$

Since AA the values of pK_{a1} and pK_{a2} are 4.1 and 11.6, respectively, in neutral solutions (pH =7), the relative concentrations of [AAH_2], [AAH^-], and [AA^{2-}] are 0.126%, 99.9% and 0.0025%, respectively. Though the concentration of AA^{2-} is negligible, the presence of AA^{2-} substantially influence rate of the reduction of JM216 as it is shown below. Further, the calculations show that the first deprotonation of AA occurs in the O3 position and the corresponding optimal structure lies by about 8 kcal·mol^{-1} lower than corresponding structure with deprotonated oxygen in the O2 position, which is in agreement with experimental measurements.

Since satraplatin can interact with all three forms of AA, the reduction process must be described from the perspective of side reactions with a fast acido-base equilibrium condition in order to get results comparable with experimental studies of Lemma[17] and Dong.[21] In this case an effective rate constant k^{eff} can be determined as a weighted average of calculated rate constants k_1, k_2, and k_3 for the individual branches (side reactions) where the weights are given by molar fractions of the AA forms:

$$\frac{d[S]}{dt} = -\mathrm{k}_1[\mathrm{S}][AAH_2] - \mathrm{k}_2[\mathrm{S}]\,[AAH^-] - \mathrm{k}_3[\mathrm{S}][AA^{2-}]$$

$$= -\frac{k_1[H^+]^2 + k_2K_{a1}[H^+] + k_3K_{a1}K_{a2}}{[H^+]^2 + K_{a1}[H^+] + K_{a1}K_{a2}}[S][AA^{tot}] = -k^{eff}[S][AA^{tot}]\,,$$

where [S] represents concentration of satraplatin. According to this relation it makes sense to consider the rate constants k_1 or k_3 only if they are substantially higher (by several orders of magnitude) than k_2 due to dominant abundance of AAH^- protonation state at neutral pH, In the opposite case, the effective rate constant can be identified with k_2.

In our calculations we take into account all three protonation states of AA and thus the proton-assisted and outer sphere electron transfers are considered as possible mechanisms for the reduction of satraplatin. As the oxidized AA possesses keto groups in the C2 and C3 positions, the corresponding hydrogens must be

released during the reaction (cf. **Scheme 1**). In the proton-assisted electron transfer mechanism, proton H2 is moved to one of the acetato ligands inducing the electron transfer from AA moiety to the Pt(IV) complex. This mechanism is considered in the AAH_2 and AAH^- reaction branches where the corresponding proton is present. In the case of AAH_2 branch, an additional water molecule is included into the examined system serving as an acceptor of the other AA proton. Simultaneously, the water molecule helps to stabilize an arrangement of the system. In the reactants, a mutual orientation of satraplatin and AA is enforced by the hydrogen bonding between (protonated) O2 and/or O3 with a proximate acetate and possibly also a chloro ligand. If one (or both) of these oxygens is deprotonated H-bonding to amino group(s) of JM216 is established. As it can be expected, these H-bonds are particularly strong due to electrostatic enhancement. This can be demonstrated by association energy between JM216 and AA^{2-}, which is ca 15.6 kcal·mol^{-1} (cf. **Table 3**) or by electron density of 0.05 e/a.u.^{3} in the H-bond critical points (BCPs).

The obtained TS structures are displayed in **Fig. 1** and they can be characterized by a stretching vibrational mode with an imaginary frequency, which corresponds to elongation of the Pt-O(Ac) bonds and shortening of the O2-C2 and O3-C3 bonds in the AA moiety and vice versa. In the proton-assisted variant, the proton transfer between AA and an acetato ligand of JM216 is visible within this mode, too. For the outer sphere electron transfer mechanism, symmetrical elongation of both the Pt-O(Ac) bonds of ca 0.4 Å in the TS structure relative to the reactants is noticeable, while in the proton-assisted mechanism elongation of the Pt-O(Ac) distances is asymmetric due to the fact that one of the acetato ligands is simultaneously a proton acceptor, which makes this Pt-O(Ac) bond visibly longer, cf **Table 2**.

In the product state, both the acetato ligands are released and associated via H-bonds to the amino groups of the Pt(II) complex. If the acetic acid is protonated (as a result of the proton transfer from AA) the H-bond to O2 oxygen of AA stabilizes the systems and O3 oxygen is acceptor of one of the hydrogens from the satraplatin amino-group. Generally, the oxidized AA in the product supermolecule is in a very similar position to platinum complex as in the reactant one. The oxidation of ascorbic acid is connected with rearrangement of double bonds in the AA moiety, which is confirmed by elongation of the C2-C3 bond (from ca 1.37 to 1.53 Å in dependence on the original protonation state of AA) and shortening of the C2-O2 and C3-O3 bonds (from ca 1.34 to 1.21 Å).

The energy characteristics of the reduction reaction are strongly dependent on pH of the solution. For fully protonated AAH_2, e.g. in acidic environment, $\Delta G(W)$ = -10.8 kcal·mol^{-1}, when the transferred protons are located on the released acetates after the reduction process, while in basic solutions, for fully deprotonated AA^{2-} form, $\Delta G(W)$ = -28.1 kcal·mol^{-1}. The difference is connected with the protonation of

the AA moiety, as it follows from the determined redox potentials for ascorbic acid discussed in our previous study[20] or from other (experimental) works.[19] The energy relation can be substantially influenced by a choice of proton acceptors, namely by pK_a of the proton-accepting groups. In the case of fully deprotonated AA^{2-}, only the electron transfer occurs. Moreover, the negatively charged AA^{2-} anion is not very stable (lies relatively high in the energy). In the remaining two cases, AAH^- and AAH_2, the protons from AA are assumed to be accepted by acetic acid in final products, i.e. from the thermodynamic perspective, a proton transfer from water to the acetate is additionally supposed in the AAH_2 branch. Nevertheless, pKa of acetic acid is 4.76, which means that it will not be very willing to accept a proton in neutral solution (pH=7). Therefore, it can be assumed that this proton will be better stabilized by another more suitable site in a real (biological) solution.

Due to the well-known high kinetic inertness of Pt(IV) complexes, the most important parameters represent rate constants. Similarly to reaction energies, activation barriers reach a very similar height of 28.2 and 28.8 $kcal \cdot mol^{-1}$ in branches with AAH_2 and AAH^-, respectively. This would result in a very slow reaction when intracellular concentration of AA is taken into account. In the branch with AA^{2-}, the activation barrier is noticeably lower reaching only a half height in comparison with the previous cases (cf. **Table 4**). Thus, the rate constant in the AA^{2-} branch is 23 $M^{-1} \cdot s^{-1}$, i.e. by ca ten orders of magnitude higher than in the AAH_2 and AAH^- cases. This easily overweighs the very low (by ca five orders of magnitude) concentration of this protonation state. This is exactly a situation when the kinetic model for side reactions must be applied. Using the relative concentrations of each AA protonation state, the calculated effective rate constant can be estimated to $2.6 \cdot 10^{-3}$ $M^{-1} \cdot s^{-1}$. This value is in quite good agreement with measured value by Lemma et al., which is $k_{exp} = 5.1 \cdot 10^{-2}$ $M^{-1} \cdot s^{-1}$ at pH=7.12, T=298K and 5mM AA. For mM concentrations of ascorbic acid the theoretically determined half-life represents 4.4 days. As to the effective reaction Gibbs free energy, averaging over molar fraction leads to practically the identical energy as a result of the dominant protonation state (AAH^-) since the energy differences among individual AA forms varies much less than the corresponding rate constants.

Base-assisted electron transfer

In order to increase occurrence of fully deprotonated AA^{2-} form, the negatively charge cysteine (with deprotonated thiol group) was included into the supermolecular model. The pK_a value of SH group is 8.37, which is relatively close to neutral pH. Based on the Henderson-Hasselbalch equation, about 4% of Cys molecules will be in desired protonation state at pH=7. It can be assumed that glutathione (L-γ-glutamyl-L-cysteinyl-glycine, GSH) is relatively abundant in cellular environment so that the concentrations 0.5 - 10 mM and pKa(SH) of 9.12

(9.65) leads to roughly μM concentrations of the deprotonated GS^- form. In this case, the so-called 'base-assisted electron transfer' mechanism is considered. An optimal position of cysteine within the JM216:AA:Cys supermolecule is stabilized by several H-bonds as can be seen in **Fig.2**. The most important H-bond (in our model) is interaction between the thiol group and the O2 site of AA, which is involved in the crucial proton transfer responsible for possible increasing of the trace concentration of AA^{2-} and in this way for decreasing of the activation barrier of JM216…AAH^- supermolecule from 29.4 to 20.5 kcal·mol^{-1} (cf. **Table 4**). Including the Cys molecule as an acceptor of the proton leads to a decrease of the reaction Gibbs energy from -9.1 kcal·mol^{-1} to -13.2 kcal·mol^{-1} (cf **Table 3**) and lowering of the activation barrier so that a rate constant is of the same order of magnitude as the effective rate constant of the JM216:AA system without the Cys molecule. In this way, the problem of too low concentration of AA^{2-} is partially avoided (as discussed above) and the calculated rate is twice higher ($k = 5.6 \cdot 10^{-3}$ $M^{-1} \cdot s^{-1}$).Here, it is important that a base, which is ready to accept a proton, is present in the surroundings of the JM216:AA system. The total charge of the whole system is 2- similarly to the reaction branch with AA^{2-}.

Satraplatin modifications

In addition we modified JM216 in the AAH^- and AA^{2-} branches replacing one of the acetato ligands by chloroacetate or phenylacetate (we denote the structures JM216-Cl and JM216-Phe, cf **Fig. 3**). Since a proton acceptor is transferred to this derivative of acetato ligand in the AAH^- branch, the pK_a of phenylacetic (4.31) and chloroacetic acid (2.86) is a decisive factor for reaction Gibbs free energies. This energy is increased by 3.0 kcal·mol^{-1} for JM216-Phe and by 7.6 kcal·mol^{-1} for JM216-Cl compared to original JM216. On the contrary, when the AA^{2-} is considered, the reaction Gibbs free energy is lower by 2.2 (JM216-Phe) and 2.8 kcal·mol^{-1} (JM216-Cl). The explanation insists in the fact that when proton(s) need to be transferred during the reduction process (systems AAH_2 and AAH^-), modified acetic acid is less willing to accept them. On the contrary, when AA^{2-} is considered then electronegative chloro-ligand enables outer shell electron transfer at least partially due to its higher electron affinity.. Therefore the reduction is facilitated despite the fact that the ρ(BCP) of the Pt-O bonds increases in row: JM216, JM216-Cl and JM216-Phe. If we focus on the kinetics, the determined effective rate constants for JM216-Cl ($9.2 \cdot 10^{-3}$ $M^{-1} \cdot s^{-1}$) is three times higher than for satraplatin, and thus chlorination of acetato ligands should make the reduction faster. On the contrary, the value of $k_{eff} = 1.9 \cdot 10^{-5}$ $M^{-1} \cdot s^{-1}$ for JM216-Phe is by two orders lower (cf. **Table 4**).

JM576 - trans analog of satraplatin

Besides JM216, the reduction of JM576 in the presence of AA is also investigated. According to experimental results a release of chloro ligands is assumed in the reaction course.[17] In accord with the previous part, the proton-assisted and outer sphere electron transfer mechanisms are considered for this complex, too. However, only its interactions with AAH^- and AA^{2-} are evaluated. In order to stabilize the chosen structures, a water molecule is added into the systems with AAH^- and AA^{2-}. The water molecule helps to stabilize one of the leaving chloro ligands and in the case of the AAH^- reaction branch it also serves as an acceptor of the released proton, which further strengthens its interaction with the leaving chloride (in the TS the H-bond length is 1.97 Å). The discussed TS structures are depicted in **Fig. 4**. An elongation of the Pt-Cl bonds represents 0.45 Å (0.54 Å) for the chloro ligand interacting with the water molecule in system with AA^{2-} (AAH^-) (**Fig. 4a,b**) and 0.36 Å (0.38 Å) for the second chloro ligand. After the TS point, the second released chloro ligand is associated to the ammine ligand in the system with AAH^- and to proton of the hydroxyl H6-O6-group in the case of the AA^{2-} branch (for the notation see scheme 1) This leads to breaking of the intramolecular H6…O3 hydrogen bond within the AA^{2-} moiety. All other hydrogen bonds remain preserved in the structures during the whole reaction course.

As to thermodynamics, the reaction electronic energy is slightly lower in the AA^{2-} branch for the trans analog compared to JM216 which is associated with lower binding energy of the chloro ligands in JM576 than BE of the acetato ligands in JM216. The same conclusion follows also from AIM analysis of BCP's since electron density in BCP of Pt-O(acet, JM216) bond is about one fifth greater than ρ(BCP) of Pt-Cl bonds in JM576 (0.1104 $e \cdot au^{-3}$ and 0.0920 $e \cdot au^{-3}$, respectively). Nevertheless, entropic contributions turns the preference and the reaction Gibbs free energy of - 25.7 $kcal \cdot mol^{-1}$ for JM576 is by about 2.4 $kcal \cdot mol^{-1}$ less exergonic. In the system with AAH^-, its corresponding value is 7.5 $kcal \cdot mol^{-1}$ supposing that the proton from AAH^- is transferred to the water molecule. Nevertheless, considering isolated acetic acid as the final proton acceptor, the reaction Gibbs free energy represents -7.7 $kcal \cdot mol^{-1}$, which approaches the value of proton-assisted electron transfer mechanisms of satraplatin. The activation barriers of JM576 with AA are relatively lower than for the corresponding pathways of JM216. Therefore, comparing with the analogous systems of JM216, the rate constants are approximately twenty times and five times higher in AA^{2-} and AAH^- branches, respectively (cf. **Table 4**).

Determining the effective rate constant on the basis of the kinetic model for side reactions, we obtained for the JM576 complex value of $5.1 \cdot 10^{-2}$ $M^{-1} \cdot s^{-1}$, which is by one order of magnitude higher in comparison with satraplatin due to even lower activation barrier in the AA^{2-} branch (ca 12.9 $kcal \cdot mol^{-1}$). However, the

experimentally determined rate constant for this compound is still about three orders higher (21.8 $M^{-1} \cdot s^{-1}$). This represents ca 4 $kcal \cdot mol^{-1}$ lower activation barrier, which seems to be above accuracy of method used and some other TS should be searched.

Electron density distribution

The most distinct changes in electron density distribution occur in the proximity of Pt atom and in the vicinity of C2 and C3 carbons in the AA moiety. During the reduction of satraplatin the partial charge on Pt(IV) nucleus decreases from 1.25 e to 0.56 e. For JM576 analog the decrease is a little bit lower, starting from similar Pt(IV) value of 1.24 e but reducing to the final partial charge of 0.77 e on the corresponding Pt(II) center. This is caused by the release of the axial chloro ligands, which are more diffuse and thus they donate more electron density to Pt atom in comparison with acetato ligands remaining coordinated in the reduced form of JM576. As a consequence of transferred electrons, partial charges on equatorial ligands also slightly decrease and the change of the total charge in the equatorial plane Pt-N(cha)-N(ammine)-Cl-Cl of JM216 varies from -1.0 to -1.1 e. As to AA moiety, the largest increase of the partial charge (by 0.4 e) is observed on the C2 atom. Generally, in this region (C3, O2, and O3 atoms) the increase from 0.15 e to 0.35 e can be noticed, demonstrating that the oxidation of AA is connected mainly with a rearrangement in this part of AA. The same conclusion follows from an increase of the electronic density in BCPs on the C2-O2 and C3-O3 bonds by 0.06-0.13 $e \cdot au^{-3}$. Consistently, the electron density in the BCP of the C2-C3 bond decreases by 0.05-0.08 $e \cdot au^{-3}$ The lowest change corresponds to the AA^{2-} branch while the highest one to AAH_2 protonation form.

In TS structures, the partial charge of the Pt atom in JM216 decreases to 1.04 e in comparison with smaller reduction to 1.16 e in JM576 for in the AA^{2-} branch. Nevertheless, the change of electron density in the equatorial plane Pt-N(cha)-N(ammine)-Cl-Cl of JM216 almost reaches a half of the total charge shift in this group of atoms (0.5 e, cf last line in **Table 5**). Despite similar changes can be noticed also in the AA^{2-} moiety the charge of AAH^- in the TS structure remains nearly unchanged, which is a consequence of the proton transfer to acetate that compensates the decrease of the electron density. In fact, the proton transfer is almost completed in the TS structures which is obvious from comparison of the H-O(Ac) bond length in the TS structure (1.037 Å) and the product (0.983 Å). This corresponds with Hammond's principle since the reaction is exothermic.

The changes of the electron density along the intrinsic reaction coordinate (IRC) were analyzed for the outer sphere electron transfer (in the system consisting of JM216 and AA^{2-}). For different types of reactions[31-34] it was shown that main electronic changes occur in the so-called transition state region characterized by inflection points (α and γ) bracketing the TS structure (β-point).[35] At the α- and γ-

points, the first derivative of the potential energy with respect to the reaction coordinate (define as the reaction force) has extremes. Setting the TS β-point to the origin of IRC the inflection points are α = -2.7 Å·amu$^{1/2}$ and γ = 2.8 Å·amu$^{1/2}$, as it can be seen from **Fig. 5**. If we concentrate on changes of the electronic density in BCPs, it is evident that they occur mainly in the area of this region as it is depicted in **Fig. 6**. This is valid not only for breaking of Pt-O(Ac) bonds but also for changes in C2-C3, C2-O2, and C3-O3 bond where character is altered from the enol to keto form. Similar conclusions can be drawn from Mrozek-Nalewajski bond indexes or the partial charge analysis (not shown here).

To appraise spontaneity of an electron density rearrangement, the electronic chemical potential μ can be approximated based on HOMO, LUMO eigenvalues.

$$\mu = -\frac{1}{2}(IP + EA) \approx \frac{1}{2}(E(HOMO) + E(LUMO)),$$

A rearrangement of the electron density is spontaneous when the magnitude of chemical potential decreases along the IRC. For this purpose, a quantity called reaction elecronic flux J (REF)[34]was introduced according to the definition:

$$J(\xi) = -\frac{\partial \mu}{\partial \xi},$$

where $\partial\xi$ denotes a change in a reaction coordinate. When the calculated REF is positive, the changes in electron density distribution are spontaneous. The course of REF was explored in the outer sphere electron transfer from AA^{2-} to JM216 accompanied by realese of the axial acetato ligands. The flux is positive in the reactant region and monotonously decreasing, finally becoming negative shortly beyond TS at ξ = 1.1 Å·amu$^{1/2}$. It means that the initial electron transfer represents a spontaneous process. The negative area is connected with non-spontaneous Pt-O(Ac) bond breaking with the lowest value just before γ-point. Finally, REF becomes positive at ξ = 3.7 Å·amu$^{1/2}$ on IRC (cf. **Fig. 7**), which should correspond with the point where the bonds to the axial ligands cease to exist.

The ETS-NOCV analysis[36,37] was also performed for this IRC. The decomposition of the interaction energy from the reactant perspective (the system is divided into two fragments – satraplatin and AA^{2-}) into the electrostatic, Pauli repulsion and orbital term is drawn in **Fig. 8**. The bonding energy for the reactant is much higher than the association energies presented in **Table 3** due to the fact that this analysis is performed in gas phase and AA^{2-} moiety is negatively charged (-2 e). The total bonding energy lowers from -96 kcal·mol^{-1} for the reactant to -192 kcal·mol^{-1} for the product. As it can be expected, the main contribution represents the orbital interaction, since we consider outer sphere electron transfer and thus the transfer from originally occupied orbitals of the AA^{2-} fragment to virtual orbitals on JM216 is clearly visible there (cf. **Fig. 8**). This shift of the electron density can be demonstrated in the terms of the deformation density, which can be further

decomposed into the natural orbitals for chemical valence (NOCV).[38] The lowest orbital pair obtained after diagonalization of the deformation density matrix for the TS structure is depicted in **Fig. 9** and it corresponds to the regarded electron transfer from the AA moiety (decreasing density - red region) to the Pt complex (increasing density - blue region). As to eigenvalue it represents more than 80% of the total orbital interaction. The steric interaction, a sum of the electrostatic interaction and the Pauli repulsion, increases from -27 kcal·mol^{-1} to 25 kcal·mol^{-1} in the course of the reaction, which is connected with the fact that AA^{2-} is located in an ideal position in the reactant part of IRC, which becomes subsequently less and less 'optimal' .

Conclusion

Two different reaction mechanisms – proton-assisted and outer sphere electron transfer – were investigated for the reduction reaction of satraplatin with ascorbic acid. As the ascorbic acid occurs in the solution in three different protonation forms, the kinetic model for side reactions was employed. This model provides the effective rate constants in fairly good agreement with experimental results. Since a low activation barrier was found in the outer sphere mechanism of AA^{2-}, whose concentration is very low at neutral pH, it was also demonstrated that the reaction rate increases in presence of an appropriate base in the solution. The rearrangement of electron density distribution during the reduction in the AA^{2-} branch represents a spontaneous process except a part of IRC linked with the Pt-O(Ac) bond-breaking process.

The reduction of the trans analog of satraplatin, compound JM576, via 'proton-assisted' and the outer sphere electron mechanism was also employed. The effective rate constant is by about one order of magnitude higher, but in comparison with experimental data its magnitude is still too low, so it is not still certain whether another reaction mechanism should not be considered.

Acknowledgement:

Authors are grateful to Grant Agency of Czech Republic project No 16-06240S for supporting this study. Additional support (for FŠ) was obtained from the Grant Agency of Charles University. No.1145016. Access to computing facilities owned by parties and projects contributing to the National Grid Infrastructure MetaCentrum, provided under the program ‘Projects of Large Infrastructure for Research, Development, and Innovations’ (LM2010005) is highly appreciated.

References:

(1) Choi, S.; Vastag, L.; Leung, C.-H.; Beard, A. M.; Knowles, D. E.; Larrabee, J. A. *Inorg. Chem.* **2006**, *45*, 10108.

(2) Šebesta, F.; Burda, J. V. *Chem. Eur. J.* **2016**, *22*, 1037.

(3) Šebesta, F.; Burda, J. V. *The Journal of Physical Chemistry B* **2017**, *121*, 4400.

(4) Ariafard, A.; Tabatabaie, E. S.; Aghmasheh, S.; Najaflo, S.; Yates, B. F. *Inorganic Chemistry* **2012**, *51*, 8002.

(5) Ariafard, A.; Ghohe, N. M.; Abbasi, K. K.; Canty, A. J.; Yates, B. F. *Inorganic Chemistry* **2013**, *52*, 707.

(6) Akshintala, S.; Marcus, L.; Warren, K. E.; Murphy, R. F.; Sissung, T. M.; Srivastava, A.; Goodspeed, W. J.; Goodwin, A.; Brewer, C. C.; Zalewski, C.; King, K. A.; Kim, A.; Figg, W. D.; Widemann, B. C. *Pediatric Blood & Cancer* **2015**, *62*, 603.

(7) Bhargava, A.; Vaishampayan, U. N. *Expert Opinion on Investigational Drugs* **2009**, *18*, 1787.

(8) Bradáč, O.; Zimmermann, T.; Burda, J. V. *J. Mol. Model.* **2013**, *19*, 1669.

(9) Raynaud, F. I.; Mistry, P.; Donaghue, A.; Poon, G. K.; Kelland, L. R.; Barnard, C. F. J.; Murrer, B. A.; Harrap, K. R. *Cancer Chemotherapy and Pharmacology* **1996**, *38*, 155.

(10) Basolo, F.; Pearson, R. G. In *Advances in Inorganic Chemistry and Radiochemistry*; Emeleus, H. J., Sharpe, A. G., Eds.; Academic Press: 1961; Vol. Volume 3, p 1.

(11) Basolo, F.; Messing, A. F.; Wilks, P. H.; Wilkins, R. G.; Pearson, R. G. *Journal of Inorganic and Nuclear Chemistry* **1958**, *8*, 203.

(12) Ravera, M.; Gabano, E.; Zanellato, I.; Bonarrigo, I.; Escribano, E.; Moreno, V.; Font-Bardia, M.; Calvet, T.; Osella, D. *Dalton Transactions* **2012**, *41*, 3313.

(13) Carr, J.; Tingle, M.; McKeage, M. *Cancer Chemotherapy and Pharmacology* **2006**, *57*, 483.

(14) Wexselblatt, E.; Gibson, D. *Journal of Inorganic Biochemistry* **2012**, *117*, 220.

(15) Pichler, V.; Goschl, S.; Schreiber-Brynzak, E.; Jakupec, M. A.; Galanski, M.; Keppler, B. K. *Metallomics* **2015**, *7*, 1078.

(16) Choi, S.; Filotto, C.; Bisanzo, M.; Delaney, S.; Lagasee, D.; Whitworth, J. L.; Jusko, A.; Li, C.; Wood, N. A.; Willingham, J.; Schwenker, A.; Spaulding, K. *Inorg. Chem.* **1998**, *37*, 2500.

(17) Lemma, K.; Sargeson, A. M.; Elding, L. I. *Journal of the Chemical Society, Dalton Transactions* **2000**, 1167.

(18) In *The Merck Index - An Encyclopedia of Chemicals, Drugs, and Biologicals*; O'Neil, M. J., Ed.; Merck and Co., Inc.: Whitehouse Station, NJ, 2006, p 136.

(19) Ball, E. G. *Journal of Biological Chemistry* **1937**, *118*, 219.

(20) Šebesta, F.; Baxová, K.; Burda, J. V. *Inorganic Chemistry*, submitted.

(21) Dong, J.; Ren, Y.; Huo, S.; Shen, S.; Xu, J.; Tian, H.; Shi, T. *Dalton Transactions* **2016**, *45*, 11326.

(22) Ejehi, Z.; Ariafard, A. *Chemical Communications* **2017**, *53*, 1413.

(23) Becke, A. D. *The Journal of Chemical Physics* **1993**, *98*, 5648.

(24) Grimme, S.; Antony, J.; Ehrlich, S.; Krieg, H. *The Journal of Chemical Physics* **2010**, *132*, 154104.
(25) Grimme, S.; Ehrlich, S.; Goerigk, L. *J. Comp. Chem.* **2011**, *32*, 1456.
(26) Klamt, A.; Schuurmann, G. *J Chem. Soc.-Perkin Transactions 2* **1993**, 799.
(27) Zimmermann, T.; Burda, J. V. *J. Chem. Phys.* **2009**, *131*, 135101.
(28) Barone, V.; Cossi, M.; Tomasi, J. *J. Chem. Phys.* **1997**, *107*, 3210.
(29) Wertz, D. H. *J. Am.chem. Soc.* **1980**, *102*, 5316.
(30) Cheng, M.-J.; Nielsen, R. J.; Goddard Iii, W. A. *Chemical Communications* **2014**, *50*, 10994.
(31) Inostroza-Rivera, R.; Herrera, B.; Toro-Labbe, A. *Physical Chemistry Chemical Physics* **2014**, *16*, 14489.
(32) Cortés-Arriagada, D.; Gutiérrez-Oliva, S.; Herrera, B.; Soto, K.; Toro-Labbé, A. *The Journal of Chemical Physics* **2014**, *141*, 134701.
(33) Giri, S.; Inostroza-Rivera, R.; Herrera, B.; Núñez, A. S.; Lund, F.; Toro-Labbé, A. *Journal of Molecular Modeling* **2014**, *20*, 2353.
(34) Flores-Morales, P.; Gutiérrez-Oliva, S.; Silva, E.; Toro-Labbé, A. *Journal of Molecular Structure: THEOCHEM* **2010**, *943*, 121.
(35) Toro-Labbé, A. *J. Phys. Chem. A* **1999**, *103*, 4398.
(36) Mitoraj, M.; Michalak, A.; Ziegler, T. *J. Chem. Theor. Comput.* **2009**, *5*, 962.
(37) Mitoraj, M. P.; Parafiniuk, M.; Srebro, M.; Handzlik, M.; Buczek, A.; Michalak, A. *J. Mol. Model.* **2011**, *17*, 2337.
(38) Michalak, A.; Mitoraj, M.; Ziegler, T. *J. Phys. Chem. A* **2008**, *112*, 1933.

Tables:

Table 1: Reduction potentials (in mV) for satraplatin, its trans-configuration JM576 and ascorbic acid.

	Current model	B3LYP-GD3BJ+W[c]	CCSD(T)	CCSD(T)+W[c]	Experiment
JM216	552	476	276	8	-53±60[a]
JM576	882				
AAH_2	976	853	361	346	326[b]
AAH^-	668	491	48	41	51 [b]
AA^{2-}	-170	-207	-549	-546	

a) Ref. 16, b) Ref. 19, c) W denotes inclusion of Wertz's corrections

Table 2: Significant bond lengths (in Å) in the optimized reactants, TS and products structures.

	AAH_2			AAH^-			AA^{2-}			AAH^- + Cys		
	Re	TS	Pr	Re	TS	Pr	Re	TS	Pr	Re	TS	Pr
Pt-O(Ac)	2.057	2.719	4.134	2.036	2.545	4.107	2.032	2.452	3.984	2.039	2.456	4.071
Pt-O(Ac')	2.024	2.369	3.538	2.030	2.322	4.107	2.032	2.447	3.902	2.030	2.410	3.592
Pt – Cl	2.375	2.383	2.372	2.388	2.395	2.381	2.400	2.411	2.381	2.376	2.405	2.390
Pt – Cl‘	2.377	2.402	2.399	2.378	2.391	2.384	2.399	2.405	2.383	2.387	2.406	2.392
Pt-N(NH_3)	2.058	2.052	2.040	2.057	2.059	2.047	2.042	2.050	2.051	2.051	2.055	2.047
Pt- N(cha)	2.084	2.078	2.069	2.075	2.075	2.058	2.069	2.064	2.061	2.081	2.070	2.054
C2 - C3	1.354	1.441	1.532	1.376	1.439	1.529	1.309	1.446	1.512	1.380	1.444	1.523
C2 - O2	1.369	1.256	1.204	1.375	1.273	1.207	1.342	1.265	1.213	1.372	1.261	1.211
C3 - O3	1.333	1.262	1.216	1.284	1.252	1.208	1.297	1.252	1.222	1.287	1.262	1.215

Table 3: Reaction and association energies for the considered individual reaction mechanisms. Energies are in kcal·mol^{-1}.

Reaction energy	ΔE_O	ΔG_O	$\Delta G_O(W)$	ΔE	ΔG	$\Delta G(W)$
AAH_2, JM216	5.7	-23.1	-5.8	10.8	-27.2	-10.8
AAH^-, JM216	14.2	-15.6	0.8	4.3	-25.5	-9.1
AA^{2-}, JM216	-5.1	-36.0	-19.6	-13.6	-44.5	-28.1
AAH^-, Cys, JM216	11.4	-21.1	-28.5	2.9	-29.6	-13.2
AAH^-, JM216-Cl	20.8	-10.6	6.3	13.1	-18.4	-1.5
AA^{2-}, JM216-Cl	-9.9	-40.3	-23.5	-17.3	-47.7	-15.6
AAH^-, JM216-Phe	20.9	-12.9	4.5	10.4	-23.5	-6.1
AA^{2-}, JM216-Phe	-4.1	-36.2	-18.9	-15.6	-47.6	-30.3
AAH^-, JM576	31.0	11.4	31.0	12.6	-7.0	3.1
AA^{2-}, JM576	-16.7	-38.0	-16.7	-14.1	-35.4	-25.7
Association energy	ΔE_O	ΔG_O	$\Delta G_O(W)$	ΔE	ΔG	$\Delta G(W)$
AAH_2, JM216	-17.8	11.8	-3.5	-8.0	21.6	6.2
AAH^-, JM216	-12.2	2.0	-7.3	-8.0	6.2	-3.1
AA^{2-}, JM216	-23.0	-9.1	-18.4	-15.5	-1.6	-10.9
AAH^-, Cys, JM216	-26.3	3.3	16.4	-11.7	17.9	-0.5
AAH^-, JM216-Cl	-12.5	2.5	-6.9	-8.9	6.0	-3.4
AA^{2-}, JM216-Cl	-24.0	-10.5	-19.9	-21.2	-6.6	-16.0
AAH^-, JM216-Phe	-12.8	1.9	-7.5	-5.9	8.7	-0.6
AA^{2-}, JM216-Phe	-24.1	-9.5	-18.9	-21.2	-6.6	-16.0
AAH^-, JM576	-16.5	10.8	-4.6	-8.6	18.7	3.3
AA^{2-}, JM576	-23.8	0.9	-14.5	-12.7	12.0	-3.4

Table 4: Activation barriers and corresponding rate constants for the individual reaction mechanisms. Energies are in kcal·mol^{-1} and rate constants in $M^{-1}\cdot s^{-1}$.

Activation barriers	ΔE_O	ΔG_O	$\Delta G_O(W)$	ΔE	ΔG	$\Delta G(W)$	$k(W)$	k_{eff}
AAH_2, JM216	46.3	36.2	36.2	38.3	28.2	28.2	1.4E-08	
AAH^-, JM216	34.5	29.0	29.1	34.2	28.8	28.8	4.7E-09	2.6E-03
AA^{2-}, JM216	19.0	14.1	14.1	19.7	14.7	14.7	1.1E+02	
AAH^-, Cys, JM216	25.1	19.5	22.7	26.1	20.5	20.5	5.6E-03	5.6E-03
AAH^-, JM216-Cl	35.2	27.3	27.4	34.5	26.6	26.7	1.7E-07	9.2E-03
AA^{2-}, JM216-Cl	16.3	13.1	13.1	17.2	13.9	14.0	3.7E+02	
AAH^-, JM216-Phe	31.1	29.4	29.4	32.5	30.8	30.8	1.5E-10	1.9E-05
AA^{2-}, JM216-Phe	18.2	15.5	15.5	20.3	17.6	17.6	7.5E-01	
AAH^-, JM576	32.3	28.1	28.12	31.9	27.7	27.7	2.8E-08	5.1E-02
AA^{2-}, JM576	8.9	8.3	8.3	13.5	12.9	12.9	2.0E+03	

Table 5: NPA charges (in e) determined at the B3LYP-GD3BJ/6-31++G**/IEFPCM/UAKS level.

	AAH_2			AAH^-			AA^{2-}			AAH^- + Cys		
	Re	TS	Pr	Re	TS	Pr	Re	TS	Pr	Re	TS	Pr
Pt	1.249	0.973	0.563	1.253	1.041	0.571	1.266	1.038	0.562	1.251	1.038	0.557
O(Ac)	-0.739	-0.740	-0.843	-0.687	-0.736	-0.857	-0.692	-0.737	-0.841	-0.712	-0.767	-0.819
O(Ac‘)	-0.676	-0.699	-0.745	-0.677	-0.706	-0.857	-0.687	-0.727	-0.787	-0.683	-0.721	-0.823
Cl	-0.468	-0.557	-0.593	-0.496	-0.576	-0.605	-0.532	-0.618	-0.613	-0.471	-0.587	-0.600
Cl‘	-0.474	-0.522	-0.514	-0.466	-0.570	-0.601	-0.535	-0.613	-0.622	-0.489	-0.580	-0.609
$N(NH_3)$	-0.995	-1.018	-1.022	-0.990	-1.030	-1.032	-0.986	-1.012	-1.033	-0.987	-1.020	-1.036
N(cha)	-0.798	-0.824	-0.827	-0.800	-0.819	-0.819	-0.799	-0.825	-0.820	-0.790	-0.818	-0.825
O2	-0.769	-0.644	-0.476	-0.761	-0.658	-0.471	-0.905	-0.705	-0.544	-0.795	-0.671	-0.513
O3	-0.724	-0.663	-0.557	-0.810	-0.676	-0.506	-0.843	-0.695	-0.625	-0.804	-0.705	-0.552
C2	0.077	0.271	0.463	0.031	0.221	0.454	0.054	0.253	0.428	0.026	0.227	0.425
C3	0.343	0.442	0.556	0.363	0.410	0.515	0.318	0.414	0.540	0.350	0.366	0.534
AA	-0.079	-0.664	0.081	-0.972	-0.886	0.005	-1.807	-0.970	-0.251	-1.085	-1.035	-0.198
Ac	-0.568	-0.537	-0.929	-0.558	-0.545	-0.957	-0.578	-0.768	-0.954	-0.571	-0.728	-0.948
Ac‘	-0.531	-0.667	-0.545	-0.563	-0.677	-0.957	-0.566	-0.713	-0.714	-0.543	-0.722	-0.747
$PtN_2H_5Cl_2$	0.825	0.316	-0.156	0.827	0.322	-0.269	0.701	0.214	-0.313	0.828	0.296	-0.288

Table 6: Changes of NPA charges determined at the B3LYP-GD3BJ/6-31++G** /IEFPCM/UAKS level and bond lengths in optimized structures in the considered outer sphere electron transfer mechanism for trans analogue JM576.

	Charges (e)					
	AAH^-, JM576			AA^{2-}, JM576		
	Re	TS	Pr	Re	TS	Pr
Pt	1.241	1.142	0.766	1.245	1.161	0.772
Cl	-0.458	-0.724	-0.926	-0.454	-0.748	-0.937
Cl‘	-0.465	-0.683	-0.838	-0.485	-0.687	-0.947
O(Ac)	-0.689	-0.724	-0.742	-0.663	-0.706	-0.722
O(Ac‘)	-0.698	-0.733	-0.725	-0.704	-0.729	-0.746
AA	-0.981	-0.833	-0.096	-1.838	-0.992	-0.042
$Pt(Ac)_2(NH3)(cha)$	0.086	-0.332	-0.722	0.018	-0.374	-0.883
cyclohexyl	-0.534	-0.591	-0.594	-0.558	-0.599	-0.617
	Bond lengths (Å)					
	AAH^-, JM576			AA^{2-}, JM576		
	Re	TS	Pr	Re	TS	Pr
Pt – Cl	2.364	2.743	4.920	2.359	2.716	4.301
Pt – Cl‘	2.364	2.900	7.900	2.371	2.824	4.427
Pt – O(Ac)	2.029	2.038	2.053	2.027	2.049	2.038
Pt – O(Ac‘)	2.033	2.052	2.027	2.031	2.048	2.038
C2 - C3	1.378	1.447	1.524	1.390	1.446	1.535
C2 - O2	1.369	1.263	1.210	1.330	1.262	1.205
C3 - O3	1.288	1.252	1.214	1.304	1.255	1.208

Scheme 1: Oxidation of ascorbic acid at neutral pH. Numbering for important oxygen atoms is stated in parenthesis.

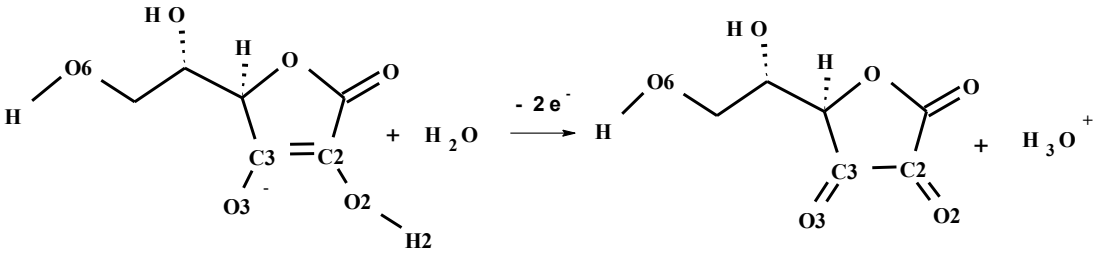

Capture for Figures:

Figure 1: Optimized structures of transition states for proton assisted electron transfer mechanism in the AAH_2 (**A**), AAH^- (**B**) branches and for outer sphere electron transfer mechanism in the AA^{2-} branch (**C**).

Figure 2: Optimized structures of transition state for the base assisted electron transfer mechanism, where the base is represented by Cys^-.

Figure 3: Modifications of satraplatin – JM216-Cl and JM216-Phe.

Figure 4: Optimized structures of transition states for the outer sphere electron transfer on JM576 in the AA^- (**A**), AA^{2-} (**B**) branches.

Figure 5: Reaction profile for reduction of satraplatin in the presence of AA^{2-} and the course of the reaction force along the reaction coordinate.

Figure 6: Magnitude of the electron density in BCPs on the selected bonds in the course of the reduction of JM216 in the AA^{2-} branch.

Figure 7: Course of the electronic chemical potential μ and reaction electronic flux J during the reduction of JM216 in the AA^{2-} branch.

Figure 8: Decomposition of the total bonding energy from the ETS-NOCV analysis from the reactant perspective (partitioning into AA^{2-} and the Pt(IV) complex). The course of electrostatic interaction, Pauli repulsion and orbital interaction is depicted.

Figure 9: Contours of leading term $\Delta\rho_1$ of deformation density from the ETS-NOCV analysis. Blue regions correspond to an increase of electron density and red ones to a decrease. The value of deformation density on contours is ± 0.003 $e \cdot au^{-3}$.

Figures:

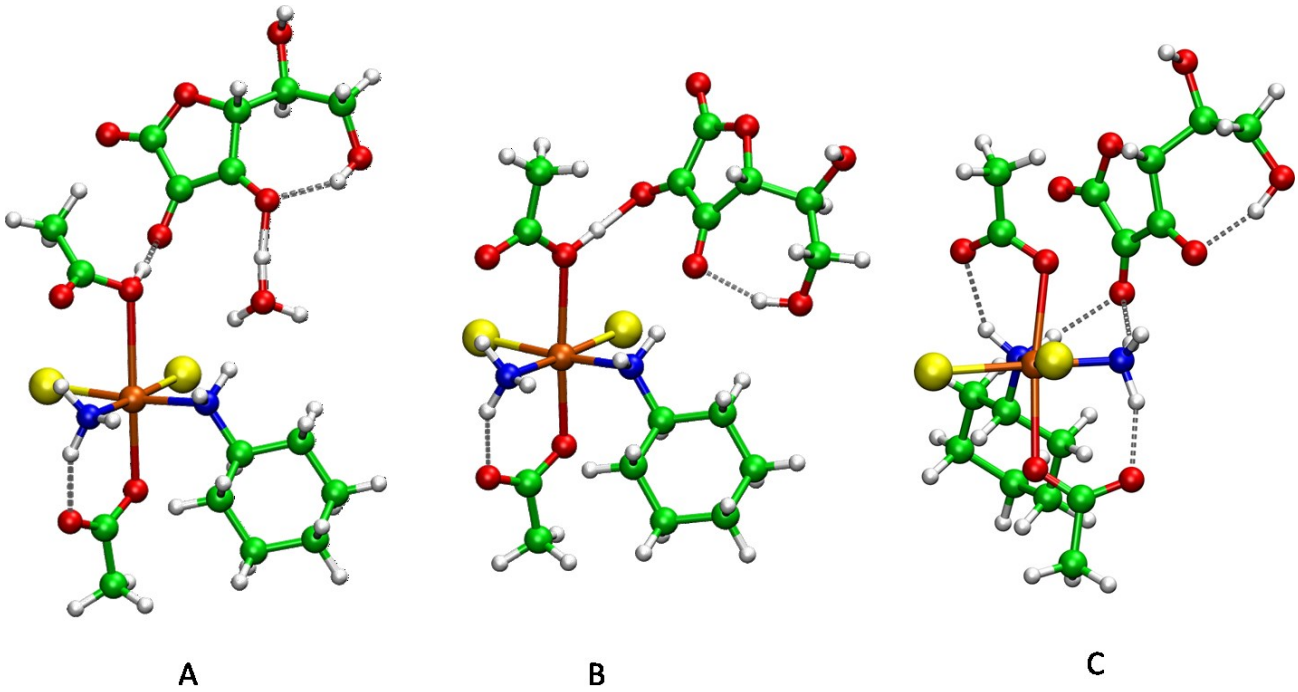

Figure 1

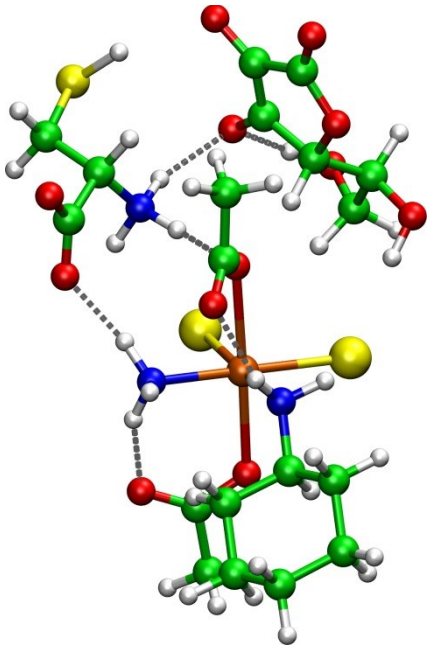

Figure 2

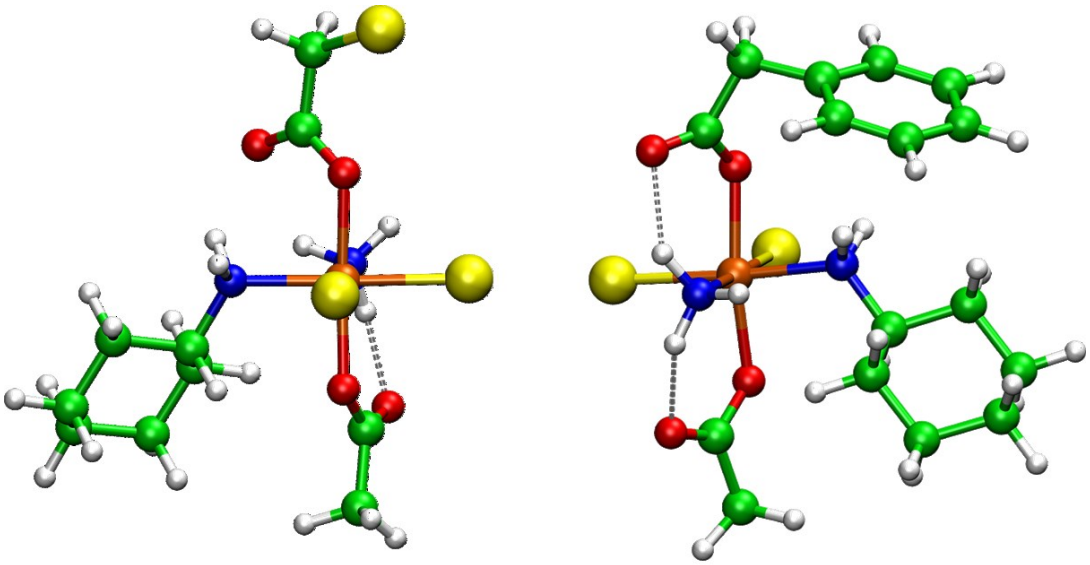

Figure 3

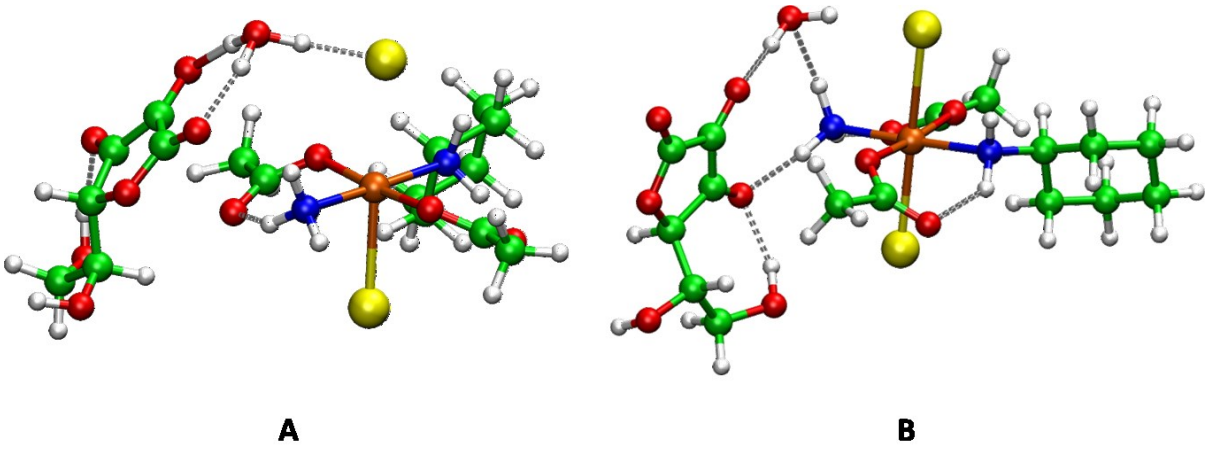

Figure 4

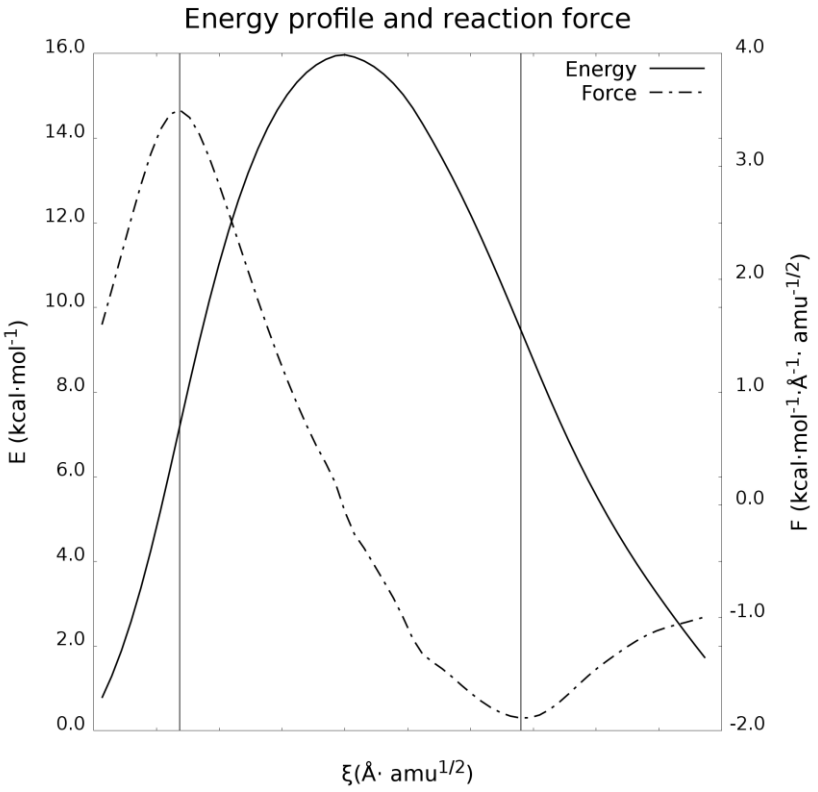
Energy profile and reaction force
Energy
Force
E (kcal·mol-1)
F (kcal·mol-1·Å-1· amu-1/2)
ξ(Å· amu1/2)
16.0
14.0
12.0
10.0
8.0
6.0
4.0
2.0
0.0
4.0
3.0
2.0
1.0
0.0
-1.0
-2.0

Figure 5

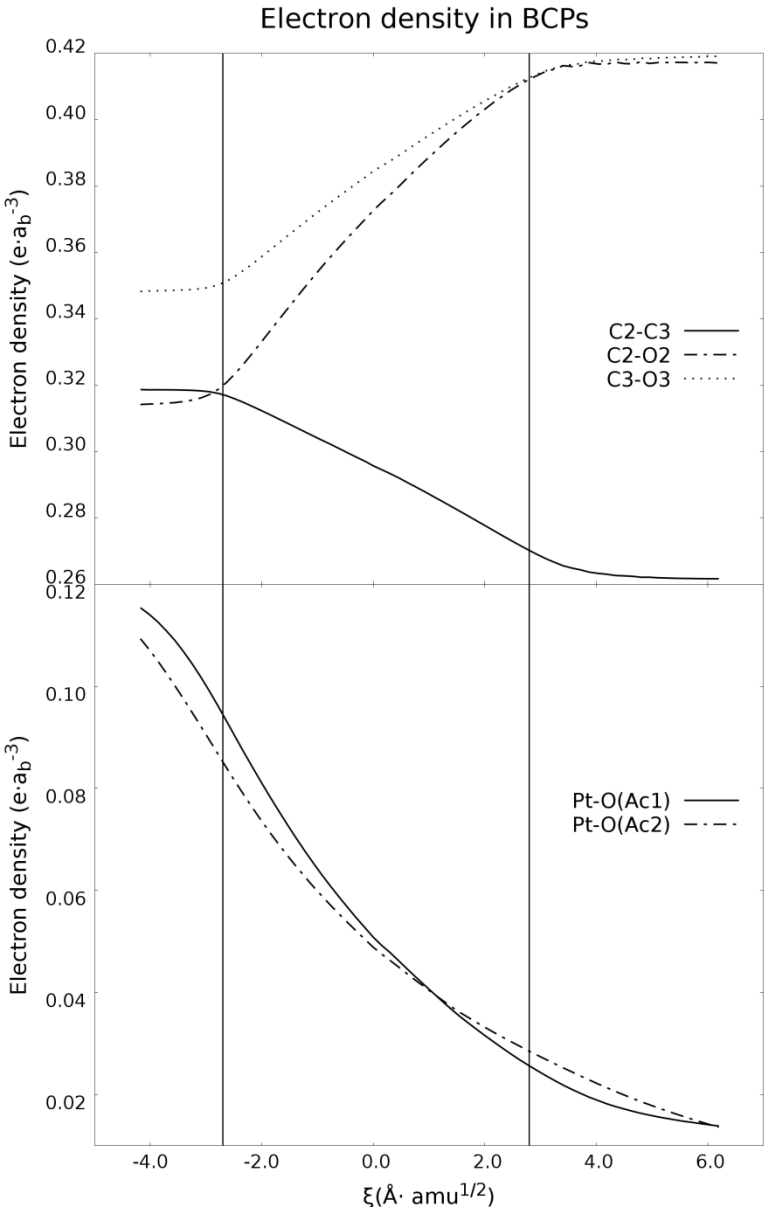
Electron density in BCPs
Electron density (e·a$_b^{-3}$)
0.42
0.40
0.38
0.36
0.34
0.32
0.30
0.28
0.26
C2-C3
C2-O2
C3-O3
Electron density (e·a$_b^{-3}$)
0.12
0.10
0.08
0.06
0.04
0.02
Pt-O(Ac1)
Pt-O(Ac2)
-4.0
-2.0
0.0
2.0
4.0
6.0
ξ(Å· amu$^{1/2}$)

Figure 6

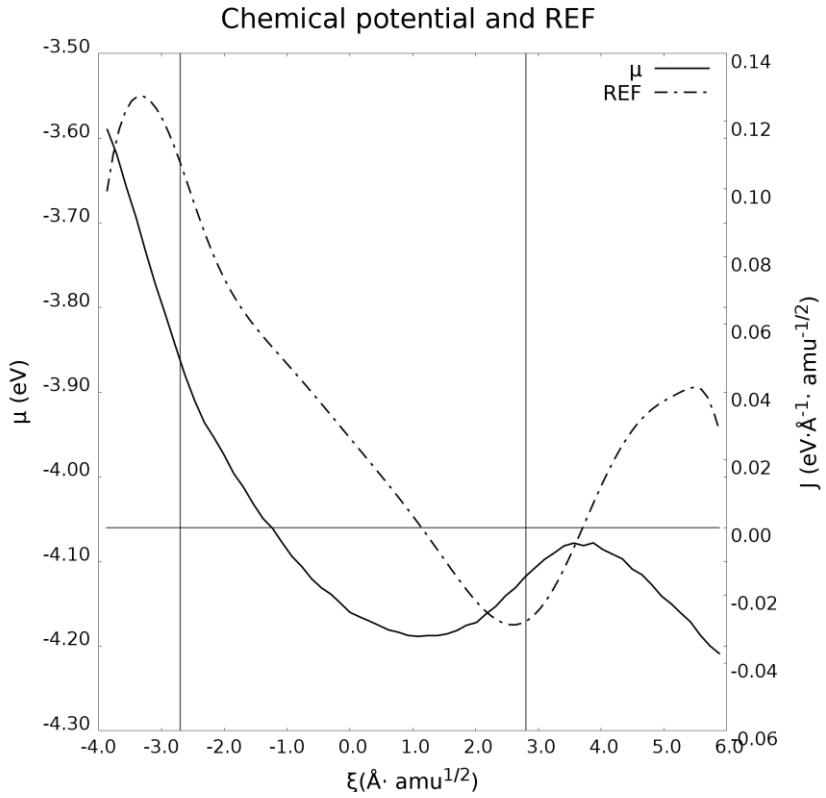
Chemical potential and REF
μ
REF
μ (eV)
J (eV·Å-1· amu-1/2)
ξ(Å· amu1/2)
-3.50
-3.60
-3.70
-3.80
-3.90
-4.00
-4.10
-4.20
-4.30
0.14
0.12
0.10
0.08
0.06
0.04
0.02
0.00
-0.02
-0.04
-0.06
-4.0
-3.0
-2.0
-1.0
0.0
1.0
2.0
3.0
4.0
5.0
6.0

Figure 7

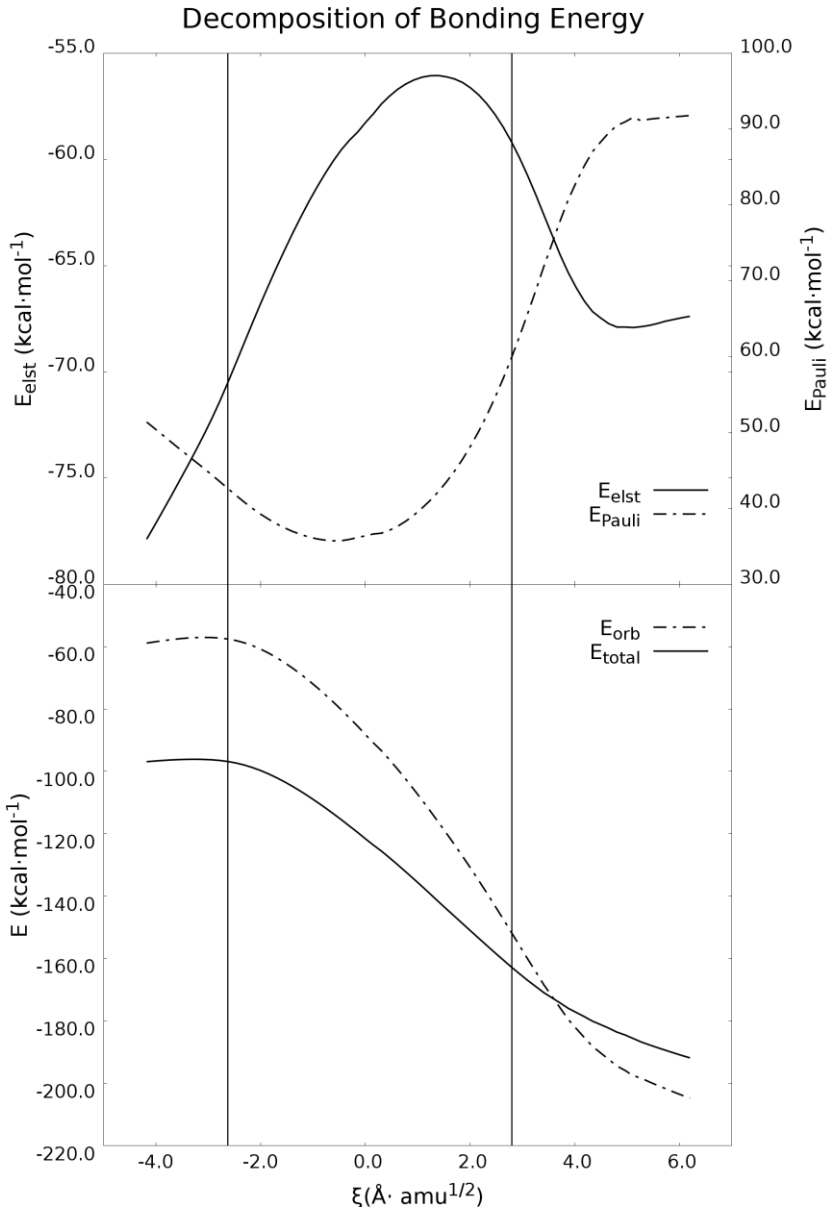
Decomposition of Bonding Energy
E_elst (kcal·mol^-1)
E_Pauli (kcal·mol^-1)
E_elst
E_Pauli
E_orb
E_total
E (kcal·mol^-1)
ξ(Å· amu^1/2)

Figure 8

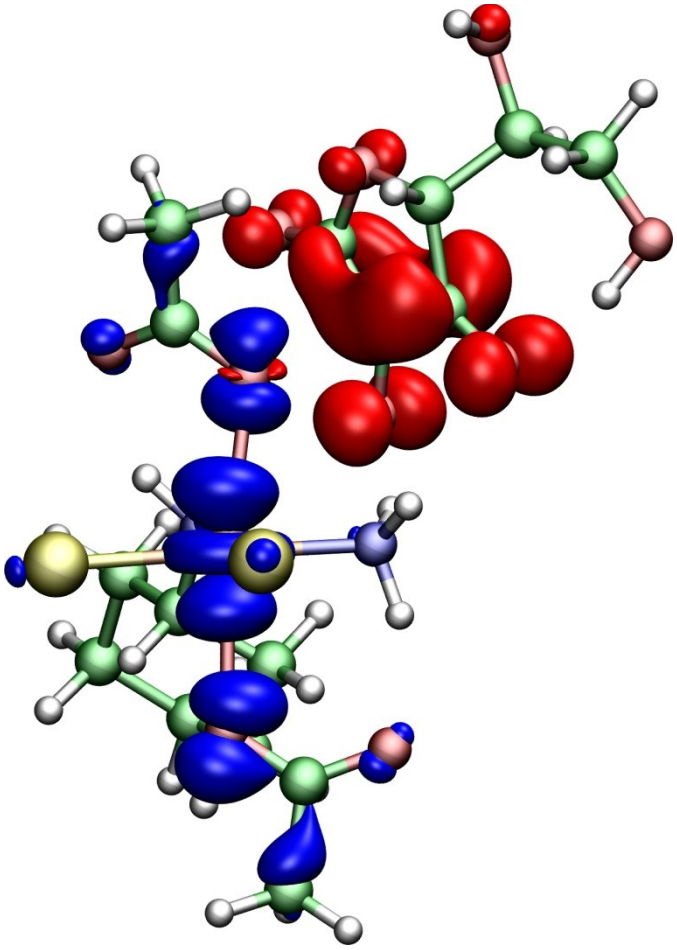

Figure 9

The Influence Of The Metal Cations and Microhydration On The Reaction Trajectory Of The N3 ↔ O2 Thymine Proton Transfer. Quantum Mechanical Study

Filip Šebesta,[1] Mateusz Z. Brela,[2] Silvia Diaz,[4] Sebastian Miranda,[4] Jane S. Murray,[3] Soledad Gutiérrez-Oliva,[4] Alejandro Toro-Labbé,[4] Artur Michalak,[2] Jaroslav V. Burda[1*]

[1]Department of Chemical Physics and Optics, Faculty of Mathematics and Physics, Charles University, Ke Karlovu 3, 112 16 Prague, Czech Republic
[2]Department of Theoretical Chemistry, Faculty of Chemistry, Jagiellonian University, R. Ingardena 3, 30-060 Cracow, Poland
[3]Department of Chemistry, University of New Orleans, New Orleans, LA 70148, USA
[4]Laboratorio de Química Teórica Computacional (QTC), Facultad de Química, Pontificia Universidad Católica de Chile, Vicuña Mackenna 4860, Casilla 306, Correo 22, Santiago, Chile

[*] email address of the corresponding author: burda@karlov.mff.cuni.cz

Abstract

This study involves the intramolecular proton transfer (PT) process on a thymine nucleobase between N3 and O2 atoms. We explore a mechanism for the PT assisted by hexacoordinated divalent metals cations, namely Mg^{2+}, Zn^{2+}, and Hg^{2+}. Our results point out that this reaction corresponds to a two-stage process. The first involves the proton transfer from one of the aqua ligands towards O2. The implications of this stage are the formation of a hydroxo anion bound to the metal center and a positively charged thymine. In order to proceed to the second stage a structural change is needed to allow the negatively charged hydroxo ligand to abstract the N3 proton, which represents the final product of the PT reaction. In the presence of the selected hexaaqua cations the activation barrier is at most 8 kcal/mol.

Introduction

Interactions of metal cations with nucleobases affect properties and behavior of DNA/RNA significantly. It is well known that metal cations, such as Mg^{2+}, naturally associated with nucleic acids govern their 3D folding and trigger or enhance many biophysical and biochemical processes.[1,2] A special case of these interactions concerns modified base pairs, in which hydrogen bonding is replaced by a metal-mediated interaction.[3] Even canonical base pairs that occur naturally in DNA/RNA molecules can be involved in such metal cross-links. It is clear that the functioning of such modified base pairs is completely different than the behavior of standard Watson–Crick base pairs. A spatial occupation of the pyrimidine-metal-pyrimidine

structure within the DNA duplex fits standard Watson–Crick purine–pyrimidine base pairs. The mispaired structures like thymine-thymine (T-T) and cytosine-cytosine (C-C) are very sensitive to metal cations. For example, a silver cross-link was studied in the C-Ag(I)-C base pair[4,5] and structures like imidazole-Ag-imidazole appeared to be a functional alternative to normal pyrimidine bases.[6,7]

The T-Hg(II)-T metal cross-linked base pair is probably one of the best structurally resolved from these base pairs. This structure was found by means of the ^{2}J(N3,N3) NMR spin–spin coupling.[8] The heavy metal bonding to the N3 site of thymine was also assigned by Raman spectroscopy.[9,10] Recently the B-DNA hexadecamer structure with two subsequent T-Hg(II)-T base pairs was characterized by NMR spectroscopy.[11] Also, the enthalpy and entropy of the formation process were measured by the isothermal titration calorimetry.[12] In our previous computational study we explored the above mentioned process confirming the thermodynamic characteristics of the reaction suggesting the detailed mechanism.[13,14] We recognized also the importance of proton transfer as a key step for both primary metal-adduct formation as well as for the consequent completing of the cross-link structure. Therefore, we decided to examine the proton transfer process as a separate reaction under the influence of hydrated metal cations and compare the reaction characteristics.

Interactions of Mg^{2+}, Zn^{2+}, and Hg^{2+} with nucleobases (especially purine bases) were explored several times before. [15-18] The interaction of the Hg^{2+} cation with thymine can be put to a recent context with intensive studies on a selective interaction of mercury, which preferentially binds to this nucleobase and especially to TT mispairs. [8,11-13,19-23]

Methods

Reaction pathway

The reaction force $F(\xi)$ is defined[24] as the negative gradient of the potential energy $V(\xi)$ of a chemical or physical process along a reaction coordinate ξ:

$$F(\xi) = -\frac{\partial V(\xi)}{\partial \xi} \quad \text{(eq. 1)}$$

where ξ is used for the intrinsic reaction coordinate (IRC or just RC). The reaction force is used to define reaction regions along the reaction coordinate, this helps distinguish the different mechanisms that might be operating to drive the entire chemical process. For a one-step process in which reactants and products are separated by an energy barrier, as shown in Scheme 1, the reaction force presents two critical points, a minimum at $\xi = \alpha$ and a maximum at $\xi = \gamma$, these critical points allow to define three reaction regions along R. The reactant region goes from the reactant to the force minimum ($\xi = \alpha$) ; the transition state region going from the force minimum to the force maximum ($\xi = \gamma$); and the product region defined from the force maximum until the products. On the other hand, the reaction‑force constant $k(\xi)$ is the negative derivative of $F(\xi)$ $[k(\xi) = -\partial F(\xi)/\partial \xi]$, which should be negative throughout that entire region, between the so-called α and γ points defined as points with zero second derivative.

A typical $V(\xi)$ profile with corresponding $F(\xi)$ for a process with a single energy barrier is drawn in **Scheme 1**. Minimum and maximum on the reaction force $F(R)$ occur at the inflection points of $V(\xi)$, $\xi = \alpha$ and $\xi = \gamma$.

Examining a variety of reactions – proton transfers, molecular rearrangements, conformational changes, S_N2 substitution, bond dissociation/formation – these regions maintain some characteristic features. Passing from the reactants to the α point, structural changes are dominant: bond stretching, angle bending, various rotations and deformations, etc. In this way the reactants are prepared for subsequent steps while an increasingly negative (retarding) reaction force $F(\xi)$ can be seen till reaching the greatest magnitude at point α. Here, the system can be considered as an activated form of the reactants.

The middle section, between points α and γ, represents a transition region. In this part structural factors are still important. However, electronic changes dominate within this region: creation and annihilation of bond critical points (according to Bader AIM theory[25]), extensive variations of properties such as orbital energies, electrostatic potentials, etc. These changes are connected with a positive and increasing driving force that diminishes and then balances the retarding forces, at $\xi = \beta$ (TS structure), which is also linked with maximum of the reaction potential $V(\xi)$. At the point γ, force $F(\xi)$ reaches its highest positive value, which marks the end of the transition region. The system can be regarded as activated states of the products at this point. In the third region, after point γ, structural changes, which lead products to their final optimal form, dominate. Considering this partitioning of a reaction coordinate, natural decomposition of activation energy into two components can be introduced:

$$\Delta E_{act} = V(\beta) - V(reactants) = [V(\beta) - V(\alpha)] + [V(\alpha) - V(reactants)] = W_2 + W_1 \ .$$

W_1 introduces the energy, which is required in order to get from the optimal reactant structure to α point, primarily to overcome resistance to the structural changes. W_2 is the energy connected with the electronic changes passing to the transition state (α → β). In analogous way W_3 is associated with the electronic changes from the transition state β to γ, and W_4 as energy released passing from γ point to the reaction minimum.

Chemical potential and reaction electronic flux

The chemical potential represents a global electronic property, which classifies the reactivity of the electronic systems. It has been defined within density functional theory as:[26]

$$\mu = \left(\frac{\partial E}{\partial N}\right) = -\chi$$

where χ is electronegativity,[27,28] characterizing the tendency of the electronic cloud to escape from an equilibrium.[29] Within the finite difference approximation, it can be expressed by:[30]

$$\mu = -\frac{1}{2}(IP + EA) = \frac{1}{2}(HOMO + LUMO) \quad \text{. (eq. 2)}$$

IP and EA stand for the first ionization potential and electron affinity of the system, respectively. This equation can be used for estimation of the chemical potential along the reaction coordinate (ξ). For deeper understanding of the electronic changes along a reaction coordinate, a reaction electronic flux (REF) descriptor has been recently introduced.[31,32] REF represents changes of the chemical potential considered as a charge density gradient between two points on the reaction coordinate, it measures the electronic activity taking place during the chemical reaction. The REF is defined as:

$$J(\xi) = -\left(\frac{\partial \mu}{\partial \xi}\right).$$

The course of *J(ξ)* enables to identify the areas of the reaction coordinate where important charge transfer and polarization occur. In analogy with classical thermodynamics, areas of $J > 0$ corresponds to spontaneous reorganization of the electron density that is driven by bond forming/strengthening process; and areas of $J < 0$ can be connected with non-spontaneous change of the electron density that is driven by bond weakening/breaking processes.

Decomposition of the Reaction-Energy and the Reaction-Force Profiles

The analysis of the changes in the electronic structure along the reaction pathways, going beyond the typical analysis limited to the stationary points, was pioneered by

Morokuma et al.[33-36] The fragment representation of considered systems gave the possibility to describe the electronic changes in term of bond-breaking and bond-formation. Bickelhaupt et. al.[37,38] proposed the *activation strain model* (ASM), originally intended to provide information about origin of the activation barriers in different reactions. In this approach the reaction energy profile, $\Delta E(\xi)$, is decomposed into two contributions: the *distortion energy* accounting for the structural deformation of fragments A and B:

$$\Delta E_{dist}(\xi) = \Delta E_A(\xi) + \Delta E_B(\xi),$$

and the interaction between them, $\Delta E_{int}(\xi)$:

$$\Delta E(\xi) = \Delta E_{dist}(\xi) + \Delta E_{int}(\xi) \qquad \text{(eq. 3)}$$

In the ETS bond-energy decomposition method [39-41] applied in this work, the overall interaction (bonding) energy for a given molecular geometry (here: a point at the reaction path, ξ) is decomposed into the electrostatic (ΔE_{elstat}), Pauli repulsion (ΔE_{Pauli}) and orbital interaction (ΔE_{orb}) components:

$$\Delta E_{int}(\xi) = \Delta E_{elstat}(\xi) + \Delta E_{Pauli}(\xi) + \Delta E_{orb}(\xi) \quad \text{(eq. 4)}$$

The first term, ΔE_{elstat}, corresponds to the electrostatic interaction between the frozen charge distributions of the two distorted fragments in the considered system geometry. The second term, ΔE_{Pauli}, accounts for the repulsive interaction between occupied orbitals of the two fragments. The orbital interaction term, $\Delta E_{orb}(\xi)$, represents the stabilizing component due to the interaction of the occupied orbitals of one fragment with virtual orbitals of the other subsystem, leading to bond formation; this term includes as well the intra-fragment polarization, emerging from the mixing of occupied and virtual orbitals of the same fragment.
Following the ASM energy decomposition, the reaction force of eq. 1 can be similarly represented as sum of the distortion and interaction contributions:

$$F(\xi) = -\frac{\mathrm{d}\Delta\mathrm{E}(\xi)}{\mathrm{d}\xi} = -\frac{\mathrm{d}\Delta\mathrm{E}_{\mathrm{dist}}(\xi)}{\mathrm{d}\xi} - \frac{\mathrm{d}\Delta\mathrm{E}_{\mathrm{int}}(\xi)}{\mathrm{d}\xi} = F_{dist}(\xi) + F_{int}(\xi) \qquad \text{(eq. 5)}$$

The reaction-force components defined by eq. 5 were used in a discussion of the forces driving/retarding the chemical reaction by Politzer *et al.*[42]

Further decomposition of the interaction part of the reaction force, $F_{int}(\xi)$ into the ETS components was recently proposed by Diaz *et al.* [43]:

$$\frac{d\Delta E_{int}(\xi)}{d\xi} = \frac{d\Delta E_{Pauli}(\xi)}{d\xi} + \frac{d\Delta E_{elstat}(\xi)}{d\xi} + \frac{d\Delta E_{orb}(\xi)}{d\xi}$$

$$F_{int}(\xi) = F_{Pauli}(\xi) + F_{elstat}(\xi) + F_{orb}(\xi) \qquad \text{(eq. 6)}$$

Here, $F_{elstat}(\xi)$ is the electrostatic-interaction force, $F_{Pauli}(\xi)$ is Pauli-repulsion force, and $F_{orb}(\xi)$ is the orbital-interaction force. It should be mentioned that the latter term can be further decomposed[43] into the ETS-NOCV components, following the NOCV decomposition of $\Delta E_{orb}(\xi)$ term.[44-46]

It should be emphasized that a choice of the fragments may be not intuitive for all points on the pathway of a given chemical reaction. We have emphasized this difficulty in previous papers,[43,47] discussing two different fragmentation schemes, leading to a description "from the reactant perspective" and "from the product perspective", based on the partitioning "natural" to the reactants and products, respectively. It should be further stressed that depending on the fragmentation of the system ("reactant" or "product" perspective) the driving and retarding components can be included in different ETS-NOCV reaction-force terms since one partitioning is focused on the bond-formation processes, while the other - on bond-breaking.[43]

Computational Details

All the systems were optimized at the B3LYP/6-31G(d) computational level using G09 program package[48] Transition metals (Zn, Hg) were described by energy-adjusted quazirelativistic Stuttgart's pseudopotentials.[49,50] Frequency analysis confirmed the proper character of the obtained structures of all the minima and transition states. Algorithm of Intrinsic Reaction Coordinate (IRC) method[51] was used for the determination of the proton transfer reaction profiles. The proton transfer (PT) from N3 to O2 site of thymine (standard numbering is according to Saenger[52]) was explored in isolated nucleobase and micro-hydrated thymine with one water molecule associated in the proximity of the N3 position where it mediates proton transfer between both N3 and O2 sites. Further, an influence of the naked and hydrated (with three and five water molecules) Mg^{2+}, Zn^{2+}, and Hg^{2+} metal cations coordinated to the O4 thymine site was examined. Finally, the main goal of the study was explored - an effect of H-bonded hexaaqua-cations of the above-mentioned metals on PT of thymine was explored. In these structures, two aqua ligands are associated with the O4 and O2/N3 sites and proton transfer occurs via two-step reaction mechanism, cf. **Scheme 2**. In this two-step mechanism the reaction coordinate ξ is taken as a merge of RCs of the both reaction steps: i) movement of a proton from O(w)...H...O2 and ii) N3...H...O(w). This 'unification' of both steps is possible since both RC are sharing the intermediate structure, which is end of the first step and starting point on RC of the second step.

Partial charges from natural population analysis (NPA)[53] together with Bader's 'Atoms in Molecules' (AIM) electron densities in Bond Critical Points (BCP)[25] were evaluated using Keith's AIMAll program.[54] Change of the chemical potential was estimated from the eq. 2 and consequently the reaction electronic flux[55]

along the RC was evaluated. Nalewajski-Mrozek bond order analysis,[56] the ETS-NOCV, and S-O coupling calculation with the ZORA method[57] were performed using B3LYP exchange-correlation functional and standard triple-ζ basis with two sets of polarization functions in the Amsterdam Density Functional (ADF) [58-61] program. It should be emphasized that the single-point ADF calculations were performed for each Gaussian-IRC point.

Results and Discussion

Energy and Reaction Force Profiles

An energy profile for the PT was explored in presence of solvated divalent metal cations - hexaaqua form of Mg^{2+}, Zn^{2+}, and Hg^{2+}. These profiles together with individual structures are displayed in **Fig. 1**. Generally, the reactant structures for metal assisted PT have two aqua ligands H-bonded to the O2 and O4 thymine sites. These profiles have quite a different shape in comparison with reaction profile for PT of a) isolated thymine, b) thymine in the presence of one explicit water or c) thymine with the metal cation coordinated to the O4 site of the nucleobase. Corresponding reaction profiles are collected in **Table S1** and in **Fig. S1** and **S2** presented in Supplementary Information.

The reaction in presence of $[Zn(H_2O)_6]^{2+}$ (**R2**) and $[Hg(H_2O)_6]^{2+}$ (**R3**) is connected with energy profile where two TSs are clearly distinguishable. The first PT is connected with TS1 maximum, which leads to formation of thymine cation $(thymine\text{-}H)^+$ and hydroxo-ligand coordinated to metal. The first energy barrier is about 3 kcal/mol, followed by a meta-stable intermediate, which lies ca 0.5 kcal/mol lower for both Zn^2 and Hg^{2+} complexes, cf. **Fig 1b** and **c**. Then, the second PT occurs with an energy barrier of 2.5 and 4.3 kcal/mol above the metastable intermediate structure for the Zn^2 and Hg^{2+} system, respectively. This means that in the case of Hg-containing structure the second PT is the rate-limiting step of the reaction. Nevertheless, it would be very difficult to distinguish or detect the intermediate structure due to very low TS barriers and thus very fast reaction occurrence. Interestingly, the **R2** and **R3** reactions differ from the thermodynamical point of view. While the complete reaction is slightly exothermic (by -1.6 kcal/mol) in the Zn case, the endothermic course is predicted in presence of Hg^{2+} cation by 4.3 kcal/mol. Final product structures can be obtained by an additional rearrangement of aqua-ligands after ending in the last IRC geometry (local reaction minimum), which leads in the Zn^{2+} case to further energy decrease from ca 3.5 kcal/mol to -1.6 kcal/mol.

The potential energy curves of PT reaction assisted by $[Mg(H_2O)_6]^{2+}$ (**R1**) is displayed in **Fig. 1a** and shows a marked shoulder followed by only one maximum. Even though two maxima were expected (one for each proton transfer) the profile indicates that when the energy needed for transfer of the first proton is reached (~ 5

kcal/mol), it generates a highly unstable species due to the inability of the Mg^{2+} cation to stabilize the negatively charged hydroxyl ion in the vicinity of positively charged thymine, see e.g. bond order analysis below. Thus, energy of such an activated complex continues increasing until the second proton transfer takes place with the energy barrier of 7.9 kcal/mol. This is followed by the stabilization and relaxation of the system. From a thermodynamic point of view, the reaction is mildly endothermic where the product is about 4.1 kcal/mol higher in energy than the reactant. A separation between both PT processes along the reaction coordinate is a consequence of the sufficient stabilization of the Zn, and Hg charged intermediate. Also, both PTs in **R1** of the Mg^{2+} system occur in a substantially closer region (shorter RC). This becomes clear after the normalization of the reaction coordinate.

Since the reaction profiles are similar for both Zn^{2+} **(R2)** and Hg^{2+} (**R3**) complexes, further only **R3** reaction will be discussed from the point of the reaction force profile. In **R3,** eight regions can be defined. The W_1 area (reactants→α) corresponds to mainly structural relaxation (ca 2.7 kcal/mol), while the electronic change parts - W_2 (α→β) and W_3 (β→γ) are connected with values of 0.24 and 0.07 kcal/mol, respectively. The first two magnitudes define the non-spontaneous structural (W_1) and electronic (W_2) activity bringing the system to the first PT, and spontaneous (W_3) activity, which represents a subsequent electronic relaxation. The following structural reordering demonstrates a very flat surface, according to the energy of 0.75 kcal/mol linked with W_4 area (γ→intermediate), cf. **Table 1**. Next, an important reorinetation prepares the system for the second PT. Here the aqua ligand reorients into the proper direction. The contribution of this structural modification is determined by the value of W_1' (4.07 kcal/mol) being the main contribution to the energy barrier. W_x' represents the same energy as W_x but the primed version concerns the second reaction step. The electronic reorganization associated to the PT process is defined by W_2' and W_3' with values of 0.23 and 0.08 kcal/mol, respectively. The final relaxation to the product geometry stabilizes the whole system by additional 2 kcal/mol.

As to the magnesium-containing system, the initial work determined by the value of W_1 is higher than in the Hg^{2+} case (4.2 kcal/mol). It implies that for Mg^{2+} structure, larger structural rearrangements needs to be carried out in order to prepare the system for the first PT than in the **R3** case. Since a true TS is missing for the first PT - as observed from **R1** potential energy curve (**Fig. 1a**), the reaction force of this profile is reduced into six regions (W_1, W_2+W_3, $W_4 = W_1'$, W_2', W_3' and W_4') only. When the reaction force profile is considered (dash blue line in Fig 1), it can be noticed that after the first negative minimum there is no crossing through zero to positive values on **R1** near this minimum, which would indicate a TS structure formed after the first PT. For this particular case, other strategy how to partition the reaction coordinates has to be chosen and the second derivative of the potential

energy - the reaction-force constant is taken into consideration. In this way, at the minimum of reaction force (the α-point at ξ = 0.21) is defined. Shortly afterwards, a maximum of reaction force at ξ = 0.25 can be use for the determination of the end of $W_2 + W_3$) region of RC with energy of 5.6 kcal/mol. Despite the fact that this minimum is still in negative values, the reaction-force constant curve has zero in this point. After this γ-point, the $W_4 = W_1'$ section starts, which can be considered as a region of predominating structural changes before the second PT is reached. These considerations are also consistent with REF characteristics as it can be seen in a discussion below, where not much electronic changes occur in the range ξ = 0.25 - 0.5. Then, just before the TS another local minimum of the reaction force appears defining the boundary between W_1' and W_2' (ξ = 0.52) regions (α' point) at 7.7 kcal/mol. The region of W_2' is connected with another electronic changes. Then RC passes through the only true TS (β'-point, ξ = 0.53) and the γ ' point at ξ = 0.54. These electronic changes are linked with very small energy differences of 0.2 kcal/mol within very short range of RC. Consequently structural relaxation follows, which leads to the final product represented by a relatively large energy release of 3.8 kcal/mol.

From the analysis of **R1** - **R3** energy profile components, it is possible to infer that the contributions of the electronic effects into the reaction mechanism are small, particularly depicted from the values of W_2, W_3, W_2' and W_3' of all RC. Thus, despite the apparent complexity of the mechanism, it seems that the energy barriers are mainly driven by the structural changes needed to perform the reaction.

Structural changes along the metal assisted PT

At the beginning, the regular thymine is associated with the solvated metal cation by two H-bonds at the O2 and O4 sites. Based on the division of reaction coordinate according to the reaction force, first minimum (α-point) is located at ca ξ = 0.2 of all the normalized reaction coordinates. It is important to mention that after the γ-points, the H-bonded proton of the aqua ligand is transferred to the O2 site of the nucleobase forming the positively charged thymine cation and the 1+ charged $[M(H_2O)_5(OH)]^+$ cation. Notice that a completely opposite situation occurs in water-assisted PT where ion pair: {thymine$^-$: H_3O^+} is formed in TS structure. Actually, the first PT starts by approaching oxygen of the aqua ligand to H(N3) before the α–point is reached, in the area of predominately structural changes. After the γ-point the distance between (O2-)H and oxygen of hydroxo group increases forming the above mentioned ionic pair. Then the (N3-)H…O(aq) H-bonding interaction increases. In the close vicinity of the second TS on the **R2** and **R3** profiles and the only TS of the **R1** profile, the convex character of the potential energy curve ends in the second α'-point. In this area the cleavage of N3-H and second PT to the temporarily existing hydroxo-ligand

occurs. Finally, in product state, the thymine enol-tautomer is associated with the solvated metal cation by two H-bonds at the N3 and O4 sites.

In the thymine systems with the Zn^{2+} and Hg^{2+} solvated cations, the stable 1+ charged $[M(H_2O)_5(OH)]^+$ complexes is predicted in shallow local minimum (2.7 and 2.1 kcal/mol above the reactant for Hg and Zn complexes, respectively). It means that $[Hg(H_2O)_5(OH)]^+$ is stabilized by nearly 1kcal/mol while only by 0.5 kcal/mol in the Zn case. From the comparison of RC of the three metal cations an important difference in their chemical behavior is noticeable - an additional stability of the Zn^{2+} and Hg^{2+} over Mg^{2+} cation due to ability of transition metals to form dative bonds. The coordination-covalent character of Zn and Hg metals is visible e.g., from electron densities in bond critical points (ρ_{BCP}). While in isolated hexaaqua cations the ρ_{BCP}(M-O) density is 0.031 in the Mg^{2+} case the analogous values for the Zn^{2+} and Hg^{2+} cations are visibly higher: 0.053, and 0.047 e/au^3, respectively. This feature is also demonstrated in the course of the M-O bond order of the aqua-ligand assisted in PT for all the metals displayed in **Fig. 4**.

As to the influence of environment, no substantial changes can be assumed since the most important water molecules, which directly mediate the PT, are already presented in our models so that only minor changes can be expected if a more extended solvation shell would be introduced either by including explicit water molecules e.g., in QM/MM simulations[62-67] or indirectly using implicit solvation models (SMx[68,69] or PCM[70,71]).

Energies of other forms of N3 → O2 PT in thymine system

For a complete energetic picture we evaluate within the same computational model also PT in isolated thymine, thymine with a water molecule (water-assisted PT) and PT in the presence of directly coordinated metal cations to the O4 site of nucleobase. The energy characteristics of these reaction coordinates are collected in **Table S1**. An endothermic course of about 21 kcal/mol with height of the activation barrier of ca 50 kcal/mol was found for isolated thymine. The energy increases from reactant to α-point (W_1) by about 35 kcal/mol demonstrating there is a large energy penalty in the area with dominant structural reorganization. In the region of electronic changes (W_2) only half of this energy is necessary - 18 kcal/mol. These values can be easily understood since breaking of the N3-H bond is energetically quite demanding without practically any compensation from O2--H formation energy. The reaction coordinate for PT mediated by water molecule does not start from the global minimum where the water molecule is associated to thymine by two H-bonds at the O2 and N1 sites. In the reactant minimum, the water molecule has to be associated with thymine between O2 and N3 sites. In this model the reaction is about 15 kcal/mol endothermic. However, the activation barrier is substantially decreased by about 30kcal/mol. The reaction profiles (energy, reaction force, and reaction-force

constant) are showed for isolated thymine in **Fig. S1a,** and for water assisted PT in **Fig. S1b** of the Supplementary Information**.**

An interesting modification of the above-discussed system was obtained when the divalent metal cations (Mg^{2+}, Zn^{2+}, and Hg^{2+}) were coordinated to the O4 position of thymine either in the naked form or coordinated by three and five water molecules. From the **Table S1,** it can be noticed that the reaction becomes exothermic in all these cases. This character is caused by higher electrostatic repulsion between the metal cation (even in the hydrated form) and positively charged hydrogen bound to the N3 position in comparison with analogous repulsion after PT when this proton is moved to the more remote O2 site. (Charge of this 'active' hydrogen is ca $\delta \approx 0.4$ e according to NPA analysis). The hydration shell of the cation shields its positive charge so that the reaction becomes less exothermic in comparison with the bare cation. This clearly confirms the electrostatic origin of the reaction driving force. Then practically thermoneutral course of PT in presence of the pentaaqua cations can be easily understood. Metalation in the O4 position also lowers the activation barrier by about 10 kcal/mol. The reaction coordinates for the Mg^{2+} cation (bare as well as hydrated) are displayed in **Fig**. **S2** of the Supplementary Information.

Analyses of Electronic Properties

Thymine N3-O2 Proton Transfer assisted by single water molecule

Comparing PT in the isolated thymine and in presence of the associated water molecule it can be noticed that ρ_{BCP} of H-bond between (N3-)H…O(w) (0.032 e/au^3) increases to 0.159 e/au^3 passing from the reactant to the TS structure with a simultaneous decrease of ρ_{BCP} of the N3-H bond from 0.310 to 0.075 e/au^3. Two nearly simultaneous PT's occur in the close proximity of the TS structure of the thymine...water system. After the breaking of N3-H bond, another proton from water starts to move to O2 thymine site. From the AIM analysis, it can be noticed that visibly larger densities in BCP's of both active (transferring) protons with O(w) occurs, which indicates presence of H_3O^+ particle. This picture together with the fact that the interatomic distances are clearly in favor of hydronium cation lead to a conclusion that the TS structure of thymine...water system should be considered as a ion-pair: {thymine^{--} and H_3O^+}. A simultaneous cleavage of N3-H and formation of H-O(w) bonds are responsible for a large decrease of the activation barrier of the PT process from 51 (in isolated thymine) to 21 kcal/mol in the case of thymine...water associated complex. Similar situation is described also in paper of Yepes et al.[72] The assisted mechanism of hydrated metal cations summarized in **Table 1** can be basically considered as an asynchronous analog of this mechanism where a different role of water/aqua ligand can be noticed. By asynchronous mechanism we understand transfer of one proton first forming intermediate structure subsequently

followed by second PT leading to final reaction product. While in this TS a ion-pair { thymine$^-$ and H_3O^+ } structure is formed in system water...thymine, in presence of hydrated metal cations other ion-pair {$[M(H_2O)_5(OH)]^+$ and thymine$^+$} occur in the intermediate structure - either stable (Zn^{2+} and Hg^{2+}) or unstable (Mg^{2+}).

PT assisted by hydrated metal cations

Electronic analyses were performed for geometries of all the stationary points. In the case of Mg^{2+} reaction coordinate, another (unstable) structure from reaction coordinate $\xi = 0.24$ is included since this structure should, at least to some extent, correspond to the TS1 point of the other metal cations. **Table 2** contains bond distances of the structures involved in PT. Generally, only small variations of O4…H-O(aq) distance demonstrate that this H-bond is always present without any substantial response to PT. Basically the key changes occur in the vicinity of the N3 and O2 sites of thymine and the corresponding aqua-ligand. All the changes can be also mapped to variations of ρ_{BCP} obtained from Bader's AIM method, which are summarized for corresponding bonds of all three cations in **Table 3,** and NPA partial charges collected in **Table 4**. In **Fig. 2,** changes of ρ_{BCP} are displayed for selected bonds within **R2** of Zn^{2+} cation. The structural changes induced by switching between keto-enol forms of thymine due to PT are demonstrated on C2-N3 and C2-O2 distances on the reaction coordinate (cf. **Table 2)** and in the case of Zn^{2+} complex the changes in bonding distances can be compared in **Fig. 3** where variation of bond orders within RC are displayed. Practically identical figures were obtained also for BCP densities and bond-orders in systems with the remaining two metals (Mg^{2+} and Hg^{2+}). From **Fig. 2** and **Fig. 3**, clear decrease of C2=O2 (1.7) bond order to C2-O2 (1.1) is visible simultaneously with increase of C2-N3 (1.1) bond to C2=N3 (1.4). Similarly breaking of the N3-H bond and forming of the O2-H bond are apparent.

Comparing the averaged M-O(aq) bond lengths it can be noticed that the distances increase from Mg to Hg: d(Mg-O) < d(Zn-O) << d(Hg-O) Despite the increasing M-O distances, the NPA partial charge of the metal cation decreases in the opposite order Mg > Zn > Hg (cf. **Table 4**) demonstrating the higher extent of donation from oxygen atoms. However, BCP electron densities can be considered as a more appropriate tool for estimation of the strength of the coordination- covalent bond. These values are displayed in **Table 3**. From this table, it follows that the highest ρ_{BCP} of M-O bond belongs to the Zn^{2+} complexes. The Hg-O densities are only slightly smaller than in the case of Zn^{2+} complexes. As one can expect the Mg^{2+} structures display the smallest portion of covalent contributions.

Besides comparison of the individual metal cations, it is interesting to examine changes in various properties along the reaction coordinate. A very strong H-bond of aqua-ligand associated to the O4 site is one of the striking features. The

corresponding ρ_{BCP} is around 0.06 e/au^3 in the reactant and product state, which is twice the value of water associated to thymine without polarization effects by any cation. This density is partially reduced during the reaction course, cf. **Table 4**. A similar, only slightly weaker, H-bond exists between aqua-ligand and the O2 site (in reactant) and the N3 site (in product) of thymine. Observing changes in BCP densities for bonds involving the H3 and H2 protons, one can get some additional insight to the reaction course. These densities start from ca 0.02 , for a weak H-bond, to 0.34 e/au^3, for a fully established covalent bond. Usual values for TS structures and intermediates are in the range of 0.1 - 0.2 e/au^3. From this perspective also the 'ξ = 0.24' structure of the Mg^{2+} cation exhibits a similar behavior.

Reaction Electronic Flux and Bond Order Analysis

The reaction electronic fluxes of **R1, R2,** and **R3** (presented in **Fig. 5)** show a well-defined behavior along the reaction coordinate with two main peaks that define regions where the two PT take place. In the case of **R3** the intensity of the variation of the REF is so small that only fluctuations around the zero regime are observed, however well defined positive and negative peaks show up in the region of the first proton transfer. The REF analysis allowed us to confirm the dominant character that the conformational changes have on the reaction mechanism. Only minor electronic activity can be observed in very narrow areas of RC around the PT processes. In all cases, the first PT and the chemical events that accompany it represent the electronic spontaneous processes, this means that OH bond formation process drives the reaction at this point. According to the bond order analysis depicted on **Fig. 3**, the main events that occur in the region associated to the first peak are the O_{aq}-H bond breaking from the aqua ligand and the O2-H bond formation on the thymine base. These are accompanied by a partial decrease of the bond order of the C2=O2 double bond and an increase of the C2-N3 single bond (cf. **Fig 3**). Meanwhile, the second peak that corresponds to the next PT comprise the non-spontaneous electronic reorganization, involving the dissociation of the N3-H bond coupled to the formation of the new O_{aq}-H from the hydroxo-ligand. his step also completes formation of the C2=N3 and C2-O2 bonds, i.e. enol structural form.

The larger separation of the two peaks in the REF profile of **R2** and **R3,** with respect to **R1,** denotes a difference in the chemical events that take place along its reaction coordinate as discussed above. This is associated with the nature of the metal center, where Zn^{2+} and Hg^{2+} cations are able to accept some portion of electron density from the hydroxo anion and in this way stabilize the 1+ charged intermediate. This situation is depicted in **Fig. 4** where the variation of the bond order of the M-O bond for oxygen from the anionic ligand is displayed. This bond order increases in the region located between the peaks corresponding to the PT processes in the Zn-O and Hg-O cases, while only a marginal increase can be

observed for the Mg^{2+} complex. Thus, the inability of Mg^{2+} to accept electron density from the hydroxo ligand is also responsible for a different shape of the energy profile of the system with the magnesium cation and to a slightly higher energy barrier, as well. Besides the difference related to the stabilization of the charged intermediate species, all the other chemical changes occur in a similar fashion for the all three metal cations, i.e. with similar behavior during the whole reaction coordinate. One important point, which should be mentioned, is the fact that REF is substantially weaker in the system with the mercury cation, cf. **Fig. 5**. This is the reason why its course looks so 'rugged' or 'bumpy'.

In order to elucidate various shapes of REF, all IRC geometries of the system with Zn^{2+} cation were modifies so that zinc atom was replaced in by point charge varied in a series: 0.0 e, 0.5 e, 0.75 e, and 1.0 e. This charge was used for polarization of a single water molecule placed in the positions of original aqua ligand, which assisted the PT's. In this way another series of REF was obtained and the plots are displayed in **Fig. 6**. From this figure, it can be noticed how the spontaneity of the PT processes is changed. In the case of non-polarized water molecule the first PT has to be forced (non-spontaneous course) while the second PT is spontaneous – returning one proton to the hydroxyl anion and recombining water molecule. On the contrary, in higher polarization of this water molecule (using 0.75 and 1.00 e point charge) the first PT is already spontaneous. An interesting situation occurs for point charge of 0.5 e where each of PT exhibits in the vicinity of the corresponding TS both spontaneous and non-spontaneous characters, which indicates that within these PT's the bond formation and bond breaking play an roughly equivalent role.

Decomposition of the Reaction-Energy and the Reaction-Force Profiles

In this part of the study, we consider a comparison of the examined proton transfer processes on thymine nucleobase assisted by hexacoordinated complexes of divalent metals cations, Mg^{2+}, Zn^{2+} and Hg^{2+}. We consider decomposition of the reaction energy following eqs. 3 and 4, and of the reaction force following eqs. 5 and 6. Two ways of partitioning of the system into the fragments are shown in **Fig. 7**. In the "reactant partitioning" thymine and hexacoordinated divalent metals cation are the fragments, see panel *a* of **Fig. 7**. In the "product partitioning", the first fragment includes enol form of thymine with the proton transferred from N3 nitrogen to O2 oxygen, and the second part consists of the hexacoordinated divalent metal cations, see panel *b* of **Fig. 7**.

The goal of the presented ETS-NOCV analysis with two fragmentation schemes is the quantitative assessment of the reaction-driving and reaction-retarding force components resulting from the observed bond-breaking and bond-formation processes. Therefore, we will not discuss in detail all the ETS-NOCV components of

the reaction-energy and the reaction-force profiles (reported in Supplementary Information, **Figs. S3-S13**; the corresponding values for stationary points are collected in **Tabs. S2-S8**). Instead, we will elucidate the "driving" and "retarding" force terms, based on the sums of the appropriate ETS-NOCV contributions for a given partitioning scheme.

Depending on the fragmentation of the system ("reactant" or "product") the driving and retarding components are included in different ETS-NOCV reaction-force terms. Namely, in the "reactant partitioning" scheme, the electrostatic and orbital-interaction energy terms are decreasing (getting more stabilizing), thus leading to the positive reaction force contributions (driving the reaction), $F^R_{drive}(\xi)$. For this partitioning the distortion and the Pauli-repulsion energy components are increasing, thus giving rise to the negative reaction-force contribution (retarding the reaction), $F^R_{retard}(\xi)$. For the "product partitioning" (see **Fig. 7b**), the "driving force", $F^P_{drive}(\xi)$, is composed of the distortion and Pauli-repulsion terms, while the "retarding force", $F^P_{retard}(\xi)$, consists of the electrostatic and orbital interaction contributions. The reaction energy- and force-components grouped as discussed above, are presented in **Fig. 8** for three considered reactions. The left panel presents the "reactant partitioning", while right - the "product partitioning".

Firstly, let us consider the "reactant partitioning" depicted in the left panel of **Fig. 8**. One can see that the sum of the distortion energy and Pauli repulsion components increase rapidly in two regions associated with transition states for the two elementary steps. At the same time, the sum of the electrostatic and orbital interaction energy components decreases substantially in the same TS regions. Namely, the first pronounced change in energy components is associated with the proton transfer from aqua-ligand to O2 site of thymine forming thymine$^+$ cation$^+$ plus monohydroxo-pentaaqua metal complex after the first PT. The driving force component, $F^R_{drive}(\xi)$, defined as the sum of orbital interaction and electrostatic force terms, reveals formation of the O2–H bond, while the retarding force contribution, $F^R_{retard}(\xi)$, (sum of the distortion and Pauli repulsion force terms) exposes the O(aq)–H bond-breaking process. The values of the extremes of the force profiles are collected in **Table S2**. The PT assisted by the Hg^{2+} complex has the largest absolute values of the retarding and driving forces at the first TS, -159 kcal/(mol. a_0 amu$^{1/2}$), and 161 kcal/(mol. a_0 amu$^{1/2}$), respectively. The opposite situation is presented at the second TS, where PT assisted by the Hg^{2+} complex has the smallest absolute values of the retarding and driving forces, compared to other studied systems.

In the second partitioning, the sum of the electrostatic and orbital contributions becomes less stabilizing along the reaction pathway, see the right panel of **Fig. 8**. Two distinctive steps are observed in the reaction energy profiles for both,

the "product partitioning", and the "reactant partitioning". In the first step, the Mg^{2+} complex exhibits the largest retarding force among the studied systems. The second step in the "product partitioning" is associated with the N3–H bond-breaking process (involving the H3 hydrogen atom in **Fig. 7**). Thus, in this process the catalytic effect should be elucidated by metal influence on the hydroxo-group, cf. also discussion to **Fig. 6** and role of point charges on ligand polarization. Therefore, it is not surprising that the retarding force component, $F_{retard}^{P}(\xi)$ (comprising here the orbital interaction and electrostatic terms) changes in the order: Hg (-142 kcal/(mol. a_0 $amu^{1/2}$)), Zn (-148 kcal/(mol. a_0 $amu^{1/2}$)), Mg (-152 kcal/(mol. a_0 $amu^{1/2}$)). It should be also stressed that the limiting process for the Hg^{2+} complex is the first PT, while for the Zn^{2+} and Mg^{2+} systems, it is the second proton transfer that exhibits the highest activation barrier. Therefore, the relatively small value of the retarding force may rationalize the fact that the smallest activation barrier is observed for Zn^{2+} cation, as presented in **Table 1**.

The Influence of Relativistic Spin-Orbit Interaction in the Hg(II) complexes

In the case of Hg^{2+} complexes with thymine the relativistic calculation at the ZORA level were performed at all the stationary points of RC in order to explore the influence of heavy metal element. In **Table S9** the modification of energy profile under the relativistic S-O effect can be noticed. Comparing these values with the results from scalar calculations, it follows that S-O coupling values cause further small stabilization of all the stationary structures but not of the reactants and products. The explanation can be traced simply in shortening of the Hg-O(hydroxo) bond. In this way relativistic effects can slightly more influence electronic density in closer vicinity of the heavy metal cation in comparison with the (longer) Hg-O(aqua) bond, which is present in reactant and product. Nevertheless, all the changes are quite negligible.

Conclusion

In this study the proton transfer from the N3 to O2 sites of thymine was explored using DFT technique at the B3LYP/6-31G(d) computational level in the gas phase.

It was found that a relatively high activation barrier exists in the case of isolated base. Including single water molecule as a proton transferring medium leads to substantial reduction of the barrier height (from 51 to 22 kcal/mol). Nevertheless, a very pronounced decrease of the barrier occurs when a hydrated cation is associated to the nucleobase by formation of two H-bonds. In presence of the hexaaqua cation the barrier for PT is reduced to, at most, 8 kcal/mol in the case of Mg^{2+} complex. The lowest activation barrier was found for thymine in presence of

$[Zn(H_2O)_6]^{2+}$ cation - only 5 kcal/mol. This means that such a proton transfer can occur very quickly and easily.

REF analysis shows that all important electronic changes occur within very short parts of RC connected with TS structures, in very close proximity of the TS and/or at ξ = 0.24 point in the case of Mg^{2+} case. In this way the different coordination pattern of biologically important Mg and Zn metal cations towards negatively charged OH^- anions is clearly elucidated. The ETS-NOCV decomposition scheme allows us to discuss the retarding and driving forces as components of the reaction force profiles. The changes in the electronic structure are reflected by peaks in the profiles of the reaction force components. The extremes of the forces are located in the close TS regions in accord with REF analysis.

Acknowledgement

The authors (JVB) are grateful for support provided by the Grant Agency of Czech Republic project No 16-06240S. Additional support (for FŠ) was obtained from the Grant Agency of Charles University. No. 1145016. Access to computing and storage facilities owned by parties and projects contributing to the National Grid Infrastructure MetaCentrum, provided under the program 'Projects of Large Infrastructure for Research, Development, and Innovations' (LM2010005) is highly appreciated. The calculation results based on ADF were obtained using PL-Grid Infrastructure and resources provided by ACC Cyfronet AGH (Academic Computer Centre Cyfronet, University of Science and Technology).

The Supporting Information is available free of charge via the Internet at http://….

References:

1. Sigel, H. Chem Soc Reviews 1993, 255-267.
2. Sigel, A.; Sigel, H.; Sigel, R. K. O. Structural and Catalytic Roles of Metal Ions in RNA; RSC Cambridge, 2011.
3. Megger, D. A.; Muller, J. Nucleic Acids with Purine- and Pyrimidine-Derived Nucleosides: RSC, Cambridge, 2012.
4. Megger, D. A.; Fonseca Guerra, C.; Bickelhaupt, F. M.; Müller, J. J Inorg Biochem 2011, 105(11), 1398-1404.
5. Sponer, J.; Sabat, M.; Burda, J. V.; Leszczynski, J.; Hobza, P.; Lippert, B. J Biol Inorg Chem 1999, 4(5), 537-545.
6. Johannsen, S.; Megger, N.; Böhme, D.; SigelRoland, K. O.; Müller, J. Nat Chem 2010, 2(3), 229-234.
7. Petrovec, K.; Ravoo, B. J.; Muller, J. Chem Commun 2012, 48(97), 11844-11846.
8. Tanaka, Y.; Oda, S.; Yamaguchi, H.; Kondo, Y.; Kojima, C.; Ono, A. J Am Chem Soc 2007, 129(2), 244-245.

9. Uchiyama, T.; Miura, T.; Takeuchi, H.; Dairaku, T.; Komuro, T.; Kawamura, T.; Kondo, Y.; Benda, L.; Sychrovský, V.; Bouř, P.; Okamoto, I.; Ono, A.; Tanaka, Y. Nucleic Acids Res 2012, 40(12), 5766-5774.
10. Benda, L.; Straka, M.; Sychrovský, V.; Bouř, P.; Tanaka, Y. J Phys Chem A 2012, 116(32), 8313-8320.
11. Yamaguchi, H.; Šebera, J.; Kondo, J.; Oda, S.; Komuro, T.; Kawamura, T.; Daraku, T.; Kondo, Y.; Okamoto, I.; Ono, A.; Burda, J. V.; Kojima, C.; Sychrovský, V.; Tanaka, Y. Nucleic Acid Res 2014, 42, 4094-4099.
12. Torigoe, H.; Ono, A.; Kozasa, T. Chem – Eur J 2010, 16(44), 13218-13225.
13. Šebera, J.; Burda, J.; Straka, M.; Ono, A.; Kojima, C.; Tanaka, Y.; Sychrovský, V. Chem – Eur J 2013, 19(30), 9884-9894.
14. Šebesta, F.; Burda, J. V. J Comput Chem 2017, submitted.
15. Burda, J. V.; Šponer, J.; Hobza, P. J Phys Chem 1996, 100, 7250-7255.
16. Burda, J. V.; Šponer, J.; Leszczynski, J.; Hobza, P. J Phys Chem B 1997, 101, 9670-9677.
17. Šponer, J.; Burda, J. V.; Sabat, M.; Leszczynski, J.; Hobza, P. J Phys Chem A 1998, 102, 5951-5957.
18. Varnali, T.; Tozumcalgan, D. Struct Chem 1995, 6(4-5), 343-348.
19. Tanaka, Y.; Ono, A. Dalton Trans 2008(37), 4965-4974.
20. Benda, L.; Straka, M.; Tanaka, Y.; Sychrovsky, V. Phys Chem Chem Phys 2011, 13(1), 100-103.
21. Ito, T.; Nikaido, G.; Nishimoto, S. I. J Inorg Biochem 2007, 101, 1090-1093.
22. Miyake, Y.; Togashi, H.; Tashiro, M.; Yamaguchi, H.; Oda, S.; Kudo, M.; Tanaka, Y.; Kondo, Y.; Sawa, R.; Fujimoto, T.; Machinami, T.; Ono, A. J Am Chem Soc 2006, 128(7), 2172-2173.
23. Voityuk, A. A. J Phys Chem B 2006, 110(42), 21010-21013.
24. Toro-Labbé, A. J Phys Chem A 1999, 103(22), 4398-4403.
25. Bader, R. F. W. Atoms in Molecules: A Quantum Theory; Oxford Univ. Press: Oxford, 1990.
26. Geerlings, P.; De Proft, F.; Langenaeker, W. Chem Rev 2003, 103(5), 1793-1874.
27. Sen, K. D.; Jorgensen, C. K. Electronegativity: Structure and Bonding; Springer-Verlag: Berlin, 1987.
28. Pearson, R. G. J Am Chem Soc 1985, 107(24), 6801-6806.
29. Parr, R. G.; Donnelly, R. A.; Levy, M.; Palke, W. E. J Chem Phys 1978, 68(8), 3801-3807.
30. Parr, R. G.; Yang, W. Density Functional Theory of Atoms and Molecules; Oxford University Press: Oxford, 1989.
31. Herrera, B.; Toro-Labbé, A. J Phys Chem A 2007, 111(26), 5921-5926.
32. Echegaray, E.; Toro-Labbé, A. J Phys Chem A 2008, 112(46), 11801-11807.
33. Morokuma, K. J Chem Phys 1971, 55(3), 1236-1244.
34. Kitaura, K.; Morokuma, K. Int J Quantum Chem 1976, 10(2), 325-340.
35. Nagase, S.; Morokuma, K. J Am Chem Soc 1978, 100(6), 1666-1672.
36. Joshi, B. D.; Morokuma, K. J Chem Phys 1977, 67(11), 4880-4883.
37. Bickelhaupt, F. M. J Comput Chem 1999, 20(1), 114-128.
38. Fernandez, I.; Bickelhaupt, F. M. Chem Soc Rev 2014, 43(14), 4953-4967.
39. Ziegler, T.; Rauk, A. Theor Chim Acta 1977, 46(1), 1-10.
40. Ziegler, T.; Rauk, A. Inorg Chem 1979, 18(7), 1755-1759.
41. Ziegler, T.; Rauk, A. Inorg Chem 1979, 18(6), 1558-1565.

42. Politzer, P.; Murray, J. S.; Yepes, D.; Jaque, P. J Mol Model 2014, 20(8), 2351.
43. Díaz, S.; Brela, M. Z.; Gutiérrez-Oliva, S.; Toro-Labbé, A.; Michalak, A. J Comput Chem 2017, accepted.
44. Mitoraj, M.; Michalak, A. J Mol Model 2007, 13(2), 347-355.
45. Michalak, A.; Mitoraj, M.; Ziegler, T. J Phys Chem A 2008, 112(9), 1933-1939.
46. Mitoraj, M.; Michalak, A.; Ziegler, T. J Chem Theor Comput 2009, 5, 962.
47. Mitoraj, M. P.; Parafiniuk, M.; Srebro, M.; Handzlik, M.; Buczek, A.; Michalak, A. J Mol Model 2011, 17(9), 2337.
48. Frisch, M. J.; Trucks, G. W.; Schlegel, H. B.; Scuseria, G. E. R., M. A.; Cheeseman, J. R.; Scalmani, G.; Barone, V.; Mennucci, B.; Petersson, G. A.; Nakatsuji, H.; Caricato, M.; Li, X.; Hratchian, H. P.; Izmaylov, A. F.; Bloino, J.; Zheng, G.; Sonnenberg, J. L.; Hada, M.; Ehara, M.; Toyota, K.; ; Fukuda, R. H., J.; Ishida, M.; Nakajima, T.; Honda, Y.; Kitao, O.; Nakai, H.; Vreven, T.; Montgomery, Jr., J. A.; Peralta, J. E.; Ogliaro, F.; Bearpark, M.; Heyd, J. J.; Brothers, E.; Kudin, K. N.; Staroverov, V. N.; Kobayashi, R.; Normand, J.; ; Raghavachari, K. R., A.; Burant, J. C.; Iyengar, S. S.; Tomasi, J.; Cossi, M.; Rega, N.; Millam, N. J.; Klene, M.; Knox, J. E.; Cross, J. B.; Bakken, V.; Adamo, C.; Jaramillo, J.; Gomperts, R.; Stratmann, R. E.; Yazyev, O.; Austin, A. J.; Cammi, R.; ; Pomelli, C. O., J. W.; Martin, R. L.; Morokuma, K.; Zakrzewski, V. G.; Voth, G. A.; Salvador, P.; Dannenberg, J. J.; Dapprich, S.; Daniels, A. D.; Farkas, Ö.; Foresman, J. B.; Ortiz, J. V.; Cioslowski, J.; Fox, D. J. . Gaussian, Inc, 2009, Wallingford CT.
49. Küchle, W.; Dolg, M.; Stoll, H.; Preuss, H. J Chem Phys 1994, 100(10), 7535-7542.
50. Andrae, D.; Haussermann, U.; Dolg, M.; Stoll, H.; Preuss, H. Theor Chim Acta 1990, 77(2), 123-141.
51. Winter, M.; [The University of Sheffield and WebElements Ltd, UK]. 2011, p WebElements: the periodic table on the WWW
52. Saenger, W. Principles of Nucleic Acid Structure; Springer-Verlag: New York, 1983.
53. Weinhold, F.; University of Wisconsin, Madison, Wisconsin 53706: Wisconsin, 2001.
54. Keith, T. A.; http://aim.tkgristmill.com, 2009.
55. Toro-Labbe, A.; Gutierrez-Oliva, S.; Concha, M. C.; Murray, J. S.; Politzer, P. J Chem Phys 2004, 121(10), 4570-4576.
56. Nalewajski, R. F.; Mrozek, J.; Michalak, A. Int J Quantum Chem 1997, 61(3), 589-601.
57. van Lenthe, E.; Snijders, J. G.; Baerends, E. J. J Chem Phys 1996, 105, 6505-6514.
58. te Velde, G.; Bickelhaupt, F. M.; Baerends, E. J.; Fonseca Guerra, C.; van Gisbergen, S. J. A.; Snijders, J. G.; Ziegler, T. J Comput Chem 2001, 22(9), 931-967.
59. Baerends, E. J.; Ellis, D. E.; Ros, P. Chem Phys 1973, 2(1), 41-51.
60. te Velde, G.; Baerends, E. J. J Comput Phys 1992, 99(1), 84-98.
61. Fonseca, C. G.; Visser, O.; Snijders, J. G.; TeVelde, G.; Baerends, E. J. In In Methods and Techniques in Computational Chemistry; METECC-95 Clementi, E.; Corongiu, G., Eds.; STEF: Cagliari, Italy, 1995, p 305.
62. Bakowies, D.; Thiel, W. J Comput Chem 1996, 17(1), 87-108.
63. Gao, J. Acc Chem Res 1996, 29(6), 298-305.

64. Luque, F. J.; Reuter, N.; Cartier, A.; Ruiz-Lopez, M. F. J Phys Chem A 2000, 104, 10923-10931.
65. Olsson, M. H. M.; Hong, G. Y.; Warshel, A. J Am Chem Soc 2003, 125(17), 5025-5039.
66. Thompson, M. A. J Phys Chem 1996, 100, 14492-14507.
67. Tongraar, A.; Liedl, K. R.; Rode, B. M. J Phys Chem A 1997, 101, 6299-6309.
68. Cramer, C. J.; Truhlar, D. G. In Reviews in Computational Chem; Lopkowitz, K. B.; Boyd, D. B., Eds.; VCH Publishers, Inc.: New York, 1995, p 1-72.
69. Kelly, C. P.; Cramer, C. J.; Truhlar, D. G. J Chem Theory Comput 2005, 6, 1133-1152.
70. Bonaccorsi, R.; Palla, P.; Tomasi, J. J Am Chem Soc 1984, 106, 1945-1950.
71. Miertus, S.; Scrocco, E.; Tomasi, J. Chem Phys 1981, 55(1), 117-129.
72. Yepes, D.; Murray, J. S.; Santos, J. C.; Toro-Labbé, A.; Politzer, P.; Jaque, P. J Mol Model 2013, 19(7), 2689-2697.

Table 1 Relative energies and RC of metal assisted PT (energy in kcal/mol, RCs are normalized mass weighted cartesian coordinates - mwc)

	α		β=TS1		γ		Intermediate		α'		β'=TS2		γ'		ΔE_a	ΔE_r
	ξ	E	ξ	E	ξ.	E	ξ	E	ξ	E			ξ	E		
Mg	0.20	4.2	-	-	0.25	5.6	-	-	0.52	7.7	0.53	**7.9**	0.54	7.6	7.9	**4.1**
Zn	0.19	2.6	0.21	**3.2**	0.22	3.1	0.32	**2.7**	0.61	5.1	0.62	***5.2***	0.63	5.0	3.2[a]	**-1.6**
Hg	0.24	2.7	0.25	**2.9**	0.26	2.8	0.48	**2.1**	0.77	6.2	0.78	***6.4***	0.79	6.3	4.3[b]	**4.3**

[a] first TS has higher barrier

[b] second TS has higher barrier.

Table 4 NPA partial charges of the active sites in the reaction course (in e).

	Mg				Zn					Hg				
	Rea	ξ =0.24	TS	Prod	Rea	TS1	Lm1	TS2	Prod	Rea	TS1	Lm1	TS2	Prod
M	1.386	1.380	1.376	1.376	1.295	1.285	1.276	1.279	1.278	1.260	1.232	1.216	1.226	1.238
O(H..O4)	-1.030	-1.094	-1.025	-1.041	-1.028	-1.009	-1.002	-1.010	-1.021	-1.008	-0.996	-0.993	-0.999	-1.004
H(..O4)	0.530	0.531	0.532	0.536	0.532	0.531	0.531	0.536	0.540	0.532	0.529	0.528	0.537	0.541
O4	-0.637	-0.613	-0.625	-0.667	-0.638	-0.610	-0.604	-0.635	-0.683	-0.643	-0.616	-0.609	-0.646	-0.676
N3	-0.661	-0.650	-0.662	-0.684	-0.661	-0.650	-0.646	-0.667	-0.691	-0.660	-0.649	-0.643	-0.671	-0.687
H3	0.430	0.457	0.483	0.521	0.433	0.457	0.469	0.488	0.523	0.433	0.458	0.471	0.494	0.520
O2	-0.661	-0.657	-0.650	-0.653	-0.666	-0.662	-0.655	-0.649	-0.654	-0.664	-0.660	-0.652	-0.652	-0.657
H(..O2)	0.539	0.531	0.535	0.521	0.539	0.534	0.541	0.535	0.523	0.537	0.536	0.545	0.534	0.524
O(H..O2)	-1.027	-1.123	-1.112	-1.018	-1.023	-1.110	-1.140	-1.092	-1.008	-1.013	-1.082	-1.104	-1.047	-0.995
O(aq)	-1.000	-1.009	-1.006	-0.995	-0.990	-0.998	-1.001	-0.994	-0.983	-0.979	-0.987	-0.992	-0.982	-0.974

Table 2 The distances of the most important (H-)bonds (in Å). Abbreviation Rea means reactants, Im - reaction intermediates, Prod - products.

		M-O	N3-H3	H3…O	O2..H2-O	H2-O	C2-O2	N3-C2
Mg	Rea	2.106	1.013	2.083	1.682	1.01	1.239	1.377
	ξ =0.24	2.109	1.028	1.816	1.162	1.319	1.283	1.346
	TS	2.102	1.227	1.271	0.989	2.057	1.317	1.324
	Prod	2.095	1.726	1.016	0.972	3.046	1.329	1.314
Zn	Rea	2.127	1.016	2.138	1.646	1.02	1.239	1.377
	TS1	2.134	1.023	1.923	1.154	1.304	1.276	1.352
	Im	2.139	1.042	1.739	1.035	1.61	1.297	1.339
	TS2	2.132	1.241	1.252	0.982	2.236	1.318	1.323
	Prod	2.125	1.703	1.02	0.973	3.024	1.327	1.316
Hg	Rea	2.398	1.013	2.206	1.636	1.019	1.239	1.379
	TS1	2.413	1.022	1.959	1.165	1.279	1.274	1.354
	Im	2.437	1.039	1.761	1.027	1.628	1.297	1.34
	TS2	2.406	1.299	1.195	0.98	2.298	1.321	1.322
	Prod	2.399	1.655	1.029	0.973	2.835	1.327	1.316

Table 3 Electronic densities in BCPs of key bonds directly involved in PT (in e/au^3).

		N3-H3	H3…O	O2..H2-O	H2-O	M-O	O4…H
Mg	Rea	0.331	0.022	0.049	0.286	0.031	0.058
	ξ =0.24	0.314	0.04	0.187	0.123	0.031	0.042
	TS	0.177	0.142	0.319	0.023	0.032	0.053
	Prod	0.05	0.288	0.338	-	0.032	0.067
Zn	Rea	0.331	0.019	0.053	0.281	0.052	0.063
	TS1	0.319	0.032	0.191	0.126	0.053	0.043
	Lm1	0.3	0.047	0.271	0.059	0.053	0.040
	TS2	0.17	0.149	0.325	0.015	0.054	0.056
	Prod	0.053	0.284	0.336	-	0.054	0.070
Hg	Rea	0.33	0.017	0.054	0.282	0.047	0.062
	TS1	0.32	0.028	0.185	0.134	0.047	0.042
	Lm1	0.303	0.043	0.278	0.056	0.047	0.038
	TS2	0.145	0.172	0.328	0.013	0.047	0.054
	Prod	0.059	0.276	0.336	-	0.048	0.066

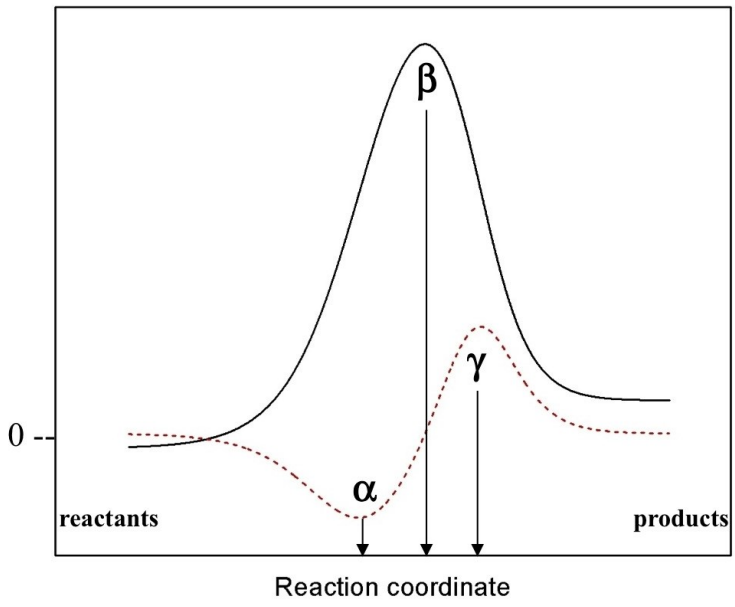

Scheme 1. Characteristic profiles along the intrinsic reaction coordinate R_c of the potential energy *V(ξ)* and the reaction force *F(ξ)*, for a process having an activation barrier in both directions. *V(ξ)* and *F(ξ)* are shown in solid and dashed lines, respectively. The zero of *F(ξ)* is indicated. The points $\xi = \alpha$ and $\xi = \gamma$ correspond to the minimum and maximum of *F(ξ)*; the transition state is at $\xi = \beta$.

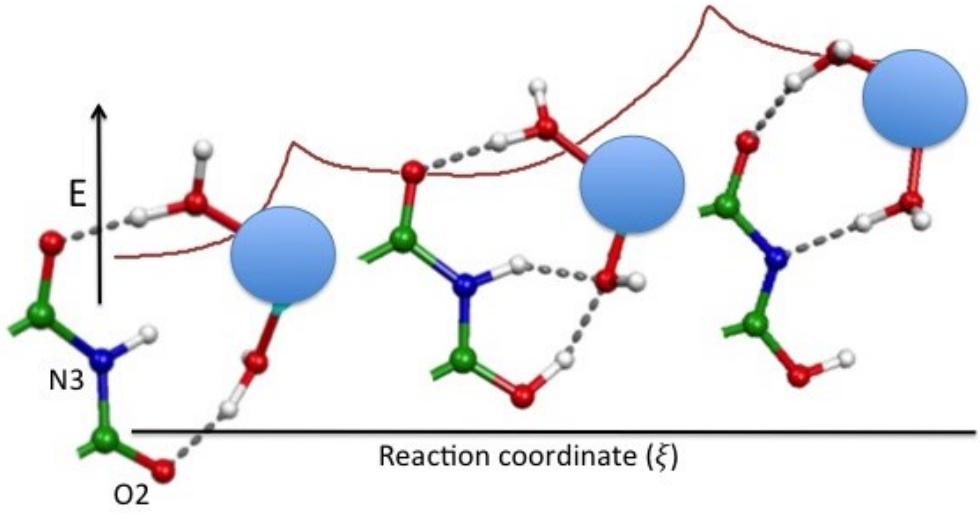

Scheme 2 Graphical description of the assisted PT process in presence of hydrated metal cations and changes in H-bonding pattern along the RC.

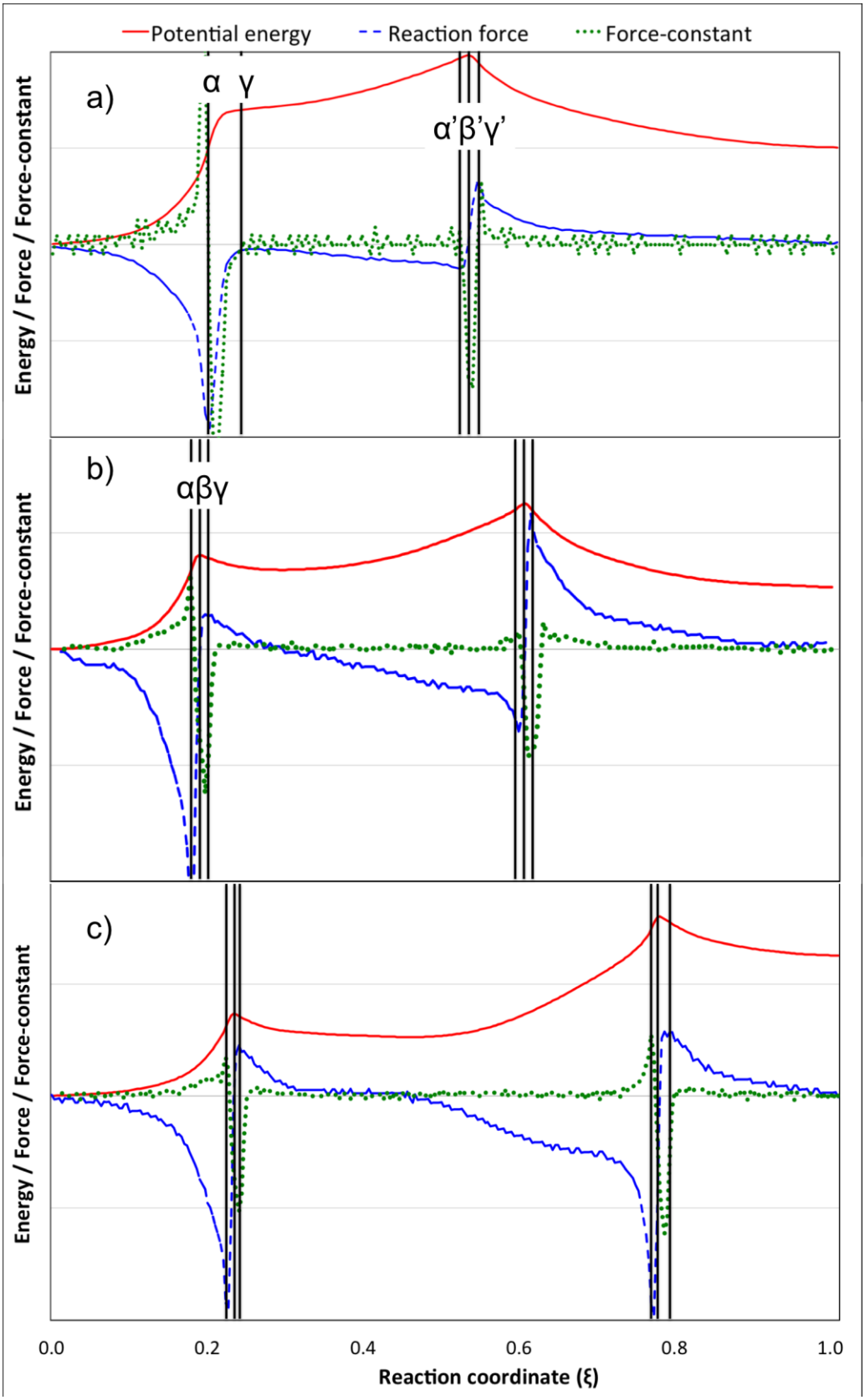

Figure 1 Reaction profiles for the metal assisted PT a) with $[Mg(H_2O)_6]^{2+}$ b) with $[Zn(H_2O)_6]^{2+}$ c) with $[Hg(H_2O)_6]^{2+}$. Energy profile (E) is in solid red line, reaction force (F) is dashed blue line and reaction-force constant (k) is green dotted line (only in the Mg^{2+} case).

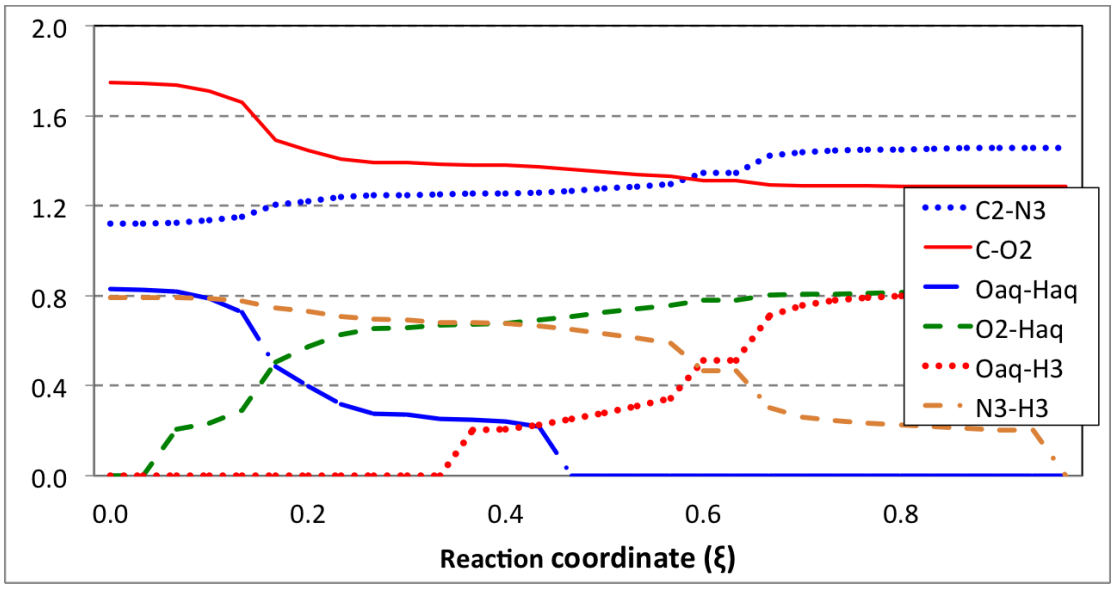

Figure 2. Bond order of the key bonds involved in both PT in the Thymine-Zn^{2+} system.

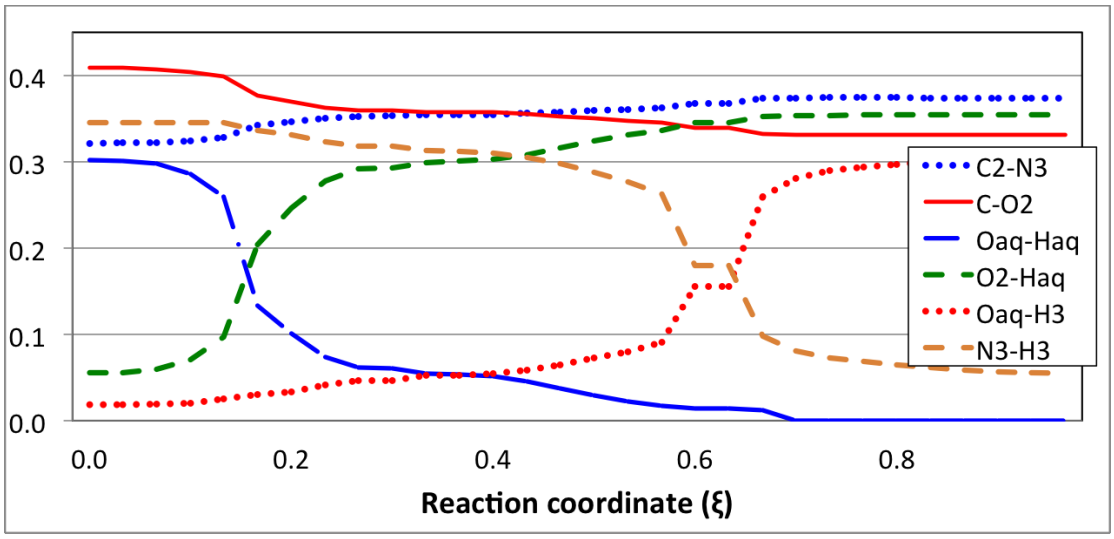

Figure 3. Electron densities in BCP's of the key bonds involved in both PT in the Thymine-Zn^{2+} system.

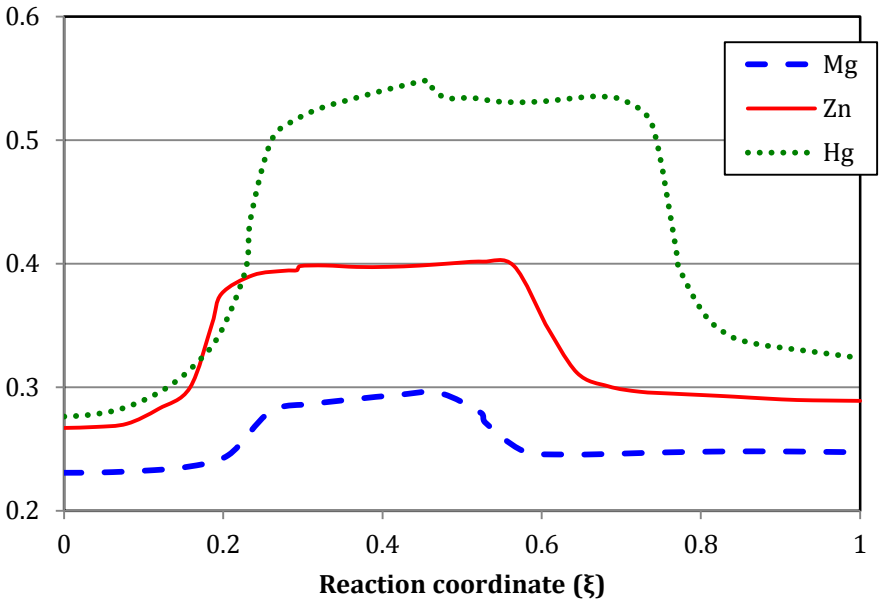

Figure 4 Bond order of M-O(aqua/hydroxo) coordination within the assisted PT.

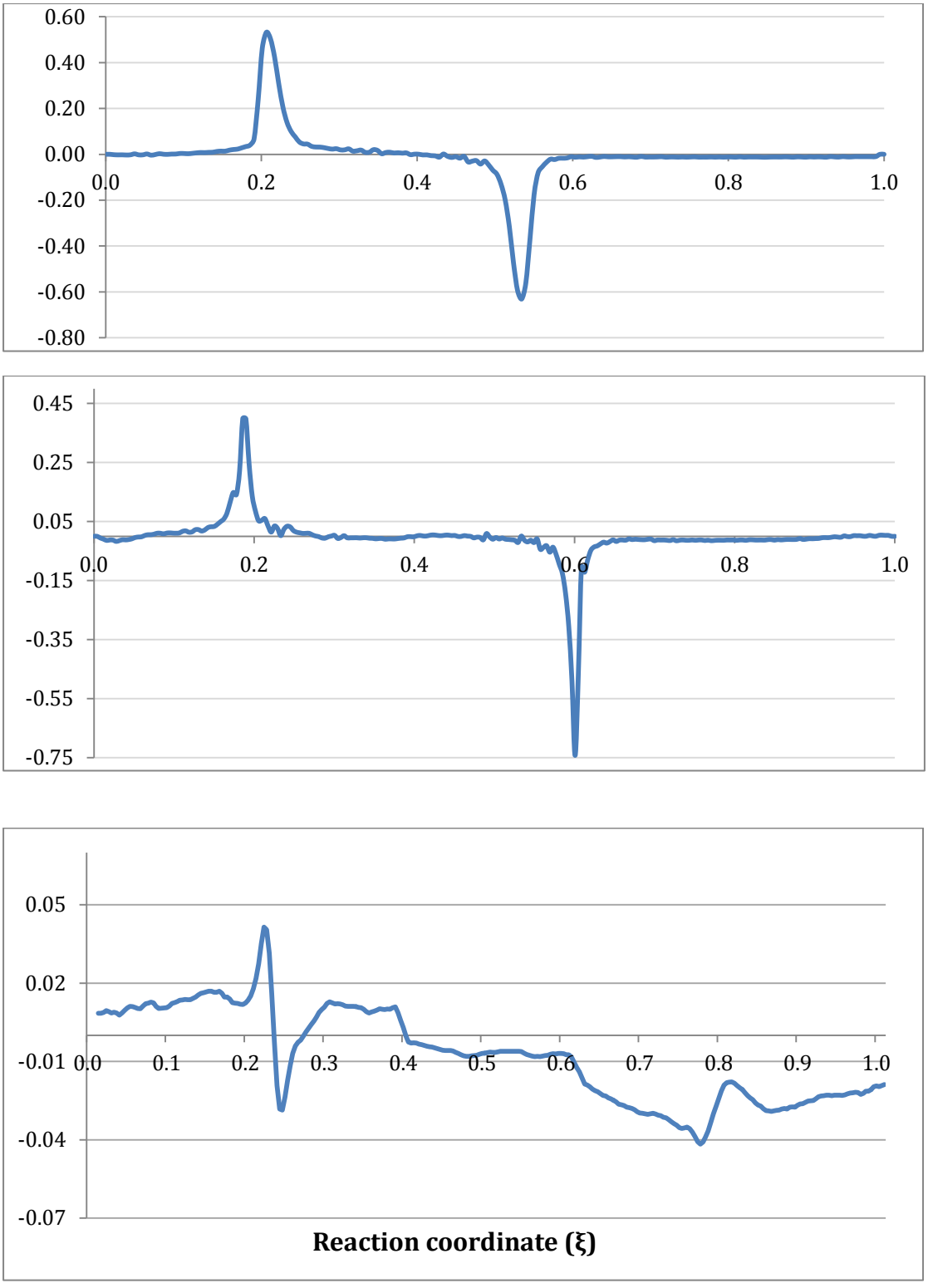

Figure 5 The REF curves for associated PT in the complex of thymine with a) Mg^{2+}, b) Zn^{2+}, and c) Hg^{2+} hydrated cations

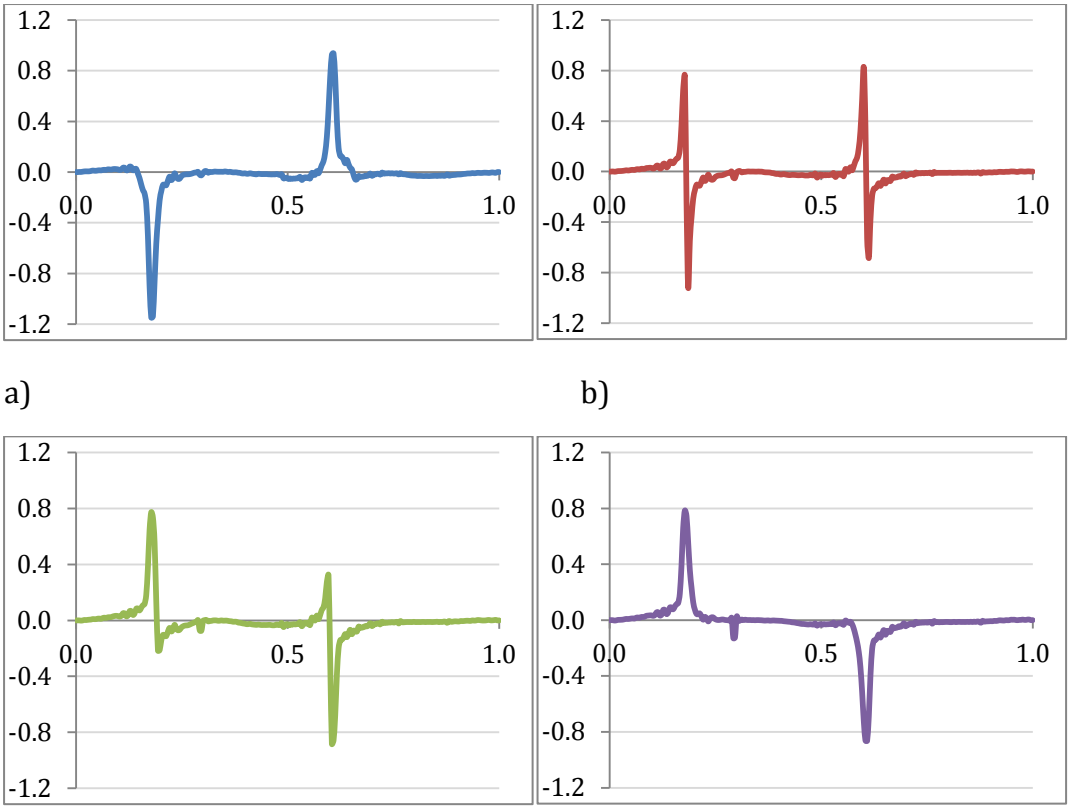

Figure 6 The REF curves for PT in thymine with one water polarized by various charge placed in the position of Zn atom: a) 0.0 e, b) 0.50 e c) 0.75 e, and d) 1.0 e.

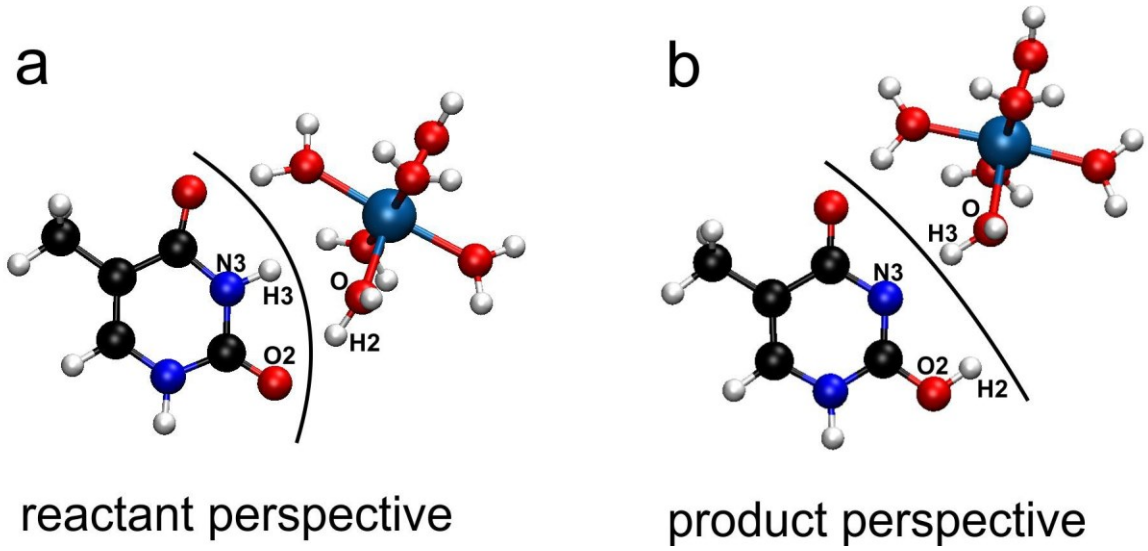

Figure 7. The reactant and product structures of proton transfer processes in thymine assisted by hexacoordinated complexes of divalent metals cations are presented. The reactant and product fragmentation schemes are indicated by the solid line: in the 'reactant perspective' and 'product perspective'.

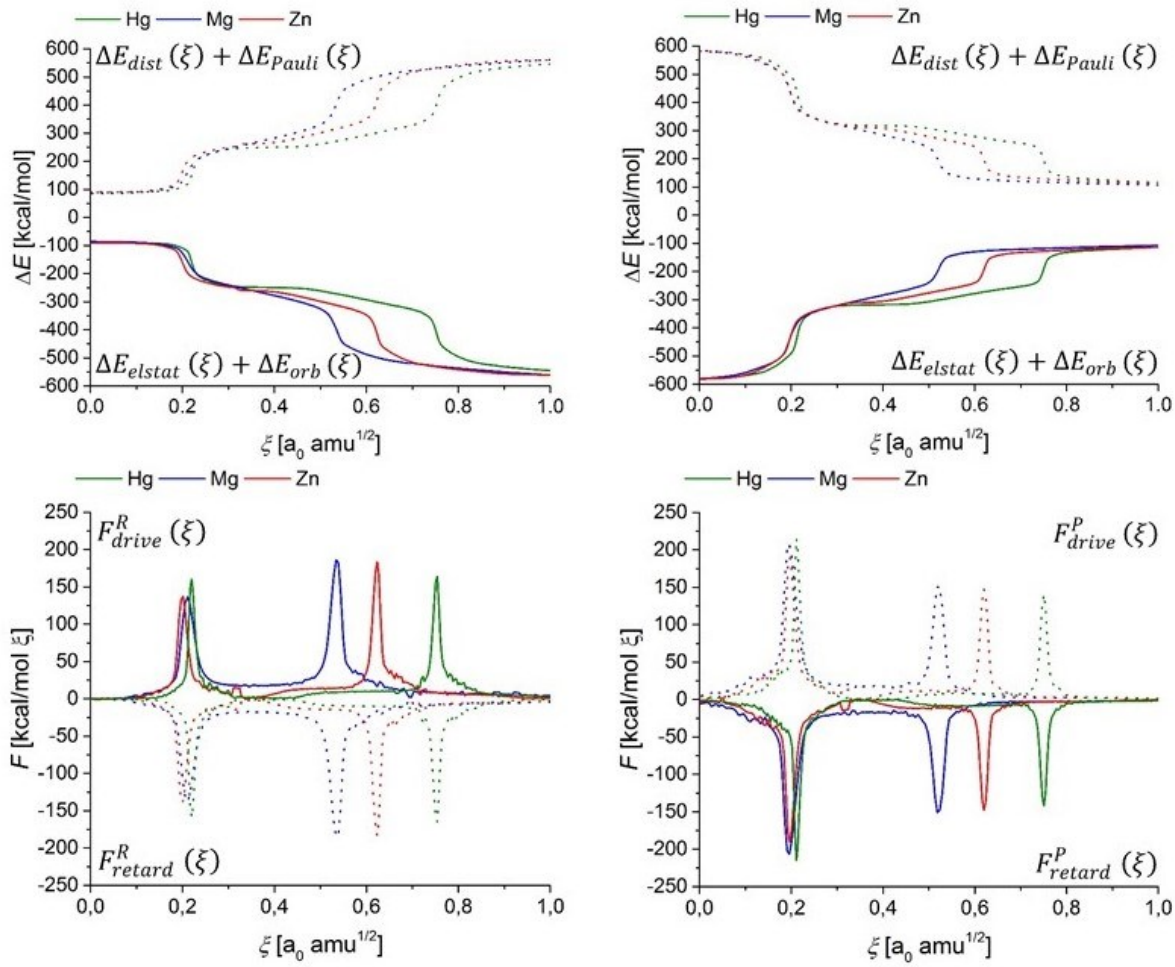

Figure 8. The top part shows the decomposed energy profiles; solid lines present the sum of the electrostatic energy and the orbital-interaction energy, $\Delta E_{elstat}(\xi) + \Delta E_{orb}(\xi)$; dashed lines present the sum of the Pauli repulsion energy and the distortion energy, $\Delta E_{dist}(\xi) + \Delta E_{Pauli}(\xi)$; for the reactant partitioning (left part) and the product partitioning (right part). The bottom part presents the corresponding reaction force components for the reactant and product partitioning respectively. The three analyzed systems: thymine with hexacoordinated divalent metals cations are color coded: green - Hg^{2+}, blue - Mg^{2+} and red - Zn^{2+}.

QM/MM Umbrella sampling MD Study of Thymine Interaction with Mercury Cation in Explicit Water Solution.

*Filip Šebesta,[a] Vladimír Sychrovský,[b] Yoshiyuki Tanaka,[c] and Jaroslav V. Burda[a] **

[a)] Department of Chemical Physics and Optics, Faculty of Mathematics and Physics, Charles University in Prague, Ke Karlovu 3, 121 16 Prague, Czech Republic
[b)] Institute of Organic Chemistry and Biochemistry, v.v.i., Academy of Sciences of the Czech Republic, Flemingovo náměstí 2, 166 10, Prague, Czech Republic
[c)]Tohoku University, Grad Sch Pharmaceut Sci, Lab Mol Transformat, Aoba Ku, Sendai, Miyagi 9808578, Japan

* corresponding author

Introduction

The protonation of DNA bases plays a crucial role for metal binding, particularly during formation of metal bridged mismatches.[1] Occurence of such structures has been confirmed experimentally. In the case of the Ag(I) cation, there is an evidence of formation of C(N3)-Ag-C(N3) linkage[2] and further of metal-bridged imidazole-Ag(I)-imidazole pairs. Presence of the latter structural motif in a DNA oligomer with ^{15}N-labelled imidazole mismatches was proved based on $^{1}J(^{15}N,^{107/109}Ag)$ couplings from NMR measurements. Analogously, in 2007 formation of T(N3)-Hg(II)-T(N3) linkages was confirmed in the case of thymine mismatches based on ^{15}N NMR chemical shifts and ^{15}N-^{15}N J couplings.[3] The first crystal structure of the consecutive mercury linkages was published for the DNA dodecamer d(CGCGATTTCGCG) with T:T mismatches seven years later.[4] Using the isothermal titration calorimetry, the reaction Gibbs free energy of -8 kcal·mol^{-1} corresponding to formation of the T(N3)-Hg(II)-T(N3) linkage was obtained,[5] which is in accord with the calculated value at the ONIOM QM/QM level for a three base-pair model by Yamaguchi et al.[6] A detailed reaction mechanism was proposed by Šebera et al.[1] and corresponding energy profile was calculated at ONIOM B3LYP/BP86 level for the same three base-pair model with the $[Hg(H_2O)_4OH]^+$ complex. In the beginning of the reaction the hydrated mercury cation $[Hg(H_2O)_4OH]^+$ is located in the major groove in the proximity of the T:T mismatch. In the first step, proton transfer (PT) from one of the nitrogen N3 atoms to

the hydroxo ligand occurs and subsequently the first Hg-N3 bond is formed. The activation barrier of 2.9 kcal·mol^{-1} associated with this PT is very low. The reaction continues with the second PT from nitrogen N3 to oxygen O2 on the opposite thymine moiety. This keto-enol transfer is assisted by a water molecule released from the original $[Hg(H_2O)_4OH]^+$ cation. This step is connected with a significantly higher activation barrier of 16.5 kcal·mol^{-1} followed by a release of aqua ligands and coordination of the Hg(II) cation to oxygen O4 of the second thymine. The N3-Hg(II)-N3 linkage is not formed until the transferred proton from O2 is released. The occurrence of the discussed linkages can be detected using Raman spectroscopy by a characteristic Raman marker band, which corresponds to the C4=O4 bond stretching mode.[7] Important frequency shifts were also qualitatively reproduced using DFT and MP2 methods for the model $(TpT{\cdot}Hg)_2$ system.[8]

Since a DNA sequence with T:T mismatches is an efficient target for Hg(II) cations, it can be used for detection of mercury pollution in environment. In addition, several metal cations can be kept between consecutive pyrimidine-pyrimidine mismatches,[4,9] which leads to an idea that such a material can be used for construction of electric nano-devices.

In this study, we focus on detailed description of the first Hg-N3 coordination as a intiating step of the mercury cation binding to a T:T mismatch. Šebera et al.[1] determined the height of activation barriers within the proposed reaction using a relatively small model – N1-methylthymine with the $[Hg(H_2O)OH]^+$ complex. Therefore, we decided to reinvestigate this problem using a different description. Since the dynamic effects can play an important role in proton transfers, the QM/MM umbrella sampling MD method is selected. N1-methylthymine remains as a model structure in our calculations, however, the hydrated Hg^{2+} cation is represented by $[Hg(H_2O)_5(OH)]^+$ or $Hg(H_2O)_4(OH)_2$ clusters with explicit solvent at MM level. Thus, two possible protonation states are considered and the resulting reaction courses are compared. For comparison, static DFT calculations are performed for mono- and dihydroxo complexes with four ligands tetra-coordinated mercury caton i.e. $Hg(H_2O)_3(OH)]^+$ or $Hg(H_2O)_2(OH)_2$.

Computational details

QM/MM MD calculations were carried out using QMS 1.7 interface[10] combining Gaussian 09[71] and Amber 11[72] programs for QM and MM parts,

respectively. Topology files for solvated QM parts: a) thymine + $[Hg(H_2O)_5(OH)]^+$ and b) thymine + $Hg(H_2O)_4(OH)_2$ were prepared using the AmberTools15 package. QM part was initially optimized at the B3LYP/6-31+G(d)/MWB60 level using the IEFPCM/UFF solvation model. Based on the electrostatic potential calculated for the optimized geometries at the B3LYP/6-31++G(d,p)/MWB60 level, RESP charges for the isolated parts were determined within the *respgen* and *resp* utilities. Amber ff10 parameters are used for a description of the thymine, GAFF (General Amber Force Field) for description of ligands and parameters connected with the Hg(II) cation were taken from our previous study.[73] Since we employ the subtractive scheme of the QM/MM method, accuracy of the bonding parameters for the QM part does not play important role since MM bonding energy of this part is completely subtracted within QM/MM calculation.

The QM part was surrounded with ca 1000 TIP3P water molecules in order to include water solution. The temperature of these systems was initially equilibrated to 300 K in 100 ps NVT simulation using Berendsen thermostat. Subsequently, the pressure in the systems was settled at 1 atm in 400 ps NPT simulation using Langevin dynamics. In both equilibration steps, periodic boundary conditions (PBC) with cut off of 10 Å were applied. The time step of 2 fs was used together with SHAKE constraint algorithm. During all pure MM runs, the QM part was kept frozen. A rectangular simulation box with length of edges of ca 30 Å to 35 Å was

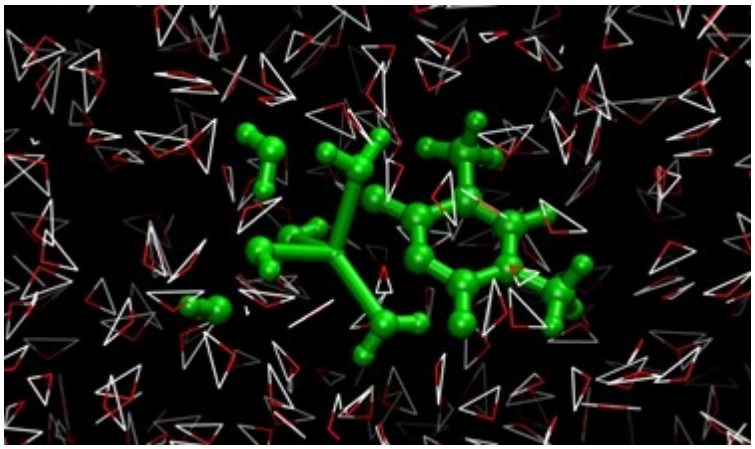

Figure 1: Partitioning of the system in the dihydroxo branch. The green-colored molecules represent the QM part.

obtained as the result. This step is important due to the fact that QMS interface does not enable running a NPT simulation and the size of the box remains fixed in the following calculations.

The equilibrated systems were re-heated within QM/MM MD simulations from 10 K to 298 K with the unrestricted QM part (for partitioning see **Fig 13**). The QM region was described at the B3LYP-GD3BJ/LANL2DZ level. Polarization of the wave function by surrounding water molecules was included using the electronic embedding when a term corresponding to electrostatic interaction with all solvent molecules and counterions was added into the QM Hamiltonian. The previous MM parametrization was maintained. The systems were developed using Velocity Verlet propagator with the time step of 0.5 fs.

After 2.5 ps temperature equilibration with the Berendsen thermostat, the Umbrella Sampling MD was performed. For this purpose the reaction coordinate was mapped to the distance between the Hg^{2+} cation and nitrogen N3. The system was localized along the reaction coordinate by a set of harmonic potentials with the force constant of 70 kcal·mol^{-1} restraining the Hg-N3 distance. Centers of the bias potentials were by 0.2 Å apart in order to form a set of overlapping windows. Moreover, in the vicinity of the transition state (the Hg-N3 distance in the range 3.6 Å and 2.6 Å), extra windows were considered. They were characterized by the distance of 0.1 Å between their minima with the higher force constant of 150 kcal·mol^{-1}. This should ensure a sufficient sampling of the transition region.

Propagation lasted 10 ps in each window and the temperature was kept at 298 K by Langevin dynamics. Structures from each twetieth step (i. e. each 10 fs) were collected and the QM/MM energy was reevaluated using larger bases set 6-31+G(d)/MWB60 (B2) in the QM calculations. Obtained probability distributions from all windows were further processed using Weighted Histogram Analysis Method (WHAM) and Umbrella Integration (UI) technique in order to determine a free energy profile for the studied reactions. Finally, the obtained profiles were corrected using the Free Energy Perturbation (FEP) approach where shifts in Gibbs free energy

$$\Delta G_{FEP} = G_{6-31+G(d)/MWB60} - G_{LANL2DZ}$$
$$= -k_b T ln \left\langle exp\left\{\frac{-E_{6-31+G(d)/MWB60} - E_{LANL2DZ}}{k_b T}\right\}\right\rangle_{LANL2DZ}$$

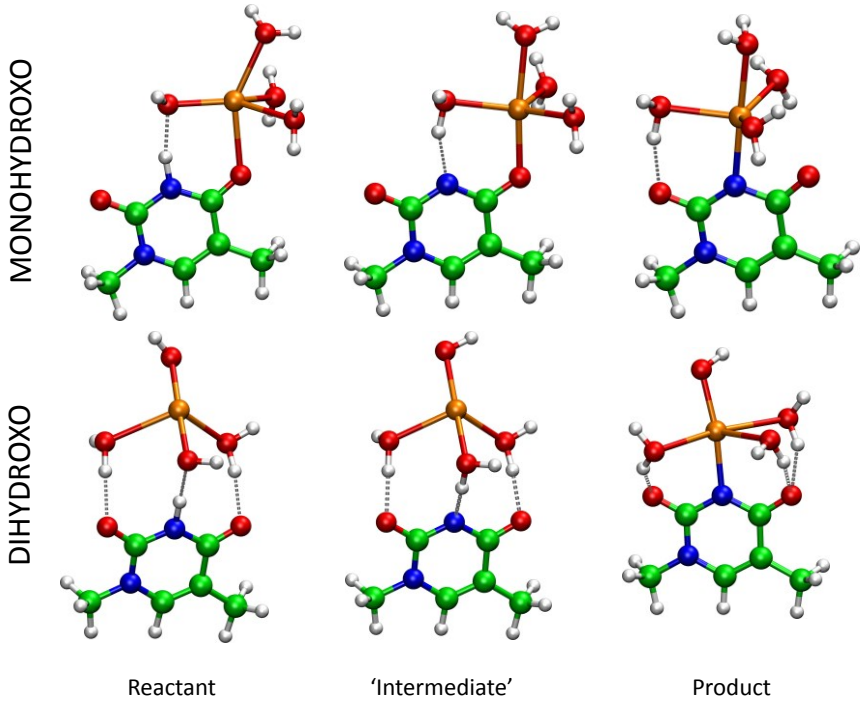

Figure 2: Geometries of optimized minima within the mono- and dihydroxo branches at the DFT level.

were determined from the differences between calculations with larger and smaller basis set.

DFT static calculations were carried out for model systems consisted of thymine and $[Hg(H_2O)_3(OH)]^+$ and $Hg(H_2O)_2(OH)_2$ complexes using Gaussian 09. The structures were optimized with the ω-B97XD functional, the 6-31+G(d) basis set, and Stuttgart's pseudopotential MWB60 for the mercury cation. The surrounding solvent was simulated using the C-PCM/Klamt implicit solvation model. At the same level, the frequency analysis was performed. The final electronic energies were obtained by singlepoint (SP) calculations at the B3LYP-GD3BJ/6-311++G(2df,2pd)/MWB60 level using the DPCM/scaled-UAKS solvation model[11] with Wertz's corrections[12,13] to Gibbs free energy.

Structural changes within the reaction course

In QM/MM MD simulation, the hydrated mercury cation is pulled to nitrogen N3 from the Hg-N3 distance (hereinafter denoted ξ) of 5.6 Å. Regardless whether the mono- or dihydroxo Hg^{2+} cluster is considered, interaction with thymine moiety

is initially mediated by a water molecule whose position is stabilized by H-bond to hydrogen H3. In fact, the Hg^{2+} cation is not hexa-coordinated. It follows from the DFT calculations that in the dihydroxo (DH) complex, the coordination number of mercury is four where the Hg-O bonds (2.1 Å) to hydroxo ligands are significantly shorter than the bonds to aqua ligands (2.6 Å). In the monohydroxo (MH) complex, an arrangement of the first solvation shell is very similar. Hg-O(H_2O) bonds are 2.3-2.4 Å and occurrence of usually five-coordinated clusters is observed in the simulations.

Shortening the Hg-N3 distance, a H-bond between an aqua ligand and oxygen O4 is established. When ξ is below 5 Å, the H-bond between the hydroxo ligand and hydrogen H3 is observed in the systems. More exactly, it is present from ξ = 4.9 Å and ξ = 4.7 Å in the MH and DH branches, respectively. The first evidence of proton transfer is noticed from $\xi \approx$ 4.2 Å (MH) and $\xi \approx$ 3.9 Å (DH) and the transferred proton becomes a part of aqua ligand when the ξ reaches 3.2 Å (MH) and 3.3 Å (DH), respectively. The difference between both MH and DH branches in the region of the proton transfer dwells in the fact that while the DH complex is stabilized by H-bonds to the keto groups of the thymine moiety, in the MH branch the Hg^{2+} cation is directly coordinated to the oxygen O4. This coordination is noticeable from ξ = 3.7 Å and the Hg-O4 bond length achieves its minimum (approximately 2.25 Å) for ξ = 3.3 Å. Subsequently, the aqua ligand moves away from vicinity of nitrogen N3 and the Hg-N3 bond is formed. In the products, the structures are stabilized by H-bonds between aqua ligands and oxygens O2 and O4 of the thymine moiety in the same way as in ref. 14. In the DH branch, the remaining OH ligand is located in the trans-position to nitrogen N3. It should be remarked that proton transfers between aqua and hydroxo ligands were observed in the simulations. If the systems were not sufficiently equilibrated in the windows close to the products, the keto-enol transfer could be noticed.

The static DFT calculations were performed for the four-coordinated MH and HD complexes. In the reactants, the DH complex is stabilized by three H-bonds between its aqua ligands and both keto groups of the thymine and the hydroxo ligand and the hydrogen H3. In the case of the MH complex, the Hg^{2+} cation is already coordinated to the oxygen O4 (cf. **Fig. 2**). At the optimization level, two transition states are determined. The first one (**TS1**) corresponds to proton transfer from the N3 position to the hydroxo ligand forming a meta-stable intermediate (**Im**). The second

one (**TS2**) is associated with binding of the Hg^{2+} cation to the free N3 position. The products are stabilized in the same way as in the QM/MM simulations. Nevertheless, the first transition state **TS1** in the both branches is not real. It suffices to add the entropic contributions to the electronic energy at the optimization level and the Gibbs free energy increases towards the 'intermediate' in the DH branch. The **TS1** structure in the MH branch becomes unreal at the level of the SP calculations. As a result, the only real transition state (**TS2**) is obtained. The Hg-N3 and Hg-O4 (solely for the MH branch) distances are presented in **Table 1** for comparison with the geometry parameters received in the QM/MM simulations. They will be discussed together with the QM/MM free energy profiles in detail.

Free energy profiles

The association of the mercury complex with methylthymine represents a slightly exergonic process (cf. **Fig. 3**) at the level of the static DFT calculations. Let's set energy of the reactants to zero for needs of a following discussion. The 'first activation barrier' associated with the N3↔OH proton transfer (**TS1**) lies 7.6 kcal·mol^{-1} high in the MH branch and the energy of followed-up 'intermediate' is 8.0 kcal·mol^{-1}. An energy of the corresponding alleged **TS1** state in the DH branch is slightly lower (6.2 kcal·mol^{-1}) and Gibbs free energy of the subsequent 'intermediate' state represents 8.1 kcal·mol^{-1}. Since the Gibbs free energy increases up to 'second' transition state **TS2** in both MH and DH branches within SP calculations, the resulting activation barriers are 10.4 and 12.3 kcal·mol^{-1} high, respectively (cf. **Table 2**). In MH branch, breaking of N3…H(OH) H-bond is

	Monohydroxo		*Dihydroxo*
	Hg-N3	Hg-O4	Hg-N3
Reactant	3.511	2.455	3.873
TS1	3.365	2.313	3.735
Im	3.236	2.209	3.734
TS2	3.037	2.201	3.102
Product	2.213	2.752	2.161

Table 1: The Hg-N3 and Hg-O4 (only for monohydroxo branch) distances (in Å) for the systems in stationary points along the reaction coordinate determined at the DFT level.

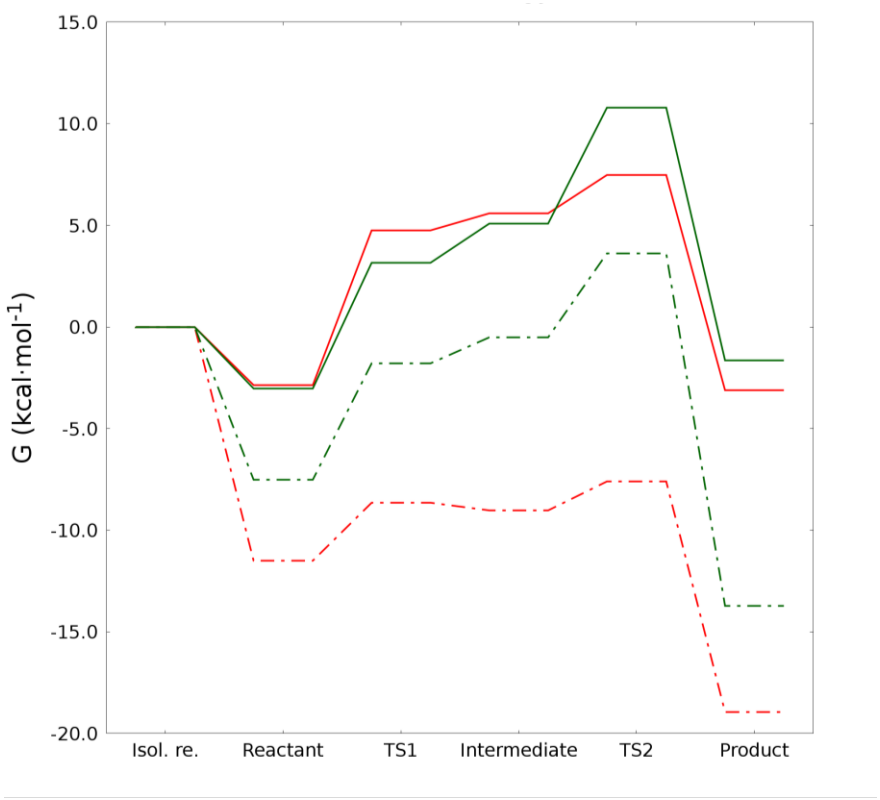

Figure 3: The calculated Gibbs free energy profiles at the DFT level. The red lines correspond to the monohydroxo branch and the green lines to the dihydroxo branch. The energy profiles obtained at the B3LYP-GD3BJ/6-311++G(2df,2pd)/MWB60/IEF-PCM/scaled-UAKS level are depicted by the full lines while profiles determined at the ω-B97XD/6-31+G(d)/MWB60/C-PCM/Klamt level by dash-dotted lines. Wertz's corrections are included.

partially compensated by formation of H-bonds to the keto groups of the thymine moiety.

In total, binding of the hydrated Hg^{2+} cation into the N3 position represents a slightly exergonic process where the reaction Gibbs free energy is -1.7 and -3.1 kcal·mol^{-1} in the DH and MH branches, respectively. If the non-electrostatic solvation contributions are included, Gibbs association energies of reactants are nearly zero and the total reaction is slightly endergonic (0.34 (MH), 2.3 kcal·mol^{-1} (DH)). The activation barriers remain almost unchanged.

The free energy profiles obtained from the QM/MM simulation are much closer to results obtained at the optimization level than to the SP calculations (cf. **Fig. 3,4**). Here, only the profile included FEP corrections will be discussed. Owing to the fact that FEP corrections are evaluated using the 6-31+G(d)/MWB60 basis set, the QM/MM profiles exhibit similar characteristics as the results obtained at the optimization level. The reaction starts with the large decrease of roughly 7 kcal·mol^{-1}

corresponding to association of the reactant. In the DFT calculations at the optimization level, the free energy decreases even more. In the MH branch, a low barrier of 4.1 kcal·mol^{-1} related to the H3↔OH proton transfer immediately follows. Its peak corresponds to ξ = 4.4 Å. The structure is subsequently stabilized by coordination of the Hg^{2+} cation to the O4 position towards the second minimum on the RC. In the reactant optimized at the DFT level, the Hg-O4 bond is already established and ξ = 3.5 Å, which roughly corresponds with a groove in the energy profile at ξ = 3.7 Å (cf. **Fig 4**). The second barrier of 2.5 kcal·mol^{-1}, which is associated with the Hg-N3 bond formation, is little higher than it follows from the DFT calculations. In the DH branch, solely one activation barrier of 4.8 kcal·mol^{-1} is obtained, which is a significantly lower value in comparison with the DFT calculations. On the other hand, a small plateau can be recognized during the energy increase at ξ = 3.7 Å, which exactly corresponds to the Hg-N3 distance in the unreal intermediate. A final decrease of energy by more than 10 kcal·mol^{-1} is similar to the DFT results in both branches.

	Optimization			*SP calculations*			
DH	*ΔE*	*ΔG*	*ΔG(W)*	*ΔE*	*ΔG*	*ΔG(W)*	*ΔG(W+n)*
Reaktant	-14.4	1.1	-7.5	-9.9	5.5	-3.0	0.0
TS1	-7.8	6.8	-1.8	-2.9	11.7	3.1	4.9
Intermediate	-8.0	8.1	-0.5	-2.4	13.7	5.1	6.9
TS2	-5.9	12.2	3.6	1.3	19.4	10.8	12.3
Produkt	-19.7	-5.1	-13.7	-7.6	7.0	-1.7	2.3
MH	*ΔE*	*ΔG*	*ΔG(W)*	*ΔE*	*ΔG*	*ΔG(W)*	*ΔG(W+n)*
Reaktant	-15.3	-2.9	-11.5	-6.7	5.7	-2.9	0.4
TS1	-10.6	-0.1	-8.6	2.9	13.4	4.8	7.6
Intermediate	-12.9	-0.4	-9.0	1.7	14.2	5.6	8.7
TS2	-12.8	1.0	-7.6	2.3	16.1	7.5	10.7
Produkt	-23.0	-10.3	-18.9	-7.1	5.5	-3.1	0.3

Table 2: Energy of stationary points along the reaction coordinate determined at the optimization and SP calculation level within DFT calculations. The zero energy corresponds to isolated reactants. All energies are in kcal·mol^{-1} and *W* in parenthesis denotes inclusion of Wertz's corrections and *n* addition of the non-electrostatic solvation contributions.

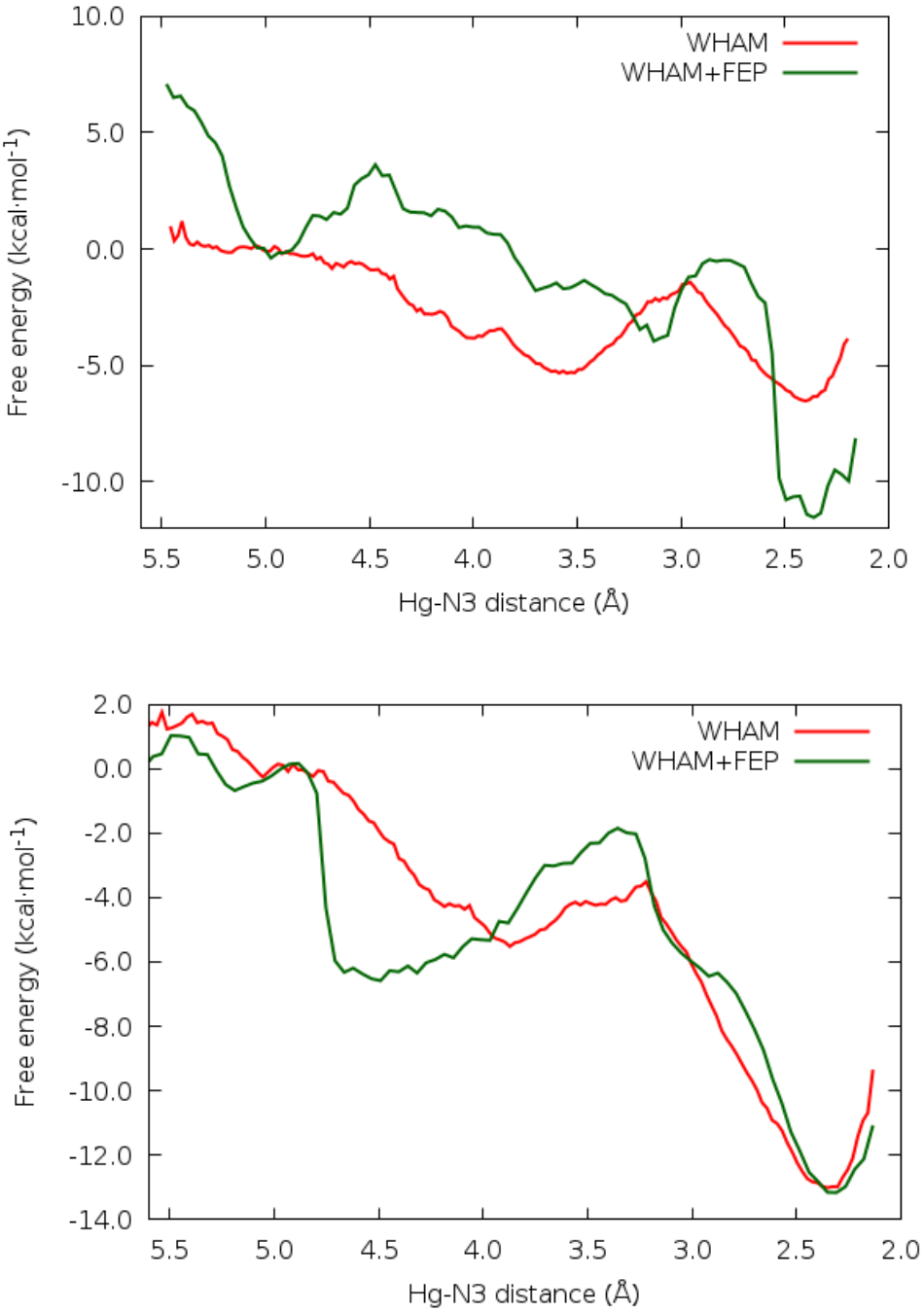

Figure 4: The free energy profiles determined using the QM/MM umbrella sampling MD simulations. The total profiles are constructed using the WHAM method (red lines). The profiles are subsequently corrected by FEP correction determined at the B3LYP-GD3BJ/6-31+G(d)/MWB60 level (green lines). The above plot corresponds to the monohydroxo system and the below one to the dihydroxo branch.

Conclusion

The QM/MM energy profiles with the FEP correction in the MH and DH branches exhibit similar characteristics as the profiles obtained at the w-B97XD/6-31+G(d). Nevertheless, the activation barrier in the case of DH complex is about twice lower within the QM/MM simulations. It should be remarked that employment of Wertz's corrections in static DFT calculation is crucial for obtaining similar profiles. In fact, the initial energy decrease, which accompanies the association of the reactants, is obtained only when the Wertz's corrections are included. In addition, it can be seen that the N3↔OH proton transfer is a dynamical process that occurs in the range of the Hg-N3 distances from more than 4.0 Å to 3.3 Å. On the basis of the SP calculations, only one activation barrier is present in both branches. Its height is 10.4 and 12.3 kcal·mol^{-1} in the MH and DH branches, respectively. Moreover, the rate determining steps in the QM/MM calculations correspond with barrier of 4-5 kcal·mol^{-1}. From this perspective, the barrier of 2.9 kcal·mol^{-1} suggested for the considered process by Šebera et al.[1] is underestimated.

Acknowledgement:

Authors are grateful to Grant Agency of Czech Republic project No 16-06240S for supporting this study. Additional support (for FŠ) was obtained from the Grant Agency of Charles University. No.1145016. Access to computing facilities owned by parties and projects contributing to the National Grid Infrastructure MetaCentrum, provided under the program 'Projects of Large Infrastructure for Research, Development, and Innovations' (LM2010005) is highly appreciated.

References:

(1) Šebera, J.; Burda, J.; Straka, M.; Ono, A.; Kojima, C.; Tanaka, Y.; Sychrovský, V. *Chem. – Eur. J.* **2013**, *19*, 9884.

(2) Megger, D. A.; Müller, J. *Nucleosides, Nucleotides and Nucleic Acids* **2010**, *29*, 27.

(3) Tanaka, Y.; Oda, S.; Yamaguchi, H.; Kondo, Y.; Kojima, C.; Ono, A. *J. Am. Chem. Soc.* **2007**, *129*, 244.

(4) Kondo, J.; Yamada, T.; Hirose, C.; Okamoto, I.; Tanaka, Y.; Ono, A. *Angewandte Chemie International Edition* **2014**, *53*, 2385.

(5) Torigoe, H.; Ono, A.; Kozasa, T. *Chem. – Eur. J.* **2010**, *16*, 13218.

(6) Yamaguchi, H.; Šebera, J.; Kondo, J.; Oda, S.; Komuro, T.; Kawamura, T.; Daraku, T.; Kondo, Y.; Okamoto, I.; Ono, A.; Burda, J. V.; Kojima, C.; Sychrovský, V.; Tanaka, Y. *Nucleic Acid Res.* **2014**, *42*, 4094.

(7) Uchiyama, T.; Miura, T.; Takeuchi, H.; Dairaku, T.; Komuro, T.; Kawamura, T.; Kondo, Y.; Benda, L.; Sychrovský, V.; Bouř, P.; Okamoto, I.; Ono, A.; Tanaka, Y. *Nucleic Acids Res.* **2012**, *40*, 5766.

(8) Benda, L.; Straka, M.; Sychrovský, V.; Bouř, P.; Tanaka, Y. *J. Phys. Chem. A* **2012**, *116*, 8313.

(9) Benda, L.; Straka, M.; Tanaka, Y.; Sychrovsky, V. *Phys. Chem. Chem. Phys.* **2011**, *13*, 100.

(10) Futera, Z.; Burda, J. V. *J. Comput. Chem.* **2014**, *35*, 1446.

(11) Zimmermann, T.; Burda, J. V. *J. Chem. Phys.* **2009**, *131*, 135101.

(12) Wertz, D. H. *J. Am.chem. Soc.* **1980**, *102*, 5316.

(13) Cheng, M.-J.; Nielsen, R. J.; Goddard Iii, W. A. *Chemical Communications* **2014**, *50*, 10994.

(14) Šebesta, F.; Brela, M. Z.; Diaz, S.; Miranda, S.; Murray, J. S.; Gutiérrez-Oliva, S.; Toro-Labbé, A.; Michalak, A.; Burda, J. V. *Journal of Computational Chemistry* **2017**, in print.

JCTC Journal of Chemical Theory and Computation

Article

pubs.acs.org/JCTC

Estimation of Transition-Metal Empirical Parameters for Molecular Mechanical Force Fields

Filip Šebesta, Vladislav Sláma, Josef Melcr, Zdeněk Futera,[†] and Jaroslav V. Burda*

Department of Chemical Physics and Optics, Faculty of Mathematics and Physics, Charles University, Ke Karlovu 3, 121 16 Prague 2, Czech Republic

Supporting Information

ABSTRACT: Force-field parameters of the first row transition metals together with a few additional common elements such as those from the second (Rh, Ru) and third (Hg, Pt) rows of elements in ligated forms were determined based on the density functional theory calculations. Bonding characteristics were determined by averaging metal−ligand force constants in optimal geometries from several chosen complexes of each metal in the most common oxidation numbers and structural arrangements. Parameters of Lennard-Jones potential were determined based on a supermolecular model. Our determined molecular mechanical parameters are compared with presently available parameters published by other groups. We performed two different kinds of testing in order to demonstrate the reliability of these parameters in the case of ligated metallo complexes. First, the nonbonding potential was constructed for an additional set of 19 larger systems containing common complexes with organic molecules. The second test compares the Pt−O and Pt−H radial distribution functions for cisplatin in a box of TIP3P water with lately published studies.

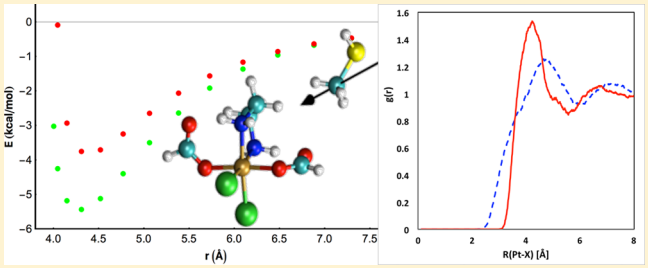

INTRODUCTION

Molecular mechanical (MM) simulations of transition metal elements represent one of the less reliable tasks in the present computational chemistry. The reason for this unpleasant fact is connected with several aspects. All the force-field parameters are highly sensitive to the (partial) charge of the metal cation. However, this charge is far from being at least approximately constant, and its value might be affected by many factors, for instance by switching the oxidation state of the metal, the nature of the coordinated ligands, the solvation, and/or other environmental factors. All these factors represent too variable conditions for a reasonably accurate molecular mechanical description of metallic systems regardless of whether the metal undergoes some chemical changes or not. Nevertheless, the MM simulation can be basically performed with a reasonable accuracy for a particular coordination sphere when only well-parametrized ligands of the metal interact with the complex surrounding. This is especially the case of a combined quantum mechanical/molecular mechanical (QM/MM) method (such as ONIOM[1] or our recent code QMS[2]) where the metal and its closest neighborhood are calculated at the QM level. However, the MM potential is used for the description of their interaction with the surrounding molecular environment. In these cases, a force field optimized for transition metals can work relatively well. Nevertheless, there are still a few systematic sets of reliable empirical parameters available. Usually one can find reports devoted to some specific metals or group of metals such as in ref 3. Lennard-Jones (LJ) parameters for hydration of various metal cations are explored by Li et al.[4] From this study, data for the mercury cation can be compared. Among others, we mention also relevant works of Zhao et al.,[5] Torras and Alemán,[6] Bernardes et al.,[7] Babu and Lim,[8] Stole and Karplus,[9] or Heiz et al.[10] However, most of these works explore interactions of naked metal cations with their surroundings while our contribution is based on interactions of already coordinated metal cations.

In this contribution we present a systematic collection of force-field parameters based on the AMBER Tools recipe[11] utilizing RESP partial charges.[12] We determined the Lennard-Jones nonbonding parameters of the transition metals in various oxidation states and coordination patterns. The parameters are fitted to reproduce density functional theory (DFT) calculations. Further, metal−ligand M−X bonding parameters and X−M−Y valence angle parameters were determined for the most common ligated groups using harmonic potentials. Besides the first row of transition metals, also Ru, Rh, Pt, and Hg cations in their most common oxidation states are considered here.

METHODS

The bonding parameters were determined in five homoligated and three electroneutral complexes for each regarded metal cation (by the term homoligated we mean a complex with the same ligands). The H_2O, NH_3, CO, Cl^-, and SH^- ligands were considered in both cases, i.e., five (charged) homoligated complexes and three neutral complexes where combination of (i) H_2O and SH^- or (ii) NH_3 and Cl^- or (iii) CO and Cl^- ligands

Received: April 24, 2016
Published: June 23, 2016

DOI: 10.1021/acs.jctc.6b00416
J. Chem. Theory Comput. 2016, 12, 3681−3688

was used so that the number of negatively charged ligands compensated for the charge of the given metal cation. The coordination numbers Z of the metals in the complexes were 4, 5 (trigonal bipyramids of Mn(II)), and 6 according to the highest stability of the given complex. Octahedral and square-planar structures were usually found as the most stable. In the planar complexes both cis- and trans-configurations were examined. In the octahedral complexes just the configurations drawn in Scheme 1 were considered to determine bond and valence-angle

Scheme 1. Configurations of Neutral Complexes in Various Oxidation States[a]

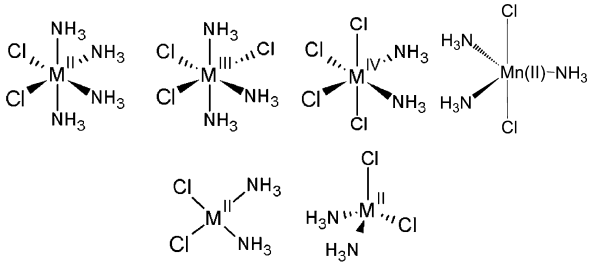

[a]Complexes with NH_3 and Cl^- ligands are presented as an example.

parameters. In the case of vanadium(III) also pentacoordinated oxo complexes with homogeneous ligands were taken into account as depicted in Scheme 2.

Scheme 2. Vanadium Tetraammine−Oxo Complex

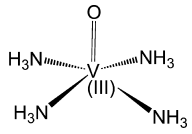

All quantum chemical calculations were performed with Gaussian 09 program for determination of electronic structure. The considered structures were optimized in the gas phase at the ω-B97XD/6-31+G(d) computational level. The Stuttgart−Dresden (SDD) effective core potentials[13] were used for the transition metal atoms, and the original set of atomic pseudoorbitals were extended by diffuse and polarization functions whose exponents are collected in Table S1 in the Supporting Information (SI). Usually, several possible multiplicities for the regarded complexes were explored in order to find the most stable spin state.

In the next step, a rigid potential energy surface (rPES) scan was performed changing either the metal−ligands bond length or the angle between ligands (by asymmetric movement of one of the ligands). We did not performed a relaxed PES scan since all the bonding parameters have only approximate character based on averaging several M−X (metal−other element) bonds. These bonding energies vary by more than 20 kcal/mol within the set of chosen complexes. The value of the relevant force constant was obtained by fitting the harmonic potential $E(x) = k/2(x - x_0)^2$ (k represents the force constant; x_0 is the equilibrium value) to the calculated energy profile. Four energy points, symmetrically displaced around the equilibrium value, were used for the fitting procedure. The alternative way for acquiring the searched force constants would be to perform analysis of the Hessian matrix eigenvalues and eigenvectors. However, it is not always easy to separate individual bonding and (especially) valence-angle modes in this approach.

The final bonding parameters were obtained by averaging of the obtained values for the given type of bond in the homoligated and neutral complexes. In the case of bonding angles, only one parameter, the averaged X−M−Y angle force constant, was determined for each metal. For the application of these angle parameters, we suggest adjusting the ϑ_0 value according to the optimized geometry of a particular structure of interest. The individual constants are sensitive to the type and structural arrangement of the ligands. Nevertheless, since these constants are relatively small, they can be averaged for several kinds of ligands and used with coordination, which follows from a theoretically predicted structure (e.g., based on the theory of hybridization, ligand field theory, and so on; i.e., ca. 90° in octahedral or square-planar structures) without geometry optimization as reasonable approximation, too.

The LJ parameters were determined using a supermolecular approach. The supermolecule consists of a neutral metal complex and a "testing" molecule. As neutral complexes, $M(NH_3)_xCl_y$ and $M(H_2O)_x(SH)_y$ structures, were chosen and combined with one of the NH_3, CH_4, or H_2O testing molecules. Varying the distance between a complex and a testing molecule, the dependencies of the energy on the relevant geometry parameters were obtained. In analogy to determination of the bonding parameters, the rPES scans at the ω-B97XD/6-31+G(d)/SDD computational level were applied here as well.

Seeking for the nonbonding parameters started with the determination of partial charges q_i, which were fitted by the RESP module of the AMBER Tools program suite[11] for the chosen complexes. In order to preserve compatibility of our results with GAFF (General Amber Force Field), the electrostatic potentials for the RESP procedure were computed at the HF/6-31G(d) level using the Merz−Singh−Kollmann scheme.[14] Required atomic radii of the transition metals were taken from the "Web of Elements" database [online: http://www.webelements.com/], and they are collected in Table S1. The RESP partial charges were consistently calculated for all the isolated complexes and testing molecules.

From the rPES scanned energies, classical electrostatic contribution

$$E_{\mathrm{elst}} = \frac{1}{2}\sum_{i,j}^{N}\frac{1}{4\pi\varepsilon_0}\frac{q_i q_j}{r_{ij}} \tag{1}$$

was subtracted. For this purpose, the RESP charges obtained on the isolated molecules and the isolated metal complexes were used supposing that the partial charges remain constant during the rPES scan and reproduce the electrostatic interaction reasonably. This assumption is consistent with the performance of the common MM/MD simulation techniques. Further, the nonbonding interactions between the ligands from the metal complex and all atoms of the testing molecule had to be subtracted using known atomic LJ parameters from GAFF. To evaluate the LJ energy contribution, we used the following formula:

$$E_{\mathrm{vdW}} = \frac{1}{2}\sum_{i,j}^{N}\varepsilon_{ij}\left(\left(\frac{r_{ij}^0}{r_{ij}}\right)^{12} - 2\left(\frac{r_{ij}^0}{r_{ij}}\right)^{6}\right) \tag{2}$$

DOI: 10.1021/acs.jctc.6b00416
J. Chem. Theory Comput. 2016, 12, 3681−3688

Table 1. Averaged Parameters of the Bonding Harmonic Potential: Force Constants [k, (kcal/mol)/Å^2] and Equilibrium Distances [r^0, Å][a]

	M−Cl			M−N		M−O		M−S		M−C		
	k	r^0	r^{CSD}	k	r^0	k	r^0	k	r^0	k	r^0	shape[b]
Cu(I)	125	2.4	2.3 (702)	104	2.1			109	2.4	142	2	T_d
Ti(II)	185	2.4	2.5 (8)	109	2.3	120	2.2	173	2.5	104	2.3	O_h
Cr(II)	169	2.4	2.4 (32)	147	2.1	143	2.1	152	2.4	99	2.3	O_h/SqPl
Mn(II)	157	2.4	2.4 (259)	91	2.3	104	2.3	150	2.4	47	2.5	O_h/TrBiP
Fe(II)	148	2.4	2.3 (368)	91	2.3	151	2.1	131	2.4	139	2.1	O_h
Co(II)	123	2.4	2.3 (656)	94	2.2	97	2.2	131	2.4	55	2.3	O_h
Ni(II)	221	2.2	2.3 (574)	219	2.0	230	1.9	210	2.3	169	1.9	SqPl
Cu(II)	172	2.3	2.4 (2227)	203	2.1	123	2.1	146	2.3	102	2.1	SqPl/O_h
Zn(II)	211	2.2	2.3 (1105)	201	2.1	187	2.1	179	2.4	137	2.3	T_d
Ru(II)	219	2.4	2.4 (1232)	200	2.2	183	2.2	221	2.4	295	2.0	O_h
Rh(II)	211	2.4	2.5 (55)	202	2.2	205	2.2	186	2.4	198	2.1	SqPl
Pt(II)	274	2.3	2.3 (1791)	301	2.1	262	2.1	273	2.3	370	2.0	SqPl
Hg(II)	206	2.5	2.5 (455)	121	2.4	120	2.4	169	2.6	83	2.6	T_d/T[b]
Sc(III)	166	2.5	2.5 (12)	142	2.3	172	2.2	106	2.6	100	2.5	O_h
V(III)	115	2.4	2.3 (54)	173	2.2	200	2.1	145	2.4	145	2.2	O_h
Cr(III)	169	2.4	2.3 (132)	165	2.1	217	2.0	126	2.4	145	2.2	O_h
Mn(III)	179	2.3	2.4 (74)	130	2.2	142	2.1	147	2.4	139	2.2	O_h
Fe(III)	162	2.4	2.3 (542)	141	2.2	166	2.1	147	2.4	104	2.3	O_h
Co(III)	185	2.4	2.3 (257)	226	2.1	176	2.0	277	2.3	221	2.1	O_h
Ru(III)	197	2.4	2.4 (258)	241	2.2	255	2.1	174	2.4	218	2.1	O_h
Rh(III)	208	2.4	2.4 (464)	255	2.1	282	2.1	181	2.4	255	2.0	O_h
Ti(IV)	280	2.3	2.3 (327)	209	2.1	300	2.0	214	2.4	142	2.3	O_h/T_d
Pt(IV)	295	2.3	2.3 (391)	300	2.1	293	2.1	265	2.4	286	2.1	O_h

[a]The parameters are divided according to the oxidation numbers in order to make the mutual comparison of metal cations easier. [b]SqPl, square planar; TrBiP, trigonal bipyrimidal; T_d, tetrahedral coordination in homoligated complexes; T, T-shape arrangement in electroneutral complexes; O_h, octahedral coordination.

The ε_{ij} and r^0_{ij} can be constructed from atomic LJ parameters ε_i and r_i^0 defined in GAFF. In AMBER, the Lorentz−Berthelot approach is used:

$$\varepsilon_{ij} = \sqrt{\varepsilon_i \varepsilon_j}, \qquad r_{ij}^0 = r_i^0 + r_j^0 \tag{3}$$

The following GAFF atom types were assigned to atoms in the ligands and the testing molecules: NH_3, *n3*, *hn*; H_2O, *ow*, *hw*; CH_4, *c3*, *hc*; CO, *c*, *o*; SH^-, *sh*, *hs*; Cl^-, *cl*.

Resulting energy profiles for pure LJ interaction of the given metal cation with atoms in all testing molecules were fitted simultaneously obtaining just one (averaged) pair of LJ parameters. The nonlinear least-squares Marquardt−Levenberg algorithm, implemented in Gnuplot v. 4.6, was used for the fitting.[15] Within the fitting procedure some points from the closer contacts of both molecules had to be discarded due to partial formation of covalent bonding. These cases might affect the course of the QM potential mainly close to the minimum energy region and at the beginning of the repulsive branch of the LJ potential. However, these effects should not be regarded in the MM description. They also cause that the repulsive part of the LJ interaction of a metal and a testing molecule was determined with some uncertainties especially in the case of octahedral structures. Unfortunately, this part is important for correct determination of an equilibrium distance r^0, too. In our model for determination of LJ parameters we restricted ourselves to rPES without BSSE. Of course, relaxed PES even including BSSE correction (as performed in some other studies) can lead to a more accurate QM interaction hypersurface (interaction curve in our case[6,16]). Nevertheless, we expect that approximation of fixed partial charges represents in metallic systems so crude an approach that a tiny improvement of QM surfaces by both relaxed PES and BSSE corrections can be easily neglected.

RESULTS AND DISCUSSION

Bonding Parameters. Applying the above-described procedure, a set of harmonic potential parameters for metallic bonds (M−X) was obtained and is collected in Table 1 together with the approximate coordination arrangement. Both the force constants and the equilibrium distances listed in the table are averages of values obtained from all the explored complexes where the same kind of bond(s) occurred. Nevertheless, we recommend using the force constants presented here with optimal distances r^0 for a specific complex (if possible), since the metal−ligand distances can deviate from optimal bond lengths in complexes chosen in our study. In this way, more accurate binding energies will result from the MM/MD simulations. In the searched literature, the bonding parameters are very seldom published probably because of the reasons mentioned in Introduction.

From Table 1 it can be noticed that generally the lowest force constant occurs for monovalent cations (Cu(I) in our case) because of the smallest electrostatic enhancement. A similar explanation holds even for the metal−carbon binding since the carbonyl ligand used in the fitting procedure has a relatively small dipole moment. In accord with this argument, the highest-value force constants can be expected for ions with oxidation number four, which is also confirmed from the last two lines of Table 1.

The average M−Cl bond lengths for each metal cation were also obtained from the Cambridge Structural Database (CSD). For the given metal all structures, which contain M−Cl bond,

DOI: 10.1021/acs.jctc.6b00416
J. Chem. Theory Comput. 2016, 12, 3681−3688

were searched. Simultaneously two restrictions were applied: *R*-factor lower than 0.05 and no errors. The *R*-factor is defined as

$$R = \frac{\sum ||F_{obs}| - |F_{calc}||}{\sum |F_{obs}|}$$

where F_{obs} and F_{calc} are experimentally observed and calculated structure factors, respectively. Only the database records with explicitly specified information about valence (e.g., "manganese-(iii)" for Mn(III)) were considered. If the data record satisfied the mentioned conditions, information about the M−Cl bonds was collected, and its average value is given in Table 1, column r^{CSD}. In parentheses also the frequency of occurrence is added. Comparing both M−Cl distances one can see a reasonable accord in computationally predicted values with experimentally obtained data. All the differences are always within 0.1 Å Therefore, we can conclude that the chosen level of calculation is fairly reliable.

In the case of the harmonic potential of the valence angle, the force constants were averaged for all explored ligands to the single X−M−Y value. This value can serve as an approximate estimation of the particular force constant. The averaged valence-angle force constants are presented in Table 2. The specific value depends rather strongly on other ligands present in the complex. Moreover, the approximate value of the equilibrium valence angle follows from the coordination number of the given metal cation, e.g., 90° in square-planar complexes. If a more accurate harmonic potential is required, then the valence angle ϑ_0 should be used from the optimized structure of the given complex in the same way as that for the M−X bond distance. In all cases valence-angle force constants refer to the smaller angle (usually 90°, never 180°). This is also how the averaging of all the valence-angle force constants for the given metal cation was performed.

Table 2. Averaged Force Constants of Valence-Angle Harmonic Potential [*k*, (kcal/mol)/rad^2] and Approximate Symmetry of Explored Metallic Complexes[a]

	k	shape
Cu(I)	30.0	T_d
Ti(II)	70.0	O_h
Cr(II)	75.0	O_h/SqPl
Mn(II)	40.0	O_h/TrBiP
Fe(II)	60.0	O_h
Co(II)	80.0	O_h
Ni(II)	120.0	SqPl
Cu(II)	105.0	SqPl/O_h
Zn(II)	35.0	T_d
Ru(II)	95.0	O_h
Rh(II)	100.0	SqPl
Pt(II)	110.0	SqPl
Hg(II)	30.0	T_d/T[b]
Sc(III)	60.0	O_h
V(III)	85.0	O_h
Cr(III)	75.0	O_h
Mn(III)	65.0	O_h
Fe(III)	110.0	O_h
Co(III)	120.0	O_h
Ru(III)	110.0	O_h
Rh(III)	90.0	O_h
Ti(IV)	85.0	O_h/T_d
Pt(IV)	115.0	O_h

[a]Optimal value of the bond angle ϑ_0 is taken according to the geometrical shape of the complex. [b]SqPl, square planar; TrBiP, trigonal bipyrimidal; T_d, tetrahedral coordination in homoligated complexes; T, T-shape arrangement in electroneutral complexes; O_h, octahedral coordination.

With regard to torsion angles, which are also used in MM potentials, no force-field constants were systematically searched here. Although the considered geometries require torsional potentials for H−(N/O/S)−M−X angles, the related force constants fluctuate usually in a range from 0.3 to 3.0 (kcal/mol)/rad^2. We omitted these energy terms by setting the force constants to zero. We should keep in mind that in the neighborhood of the metal center steric and electrostatic repulsions are so dominant that they easily override subtle effects such as torsion-angle energies.

The bonding parameters calculated in our work can be compared with several results found in the literature. Yao et al.[3a] published both the bonding and LJ parameters for Pt(II). Their Pt−N bonding force constant is 366 (kcal/mol)/Å^2, which is about 60 (kcal/mol)/Å^2 higher than our value probably due to the explicit consideration of the relatively strongly donating N7 site of purine bases. On the contrary Lienke et al.[3b] presented the force constant for the Pt−Cl bond, and their value is about a similar amount of energy (ca. 60 kcal/mol) lower than our estimation.

Nonbonding Interactions. The most important parameters, which also influence atoms in the outer part of QM/MM calculations, are the atomic charges and constants of the Lennard-Jones potential. Therefore, the main attention was paid to determination of these parameters in previous works.[4−13,22] As we already discussed, assignment of the atomic charges, which are required for evaluation of the electrostatic interaction, represents a serious problem. In practice, these charges are highly influenced by the closest neighborhood, and they may change substantially even within a single MD simulation due to varying polarization of the coordination shell. Since only a single (constant) value is required as a partial charge in common MM/MD calculations (within nonpolarizable force fields), the RESP charges were used in this study in accord with all the AMBER force fields. However, this limitation causes by far the largest error in the MM calculations. The averaged RESP charges from the complexes used in our study are displayed in Table 3. Yet, these charges should be used just for illustration, and calculation of RESP charges is strongly recommended for any particular complex. Otherwise severe deviations from "at least partially realistic" behavior must be expected.

The optimal atomic LJ parameters ε_i and r_i^0 for metal cations are collected in Table 3. In contrast to the bonding parameters, a relatively large set of LJ potentials is available in the literature. Nevertheless, interactions of the bare metal cations with their neighborhood were expected in most of the previous studies.[7−9,11,13] And, in this way, relatively smaller energy parameters ε_i were obtained together with relatively larger parameter r^0. In our approach we employed two neutral complexes with testing molecules (methane, ammonia, and water). Based on calculated RESP charges and known other-atom LJ parameters, we obtained by least-squares fitting the required ε_i and r_i^0 for the given metal cation. These parameters form a two-dimensional surface, which has often a very flat minimum; cf. Figure 1. In comparison with similar results for transition metals published by others,[4−6,8] our estimations have a little bit larger ε and slightly smaller r^0 parameter. As follows from Figure 1, it is not surprising that sets of other pairs of ε_i, r_i^0 can also

DOI: 10.1021/acs.jctc.6b00416
J. Chem. Theory Comput. 2016, 12, 3681−3688

Table 3. RESP Partial Charges q (e), Lennard-Jones Parameters ε_i (kcal/mol) and r^0 (Å), and RMSD (kcal/mol) of the Performed Fit

	q	ε_i	r^0	RMSD
Cu(I)	0.652	2.148	2.668	6.503
Ti(II)	1.175	0.917	2.869	17.067
Cr(II)	0.869	1.518	2.734	10.233
Mn(II)	1.018	1.089	2.904	22.034
Fe(II)	1.032	0.698	2.969	17.683
Co(II)	1.010	1.196	2.805	20.342
Ni(II)	0.605	2.650	2.720	12.760
Cu(II)	0.771	3.772	2.801	104.367
Zn(II)	0.697	1.095	2.847	8.248
Ru(II)	0.872	0.418	2.939	36.045
Rh(II)	0.507	3.946	2.715	16.369
Pt(II)	0.276	5.073	2.670	13.986
Hg(II)	0.661	1.955	2.801	7.743
Sc(III)	1.207	0.110	3.330	34.671
V(III)	1.012	1.904	2.767	45.973
Cr(III)	1.063	0.782	2.847	25.055
Mn(III)	0.833	0.069	2.367	19.731
Fe(III)	0.876	0.122	3.086	23.742
Co(III)	0.916	0.952	2.946	18.675
Ru(III)	0.790	1.644	2.832	26.477
Rh(III)	1.236	1.092	2.896	20.757
Ti(IV)	0.753	1.174	3.747	5.092
Pt(IV)	0.440	0.141	3.272	16.893

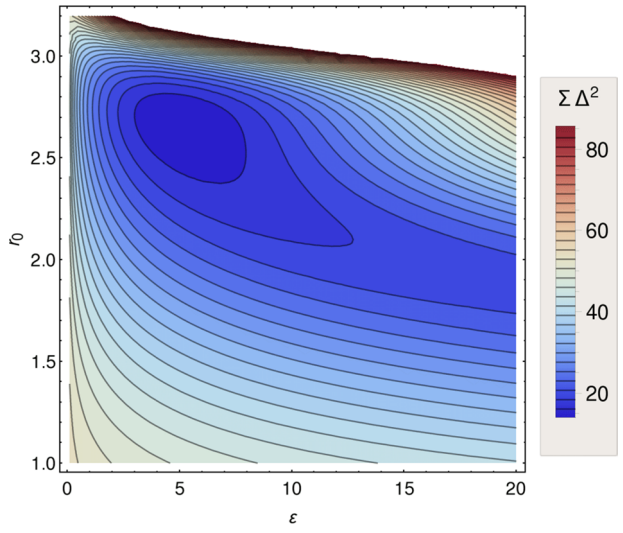

Figure 1. Surface of the least-squares fits ($\Sigma\,\Delta^2$) of atomic LJ parameters ε and r_0 for Pt(II) complexes interacting with the testing molecules.

give reasonable and reliable results since they may fit to the flat "valley" shown in Figure 1. We hope that an advantage of our parameters dwells in the fact that they were optimized for the set of metal complexes interacting with several molecules and, in this way, they are more general.

Verification of the LJ Parameters. To show how reliable our parameters are, we present here an extensive set of verification examples. It involves two kinds of tests, which are especially focused on the correct behavior of the nonbonding parameters.

First, an additional collection of larger complexes and testing molecules was chosen in order to demonstrate how the determined nonbonding potentials match with the DFT calculations (at the same level as the previous rPES scans). For each metal, we took several common complexes from the literature and let them interact with common small organic molecules. Altogether we are presenting 19 systems (as supermolecules): Co(II), $Co(en)_2Cl_2$/acetone (en = ethylendiamine); Cr(III), $Cr(acac)_3/CH_2O$ (acac = acetylacetonate); Cu(II), **Cu(II)−ATSM/$CO(NH_2)_2$** (ATSM = diacetylbis(*N*(4)-methylthiosemicarbazonato); Fe(II), $Fe(C_5H_5)(CO)_2Cl$/acetone; Hg(II), $Hg(CH_3COO)(CH_3CH_2)$/cyclopentadiene and **Hg(CH_3COO) (CH_3CH_2)/ethanol**; Mn(III), $Mn(acac)_3$/pyrrole; Ni(II), $Ni(en)_2Cl_2/CH_2Cl_2$; Pt(II), **PtCl(en)OH/$(CH_3)_3N$**; Pt(IV), $Pt(HCOO)_2Cl_2(en)/CH_3SH$; Rh(III), $Rh(H_2O)Cl_3(imidazole)_2/CH_3OCH_3$; Ru(III), **hydrated NAMI/$HCOOCH_3$**, (NAMI = *trans*-[$Ru(H_2O)Cl_3$(imidazole)(dimethyl sulfoxide-*S*)] (in geometrical arrangements a and b); Sc(III), $Sc(acac)_3/CH_3PH_2$; Ti(IV), $Ti(acac)_2Cl_2/HCOOCH_3$ and titanocene/CH_3OCH_3 (titanocene = dichloride bis(η^5-cyclopentadienyl)titanium(IV)); V(III), $V(acac)_3$/glycine; Zn(II), Zn(salen)/$COCl_2$ (salen = *N*,*N*′-bis(salicylidene)ethylendiamine dianion and Zn(salen)/furan. The four underscored and bold marked systems from the list above are presented in Figure 2 and discussed in the text; the remaining systems are placed in SI Figure S2 for the sake of clarity. Supermolecular structures with trajectories labeled by arrows, for systems presented in Figure 2, are displayed in Figure 3, and the remaining cases are collected in Figure S3.

In analogy to the fitting procedure, the QM energy profiles were determined for the given supermolecule using the rPES method, and after subtracting the electrostatic term (using the RESP charges calculated on isolated parts in the optimal geometry), the van der Waals interactions were determined and compared with LJ potential based on the force-field parameters from Table 1. Three of the four representative systems in Figure 2 display quite acceptable agreement between DFT and the MM description (cf. Figure 2a,c,d). In Figure 2c, a nearly perfect match concerns the nonbonding minimum at 4.3 Å in the case of the Pt(II) complex interaction with trimethylamine. The extent of Pt(II)···$(CH_3)_3N$ stabilization energy predicted by MM method is in very good accord with the DFT results. The system of the Ru(III) complex with methyl formate (Figure 2d) exhibits a fair match of the Ru−O distance in the energy minimum, but the interaction energy is lower than the corresponding QM value. On the other hand, the system with a "not-so-good" agreement is demonstrated in Figure 2b, namely, $Hg(CH_3COO)(CH_3CH_2)$ complex interacting with ethanol where the extent of deviation belongs to one of the worst cases. Here, the repulsive branch prevails in much longer distances at the MM level in comparison with the DFT calculations. This can be explained by forming an attractive interaction between alcohol and acetic acid as a ligand of the Hg(II) complex. A similar explanation can be also used in the case of $Hg(CH_3COO)(CH_3CH_2)$ with cyclopentadiene and Zn(salen) with furan (Figure S2d,o)

The second test is based on the comparison of Pt−O_w and Pt−H_w radial distribution functions (RDFs) for cisplatin complex in neutral dichloro-form (*cis*-$Pt(NH_3)_2Cl_2$) and diaqua-form ([*cis*-$Pt(NH_3)_2(H_2O)_2]^{2+}$) in water solution (O_w and H_w stand for oxygen and hydrogen of water molecules, respectively). For these systems, the MD simulations were performed in a periodic TIP3P[17] water box and obtained RDFs were compared with results known from the literature.[3c,16a,18] Additional examples of calculations of the Pt(II) complexes within the explicit water solution can be also found in ref 19. The study of Lopes et al.[3c] deals with the solvated cisplatin simulated with Monte Carlo

DOI: 10.1021/acs.jctc.6b00416
J. Chem. Theory Comput. 2016, 12, 3681−3688

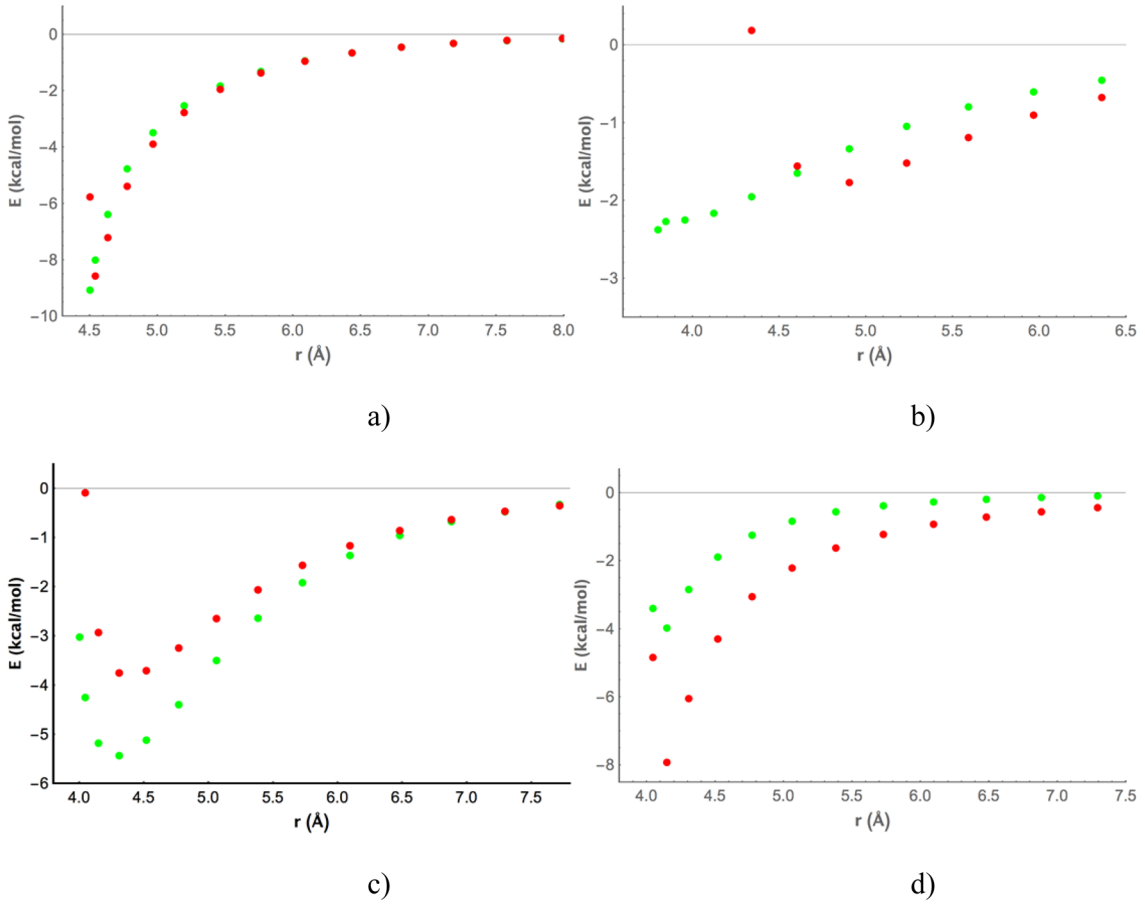

Figure 2. Comparison of QM (green dots) and MM (red dots) nonbonding potentials: (a) Cu(II), Cu(II)−ATSM/$CO(NH_2)_2$; (b) Hg(II), $Hg(CH_3COO)$ (CH_3CH_2)/ethanol; (c) Pt(II), PtCl(en)OH/ $(CH_3)_3N$; (d) Ru(III), hydrated NAMI/$HCOOCH_3$ (arrangement a).

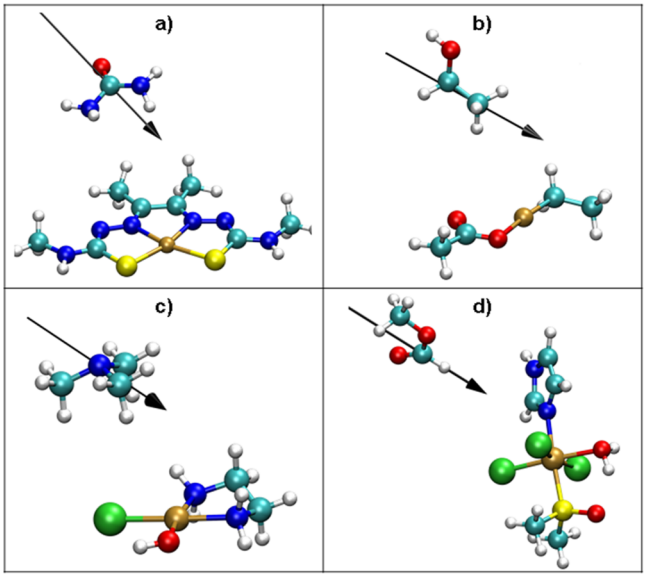

Figure 3. Supermolecular models with trajectories indicated by arrows for systems from Figure 2.

authors obtained ε(Pt) = 1.05 kcal/mol and σ = 3.66 Å. Their energy parameter is rather small compared to ours but together with a larger value of σ it can fit to the "flat optimal valley" from Figure 1. In the discussed study the authors explicitly considered in their fitting procedure both possible water orientations (with hydrogen and oxygen) in axial interaction site, as presented in Figure 4. These two possibilities are known from the literature as

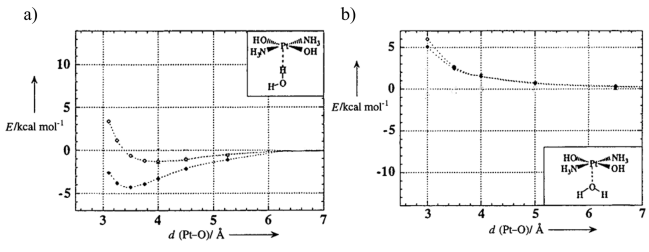

Figure 4. HF (empty circle) and MP2 (solid circle) energy profile for approaching water to hydrated cisplatin along the axial line: (a) by hydrogen atom; (b) by oxygen (reprinted with kind permission from ref 16b. Copyright 2000 John Wiley & Sons).

method where the LJ parameters were determined in a way similar to that of our work, by fitting to the ab initio potential obtained at the (MP2/LANL2DZ/6-31G(d,p) computational level. The water solution was simulated by the TIP3P model and partial charges received from the CHelpG procedure.[20] The

the closest interacting sites between platinum and water—for a further discussion see, e.g., refs 16b and 21. The Pt−O_w and Pt−H_w RDFs from the study of Lopes[3c] are depicted in Figure 5a. In another work[16a] classical MD simulations were performed with the frozen molecular geometry of cisplatin (optimized by the MP2/6-31+G(d,p) ab initio method). Instead of the LJ potential,

DOI: 10.1021/acs.jctc.6b00416
J. Chem. Theory Comput. 2016, 12, 3681−3688

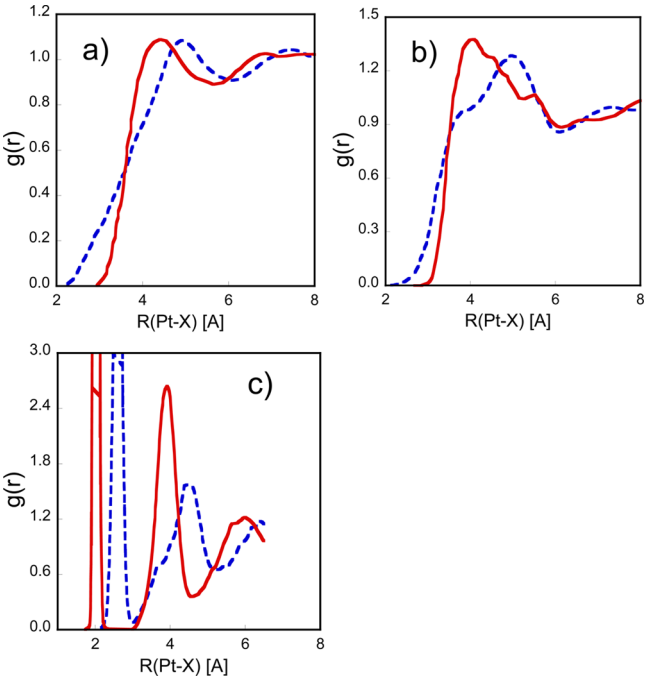

Figure 5. Pt−O_w (solid red lines) and Pt−H_w (dashed blue lines) radial distribution functions of the cisplatin complex in water solution. Sources for plots: (a) Lopes et al. (adapted with permission from ref 3c; copyright 2006 American Chemical Society); (b) Melchior et al. (adapted with permission from ref 16a; copyright 2013 American Chemical Society) (RDF curves correspond to dichloro form); (c) Beret et al. (adapted with permission from ref 18; copyright 2008 American Chemical Society) (plots of RDF regard diaqua form of cisplatin).

the interaction energy between cisplatin and the surrounding water was estimated using a series of terms:

$$V(r_{ij}) = \sum_{i}^{\text{cisDDP}} \sum_{j}^{\text{water}} \left(\frac{C_{ij}^{\ 4}}{r_{ij}^{\ 4}} + \frac{C_{ij}^{\ 6}}{r_{ij}^{\ 6}} + \frac{C_{ij}^{\ 8}}{r_{ij}^{\ 8}} + \frac{C_{ij}^{\ 12}}{r_{ij}^{\ 12}} \right) + \frac{q_i q_j}{r_{ij}}$$

where coefficients C_{ij} were fitted from the ab initio calculations and partial charges determined by ESP Merz−Singh−Kollman method[14] for isolated cisplatin. Their periodic box was of approximately the same size as in our work and the study of Lopes et al.,[3c] which is ca 31 Å. A slightly different model of water was used (SPC/E). The resulting RDFs are placed in Figure 5b. Comparing these two RDFs with our results (shown in Figure 6),

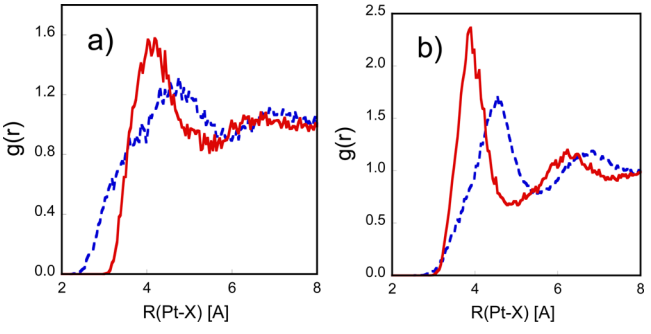

Figure 6. Pt−O_w (solid red lines) and Pt−H_w (dashed blue lines) radial distribution functions of the cisplatin (a) in dichloro ($Pt(NH_3)_2Cl_2$) and (b) diaqua complex ($[Pt(NH_3)_2(H_2O)_2]^{2+}$) in water solution based on LJ parameters for Pt from Table 3. RDF of Pt-Ow.

it can be noticed that the parametrizations used in studies 3c and 16a are able to predict the correct size of mesoshell water at ca. 3.6−3.9 Å above the square-planar platinum complex. In our case the first peak has a maximum around 3.9−4.1 Å slightly depending on the type of cisplatin complex (if the hydrated form is used or not). The integral under the Pt-Ow RDF curve from 2.1 to 3.75 Å for cisplatin (or to 3.65 Å for its hydrated form) gives two oxygen atoms that correspond to mesoshell water. These two water molecules can be located in the vicinity of the Pt atom from above and below the complex plane. The other three water molecules in the distance between 3.8 and 4.1 Å from Pt atom interact with ammine ligands. Also, the predicted number of water molecules in the first solvation shell is estimated to be between 15 and 17, which is in fair accord with the study of Platts.[22] The last compared RDFs come from probably the most accurate study using the ab initio Car−Parrinello (CPMD) method with PBE exchange and correlation functional.[18] In this case, a slightly different complex was considered: charged tetraaqua cation $[Pt(H_2O)_4]^{2+}$ in a (relatively smaller) periodic box of water (ca. 13 Å). Nevertheless, since the CPMD method is used, such a box represented contemporary computational limits. The RDFs from study 18 are shown in Figure 5c. From these calculations (as well as from the previously mentioned RDFs[3c,16a]), it follows that our Pt−O_w distance of the first maximum is close to their value of ca. 3.8−4.0 Å. In comparison with the optimal value of the Pt−O_w interaction (3.4 Å) determined by QM calculations by Kozelka (Figure 4a), our distances are a little bit larger. However, the direct comparison is not plausible because of several reasons: (a) our system is slightly different (cisplatin and diaquacisplatin while in the Kozelka's case dihydroxotransplatin); (b) our calculations are based on dynamical simulations where we are working with RDF, and it should be also kept in mind that some elongation comes from the dynamical character of our models. Nevertheless, when we integrate RDF, first water "occurs" at 3.6 Å and the second at 3.8 Å.

With regard to Pt−H_w RDF, only the CPMD study is able to predict the position of the first hydrogen maximum as suggested by Kozelka et al.[16b] and as it is presented in Figure 4a. From Figure 4b it can be also seen that the Pt−O_w direct interaction should not be actually considered attractive at all. For the clear proof of this Pt···H_w interaction, authors of the CPMD study nicely involve decomposition of RDF into three parts—axial, intermediate, and equatorial—since from the total Pt−H_w RDF is not completely clear, which hydrogen atoms contributes to the first (relatively very broad) 2.5 Å peak. In our MD simulation this particular point is not relevant since we are dealing with cisplatin and the MM method can easily distinguish between the TIP3P water and QM ammonia hydrogen atoms or hydrogens of directly coordinated aqua ligands. Nevertheless, besides this CPMD study none of the classical MD studies[3c,16a] or our simulations is able to detect the Pt···H interaction. The reason for this dwells in the fact that in the used water models the LJ parameters for H_w atoms are not considered. Thus, the former increase of H_w−Pt RDF in the case of cisplatin has a purely electrostatic origin. Therefore, in the case of hydrated cisplatin no such interaction can be visible at all.

Finally with regard to this testing system it should be stressed that despite various forms of cisplatin (and transplatin in the Kozelka's study) being compared, it can be concluded that relevant parts of RDFs concerning the distance of the closest water and number of waters in the mesoshell are in fair accord

DOI: 10.1021/acs.jctc.6b00416
J. Chem. Theory Comput. 2016, 12, 3681−3688

with available results of other studies giving a reasonable credit to our parameters, too.

CONCLUSIONS

In this study we searched for the force-field parameters of the first row transition metals plus some additional common metals Ru, Rh, Pt, and Hg in ligated forms. The DFT calculations at the ω-B97XD/6-31+G(d) computational level were employed to get reference data for fitting force-field parameters. Bonding characteristics were determined by averaging metal−ligand force constants and optimal bond distances from several different complexes of each metal cation in the most frequent oxidation states and coordination numbers. Only a single indicative value for valence-angle force constant is presented for each metal cation due to the large variance of this value. For higher accuracy the authors recommend to optimize examined complexes for receiving optimal distances and valence angles in each individual case. Also, RESP charges are required in the optimal structure for more accurate estimation of electrostatic energy. The supermolecular model was utilized for determination of parameters for the Lennard-Jones potential.

In the final part two different tests are provided in order to support good accuracy and reliability of these parameters for ligated metallo complexes. First, the construction of nonbonding potential for an additional set of 19 larger systems containing common complexes and organic molecules based on literature was performed and compared with the DFT reference calculations. The second example compares the radial distribution functions of solvated cisplatin with several published results.

ASSOCIATED CONTENT

Supporting Information

The Supporting Information is available free of charge on the ACS Publications website at DOI: 10.1021/acs.jctc.6b00416.

Atomic radii and polarization and diffuse functions, description of determination of LJ parameters, orientation of testing molecules, comparison of QM and MM nonbonding potentials, and supermolecular models with trajectories indicated (PDF)

AUTHOR INFORMATION

Corresponding Author

*E-mail: burda@karlov.mff.cuni.cz.

Present Address

†University College Dublin (UCD), School of Chemical & Bioprocess Engineering, Belfield, Dublin 4, Ireland

Notes

The authors declare no competing financial interest.

ACKNOWLEDGMENTS

We are grateful to the Grant Agency of Czech Republic Project No 16-06240S for supporting this study. Additional support (for F.Š.) was obtained from the Grant Agency of Charles University, No. 532212. Access to computing and storage facilities owned by parties and projects contributing to the National Grid Infrastructure MetaCentrum, provided under the program "Projects of Large Infrastructure for Research, Development, and Innovations" (LM2010005) is highly appreciated.

REFERENCES

(1) Dapprich, S.; Komáromi, I.; Byun, K. S.; Morokuma, K.; Frisch, M. J. *J. Mol. Struct.: THEOCHEM* **1999**, *461-462*, 1−21.

(2) (a) Futera, Z.; Burda, J. V. *J. Comput. Chem.* **2014**, *35*, 1446−1456. (b) Futera, Z.; Sodeyama, K.; Burda, J. V.; Einaga, Y.; Tateyama, Y. *Phys. Chem. Chem. Phys.* **2014**, *16*, 19530−19539.

(3) (a) Yao, S.; Plastaras, J. P.; Marzilli, L. G. *Inorg. Chem.* **1994**, *33*, 6061−6077. (b) Lienke, A.; Klatt, G.; Robinson, D. J.; Koch, K. R.; Naidoo, N. *Inorg. Chem.* **2001**, *40*, 2352−2357. (c) Lopes, J. F.; de A. Menezes, V. S.; Duarte, H. A.; Rocha, W. R.; De Almeida, W. B.; Dos Santos, H. F. *J. Phys. Chem. B* **2006**, *110*, 12047−12054.

(4) Li, X.; Tu, Y.; Tian, H.; Ågren, H. *J. Chem. Phys.* **2010**, *132*, 104505.

(5) Zhao, L.; Liu, L.; Sun, H. *J. Phys. Chem. C* **2007**, *111*, 10610−10617.

(6) Torras, J.; Alemán, C. *J. Phys. Chem. B* **2013**, *117*, 10513−10522.

(7) Bernardes, C. E. S.; Canongia Lopes, J. N.; da Piedade, M. E. M. *J. Phys. Chem. A* **2013**, *117*, 11107−11113.

(8) Babu, C. S.; Lim, C. *J. Phys. Chem. A* **2006**, *110*, 691−699.

(9) Stote, R. H.; Karplus, M. *Proteins: Struct., Funct., Genet.* **1995**, *23*, 12−31.

(10) Heinz, H.; Vaia, R. A.; Farmer, B. L.; Naik, R. R. *J. Phys. Chem. C* **2008**, *112*, 17281−17290.

(11) Case, D. A.; Darden, T. A.; Cheatham, T. E.; Simmerling, C. L.; Wang, J.; Duke, R. E.; Luo, R.; Walker, R. C.; Zhang, W.; Merz, K. M.; Roberts, B.; Wang, B.; Hayik, S.; Roitberg, A.; Seabra, G.; Kolossvary, I.; Wong, K. F.; Paesani, F.; Vanicek, J.; Liu, J.; Wu, X.; Brozell, S.; Steinbrecher, T.; Gohlke, H.; Cai, Q.; Ye, X.; Wang, J.; Hsieh, M. J.; Cui, G.; Roe, D. R.; Mathews, D. H.; Seetin, M. G.; Sagui, C.; Babin, V.; Luchko, T.; Gusarov, S.; Kovalenko, A.; Kollman, P. A. *AMBER 11*; University of California: San Francisco, CA, USA, 2010.

(12) (a) Bayly, C. I.; Cieplak, P.; Cornell, W.; Kollman, P. A. *J. Phys. Chem.* **1993**, *97* (40), 10269−10280. (b) Cornell, W. D.; Cieplak, P.; Bayly, C. I.; Kollmann, P. A. *J. Am. Chem. Soc.* **1993**, *115*, 9620−9631.

(13) (a) Andrae, D.; Haussermann, U.; Dolg, M.; Stoll, H.; Preuss, H. *Theor. Chim. Acta* **1990**, *77*, 123−141. (b) Andrae, D.; Haussermann, U.; Dolg, M.; Stoll, H.; Preuss, H. *Theor Chim Acta* **1991**, *78*, 247−266. (c) Nicklass, A.; Dolg, M.; Stoll, H.; Preuss, H. *J. Chem. Phys.* **1995**, *102* (22), 8942−8952.

(14) Singh, U. C.; Kollman, P. A. *J. Comput. Chem.* **1984**, *5*, 129.

(15) Williams, T.; Kelley, C. *GnuPlot v. 4.6 An Interactive Plotting Program*; http://gnuplot.info, Minnesota, Sep. 1, 2014.

(16) (a) Melchior, A.; Martínez, J. M.; Pappalardo, R. R.; Marcos, E. S. *J. Chem. Theory Comput.* **2013**, *9*, 4562−4573. (b) Kozelka, J.; Berges, J.; Attias, R.; Fraitag, J. *Angew. Chem., Int. Ed.* **2000**, *39*, 198−199.

(17) Jorgensen, W. L.; Chandrasekhar, J.; Madura, J. D.; Impey, R. W.; Klein, M. L. *J. Chem. Phys.* **1983**, *79*, 926−935.

(18) Beret, E. C.; Martinez, J. M.; Pappalardo, R. R.; Marcos, E. S.; Doltsinis, N. L.; Marx, D. *J. Chem. Theory Comput.* **2008**, *4* (12), 2108−2121.

(19) (a) Carloni, P.; Sprik, M.; Andreoni, W. *J. Phys. Chem. B* **2000**, *104*, 823−835. (b) Naidoo, K. J.; Klatt, G.; Koch, K. R.; Robinson, D. J. *Inorg. Chem.* **2002**, *41*, 1845−1849. (c) Torrico, F.; Pappalardo, R. R.; Marcos, E. S.; Martinez, J. M. *Theor. Chem. Acc.* **2006**, *115*, 196−203.

(20) Breneman, C. M.; Wiberg, K. B. *J. Comput. Chem.* **1990**, *11*, 361−373.

(21) Berges, J.; Fourré, I.; Pilmé, J.; Kozelka, J. *Inorg. Chem.* **2013**, *52*, 1217−1227.

(22) Robertazzi, A.; Platts, J. A. *J. Comput. Chem.* **2004**, *25* (8), 1060−1067.

DOI: 10.1021/acs.jctc.6b00416
J. Chem. Theory Comput. 2016, 12, 3681−3688

Metal Interactions with Nucleobases, Base Pairs, and Oligomer Sequences; Computational Approach

Jaroslav V. Burda and Filip Šebesta

Contents

Abstract

This chapter concerns some of the computational studies devoted to interactions of metal cations with nucleobases, nucleotides, and short oligonucleotides considered as DNA/RNA models. Our topic is fairly complex, therefore the results obtained using mainly ab initio and DFT methods are discussed. The first part focuses on the interactions of isolated bases with metal cations either in bare, hydrated, or ligated forms. We begin with interactions of naked cations with nucleobases in gas phase. Subsequently, solvation effects using polarizable continuum models are analyzed together with a comparison to explicitly hydrated ions. In the second part, adducts of various metals with base pairs and oligomeric models of DNA/RNA are discussed. Separate sections are devoted to complexes

J.V. Burda (✉) • F. Šebesta
Faculty of Mathematics and Physics, Charles University in Prague, 12116 Prague 2, Czech Republic
e-mail: burda@karlov.mff.cuni.cz

J. Leszczynski et al. (eds.), *Handbook of Computational Chemistry*,
DOI 10.1007/978-94-007-6169-8_36-2

of promising anticancer drugs. Stacked bases and larger systems (quadruplexes) studied by semiempirical and QM/MM methods are mentioned in the last part.

Introduction

This chapter provides a brief overview of recent model calculations and simulations of metal-cation interactions with nucleic acid (NA) bases, base pairs, and short oligomeric models. From historical reasons, alkali metals and metals of alkaline earth are discussed first. All possible forms of metal cations are considered, starting with bare ions, which were mostly studied in older papers. Later, complexes with their first solvation shell or in ligated form are reviewed. Despite the simplicity and the fact that bare cations overestimate the bonding energies because of exaggerated contribution of Coulomb interaction, these models enable a clear insight into the basic bonding characteristics and other electronic properties. Many studies are focused on transition metal complexes, motivated by anticancer activity of cisplatin and other possible metallodrugs. While the electrostatic contribution dominates in the interaction of alkali metals, the coordination covalent term is important in the complexes of transition metals.

In general, the structure and function of DNA are modified by metal ions. These ions can interact with many sites in DNA (Saenger 1983; Sigel 1993), including the phosphate groups, the sugar moiety, and the NA bases. Although the metal cations usually interact with the phosphate group and, to a lesser extent, with bases, cation-base interactions are involved in many important biophysical processes, such as different stabilization of DNA triple helices (Potaman and Soyfer 1994), stabilization of quadruple helices (Hud et al. 1996), and stabilization of the ribose-base stacking in Z-DNA (Egli and Gessner 1995). It is assumed that the interaction of a divalent cation with the base can cause a significant polarization of the bases associated with stabilization of certain H-bonded base pairs and other interactions (Hud et al. 1996; Egli and Gessner 1995; Anwander et al. 1990; Santangelo et al. 2010). However, some ions do not interact with nucleic acids in a direct manner but rather contribute to unspecific loose ion atmosphere around the nucleic acids (Chu et al. 2008). While theoretical studies usually deal with binding of cations to DNA, the RNA-cation binding is much more biochemically important and diverse. Many folded RNAs contain indispensable specific structural ions, which may also be directly involved in RNA catalysis (Draper et al. 2005; Banas et al. 2009; Lilley and Eckstein 2008).

In the DNA double helix, the known sites for the cation coordination are mainly the N7 atoms of purines sometimes supported by forming the chelate structure involving also O6 atom of guanine. Some other sites, such as N3 of cytosine or thymine and N1 of adenine, are usually blocked by the hydrogen bonding. Nevertheless, several experimental as well as theoretical examples of coordination into this position exists especially in the metal bridges like cytosine-silver-cytosine (Šponer et al. 1999a) or thymine-mercury-thymine (Yamaguchi et al. 2014; Šebera et al. 2013a) as mentioned below. It should be noted that the metal cation interactions

are not restricted only to the NA bases and the cation can simultaneously interact with the phosphate group. The coordinated metal cations can interact with the NA base directly (inner-sphere coordination) or mediated by a water molecule, which links the NA base with the metal cation (outer-sphere coordination) (Sigel 1993; Egli et al. 1991). Experimental studies on 5′-monophosphates revealed the following order of macrochelate coordination involving the N7 position of purines: GMP > IMP (I – inosine) > AMP (Sigel 1993). This order was explained as a result of different basicity of the N7 sites of guanosine, inosine, and adenine. It also correlates with the dipole moments of NA bases.

Properties of Metal Adducts with Nucleobases

Interactions of Bare Cations with Bases

The first models investigated in connection with metal-nucleobases interactions employed bare cations. One of the pioneering studies, which considered the influence of water and divalent ions on the base pairing, was published in 1970 by Rozsnyai and Ladik (1970). Later Del Bene (1984) explored interactions of naked Li^+ cation with all DNA bases. In this work, all basic features of modern quantum chemical calculations are already present – the structures were optimized at the HF/STO-3G level with single point calculations (SP) using double-zeta basis set (6-31G). As the most stable adduct, the [Li-(Gua-O6,N7)]$^+$ chelate was found (with association energy of 78.4 kcal/mol – which can be compared with more recent value of 78.3 at MP2/6-31G(d,p) (Burda et al. 1996)) followed by cytosine complex [Li-(Cyt-O2,N3)]$^+$ (77.1 kcal/mol). The association energy of the most stable adenine conformer [Li-(Ade-N3)]$^+$ was estimated to be substantially lower – 48.4 kcal/mol (40.4 at MP2 (Burda et al. 1996)). These energies clearly demonstrate the dominant role of the monopole (cation)-dipole moment (nucleobase) electrostatic interaction. When the multipolar formula for energy evaluation between monopole and dipole is considered, $E = q_{Li} \cdot \mu_{gua} / R^2{}_{Li-gua}$, then ca 92 kcal/mol can be obtained for Li charge of 0.84 e, guanine dipole moment of 7.28 D, and mutual distance of 2.09 Å (supposing a collinear orientation of cation and vector of dipole moment (cf. for instance Burda and Gu 2008; Futera et al. 2009a)). In the study, both O2 and O4 thymine complexes were predicted to be more stable than the adenine adducts by about 10 kcal/mol. Closely after this keystone study, another work dealing with interactions of the A-T and G-C base pairs with Li^+ cation appeared (Del Bene 1985). In the most stable Li^+-A-T conformer, the Li cation was coordinated to O2 site of thymine. In the G-C pair, the N3 position of guanine was preferred by 4 kcal/mol over O6, N7 chelate structure. This A-T and G-C base pair was later explored with extended set of metal cations (Burda et al. 1997) roughly confirming all these results. We would like to address here one important point. The numbers above, as well as many other numerical values in this study, refer to gas phase interactions of metal cations with nucleic acids components. Such interactions are dominated by the electrostatic effects, which are

Table 1 Preferred sites for metalationand protonation

Base	Metalation	Protonation
Adenine	N7 > N1	N1 > N7
Cytosine	N3	N3
Guanine	N7 > N1	N7 > N1
Thymine, uracil	O2 > O4	O4 > O2

substantially (sometimes almost completely) extinct in nucleic acids as well as in typical bioinorganic experiments. This needs to be kept in mind while the results are interpreted. For more discussion of various aspects of the interplay between the gas phase interactions and real systems, see, e.g. refs. (Šponer et al. 2001; Schmidt et al. 2002; Burda et al. 2003; Petrov et al. 2005).

Metal coordination sites in natural nucleotides are: (a) oxygen atoms of phosphate groups where cations neutralize the negative charge (these sites can be considered quite unspecific for any cation), (b) hydroxyl groups of sugar moiety usually chosen by alkali metals or metals of alkaline earth, (c) nitrogen atoms of heterocyclic bases – especially N1, N3, and N7 atoms of purine and N3 of pyrimidine bases, which exhibit large affinity to cations or generally electrophiles (In DNA/RNA oligomeric sequences, only sites in minor or major groove are accessible for interactions. It means that solely the N3 and N7 sites of purine bases are available for the interactions.), and (d) oxygens of keto-groups (O2 of cytosine, O6 of guanine, and O2, O4 of thymine and uracil) as positions for binding of "hard" cations, e.g., alkali metals (and less frequently for transition metal). Preference for individual hetero atoms in all five NA bases was explored for Ru(II) cation also in study of Futera (Futera et al. 2009a) demonstrating the preference for N7 site of purine bases and (after deprotonation) N3 of pyrimidine.

Comparing cation coordination and protonation of these active sites, large similarities can be noticed in the case of guanine, cf. Table 1. On the contrary, more remarkable differences are observed for adenine, uracil, or thymine. Unfortunately, deprotonation of N3 in thymine/uracil is not considered.

Coordination of the Mg^{2+} cation to purine DNA bases was recently explored in many experimental as well as computational studies (e.g., ref. (Elmahdaoui and Tajmirriahi 1995; Sychrovsky et al. 2004)), where bonding properties of selected mono- and divalent metal cations with the N7 position of guanine and adenine were examined.

The interaction of bare monovalent (alkali metals and coinage metals) and divalent (alkaline earth and zinc group metals) cations with the N7 site of purine NA bases was investigated in gas phase using the MP2/6-31G(d,p)//HF/6-31G(d,p) level of theory (Burda et al. 1996). The stabilization energies of base…M complexes were determined according to the formula:

$$\Delta E^{\mathrm{Stab}} = -\left[E^{\mathrm{Complex}} - \left(E^{\mathrm{base}}_{BSSE} - E^{\mathrm{metal}}_{BSSE}\right)\right] + \Delta E^{\mathrm{base}}_{\mathrm{deform}} \quad (1)$$

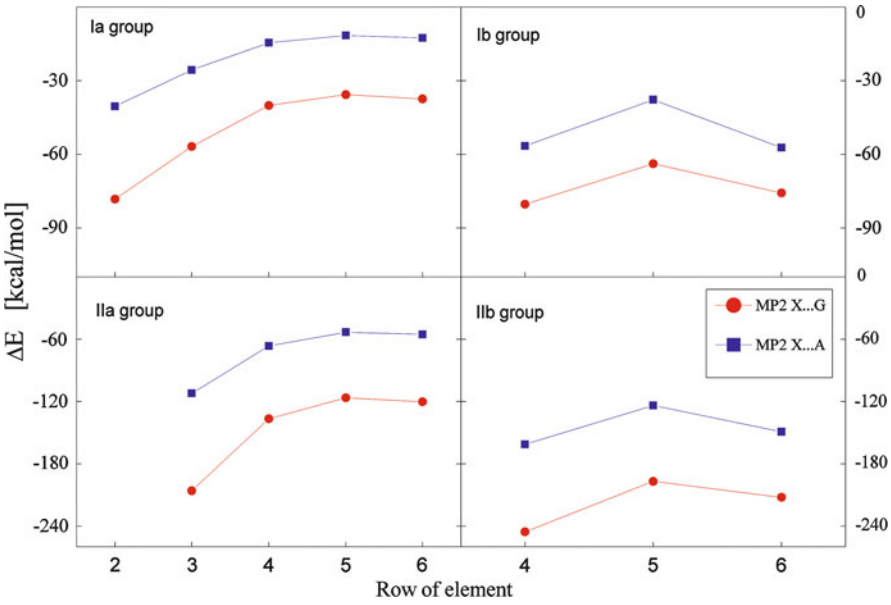

Fig. 1 Stabilization energies of metal-base complexes for Ia, Ib, IIa, and IIb metal cations interacting in N7(O6) position of the base

Here the E_{BSSE}^{base} represents total energy of the base (adenine or guanine) within the basis set superposition error (BSSE) scheme of Boys Bernardi (Boys and Bernardi 1970). The results are displayed in Fig. 1 and it is evident that the values for guanine complexes are systematically nearly twice as large as those of adenine. This is due to the larger dipole moment of guanine and also its more favorable orientation close to the direction forming M-N7 bond, as it can be seen in Fig. 2a, c. The stabilization energies of the complexes with divalent ions are larger than those with monovalent ions and, as could be expected, the stabilization energies decrease with increasing atomic number of the metal ions. The only exception is revealed for the Au^+ and Hg^{2+} complexes where, due to the more pronounced relativistic effects, the respective stabilization energies are larger than the energies of the preceding cations (Ag^+ and Cd^{2+}).

In the coinage and zinc-group metal complexes, the bonding interaction is markedly stronger in comparison with coordination of the Ia and IIa metals. This is due to the presence of lower-energy vacant s-orbitals (compared with the same orbitals of the alkali metals), enabling to some extent the dative bonding into these orbitals from the occupied MO's of the bases. This leads to the increase of covalent character of the interaction that explains the basic difference between coordination of, e.g., K^+ and Cu^+ cations.

Complexes with Li^+ bare cation were computationally explored in gas phase by Russo et al. (Russo and Toscano 2001) at the DFT(B3LYP) level within several

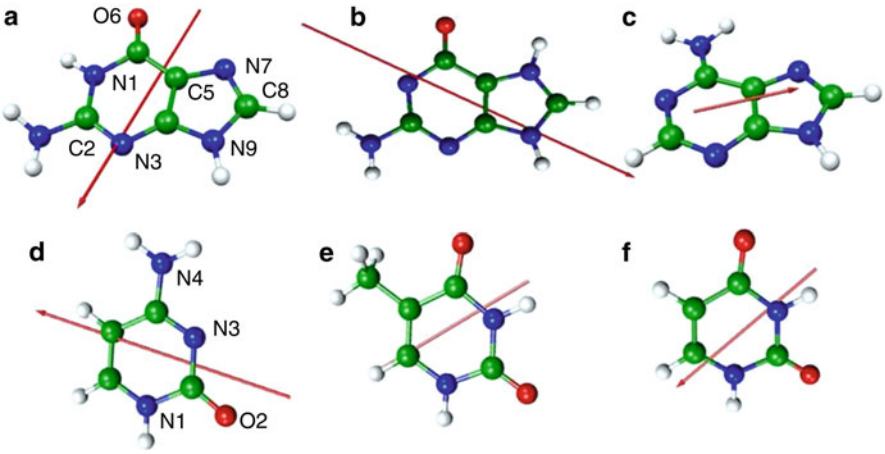

Fig. 2 Orientation and size of dipole moments in the isolated NA bases: (**a**) guanine – 6.98 D, (**b**) N7 protonated guanine tautomer – 9.16 D, (**c**) adenine – 2.43 D, (**d**) cytosine – 6.64 D, (**e**) thymine – 4.47 D, (**f**) uracil – 4.54 D determined at B3LYP/6-311++G(2df,2pd)//B3PW91/6-31G(d,p) in gas phase. Standard atom numbering is used (e.g., textbook of Saenger (1983))

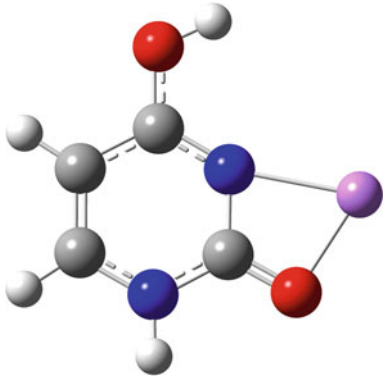

Fig. 3 Structure of the $[Li\text{-}(Ura\text{-}O2,N3)]^+$ cation (enol form of O2,N3-chelate)

basis sets. They found that the most stable complex of adenine with lithium is imino-tautomer with N6,N7 coordination. In this way, a five-membered chelate is formed where Li^+-N6 bond is 1.971 Å, and Li^+-N7 distance is 2.022 Å. The remaining explored (amino) structures, $[Li\text{-}(Ade\text{-}N3,N9)]^+$, $[Li\text{-}(Ade\text{-}N6,N7)]^+$, and $[Li\text{-}(Ade\text{-}N3)]^+$, lie by about 2, 10, and 15 kcal/mol higher on the potential energy surface. In the guanine adducts, the most stable structure is $[Li\text{-}(Guan\text{-}O6,N7)]^+$ followed by chelate $[Li\text{-}(Gua\text{-}N3,N9)]^+$, its enol form, and the enol form of the (O6,N7)-chelate, which are by 11, 12, and 15 kcal/mol less stable. The most stable complex with uracil is $[Li\text{-}(Ura\text{-}O4)]^+$ adduct. The chelate structures $[Li\text{-}(Ura\text{-}O2,N3)]^+$ (cf. Fig. 3) and $[Li\text{-}(Ura\text{-}O4,N3)]^+$ lie about 3 and 7 kcal/mol above the global minimum and the $[Li\text{-}(Ura\text{-}O2)]^+$ adduct is about 5 kcal/mol above the

O4-conformer. This fact indicates the electrostatic origin of the interaction when one considers the direction of the uracil dipole moment. In the cytosine complexes, the $[Li\text{-}(Cyt\text{-}O2,N3)]^+$ structure is the most stable minimum followed by enol-tautomer of $[Li\text{-}(Cyt\text{-}N1,O2)]^+$ (where N1 proton is transferred to O4 site) and the enol form of $[Li\text{-}(Cyt\text{-}O2,N3)]^+$. These two complexes lie about 12 and 17 kcal/mol higher on the potential energy surface. The same strategy was also applied for evaluation of Mg^{2+} and Ca^{2+} in their next paper (Russo et al. 2003). Later Marino et al. (2007, 2010) and Bagchi et al. (2012) performed DFT calculations on the interaction of naked zinc group metals with NA bases in gas phase obtaining qualitative agreement with our energies (Burda et al. 1996). Moreover pyrimidine bases are explored, too. Altogether, the preference for binding to various NA bases is G > C > A > T > U. We performed another study on the Ru(II)Cl(en)(arene) piano-stool complex where various sites of all NA were also investigated (Futera et al. 2009a). In this study ligated Ru(II) cation, similar preferences followed for gas phase calculations: G > A > C > T > U. When solvated (CPCM) model was considered, the order of binding preferences changed: G > C > T > U > A. Nevertheless, it should be stated that the difference between binding to G and A is only about 9 kcal/mol and all three last bases (T, U, and A) are in 1 kcal/mol energy span.

The coordination of divalent metal cations with the phosphate group of various nucleotides (GMP, AMP, UMP, and CMP) was studied (probably) for the first time by Varnali (Varnali and Tozumcalgan 1995). In her study semiempirical PM3 method was used. From the results it follows that the most stable metal adducts are formed with the phosphate group of AMP closely followed by CMP for all explored metals.

The calculations of the NMR spin-spin coupling constants and the NMR shifts of the direct and water-mediated binding of divalent metal cations to guanine were performed by Sychrovský (Sychrovsky et al. 2004). The intermolecular coupling constants ^1J(X, O6) and ^1J(X, N7) ($X = Mg^{2+}$, Zn^{2+}) were unambiguously assigned to the specific binding motif of the hydrated cation with O6 and N7 sites of guanine. The calculated coupling constants ^1J(Mg, O6) and ^1J(Zn, O6) are 6.2 and −17.5 Hz for the inner-shell complex where the cation directly interacts with the guanine O6 position. For the inner-shell coordination of the cation at nitrogen N7, the calculated coupling constants ^1J(Mg,N7) and ^1J(Zn,N7) are 5.6 and −36.5 Hz, respectively. When the cation binding is water-mediated, the corresponding coupling constants are zero. The calculated NMR shifts $\delta(N7) = -15.3$ and −12.2 ppm upon the coordination of Mg^{2+} and Zn^{2+} ion are similar to the NMR shift of 19.6 ppm toward the high field measured by Tanaka (Tanaka et al. 2002) for the coordination of Cd^{2+} to the N7-guanine site.

The B3LYP/6-311 + G(2df,2p) level was used to explore geometry of all possible adducts originating from the interaction of Cu^{2+} cation with the most stable tautomers of NA free bases (Marino et al. 2004). Several attachment sites for both purine and pyrimidine bases have been taken into account for possible formation of both monoadducts and chelates. It was concluded that the copper ion Cu(II) has the highest affinity for the most stable tautomer of guanine base. Further, a comparison of various divalent metal cation complexes (Zn, Cu, Ni) with hypoxanthine and

uracil was performed by Matsubara (Matsubara and Hirao 2002). The B3LYP level stabilization energies of both M(II)-hypoxanthine and M(II)-uracil complexes reflect the strength of the M-N(base) interaction giving the same stability sequence Zn > Cu > Ni for both bases.

Metal Interactions in Implicit Solvent Model

The calculated interaction energies of the bare cations with nucleobases have revealed a great overestimation of the electrostatic interaction in comparison with experimental samples. This overestimation is clearly due to the uncompensated charge of the bare cation in the gas-phase calculation compared to water solution where the charge of the cation is screened by solvent molecules. In this way, the electrostatic part of the metal-base interaction is substantially reduced. A role of the electrostatic contribution in the case of the Pt-base coordination will be enlightened later. The approach of implicit solvent models is very popular in many variants (COSMO (Frank Eckert 2006; Klamt and Schuurmann 1993), PCM (Mennucci et al. 1998; Miertus et al. 1981), SMD (Marenich et al. 2009), GBM (Roux et al. 1990; Mukhopadhyay et al. 2014) etc.), and there is a large number of such studies. Here only a few recent works will be mentioned for illustration.

In 2008, Ai et al. (2008) published a study on the tautomer equilibrium of adenine in presence of Zn^{2+} cation at the DFT level (B3LYP/6-311 + G**). It was found that the $[Zn\text{-}(Ade\text{-}N6,N7)]^{2+}$ imino complex is the most stable structure in accord with the gas-phase calculations of Kabeláč (Kabeláč and Hobza 2006). The latter calculations explored tautomers of all DNA bases in presence of bare Na^+, Mg^{2+}, and Zn^{2+} cations evaluated at the RI-MP2/TZVPP level of theory.

The binding of first-row transition metal monocations (Sc^+-Cu^+) to N7 of guanine and N7 or N3 of adenine nucleobases was studied using the DFT approach with B3LYP functional. The electrostatic character of these interactions is mainly represented by metal-ligand repulsion. The M^+-guanine binding energies are about 18–27 kcal/mol larger than those of M^+-adenine, when the differences decrease along the row (Noguera et al. 2008).

Another study on an interaction of bare cations with metabolite of purine bases-uric acid should be mentioned (Allen et al. 2006). Geometries of the complexes of Li^+, Na^+, K^+, Be^{2+}, Mg^{2+}, and Ca^{2+} metal cations with various nucleophilic sites of uric acid were optimized at the B3LYP/6-311++G(d,p) level. Single point energy calculations were performed at the MP2/6-311++G(d,p) level. It was found that cations mainly form chelate structures with a bidentate coordination. In the gas phase, the most preferred position for the interaction of Li^+, Na^+, and K^+ monovalent cations is between the N3 and O2 sites, while all divalent cations prefer coordination between the N7 and O6 sites of the urate. However, it was simultaneously shown that the incorporation of aqueous solution in the model has a significant impact on the relative stability of various complexes. The global minimum of urate with Mg^{2+} and Ca^{2+} cations is represented by the O2,N3-chelates in analogy with monovalent cations. Moreover, the relative energy differences are

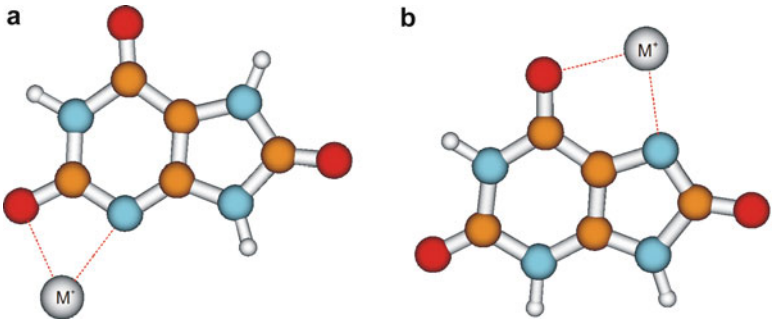

Fig. 4 The optimized structures of the metal complexes with urate: (**a**) O2,N3-chelate, (**b**) O6,N7-chelate

very small. Especially for the Ca^{2+} structures, energies of all conformers are practically in the 2 kcal/mol range. The most stable structures are depicted in Fig. 4.

Metal cation binding to deoxyguanosine monophosphate was examined by Bouř (Andrushchenko and Bour 2009). Infrared spectra of complexes with Na^{+}, Mg^{2+}, Ca^{2+}, Ni^{2+}, Cu^{2+}, Zn^{2+}, and Cd^{2+} cations were recorded and interpreted on the basis of the density functional theory. The solvation effects were simulated by PCM and cluster models (combined explicit solvent and PCM). The coordination to the guanine N7 position was considered and the obtained calculated spectra predict a blueshift of the characteristic 1578 cm^{-1} frequency, in accord with experimental data. Metal binding to the phosphate group causes significant spectral changes in the sugar-phosphate vibration region but also notable frequency shifts of the carbonyl vibrations. The Cu^{2+} and Zn^{2+} cations induce the largest changes in measured vibrational absorption, which corresponds to the computationally determined strong interaction energies in the N7-complexes. The Cu^{2+} binding to guanine was revealed to be a two-step process, which was also confirmed by the microcalorimetry titration curve.

Interactions of Explicitly Hydrated Cations

The most realistic approach to the description of metal cation interactions with nucleobases is represented by a model of the explicitly hydrated cations – usually up to hexacoordinated cations. Recently, explicit hydration has been used in connection with implicit solvation shell (combined model), e.g., in the study for hydration of Ag^{+} by Martínez et al. (1997), for acid-base properties of goethite surface model (Aquino et al. 2008) or for modeling of electrified interfaces (Benedikt et al. 2013) or already mentioned study of Bouř (Andrushchenko and Bour 2009).

Table 2 Interaction energies in the complexes of solvated cation (Mw)-(N7)purine (G/tG/A)

	$\Delta E_{\text{Mw-G}}$	$\Delta E_{\text{Mw-tG}}$	ΔE_{MG} bare	$\Delta E_{\text{Mw-A}}$	ΔE_{MA} bare
Mg^{2+}	**−89.3**	**−84.8**	−198.7	**−46.0**	−107.9
Ca^{2+}	**−82.6**	**−80.1**	−133.9	**−33.5**	−61.6
Sr^{2+}	**−76.0**	**–**	–	**−28.9**	−48.9
Ba^{2+}	**−71.2**	**−71.4**	−118.3	**−28.1**	−54.4
Zn^{2+}	**−93.8**	**−90.1**	−237.2	**−53.7**	−152.9
Cd^{2+}	**−87.9**	**−107.6**	−192.6	**−45.9**	−116.6
Hg^{2+}	**−94.3**	**−149.2**	−208.0	**−55.3**	−141.1

Hydrated Alkaline Earth and Zinc-Group Metal Cations

One of the first studies on this topic was published by Šponer et al. (1998a). In the study, pentaaqua cation adducts (of Mg^{2+}, Ca^{2+}, Sr^{2+}, Ba^{2+}, Zn^{2+}, Cd^{2+}, and Hg^{2+}) to the N7 position of guanine were explored at the MP2/6-31G*//HF/6-31G* level. Quasi-relativistic energy-averaged Stuttgart pseudopotentials were used for the description of the third and higher-row cations. The interaction between hydrated cation and guanine is significantly reduced compared to the guanine-unsolvated cation model, cf. Table 2. The cations of IIb group together with Mg^{2+} are tightly bound to the N7 atom of guanine, whereas the O6 site is involved in H-bonding with the aqua ligands from the metal hydration shell. The metals with greater radius (Ca^{2+}, Sr^{2+}, and Ba^{2+}) prefer simultaneous coordination to the N7 and O6 atoms of the base. Also, the cation-guanine distance increases with the atomic number. The energy difference between the N7 and N7-O6 types of coordination is rather small. Relativistic effects are apparent in the case of Hg^{2+}, similarly to the complexes with the bare cation reported above (Burda et al. 1996). The Zn^{2+} and Mg^{2+} cations show a different balance between the cation-base and cation-water interactions. While the Zn^{2+}cation is bound more tightly to the base (93 kcal/mol) and its water shell is more flexible (203 kcal/mol), a different situation (with stronger metal-water binding) was found in the Mg^{2+} complex. The binding energy of the $Mg(H_2O)_5{}^{2+}$ cation with N7 position of guanine in GC pair is approximately 89 and binding energy of five water molecules with Mg(GC) complex is about 220 kcal/mol. The different binding picture for Zn and Mg cations can be partly explained as a shift from the interaction between nucleobase and hydrated cation (Mg) toward the hydration of a metalated base (Zn).

It follows from Table 2 that despite the substantial reduction of the M-N7 interaction energy, the ratio of the energies for guanine and adenine remains approximately equal to two, similarly to the results obtained in the study of the bare cations (Burda et al. 1996). This confirms the dominant role of electrostatic term in these complexes. In platinum complexes, substantially higher coordination-covalent contribution is demonstrated in the limit of total charge going to zero (cf. in Figs. 9 and 15, below).

The tautomeric equilibrium and hydrogen bonding in nucleotide 2′-deoxyguanosine monophosphate in interaction with hydrated $[Mg(H_2O)_4]^{2+}$

cation were studied at the MP2/cc-pVDZ//B3LYP/cc-pVDZ and B3LYP/aug-cc-pVTZ//B3LYP/cc-pVDZ levels of theory by Gorb (Kosenkov et al. 2008). The Mg^{2+} ion forms two inner-shell contacts with the nucleotide, similar to small phosphorylated molecules under physiological conditions. The hydrated magnesium cation in the presence of the phosphate group can change the guanine tautomeric equilibrium in comparison to free guanine. The canonical O6-oxo form of guanine is more stable (by 6–8 kcal/mol) than the 06-hydroxo form in anticonformation. The interaction with Mg^{2+} ion is capable to suppress a spontaneous transient formation of the rare tautomer. The question, which coordination mode of hydrated Mg^{2+} cation with DNA is dominant (direct metal-N7 coordination or indirect interaction by water molecule through the polarized H-bonding), was addressed by Bandyopadhyay (Bandyopadhyay and Bhattacharyya 2003). Based on HF and DFT calculations, the authors show that both binding modes are of a similar importance.

An interesting situation was revealed when interactions of thioguanine (tG) base was explored (Šponer et al. 1999b). In accord with the Pearson HSAB principle (Parr and Pearson 1983), a stronger interaction with S6 site of thioguanine is observed for the heavier transition metal cations, as can be seen by corresponding columns $\Delta E_{\text{Mw-G}}$ and $\Delta E_{\text{Mw-tG}}$ in Table 2. While a mild weakening of the binding energy is even visible in the case of alkaline earth cations (Mg^{2+}, Ca^{2+}), a very robust adduct is formed with the Hg^{2+} cation. This strong coordination is also partially the consequence of a smaller number of water molecules in the first hydration shell. Due to this strong Hg-S coordination, two water molecules are pushed out from the first hydration shell. Optimized N7,S6-chelate structure resembles the arrangement with the bare cation, cf. Fig. 5b. However, a shorter Hg-S distance (2.50 Å) was obtained comparing the Hg-N bond (2.57 Å). A similar chelate structure was also found in the Cd^{2+} complex, despite the coordination with four water molecules, cf. Fig. 5c. A slightly longer Cd-S distance (2.67 Å)

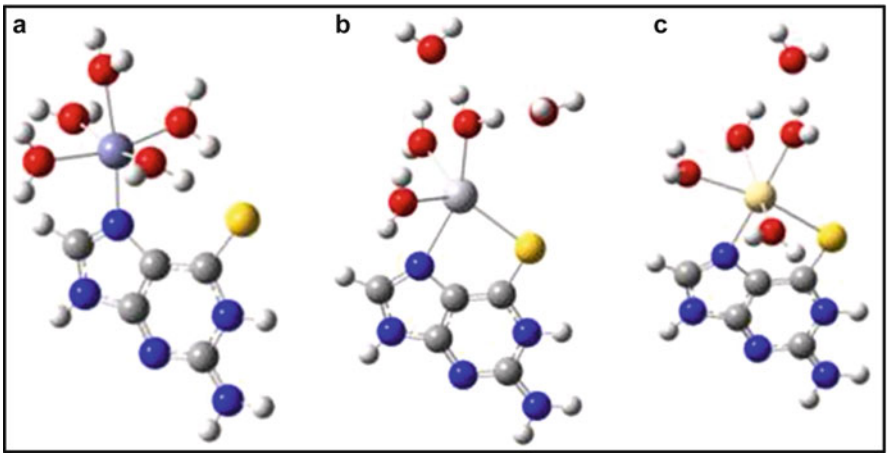

Fig. 5 Different cases of hydrated-metal coordination to thioguanine: (**a**) Zn, (**b**) Hg, and (**c**) Cd

than Cd-N (2.40 Å) was obtained in that structure. In the remaining complexes no direct metal-sulphur interaction was found at the HF/6-31G* optimization level. Nevertheless, using the DFT level, slightly different coordination pattern is revealed for Mg and Zn cations. The preferred structure contains six coordinated cation sphere but only with four water molecules similar to the chelate arrangement of the Cd^{2+} complex (Šponer et al. 1999b) as shown in the Fig. 5c.

Possible binding of hydrated cations to nucleobases in a cation-pi manner led to the conclusion that such interactions are very unlikely in the case of nucleic acids as they are outcompeted by conventional cation binding patterns. The suggestion of existence of cation-pi interactions in DNA was shown to be a case of misinterpretation of structural data (Šponer et al. 2000a).

Later extended study by Rulisek (Rulisek and Šponer 2003) explored adducts of hydrated divalent metal cations (Mg^{2+}, Cu^{2+}, Zn^{2+}, and Cd^{2+}) to the guanine N7 position interacting in outer- and inner-shell manner with an anionic phosphate group. The results obtained by the B3LYP and MP2 computational level are compared. Their calculations illustrate that the cations have a different balance of water-cation and N7-cation binding, leading to selectivity toward the N7 binding in the following order: $Cu^{2+} >> Zn^{2+} = Cd^{2+} > Mg^{2+}$. It is consistently reflected by changes of interatomic distances upon cation substitution, changes of both absolute electronic and interaction energies. The energetics of the cation selectivity is typically on a scale of 3–10 kcal/mol. The calculations demonstrate that the inner-shell binding to the phosphate is more stable than the outer-shell binding. Nevertheless, this does not mean that such a conclusion can be generalized for real samples where the phosphate group is included in the form of sugar-phosphate backbone.

Complexes of Hydrated Copper Cations with Guanine

Interaction of hydrated Cu(I)/Cu(II) cations with guanine represents another interesting explored system. In this case also redox properties under hydration can be compared to copper complexes with water and ammonium ligands (Pavelka et al. 2008; Burda et al. 2005). One of the examined features of the copper complexes involves the number of coordinated ligands. While the Cu(I) complexes prefer two-coordinated structures, the geometry of Cu(II) complexes has usually the coordination number four or five, in accord with the small inorganic copper complexes studied previously (Pavelka and Burda 2005; Pavelka et al. 2006). Also, the affinity of various active sites of the metalated guanine for water molecules in comparison with nonmetalated (isolated) base was explored. The resulting preference for individual conformers determined at the B3LYP/6-311++G(2df,2pd) level can be seen in Table 3 and the most stable structures are displayed in Fig. 6. The affinity of individual sites of the isolated bases was explored by Poltev et al. (1996) using empirical potentials. They found that in the case of guanine hydration by a single water molecule, the global minimum structure has one water molecule between O6 and N1 sites, followed by the N1-N2 water adduct. The N9 position was not considered since this position is not accessible in nucleosides. In another study (Colominas et al. 1996), various tautomeric forms of guanine and cytosine

Table 3 The relative differences of Gibb's free energies ΔG and stabilization energies ΔE^{Stab} and Cu-N7 and Cu-O binding energies for the selected conformers in kcal/mol

Conformer	ΔG	ΔE^{Stab}	E(Cu-N)	E(Cu-O)
1	0.0	−168.4	83.4	60.4
2	1.1	−167.9	81.0	59.9
3	2.6	−165.3	80.4	60.7
4	3.5	−166.5	74.4	60.6
5	3.6	−167.7	76.5	60.1

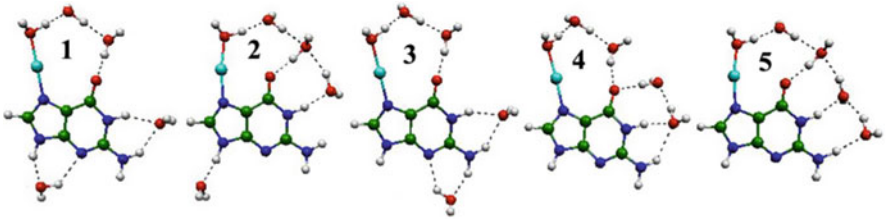

Fig. 6 The most stable conformers of $[Cu(H_2O)_5(N7\text{-guanine})]^+$ complex

Table 4 Relative differences of Gibbs energies $\boldsymbol{\Delta G}$ and stabilization energies $\boldsymbol{\Delta E^{stab}}$ (in kcal/mol) with respect to global minima structure. Abbreviation *c.n.* stands for the coordination number and *struct.* is used for identification of the optimized structure in Fig. 7

System	*c.n.*	*Struct.*	$\boldsymbol{\Delta G^{total}}$	$\boldsymbol{\Delta\Delta E^{stab}}$
$[CuG(H_2O)_4]^{2+}$	4	*4b*	2.2	4.6
	4^{chel}	*4j*	0.0	0.0
	4^{chel}	*4 k*	2.0	1.0
	5^{chel}	*4 g*	4.3	4.9
$[CuG(H_2O)_5]^{2+}$	4	*5a*	2.8	0.0
	4^{chel}	*5w*	0.0	1.7
	4^{chel}	*5y*	1.1	1.0
	5^{chel}	*5 h*	6.4	5.4

and their influence on Watson-Crick H-bonding were explored. From these results, it is clear that there is no substantial change due to the polarization effects of Cu(I) cation revealed by semiempirical methods, in comparison with the MP2 approach. Also, metal-N7 binding energies can be compared with results of our earlier studies (Burda et al. 1996, 1997) on metal coordination to the purine DNA bases. Despite the fact that in the earlier investigations only bare cations were considered at the MP2/6-31G(d)//HF/6-31G(d) level, the interaction energy is fairly similar to the analogous energies of these hydrated structures.

The adducts of the hydrated copper(II) cation with guanine were explored in the study of Pavelka (Pavelka et al. 2006). Various numbers of water molecules were considered in combination with the different coordination pattern of the Cu^{2+} cation. The most stable structures are summarized in Table 4 and displayed in Fig. 7. The full set of investigated structures can be viewed in the original paper (Pavelka et al. 2006).

From this study it follows that the penta-coordination of Cu(II) in these complexes is visibly less convenient than that in the case of the small inorganic complexes (for both aqua ligands (Burda et al. 2004) or mixed aqua-ammine ligands

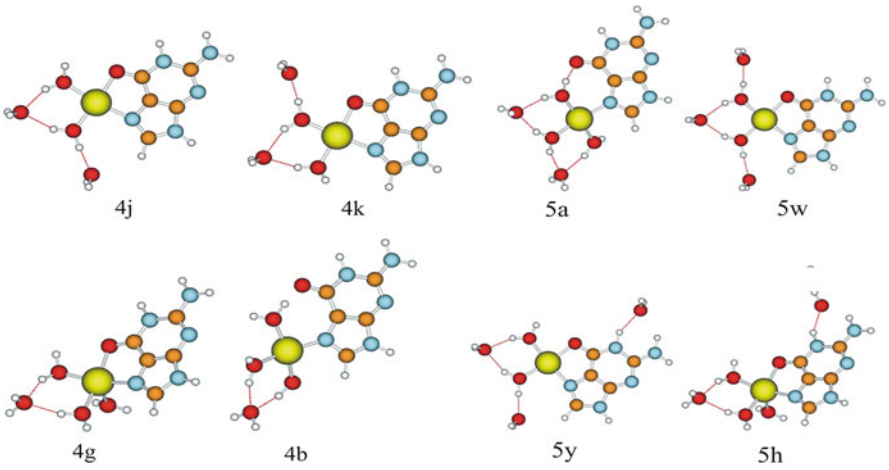

Fig. 7 The most stable structures of Cu-guanine complexes with four and five water molecules

(Pavelka and Burda 2005)). The Cu(I) complexes do not create chelate structures since linear monoaqua form with the remaining water molecules in the solvation shell is substantially more stable. In the monoaqua Cu(I) and Cu(II) complexes, the strength of Cu-N7 bond (−81/-230 kcal/mol for Cu(I)/Cu(II)) and Cu-O(aq) bond (−35/-46 kcal/mol) roughly follows formal electrostatic relationship. The higher preference for N7 coordination in Cu(II) complex is related to the possibility of the higher electron transfer from more polarizable nitrogen atom.

Interactions with Platinum Metal Complexes

One of the most frequently studied metals in connection with nucleobases is platinum. Since late sixties when B. Rosenberg published his study on anticancer activity of cisplatin (Rosenberg et al. 1965, 1969), a lot of effort is devoted to this compound and its derivatives, as well as to some other transition metal complexes where similar activities can be expected. One of the early calculations was performed by Basch et al. (1986) and by Lipinski (1989). Since then a vast number of both experimental and theoretical studies can be found in literature on this topic, especially on platinum interactions with nucleobases, nucleotides, and other DNA models. One of the most important questions, which need to be solved, concerned tautomeric equilibria due to the possible point mutations. This topic was addressed in several studies considering various nucleobases. Metallodrugs are generally expected to coordinate predominately in the major groove of genomic DNA. Therefore our discussion starts with the interaction in N7 position of purine bases.

An interesting study on the difference between protonation and metalation of the N7 position of deoxyguanosine was published by Baik et al. (2002). While under

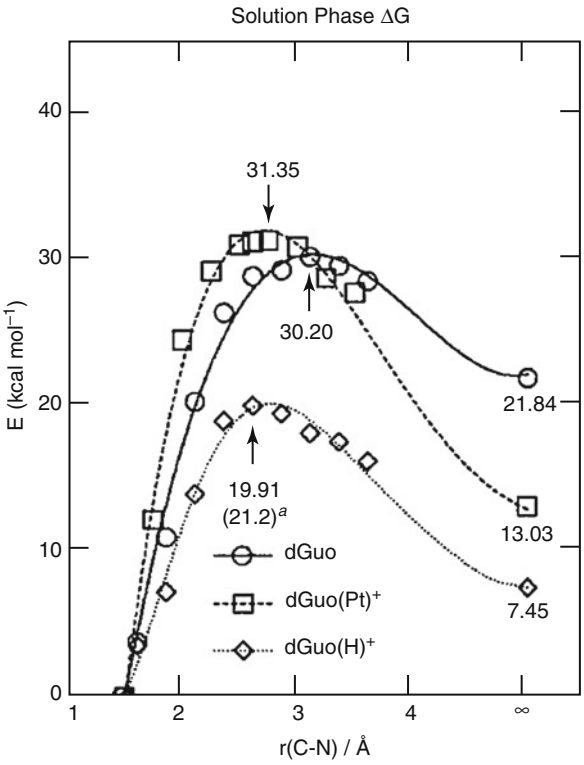

Fig. 8 Reaction free energy profile for dissociation of N9-C1′ glycoside bond of dGuo, dGuo(H)$^+$, and dGuo(Pt)$^+$ in solvent

protonation the glycoside N9-C1′ bond breaks, the Pt(II) adduct does not change the strength of the glycosidic bond substantially, as can be noticed from the Fig. 8.

The Tautomeric Equilibrium of the Metalated Nucleobases

Several platinum complexes with varying total charge were explored at B3LYP/6-31G(d) level (Burda et al. 2000): neutral trans-dichloro-ammine-platinum, +1 charged trans-diammine-chloro-platinum, and +2 charged triammine-platinum. Two tautomers of guanine were considered – keto and enol forms as well as N6-amino and syn- and anti-imino forms of adenine. In this way the role of electrostatic contribution could be elucidated. Despite the gas-phase calculations, the bonding energy and tautomeric relations in solvent can be easily estimated. In Fig. 9, the relative tautomeric stabilization energies are displayed for adenine and guanine.

From this figure it follows that the trans-imino-tautomer of adenine is better stabilized under platination, which could lead to mispairing. In the case of guanine, the regular keto form is more stable for charged complexes. Moreover, the enol preference in the electroneutral complex is caused by the additional H-bonding stabilization between platinum ligand (aqua or chloro) with hydrogen from the enol group (cf. Fig. 10a). Such stabilization may not be present in solvent due to competitive H-bonding interactions with other water molecules. This study in

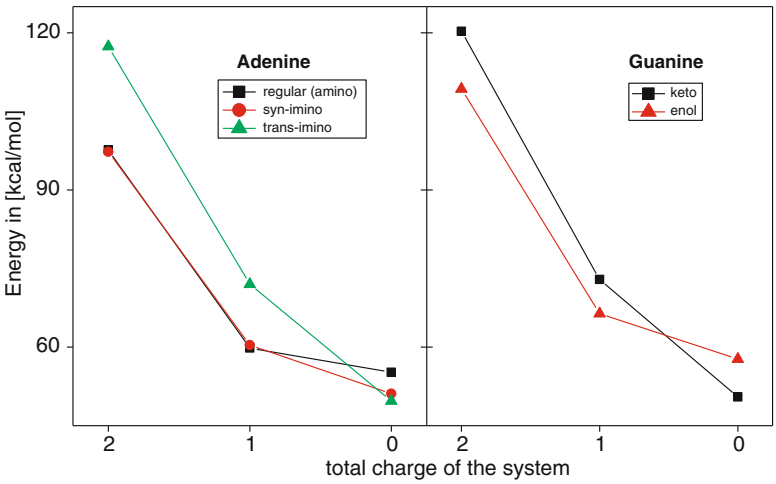

Fig. 9 Stabilization energies of the platinum-base complexes in dependence on total charge of the (**a**) Pt-adenine and (**b**) Pt-guanine complex

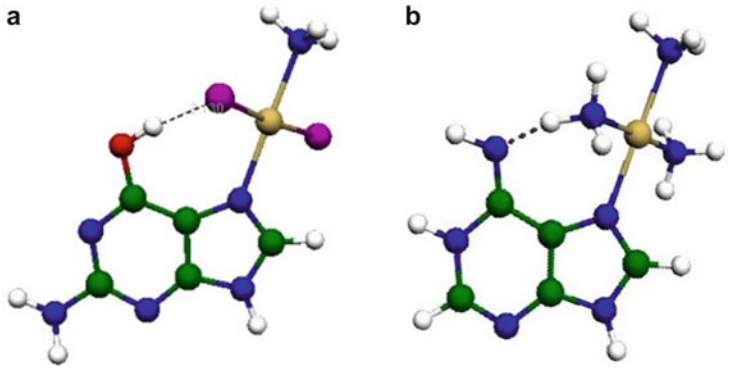

Fig. 10 Structure of platinum(II) complexes with (**a**) enol-tautomer of guanine and (**b**) trans-imino-tautomer of adenine

general suggests that the largest part of the tautomeric effects of the N7 platination is due to gas phase effects, which are assumed to be annihilated in real assays.

Metalation of the exocyclic amino group of cytosine and adenine nucleobases was explored in the case Pt(II) and Hg(II) complexes (Šponer et al. 1999c). It induces protonation of the N3 site of cytosine and N1 site of adenine. Hence, it causes a proton shift from an exocyclic to an endocyclic N atom (similar to situation in Fig. 10b). In this way the metal-assisted process can lead to the generation of rare nucleobase tautomers. The calculations demonstrate that metalation of the exocyclic amino group of nucleobases significantly increases the protonation energy of the aromatic rings of nucleobases by about 30–34 kcal/mol for the Pt(II) adduct and by about 10–14 kcal/mol for the Hg(II) adduct. This study demonstrates a

tautomeric shift that is caused by changes of the electronic structure of nucleobases and is unrelated to electrostatic effects. Thus, authors suggested a separation of purely electrostatic effects from nonelectrostatic (molecular orbital) contributions. The former ones are expected to be rather unimportant in aqueous solution or x-ray crystallography experiments, where the systems are overall strictly neutral. The nonelectrostatic contributions are assumed to remain insensitive to the environment and fully expressed under usual experimental conditions.

Rare tautomers of 1-methyluracil (MeUH) and 1-methylthymine (MeTH) in coordination with Pt(II) complexes were explored by van der Wijst et al. (2009). Comparing the calculations in gas phase and water, the influence of the solvation effects was estimated. They also showed that relative stabilization energies of the Pt(II) complexes with various tautomers of MeUH and MeTH differ from the isolated tautomers. This leads to the conclusion that some rare tautomers may become favored under metalation.

Recently, a reduction mechanism of $Pt^{IV}(DACH)Cl_4$ in the presence of dGMP was explored (Šebesta and Burda 2016). The first step represents a substitution reaction of a chloro-ligand by dGMP followed by a nucleophilic attack of phosphate or sugar oxygen to the C8 position of guanine. Subsequently, the reduction reaction occurs forming the $Pt^{II}(DACH)Cl_2$ complex. The whole process is completed by hydrolysis. Two different pathways for the substitution reaction were examined: direct associative and Basolo-Pearson autocatalytic mechanism. While activation barriers for direct association were too high, the barriers based on Basolo-Pearson mechanism are used for estimation of the rate constants (according to Eyring's TST) and are compared with experimental values. It was found that the rate determining step is the nucleophilic attack with a slightly faster performance in 3′-dGMP branch than in 5′-dGMP with the activation barrier of 21.1 and 20.4 kcal $\cdot$ mol^{-1} comparing with experimental values of 23.8 and 23.2 kcal $\cdot$ mol^{-1}, respectively. The reduction reaction is connected with the electron flow from guanine to Pt complex (cf. Fig. 11).

The product of reduction reaction is a chelate structure, which dissociates within the last reaction – hydrolysis. The whole redox process (substitution, reduction, and hydrolysis reactions) is exoergic by 34 and 28 kcal $\cdot$ mol^{-1} for 5′-dGMP and 3′-dGMP, respectively.

Interaction of Nucleobases with Half-Sandwich Ru(II) Complexes

Recently, computations on ruthenium complexes with nucleobases were published by Futera (Futera et al. 2009b). In his comprehensive study, interactions of piano-stool ruthenium metallodrug with nucleobases were investigated. In the same study, the reaction profile of the chloro-ligand replacement by water molecule and the role of the arene-ring size were also explored. From the point of this review, an important part of Futera's study deals with interactions of Ru(II) with various sites of all the nucleobases in vacuum and in the implicit solvent model. For the optimized structures, the bonding and stabilization energies were determined. Characteristics of the most stable conformers are summarized in Table 5. From the Table 5 it follows that in the case of purine bases, the most stable adenine structure (Ru-(Ade-N1) conformer) differs from the most stable guanine complex (Ru-(Gua-N7) conformer)

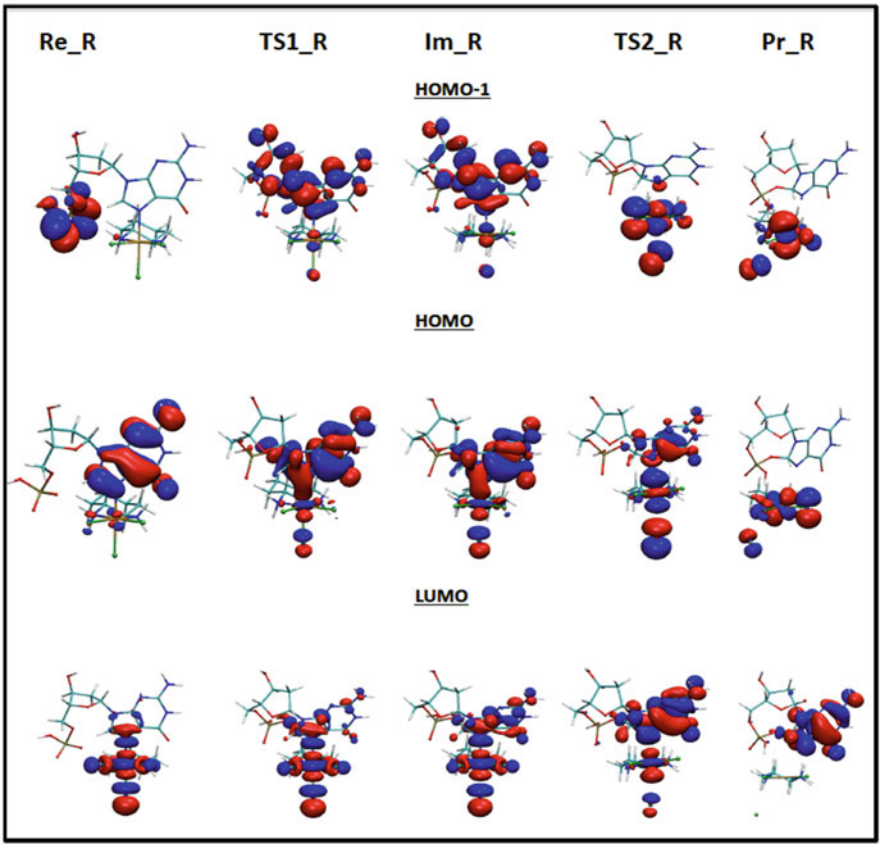

Fig. 11 Electronic flux from HOMO to LUMO of the supermolecular Tetraplatin/dGMP system

as revealed in the gas-phase calculations. Nevertheless, in the PCM model, the N7-conformer represents the most stable form of the both purine nucleobases. This change of the Ru-adenine global minimum follows from the general reduction of the electrostatic forces, which are substantially screened in PCM approaches. In gas phase, the Ru-(Ade-N1) coordination is enhanced by favorable orientation of the adenine dipole moment of about 2.70 D (determined at the MP2/6-31++G(d,p), gas-phase level) aiming in N1-C8 direction while the guanine dipole of 6.36 D points in N7-N3 direction, as can be seen in Fig. 2. Even larger dipole moment was predicted for N1-guanine tautomer with proton transferred to N7 atom ($\mu = 9.55$ D). This dipole moment correlates with the fact that the Ru-(Gua-N1) adduct exhibits the highest ΔE^{BE}(Ru-(base-N)) binding energy among all the explored complexes (interestingly, in both gas phase and PCM approach). The analogous effect of decreased electrostatic enhancement is also responsible for the change in energy preference in the case of cytosine adducts. The Ru-(Cyt-O2) structure becomes the least stable in implicit water model (by more than 7 kcal/mol) and the most

Table 5 Binding and stabilization energies (in kcal/mol)

	Ru(bz)(A-N1)		Ru(bz)(A-N3)		Ru(bz)(A-N7)		Ru(cym)(A-N7)	
Adenine	g.p.	COSMO	g.p.	COSMO	g.p.	COSMO	g.p.	COSMO
$\Delta E^{BE}(A)$	−72.7	−48.7	−69.1	−47.7	−69.7	−50.3	−65.4	−50.2
ΔE^{Stab}	431.1	389.2	426.9	387.9	426.2	390.0	441.4	396.5
Guanine	Ru(bz)(G-N1)		Ru(bz)(G-N3)		Ru(bz)(G-N7)		Ru(cym)(G-N7)	
$\Delta E^{BE}(G)$	−103.9	−59.7	−56.4	−45.3	−90.7	−56.0	−86.1	−57.2
ΔE^{Stab}	442.7	390.9	412.6	384.7	449.7	395.3	465.6	383.3
Cytosine	Ru(bz)(C-N1)		Ru(bz)(C-N3)		Ru(bz)(C-O2)			
$\Delta E^{BE}(C)$	−89.5	−56.0	−79.0	−52.8	−84.0	−45.9		
ΔE^{Stab}	441.1	392.6	438.4	392.2	444.6	389.2		
Thymine	Ru(bz)(T-N1)		Ru(bz)(T-N3)		Ru(bz)(T-O2)		Ru(bz)(T-O4)	
$\Delta E^{BE}(T)$	−65.0	−46.5	−82.8	−51.3	−53.9	−31.3	−60.0	−34.7
ΔE^{Stab}	407.4	372.3	424.9	380.3	412.5	374.0	420.2	376.2
Uracil	Ru(bz)(U-N1)		Ru(bz)(U-N3)		Ru(bz)(U-O2)		Ru(bz)(U-O4)	
$\Delta E^{BE}(U)$	−61.6	−45.9	−79.8	−51.1	−50.8	−31.7	−59.1	−34.3
ΔE^{Stab}	403.2	371.2	422.7	380.5	410.5	375.3	419.3	377.3

stable adduct is Ru-(Cyt-N1) closely followed by the Ru-(Cyt-N3) complex with practically the same stabilization and total electronic energies. The thymine and uracil bases favor the N3 coordination regardless the environment. This preference is in accord with different orientation of the dipole moment of uracil and thymine in comparison with cytosine (cf. Fig. 2). Another computational study dealing with interaction of different forms of ruthenium complexes with DNA bases was published recently (Besker et al. 2007). Here similar binding energies (in comparison to Futera's work) were obtained for relevant structures in both gas phase and PCM.

Molecular mechanism for the replacement of chloro-ligand by water and subsequently of aqua-ligand by nucleobase was also explored by Futera (Futera et al. 2009c). Similarly to the platination process, the hydration reaction is mildly endoergic ($\Delta G = 2$ kcal/mol). Formation of the guanine adduct is exoergic by ca 7 kcal/mol. Nevertheless, all these reactions are faster in the case of the ruthenium complex (in equimolar concentrations) since the activation barriers are lower, e.g., the values for replacement of both adenine and guanine are about 18 kcal/mol while in the cisplatin case analogous barriers are ca 20 kcal/mol (cf. Table 8). Moreover, while "simple" mechanism was found in adenine reaction (as displayed in Fig. 12a), a two-step reaction mechanism was suggested for the guanine replacement (Fig. 12b).

In these mechanisms, a lower activation barrier for the substitution by adenine corresponds to higher rate constant (1.7 $M.s^{-1}$ vs. 0.5 $M.s^{-1}$). Nevertheless, since the minimum associated with the reaction coordination ("direct reactant") of adenine is about 4 kcal/mol higher than the global minimum it means the concentration of the conformer corresponding to this local minimum will be by

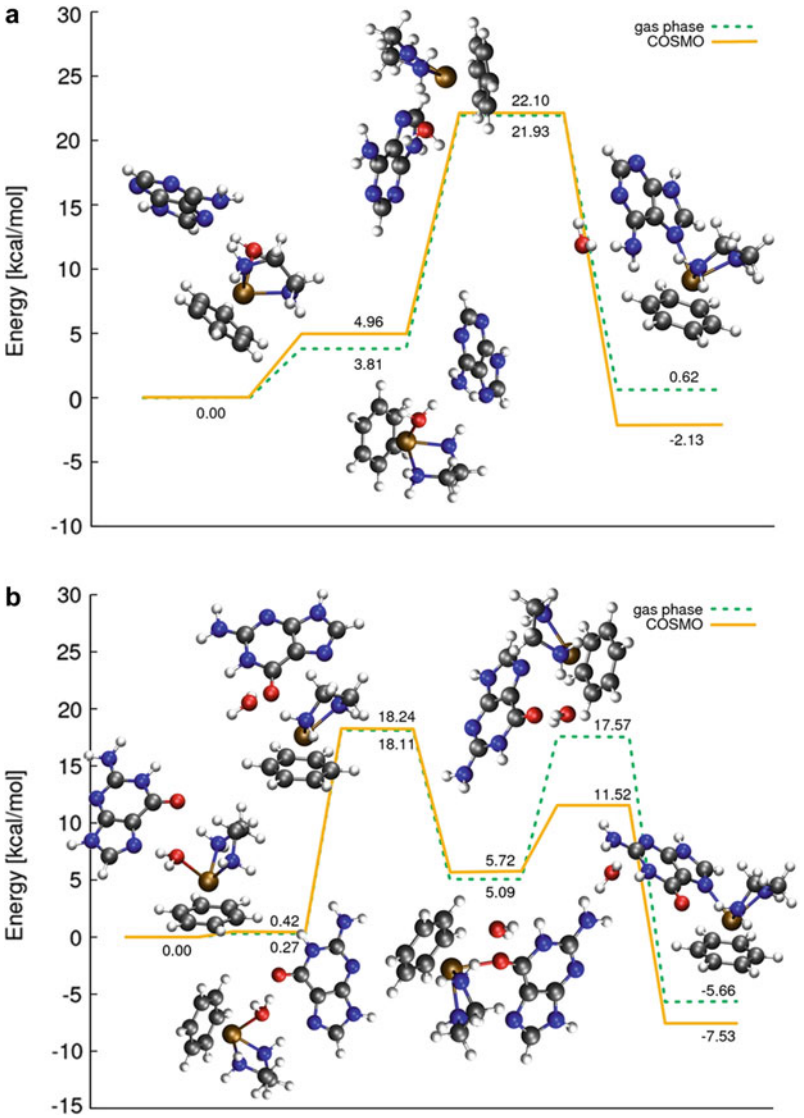

Fig. 12 (**a**) Reaction coordinate for replacement of water by adenine and (**b**) guanine

three orders of magnitude lower (according to the Boltzmann equilibrium law). A different situation occurs for the analogous local minimum of guanine. Here the instant concentration (under assumption of equilibrium) of the local reaction minimum is comparable to the global minimum and therefore, the real reaction rate will be actually substantially higher in the reaction with guanine.

Osmium complexes were also considered as possible metallodrugs. The hydrogenation energies of various nitrogen heterocycles in the presence of osmium tetraoxide were investigated and published by Deubel (2003). While hydrogenation of pyrimidine bases is exothermic, the purine C4-C5 bond does not have a tendency to hydrogenate.

Another study on tautometic equilibria and connected proton transfer (PT) from the N3 site to O2 site of thymine was explored by Burda et al. (2016). It is shown that PT in the presence of additional water molecule reduces activation barrier from 51 kcal/mol to ca 22 kcal/mol. Nevertheless, when solvated cations ($[Mg(H_2O)_6]^{2+}$, $[Zn(H_2O)_6]^{2+}$, and $[Hg(H_2O)_6]^{2+}$) are coordinated to the O2 and O4 site of thymine by two of their aqua ligands, then further reduction of the activation barrier to ca 6–8 kcal/mol was observed due to polarization of these ligands.

The Metal Coordination to Multiple Nucleobase Systems

Interaction with Base Pairs

Metal Cations from Ia, Ib, IIa, and IIb Groups

An influence of metal coordination in major groove on the enhancement of base pairing was explored by Burda et al. (1997). The energy decomposition for these systems requires, besides total stabilization and pair energies, also the nonadditive three-body contribution.

The studied complexes were partitioned into three subsytems: the two bases (B_1, B_2) and a metal cation (M). The total stabilization energy (ΔE^{Stab}) is, within the BSSE counterpoise error, defined as:

$$\begin{aligned}\Delta E^{\mathrm{Stab}} = -\{E(B_1, B_2, M) - [E(B_1, gB_2, gM) \\ + E(gB_1, B_2, gM) + E(gB_1, gB_2, M)]\}\end{aligned} \tag{2}$$

where E(B_1, B_2, M) represents the total energy of the whole complex, and, e.g., E(B_1, gB_2, gM) is a total energy of the base B_1 in the presence of the basis functions on the ghost systems B_2 and M. Alternatively, the total stabilization energy ΔE can be expressed in terms of pair stabilization energies and the three-body contribution:

$$\Delta E^{\mathrm{Stab}} = E(B_1 - B_2) + E(B_1 - M) + E(B_2 - M) + E(3) \tag{3}$$

where each pair-stabilization energy is calculated within the BSSE scheme. For example, the E(B_1-B_2) energy can be determined from formula:

$$E(B_1 - B_2) = -\{E(B_1, B_2, gM) - [E(B_1, gB_2, gM) + E(gB_1, B_2, gM)]\} \tag{4}$$

Besides these pairwise energies, interactions of one subsystem of the complex (metal or pyrimidine) with the remaining part were also evaluated. The interaction of thymine with (metal + adenine) subsystem can be determined as:

$$E(MA-T) = -\{E(A,T,M) - [E(A,gT,M) + E(gA,T,gM)]\} \quad (5)$$

The whole systems can be regarded as a composition of a strongly bonded metal cation-purine base part plus two weak interactions: metal cation-remote pyrimidine base and Watson-Crick H-bonded base pair. The latter two terms represent only a small perturbation of the first one, and their mutual influence is basically very small. Therefore, it is not surprising that similar geometry and energy parameters for metal coordination were obtained, comparing with the analogous characteristics in ref. (Burda et al. 1996). Also, the obtained geometries match well with the results reported by Anwander et al. (1990) for complexes with Ca^{2+}, Mg^{2+}, and Zn^{2+}. Some small differences originate from a smaller basis set, which they have used: too short distances between the purine base and the metal cation, especially for the Zn^{2+} complexes (our calculations predict 1.95 Å for the Zn^{2+}GC complex, while Anwander reported 1.72 Å).

The metal cation significantly influences the geometry of the base pair. The (C)O2 . . . H-N2(G) H-bond lengths in the GC complexes are systematically reduced, in comparison with the isolated pair. This reduction is the largest for bivalent ions (up to 0.3 Å). The central H-bond N3-H . . . N1 remains practically unchanged, and the third N4-H . . . O6 H-bond, which is the closest one to the metal cation, is significantly lengthened in comparison with the isolated GC pair. The elongation is again the largest for bivalent ions (0.65 Å in Zn^{2+}GC and Mg^{2+}GC). In the AT pair, the metal cations affect the H-bonds in a different way. The (T)O4 . . . H-N6 H-bond, which is closer to the metal-ion coordination site, shows a substantial shortening (0.35 Å in complexes with Zn^{2+} and Mg^{2+}), while the other H-bond (N3-H . . . N1) is lengthened (by 0.18 Å in Zn^{2+}AT complex). The geometric rearrangements of the pair structures can be regarded as rotation around the center of the pyrimidine ring towards the metal cation in the case of the AT pair and away from it in the case of the GC pair.

Basically, the same dependencies of the stabilization energies on increasing atomic numbers of metal cations are observed in metal-purine-pyrimidine complexes like in previously published metal-purine species (Burda et al. 1996). Stabilization energies of complexes with divalent ions are larger than those of monovalent ions, and M-GC stabilization energies are larger than those for M-AT complexes. Both conclusions reflect the dominant role of the ion-dipole electrostatic contribution to the stabilization energy of these complexes.

Compared with the study of Anwander (Anwander et al. 1990), a very close agreement was obtained for complexes of Ca^{2+} with base pairs (within 5 kcal/mol). However, larger differences were found in Mg^{2+}-containing systems ($\approx$20 kcal Mg^{2+}-AT and $\approx$40 kcal Mg^{2+}-GC; the values in our work describe larger stabilization – for both base pairs). Nevertheless, the use of a minimal basis set (MBS) for zinc (all-electron calculations) nearly doubles the

stability (ΔE^{HF}(MBS:Zn^{2+}-GC) = 448 kcal/mol vs. our value ΔE^{HF}(AREP:Zn^{2+}-GC) = 254 kcal/mol and ΔE^{HF}(MBS:Zn^{2+}-AT) = 328 kcal/mol vs. ΔE^{HF}(AREP:Zn^{2+}-AT) = 158 kcal/mol).

The H-bond WC interactions in the AT pair within the geometries of M-AT complexes are systematically weakened in comparison with the isolated optimized AT pair (ΔE^{MP2} = 12.3 kcal/mol). This weakening, which is larger for divalent ions amounts to about 4 kcal/mol, leading to AT pairing energy of ca 8 kcal/mol. A similar weakening of H-bonds was expected to occur in the M-GC complexes (cf. Table 6). However, it was found that ΔE^{MP2} of H-bonds in the GC pair within the M-GC complexes are a little stronger (with Ca^{2+}-Ba^{2+} exceptions) than those of the H-bonds in the isolated GC pair ($\Delta E^{MP2} = -26.3$ kcal/mol). It can be shown that these changes correspond to the geometry deformation under the metal coordination. From the energy decomposition it can be concluded that the H-bond strength of GC or AT pair, calculated as a pairwise interaction energy within the optimized M-GC or M-AT complexes, is influenced by cations only marginally. However, metal cations bound to the WC base pairs dramatically (directly or indirectly) change many characteristics of the base pairing. Actually, one should not consider pairwise energies of the G-C and A-T pairs but the MG-C and MA-T H-bonding energies and these values are systematically higher – up to 24 kcal/mol for A- T and 48 kcal/mol for G-C H-bonding in the presence of Zn^{2+} cation. It amounts to nearly two times enhancement of the original base pairing energy.

Similar conclusions are also reported in other studies on the metal-nucleobases interactions. A trimer base arrangement was explored using a similar computational model. The enhancement of G.GC(rH), G.GC(H), A.AT(rH), T.AT(H) and some other base interactions including reverse Hoogsteen pairs GG(rH) and AA(rH) was proved in the presence of Li^+ and Ca^{2+} cations (Šponer et al. 1997). A study on the strength of H-bonding of WC base pairing under metalation at various active sites of bases concluded that the N3(Adenine) site available in the minor groove has higher chances for platination, in comparison with the N7-site of the base (Zhang and Huang 2007).

The results of investigation on Cu^+/Cu^{2+} interaction with AT and GC pairs were published by Sodupe's group (Noguera et al. 2004, 2007). The influence of metal cations coordinated to N7 of guanine on the intermolecular proton-transfer reaction in guanine-cytosine base pair was studied with the B3LYP density functional. Gas phase metal cation interaction stabilizes the ion pair structure derived from the N1-N3 single-proton-transfer reaction, the effects being more pronounced for the divalent cation than for the monovalent one. For Cu^{2+}-GC, the reaction is largely favored due to both electrostatic and oxidative effects. Hydration of the metal cation reverts this trend due to the screening of electrostatic effects.

In the section on the interaction of hydrated metal complexes, Šponer's study (Šponer et al. 1998a) was mentioned where in addition to purine nucleobases, the GC, AT, and AA base pairs were also considered. Since the metal-purine base interaction is not substantially influenced by the remote pyrimidine base we will

Table 6 Enhancement of Watson-Crick base pairing energy under the metalation. (in kcal/mol) (energies calculated at the MP2/6-31G** level)

Metal	E(M-A)	E(A-T)[a]	E(M-AT)	E(MA-T)	E(M-A-T)	E(M-G)	E(G-C)[a]	E(M-GC)	E(MG-C)	E(M-G-C)
Cu^{+}	−54.5	−12.0	−58.6	**−16.1**	−70.5	−79.9	−27.2	−86.1	**−33.3**	−113.3
Ag^{+}	−36.0	−12.0	−40.0	**−16.0**	−52.0	−64.2	−27.0	−69.0	**−31.8**	−96.1
Au^{+}	−55.0	−12.0	−59.1	**−16.1**	−71.1	−75.9	−27.0	−81.8	**−32.9**	−108.8
Zn^{2+}	−152.9	−10.8	−165.9	**−23.8**	−176.7	−237.2	−26.1	−259.4	**−48.2**	−285.4
Cd^{2+}	−116.6	−10.9	−129.3	**−23.6**	−140.2	−192.6	−25.9	−211.3	**−44.6**	−237.2
Hg^{2+}	−141.1	−10.9	−153.8	**−23.7**	−164.7	−207.9	−25.9	−228.0	**−45.9**	−253.9
Mg^{2+}	−107.9	−10.8	−120.7	**−23.5**	−131.5	−198.6	−25.9	−217.8	**−45.1**	−243.8
Ca^{2+}	−61.6	−11.1	−73.1	**−22.6**	−84.2	−133.8	−25.7	−146.9	**−38.8**	−172.6
Sr^{2+}	−48.9	−11.2	−59.8	**−22.1**	−71.0					
Ba^{2+}	−51.4	−11.2	−62.3	**−22.1**	−73.5	−118.8	−25.6	−130.4	**−37.2**	−156.0

focus on the base pair enhancement and some changes observed in comparison with the study on bare metal cations complexes (Burda et al. 1997). The strength of the guanine-cytosine Watson-Crick base pair is enhanced by ca. 20–30 % due to the coordination of the hydrated cation, while in the case of bare cations this enhancement was about 60–90 %.

In the study of Oliva et al.(Oliva and Cavallo 2009), an impact of binding of hydrated Mg^{2+}, Mn^{2+}, Co^{2+} to the N7 position of guanine on Watson-Crick and reverse Watson-Crick base-pairs was investigated at the MP2 level. The combined model, where implicit solvent (COSMO) is considered together with an explicit first hydration shell of the cation shows that the stabilization effect of metalation on Watson-Crick geometry is rather weak – from 0.1 kcal/mol for Mg^{2+} to 0.8 kcal/mol for Co^{2+} cation. In the case of reverse Watson-Crick base pair, the stronger stabilization was determined in the range from 1.7 kcal/mol for Mg^{2+} and Mn^{2+} to 2.2 kcal/mol for Co^{2+}, which is in accord with our previous study (Šponer et al. 1998a). It was also shown that for the hexahydrated cations, the binding energies increase in the order $Mg^{2+} < Mn^{2+} < Co^{2+}$. The lowest stability of Mg^{2+} cation can be explained by missing back-donation from the aromatic ring of the guanine to empty d orbitals of metal. An impact of metalation of GC base-pair by hydrated Mg^{2+}, Ca^{2+}, Zn^{2+}, Cu^{2+} on vibrational spectra was studied using SIESTA code by Morari et al. (2012, 2014) clearly showing the effect of adduct formation.

An interesting comparison of Zn^{2+} and Mg^{2+} hydrated cations in Pu-Pu-Py triplexes was carried out (Šponer et al. 1998b) where a hydrated metal is coordinated to the N7 position of purine base attached to the Watson-Crick base pair. Using this model, metal assisted triplex stabilization was studied. It was shown that in both A.A and GG, the Hoogsteen pairing is strengthened under metalation. A substantially stronger enhancement of (MG).G pairing was revealed (19.8 and 20.4 kcal/mol for Mg^{2+} and Zn^{2+} cations, respectively), in comparison with similar adenine structures where no additional stabilization was practically detected (only about 2.7 kcal/mol for both metal cations). In another study (Šponer et al. 1999d), a more extended set of divalent metal cations (Mg^{2+}, Ca^{2+}, Sr^{2+}, Ba^{2+}, Zn^{2+}, Cd^{2+}, and Hg^{2+}) hydrated by five water molecules was explored with rAA and AT base pairs interacting with N7 site of adenine confirming the previously obtained results.

Rare tautomers of NA bases are important from the point of view of the global mutagenicity of DNA. Their formation by proton transfer between N1(G) and N3(C) in canonical Watson-Crick base pair was studied by Céron-Carrasco et al. (Ceron-Carrasco and Jacquemin 2011), extended later using ONIOM (QM/QM) method (Ceron-Carrasco et al. 2012b) for metalated B-form d(G-C,Mg-G-C,G-C) trimer. These authors explored also cisplatin cross-linked ds-DNA 5′-d(AG*G*C)-3′ (Ceron-Carrasco et al. 2012a) tetramer. In the latter case, the calculations of PT energy profile were performed using ONIOM approach at M06-2X/6-311++G(d,p):AMBER(UFF) level with both crosslinked G*C base pairs and cisplatin in the QM part. LANL2DZ basis set was used for a description of Pt atom. The formation of the rare tautomer in crosslinked G*C pairs through the PT is characterized by an increase of the electronic energy by 9–12 kcal/mol if the considered DNA arrangement is close to the experimental NMR structure (Wu

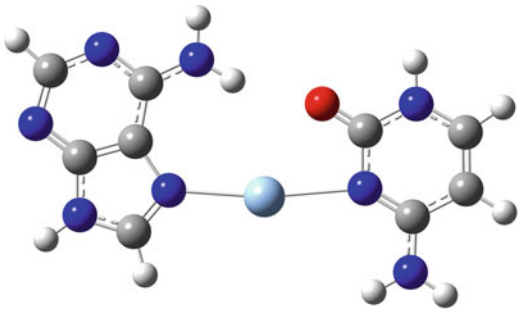

Fig. 13 Cytosine-M^+-Adenine complexes, M = (Cu, Ag, Au)

et al. 2007). The corresponding activation barriers are only by 0.2–0.5 kcal/mol higher than reaction energy in the given case. In the former case, the hydrated Mg^{2+} cation is coordinated to nitrogen N7 of guanine. The reaction energy of 3.2 kcal/mol and the activation barrier of 8.0 kcal/mol for the considered N1(G) to N3(C) proton transfer were determined at M06-2X/6-311++G(d,p):B97-D/6-31+G(d)/PCM level. The inner part was consisted of GC base pair and hydrated Mg^{2+} cation.

An interesting idea is related to a replacement of proton in H-bonding by metal. Nowadays, these metal mediated NA base structures are highly investigated for the purpose of obtaining novel materials which might be employed as, for example, electric, fluorescent, or luminescent sensors. In this way, the noncanonical A-C base pair was examined with the coinage metal cations (Cu^+, Ag^+, and Au^+) used as a bridge between both bases (Šponer et al. 1999e), cf. Fig. 13. A possibility of additional water coordination to the metal was also considered. In the original paper, it is concluded that these metal bridged complexes are substantially more stable than original (protonated) base pair. The water coordination does not influence the strength of the metal bridge substantially; nevertheless, its presence has some impact on the geometry of the complexes. Comparing bonding properties of all three metal cations, it was found that Ag cation coordinates relatively weakly, which is in good accord with the previous results (Burda et al. 1996, 1997). Slightly shorter bond length d(M-N7-Adenine) than d(M-N3-Cytosine) contradicts the estimated bonding energies since ΔE^{M-A} is smaller than ΔE^{M-C}. This can be explained by two facts: (a) the electrostatic contribution to the metal coordination is much smaller in adenine case (see the size and orientation of the dipole moments of both bases in Fig. 2) and (b) the metal-cytosine interaction cannot be considered purely of the M-N3 character since the M-O2 contribution plays a nonnegligible role too.

Schreiber et al. (Schreiber and Gonzalez 2007a) explored the Ag(I) adducts with DNA base and the influence of Ag(I) coordination for adenine-cytosine mispairing. Their calculations show that in gas phase the canonical form of cytosine is stabilized upon metalation, whereas the lowest energy structure of Ag-adenine corresponds to the imino tautomer. The most stable metalated adenine-cytosine mispair is formed from the canonical cytosine and adenine tautomers. Other types of A-C pairs (e.g., reverse Wobble) were found much less stable. The same authors also performed

an interesting study dealing with the role of Ag(I) cation on electronic spectra of the A-C pairs using very accurate MS-CASPT2 approach (Schreiber and Gonzalez 2007b).

Stability of silver-mediated cytosine:cytosine or cytosine:adenine mismatches was also studied in implicit solvent in more recent studies (Megger et al. 2011a; Fortino et al. 2015). In the case of C:C mismatch, the Ag^+ cation is coordinated to both N3 nitrogen atoms and the trans arrangement of cytosines is favorable since it enables formation of the weak hydrogen bond O2 $\cdots$ H-N4 (2.13 Å). The presence of this hydrogen bond simultaneously causes that N3-Ag-N3 angle is about 160°. Counterpoise corrected binding energy (BE) for described base pair is 34 kcal/mol at B3LYP-D3/6-311++G(2df,2pd)/SDD/COSMO level while the gas phase BE is 43 kcal/mol according to ref. (Fortino et al. 2015).

In contrast to rather planar geometry of C-Ag-C structure, one of the pairs in DNA dimer d(C-Ag-C)$_2$ is characterized by rather large propeller twist of 78°. The Ag $\cdots$ Ag distance (3.9 Å) in the optimized dimer structure is comparable with Hg $\cdots$ Hg distance of 3.8–3.9 Å in (T-Hg-T)$_2$ dimer (Benda et al. 2011). BE of dimer (73 kcal/mol) shows that this energy is practically additive.

Considering C-Ag-A base pair, the Hoogsteen arrangement, where Ag^+ ion is coordinated to N7(A) and N3(C) nitrogen atoms, is more favorable than the Watson-Crick type. The corresponding energy difference is 5.9 and 2.3 kcal/mol for C-Ag-A monomer and (C-Ag-A)$_2$ dimer, respectively.

It was found that if concentration of Ag^+ ions is sufficient, stabilization through two Ag^+ ions becomes preferable in the case of thymine:1,3-dideazaadenine (D) base pair (Megger et al. 2011b). In addition to usual N7(D)-Ag-N3(T) linkage, the second Ag^+ ion is coordinated to N6(D) nitrogen and O4(T) oxygen. The optimized mutual distance between Ag atoms is 2.88 Å. The energy difference of 24 kcal/mol between the base pair with two Ag linkage atoms and the base pair with one linkage N7(D)-Ag-N3(T) plus monohydrated Ag^+ ion was determined at the ZORA-BLYP-D/TZ2P/COSMO level.

Interestingly, possibility of the so-called M-DNA crosslink stabilization of GC base pairs by divalent zinc has been investigated by Fuentes-Cabrera et al. (2007). Further, stabilizations of the base pair of Watson-Crick (AT, AU, GC), Hoogsteen (AT, AU), and Wobble (GU) type by Ib transition metals – Cu^+, Ag^+, and Au^+ cations – were explored (Marino et al. 2012). Additionally, 1-deazaadenine instead adenine was considered in the case of the Hoogsteen type base pairs. The metal cation is coordinated to N7 nitrogen of purine bases and N3 nitrogen of pyrimidine bases in these structures except for N1(G)-M-O2(U) linkage in Wobble base pair. In order to maintain one strong hydrogen bond in Watson-Crick base pairs after incorporation of the metal ion, angle N3-M-N7 is not exactly 180°, but it is in the range from 150° to 180°. The coordination of the metal cation causes an increase of binding energies (determined at the B3LYP-D3 level in gas phase) about 20–35 kcal/mol in comparison with hydrogen-bonded base pairs. Independently on the base pairs and type of binding, stabilization by Cu^+ and Au^+ cations is comparable, while in the case of Ag^+ ion, the binding energy is about 10–20 kcal/mol lower in agreement with (Šponer et al. 1999e).

A detailed study of formation of (T)N3-Hg-N3(T) linkage was performed by Šebera et al. (2013b) The ds-DNA was modeled as trimer G-C, T-T, T-Hg^{II}-T, and the ONIOM (B3LYP/6-31G(d)/SDD:BP86/LANL2DZ with implicit water solvent IEF-PCM/UFF) was used. The initial step represents proton transfer from N3 to hydroxo ligand of hydrated Hg^{2+} ion and subsequent formation of the first Hg-N3(T1) bond. This step is slightly endergonic ($\Delta G_r = 1.4$ kcal/mol) and is related to the very low barrier of 2.9 kcal/mol. The reaction proceeds with the second proton transfer from N3(T2) to O2(T2) (tautomerization) or to another hydroxo ligand of Hg^{2+} ion if it is present. The activation barrier corresponding to tautomerization is 16.5 kcal/mol high, while for proton transfer to the hydroxo ligand the barrier is about 3 kcal/mol lower. The total reaction Gibb's energy is −9.5 kcal/mol and the bond length of both Hg-N3 bonds is 2.15 Å, when the deprotonated product at O2 position was considered.

In order to show changes in electronic properties after formation of Hg^{II} linkage between thymine: thymine mismatch, a charge transfer from donor Ap to acceptor G in ds-DNA tetramer sequence Ap-T-A-G was studied in the low temperature region (Kratochvílová et al. 2014). Electronic coupling $|J_{Ap,G}|$ between Ap and G bases determined using relativistic ZORA at the B3LYP/TZ2P/COSMO level shows that the value of $|J_{Ap,G}|$ increases about 4–5 meV after formation of the Hg^{II} linkage compared to T-T mismatch structure. When the structure of the metal-mediated mismatch is preserved and just Hg atom is removed, the value of $|J_{Ap,G}|$ decreases only by 1 meV. Hence, it was concluded that the structure of the thymine-thymine mismatch is more important for the charge transfer than the presence of Hg^{2+} cation.

Also differences in Raman spectra related to formation of T-Hg^{II}-T linkage were investigated both experimentally and theoretically (B3LYP-D2/6-31+G**/COSMO) (Benda et al. 2012). Spectral shifts are fairly small for both experimental and calculated spectra. However, calculated spectra provide usually slightly overestimated values compared to the experiment. An exception represents the vibrational mode corresponding to C = O stretching (1664 cm^{-1} in TpT), where the red shift of −77 cm^{-1} was observed.

The stability of dimer Tp-Hg-T · T-Hg-Tp with two Hg^{2+} ions was verified for RNA analogue U-Hg-U · U-Hg-U dimer at the spin-component-scaled MP2 level (Benda et al. 2011). The equilibrated distance d(Hg ··· Hg) was determined to 3.8–3.9 Å. Simultaneously, a metallophilic attraction (dominance of a dispersion interaction over repulsive electrostatic one) between Hg atoms was estimated in the range from −1.1 to −0.7 kcal/mol according to a mutual arrangement of the metal-mediated base pairs. The trimeric systems $(T\text{-}Hg\text{-}T)_3$ and $(U\text{-}Hg\text{-}U)_3$ were studied by Marino et al. (Marino 2014) at B3LYP-D3(M06-L)/TVP level in the gas phase. The vertical binding energies between layers were 29.8 and 30.8 kcal/mol for $(T\text{-}Hg\text{-}T)_3$ and $(U\text{-}Hg\text{-}U)_3$, respectively. The binding energies of Hg^{2+} ion in T-Hg-T and U-Hg-U monomers was also determined and their values are 200 and 186 kcal/mol.

Study focused on Ag-mediated Hoogsteen-type base pairs containing cytosine and modified 1,3-dideazapurine and 1-deazapurine at exocyclic O6 position with hydroxo, methoxo, fluoro, chloro, and bromo group was published (Megger et al. 2011a). It was concluded that BE were always lower in comparison with the

mediated C-Ag-G base pair except the base pair containing 1,3-dideaza-6-hydroxopurine, which is characterized by the same energy.

Interactions of Hydrated Cations with Nucleotides

Šponer et al. (2000b) studied the coordination of hydrated zinc and magnesium group divalent cations to the N7 position of purine nucleotides. They showed that the sugar-phosphate backbone provides a significant screening of the metal charge, while the backbone geometry is affected by the cation. Polarized water molecules of the cation hydration shell form very strong hydrogen bond bridges between the cation and the anionic oxygen atoms of the phosphate group. Weaker hydrogen bonds are formed between the cation hydration shell and the exocyclic purine X6 atoms. The cation binding to N7 of adenosine monophosphate forces the adenine amino group to adopt nonplanar conformation. Its nitrogen atom serves as an H-acceptor for a water molecule from the cation hydration shell. Cation binding to N7 does not lead to any major changes in the geometry of the base pairing. However, the stability of the base pairing can be increased by polarization of the purine base by the cation and by long-range electrostatic attraction between the hydrated cation and the other nucleobase. The stability of guanine-cytosine Watson-Crick base pairing is enhanced by the polarization mechanism while the stability of the adenine-thymine Watson-Crick base pair is amplified by the electrostatic effects as shown in the case of base pairs model discussed previously (Burda et al. 1997). Also, the guanine-guanine reverse-Hoogsteen base pairing is stabilized by both contributions while the adenine-adenine reverse-Hoogsteen system is not influenced by the cation. Binding of a cation to the N7 of guanine promotes transfer of its H1 proton to the N3 acceptor site of cytosine. However, the negatively charged backbone exerts a significant screening effect on this potentially mutagenic process, and the probability of such a proton transfer in DNA should be only moderately enhanced by a cation binding.

A comprehensive study dealing with a coordination of hydrated cations Zn(II) and Mg(II) to guanosine 5′ monophosphate was performed by Gresh (Gresh et al. 2003) in order to obtain parameters for polarizable molecular mechanics for metal-DNA and metal-RNA simulations.

An important role of the position of Mg^{2+} ion in the active site of hepatitis delta virus (HDV) ribozyme during its self-cleaving process was described by Mlynsky et al. (2015) using the ONIOM method implemented in Gaussian 09. The reaction starts with deprotonation of O2′-H(U-1) group in the active site of HDV, which is followed by the nucleophilic attack of O2′-(U-1) on phosphorus of the scissile phosphodiester. As a consequence, the P-O5′(G1) bond is broken and O5′ position is saturated by the proton from C75 (cf. Fig. 14). The protonated state at the N3 position of $C75H^{+}$, which occurs with only low probability, was considered as a reactant (estimated pKa for this protonation is 8.8–11.2) together with $[Mg(H_2O)_nOH]^{+}$ used as Brønsted base. The experimentally determined pKa constant for hydrated Mg^{2+} ion is 11.4. On the basis of estimated pKa constants, the Gibbs energy correction for considered protonation state of reactant was 8.3 kcal/mol. In ONIOM calculations (BLYP/6-31 + G(d,p):AMBER(ff99bsc0χOL3), reoptimized with hybrid MPW1K functional), the authors considered eight pathways with the different

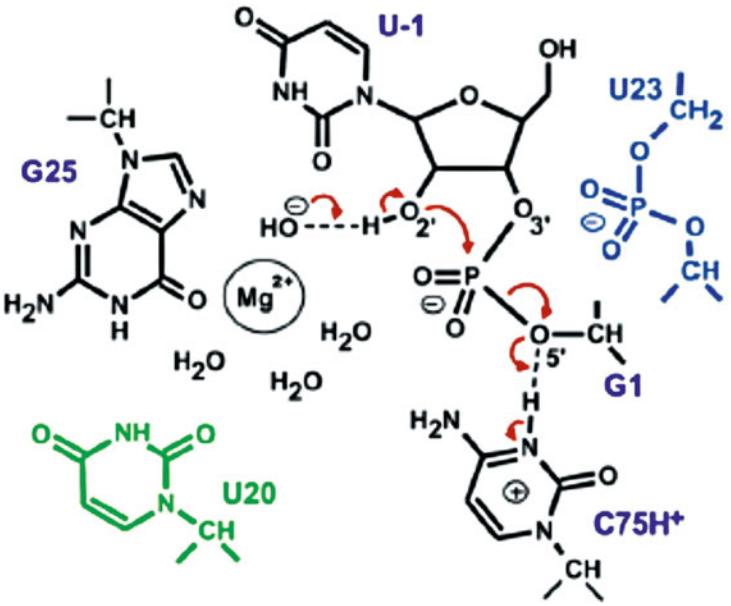

Fig. 14 Active site of HDV ribozyme with coordinated Mg^{2+} cation. Electron transfers during the self-cleavage process are depicted by *arrows*

position of Mg^{2+} ion coordination in reactants based on previous MD simulations. The QM part contained hydrated Mg^{2+} cation, uracil U-1, G1 guanosine, cytosine C75, and guanine G25. The resulting Gibbs energy barriers are in the range from 14.2 to 28.8 kcal/mol and the lowest barrier (14.2 kcal/mol) corresponds to the initial coordination of Mg^{2+} cation to O2(U-1) and O2′(U-1).

Enhancement of Base Pairing by Pt Complexes

Several studies related to platinum metal interactions with base pairs and the influence of metal complexes on the strength of pairing should be mentioned.

Molecular structures of several Pt complexes with the Watson-Crick AT and GC base pairs were optimized using the B3LYP method. The interaction energies were analyzed using B3LYP and MP2 approaches (Burda et al. 2001). Platination causes some distortion in the H-bond arrangement of the base pairs. The pyrimidine bases rotate around their centre of mass under the influence of the charged Pt entities. This effect is quite general and was already discussed above (Burda et al. 1997; Šponer et al. 1998a, 1999b). The metal-binding affects the strength of individual H-bonds involved in the base pairing. It was concluded that ligands attached to the Pt(II) cation form rather strong intramolecular H-bonds with the X6 exocyclic site

of purine bases. The adenine amino group adopts a pyramidal-rotated geometry and its nitrogen serves as H-bond acceptor for the ammine ligands of cisplatin.

The Pt-binding has a comparable effect on the base pairing stability as binding of hydrated metals of IIa and IIb groups. In the electroneutral form, the Pt-adducts does not practically influence the base pair stability. Charged Pt adducts substantially strengthen the stability of GC base pair via polarization effects. The influence of the +2 charged Pt-adduct is even larger compared with hydrated metals of IIa and IIb groups. No such polarization effects have been revealed for the AT base pair. However, gas-phase stability of this pair is effectively enhanced by long-range electrostatic interaction between the charged metal group and thymine.

The dependence of the stabilization and Pt-N7 binding energies on the total charge of the complex is displayed in Fig. 15a. Here, the role of electrostatic contributions is clearly demonstrated for the both kinds of energies. Interestingly, in electroneutral complexes, the Pt-N7 binding energies are similar in guanine and adenine structures (≈50 kcal/mol corresponding to "pure" coordination covalent contribution). In the Fig. 15b, the base pairing energies are drawn showing that the geometry deformations do not basically influence these values. Nevertheless, the interaction of metalated purine base with pyrimidine base is substantially strengthened, especially in the case of charged complexes (e.g., in complexes of hydrated cisplatin). It is important to point out that the effect of base pair stabilization enhancement due to cation binding has been confirmed experimentally by Sigel and Lippert (1999).

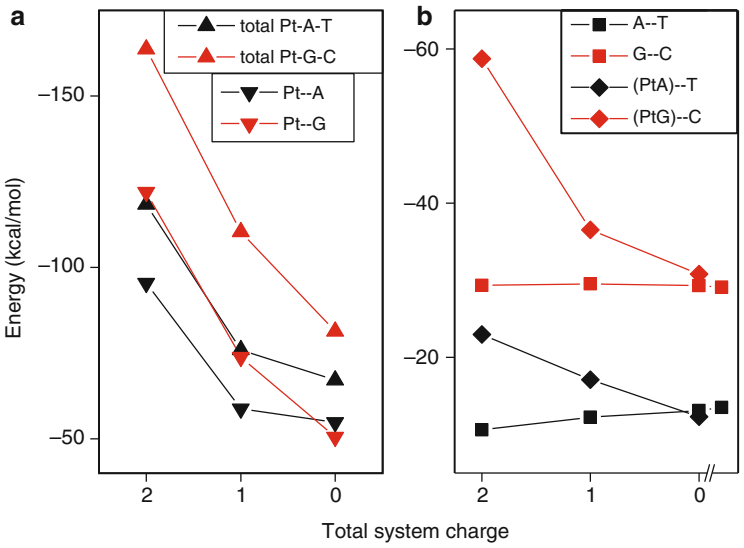

Fig. 15 (**a**) Stabilization and metalation Pt-N7 energies. (**b**) Enhancement of the Watson-Crick pairing energies for AT and GC base pairs

Table 7 Gas phase stabilization energies of the Pt-cross-linked structures (in kcal/mol)

	ΔE^{stab}(MP2)
Pt-a_2A_2	491.5
Pt-a_2AG	514.6
Pt-a_2G_2	528.3

Zilberberg et al. reported an influence of chelated cisplatin complex with guanine(O6,N7) on Watson-Crick base pairing (Zilberberg et al. 1997). In such chelate structures, more distinct perturbation of base pairing was revealed. However, such chelate binding pattern is unlikely to be relevant to experimental conditions.

Metal Cross-Linked DNA Structures

Platinum(II) Complexes

Cisplatin bridges between two consequent bases (1,2-GpG) are believed to be the key structure for triggering the apoptotic process. Recently, several studies on these cross-linked structures have been published. The properties of Pt-bridges were explored (Burda and Leszczynski 2003; Zeizinger et al. 2004) showing that relatively strong Pt-N7 coordination is formed. The process of the aqua ligand replacement by a nucleobase is mildly exoergic in both steps forming: (a) a monofunctional adduct and, consequently, (b) the cross-linked structure. Stabilization energies of the Pt-GG, Pt-GA, and Pt-AA bridges are collected in Table 7. The relative amount of these values correlates well with the abundance of individual structures in real samples, assuming the gas-phase calculations require some additional rescaling in correspondence to the reduced electrostatic interactions in solvent.

An influence of the sugar phosphate backbone on the strength of Pt-bridge was also examined (Zeizinger et al. 2004). An additional stabilization of the Pt cross-linked structures appeared as a result of the interaction between negatively charged phosphate group and the Pt cation.

One of the first papers studying transition states of the replacement aqua ligand by nucleobase was published by Chval (Chval and Sip 2003). His model was based on the gas-phase calculations and the estimated activation barrier is too low in comparison with the experimental value. This situation was improved in studies of Raber (Raber et al. 2005) and Baik (Baik et al. 2003). They have taken into account the hydration effects employing implicit solvent model. Especially, Raber's results are in fairly good accord with experimental data. Activation barriers of monoaqua and diaqua Pt(II) complexes are summarized in Table 8 for both guanine and adenine replacement of the first and second leaving (aqua) ligand. In Table 9, the activation barriers for second and third generation Pt(II) drugs – oxaliplatin, nedaplatin, and carboplatin – are displayed (Alberto et al. 2011), where higher barriers also occur in the case of adenine. According to the calculation of oxaliplatin, the second reaction step should be visibly more energy demanding.

Table 8 Activation barriers of the substitution reaction for the aqua ligand replacement by purine base (in kcal/mol)

1st step	Chloro-aqua	Diaqua
Guanine	21.4[a]	19.5[a]
	25.6[b]	21.8[b]
	14[c]	17.9[c]
		18.3[d]
Adenine	24.0[a]	24.8[a]
	37.6[b]	34.5[b]
	14.5[c]	14.5[c]
2nd step		
GG hh		22.5[a]
		23.4[e]
GA hh		28.6[a]

[a]Ref. (Raber et al. 2005)
[b]Ref. (Baik et al. 2003)
[c]Ref. (Chval and Sip 2003), experimental data
[d]Ref. (Arpalahti and Lippert 1990)
[e]Ref. (Bancroft et al. 1990)

Table 9 Activation barriers for the substitution of the aqua ligand by N7-guanine or N7-adenine in the case of oxaliplatin, nedaplatin, and carboplatin(Alberto et al. 2011) (in kcal/mol)

	Guanine	Adenine
	Monoaqua	
Oxaliplatin	10.2	17.1
Nedaplatin	24.9	26.0
Carboplatin	13.2	25.1
	Diaqua	
Oxaliplatin	21.4	24.1

A comprehensive study on formation of Pt-N7 cross-links between fully hydrated oxaliplatin – cis-$[Pt(DACH)(H_2O)_2]^{2+}$ (DACH = cyclohexane-1R,2R-diamine) – and double-stranded pGpG·CpC dinucleotide was performed by Chval et al. (2013). Structures were optimized in the implicit solvent model at the RI-TPSS-D/MWB-60(f)/def2-SV(P)/COSMO level and the energy profile and interaction energies were subsequently obtained at the ω-B97XD/MWB-60(2f)/6-311 + G-(2d,2p)/IEFPCM/UFF and B3LYP-D/MWB-60(2f)/def2-TPZVPP/COSMO levels. The whole reaction mechanism is depicted in Fig. 16. In the study, both $5' \rightarrow 3'$ and $3' \rightarrow 5'$ binding directions to the DNA dimer were investigated. The reaction energies for the monoadduct formation are −3.3 kcal/mol and −1.8 kcal/mol, respectively. The subsequent cross-link formation from the monoadduct is connected with releasing of −1.0 and −8.5 kcal/mol, respectively. Formation of the first Pt-N7 bond represents the rate-limiting step and the binding to N7 (5′G) is slightly kinetically preferred over N7(3′G). The corresponding activation barrier is 21.2 kcal/mol. The following chelation reaction is more favorable in the $3' \rightarrow 5'$ direction (activation barrier of 17.1 kcal/mol) in agreement with the experimental measurements. Formation of each Pt-N7 bond leads to an increase

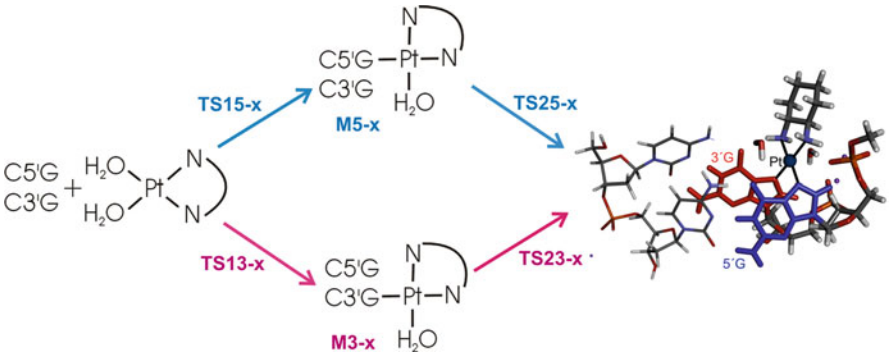

Fig. 16 Scheme of the reaction mechanism for formation of the cross-linked structure by fully hydrated oxaliplatin

of the stabilization between the ds(pGpG) and the Pt(DACH) fragments by about 15 kcal/mol in aqueous solution. Further, the solvent-phase pairing energies are enlarged by about 10 % with respect to the pGpG · CpC dinucleotide itself and do not visibly depend on the number of Pt-N7 bonds for most of the platinated structures. Simultaneously, hydrogen bond O6(G) · · · H4(C) is weakened as a consequence of interaction between amino group of Pt(DACH) and O6 (G). Nevertheless, the described weakening is compensated by strengthening of H1(G) · · · N3(C) and H2(G) · · · O2(C) H-bonds.

An arrangement of two adjacent guanosines (G), which are cross-linked by kiteplatin (cis-Pt(1,4-DACH)Cl_2), were studied by Margiotta et al. (2015) in the case of cis-Pt(1,4-DACH)d(GpG), cis-Pt(1,4-DACH)d(GGTTT), and cis-Pt(1,4-DACH)d(TGGT). An initial systematic conformation search at the LFMM (Ligand Field Molecular Mechanics) (Deeth 2001; Deeth et al. 2009) level for cis-Pt(1,4-DACH)d(GpG) was followed-up by reoptimization in gas and also aqueous phase using the semiempirical PM6-DH2 method (Korth et al. 2010; Řezáč et al. 2009). It was determined that the head to head arrangement of anticonformers of Gs is preferred over the head to tail arrangement by 6 kcal/mol (in solvent), which is in accord with experimental measurements.

Binding energies of cisplatin, oxaliplatin [(cyclohexane-1R,2R-diammine)-oxalato platinum(II)], and kiteplatin (Fig. 17) are mutually compared by Mutter et al. (2015). The strongest binding energy was determined for cisplatin if the interaction of Pt complexes with GpG · CpC dimer was considered at the DFT level (B97-D/TZVP). Binding energies of kiteplatin and oxaliplatin are comparable. This trend is independent on the fact whether the system is in the gas phase or in the water solution represented by COSMO solvent model. Nevertheless, when the GpG · CpC dimer is replaced by octamer (ds-CCTGGTCC) and QM/MM approach was used, the binding energies of cisplatin are the weakest, then follows kiteplatin and the strongest interaction shows oxaliplatin (cf. Table 10). In another study (Gkionis et al. 2013), the interactions of heptaplatin ([2-(1-Methylethyl)-1,3-dioxolane-4,5-dimethanamine-*N*,*N*′]-[propanedioato(2-)-*O*,*O*′]-platinum(II)) and lobaplatin

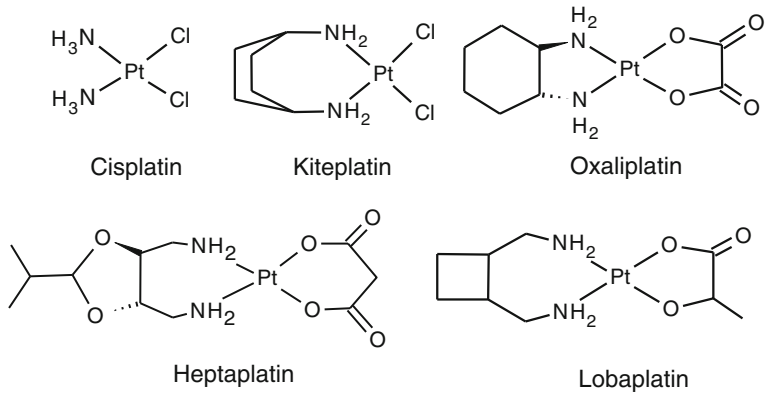

Fig. 17 Structure of the selected Pt(II) drugs

Table 10 Binding energies of cisplatin, oxaliplatin, and kiteplatin to DNA dimer GpG · CpC and octamer ds-CCTGGTCC (in kcal/mol) (Mutter et al. 2015)

	DFT BE[a)] Dimer	ONIOM BE[b)] Octamer
Cisplatin	−129.6	−245.4
Oxaliplatin	−122.6	−299.6
Kiteplatin	−122.0	−282.4

[a]Counterpoise corrected binding energies determined at the B97-D/TZVP/COSMO
[b]Binding energies determined the BH and H/SDD/6-31+G(d,p):AMBER/parm99

(1,2-diammino-methyl-cyclobutane-platinum(II)-lactate) (besides oxaliplatin and cisplatin) with the same octamer were investigated and it was determined that the binding energies are about 38 kcal/mol and 28 kcal/mol, resp., higher than for oxaliplatin. In the former paper, (Mutter et al. 2015) was also mentioned an interesting trend that when the DNA dimer, tetramer, octamer, and dodecamer is considered, the ONIOM binding energy of kiteplatin increases towards octamer, however it is (slightly) smaller for dodecamer. Basically it is a question why binding energy should increase so dramatically with increasing size of the system and it is pity that some deeper analysis (or energy decomposition) is not present.

Ruthenium(II) Complexes

An interesting continuation of the investigations of the "piano-stool" Ru(II) complexes with DNA base mentioned from section "▸ Properties of Metal Adducts with Nucleobases" represents formation of Ru(II) cross-linked structures studied using hybrid ONIOM and QM/MM Umbrella sampling-MD by Futera et al. (Futera and Burda 2014; Futera et al. 2012). An interaction of piano stool complexes with DNA is to some extent similar to cisplatin. The considered representative of piano stool complexes, $[Ru^{II}(\eta^6\text{-benzene})(en)Cl]^+$, must be initially activated by hydration reaction. Subsequently, the Ru(II) complex/DNA monoadduct is formed with the bond between Ru and N7 nitrogen of one of the adjacent guanines G*. Formation of

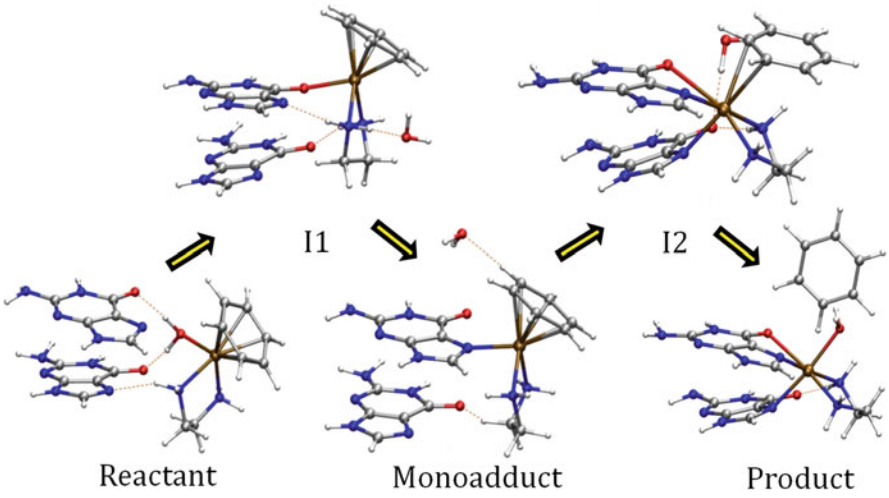

Fig. 18 Formation of Ru(II) cross-link in the presence of hydrated $[Ru^{II}(\eta^6\text{-benzene})(en)Cl]^+$ complex

the Ru(II) cross-link is completed by binding of the complex to N7 position of the second guanine G* (cf. Fig. 18).

The free energy profile in QM/MM MD approach was built using the umbrella sampling approach together with weighted histogram analysis (WHAM) and umbrella integration (UI) methods at the B97D/LANL2DZ:AMBER(parm03) level. Additionally, the FEP (free energy perturbation) corrections determined at B3LYP/SDD/6-31++G(d,p) level were added to increase the accuracy of the model. The ds-DNA was modeled by decamer structure with 5′-AATGG1*G2*ACCT-3′ sequence. The QM core consists of the piano-stool complex and one explicit water molecule in hydration reaction and of hydrated Ru(II) complex and both adjacent guanines G* in the remaining reactions.

For hydration reaction with smaller quantum core, the B3LYP/SDD/6-31G level was used. The Gibb's free reaction energy corresponding to this activation process is 2 kcal/mol and the activation barrier of 19.5 kcal/mol is in good agreement with experimental value (21.1 kcal/mol) (Wang et al. 2005). Formation of the monoadduct and subsequent cross-linked structure leads to decrease of total ΔG energy of the system by 3.4 kcal/mol and 9.5 kcal/mol, respectively. The most stable form of the monoadduct, i.e., with Ru-N7(G1*) coordination, is not formed directly; the substitution goes through a structure where Ru-O6(G1*) is formed first as an reaction intermediate. Similarly to the study (Chval et al. 2013) mentioned above, coordination of the Ru complex to guanine G represents the rate-determining step characterized with the activation barrier of 21.1 kcal/mol in the two step mechanism. Formation of the (G1*)N7-Ru-N7(G2*) cross-linked chelate complex is connected with release of the arene ligand, which is initially η^6-coordinated. In the products, Ru-N7(G2*) bond to the 3′-end guanine is substantially weaker

which is documented by bonding energies of −47 kcal/mol and −35 kcal/mol for Ru-N7(G1*) and Ru-N7(G2*), respectively. The previous ONIOM calculations at the B3LYP/6-31++G(d,p):AMBER(ff96) level (Futera et al. 2012), where the ds-DNA hexamer 5′-GCG*G*GC-3′ model was used, predict higher activation barriers by about 4 kcal/mol for monoadduct formation in the two-step mechanism and by about 2 kcal/mol for direct monoadduct formation.

Ions in DNA Quadruplexes

The infrared (IR) and vibrational circular dichroism (VCD) spectra of guanosine-5′-hydrazide have been measured and analyzed on the basis of ab initio modeling (Setnicka et al. 2008). The B3LYP/6-31G(d,p) calculations predict that guanine, forming a clear solution in deuterated DMSO, is present in monomeric form in this solvent, whereas strong gelation in a phosphate buffer is due to the formation of a guanine-quartet structure. Here, the four bases are linked by hydrogen-bonded guanine moieties and stabilized by an alkali metal cation. The DFT prediction of the IR and VCD spectra are based on the nearly planar quartet structure, which is slightly distorted from the C_{4h} symmetry. The guanine bases interact via four Hoogsteen-type hydrogen bonds and a sodium cation is positioned in the middle of the guanine quartet. The obtained results are in very good agreement with the experimental spectra, indicating that calculated structure is highly probable in the gel state.

The guanine quartets were examined also by Gu and Leszczynski (2000). The normal four-stranded Hoogsteen-bonded G-quartet structures were optimized in the gas-phase with a monovalent cations obtaining the stability order $Li^+ > Na^+ > K^+$. However, after the correction on solvent effects, the stability sequence of the monovalent cation − guanine-tetrad complexes follows the opposite trend $K^+ > Na^+ > Li^+$. The preferential binding of potassium over sodium and lithium in water solutions reproduces the experimental ion selectivity of the guanine quadruplex. Moreover, the weak stabilization energy of the K^+-G-quartet in the coplanar form corresponds with the fact that the potassium cation tends to locate between two successive quartets. These results are in accord with the study of Hud et al. (1998) on the ion selectivity of the guanine quartets in water solutions, which are govern by the relative free energies of hydration. The experimental data on the cation-oxygen distances in the sodium ion complex are 2.34 ± 0.02 Å. This value matches the HF value of 2.33 Å. The slightly shorter Na^+-O6 distance were predicted by the DFT approach together with a significant shortening of the hydrogen bonds suggesting an overestimation of the H-bonding in the guanine quartets at the DFT level. A very comprehensive study on metal-quartet interactions has been published also by Meyer et al. (Meyer et al. 2001). It is to be noted, however, that, in principle, accurate studies of quadruplex-ion interactions would require inclusion of the whole solvated quadruplex fragment, due to the unique balance of molecular interactions in such a noncanonical structure (Šponer and Špackova 2007).

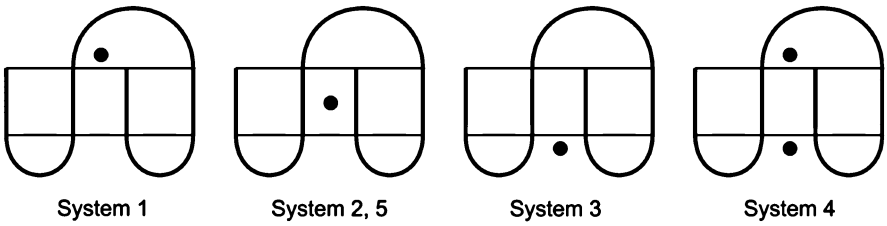

Fig. 19 An initial localization of ion(s) in 15-TBA in five studied systems

Apart from papers concerning guanine stems, duplexes consisting of all NA and isoguanie (iG) tetrads and iG pentads were investigated by Meyer et al. (Meyer et al. 2005, 2007; Meyer and Sühnel 2008) where K^+ or Na^+ ion was used for stabilization of these structures.

Seven distinct folds of two-quartet G-DNA stem which is stabilized by monovalent K^+ ion were studied using the large-scale QM calculation (Šponer et al. 2013). In contrast to the previous studies by Meyer (Meyer and Sühnel 2008), dispersion is included in the model. Optimization of the structures was performed at the RI-TPSS-D3/TZVP/COSMO level and results were compared to few MD approaches. It was shown that the relative stability of 5′-anti-anti-3′ GpG steps (AA) in G-stems is underestimated in comparison with 5′-syn-anti-3′ steps (SA) at the MM level. The final reevaluated stability order (due to the MM approach) gives that the AA arrangement is the most stable followed by SA step lying by 1.2 kcal/mol higher. An exception represents the terminal SA step at the 5′-end, which is by 3.2 kcal/mol more stable than the AA arrangement.

A localization of an ion in the quadruplex stem was investigated at the QM/MM MD level by Reshetnikov et al. (2011). As the model structure, the thrombin-binding aptamer (structure 15-TBA in PDB database) was chosen. The QM part was consisted of all nucleic acid bases (except T7) and K^+ or Ba^{2+} ions and was considered at the DFT level using the PW91 functional. The initial position (upper, central, lower) of ion(s) in five studied systems is depicted in Fig. 19. In systems 1–4, K^+ ion was present, while Ba^{2+} ion was considered in system 5. It was concluded that only the central binding site is stable, since the ion in the systems 1 and 3 moved to the center of the stem. Further in system 4, the lower ion was released and the upper one moved to the center.

The study of Gkionis et al. (2014) explored an ion binding in guanine stems at the DFT-D3 and the MM level (Cornell force field (Cornell et al. 1995)). Series of PES scans of binding of one ion (Li^+, Na^+, and K^+) to two- and three-quartet stems (without the sugar-phosphate backbone) and subsequent PES scans for binding of the second cation were performed for this purpose. In the single-ion case, the difference between the DFT-D3 and MM approach becomes acceptable, when the implicit solvent (COSMO in QM calculations and MM-PBSA (Poisson-Boltzmann surface area)) is concerned as the model. However, in the gas phase, a more attractive potential inside the channel for single-ion case was obtained at the

MM level. A different situation occurs in a multi-ion case. The problem dwells in the missing polarization in the MM calculations. Symmetry adapted perturbation theory (SAPT0) energy decomposition showed substantially weaker electrostatic repulsion between ions at QM level, where the ions can be polarized. Same results followed from the QTAIM analysis. Authors concluded that system with more than one cation cannot be even described correctly with fixed charged model, where the reduced charge on ions in MM simulation is considered.

Noncovalent interactions in two or three stacked guanine or xanthine quartets containing one or two univalent cations (Na^+, K^+) were also investigated at DFT-D3 level by Yurenko et al. (2014). The study shows a structural and energetic compatibility between guanine and xanthine quadruplexes. The hydrogen bonding, ion coordination, and base stacking contributions to the total internal stabilization are compared. The determined contribution of hydrogen bonding is practically independent on the size of the system, and it approximately corresponds to 50 % of the total noncovalent interaction. On the contrary, electrostatic repulsion between cations in trimer systems causes a slight decrease of a share of ion coordination on the total stability, which represents 34–41 % of interaction energy for the duplex. A higher influence of K^+ ion on weakening of hydrogen bonds in the duplex compared to Na^+ cation is caused by stronger interaction with O6 atom given by its larger ionic radius is also mentioned. In general, the absolute values of the energy of ion binding to the considered quadruplex structures are higher for Na^+ than for K^+. An Energy decomposition analysis further shows that the orbital contribution to ion binding is not negligible in comparison with the electrostatic term. Hence, it was concluded that ions interaction in the stem channel cannot be described purely by an electrostatic model.

A similar topic was examined also by Ida (Ida and Wu 2008). In this study, molecular dynamics was employed exploring G-quadruplex stabilized by Na and Rb cations, which were found to be tightly bound to the quadruplex structure. Moreover, in d(G(4)T(4)G(4)) sequences, the Na^+ ions are found to be located in the diagonal T-4 loop region of the G-quadruplex, which is formed by two strands of d(G4T4G4) sequence. The authors proposed that the loop Na^+ ion is located above the terminal G-quartet, coordinating to four guanine 06 atoms from the terminal G-quartet, one O2 atom from a loop thymine base, and one water molecule. The Na^+ coordination was also supported by quantum chemical calculations on ^{23}Na chemical shifts.

Conclusions

In this review, the results of some of the recent investigations on metal interactions with nucleobases, base pairs, and larger models (including base stacking or oligomer sequences) are summarized.

The studies dealing with metal cations (in naked, hydrated, and ligated forms) provide various details on their interactions with nucleobases, however such models are in many cases oversimplified. Despite the fact that some sites on the isolated nucleobase (especially in adenine) exhibits higher affinity to metal cations, in DNA

helix not all of them are available for interactions since they are involved in H-bonding (purine N1 site) or in the glycosidic bond (N9 site).

All forms of metal cations enhance the Watson-Crick base pairing interaction if their positive charge is not fully compensated. The different mechanism for the AT and GC adducts was revealed. While in AT the direct electrostatic link between remote thymine (negatively charged O4) and metal cation exists, in the GC pair the nonadditive three-body term is important since the positively charged NH_2(C) exogroup is in the proximity of the metal cation.

Clearly, metalation at the N7 position leads into many new, exceptional properties of the studied systems that are dependent on characteristics of involved metals. Some of them are discussed in details in various parts of this text.

Acknowledgments The study was supported by projects Grant Agency of the Czech Republic (GAČR) No. 16-06240S. The authors thank the Meta-Centers in Prague (Charles University and Czech Technical University), Brno (Masaryk University), Pilsen (University of West Bohemia) for the generous support of the computational resources.

Bibliography

Ai, H. Q., Yang, A. B., & Li, Y. G. (2008). Theoretical study on the interactions between Zn2+ and adenine isomers in aqueous phase. *Acta Physico-Chimica Sinica, 24*(6), 1047–1052.

Alberto, M. E., Butera, V., & Russo, N. (2011). Which one among the Pt-containing anticancer drugs more easily forms monoadducts with G and A DNA bases? A comparative study among oxaliplatin, nedaplatin, and carboplatin. *Inorganic Chemistry, 50*(15), 6965–6971. doi:10.1021/ic200148n.

Allen, R. N., Shukla, M. K., Burda, J. V., & Leszczynski, J. (2006). Theoretical study of interaction of urate with Li^+, Na^+, K^+, Be^{2+}, Mg^{2+}, and Ca^{2+} metal cations. *Journal of Physical Chemistry A, 110*, 6139–6144.

Andrushchenko, V., & Bour, P. (2009). Infrared absorption detection of metal ion-deoxyguanosine monophosphate binding: Experimental and theoretical study. *Journal of Physical Chemistry B, 113*(1), 283–291. doi:10.1021/jp8058678.

Anwander, E. H. S., Probst, M. M., & Rode, B. M. (1990). The influence of Li+, Na+, Mg2+, Ca2+, and Zn2+ ions on the hydrogen bonds of the Watson-Crick base pair. *Biopolymers, 29*, 757–769.

Aquino, A. J. A., Tunega, D., Haberhauer, G., Gerzabek, M. H., & Lischka, H. (2008). Acid–base properties of a goethite surface model: A theoretical view. *Geochimica et Cosmochimica Acta, 72*, 3587–3602.

Arpalahti, J., & Lippert, B. (1990). Coordination of aquated cis-platinum(II) diamines to purine nucleosides. Kinetics of complex formation. *Inorganic Chemistry, 29*, 104–109.

Bagchi, S., Mandal, D., Ghosh, D., & Das, A. K. (2012). Density functional theory study of interaction, bonding and affinity of group IIb transition metal cations with nucleic acid bases. *Chemical Physics, 400*, 108–117. doi:10.1016/j.chemphys.2012.03.003.

Baik, M.-H., Friesner, R. A., & Lippard, S. J. (2002). Theoretical study on the stability of N-glycosyl bonds: Why does N7-platination not promote depurination? *Journal of the American Chemical Society, 124*, 4495–4503.

Baik, M. H., Friesner, R. A., & Lippard, S. J. (2003). Theoretical study of cisplatin binding to purine bases: Why does cisplatin prefer guanine over adenine? *Journal of the American Chemical Society, 125*(46), 14082–14092.

Banas, P., Jurecka, P., Walter, N. G., Šponer, J., & Otyepka, M. (2009). Theoretical studies of RNA catalysis: Hybrid QM/MM methods and their comparison with MD and QM methods. *Methods, 49*, 202–216.

Bancroft, D. P., Lepre, C. A., & Lippard, S. J. (1990). Platinum-195 NMR kinetic and mechanistic studies of cis- and trans-diamminedichloroplatinum(II) binding to DNA. *Journal of the American Chemical Society, 112*, 6860–6867.

Bandyopadhyay, D., & Bhattacharyya, D. (2003). Different modes of interaction between hydrated magnesium ion and DNA functional groups: Database analysis and ab initio studies. *Journal of Biomolecular Structure & Dynamics, 21*(3), 447–458.

Basch, H., Krauss, M., Stevens, W. J., & Cohen, D. (1986). Binding of $Pt(NH_3)_3{}^{2+}$ to nucleic acid bases. *Inorganic Chemistry, 25*, 684–688.

Benda, L., Straka, M., Tanaka, Y., & Sychrovsky, V. (2011). On the role of mercury in the non-covalent stabilisation of consecutive U-HgII-U metal-mediated nucleic acid base pairs: Metallophilic attraction enters the world of nucleic acids. *Physical Chemistry Chemical Physics, 13*(1), 100–103. doi:10.1039/C0CP01534B.

Benda, L., Straka, M., Sychrovský, V., Bouř, P., & Tanaka, Y. (2012). Detection of mercury–TpT dinucleotide binding by Raman spectra: A computational study. *The Journal of Physical Chemistry. A, 116*(32), 8313–8320. doi:10.1021/jp3045077.

Benedikt, U., Schneider, W. B., & Auer, A. A. (2013). Modelling electrified interfaces in quantum chemistry: Constant charge vs. constant potential. *Physical Chemistry Chemical Physics, 15*, 2712–2724.

Besker, N., Coletti, C., Marrone, A., & Re, N. (2007). Binding of antitumor ruthenium complexes to DNA and proteins: A theoretical approach. *Journal of Physical Chemistry B, 111*(33), 9955–9964. doi:10.1021/jp072182q.

Boys, S. F., & Bernardi, F. (1970). The calculation of small molecular interactions by the differences of separate total energies. Some procedures with reduced errors. *Molecular Physics, 19*, 553–566.

Burda, J. V., & Gu, J. (2008). A computational study on DNA bases interactions with dinuclear tetraacetato-diaqua-dirhodium(II, II) complex. *Journal of Inorganic Biochemistry, 102*, 53–62.

Burda, J. V., & Leszczynski, J. (2003). How strong can the bend be on a DNA helix from cisplatin? DFT and MP2 quantum chemical calculations of cisplatin-bridged DNA purine bases. *Inorganic Chemistry, 42*(22), 7162–7172.

Burda, J. V., Šponer, J., & Hobza, P. (1996). Ab Initio study of the interaction of guanine and adenine with various mono- and bivalent metal cations (Li^+, Na^+, K^+, Rb^+, Cs^+; Cu^+, Ag^+, Au^+; Mg^{2+}, Ca^{2+}, Sr^{2+}, Ba^{2+}; Zn^{2+}, Cd^{2+}, and Hg^{2+}). *Journal of Physical Chemistry, 100*(17), 7250–7255.

Burda, J. V., Šponer, J., Leszczynski, J., & Hobza, P. (1997). Interaction of DNA base pairs with various metal cations (Mg^{2+}, Ca^{2+}, Sr^{2+}, Ba^{2+}, Cu^+, Ag^+, Au^+, Zn^{2+}, Cd^{2+}, and Hg^{2+}): Nonempirical ab initio calculations on structures, energies, and nonadditivity of the interaction. *Journal of Physical Chemistry B, 101*(46), 9670–9677.

Burda, J. V., Šponer, J., & Leszczynski, J. (2000). The interactions of square platinum(II) complexes with guanine and adenine: A quantum-chemical ab initio study of metalated tautomeric forms. *Journal of Biological Inorganic Chemistry, 5*(2), 178–188.

Burda, J. V., Šponer, J., & Leszczynski, J. (2001). The influence of square planar platinum complexes on DNA base pairing. An ab initio DFT study. *Physical Chemistry Chemical Physics, 3*(19), 4404–4411.

Burda, J. V., Šponer, J., Hrabáková, J., Zeizinger, M., & Leszczynski, J. (2003). The influence of N-7 guanine modifications on the strength of Watson-Crick base pairing and guanine N-1 acidity: Comparison of gas-phase and condensed-phase trends. *Journal of Physical Chemistry B, 107*(22), 5349–5356.

Burda, J. V., Pavelka, M., & Simanek, M. (2004). Theoretical model of copper Cu(I)/Cu(II) hydration. DFT and ab initio quantum chemical study. *Journal of Molecular Structure (THEOCHEM), 683*(1–3), 183–193. doi:10.1016/j.theochem.2004.06.013.

Burda, J. V., Shukla, M. K., & Leszczynski, J. (2005). Theoretical model of the aqua-copper [Cu(H2O)5] + cation interactions with guanine. *Journal of Molecular Modeling, 11*, 362–369.

Burda, J. V., Murray, J. S., Gutierrez-Oliva, S., Politzer, P., & Toro-Labbe, A. (2015). *Journal of Chemical Theory and Computation*. Submitted.

Ceron-Carrasco, J. P., & Jacquemin, D. (2011). Influence of Mg2+ on the guanine-cytosine tautomeric equilibrium: Simulations of the induced intermolecular proton transfer. *Chemphyschem, 12*(14), 2615–2623. doi:10.1002/cphc.201100264.

Ceron-Carrasco, J. P., Jacquemin, D., & Cauet, E. (2012a). Cisplatin cytotoxicity: A theoretical study of induced mutations. *Physical Chemistry Chemical Physics, 14*(36), 12457–12464. doi:10.1039/C2CP40515F.

Ceron-Carrasco, J. P., Requena, A., & Jacquemin, D. (2012b). Impact of DFT functionals on the predicted magnesium-DNA interaction: An ONIOM study. *Theoretical Chemistry Accounts*, *131*(3). doi:10.1007/s00214-012-1188-9.

Chu, V. B., Bai, Y., Lipfert, J., Herschlag, D., & Doniach, S. (2008). A repulsive field: Advances in the electrostatics of the ion atmosphere. *Current Opinion in Chemical Biology, 12*, 619–625.

Chval, Z., & Sip, M. (2003). Transition states of cisplatin binding to guanine and adenine: Ab initio reactivity study. *Collection of Czechoslovak Chemical Communications, 68*, 1105–1118.

Chval, Z., Kabelac, M., & Burda, J. V. (2013). Mechanism of the cis- Pt(1R,2R-DACH)(H2O)(2)(2+) intrastrand binding to the double-stranded (pGpG)center dot(CpC) dinucleotide in aqueous solution: A computational DFT study. *Inorganic Chemistry, 52*(10), 5801–5813. doi:10.1021/ic302654s.

Colominas, C., Luque, F. J., & Orozco, M. (1996). Tautomerism and protonation of guanine and cytosine. Implications in the formation of hydrogen-bonded complexes. *Journal of the American Chemical Society, 118*(29), 6811–6821.

Cornell, W. D., Cieplak, P., Bayly, C. I., Gould, I. R., Merz, J., Kenneth, M., Ferguson, D. M., Spellmeyer, D. C., Fox, T., James Caldwell, J. W., & Kollman, P. A. (1995). A second generation force field for the simulation of proteins, nucleic acids, and organic molecules. *Journal of the American Chemical Society, 117*, 5179–5197.

Deeth, R. J. (2001). The ligand field molecular mechanics model and the stereoelectronic effects of d and s electrons. *Coordination Chemistry Reviews, 212*(1), 11–34. doi:10.1016/S0010-8545(00)00354-4.

Deeth, R. J., Anastasi, A., Diedrich, C., & Randell, K. (2009). Molecular modelling for transition metal complexes: Dealing with d-electron effects. *Coordination Chemistry Reviews, 253*(5–6), 795–816. doi:10.1016/j.ccr.2008.06.018.

Del Bene, J. E. (1984). Moleculat orbital study of the Li+ complexes of the DNA bases. *Journal of Physical Chemistry, 88*, 5927–5931.

Del Bene, J. E. (1985). Molecular orbital theory of the hydrogen bond. *Journal of Molecular Structure, 124*, 201–212.

Deubel, D. V. (2003). Reactivity of osmium tetraoxide towards nitrogen heterocycles: Implications for the molecular recognition of DNA mismatch. *Angewandte Chemie, International Edition, 42*(17), 1974–1977. doi:10.1002/anie.200250462.

Draper, D. E., Grilley, D., & Soto, A. M. (2005). Ions and RNA folding. *Annual Review of Biophysics and Biomolecular Structure, 34*, 221–243.

Egli, M., & Gessner, R. V. (1995). Stereoelectronic effects of deoxyribose O4′ on DNA conformation. *Proceedings of the National Academy of Sciences of the United States of America, 92*, 180–184.

Egli, M., Williams, L. D., Fredericks, C. A., & Rich, A. (1991). DNA-nogalamycin interactions. *Biochemistry, 30*, 1364.

Elmahdaoui, L., & Tajmirriahi, H. (1995). A comparative-study of Atp and Gtp complexation with trivalent Al, Ga and Fe cations – Determination of cation-binding site and nucleotide conformation by ftir difference spectroscopy. *Journal of Biomolecular Structure & Dynamics, 13*(1), 69–86.

Fortino, M., Marino, T., & Russo, N. (2015). Theoretical study of silver-ion-mediated base pairs: The case of C–Ag–C and C–Ag–A systems. *The Journal of Physical Chemistry. A, 119*(21), 5153–5157. doi:10.1021/jp5096739.

Frank Eckert, A. K. (2006). Accurate prediction of basicity in aqueous solution with COSMO-RS. *Journal of Computational Chemistry, 27*(1), 11–19.

Fuentes-Cabrera, M., Sumpter, B. G., & Šponer, J. E. (2007). Theoretical study on the structure, stability, and electronic properties of the guanine–Zn–cytosine base pair in M-DNA. *Journal of Physical Chemistry B, 111*, 870–875.

Futera, Z., & Burda, J. V. (2014). Reaction mechanism of Ru(II) piano-stool complexes: Umbrella sampling QM/MM MD study. *Journal of Computational Chemistry, 35*, 1446–1456.

Futera, Z., Klenko, J., Šponer, J. E., Šponer, J., & Burda, J. V. (2009a). Interactions of the "Piano-stool" [Ruthenium(II)(g6-arene)(en)Cl]1 complexes with water and nucleobases; ab initio and DFT study. *Journal of Computational Chemistry, 30*, 1758–1770.

Futera, Z., Klenko, J., Šponer, J. E., Šponer, J., & Burda, J. V. (2009b). Interactions of the "piano-stool" [ruthenium(II)(arene)(en)Cl] complexes with water and nucleobases; ab initio and DFT study. *Journal of Computational Chemistry, 30*, 1758.

Futera, Z., Klenko, J., Šponer, J. E., Šponer, J., & Burda, J. V. (2009c). Interactions of the "Piano-stool" ruthenium(II)(eta(6)-arene)(en)Cl (+) complexes with water and nucleobases; A initio and DFT study. *Journal of Computational Chemistry, 30*(12), 1758–1770. doi:10.1002/jcc.21179.

Futera, Z., Platts, J. A., & Burda, J. V. (2012). Binding of piano-stool Ru(II) complexes to DNA; QM/MM study. *Journal of Computational Chemistry, 33*, 2092–2101.

Gkionis, K., Mutter, S. T., & Platts, J. A. (2013). QM/MM description of platinum-DNA interactions: Comparison of binding and DNA distortion of five drugs. *RSC Advances, 3*(12), 4066–4073. doi:10.1039/C3RA23041D.

Gkionis, K., Kruse, H., Platts, J. A., Mládek, A., Koča, J., & Šponer, J. (2014). Ion binding to quadruplex DNA stems. Comparison of MM and QM descriptions reveals sizable polarization effects not included in contemporary simulations. *Journal of Chemical Theory and Computation, 10*(3), 1326–1340. doi:10.1021/ct4009969.

Gresh, N., Šponer, J. E., Špačková, N., Leszczynski, J., & Šponer, J. (2003). Theoretical study of binding of hydrated cations Zn(II) and Mg(II) to guanosine 5′ monophosphate. Towards polarizable molecular mechanics for DNA and RNA. *The Journal of Physical Chemistry B, 107*, 8669–8681.

Gu, J. D., & Leszczynski, J. (2000). A remarkable alteration in the bonding pattern: An HF and DFT study of the interactions between the metal cations and the Hoogsteen hydrogen-bonded G-tetrad. *Journal of Physical Chemistry A, 104*(26), 6308–6313.

Hud, N. V., Smith, F. W., Anet, F. A. L., & Feigon, J. (1996). The selectivity for K+ versus Na + in DNA quadruplexes is dominated by relative free energies of hydration: A thermodynamic analysis by 1H NMR. *Biochemistry, 35*(48), 15383–15390.

Hud, N. V., Schultze, P., & Feigon, J. (1998). Ammonium ion as an NMR probe for monovalent cation coordination sites of DNA quadruplexes. *Journal of the American Chemical Society, 120*, 6403–6408.

Ida, R., & Wu, G. (2008). Direct NMR detection of alkali metal ions bound to G-quadruplex DNA. *Journal of the American Chemical Society, 130*, 3590–3594.

Kabeláč, M., & Hobza, P. (2006). Na^+, Mg^{2+}, and Zn^{2+} binding to all tautomers of adenine, cytosine, and thymine and the eight most stable keto/enol tautomers of guanine: A correlated ab initio quantum chemical study. *Journal of Physical Chemistry B, 110*, 14515–14523.

Klamt, A., & Schuurmann, G. (1993). Cosmo – A new approach to dielectric screening in solvents with explicit expressions for the screening energy and its gradient. *Journal of the Chemical Society, Perkin Transactions, 2*(5), 799–805.

Korth, M., Pitoňák, M., Řezáč, J., & Hobza, P. (2010). A transferable H-bonding correction for semiempirical quantum-chemical methods. *Journal of Chemical Theory and Computation, 6*(1), 344–352. doi:10.1021/ct900541n.

Kosenkov, D., Gorb, L., Shishkin, O. V., Šponer, J., & Leszczynski, J. (2008). Tautomeric equilibrium, stability, and hydrogen bonding in 2'-deoxyguanosine monophosphate complexed with Mg^{2+}. *Journal of Physical Chemistry B, 112*, 150–158.

Kratochvílová, I., Golan, M., Vala, M., Špérová, M., Weiter, M., Páv, O., Šebera, J., Rosenberg, I., Sychrovský, V., Tanaka, Y., & Bickelhaupt, F. M. (2014). Theoretical and experimental study

of charge transfer through DNA: Impact of mercury mediated T-Hg-T base pair. *The Journal of Physical Chemistry B, 118*(20), 5374–5381. doi:10.1021/jp501986a.

Lilley, D. M. J., & Eckstein, F. (2008). *Ribozymes and RNA catalysis*. Cambridge: Royal Society of Chemistry.

Lipinski, J. (1989). Electronic structure of platinum(ii) antitumor complexes and their interactions with nucleic acid bases. Part ii. *Journal of Molecular Structure (THEOCHEM), 201*, 295–305.

Marenich, A. V., Cramer, C. J., & Truhlar, D. G. (2009). Universal solvation model based on solute electron density and a continuum model of the solvent defined by the bulk dielectric constant and atomic surface tensions. *Journal of Physical Chemistry B, 113*, 6378–6396.

Margiotta, N., Petruzzella, E., Platts, J. A., Mutter, S. T., Deeth, R. J., Ranaldo, R., Papadia, P., Marzilli, P. A., Marzilli, L. G., Hoeschele, J. D., & Natile, G. (2015). DNA fragment conformations in adducts with Kiteplatin. *Dalton Transactions, 44*(8), 3544–3556. doi:10.1039/C4DT01796J.

Marino, T. (2014). DFT investigation of the mismatched base pairs (T-Hg-T)3, (U-Hg-U)3, d(T-Hg-T)2, and d(U-Hg-U)2. *Journal of Molecular Modeling, 20*(6), 1–5. doi:10.1007/s00894-014-2303-8.

Marino, T., Toscano, M., Russo, N., & Grand, A. (2004). Gas-phase interaction between DNA and RNA bases and copper(II) ion: A density functional study. *International Journal of Quantum Chemistry, 98*(4), 347–354.

Marino, T., Mazzuca, D., Toscano, M., Russo, N., & Grand, A. (2007). Gas phase interaction of zinc ion with purine and pyrimidine DNA and RNA bases. *International Journal of Quantum Chemistry, 107*, 311–320.

Marino, T., Mazzuca, D., Russo, N., Toscano, M., & Grand, A. (2010). On the interaction of rubidium and cesium mono-, strontium and barium bi-cations with DNA and RNA bases. A theoretical study. *International Journal of Quantum Chemistry, 110*(1), 138–147. doi:10.1002/qua.22076.

Marino, T., Russo, N., Toscano, M., & Pavelka, M. (2012). Theoretical investigation on DNA/RNA base pairs mediated by copper, silver, and gold cations. *Dalton Transactions, 41*(6), 1816–1823. doi:10.1039/C1DT11028D.

Martínez, J. M., Pappalardo, R. R., & Marcos, E. S. (1997). Study of the Ag^{+} hydration by means of a semicontinuum quantum-chemical solvation model. *Journal of Physical Chemistry A, 101*, 4444–4448.

Matsubara, T., & Hirao, K. (2002). Density functional study of the binding of the cyclen-coordinated M(II) (M = Zn, Cu, Ni) complexes to the DNA base. Why is Zn better to bind? *Journal of Molecular Structure (THEOCHEM), 581*, 203–213.

Megger, D. A., Fonseca Guerra, C., Bickelhaupt, F. M., & Müller, J. (2011a). Silver(I)-mediated Hoogsteen-type base pairs. *Journal of Inorganic Biochemistry, 105*(11), 1398–1404. doi:10.1016/j.jinorgbio.2011.07.005.

Megger, D. A., Fonseca Guerra, C., Hoffmann, J., Brutschy, B., Bickelhaupt, F. M., & Müller, J. (2011b). Contiguous metal-mediated base pairs comprising two AgI ions. *Chemistry - A European Journal, 17*(23), 6533–6544. doi:10.1002/chem.201002944.

Mennucci, B., Cammi, R., & Tomasi, J. (1998). Excited states and solvatochromic shifts within a nonequilibrium solvation approach: A new formulation of the integral equation formalism method at the self-consistent field, configuration interaction, and multiconfiguration self-consistent field level. *Journal of Chemical Physics, 109*(7), 2798–2807.

Meyer, M., & Sühnel, J. (2008). Density functional study of adenine tetrads with N6 − H6 ⋯ N3 hydrogen bonds. *The Journal of Physical Chemistry. A, 112*(18), 4336–4341. doi:10.1021/jp710242k.

Meyer, M., Steinke, T., Brandl, M., & Suhnel, J. (2001). Density functional study of guanine and uracil quartets and of guanine quartet/metal ion complexes. *Journal of Computational Chemistry, 22*(1), 109–124.

Meyer, M., Hocquet, A., & Sühnel, J. (2005). Interaction of sodium and potassium ions with sandwiched cytosine-, guanine-, thymine-, and uracil-base tetrads. *Journal of Computational Chemistry, 26*(4), 352–364. doi:10.1002/jcc.20176.

Meyer, M., Steinke, T., & Sühnel, J. (2007). Density functional study of isoguanine tetrad and pentad sandwich complexes with alkali metal ions. *Journal of Molecular Modeling, 13*(2), 335–345. doi:10.1007/s00894-006-0148-5.

Miertus, S., Scrocco, E., & Tomasi, J. (1981). Electrostatic interaction of a solute with a continuum. A direct utilizaion of AB initio molecular potentials for the prevision of solvent effects. *Chemical Physics, 55*(1), 117–129.

Mlynsky, V., Walter, N. G., Šponer, J., Otyepka, M., & Banas, P. (2015). The role of an active site Mg2+ in HDV ribozyme self-cleavage: Insights from QM/MM calculations. *Physical Chemistry Chemical Physics, 17*(1), 670–679. doi:10.1039/C4CP03857F.

Morari, C., Bogdan, D., & Muntean, C. M. (2012). Binding effects of Mn2+ and Zn2+ ions on the vibrational properties of guanine-cytosine base pairs in the Watson-Crick and Hoogsteen configurations. *Journal of Molecular Modeling, 18*(11), 4781–4786. doi:10.1007/s00894-012-1480-6.

Morari, C., Muntean, C. M., Tripon, C., Buimaga-Iarinca, L., & Calborean, A. (2014). DFT investigation of the vibrational properties of GC Watson-Crick and Hoogsteen base pairs in the presence of Mg2+, Ca2+, and Cu2+ ions. *Journal of Molecular Modeling*, *20*(4). doi:10.1007/s00894-014-2220-x.

Mukhopadhyay, A., Aguilar, B. H., Tolokh, I. S., & Onufriev, A. V. (2014). Introducing charge hydration asymmetry into the generalized born model. *Journal of Chemical Theory and Computation, 10*, 1788–1794.

Mutter, S., Margiotta, N., Papadia, P., & Platts, J. (2015). Computational evidence for structural consequences of kiteplatin damage on DNA. *JBIC, Journal of Biological Inorganic Chemistry, 20*(1), 35–48. doi:10.1007/s00775-014-1207-5.

Noguera, M., Bertran, J., & Sodupe, M. (2004). A quantum chemical study of Cu2+ interacting with guanine-cytosine base pair. Electrostatic and oxidative effects on intermolecular proton-transfer processes. *Journal of Physical Chemistry A, 108*(2), 333–341. doi:10.1021/jp036573q.

Noguera, M., Branchadell, V., Constantino, E., Rios-Font, R., Sodupe, M., & Rodriguez-Santiago, L. (2007). On the bonding of first-row transition metal cations to guanine and adenine nucleobases. *Journal of Physical Chemistry A, 111*(39), 9823–9829. doi:10.1021/jp073858k.

Noguera, M., Bertran, J., & Sodupe, M. (2008). Cu2+/+ cation coordination to adenine-thymine base pair. Effects on intermolecular proton-transfer processes. *Journal of Physical Chemistry B, 112*(15), 4817–4825. doi:10.1021/jp711982g.

Oliva, R., & Cavallo, L. (2009). Frequency and effect of the binding of Mg2+, Mn2+, and Co2+ ions on the guanine base in Watson-Crick and reverse Watson-Crick base pairs. *Journal of Physical Chemistry B, 113*(47), 15670–15678. doi:10.1021/jp906847p.

Parr, R. G., & Pearson, R. G. (1983). Absolute hardness: Companion parameter to absolute electronegativity. *Journal of the American Chemical Society, 105*(26), 7512–7516.

Pavelka, M., & Burda, J. V. (2005). Theoretical description of copper Cu(I)/Cu(II) complexes in mixed ammine-aqua environment. DFT and ab initio quantum chemical study. *Chemical Physics, 312*, 193–204. doi:10.1016/j.chemphys.2004.11.034.

Pavelka, M., Šimánek, M., Šponer, J., & Burda, J. V. (2006). Copper cation interactions with biologically essential types of ligands: A computational DFT study. *Journal of Physical Chemistry A, 110*, 4795–4809.

Pavelka, M., Shukla, M. K., Leszczynski, J., & Burda, J. V. (2008). Theoretical study of hydrated copper(II) interactions with guanine: A computational density functional theory study. *Journal of Physical Chemistry A, 112*(2), 256–267. doi:10.1021/jp074891+.

Petrov, A. S., Lamm, G., & Pack, G. R. (2005). Calculation of the binding free energy for magnesium – RNA interactions. *Biopolymers, 77*(3), 137–154.

Poltev, V. I., Malenkov, G. G., Gonzales, E. J., Teplukhin, A. V., Rein, R., Shibata, M., & Miller, J. H. (1996). Modeling DNA hydration: Comparison of calculated and experimental hydration properties of nuclic acid bases. *Journal of Biomolecular Structure and Dynamics, 13*(4), 717–725.

Potaman, V. N., & Soyfer, V. N. (1994). Divalent metal cations upon coordination to the N7 of purines differentially stabilize the PyPuPu DNA triplex due to unequal Hoogsteen-type hydrogen bond enhancement. *Journal of Biomolecular Structure & Dynamics, 11*, 1035–1040.

Raber, J., Zhu, C., & Eriksson, L. A. (2005). Theoretical study of cisplatin binding to DNA: The importance of initial complex stabilisation. *Journal of Physical Chemistry, 109*, 11006–11015.

Reshetnikov, R. V., Šponer, J., Rassokhina, O. I., Kopylov, A. M., Tsvetkov, P. O., Makarov, A. A., & Golovin, A. V. (2011). Cation binding to 15-TBA quadruplex DNA is a multiple-pathway cation-dependent process. *Nucleic Acids Research, 39*(22), 9789–9802. doi:10.1093/nar/gkr639.

Řezáč, J., Fanfrlík, J., Salahub, D., & Hobza, P. (2009). Semiempirical quantum chemical PM6 method augmented by dispersion and H-bonding correction terms reliably describes carious types of noncovalent complexes. *Journal of Chemical Theory and Computation, 5*(7), 1749–1760. doi:10.1021/ct9000922.

Rosenberg, B., Van Camp, L., & Krigas, T. (1965). Inhibition of cell division in *Escherichia coli* by electrolysis products from a platinum electrode. *Nature, 205*(4972), 698–699.

Rosenberg, B., Van Camp, L., Trosko, J. L., & Mansour, V. H. (1969). Platinum drugs; a new class of potent antitumor agents. *Nature, 222*, 385–391.

Roux, B., Yu, H. A., & Karplus, M. (1990). Molecular basis for the born model of ion solvation. *Journal of Physical Chemistry, 94*, 4683–4688.

Rozsnyai, F., & Ladik, J. (1970). Calculation of effects of hydration and divalent metal ions on DNA base pairs. *Bulletin of the American Physical Society, 15*(3), 325.

Rulisek, L., & Šponer, J. (2003). Outer-shell and inner-shell coordination of phosphate group to hydrated metal ions (Mg2+, Cu,2 + Zn2+, Cd2+) in the presence and absence of nucleobase. The role of nonelectrostatic effects. *Journal of Physical Chemistry B, 107*(8), 1913–1923. doi:10.1021/jp027058f.

Russo, N., & Toscano, M., A. G. (2001). Lithium affinity for DNA and RNA nucleobases. The role of theoretical information in the elucidation of the mass spectrometry data. *Journal of Physical Chemistry B, 105*, 4735–4741.

Russo, N., Toscano, M., & Grand, A. (2003). Gas-phase absolute Ca2+ and Mg2+ affinity for nucleic acid bases. A theoretical determination. *Journal of Physical Chemistry A, 107*(51), 11533–11538. doi:10.1021/jp0358681.

Saenger, W. (1983). *Principles of nucleic acid structure*. New York: Springer.

Santangelo, M. G., Antoni, P. M., Spingler, B., & Jeschke, G. (2010). Can copper(II) mediate Hoogsteen base-pairing in a left-handed DNA duplex? A pulse EPR study. *ChemPhysChem, 11*, 599–606.

Schmidt, K. S., Reedijk, J., Weisz, K., Basilio Janke, E. M., Šponer, J. E., Šponer, J., & Lippert, B. (2002). Loss of Hoogsteen pairing ability upon N1 adenine platinum binding. *Inorganic Chemistry, 41*, 2855–2863.

Schreiber, M., & Gonzalez, L. (2007a). Structure and bonding of Ag(I)-DNA base complexes and Ag(I)-adenine-cytosine mispairs: An ab initio study. *Journal of Computational Chemistry, 28*, 2299–2308. doi:10.1002/jcc.20743.

Schreiber, M., & Gonzalez, L. (2007b). The role of Ag(I) ions in the electronic spectroscopy of adenine-cytosine mispairs A MS-CASPT2 theoretical study. *Journal of Photochemistry and Photobiology A: Chemistry, 190*(2–3), 301–309. doi:10.1016/j.jphotochem.2007.01.035.

Šebera, J., Burda, J. V., Straka, M., Ono, A., Kojima, C., Tanaka, Y., & Sychrovsky, V. (2013a). Formation of a thymine-Hg II -thymine metal-mediated DNA base pair: Proposal and theoretical calculation of the reaction pathway. *Chemistry - A European Journal, 19*, 9884–9894.

Šebera, J., Burda, J., Straka, M., Ono, A., Kojima, C., Tanaka, Y., & Sychrovský, V. (2013b). Formation of a thymine-HgII-thymine metal-mediated DNA base pair: Proposal and theoretical calculation of the reaction pathway. *Chemistry - A European Journal, 19*(30), 9884–9894. doi:10.1002/chem.201300460.

Šebesta, F., & Burda, J. V. (2016). Reduction process of tetraplatin in the presence of deoxyguanosine monophosphate (dGMP): A computational DFT study. *Chemistry - A European Journal, 22*, 1037–1047.

Setnicka, V., Novy, J., Bohm, S., Sreenivasachary, N., Urbanova, M., & Volka, K. (2008). Molecular structure of guanine-quartet supramolecular assemblies in a gel-state based on a DFT calculation of infrared and vibrational circular dichroism spectra. *Langmuir, 24*(14), 7520–7527. doi:10.1021/la800611h.

Sigel, H. (1993). Interactions of metal ions with nucleotides and nucleic acids and their constituents. *Chemical Society Reviews, 22*, 255–267.

Sigel, R. K. O., & Lippert, B. (1999). Pt^{II} coordination to guanine-N7: Enhancement of the stability of the Watson–Crick base pair with cytosine. *Chemical Communications,* 2167.

Šponer, J., & Špackova, N. (2007). Molecular dynamics simulations and their application to four-stranded DNA. *Methods, 43*, 278–284.

Šponer, J., Burda, J. V., Mejzlik, P., Leszczynski, J., & Hobza, P. (1997). Hydrogen-bonded trimers of DNA bases and their interaction with metal cations: Ab initio quantum-chemical and empirical potential study. *Journal of Biomolecular Structure & Dynamics, 14*(5), 613–628.

Šponer, J., Burda, J. V., Sabat, M., Leszczynski, J., & Hobza, P. (1998a). Interaction between the guanine-cytosine Watson-Crick DNA base pair and hydrated group IIa (Mg2+, Ca2+, Sr2+, Ba2+) and group IIb (Zn2+, Cd2+, Hg2+) metal cations. *Journal of Physical Chemistry A, 102*(29), 5951–5957.

Šponer, J., Sabat, M., Burda, J. V., Doody, A. M., Leszczynski, J., & Hobza, P. (1998b). Stabilization of the purine center dot purine center dot pyrimidine DNA base triplets by divalent metal cations. *Journal of Biomolecular Structure & Dynamics, 16*(1), 139–143.

Šponer, J., Sabat, M., Burda, J., Leszczynski, J., Hobza, P., & Lippert, B. (1999a). Metal ions in non-complementary DNA base pairs: An ab initio study of Cu(I), Ag(I), and Au(I) complexes with cytosine-adenine base pair. *Journal of Biological Inorganic Chemistry, 4*, 537–545.

Šponer, J., Burda, J. V., Leszczynski, J., & Hobza, P. (1999b). Interactions of hydrated IIa and IIb group metal cations with thioguanine-cytosine DNA base pair: Ab initio and density functional theory investigation of polarization effects, differences among cations, and flexibility of the cation hydration shell. *Journal of Biomolecular Structure & Dynamics, 17*(1), 61–77.

Šponer, J., Šponer, J. E., Gorb, L., Leszczynski, J., & Lippert, B. (1999c). Metal-stabilized rare tautomers and mispairs of DNA bases: N6-metalated adenine and N4-metalated cytosine, theoretical and experimental views. *Journal of Physical Chemistry A, 103*, 11406–11413.

Šponer, J., Sabat, M., Burda, J. V., Leszczynski, J., & Hobza, P. (1999d). Interaction of the adenine-thymine Watson-Crick and adenine-adenine reverse-Hoogsteen DNA base pairs with hydrated group IIa (Mg2+, Ca2+, Sr2+, Ba2+) and IIb (Zn2+, Cd2+, Hg2+) metal cations: Absence of the base pair stabilization by metal-induced polarization effects. *Journal of Physical Chemistry B, 103*(13), 2528–2534.

Šponer, J., Sabat, M., Burda, J. V., Leszczynski, J., Hobza, P., & Lippert, B. (1999e). Metal ions in non-complementary DNA base pairs: An ab initio study of Cu(I), Ag(I), and Au(I) complexes with the cytosine-adenine base pair. *Journal of Biological Inorganic Chemistry, 4*(5), 537–545.

Šponer, J., Šponer, J. E., & Leszczynski, J. (2000a). Cation – Pi and amino-acceptor interactions between hydrated metal cations and DNA bases. A quantum-chemical view. *Journal of Biomolecular Structure and Dynamics, 17*(6), 1087–1096.

Šponer, J., Sabat, M., Gorb, L., Leszczynski, J., Lippert, B., & Hobza, P. (2000b). The effect of metal binding to the N7 site of purine nucleotides on their structure, energy, and involvement in base pairing. *Journal of Physical Chemistry B, 104*(31), 7535–7544. doi:10.1021/jp001711m.

Šponer, J. E., Leszczynski, J., Glahe, F., Lippert, B., & Šponer, J. (2001). Protonation of platinated adenine nucleobases. Gas phase vs condensed phase picture. *Inorganic Chemistry, 40*, 3269–3278.

Šponer, J., Mládek, A., Špačková, N., Cang, X., Cheatham, T. E., & Grimme, S. (2013). Relative stability of different DNA guanine quadruplex stem topologies derived using large-scale quantum-chemical computations. *Journal of the American Chemical Society, 135*(26), 9785–9796. doi:10.1021/ja402525c.

Sychrovsky, V., Šponer, J., & Hobza, P. (2004). Theoretical calculation of the NMR spin-spin coupling constants and the NMR shifts allow distinguishability between the specific direct and the water-mediated binding of a divalent metal cation to guanine. *Journal of the American Chemical Society, 126*(2), 663–672.

Tanaka, Y., Kojima, C., Morita, E. H., Kasai, Y., Yamasaki, K., Ono, A., Kainosho, M., & Taira, K. (2002). Identification of the metal ion binding site on an RNA Motif from hammerhead ribozymes using ^{15}N NMR spectroscopy. *Journal of the American Chemical Society, 124*, 4595–4601.

van der Wijst, T., Guerra, C. F., Swart, M., Bickelhaupt, F. M., & Lippert, B. (2009). Rare tautomers of 1-methyluracil and 1-methylthymine: Tuning relative stabilities through coordination to Pt-II complexes. *Chemistry - A European Journal, 15*(1), 209–218. doi:10.1002/chem.200801476.

Varnali, T., & Tozumcalgan, D. (1995). Interaction of divalent metal-cations and nucleotides – A computational study. *Structural Chemistry, 6*(4–5), 343–348.

Wang, F. Y., Habtemariam, A., van der Geer, E. P. L., Fernandez, R., Melchart, M., Deeth, R. J., Aird, R., Guichard, S., Fabbiani, F. P. A., Lozano-Casal, P., Oswald, I. D. H., Jodrell, D. I., Parsons, S., & Sadler, P. J. (2005). Controlling ligand substitution reactions of organometallic complexes: Tuning cancer cell cytotoxicity. *PNAS, 102*(51), 18269–18274.

Wu, Y. B., Bhattacharyya, D., King, C. L., Baskerville-Abraham, I., Huh, S. H., Boysen, G., Swenberg, J. A., Temple, B., Campbell, S. L., & Chaney, S. G. (2007). Solution structures of a DNA dodecamer duplex with and without a cisplatin 1,2-d(GG) intrastrand cross-link: Comparison with the same DNA duplex containing an oxaliplatin 1,2-d(GG) intrastrand cross-link. *Biochemistry, 46*(22), 6477–6487.

Yamaguchi, H., Šebera, J., Kondo, J., Oda, S., Komuro, T., Kawamura, T., Daraku, T., Kondo, Y., Okamoto, I., Ono, A., Burda, J. V., Kojima, C., Sychrovský, V., & Tanaka, Y. (2014). The structure of metallo-DNA with consecutive T-HgII-T base-pairs ex-plains positive reaction entropy for the metallo-base-pair formation. *Nucleic Acids Research, 42*, 4094–4099.

Yurenko, Y. P., Novotny, J., Sklenar, V., & Marek, R. (2014). Exploring non-covalent interactions in guanine- and xanthine-based model DNA quadruplex structures: A comprehensive quantum chemical approach. *Physical Chemistry Chemical Physics, 16*(5), 2072–2084. doi:10.1039/C3CP53875C.

Zeizinger, M., Burda, J. V., & Leszczynski, J. (2004). The influence of a sugar-phosphate backbone on the cisplatin-bridged BpB models of DNA purine bases. Quantum chemical calculations of Pt(II) bonding characteristics. *Physical Chemistry Chemical Physics, 6*(10), 3585–3590.

Zhang, Y., & Huang, K. X. (2007). On the interactions of hydrated metal cations (Mg2+, Mn2+, Ni2+, Zn2+) with guanine-cytosine Watson-Crick and guanine-guanine reverse-Hoogsteen DNA base pairs. *Journal of Molecular Structure (THEOCHEM), 812*(1–3), 51–62. doi:10.1016/j.theochem.2007.02.009.

Zilberberg, I. L., Avdeev, V. I., & Zhidomirov, G. M. (1997). Effect of cisplatin binding on guanine in nucleic acid: An ab initio study. *Journal of Molecular Structure (THEOCHEM), 418*, 73.